

**INVESTIGATION OF STRUCTURAL, MAGNETIC AND  
ELECTROMAGNETIC PROPERTIES OF HEXAFERRITE COMPOSITES  
FOR MICROWAVE ABSORBER APPLICATION**

Thesis Submitted for the Award of the Degree of

**DOCTOR OF PHILOSOPHY**

in

**Physics**

By

**Manisha Thakur**

**Registration Number: 11916443**

**Supervised By**

**Dr. A. K. Srivastava (11459)**

Department of Physics (Professor)

School of Computer Science and Engineering

Lovely Professional University, Punjab, India

**Co-Supervised by**

**Dr. Charanjit Singh (21882)**

(Professor)

School of Electronics and Electrical Engineering

Lovely Professional University, Punjab, India



*Transforming Education Transforming India*

**LOVELY PROFESSIONAL UNIVERSITY, PUNJAB**

**2024**

## DECLARATION

I, hereby declared that the presented work in the thesis entitled “**Investigation of structural, magnetic, and electromagnetic properties of hexaferrite composites for microwave absorber application**” in fulfilment of degree of **Doctor of Philosophy (Ph. D.)** is outcome of research work carried out by me under the supervision of **Dr. Ajeet Kumar Srivastava**, working as **Professor**, in the **School of Computer science and Engineering** of Lovely Professional University, Punjab, India. In keeping with general practice of reporting scientific observations, due acknowledgements have been made whenever work described here has been based on findings of another investigator. This work has not been submitted in part or full to any other University or Institute for the award of any degree.

**(Signature of Scholar)**

Name of the scholar: **Manisha Thakur**

Registration No.: **11916443**

Department/school: **School of Chemical Engineering and Physical Sciences**

Lovely Professional University,

Punjab, India

## Certificate

This is to certify that the work reported in the Ph. D. thesis entitled **Investigation of structural, magnetic, and electromagnetic properties of hexaferrite composites for microwave absorber application**” submitted in fulfillment of the requirement for the award of degree of **Doctor of Philosophy (Ph.D.)** in the **School of Chemical Engineering and Physical Sciences**, is a research work carried out by **Manisha Thakur (11916443)**, is bonafide record of his/her original work carried out under my supervision and that no part of thesis has been submitted for any other degree, diploma or equivalent course.

Supervisor: **Dr. A.K. Srivastava (11459)**

Department of Physics (Professor)

School of Computer Science and Engineering

Lovely Professional University, Punjab, India

Co-Supervisor: **Dr. Charanjit Singh (21882)**

(Professor)

School of Electronics and Electrical Engineering

Lovely Professional University, Punjab, India

## Abstract

Nowadays, the proliferation of wireless communication technology and nano-electronic devices operating within the high-frequency range has led to a growing global problem of electromagnetic (EM) pollution. This excessive emission of EM waves has become a severe concern that adversely affects human health, national defense, and security. So, the quest of this issue prompts the researchers to synthesize an efficient and reliable EM suppressor i.e., microwave absorber, capable of attenuating or absorbing the intensity of unwanted radiation. An efficient microwave absorber requires better impedance matching, regulation of electromagnetic properties, low cost, broad absorption bandwidth, and the development of large dielectric/magnetic loss mechanisms. Therefore, our study is based on M-type hexaferrite, a magnetic material with appreciable saturation magnetization, and it is not possible for pure M-type hexaferrite to fulfill the above-mentioned characteristics of a microwave absorber. So, we need to focus on substituted M-type hexaferrite and their composites with spinel ferrites, a material with low coercivity, low cost, and polyaniline having a high dielectric constant. In this study, we synthesized divalent substituted M-type hexaferrite [ $\text{SrCo}_x\text{Zn}_x\text{Fe}_{(12-2x)}\text{O}_{19}$  ( $0.4 \leq x \leq 2.0$ ) and  $\text{SrCo}_{1.5z}\text{Cd}_{0.5z}\text{Fe}_{12-2z}\text{O}_{19}$  ( $0.2 \leq z \leq 1.0$ )] and trivalent substituted M-type hexaferrite [ $\text{SrCo}_{1.5z}\text{La}_{0.5z}\text{Fe}_{12-2z}\text{O}_{19}$  ( $0.0 \leq z \leq 0.5$ ) and  $\text{Sr}(\text{CoCr})_x\text{Fe}_{(12-2x)}\text{O}_{19}$  ( $0.0 \leq x \leq 1.0$ )] using sol-gel auto-combustion methodology. Composites of divalent/trivalent substituted hexaferrite [ $\text{SrCo}_{1.5z}\text{La}_{0.5z}\text{Fe}_{12-2z}\text{O}_{19}$  (80%) +  $\text{Fe}_3\text{O}_4$  (20%) ( $0.0 \leq z \leq 0.5$ ),  $\text{SrCo}_x\text{Zn}_x\text{Fe}_{(12-2x)}\text{O}_{19}$  (80%) + PANI (20%) ( $0.4 \leq x \leq 2.0$ ),  $\text{Sr}(\text{CoCr})_x\text{Fe}_{(12-2x)}\text{O}_{19}$  (80%) +  $\text{CoFe}_2\text{O}_4$  (20%) ( $0.0 \leq x \leq 1.0$ ) and  $\text{SrCo}_{1.5z}\text{Cd}_{0.5z}\text{Fe}_{12-2z}\text{O}_{19}$  (80%) + PANI (20%) ( $0.2 \leq z \leq 1.0$ )].

The synthesized samples were characterized to investigate the structural, morphological, dielectric, electrical, hysteresis, and microwave absorption properties. To investigate the mentioned properties, various techniques were employed such as X-ray Diffraction (XRD), Field Emission Scanning Electron Microscopy (FESEM), Fourier Transform Infrared Spectroscopy (FTIR), Energy Dispersive X-ray Analysis (EDX), Impedance Analyzer, Vibrating Sample Magnetometer (VSM), Mössbauer analysis, and Vector-Network Analyzer (VNA).

M-type hexaferrite substituted with cobalt and lanthanum with composition  $\text{SrCo}_{1.5z}\text{La}_{0.5z}\text{Fe}_{12-2z}\text{O}_{19}$  ( $0.0 \leq z \leq 0.5$ ) were synthesized by auto-combustion Sol-gel



methodology. XRD study indicates that prepared specimens exhibit a hexagonal magnetoplumbite phase without any secondary peak. FTIR spectra revealed the existence of an absorption band in the IR range of  $600\text{-}380\text{ cm}^{-1}$ , which was predicted to be due to Fe-O vibrations. The micrographs showed an enhancement in the inter-grain connectivity of grains with substitution. Both dielectric constant/loss tangent parameters were found to be decreased non-linearly with substitution in the low-frequency region. Analysis of Mössbauer depicts that the substituents tend to occupy spin-up 12k-2a sites of crystal lattice from  $z = 0.0$  to  $z = 0.3$ , which may elucidate the decrease observed in magnetization. The coercivity gradually decreases from  $z = 0.0$  (5026.54 Oe) to  $z = 0.5$  (862.47 Oe). The saturation magnetization initially decreases with substitution from  $z = 0.0$  to 0.3 and then increases for  $z = 0.4$  and 0.5 samples. Composition  $z = 0.2$  displayed the optimal values for  $Z_{\text{real}}$  (0.997) and  $Z_{\text{img}}$  (0.010), resulting in the highest REL (-45.61 dB) at 8.98 GHz with 8.1 mm thickness and a wide absorption bandwidth of 0.86 GHz.

The M-type hexaferrite with composition  $\text{Sr}(\text{CoCr})_x\text{Fe}_{(12-2x)}\text{O}_{19}$  ( $0.0 \leq x \leq 1.0$ ) were synthesized using auto-combustion sol-gel methodology. XRD confirms the presence of magnetoplumbite structure without the occurrence of any secondary phases. The substitution of Cr-Co ions in a crystal lattice resulted in a meager decrease in lattice constant value ' $a$ ' and a considerable decrease in lattice constant value ' $c$ '. Two prominent absorption peaks were observed in FTIR analysis in the range of  $400\text{-}600\text{ cm}^{-1}$ . The loss tangent and dielectric constant of the Cr-Co substituted SrM hexaferrite were found to be increased with substitution. The conductivity relaxation is significantly improved with Cr-Co substitution. VSM analysis showed that  $H_c$  and  $M_r$  non-linearly decreased in substituted samples. According to VNA results, the REL of the Co-Cr substituted strontium hexaferrite with 8.4 mm thickness was -36.7 dB at 9.23 GHz with an effective absorption bandwidth of 0.79 GHz.

$\text{SrCo}_x\text{Zn}_x\text{Fe}_{12-2x}\text{O}_{19}$  (Co, Zn;  $x = 0.4, 0.8, 1.2, 1.6$  and 2.0) powders were synthesized by the auto-combustion sol-gel method. Substitution of Co-Zn ions caused the formation of magnetoplumbite and a secondary phase ( $\text{CoFe}_2\text{O}_4$ ) in the structure. Increasing the Co-Zn content ratio led to a non-linear increment in crystallite size ranging from 41.9 to 49.8 nm. SEM micrographs depicted platelet-shaped hexagonal particles that were nano-scale in thickness and micro-scale in diameter.  $\text{SrCo}_{0.8}\text{Zn}_{0.8}\text{Fe}_{10.4}\text{O}_{19}$  sample shows the minimum value of AC conductivity  $3.95 \times 10^{-5}\text{ }\Omega^{-1}\text{m}^{-1}$  in the high-frequency region. The Cole-Cole plots

( $M''$  versus  $M'$ ) reveal the existence of a single semicircular arc in the  $x = 0.0$  sample, caused by the grain boundary contribution. The values of  $M_s$  and  $M_r$  in substituted samples were higher than the initial  $M_s = 75.26$  emu/g and  $M_r = 26.95$  emu/g at  $x = 0.0$ . The highest coercivity and saturation magnetization was observed as, 4159 Oe and 80 emu/g, respectively, for  $x = 2.0$ . The squareness ratio ( $M_r/M_s$ ) of  $x = 1.6$  and  $x = 2.0$  samples, was observed to be greater than 0.5, elucidating the existence of single-domain particles. VNA results revealed maximum REL of the Co-Zn substituted strontium hexaferrite with 3.3 mm thickness was -47.26 dB at 18 GHz with an effective absorption bandwidth of (REL > -10 dB) 3.3 GHz.

A sol-gel combustion technique has been adopted to synthesize Co-Cd substituted SrM hexaferrite. The XRD of incorporated samples showed the magnetoplumbite structure, accompanied by some secondary phases of  $\text{CoFe}_2\text{O}_4$ . The crystallized size evaluated from the Debye-Scherrer formulation lies in the range of 40.75 to 46.46 nm. The morphological studies of the  $z = 0.6, 0.8,$  and  $1.0$  revealed the densification of grains which enhances the inter-particle contact. The energy dispersive spectra exhibited peaks of cadmium, cobalt, strontium, oxygen, and ferrite signifying the formation of Co-Cd substituted SrM hexaferrite. In the low-frequency region, both dielectric constant/loss tangent non-monotonically increased with Co-Cd substitution. Sample  $z = 1.0$  shows the maximum value of AC conductivity  $4.2 \times 10^{-3} \Omega^{-1}\text{m}^{-1}$  in the high-frequency region. A large value of coercivity 4273.50 Oe, 3612.63 Oe, and 4551.28 Oe was observed for  $z = 0.4, 0.6,$  and  $1.0$  samples, respectively with a squareness ratio greater than 0.5, indicating the existence of single-domain particles. The maximum REL values obtained for C1, C2, C3, C4, and C5 are -41.4, -54, -27.1, -29.3, and -31.6 dB at 10.11, 8.62, 16.37, 10.47, and 9.19 GHz, respectively.

Lanthanum (La) and Cobalt (Co) doped hard Strontium ferrite ( $\text{SrFe}_{12}\text{O}_{19}$ ): soft magnetite ( $\text{Fe}_3\text{O}_4$ ) composites in (1:5 ratio by weight) with different levels of substitution from  $z = 0.0$  to  $0.5$  were successfully synthesized. The XRD analysis of all composites revealed the simultaneous existence of hard (M-type) and soft (spinel) ferrite phases without any impurity peak and  $z = 0.0$  (20%  $\text{Fe}_3\text{O}_4$  of  $\text{SrFe}_{12}\text{O}_{19}$ ) exhibited minor traces of  $\alpha\text{-Fe}_2\text{O}_3$ . FESEM micrographs displayed well-distinguished particles of M-type and spinel ferrite in  $z = 0.0$ , and it was difficult to identify them in further substitution. The maximum conductivity relaxation obtained for  $z = 0.3$ , explained through the dense/closely packed grains, agreed with FESEM micrographs. A  $\text{Fe}^{3+}$  ions replacement with Co-La ions causes a reduction in

conductivity value and is maximum for  $z = 0.4$  ( $3.26 \times 10^{-5} \Omega^{-1}m^{-1}$ ) in the high-frequency region. Both saturation magnetization and remanent magnetization increased from  $z = 0.0$  to  $z = 0.1$ , while further substitution to  $z = 0.5$  caused a gradual decrease in both parameters. The VSM measurement exhibited an increment in  $H_c$  from  $z = 0.0$  (607.79 Oe) to  $z = 0.2$  (3084.73 Oe), and it decreases to  $z = 0.5$  (1589.40 Oe) with further substitution of Co-La ions. Switching field distribution plots ( $dM/dH$  against  $H$ ) indicated the strong exchange-coupling effect between hard/soft phases for  $z = 0.0$ , and insertion of Co-La ions causes abatement in this coupling. When  $z = 0.0$  ( $SrFe_{12}O_{19}/Fe_3O_4$ ), a maximum REL of -32.96 dB (8.9 mm) at 8.326 GHz and an absorption bandwidth of 0.60 GHz for REL > -10 dB are attained.

$SrCo_xZn_xFe_{12-2x}O_{19}/PANI$  composites in 1:5 ratio by wt% with different levels of substitution from  $x = 0.0$  to 2.0 were individually synthesized by sol-gel auto combustion and in-situ polymerization technique, respectively. XRD affirmed the existence of a hexagonal phase and PANI phase with minor traces of  $\alpha-Fe_2O_4$  in  $x = 0.0$ . The morphology of composites revealed disk flower-like and hexagonal platelet-type structures of PANI and hexagonal ferrite, respectively. Substitution of Co-Zn causes a non-linear increase in dielectric constant and loss tangent. The minimum conductivity relaxation obtained for  $x = 0.0$ , is explained through the FESEM micrographs. The replacement of Fe ions with Co-Zn ions causes non-linear variation in conductivity and is maximum for  $x = 0.8$  ( $1.33 \times 10^{-2} \Omega^{-1}m^{-1}$ ) in high-frequency regions. The two semi-circular arcs in  $x = 0.8$  and a single semi-circular arc in  $x = 0.0, 0.4, 1.6,$  and  $2.0$  composites in  $Z''$  vs.  $Z'$  Cole-Cole plots. The highest coercivity and saturation magnetization were observed as, 2293 Oe and 53.3 emu/g, respectively, for  $x = 0.4$ . Substitution of Co-Zn ions resulted in a non-linear increment in dielectric and magnetic loss.

$Sr(CoCr)_xFe_{(12-2x)}O_{19}/CoFe_2O_4$  ferrite was individually fabricated via sol-gel auto-combustion methodology and composites were prepared through physical blending method. Both the peaks of M-type hexaferrite and spinel ferrite had been observed in XRD patterns. FESEM revealed a platelet-shaped hexaferrite was encapsulated with spherical-shaped spinel ferrite. Both the electric modulus and impedance spectra exhibit non-Debye behavior in all composites. The saturation magnetization and coercivity decreased with substitution from  $x = 0.0$  to 1.0. Substitution increased reflection loss from -10 dB ( $x = 0.0$ ) to -29.9 dB ( $x = 1.0$ ).

$\text{SrCo}_z\text{Cd}_{0.5z}\text{Fe}_{12-2z}\text{O}_{19}/\text{PANI}$  composites were prepared in a 1:5 ratio by wt%. X-ray diffraction patterns displayed all reflection planes of M-type hexaferrite and a broad peak of PANI. The morphology of composites explored platelet-shaped M-type hexaferrite and disk flower-shaped PANI particles. Impedance parameters showed a shift in relaxation contribution from grain boundary to grains with substitution. Coercivity and saturation magnetization parameters derived from M-H loops gradually decrease (2620 to 745 Oe) and non-linearly increase (11 to 54 emu/g), respectively with Co-Cd substitution. Substitution of Co-Cd ions resulted in a non-linear increment in dielectric and magnetic loss.

## **Acknowledgment**

I humbly acknowledge the divine presence and guidance of GOD throughout my academic journey and the completion of this thesis. It is with deep gratitude that I recognize the role of GOD in providing me the strength, and wisdom to overcome challenges and successfully reach this milestone.

First and foremost, I am deeply grateful to my supervisor **Dr. A.K. Srivastava** (Professor), and my Co-supervisor **Dr. Charanjit Singh** (Professor) for their unwavering guidance, expertise, and patience throughout the research process. Their mentorship played a pivotal role in shaping this work. I would also like to extend my gratitude to my friends Hamnesh Mahajan and Simrandeep Kour for their companionship, which has been a source of inspiration.

I am thankful to all the faculty members of the Physics Department, Central Instrumentation Facility (CIF) for their help and support during this period. I would also like to thank Dr. R.B Jotania (Department of Physics, Gujarat University, Ahmedabad, India), Dr. Sachin Kumar Godara (Department of Chemistry, Guru Nanak Dev University, Amritsar, India) and Dr. K.C. James Raju (School of Physics, University of Hyderabad, Telangana, India), for providing various support in characterization. My special thanks to non-technical/non-teaching staff, especially Nitin Kumar Yadav and Ramesh Kumar from the physics department and Manoj Kumar from the chemistry department for their co-operation.

Finally, a special appreciation to my lovely mother (Suman), my husband (Vishal Singh), my dear son (Divyam), and all the family members for their continuous support, prayers, and encouragement throughout my research journey. With a heart filled with faith and humility, I offer this work as an expression of devotion and gratitude to God. May GOD continue to guide and bless me on this academic path and in all my future endeavours.

**Manisha Thakur**

Registration No: 11916443

Date:

# TABLE OF CONTENTS

## CHAPTER-1

<b>Introduction.....</b>	<b>1</b>
<b>1.1 Electromagnetic Interference Phenomena.....</b>	<b>2</b>
<b>1.2 Microwave absorbers.....</b>	<b>5</b>
<b>1.3 Types of Microwave Absorbers .....</b>	<b>6</b>
<b>1.4 Ferrites .....</b>	<b>7</b>
<b>1.5 History of ferrites .....</b>	<b>7</b>
<b>1.6 Application of ferrites .....</b>	<b>8</b>
<b>1.7 Classification of Ferrites .....</b>	<b>10</b>
<b>1.8 M-type hexagonal ferrites.....</b>	<b>12</b>
<b>1.9 Crystal structure of M-type hexagonal ferrites.....</b>	<b>13</b>
<b>1.10 Synthesis of M-type hexaferrite .....</b>	<b>14</b>
<b>1.11 Polyaniline.....</b>	<b>15</b>

## CHAPTER-2

<b>Review of literature, Research Gap, and Objectives.....</b>	<b>18</b>
<b>2.1 Review of literature.....</b>	<b>18</b>
<b>2.2 Research Gaps.....</b>	<b>32</b>
<b>2.3 Objective of this study .....</b>	<b>33</b>

## CHAPTER-3

<b>Research Methodology and Characterization.....</b>	<b>34</b>
<b>3.1 Method of Synthesis .....</b>	<b>34</b>
<b>3.1.1 Sol-gel Auto combustion Methodology.....</b>	<b>34</b>
<b>3.1.2 Polyaniline (PANI) synthesis method .....</b>	<b>36</b>
<b>3.1.3 Synthesis of ferrite composites .....</b>	<b>37</b>
<b>3.1.4 Synthesis of Co<sup>2+</sup> and La<sup>3+</sup> substituted SrM hexaferrite with composition SrCo<sub>1.5z</sub>La<sub>0.5z</sub>Fe<sub>12-2z</sub>O<sub>19</sub> .....</b>	<b>37</b>
<b>3.1.5 Synthesis of Co<sup>2+</sup> and Cr<sup>3+</sup> substituted SrM hexaferrite with composition Sr(CoCr)<sub>x</sub>Fe<sub>(12-2x)</sub>O<sub>19</sub> .....</b>	<b>39</b>
<b>3.1.6 Synthesis of Co<sup>2+</sup> and Zn<sup>2+</sup> substituted SrM hexaferrite with composition SrCo<sub>x</sub>Zn<sub>x</sub>Fe<sub>12-2x</sub>O<sub>19</sub> .....</b>	<b>40</b>

<b>3.1.7 Synthesis of Co<sup>2+</sup> and Cd<sup>2+</sup> substituted SrM hexaferrite with composition SrCo<sub>1.5z</sub>Cd<sub>0.5z</sub>Fe<sub>12-2z</sub>O<sub>19</sub> .....</b>	<b>41</b>
<b>3.1.8 Synthesis of SrCo<sub>1.5z</sub>La<sub>0.5z</sub>Fe<sub>12-2z</sub>O<sub>19</sub> (80%) + Fe<sub>3</sub>O<sub>4</sub> (20%) ferrite composites.....</b>	<b>42</b>
<b>3.1.9 Synthesis of SrCo<sub>x</sub>Zn<sub>x</sub>Fe<sub>12-2x</sub>O<sub>19</sub> (80%) + PANI (20%) ferrite composites. ....</b>	<b>43</b>
<b>3.1.10 Synthesis of Sr(CoCr)<sub>x</sub>Fe<sub>(12-2x)</sub>O<sub>19</sub> (80%) + CoFe<sub>2</sub>O<sub>4</sub> (20%)ferrite composites .....</b>	<b>43</b>
<b>3.1.11 Synthesis of SrCo<sub>1.5z</sub>Cd<sub>0.5z</sub>Fe<sub>12-2z</sub>O<sub>19</sub> (80%) +20% PANI ferrite composites. ....</b>	<b>43</b>
<b>3.2 Characterization Technique .....</b>	<b>44</b>
<b>3.2.1 X-ray diffraction technique (XRD).....</b>	<b>44</b>
<b>3.2.2 Parameters derived from XRD data.....</b>	<b>45</b>
<b>3.2.3 Fourier Transform Infrared Spectroscopy (FTIR).....</b>	<b>46</b>
<b>3.3.4 Field Emission Scanning Electron Microscopy .....</b>	<b>47</b>
<b>3.3.5 Vibrating Sample Magnetometer (VSM).....</b>	<b>48</b>
<b>3.3.6 Parameters Derived from M-H loops .....</b>	<b>49</b>
<b>3.3.7 Mössbauer Spectroscopy .....</b>	<b>51</b>
<b>3.3.8 Impedance Analyzer .....</b>	<b>52</b>
<b>3.3.9 Parameters derived from Impedance measurements .....</b>	<b>53</b>
<b>3.3.10 Vector Network Analyzer .....</b>	<b>54</b>
 <b>CHAPTER-4</b>	
<b>Results and Discussion.....</b>	<b>56</b>
<b>4.1 Co<sup>2+</sup> - La<sup>3+</sup> substituted SrCo<sub>1.5z</sub>La<sub>0.5z</sub>Fe<sub>12-2z</sub>O<sub>19</sub> hexaferrite.....</b>	<b>56</b>
<b>4.1.1 Structural Analysis.....</b>	<b>56</b>
<b>4.1.2 Electrical Analysis .....</b>	<b>63</b>
<b>4.1.3 Magnetic Analysis .....</b>	<b>70</b>
<b>4.1.4 Mössbauer Spectra Analysis .....</b>	<b>74</b>
<b>4.1.5 Electromagnetic Analysis .....</b>	<b>77</b>
<b>4.2 Co<sup>2+</sup>- Cr<sup>3+</sup> substituted Sr(CoCr)<sub>x</sub>Fe<sub>12-2x</sub>O<sub>19</sub> hexaferrite. ....</b>	<b>94</b>
<b>4.2.1 Structural Analysis.....</b>	<b>94</b>
<b>4.2.1.1 X-ray Diffraction Analysis.....</b>	<b>94</b>
<b>4.2.2 Electrical Analysis .....</b>	<b>99</b>
<b>4.2.3 Magnetic properties .....</b>	<b>106</b>
<b>4.2.4 Electromagnetic Analysis .....</b>	<b>109</b>
<b>4.3 Co<sup>2+</sup>-Zn<sup>2+</sup> substituted SrCo<sub>x</sub>Zn<sub>x</sub>Fe<sub>12-2x</sub>O<sub>19</sub> hexaferrite.....</b>	<b>120</b>

4.3.1 Structural Analysis.....	120
4.3.2 Electrical Analysis.....	125
4.3.3 Magnetic Analysis .....	130
4.3.4 Mössbauer analysis .....	133
4.3.5 Electromagnetic Analysis .....	136
<b>4.4 Co<sup>2+</sup>-Cd<sup>2+</sup> substituted SrCo<sub>1.5z</sub>Cd<sub>0.5z</sub>Fe<sub>12-2z</sub>O<sub>19</sub> hexaferrite.....</b>	<b>152</b>
4.4.1 Structural Analysis.....	152
4.4.2 Electrical Analysis.....	158
4.4.3 Magnetic analysis .....	163
4.4.4 Mössbauer analysis .....	166
4.4.5 Electromagnetic Analysis .....	169
<b>4.5 SrCo<sub>1.5z</sub>La<sub>0.5z</sub>Fe<sub>12-2z</sub>O<sub>19</sub> (80%) + Fe<sub>3</sub>O<sub>4</sub> (20%) ferrite composites .....</b>	<b>183</b>
4.5.1 Structural Analysis.....	184
4.5.2 Electrical Analysis.....	191
4.5.3 Magnetic Analysis .....	196
4.5.4 Electromagnetic analysis .....	199
<b>4.6 SrCo<sub>x</sub>Zn<sub>x</sub>Fe<sub>12-2x</sub>O<sub>19</sub> (80%) + PANI (20%) ferrite composites.....</b>	<b>212</b>
4.6.1 Structural Analysis.....	212
4.6.2 Electrical Analysis.....	216
4.6.3 Magnetic analysis .....	224
4.6.4 Electromagnetic Analysis .....	226
<b>4.7 Sr(CoCr)<sub>x</sub>Fe<sub>12-2x</sub>O<sub>19</sub> (80%)+ CoFe<sub>2</sub>O<sub>4</sub> (20%) ferrite composites.....</b>	<b>228</b>
4.7.1 Structural analysis.....	228
4.7.2 Electrical analysis.....	231
4.7.3 Magnetic analysis .....	236
4.7.4 Electromagnetic Analysis .....	238
<b>4.8 SrCo<sub>1.5z</sub>Cd<sub>0.5z</sub>Fe<sub>12-2z</sub>O<sub>19</sub> (80%) + PANI (20%) ferrite composites.....</b>	<b>248</b>
4.8.1 Structural Analysis.....	248
4.8.2 Electrical Analysis.....	251
4.8.3 Magnetic Analysis .....	256
4.8.4 Electromagnetic Analysis .....	257



**CHAPTER-5**

**Summary and Conclusion ..... 263**

**6 Future Scope ..... 267**

**Bibliography ..... 268**

## LIST OF FIGURES

Fig. 1.1. Electromagnetic waves (EM) -----	2
Fig. 1.2. EMI phenomena-----	5
Fig. 1.3. Types of microwave absorbers-----	6
Fig. 1.4. Application of ferrites. -----	8
Fig. 1.5. Classification of ferrites. -----	10
Fig. 1.6. Types of hexaferrite -----	11
Fig. 1.7. Advantages of M-type hexaferrite -----	12
Fig. 1.8. Magnetoplumbite crystal structure of M-type hexaferrite-----	14
Fig. 1.9. Various synthesis methods of M-type hexaferrite. -----	15
Fig. 1.10. General formula of PANI-----	16
Fig. 1.11. Advantages of the Chemical oxidative polymerization technique. -----	17
Fig. 3.1. Sol-gel auto combustion process-----	35
Fig. 3.2. Schematic procedure of Sol-gel combustion -----	36
Fig. 3.3. Schematic procedure of preparing PANI.-----	37
Fig. 3.4. Chemicals along with their company for the preparation of SrCo <sub>1.5</sub> Zn <sub>0.5</sub> Fe <sub>12-2z</sub> O <sub>19</sub> . -----	38
Fig. 3.5. Chemicals along with their company for the preparation of Sr(CoCr) <sub>x</sub> Fe <sub>(12-2x)</sub> O <sub>19</sub> -----	39
Fig. 3.6. Chemicals along with their company for the preparation of SrCo <sub>x</sub> Zn <sub>x</sub> Fe <sub>(12-2x)</sub> O <sub>19</sub> . -----	40
Fig. 3.7. Chemicals along with their company for the preparation of SrCo <sub>1.5</sub> Cd <sub>0.5</sub> Fe <sub>12-2z</sub> O <sub>19</sub> . -	42
Fig. 3.8. Snapshot of Bruker D8 advance -----	44
Fig. 3.9. Schematic diagram of X-ray diffractometer-----	45
Fig. 3.10 Ray diagram of FTIR-spectrometer.-----	47
Fig. 3.11 Ray diagram of FESEM -----	48
Fig. 3.12 Schematic diagram of VSM -----	49
Fig. 3.13. Schematic diagram Mössbauer spectroscopy -----	51
Fig. 3.14. Universal impedance analyzer -----	53
Fig. 3.15. Vector network analyzer (VNA).-----	55
Fig. 4.1. XRD pattern of D-series hexaferrite.-----	59
Fig. 4.2. Rietveld refinement of synthesized samples.-----	60
Fig. 4.3. FTIR spectra of D-series -----	61
Fig. 4.4. SEM micrographs of D-series from D1 to D6 (a-f) samples. -----	62
Fig. 4.5. EDX spectra of the (a) D2, (b) D4 (b), and (c) D6 samples. -----	63
Fig. 4.6. (a) $\epsilon'$ and (b) $\epsilon''$ (c) $\tan\delta$ variation with frequency of D-series samples.-----	65
Fig. 4.7. $\sigma$ variation with frequency for D-series samples.-----	67
Fig. 4.8. (a) $M'$ (b) $M''$ (c) Cole-Cole plots ( $M''$ vs $M'$ ) variation with frequency of D1, D2, and D4 hexaferrite-----	68
Fig. 4.9. A magnified view of SEM micrographs of D1, D2, and D4 samples. -----	69
Fig. 4.10. (a) $Z'$ (b) $Z''$ (c) Cole-Cole plots ( $Z''$ vs $Z'$ ) variation with frequency of D1, D2, and D4 hexaferrite.-----	71
Fig. 4.11. Hysteresis loops of all D-series hexaferrites. -----	73
Fig. 4.12. <sup>57</sup> Fe Mössbauer spectra of all D-series hexaferrite samples. -----	75
Fig. 4.13. (a) Complex permittivity and (b) permeability plots of D-series samples in 8-12 GHz.-----	78

Fig. 4.14. (a, c, e) Dependence of REL on frequency in D1 sample. (b, d, f) $d_m^{\text{sim}}$ and $d_m^{\text{c}}$ versus frequency for $\lambda$ and $5\lambda/4$ in the D1 sample. -----	81
Fig. 4.15. (a) Dependence of REL on frequency in D2 sample. (b) $d_m^{\text{sim}}$ and $d_m^{\text{c}}$ versus frequency for $5\lambda/4$ in the D2 sample. -----	81
Fig. 4.16. (a, c) Dependence of REL on frequency in D3 sample. (b, d) $d_m^{\text{sim}}$ and $d_m^{\text{c}}$ versus frequency for $5\lambda/4$ and $9\lambda/4$ in D3 sample. -----	82
Fig. 4.17. (a) Dependence of REL on frequency in D4 sample. (b) $d_m^{\text{sim}}$ and $d_m^{\text{c}}$ versus frequency for $5\lambda/4$ in the D4 sample. -----	83
Fig. 4.18. (a, c) Dependence of REL on frequency in D5 sample. (b, d) $d_m^{\text{sim}}$ and $d_m^{\text{c}}$ versus frequency for $5\lambda/4$ in the D5 sample. -----	84
Fig. 4.19. (a) Dependence of REL on frequency in D5 sample. (b) $d_m^{\text{sim}}$ and $d_m^{\text{c}}$ versus frequency for $5\lambda/4$ in the D5 sample. -----	84
Fig. 4.20. Three-dimensional (3D) plots of reflection loss at various frequencies and thicknesses for all samples of D-series. -----	87
Fig. 4.21. (a) Dependence of $Z_{\text{in}}$ and REL in frequency (b) Dependence of REL, $Z_{\text{real}}$ , and $Z_{\text{img}}$ on frequency for D1 sample. -----	90
Fig. 4.22. (a) Dependence of $Z_{\text{in}}$ and REL in frequency (b) Dependence of REL, $Z_{\text{real}}$ , and $Z_{\text{img}}$ on frequency for D2 sample. -----	90
Fig. 4.23. (a) Dependence of $Z_{\text{in}}$ and REL in frequency (b) Dependence of REL, $Z_{\text{real}}$ , and $Z_{\text{img}}$ on frequency for D3 sample. -----	91
Fig. 4.24. (a) Dependence of $Z_{\text{in}}$ and REL in frequency (b) Dependence of REL, $Z_{\text{real}}$ , and $Z_{\text{img}}$ on frequency for D4 sample. -----	91
Fig. 4.25. (a, c) Dependence of $Z_{\text{in}}$ and REL in frequency (b, d) Dependence of REL, $Z_{\text{real}}$ , and $Z_{\text{img}}$ on frequency for D5 sample. -----	92
Fig. 4.26. (a) Dependence of $Z_{\text{in}}$ and REL in frequency (b) Dependence of REL, $Z_{\text{real}}$ , and $Z_{\text{img}}$ on frequency for D6 sample. -----	93
Fig. 4.27. Dependence of $C_0$ on the frequency of D-series samples. -----	93
Fig. 4.28. X-ray diffraction pattern of B-series sintered hexaferrite. -----	97
Fig. 4.29. FTIR spectra of B-series samples. -----	97
Fig. 4.30. Scanned Electron Micrographs of $x=0.0$ (B1) to $x=1.0$ (B6) samples. -----	99
Fig. 4.31. (a) $\epsilon'$ and (b) $\epsilon''$ variation with frequency of B1, B2, B3, and B4 sintered hexaferrite. -----	100
Fig. 4.32. Loss tangent variation with frequency of B1, B2, B3, and B4 sintered hexaferrite. -	101
Fig. 4.33. (a) $M'$ and (b) $M''$ variation with frequency of B1, B2, B3, and B4 sintered hexaferrite. -----	102
Fig. 4.34. Cole-Cole plots ( $M''$ vs $M'$ ) of B1, B2, B3, and B4 sintered hexaferrite. -----	103
Fig. 4.35. $Z'$ variation with frequency of B1, B2, B3, and B4 sintered hexaferrite. -----	104
Fig. 4.36. $Z''$ variation with frequency of B1, B2, B3, and B4 sintered hexaferrite. -----	104
Fig. 4.37. $Z''$ versus $Z'$ plots of B1, B2, B3, and B4 sintered hexaferrite. -----	105
Fig. 4.38. Variation of $\sigma$ with a frequency of B1, B2, B3, and B4 sintered hexaferrite. -----	106
Fig. 4.39. Hysteresis plots of B-series sintered hexaferrite. -----	107
Fig. 4.40. (a) Complex permittivity and (b) permeability plots of D-series samples in 8-12 GHz. -----	110
Fig. 4.41. (a, c) Dependence of REL on frequency in B3 sample. (b, d) $d_m^{\text{sim}}$ and $d_m^{\text{c}}$ versus frequency for $5\lambda/4$ in the B3 sample. -----	112

Fig. 4.42. (a) Dependence of REL on frequency in B3 sample. (b) $d_m^{\text{sim}}$ and $d_m^{\text{c}}$ versus frequency for $5\lambda/4$ in the B3 sample. -----	112
Fig. 4.43. (a, c) Dependence of REL on frequency in B5 sample. (b, d) $d_m^{\text{sim}}$ and $d_m^{\text{c}}$ versus frequency for $5\lambda/4$ in the B5 sample. -----	113
Fig. 4.44. (a, c) Dependence of REL on frequency in B6 sample. (b, d) $d_m^{\text{sim}}$ and $d_m^{\text{c}}$ versus frequency for $5\lambda/4$ and $9\lambda/4$ in the B6 sample. -----	114
Fig. 4.45. 3D plots of REL at various thickness and frequency for B3, B4, B5 and B6 sample.	116
Fig. 4.1. (a, c) Dependence of $Z_{\text{in}}$ and REL in frequency (b, d) Dependence of REL, $Z_{\text{real}}$ , and $Z_{\text{img}}$ on frequency for B3 sample-----	
-----	130
Fig. 4.47. (a) Dependence of $Z_{\text{in}}$ and REL in frequency (b) Dependence of REL, $Z_{\text{real}}$ , and $Z_{\text{img}}$ on frequency for B5 sample. -----	119
Fig. 4.48. (a, c) Dependence of $Z_{\text{in}}$ and REL in frequency (b, d) Dependence of REL, $Z_{\text{real}}$ , and $Z_{\text{img}}$ on frequency for B6 sample. -----	119
Fig. 4.49. XRD pattern of prepared specimen F1 to F5 hexaferrite. -----	123
Fig. 4.50. Refinement analysis of F2 and F5 sample. -----	123
Fig. 4.51. FTIR spectra in 400-4000 $\text{cm}^{-1}$ range of F-series hexaferrite samples. -----	124
Fig. 4.52. SEM micrographs of F-series hexaferrite samples. -----	125
Fig. 4.53. a $\epsilon'$ (b) $\epsilon''$ (c) dielectric loss tangent variation with frequency of F2, and F5 hexaferrite. -----	126
Fig. 4.54. $\sigma$ variation with frequency of F2 and F5 hexaferrite. -----	128
Fig. 4.55. (a) $M'$ (b) $M''$ variation with frequency of F2 and F5 hexaferrite. -----	128
Fig. 4.56. Cole-Cole plots ( $M''$ vs $M'$ ) variation with frequency of F2 and F5 hexaferrite -----	129
Fig. 4.57. (a) $Z'$ (b) $Z''$ (c) Cole-Cole plots ( $Z''$ vs $Z'$ ) variation with frequency of F2 and F5 hexaferrite -----	130
Fig. 4.58. Hysteresis loops of all F-series hexaferrite. -----	133
Fig. 4.59. $^{57}\text{Fe}$ Mössbauer spectra of all F-series hexaferrite samples. -----	135
Fig. 4.60. (a) Complex permittivity and (b) permeability plots of F-series samples in 12 to 18 GHz. -----	136
Fig. 4.61. (a, c, e) Dependence of REL on frequency in F1 sample. (b, d, f) $d_m^{\text{sim}}$ and $d_m^{\text{c}}$ versus frequency for $5\lambda/4$ and $9\lambda/4$ in the F1 sample. -----	138
Fig. 4.62. (a, c, e) REL dependence on frequency in the F5 sample. (b, d, f) $d_m^{\text{sim}}$ and $d_m^{\text{c}}$ versus frequency for $\lambda/4$ , $5\lambda/4$ and $9\lambda/4$ in the F5 sample. -----	139
Fig. 4.63. (a, c) REL dependence on frequency in the F3 sample. (b, d) $d_m^{\text{sim}}$ and $d_m^{\text{c}}$ versus frequency for $5\lambda/4$ and $9\lambda/4$ in the F3 sample. -----	140
Fig. 4.64. (a, c) REL dependence on frequency in the F4 sample. (b, d) $d_m^{\text{sim}}$ and $d_m^{\text{c}}$ versus frequency for $\lambda/4$ and $5\lambda/4$ in the F4 sample. -----	141
Fig. 4.65. (a, c) REL dependence on frequency in the F5 sample. (b, d) $d_m^{\text{sim}}$ and $d_m^{\text{c}}$ versus frequency for $\lambda/4$ and $5\lambda/4$ in the F5 sample. -----	142
Fig. 4.66. 3D representation of REL plots over the entire range of frequency at various thicknesses. -----	149
Fig. 4.67. $C_0$ -dependence on frequency for all samples. -----	151
Fig. 4.68. XRD pattern of prepared specimen C1 to C5 hexaferrite. -----	154
Fig. 4.69. Refinement of C1, C2, C3, C4, and C5 samples. -----	155
Fig. 4.70. FTIR spectra in 400-4000 $\text{cm}^{-1}$ range of all hexaferrite samples. -----	156

Fig. 4.71. SEM micrographs of C1, C2, C3, C4, and C5 hexaferrite samples. -----	157
Fig. 4.72. Enlarged view of C1 sample -----	158
Fig. 4.73. EDX spectra of the C1 and C4 samples. -----	158
Fig. 4.74. a $\epsilon'$ (b) $\epsilon''$ variation with frequency of C1, C3, C4 and C5 hexaferrite. -----	159
Fig. 4.75. Loss tangent variation with frequency of C1, C3, C4 and C5 hexaferrite. -----	160
Fig. 4.76. $\sigma$ variation with frequency of C1, C3, C4 and C5 hexaferrite. -----	160
Fig. 4.77. (a) $M'$ (b) $M''$ variation with frequency of C1, C3, C4 and C5 hexaferrite -----	161
Fig. 4.78. Cole-Cole plots ( $M''$ vs $M'$ ) variation with frequency of C1, C3, C4 and C5 hexaferrite. -----	162
Fig. 4.79. (a) $Z'$ (b) $Z''$ variation with frequency of C1, C3, C4 and C5 hexaferrite. -----	163
Fig. 4.80. Cole-Cole plots ( $Z''$ vs $Z'$ ) variation with frequency of MC1, MC2, MC3 and MC4 hexaferrite. -----	163
Fig. 4.81. Hysteresis loops of C1, C2, C3, C4, and C5 hexaferrite. -----	164
Fig. 4.82. $^{57}\text{Fe}$ Mössbauer spectra of C1, C2, C3, C4, and C5 hexaferrite samples. -----	167
Fig. 4.83. (a) Complex permittivity of C1, C2, C4, and C5 samples (b) Complex permittivity of C3 sample. -----	169
Fig. 4.84. (a) Complex permeability of C1, C2, C4, and C5 samples (b) Complex permeability of C3 sample. -----	170
Fig. 4.85. (a) Dependence of REL on frequency in C1 sample. (b) $d_m^{\text{sim}}$ and $d_m^c$ versus frequency for $5\lambda/4$ in the C1 sample. -----	171
Fig. 4.86. (a, c) Dependence of REL on frequency in C2 sample. (b, d) $d_m^{\text{sim}}$ and $d_m^c$ versus frequency for $5\lambda/4$ in the C2 sample. -----	172
Fig. 4.87. (a, c, e) Dependence of REL on frequency in C3 sample. (b, d, f) $d_m^{\text{sim}}$ and $d_m^c$ versus frequency for $5\lambda/4$ and $9\lambda/4$ in the C3 sample. -----	174
Fig. 4.88. (a, c) Dependence of REL on frequency in C4 sample. (b, d) $d_m^{\text{sim}}$ and $d_m^c$ versus frequency for $\lambda/4$ and $5\lambda/4$ in the C4 sample. -----	175
Fig. 4.89. (a, c, e, g) Dependence of REL on frequency in C5 sample. (b, d, f, h) $d_m^{\text{sim}}$ and $d_m^c$ versus frequency for $\lambda/4$ , $5\lambda/4$ , $9\lambda/4$ and $13\lambda/4$ in the C5 sample. -----	177
Fig. 4.90. 3D plots of REL at various thicknesses and frequencies for all samples. -----	181
Fig. 4.91. XRD pattern of DM1, DM2, DM3, DM4, DM5 and DM6 ferrite composites. -----	185
Fig. 4.92. Rietveld refinement of all DM-series samples. -----	187
Fig. 4.93. FTIR spectra of DM-series ferrite composites. -----	188
Fig. 4.94. FESEM micrographs of DM1, DM2, DM3, DM4, DM5 and DM6 ferrite composites. -----	189
Fig. 4.2. EDX spectra and elemental mapping of DM3 ferrite composite----- -----	212
Fig. 4.96. Schematic showing morphology changes from individual hard and soft phases to composites. -----	190
Fig. 4.97. (a) $\epsilon'$ variation and (b) $\epsilon''$ variation with frequency of DM1, DM2, DM3, DM4, DM5 and DM6 ferrite composites. -----	192
Fig. 4.98. $\tan \delta$ variation with frequency of DM1, DM2, DM3, DM4, DM5 and DM6 ferrite composites. -----	193
Fig. 4.99. $\sigma$ variation with frequency of DM1, DM2, DM3, DM4, DM5 and DM6 ferrite composites. -----	193

Fig. 4.100. (a) $M'$ , (b) $M''$ , and (c) Cole-Cole plot ( $M''$ vs $M'$ ) variation with frequency of DM1, DM2, DM3, DM4, DM5 and DM6 ferrite composites. -----	195
Fig. 4.101. (a) $Z'$ , (b) $Z''$ , and (c) ( $Z''$ vs $Z'$ ) variation with frequency of DM1, DM2, DM3, DM4, DM5 and DM6 hexaferrite composites. -----	196
Fig. 4.102. (a) M-H plots (b) Enlarged view of M-H plots of DM1, DM2, DM3, DM4, DM5 and DM6 ferrite composites.-----	198
Fig. 4.103. $dM/dH$ against $H$ plots of DM1, DM2, DM3, DM4, DM5 and DM6 ferrite composites.-----	199
Fig. 4.104. (a) Complex permittivity of DM1, DM2, DM3, DM4, and DM6 samples (b) Complex permittivity of DM5 sample.-----	200
Fig. 4.105. (a) Complex permeability of of DM1, DM2, DM3, DM4, and DM6 samples (b) Complex permittivity of DM5 sample.-----	200
Fig. 4.106. (a, c) Dependence of REL on frequency in DM1 sample. (b, d) $d_m^{sim}$ and $d_m^c$ versus frequency for $\lambda/4$ and $5\lambda/4$ in DM1 sample.-----	202
Fig. 4.107. (a) Dependence of REL on frequency in DM2 sample. (b) $d_m^{sim}$ and $d_m^c$ versus frequency for $5\lambda/4$ in the DM2 sample. -----	203
Fig. 4.108. (a) Dependence of REL on frequency in DM4 sample. (b) $d_m^{sim}$ and $d_m^c$ versus frequency for $5\lambda/4$ in the DM4 sample. -----	203
Fig. 4.109. (a) Dependence of REL on frequency in DM5 sample. (b) $d_m^{sim}$ and $d_m^c$ versus frequency for $9\lambda/4$ in the DM5 sample. -----	204
Fig. 4.110. (a) Dependence of REL on frequency in DM6 sample. (b) $d_m^{sim}$ and $d_m^c$ versus frequency for $5\lambda/4$ in the DM6 sample. -----	204
Fig. 4.111. 3D plots of REL as a function of thickness and frequency. -----	207
Fig. 4.112. (a, c) Dependence of $Z_{in}$ and REL in frequency (b, d) Dependence of REL, $Z_{real}$ , and $Z_{img}$ on frequency for DM1 sample. -----	209
Fig. 4.113. (a) Dependence of $Z_{in}$ and REL in frequency (b) Dependence of REL, $Z_{real}$ , and $Z_{img}$ on frequency for DM2 sample. -----	209
Fig. 4.114. (a) Dependence of $Z_{in}$ and REL in frequency (b) Dependence of REL, $Z_{real}$ , and $Z_{img}$ on frequency for DM4 sample. -----	210
Fig. 4.115. (a) Dependence of $Z_{in}$ and REL in frequency (b) Dependence of REL, $Z_{real}$ , and $Z_{img}$ on frequency for DM5 sample. -----	210
Fig. 4.116. (a, c) Dependence of $Z_{in}$ and REL in frequency (b, d) Dependence of REL, $Z_{real}$ , and $Z_{img}$ on frequency for DM6 sample. -----	211
Fig. 4.117. XRD pattern of FP1, FP2, FP3, FP4, FP5, and FP6 ferrite composites.-----	213
Fig. 4.118. Rietveld refinement of FP1 to FP6 samples. -----	214
Fig. 4.119. FTIR spectra of of FP1, FP2, FP3, FP4, FP5, and FP6 ferrite composites. -----	215
Fig. 4.120. FESEM micrographs of ferrite composites. -----	216
Fig. 4.121. $\epsilon'$ variation with frequency of FP1, FP2, FP3, FP4, FP5, and FP6 ferrite composites.-----	217
Fig. 4.122. $\epsilon''$ variation with frequency of FP1, FP2, FP3, FP4, FP5, and FP6 ferrite composites.-----	218
Fig. 4.123. $\tan\delta$ variation with frequency of FP1, FP2, FP3, FP4, FP5, and FP6 ferrite composites-----	219
Fig. 4.124. $\sigma$ variation with frequency of FP1, FP2, FP3, FP4, FP5, and FP6 ferrite composites.-----	220

Fig. 4.125. (a) $M'$ (b) $M''$ variation with frequency of FP1, FP2, FP3, FP4, FP5, and FP6 ferrite composites.-----	220
composites. -----	221
Fig. 4.3. Cole-Cole plot ( $M''$ vs $M'$ ) variation with frequency of FP1, FP2, FP3, FP4, FP5, and FP6 ferrite composites-----	246
Fig. 4.127. $Z'$ variation with frequency of FP1, FP2, FP3, FP4, FP5, and FP6 ferrite composites -----	222
Fig. 4.128. $Z''$ variation with frequency of FP1, FP2, FP3, FP4, FP5, and FP6 ferrite composites.-----	223
Fig. 4.129. ( $Z''$ vs $Z'$ ) variation with frequency of FP1, FP2, FP3, FP4, FP5, and FP6 ferrite composites.-----	223
Fig. 4.130. (a) M-H plots (b) Enlarged view of M-H plots of FP1, FP2, FP3, FP4, FP5, and FP6 ferrite composites. -----	226
Fig. 4.131. (a) Complex permittivity of FP2, FP3, FP4, and FP6 samples (b) Complex permittivity of FP1 and FP5 samples. -----	227
Fig. 4.132. (a) Complex permeability of FP2, FP3, FP4, and FP6 samples (b) Complex permeability of FP1 and FP5 samples. -----	227
Fig. 4.133. XRD pattern of BS1, BS2, BS3, BS4, BS5, and BS6 composites.-----	230
Fig. 4.134. FTIR spectra of BS1, BS2, BS3, BS4, BS5, and BS6 composites -----	230
Fig. 4.135. FESEM micrographs of BS1, BS2, BS3, BS4, BS5, and BS6 composites.-----	231
Fig. 4.136. (a) $\epsilon'$ variation and (b) $\epsilon''$ variation with frequency (c) $\tan\delta$ of BS1, BS2, BS3, BS4, BS5, and BS6 composites. -----	233
Fig. 4.137. variation with frequency of BS1, BS2, BS3, BS4, BS5, and BS6 composites.-----	233
Fig. 4.138. (a) $M'$ , (b) $M''$ , and (c) Cole-Cole plot ( $M''$ vs $M'$ ) variation with frequency of BS1, BS2, BS3, BS4, BS5, and BS6 composites. -----	234
Fig. 4.139. (a) $Z'$ , (b) $Z''$ , and (c) ( $Z''$ vs $Z'$ ) variation with frequency of BS1, BS2, BS3, BS4, BS5, and BS6 composites. -----	235
Fig. 4.140. M-H plots of BS1, BS2, BS3, BS4, BS5, and BS6 composites.-----	237
Fig. 4.141. $dM/dH$ against $H$ plots of BS1, BS2, BS3, BS4, BS5, and BS6 composites-----	237
Fig. 4.142. (a) Complex permittivity and (b) permeability plots of BS-series samples in 8.2-12.4 GHz.-----	238
Fig. 4.143. (a) Dependence of REL on frequency in BS1 sample. (b) $d_m^{sim}$ and $d_m^c$ versus frequency for $5\lambda/4$ in the BS1 sample. -----	240
Fig. 4.144. (a) Dependence of REL on frequency in BS3 sample. (b) $d_m^{sim}$ and $d_m^c$ versus frequency for $5\lambda/4$ in the BS3 sample. -----	240
Fig. 4.145. (a) Dependence of REL on frequency in BS4 sample. (b) $d_m^{sim}$ and $d_m^c$ versus frequency for $5\lambda/4$ in the BS4 sample. -----	241
Fig. 4.146. (a) Dependence of REL on frequency in BS5 sample. (b) $d_m^{sim}$ and $d_m^c$ versus frequency for $5\lambda/4$ in the BS5 sample. -----	241
Fig. 4.147. (a) Dependence of REL on frequency in BS6 sample. (b) $d_m^{sim}$ and $d_m^c$ versus frequency for $5\lambda/4$ in the BS6 sample. -----	242
Fig. 4.148. 3D plots of REL at various thicknesses and frequencies.-----	244
Fig. 4.149. (a, c) Dependence of $Z_{in}$ and REL in frequency (b, d) Dependence of REL, $Z_{real}$ , and $Z_{img}$ on frequency for BS5 sample. -----	246

Fig. 4.150. (a, c) Dependence of $Z_{in}$ and REL in frequency (b, d) Dependence of REL, $Z_{real}$ , and $Z_{img}$ on frequency for BS6 sample. -----	247
Fig. 4.151. X-ray diffraction pattern of CP series composites. -----	249
Fig. 4.152. FTIR spectra of CP series composites. -----	250
Fig. 4.153. FESEM micrographs of CP series composites. -----	251
Fig. 4.154. $\epsilon'$ variation with frequency of CP1, CP2, CP3 and CP4 composites. -----	252
Fig. 4.155. $\epsilon''$ variation with frequency of CP1, CP2, CP3 and CP4 composites. -----	252
Fig. 4.156. Loss tangent variation with frequency of CP1, CP2, CP3 and CP4 composites. ----	253
Fig. 4.157. $\sigma$ variation with frequency of CP1, CP2, CP3 and CP4 composites. -----	253
Fig. 4.158. (a) $M'$ (b) $M''$ variation with frequency of CP1, CP2, CP3 and CP4 composites. ----	254
Fig. 4.159. Cole-Cole plot ( $M''$ vs $M'$ ) variation with frequency of CP1, CP2, CP3 and CP4 composites. -----	254
Fig. 4.160. $Z'$ variation with frequency of CP1, CP2, CP3, and CP4 composites. -----	255
Fig. 4.161. $Z''$ variation with frequency of CP1, CP2, CP3, and CP4 composites. -----	255
Fig. 4.162. ( $Z''$ vs $Z'$ ) variation with frequency of CP1, CP2, CP3 and CP4 composites. -----	256
Fig. 4.163. M-H loop of CP series composites. -----	257
Fig. 4.164. (a) Complex permittivity and (b) permeability plots of CP-series samples in 12-18 GHz -----	287



## LIST OF SYMBOLS

Symbol	Description
$\epsilon^*$	Complex permittivity
$\epsilon'$	Real part of complex permittivity (dielectric constant)
$\epsilon''$	Imaginary part of complex permittivity (dielectric loss)
F	Frequency of applied field
$\mu^*$	Complex permeability
$\mu'$	Real part of complex permeability
$\mu''$	Imaginary part of complex permeability
$\epsilon_0$	Permittivity of vacuum
$\mu_0$	Permeability of vacuum
$Z^*$	Complex impedance
$Z'$	Real part of complex impedance
$Z''$	Imaginary part of complex impedance
$Z_{in}$	Normalized input impedance
$Z_0$	Characteristic impedance (free space)
D	Crystallite size
$V_{cell}$	Volume of unit cell
$\theta$	Angle of diffraction (Bragg angle)
$\rho_x$	XRD density
$\rho_{bulk}$	Bulk density
$\delta$	Dislocation density
$\epsilon$	Lattice strain
$d_{hkl}$	Interplanar spacing
hkl	Miller indices
a, c	Lattice constant
S	Surface area
P	Porosity
$N_A$	Avogadro's number
$L_A \& L_B$	Hopping length for tetrahedral & octahedral sites, respectively
$\lambda$	Wavelength
$\beta$	Full-width half maxima
$M_s$	Saturation magnetization

$H_c$	Coercivity
$H_a$	Anisotropy field
$M_r$	Remanent magnetization
$n_B$	Bohr magneton
SQR	Squareness ratio
$\chi$	Magnetic susceptibility
REL	Reflection loss
BTR	Bandwidth-to-thickness ratio
PBW	Percentage bandwidth
EAB	Effective absorption bandwidth
$d_m$	Thickness
$C_O$	Eddy current loss
$\sigma$	AC conductivity
dB	Decibel
$M_b$	Magnetization at octahedral
$M_a$	Magnetization at tetrahedral
M.W	Molecular weight
$\Omega$	ohm

---

# CHAPTER 1

## INTRODUCTION

---

The development in technological gadgets is associated with high-speed electronic devices, wireless communication, sensors, automatic control systems, radio antennae, and military platforms with stealth technology[1], [2]. In addition, an integrated circuit is used to manufacture miniature electronic devices that are smaller in size, more sophisticated, and larger in number [3]. These circuits increase the probability of generating unwanted radiation (electromagnetic interference) which harms the environment, the functioning of other electronic devices, and majorly human health[4], [5]. The electromagnetic waves (EM) waves (Fig. 1.1) generated by these high-frequency range electronic devices have been reduced or attenuated by absorbers through large dielectric/magnetic loss [6]. There is a need for knowledge about EM interference and for inexpensive materials that offer effective absorption from undesirable radiation [7], [8]. Communication systems rely on EM waves to transmit signals, which can be categorized based on their frequency band. One type of EM radiation is microwaves, which have wavelengths ranging from 1m to 1mm and frequencies between 300 MHz to 300 GHz. The different microwave frequency ranges designated by IEEE radar band designations, such as L (1-2 GHz), S (2-4 GHz), C (4-8 GHz), X (8-12 GHz), Ku (12-18 GHz), K (18-26 GHz), or Ka (26-40 GHz) band [9].

Various materials are used to absorb microwaves to enhance absorption performance in different bandwidths. In the quest for a solution to this problem, we need to synthesize an EM absorber that has low density, broad bandwidth, antioxidant capability, is lightweight, has excellent thermal stability, and is capable of absorbing EM radiation of several frequencies [10], [11]. A major advancement towards EM suppression has been achieved by developing composites comprising a blend of two or more distinct compounds [12], [13]. Over some time, researchers have demonstrated a keen interest in composites, dedicating considerable efforts to synthesizing materials that exhibit enhanced EM absorption characteristics, increased saturation magnetization, improved anisotropy constants, greater conductivity, high magnetic/dielectric loss, and other desirable attributes. These advancements make these composites better suited for a wide range of applications [14][15].

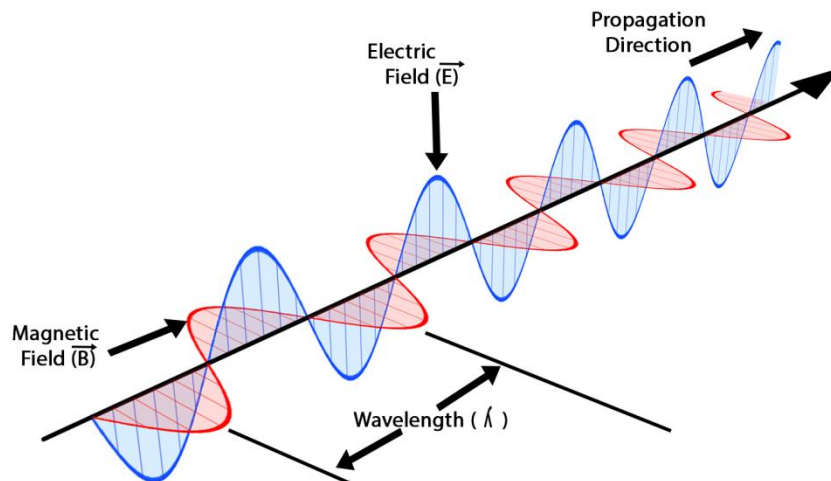


**Fig. 1.1.** Electromagnetic waves (EM) [16], [17].

## 1.1 Electromagnetic Interference Phenomena

Unwanted radiations are not solely hatched by electronic devices indeed, they also originate from various external sources such as radar and wireless communication disturbing the malfunctioning of electronic devices [18]. The prime goal of a microwave absorber (MA) is to reduce the intensity of high-frequency EM waves. The phenomena of microwave absorption are illustrated in Fig. 1.2. When high-frequency EM waves encounter the front surface of the shield, a portion of the wave gets reflected, while some portion is absorbed, and some is transmitted. To minimize wave absorption, it is essential to reflect a substantial part of waves from the front surface of the shield. Whereas the rest portion of the EM wave reaches the shield's second surface, it undergoes multiple reflections, ultimately resulting in absorption, while the remaining portion is transmitted and reaches the electronic component. Magnetic absorbers are described by two characteristics: permittivity and permeability. Both permittivity/permeability measure the effect of the electric/magnetic field within the EM wave on the material. When an incoming wave strikes the material, it gets attenuated, and energy dissipates in the form of heat. The degree of dissipation primarily depends on the frequency of the wave and the material's dielectric constant. Across different frequency ranges, the magnetic/dielectric characteristics of the material are affected by the EM absorber in numerous proportions [19][20].

### 1.1.1 Complex Permittivity/Permeability

Complex permittivity determines the material's ability to store electric potential energy under the influence of an electric field [21]. It is a complex quantity and is measured

by the ratio of the capacitance of a capacitor in the dielectric material to its capacitance in vacuum as dielectric which is called the dielectric constant.

$$\varepsilon^* = \varepsilon' - j\varepsilon'' \quad (1.1)$$

Where real part,  $\varepsilon'$  refers to the amount of energy stored (i.e., lossless mechanism) and imaginary part  $\varepsilon''$  refers to the dissipation of energy within the material (i.e., losses). A high value of dielectric loss implies maximum attenuation of the wave when it moves through the material.

Complex permeability defines the material's ability to allow electromagnetic flux to pass through it under the influence of the applied electromagnetic field [22]. The permeability arises due to the cause of the magnetic polarization of the material. It is a complex quantity and is written as [23]:

$$\mu^* = \mu' - j\mu'' \quad (1.2)$$

Where the real part,  $\mu'$  refers to the energy stored, and the imaginary part  $\mu''$  refers to magnetic loss. The high value of magnetic loss implies maximum attenuation of the wave when it moves through the material. The magnetic loss encompasses domain wall resonance, ferromagnetic resonance, hysteresis attenuation, and eddy currents. It is well established that domain wall resonance typically occurs around the 1-2 GHz frequency range. The relation between magnetic loss and hysteresis parameters is given below [24]:

$$\mu'' = \frac{M_s}{2H_a\alpha} \quad (1.3)$$

Here,  $H_a$  = anisotropy field,  $\alpha$  = extinction coefficient, and  $M_s$  = saturation magnetization

Both electric and magnetic components of EM waves participate in wavelength compression inside the material. Moreover, the energy of the wave gets attenuated, and loss occurs either in the electric or magnetic field because of the coupled EM wave nature. Permittivity/Permeability are the important parameters of most absorbers which depend upon the frequency and show a considerable variation with a small frequency range [25]. The material's effect on the wave can be determined through the behavior of  $\mu^*$  and  $\varepsilon^*$  over a frequency range. The units of permeability units are henrys/meter (H/m) and the permittivity are farads/meter (F/m).

### 1.1.2 Microwave Absorption

The frequency-dependent microwave absorption phenomena of synthesized material can be analyzed with the reflection loss (REL). According to the theory of absorbing wall, REL can be written as [26]:

$$\text{REL (dB)} = 20 \log \left| \frac{Z_{in} - Z_0}{Z_{in} + Z_0} \right| \quad (1.4)$$

Based on transmission line theory, the normalized input impedance ( $Z_{in}$ ) at the interference can be expressed as:

$$Z_{in} = Z_0 (\mu_r / \epsilon_r)^{1/2} \tanh \left[ j \frac{2\pi f t (\mu_r \epsilon_r)^{1/2}}{c} \right] \quad (1.5)$$

Where  $Z_0$  implies as characteristic impedance with value  $377\Omega$ ,  $f$  = EM wave frequency,  $t$  = thickness of the pellet,  $\epsilon_r$  - complex permittivity,  $\mu_r$  - complex permeability, and  $c$  = velocity of the EM wave (Vaccum).

### 1.1.3 Impedance Matching Mechanism

Impedance matching is an important aspect that affects the reflection loss (REL) or microwave absorption performance of material. Reflection loss (REL) depends on the impedance matching between the surrounding medium and material i.e.,  $\frac{Z_{in}}{Z_0} = 1$ . Even if a material has high dielectric/magnetic loss, it may not effectively match the impedance of free space, limiting reflection loss reduction. When  $\frac{Z_{in}}{Z_0} = 1$ , this signifies the condition of maximum signal absorption by the composition. The impedance described in Eq. 1.6 possesses a complex nature, specifically  $Z_{in} = Z_{real} + jZ_{img}$ . In an ideal scenario, when  $\frac{Z_{in}}{Z_0} = 1$ , means  $Z_{real} = 1$ , and  $Z_{img} = 0$ , all signals passing through the material are completely absorbed. However, in practical situations,  $\frac{Z_{in}}{Z_0}$  is not equal to 1 ( $Z_{real}/Z_{img}$  is not precisely close to 1, and or/0). These deviations from the ideal conditions result in a reduction in absorption efficiency. As a result,  $Z_{real}/Z_{img}$  deviates further from 1 and or/0 absorption is reduced.

### 1.1.4 Quarter-Wavelength Mechanism

According to this mechanism, a microwave signal will be absorbed within the material, when the thickness of the material is equal to the odd integer multiple of wavelength ( $n\lambda/4$ ), Mathematically [15],

$$d_m = \frac{n.c}{4f_m \sqrt{|\mu_r \epsilon_r|}} \quad , \text{ Here } n= 1, 3, 5, \dots \quad (1.6)$$

where  $d_m$  = matching thickness,  $f_m$  = matching frequency,  $n$  = an integer,  $c$  = velocity of light.

### 1.1.5 Eddy Current Losses

Eddy currents are closely associated with the skin effect within the material, and their prominence becomes more pronounced when dealing with microwave frequencies. At higher frequencies, the signal exhibits rapid variations in the time domain. This rapid fluctuation of the electric field induces a magnetic field with corresponding variations. These changes in the induced magnetic field, in turn, cause the generation of electric fields or eddy currents. These eddy currents, in opposition to the original electric current, act as impediments to the source signal (microwave signal) [27]. Consequently, they can result in substantial attenuation/absorption of the microwave signal. Mathematically,

$$C_o = \mu'' (\mu')^{-2} f^{-1} = 2\pi\mu_0\sigma t \quad (1.7)$$

Where  $\sigma$  implies conductivity.

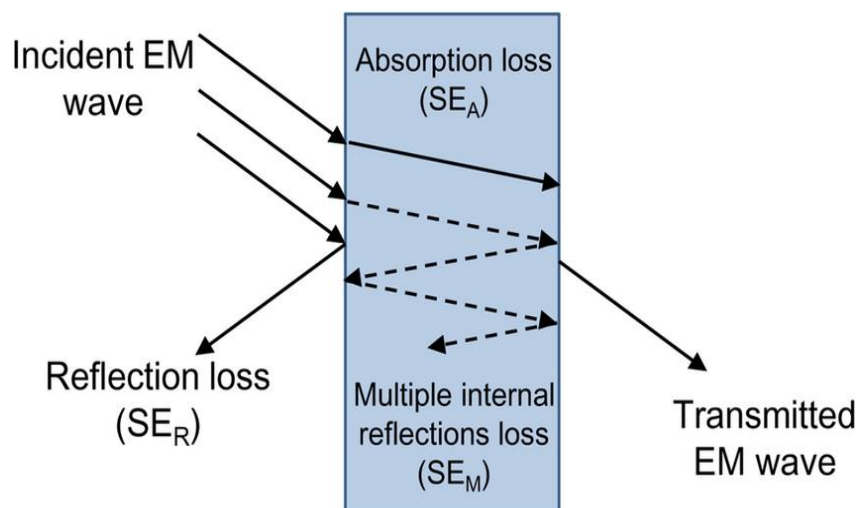


Fig. 1.2. EMI phenomena [17].

## 1.2 Microwave absorbers

Microwave-absorbing materials are predominantly designed to prevent the transmission or reflection of EM waves, which can be achieved by combining metal plates with dielectrics at specific intervals or wavelengths. The effectiveness of microwave absorbers relies on their material preparation, component arrangement, thickness, and absorption frequencies. All the advantages of an EM absorber are not fulfilled by a single material. So, we need to consider a composite of EM absorbers in which the matrix is embedded by some filler. Generally, filler involves one or more material that is responsible for absorption, and it controls how and at what frequency the material will absorb the electromagnetic wave [28][29]. For example, polyaniline, polypyrrole, wax, rubber, etc. On the other hand, matrix material will hold the

filler and protect it from mechanical and environmental damage. The matrix material is commonly selected for its physical properties such as weather resistance, flexibility, and temperature resistance.

### 1.3 Types of Microwave Absorbers

The microwave absorbers that are utilized to attenuate or absorb microwave radiation are categorized into two categories, as seen in Fig. 1.3:

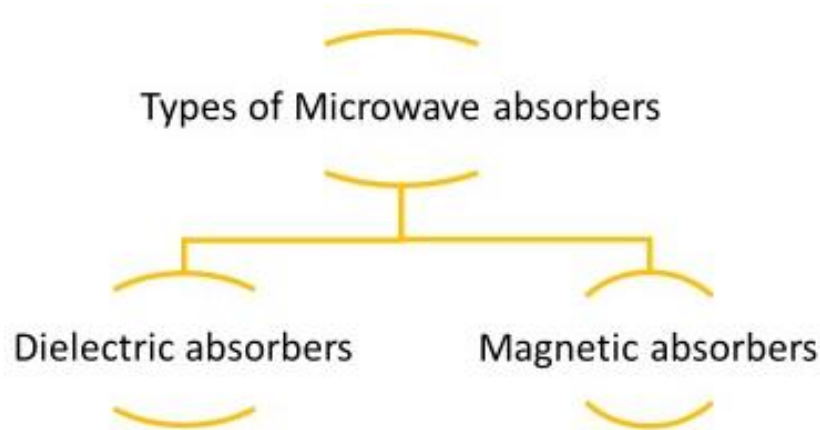


**Fig. 1.3.** Types of microwave absorbers

#### 1.3.1 Dielectric absorbers

The prime objective of dielectric absorbers is to absorb EM radiation and convert it to heat through dielectric loss. These microwave absorbers are predominately utilized as high dielectric constant/loss tangents. The material having large dielectric loss stores a substantial amount of energy from incident EM waves, while the loss factor evaluates how much of that energy is lost in the form of heat. These absorbers have several advantages, such as ease of fabrication, low cost, and tunable absorption properties. However, the dubious nature of these absorbers at high temperatures and less effectiveness at lower frequencies are some of the limitations. Some examples of dielectric absorbers are ceramic composites, carbon nanotubes (CNT), Silicon rubber, Barium titanate ( $\text{BaTiO}_3$ ), and Polymers [30][31].

#### 1.3.2 Magnetic absorbers

Unlike dielectric absorbers that depend on dielectric loss, magnetic absorbers convert EM energy into heat through magnetic hysteresis and eddy current losses in the microwave frequency range. The magnetic absorbers usually consist of ferrites or some magnetic composites, exhibiting low coercivity and high magnetic permeability. These captivating



characteristics allow them to effectively absorb EM waves in the microwave range. Some notable examples of magnetic absorbers are ferrites and iron -particles [30][31].

Constant efforts are being made to synthesize better materials, easier to use, lightweight, broad absorption bandwidth, and are cost-effective while being natural and environmentally friendly. Therefore, EM wave absorbers with wide absorption bandwidth are a requirement today. In the present research, a scheme has been employed to synthesize such a type of composite. The prime components in the composites are divalent/trivalent substituted M-type hexaferrite, spinel ferrite, and polyaniline.

## **1.4 Ferrites**

Ferrite has garnered global interest due to its exclusive combination of magnetic and insulating characteristics of the materials[32]– [35]. They are usually formed by combining iron and metal oxide material providing ferrimagnetic properties. They are primarily composed of iron oxide, and it has significant commercial importance due to their optical, magnetic, and electrical characteristics [36], [37]. Ferrites are visually dark grey or black and moderately hard and brittle. For iron, the term ferrite has been used, which originates from the Latin word, and it has different meanings in various metal technology and scientific contexts [38], [39]. Geologists describe ferrites as predominantly consisting of iron oxides, while electrical engineers anchored them as iron-based groups of materials known for their indispensable dielectric and magnetic properties [40]– [43].

## **1.5 History of ferrites**

Before the birth of Christ around the period of 800 BC, a naturally occurring magnetic material lodestone ( $\text{Fe}_3\text{O}_4$ ), consisting of ore magnetite had been discovered. These stones were in the district of Magnesia in Asia Minor, so the mineral's name became magnetite ( $\text{Fe}_3\text{O}_4$ ). Initially, it was utilized as a compass to navigate mariners without using stars. Professor Takeshi Takei put a lot of effort into improving the magnetic characteristics of this magnetite. Later, in 1600 William Gilbert discussed the magnetic characteristics of lodestones in his published work “De Magnete”. He comprehensively distinguished electricity and magnetism and provided a brief explanation of Earth's magnetic field (behaving as a giant magnet). Hans Christian Orsted (1819) established the relationship between magnetism and electricity, by observing the impact of electric current on a magnetic needle. The magnetic behavior of temperature-dependent magnetic materials was first

discovered by Pierre Curie. In 1930, a scientist Dutch physicist named Wander Johannes de Haas and his associate co-workers P.M. Van Alphen discovered that some magnetic material has inevitable magnetic properties which they termed “ferrimagnetism”. This unprecedented discovery developed the interest of researchers to do a comprehensive study on ferrimagnetic materials. During the 1930s and 1940s, H.J. Round (British physicist) conducted a lot of experiments on ferrites and investigated their unique magnetic electrical characteristics. In 1947, J. L. Snoek published the book “New Development in Ferromagnetic Materials”, wherein he outweighs the application of soft ferrite in various fields. Afterward, soft ferrites acquired commercial prevalence in all parts of the world. The basic theory of ferrimagnetic materials “spin-spin interaction” had been formulated by L. Néel (1948), and his work provides brief information about the crystal structure. Ferrites intrigue the telecommunication and electronic industry, due to the development of microwave ferrites as reported by E. Albers Schonberg. Many researchers tailored the properties of ferrites by substituting them with different kinds of cations. Over the past few years, the enormous developments in technology particularly in wire-less communication and high-speed electronic devices enhanced the demand for ferrite materials. In the following section, we discuss the applications of ferrite [44][45].

## 1.6 Application of ferrites

Ferrites have a diverse range of applications across various fields due to their unique and novel electrical, dielectric, and magnetic properties. Some notable applications are illustrated in Fig. 1.4.

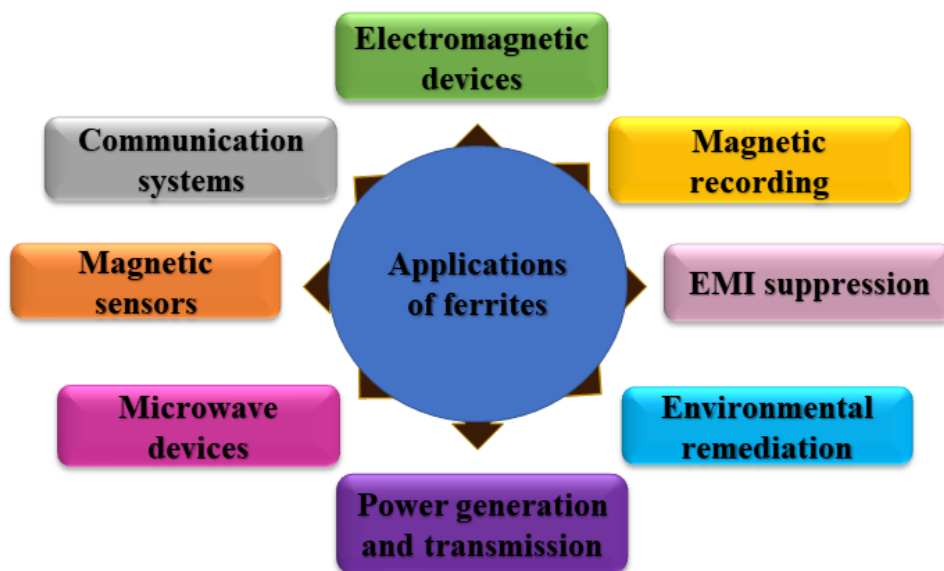


**Fig. 1.4.** Application of ferrites.

**a) Electromagnetic devices:** Ferrite cores are frequently used to suppress electromagnetic interference in electronic devices. They are placed around the cables to protect them from unwanted radiation and absorb high-frequency noise. This is important in industries, where signal quality is essential, such as telecommunication [46][47].

**b) Magnetic recording:** Ferrite particles are utilized in magnetic recording media such as audio cassette tapes and computer hard drives. By magnetizing and demagnetizing the surface, they are used to store and retrieve data [48], [49], [50], [51].

**c) Microwave devices:** Ferrites find a lot of applications in microwave devices like isolators and circulators. Isolators protect sensitive components from reflected impulses, whereas circulators are often used in radar systems and other radio frequency applications to direct the flow of signals in one direction [50], [51], [52].

**d) Magnetic sensors:** In various applications, ferrite-based sensors are used including industries, environmental monitoring, and automotive. They can detect changes in a magnetic field and are used in position sensors, speed sensors, and more [53], [54], [55].

**e) Power generation and transmission:** They have also been utilized in power supply components like transformers and chokes to reduce EM interference and improve power efficiency [58]– [60].

**f) Radio frequency identification systems (RFID):** They help to reduce interference and improve signal strength, leading to more reliable communication between RFID tags and readers [61]– [63].

**g) Medical devices:** Ferrites are also useful in medical applications such as magnetic resonance imaging machines (MRI). The high value of magnetic permeability of ferrites plays a vital role in creating strong magnetic fields required for imaging [64]– [66].

**h) Energy storage:** In energy storage systems, including inductors for energy storage applications like power supplies ferrite-based materials have been potentially used [67]– [69].

## 1.7 Classification of Ferrites

Ferrites are mainly of three different types, namely spinel, garnet, and hexagonal ferrites. The crystal structure of a ferrite influences its magnetic and physical properties. Fig. 1.5 illustrates the common classification of ferrites.

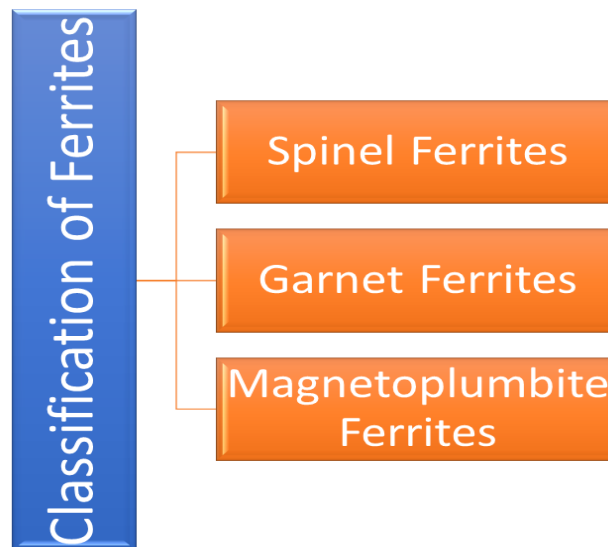


**Fig. 1.5.** Classification of ferrites.

### 1.7.1 Garnet ferrites

These ferrites consist of large trivalent rare earth ions having high magnetic moments. The formula is  $M_3^{3+}Fe_5O_{12}$ , where M = Samarium (Sm), Yttrium (Y), Gadolinium (Gd), and many more rare earth ions. Bertaut and Forrat were the first to report on the unit cell dimension and crystal structure of rare-earth iron garnets [70][71].

### 1.7.2 Spinel ferrites

Bragg and Nishikawa were the first to elaborate on the crystalline structure of spinel ferrites. These are defined as  $AFe_2O_4$  where A represents divalent cations (such as zinc, manganese, or magnesium), and B represents trivalent cations (such as iron or aluminum). In the spinel structure, the metal cations are distributed between two interpenetrating sublattices: the tetrahedral (A) and the octahedral (B) sites. They exhibit a combination of high electrical resistivity (mitigate the eddy current in the core) and high magnetic properties[13][72]. They are widely used in applications like color imaging, magnetic recording, catalytic activity, microwave devices, and biomedical and high-frequency transformers.

### 1.7.3 Hexagonal ferrites

Ferrites are highly effective microwave absorbers, primarily due to their key attributes such as low permittivity loss and affordability. Their elevated resistance and minimal losses due to eddy currents make them excellent core materials for electronic and

telecommunications. In terms of magnetic properties, ferrites are categorized into two types based on their coercivity ( $H_c$ ). Hard ferrites (high  $H_c$ ), making them resistant to demagnetization, whereas soft ferrites (low  $H_c$ ). Compared to garnet and spinel ferrites, hexaferrites exhibit anisotropic characteristics and possess a higher inherent magnetocrystalline anisotropy field. Their in-plane anisotropy results in natural resonance in the gigahertz (GHz) range, rendering them well-suited for high-frequency absorption. A group of ferrites that consist of a hexagonal-type structure is called hexagonal ferrites. The general formula is  $AFe_{12}O_{19}$  where  $A = Sr, Ba, \text{ and } Pb$ . Hexagonal ferrites possess a coercivity of 6700 Oe, Curie temperature of 502 °C, saturation magnetization ( $M_s$ ) of 72 emu/g, and excellent magnetic properties [71]. These unique characteristics enriched their applications in several technological areas such as sensors, magnetic recording, biomedicine, microwave absorbers, magnetoelectric application, radar absorbing material, low power spintronics devices, memory storage devices, electronic devices radiation shielding, higher frequency range, circulators, phase shifters, and stealth technology [74]– [77]. It has been classified into six groups based on its composition and crystalline structure as seen in Fig. 1.6 and Table 1.1:

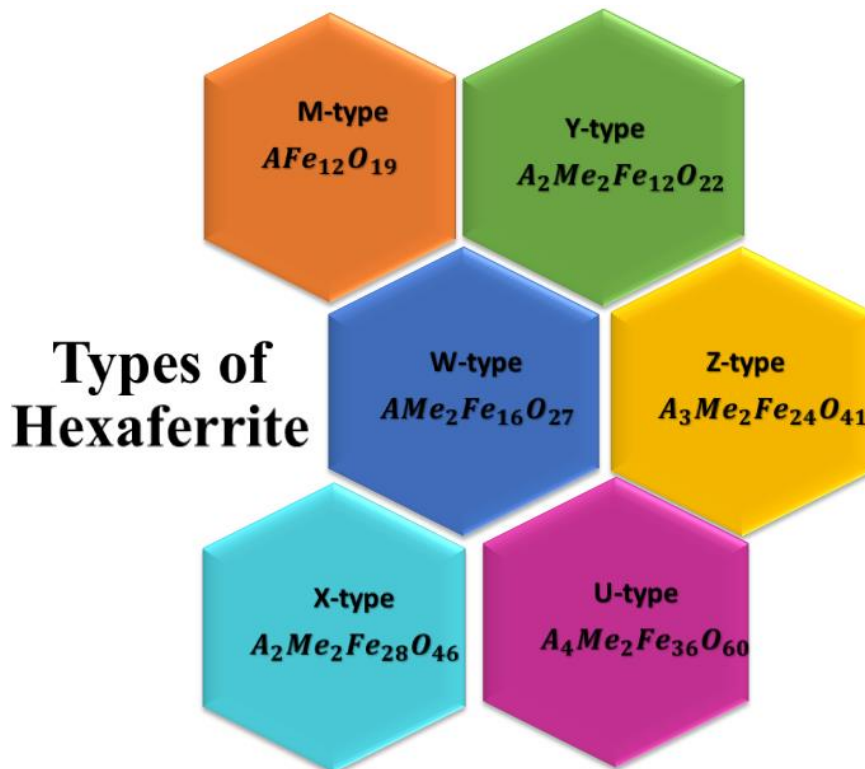


**Fig. 1.6.** Types of hexaferrite

**Table 1.1** Composition of different types of hexaferrite

Hexaferrite type	Combination	Stacking sequence	Molecular formula
<b>M</b>	M	RSR*S*	$AFe_{12}O_{19}$
<b>Y</b>	Y	TSTSTS	$A_2Me_2Fe_{12}O_{22}$
<b>W</b>	M+S	RSSR*S*S*	$AMe_2Fe_{16}O_{27}$
<b>Z</b>	M+Y	RSTSR*S*T*S*	$A_3Me_2Fe_{24}O_{41}$
<b>X</b>	2M+S	RSR*S*S*	$A_2Me_2Fe_{28}O_{46}$
<b>U</b>	2M+Y	RSR*S*T*S*	$A_4Me_2Fe_{36}O_{60}$

Where A represents Sr, Ba, Pb, Ca, etc. and Me is divalent ions Ni, Co, Zn, Cu, etc. S = spinel ( $Fe_6O_8$ ), Me = Fe, R = hexagonal ( $AFe_6O_{11}$ ) and T = hexagonal ( $AFe_8O_{14}$ ). The asterisk (\*) presents the corresponding sub-unit is rotated 180° around the hexagonal axis.

### 1.8 M-type hexagonal ferrites

Out of these above-mentioned hexagonal ferrites, M-type hexaferrite has grabbed the attention of researchers due to its wide array of applications. Fig. 1.7 illustrates the advantages of M-type hexagonal ferrites. In the following section, we focused on various brief descriptions of M-type hexaferrite, its crystal structure, and its synthesis method.

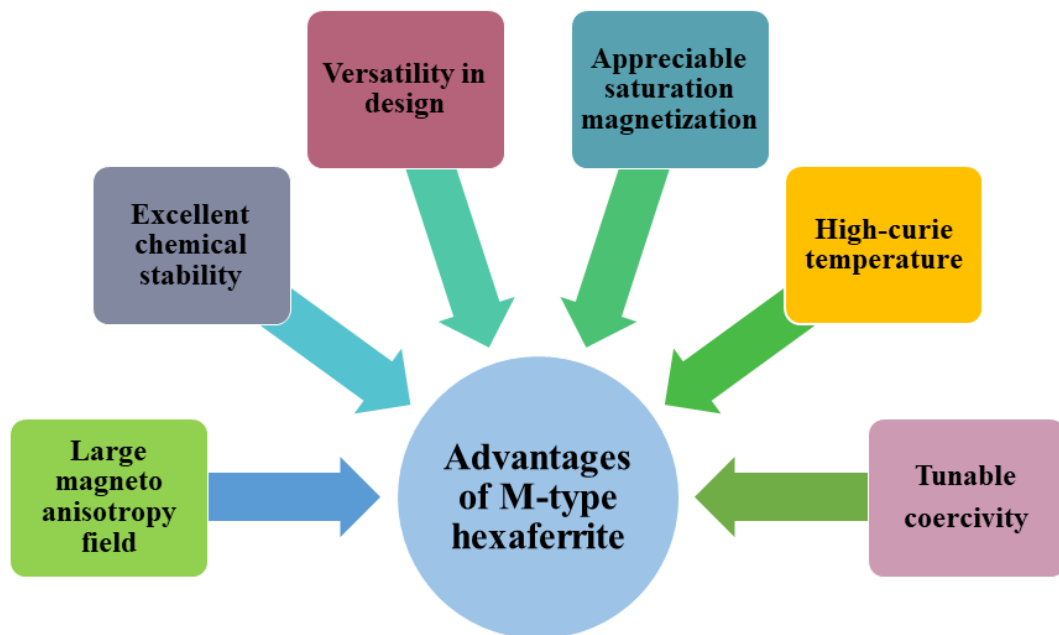


**Fig. 1.7.** Advantages of M-type hexaferrite

## 1.9 Crystal structure of M-type hexagonal ferrites

M-type hexagonal ferrites are promising materials because of their excellent properties such as high coercivity, affordable price, chemical, and thermal stability, high curie temperature, etc [78][79]. It has been extensively used for wide applications such as permanent magnets, supercapacitors, data storage, microwave devices, EM absorbers, etc. M-type hexagonal ferrite consists of a magnetoplumbite structure (Fig. 1.8) and belongs to the space group  $P6_3/mmc$ . In magnetoplumbite structure, the two spinel blocks S and  $S^*$  are connected by block R which contains barium or strontium. The stacking sequence of M-type hexagonal ferrites describes the unit cell as  $RSR^*S^*$ , where R represents a block of three layers of oxygen ions ( $O_4 - MeO_3 - O_4$ ) with composition  $[Me^{+2}Fe_6^{+3}O_{11}]^{-2}$  and S represents the spinel block of two layers of oxygen ions ( $O_4 - O_4$ ) with composition  $[Me_2^{+2}Fe_4^{+3}O_{11}]^0 (S^0)$  or  $[Fe_6^{+3}O_8]^{+2} (S^{+2})$ . The block has an asterisk on its superscript specifying that the corresponding block is rotated  $180^\circ$  around the hexagonal c-axis. The unit cell of M-type hexaferrite involves 38 ions of oxygen ( $O^{2-}$ ), 24 ions of ferric ions ( $Fe^{3+}$ ) and 2 Me ions [Me =  $Ba^{+2}$ ,  $Sr^{+2}$ ,  $Pb^{+2}$ , and  $La^{+2}$ , etc.]. The  $24Fe^{3+}$  ions are dispersed over five different sites i.e., octahedral site (2a, 12k and  $4f_2$ ), trigonal bi-pyramidal site 2b, tetrahedral site  $4f_1$ . Table 1.2 displays the site occupancy of  $Fe^{3+}$  ions over five crystallographic sites.

**Table 1.2** Site occupancy of  $Fe^{3+}$  ion at different crystallographic sites.

Site	Geometry	Spin	No. of $Fe^{3+}$ ions
2a	Octahedral	Up ( $\uparrow$ )	1
12k	Octahedral	Up ( $\uparrow$ )	6
$4f_2$	Octahedral	Down ( $\downarrow$ )	2
$4f_1$	Tetrahedral	Down ( $\downarrow$ )	2
2b	Trigonal bi-pyramidal	Up ( $\uparrow$ )	1

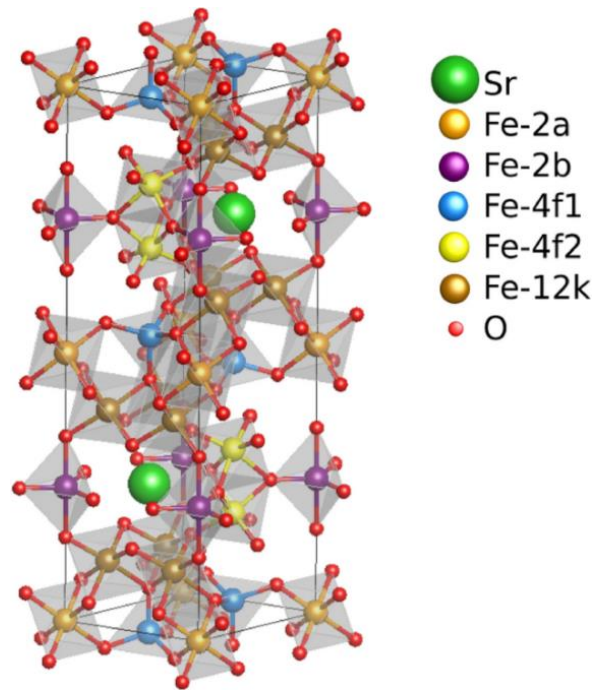


**Fig. 1.8.** Magnetoplumbite crystal structure of M-type hexaferrite [78].

### 1.10 Synthesis of M-type hexaferrite

The synthesis method plays a vital role in determining M-type hexaferrite's structural, morphological, electrical, and magnetic characteristics. The choice of synthesis method can impact crystal structures, compositions, homogeneity, morphology, scalability, time efficiency, and cost-effectiveness. There are several methods of synthesizing M-type hexaferrite, as shown in Fig. 1.9. A considerable number of researchers have employed various methods, individually or in combination, to synthesize hexaferrite. Behra and Ravi successfully produced a single-phase polycrystalline  $\text{Ba}_2(\text{Ca}_{1-x}\text{Mg}_x)_2\text{Fe}_{12}\text{O}_{22}$  using the solid-state reaction technique [79]. Bibhuti et al. [80] also prepared a polycrystalline sample of  $\text{Ba}_2\text{Mg}_2\text{Fe}_{12}\text{O}_{22}$  at 1050 °C through a solid-state reaction and confirmed its crystalline nature via XRD analysis. They observed a decrease in  $M_s$  as a dopant concentration increased, accompanied by an increase in  $H_c$ . The optimal magnetic characteristics were achieved at  $x = 0.13$ . Guo et al. [81] utilized the hydrothermal method to obtain well-dispersed nanosized  $\text{BaFe}_{12}\text{O}_{19}$  hexagonal platelets with high purity. Their experiments highlighted the essential conditions for generating high-purity  $\text{BaFe}_{12}\text{O}_{19}$ , including the use of a non-stoichiometric and iron-deficient precursor, a reaction duration of at least 24 hours, and a low reaction temperature of 210 °C. Drogenik synthesized barium hexaferrite using a controlled hydrothermal method at 280 °C, achieving  $M_s$  (40 emu/g) [82]. For preparing M-type hexaferrite materials, the sol-gel combustion method is preferred over another synthesis method. This method provides a homogenous distribution of elements, fine particles with



controlled morphology, capacity for large-scale production, fabrication of thin films, and short-time, and is cost-effective [84]– [88]. Moreover, the usage of de-ionized water as a solvent adds an environment-friendly aspect to this approach.

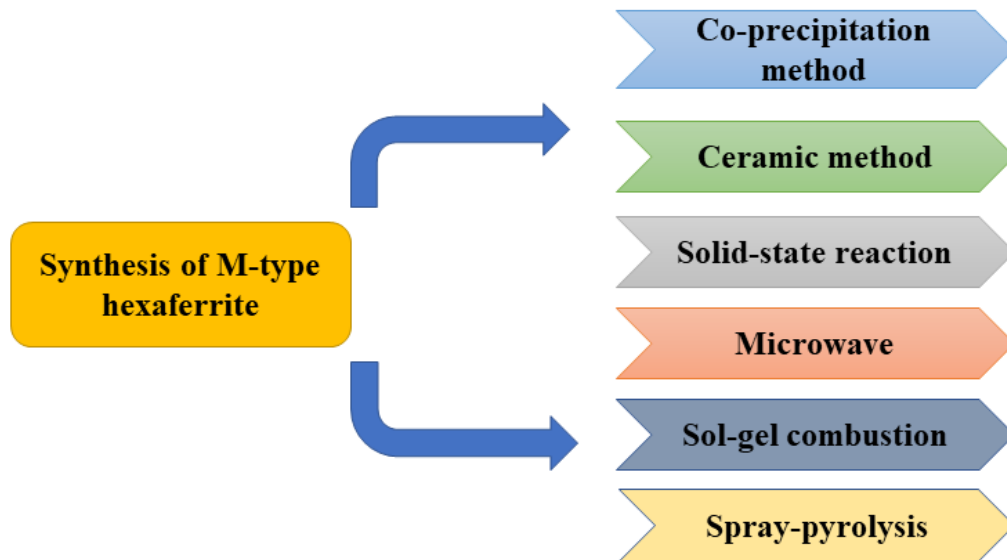


**Fig. 1.9.** Various synthesis methods of M-type hexaferrite.

## 1.11 Polyaniline

Since 1976, numerous conducting polymers have attracted a lot of attention including polypyrrole, polyaniline, and polythiophene. The discovery of conducting polymers led to the awarding of the Nobel Prize in Chemistry 2000 to MacDiarmid, Shirakawa, and Heeger. Their discovery was intriguing because it holds chemistry and condensed matter physics together. These well-known polymers were dismissed as uninteresting from the perspective of electrical materials since they are saturated and insulators. Conducting polymers are made up of an overlap of singly occupied p-orbitals in the polymer chain's backbone and have an extended p-conjugated system. Alternate single and double bonds are present between the carbon atoms of conjugated polymers. Each bond has a weaker localized p-bond in addition to a stronger localized sigma bond (holding the polymer together). These p-bonded unsaturated polymers are well suited for oxidation-reduction processes due to their ionization potentials and strong electron affinities. The conjugated polymers have fundamentally distinct electronic configurations because each carbon atom has one unpaired electron (the p-electron) because of the chemical bonding. The electron delocalization along the polymer's backbone is caused by the overlapping of p-orbitals of succeeding carbon atoms. This delocalization creates a path for mobile charge carriers along the polymer chain's backbone. As a result, the kind and number of atoms present within the repeated unit (chain symmetry)

determines the electronic structure of conducting polymers. Such polymers may have metallic and semiconducting characteristics [89]– [91].

One of the polymers that has been explored the most is polyaniline (PANI). It is due to several factors, including ease of preparation, a generally stable atmosphere, and strong electrical conductivity. As a typical PANI has poor solubility in most common organic solvents which directly results in processing difficulty. Homopolymer PANI is composed of either quinonoid or benzenoid components, or both present in varying proportions in their molecular structure, as seen in Fig. 1.10. It can be found in many oxidation states. The quinonoid form of fully oxidized pernigraniline has no hydrogen atoms connected to nitrogen atoms, while the benzenoid state of totally reduced leucoemeraldine has hydrogen atoms linked to nitrogen atoms. The redox state of PANI is determined by the percentage of benzenoid and quinonoid in PANI chains. The ratio of benzenoid to quinonoid, for partially oxidized emeraldine should ideally be 1:1, for fully reduced leucoemeraldine 1:0, and 0:1 for fully oxidized pernigraniline. These ratios can be modified by altering the synthesis process and the amount of doping. Both leucoemeraldine and pernigraniline are non-conductors by nature, however emeraldine salt, which is slightly doped, conducts electricity. Of all three types of PANI, only emeraldine is thermally stable [92]– [94].



**Fig. 1.10.** General formula of PANI [94].

The aniline monomer or its derivative is used to make PANI. In general, oxidants are free radical initiators like potassium persulphate (KPS), ammonium persulphate (APS), etc. Additionally, effective oxidants such as chloroaurate, ferric chloride, potassium dichromate, chloroaurate, etc. can also be utilized. Among all these oxidants we prefer to choose APS because of its high oxidative potential (1.94V) as compared to other oxidants such as hydrogen peroxide, potassium dichromate, ferric chloride, and cerium (IV) sulphate.

Two prime categories of synthesizing PANI are with oxidant and without oxidant. The former category involves interfacial polymerization, solid-state polymerization, microemulsion polymerization, electrospinning polymerization, plasma polymerization, ultrasonic polymerization, and chemical oxidative polymerization. While the latter category involves electrochemical polymerization. Among the techniques, the chemical oxidative polymerization (COP) technique is predominantly and widely utilized for its exceptional advantages. Fig. 1.11 illustrates the advantages of the COP technique over other preparation methods [89][94]– [97].



**Fig. 1.11.** Advantages of the Chemical oxidative polymerization technique.

---

# CHAPTER 2

## REVIEW OF LITERATURE, RESEARCH GAP, AND OBJECTIVES

---

### 2.1 Review of literature

**LjaZ M. *et al.* (2024)** analyzed the Cobalt effect on magnetic and microstructural characteristics of sol-gel routed barium-strontium hexaferrite of composition  $\text{Ba}_{0.6}\text{Sr}_{0.3}\text{Er}_{0.1}\text{Fe}_{11.5-x}\text{Al}_{0.5}\text{Co}_x\text{O}_{19}$ , where  $0.0 \leq x \leq 2$ . XRD and SEM analysis revealed the sole formation of a hexagonal phase and the homogenous dispersion of particles in all samples, respectively. The hysteresis loop technique was utilized to determine the magnetic properties. Authors reported that magnetic properties significantly enhanced with doping, saturation magnetization increased from 37.76 emu/g ( $x = 0.0$ ) to 57.12 emu/g ( $x = 1.5$ ), at  $x = 1.5$  composition  $H_a = 1.303$  kOe and  $H_c = 4.172$  kOe. Investigators generalized that synthesized samples are a potential candidate in magnetic applications [98].

**Khan M. *et al.* (2023)** enquired about sol-gel synthesized barium-strontium hexaferrite nanoparticles. They prepared composites with multi-walled carbon nanotubes (MWCNTs) via carrier fluid ultrasonication and conductive polymers through in-situ polymerization. Dielectric measurements at low frequency showed an increment in dielectric losses, with values of 304 at 100 Hz for pure nanoparticles. These losses further increased from 2721 to 7861 for ternary composites with polythiophene and polyaniline matrices, indicating effective energy dissipation behavior. The microwave absorption properties of the samples were analyzed in terms of thickness and frequency, revealing a reliance on the phenomenon of quarter wavelength. The ternary composite with a polythiophene matrix exhibited a  $\text{REL}_{\text{max}}$  of -39 dB at 7.4 GHz [99].

**Thanh T. *et al.* (2023)** employed a ball milling method to synthesize polygonal-shaped cobalt-doped strontium hexaferrite followed by heat treatment and obtained a crystallite size of approximately 24 nm. The coercivity decreased as the content of cobalt dopant increased, while the saturation magnetization exhibited the opposite trend. When incorporated into an

epoxy matrix, all Co-SrM-epoxied samples demonstrated favorable microwave absorption capabilities within the 12-18 GHz frequency range at a thickness ranging from 4-6 mm. The optimum reflection loss (REL) value achieved was -30.7 dB (99.9 % absorption of the incident wave) and it could be attributed to factors such as impedance matching, eddy current, natural resonance, and dielectric relaxation loss. These findings demonstrated the potential of Co-SrM-epoxied samples as promising microwave-absorbing materials (MAMs) for practical applications [100].

**Liu X. *et al.* (2023)** explored rare earth-doped BaM/PANI composites and studied their effect on microstructure and microwave absorption properties prepared through an in-situ polymerization process. Both doped and undoped BaM hexaferrite exhibited hexagonal-shaped flake particles. The La-doped composite exhibited a  $REL_{max}$  of -63.6 dB for 3.28 mm thickness at 7.76 GHz, while Nd-doped composites revealed a wide absorption bandwidth of 3.88 GHz at a 1.58 mm thickness. The introduction of rare earth elements reduced the limitations of electric polarization in PANI near the surface of the BaM particles. As a result, the interfaces between the rare-earth doped BaM and PANI phases experienced increased polarization [101].

**Khan K. *et al.* (2023)** revealed the influence of grain/grain boundaries and magnetic exchange coupling of soft/hard nanocomposites with varying ratios of hard ferrite, denoted as  $(MgFe_2O_4)_{100-x}/(BaFe_{12}O_{19})_x$ , were fabricated using in-situ auto-combustion sol-gel method. Analysis of the hysteresis loop at various temperatures exhibited single smooth curves and suggested a strong exchange-coupling between the hard/soft ferrite phases. The existence of a shoulder peak in the  $dM/dH$  versus  $H$  curve for the molar ratio  $x = 50$  indicated modest exchange coupling between the two phases. The incorporation of Nyquist plots for complex impedance analysis and modeling using an equivalent model circuit indicated that both grain and grain boundaries contributed to the total conduction mechanism of composites. These results suggested that the synthesized composites possess a higher impedance value, making them suitable candidates for various technical applications, including high band-pass filters and electromagnetic shielding [102].

**Gupta A. *et al.* (2023)** examined the effect of  $Zn^{2+}$  ions on sol-gel combustion synthesized  $SrFe_8Al_4O_{19}$  hexaferrite. VSM resulted in an inclination in values of  $M_s$  from  $x=0.0$  (14.88 emu/g) to 1.0 (25.54 emu/g), conversely  $H_c$  was observed to decrease from 17.93 kOe to 9.30

kOe by increasing the doping content of Zn ions. The typical dielectric behavior of hexaferrite was demonstrated by the synthesized samples, which can be explained by the Maxwell-Wagner theory [103].

**Amini M. et al. (2023)** synthesized hexagonal powders of single-phase  $MFe_{12}O_{19}$  (where  $M = Pb, Ba, Sr$ ). They employed a citrate-nitrate process, which involved adjusting the pH to 7, using an M-to-iron molar ratio of 1:11, a nitrate-to-citrate ratio of 1:1.5, and a heating temperature of 850 °C. Rietveld analysis revealed that the samples exhibited hexagonal symmetry (space group  $P6_3/mmc$ ), further validated by FTIR. Variations in the  $M_s$  of the  $MFe_{12}O_{19}$  hexaferrite were attributed to the presence of a non-magnetic layer within the grains. Moreover, the  $H_c$  of samples exhibited an increase with a rise in the average particle sizes. The dielectric measurements of the examined samples suggested the existence of localized charge carriers engaged in short-range conduction during the relaxation phase. This led to a deviation from the ideal Debye-type behavior, which ac conductivity investigations also verified [104].

**Caliskan S. et al. (2023)** comprehensively analyzed nano Sr-hexaferrite which co-substituted by Co-V ions, specifically  $Sr_{0.5}Co_{0.5}V_xFe_{12-x}O_{19}$  (NHFs), where the value of  $x$  ranged from 0.00 to 0.08. The average crystallite size of citrate combustion synthesized products yielded in the range of 37-83 nm. Mössbauer spectra indicated that the presence of  $V^{3+}$  influenced the density of electrons around  $Fe^{3+}$  ions at all sites. VSM results revealed that all samples exhibited magnetic hardness at both high and low temperatures. The values of  $M_s$ ,  $M_r$ , and  $n_B$  were dependent on the concentration of dopants, with the highest value observed at  $x = 0.04$ . The samples displayed a squareness ratio (SQR) of approximately 0.5 at all temperatures, indicating substantial anisotropy [105].

**Rana K. et al. (2023)** fabricated strontium hexaferrite using a modified conventional citrate precursor method, sintered at 800 °C and 910 °C. XRD affirmed the formation of magnetoplumbite structure at both temperatures and the obtained results were supported by Raman spectroscopy and FTIR. As the sintering temperature increased the  $M_s$  and  $H_c$  showed increments from 81 to 92 emu/g and from 107 to 262 Oe, respectively. Furthermore, the increment in sintering temperature decreased the impurity content and underwent a transition from the hard character of SrM hexaferrite to soft [106].

**Ramirez-Ayala M. et al. (2023)** comprehensively examined the magnetic, microstructural, and structural properties of neodymium (Nd) substituted strontium hexaferrite. Nd was added during the preparation of hexaferrite via the sol-gel Pechini method. The findings revealed the existence of a secondary phase in neodymium orthoferrite which would be due to the partial incorporation of Nd into the crystal structure of hexaferrite and consequently impact the magnetic properties of the hexaferrite material. The magnetic properties peaked when 2.85% weight of neodymium orthoferrite was mixed with hexaferrite resulting in a 35 % increase in the maximum energy product compared to using pure SrM hexaferrite [107].

**Mironovich A. et al. (2023)** fabricated  $\text{BaFe}_{12-2x}\text{Ni}_x\text{O}_{19}$  hexaferrite synthesized via hydrothermal technique with post-annealing. XRD and EDX analysis revealed the existence of Ni ions in the barium hexaferrite crystal lattice. The cation distribution of  $\text{Ni}^{2+}$  ions was well explained with Mössbauer and magnetic analysis. As the level of  $\text{Ni}^{2+}$  ions increased, the  $M_s$  value reduced from 65.88 emu/g to 49.13 emu/g and was associated with the site occupancy of Ni ions at 12k sites [108].

**Nishkala K. et al. (2023)** explored  $\text{Ba}_{(1-x)}\text{La}_x\text{Fe}_{12}\text{O}_{19}$  ( $x = 0, 0.1, 0.15, \text{ and } 0.20$ ) hexaferrite, which was synthesized using a combination of ball milling and a subsequent heat treatment. All the samples affirmed the existence of a single-phase magnetoplumbite structure through the Rietveld analysis of XRD patterns. FESEM showed the presence of hexagonal plate-like grains with varying sizes of grains, where the increment in La content caused a decrease in average grain size. Density measurements indicated a decrease in porosity up to La content  $x = 0.15$ , followed by a slight increase for  $x=0.20$ . Mössbauer spectroscopy revealed the absence of  $\text{Fe}^{2+}$  ions and electron delocalization following La doping. The hyperfine structure showed minimal variation with La doping. Dielectric spectroscopy revealed that the sample with La content  $x = 0.20$  exhibited the highest dielectric constant and low loss [109].

**Fasate S. et al. (2023)** reported the impact of Mn-substituted barium hexaferrites on magnetic, electrical, and dielectric properties. Using sol-gel combustion methodology they synthesized  $\text{Ba}_{1-x}\text{Mn}_x\text{Fe}_{12}\text{O}_{19}$  hexaferrite, where  $x$  ranged from 0.0 to 0.5. A decrement was observed in the DC electrical resistance with rising temperature and concentration of  $\text{Mn}^{2+}$ . The dielectric constant/loss, and loss tangent reduce with increasing frequency and with substitution of  $\text{Mn}^{2+}$  ions. The saturation magnetization of Mn-substituted hexagonal ferrite was decreased, as the level of substitution increased [110].

**Chagas P. et al. (2023)** investigated the influence of Sn-substituted strontium hexaferrite on electrical conductivity, which was synthesized using the methodology of solid-state reaction. The conductivity values for the Sn-doped SrM ceramic samples rose as the dopant cation concentration increased. Moreover, two conductive processes emerged because of the Sn<sup>4+</sup> cations being incorporated into the SrM crystal structure. At low frequencies, there was a DC-conductivity process, and a second frequency-dependent conductive process was observed at high frequencies. Based on the analysis of the activation energy, two mechanisms were identified for the conductive processes. The first mechanism involved small polaron tunneling with long-range mobility and low frequency, exhibiting spontaneous occurrence with negative activation energy. The second mechanism was related to electron hopping, following a correlated barrier model, with activation energy from 0.135 to 0.355 eV [111].

**Mohammad F.Z. et al. (2023)** examined the effect of Co-Zn substitution on BaM hexagonal ferrites with chemical composition BaCo<sub>0.5</sub>Zn<sub>0.25</sub>Fe<sub>11.25</sub>O<sub>19</sub>. The crystalline size ranged from 22.1 to 30.3 nm and morphology verified the spherical shape of the particles. The presence of nano-crystallites was confirmed by TEM analysis, which exhibited agglomeration likely due to exchange interaction between magnetic particles. The hysteresis curves demonstrated an increase in coercivity, remanent magnetization, and saturation magnetization, through the simultaneous substitution of Co and Zn ions in BaM ferrite. The VNA results indicated an increase in both permittivity and permeability with doping. Finally, at a coating thickness of 1.8mm, the effective bandwidth for absorption ( $\geq 10$  dB) increased from 2.76 to 3.60 GHz [112].

**Bilovol V. et al. (2023)** comprehensively analyzed the effect of exchange coupling in (100-x) SrFe<sub>12</sub>O<sub>19</sub>/(x)CoFe<sub>2</sub>O<sub>4</sub> composites synthesized via a ball milling process, employing several proportions of cubic and hexagonal ferrite powders as precursors (x = 10, 20, 30, and 40 %). A VSM was deployed to determine the magnetic characteristics of synthesized composites at a 1.6 T applied magnetic field. The composite containing 10 wt% CoFe<sub>2</sub>O<sub>4</sub> exhibited the highest energy product (BH)<sub>max</sub> of value 10.9 kJ/m<sup>3</sup>, which was roughly 20 % greater than that of SrFe<sub>12</sub>O<sub>19</sub>. The optimal exchange coupling improved the magnetic properties of the composite [113].



**Zareef Khan M. et al. (2022)** report the results of concentration-dependent exchange coupling in  $(1-x)$   $(\text{BaFe}_{12}\text{O}_{19})/x(\text{NiFe}_2\text{O}_4)$  ( $x = 0$  to  $1$ ) nanocomposites. Remarkably, for the  $x = 0.7$  composition, the merging of zero field-cooled and field-cooled magnetization curves indicated robust magnetic interactions within these nanocomposites. The addition of hard in soft ferrite leads to a linear increment in coercivity and saturation magnetization of soft ferrite. A pronounced increment was observed for  $x = 0.5$  and  $0.7$ , suggesting the existence of spring exchange coupling in these nanocomposites [114].

**Karnajit Singh H. et al. (2022)** conducted a comprehensive study on polycrystalline  $\text{Ba}_{0.4}\text{La}_{0.1}\text{Sr}_{0.5}\text{Al}_x\text{Fe}_{12-x}\text{O}_{19}$  hexaferrite samples synthesized using the solid-state method. The complex dielectric constant  $(\epsilon', \epsilon'')$  decreased with  $\text{Al}^{3+}$  insertion, with values at 1 MHz ranging from  $\epsilon' = 3.44$  k,  $\epsilon'' = 0.993$  k for  $x = 0$  to  $\epsilon' = 0.744$  k,  $\epsilon'' = 0.211$  k for  $x = 1$ . They observed a decrease in saturation magnetization and magnetic anisotropy  $K_1(\text{T})$ , while the anisotropy field  $H_a(\text{T})$  and coercivity  $H_c(\text{T})$  increased with temperature and  $\text{Al}^{3+}$  concentration. The combination of dielectric/magnetic responses makes the material considerable for permanent magnets and microwave applications [115].

**Shakir H. et al. (2022)** comprehended structural, morphological, magnetic properties and EM shielding of barium hexaferrite (BHF)-polypyrrole (Ppy) particles prepared via in-situ polymerization. A high wt% of BHF-Ppy composites revealed shielding effectiveness of less than  $-50$  dB in the  $0.1$  to  $20$  GHz frequency range [116].

**Chauhan C. et al. (2022)** enquired about the dielectric and magnetic characteristics of  $\text{SrFe}_{12}\text{O}_{19}/\text{NiFe}_2\text{O}_4$  nanocomposites were synthesized in the existence of crown flower extract, and their properties were investigated at various weight ratios. The nanocomposites exhibited an average crystallize size ranging from  $25$  nm to  $44$  nm. The analysis of the M-H loop revealed that the  $H_c$  (ranged from  $3181$  to  $326$  Oe) and  $M_s$  (ranged from  $57.5$   $\text{A/m}^2$  kg to  $40$   $\text{A/m}^2$  kg) decreased with an increment in the spinel phase concentration. All the synthesized nanocomposites exhibited characteristics of hard ferrites, except the 5:5 weight ratio displayed soft magnetic properties. The analysis also indicated that 7:3 and 6:4 composites showed partial exchange coupling interactions, 9:1 and 8:2 composites showed weak exchange coupling interactions, and a perfect exchange coupling interaction was observed in the 5:5 composite [117].

**Godara S. et al. (2022)** fabricated a series of  $\text{Ba}_{1-x}\text{Ca}_x\text{Fe}_{12}\text{O}_{19}$  by sol-gel technique to improve their  $\epsilon'$ ,  $M_s$ , and  $H_C$  for permanent magnets. Study of XRD confirmed the formation of magnetoplumbite structure with some secondary phases. As the content of Ca ions increased, dielectric parameters improved. With substitution, Coercivity increased from 5043-5290 Oe, while  $M_s$  was maximum for  $x = 0.2$  (72.38 emu/g) [118].

**Bozorgmehr M. et al. (2021)** explored the absorption characteristics of synthesized nanocomposites  $\text{SrZn}_{2-x}(\text{MnCa})_{x/2}\text{Fe}_{16}\text{O}_{27}$  hexaferrite prepared by co-precipitation technique and single-walled carbon nanotubes were utilized. The study concluded that with substitution the value of  $M_s$  decreased from 70 emu/g to 45 emu/g, whereas  $H_c$  increased from 145 Oe to 605 Oe. VNA study revealed that substitution causes enrichment in REL values from -22 dB to -37 dB. However, maximum REL = -42 dB was found in composition  $x = 0.4$  with 5 vol% single-walled carbon nanotube at 10.2 GHz frequency [119].

**Fang G. et al. (2021)** prepared  $\text{Ba}(\text{Zr-Ni})_{0.6}\text{Fe}_{10.8}\text{O}_{19}/\text{Fe}_3\text{O}_4$  composites at various temperatures (room temperature, 200, 400, and 600 °C). The increment in heat treatment enhanced the exchange coupling effect between hard/soft ferrites. The effective bandwidth of 6.88 GHz and the reflection loss peaked at 1.9 mm thickness of -43.08 dB. The enhanced microwave absorption was ascribed to a large magnetic loss [120].

**Tran N. et al. (2021)** synthesized  $\text{Ba}_{1-x}\text{La}_x\text{Fe}_{12}\text{O}_{19}$  with  $x = 0, 0.1, 0.3,$  and  $0.5$  by co-precipitation at 900 °C for 3 hours. When  $\text{Ba}_{1-x}\text{La}_x\text{Fe}_{12}\text{O}_{19}$  ( $x = 0.0$ ) was mixed with polyaniline (10 % wt), the absorber exhibited more than 90 % absorption of an incident wave for the thickness of 1.75-3.50 mm, with an effective bandwidth of 2.52 GHz [121].

**Singh C. et al. (2021)** comprehensively analyzed the absorption performance of  $\text{Ba}_{(1-x)}\text{Sr}_x\text{Fe}_{12}\text{O}_{19}$  and paraffin wax-prepared composites. The introduction of  $\text{Sr}^{2+}$  reduced the magnetic and dielectric loss tangent of composites. A narrow and wide REL had been observed in the  $x = 0.2$  and  $x = 0.0$  composite, respectively. While  $\text{Ba}_{0.4}\text{Sr}_{0.6}\text{Fe}_{12}\text{O}_{19}/\text{wax}$  composite showed  $-0.35\text{E-}03$  dB at 0.15 GHz [122].

**Rostami M. et al. (2021)** synthesized Co-Al-Ti doped  $\text{BaCo}_x\text{Al}_x\text{Ti}_x\text{Fe}_{12-3x}\text{O}_{19}$  /MWCNTs-epoxy resin composites by high-power ultrasonication. They explored the absorption characteristics of prepared samples in the 1-8 GHz frequency range at various levels of

substitution, from  $x = 0.0$  to  $0.4$ . All synthesized nanocomposites exhibited  $REL < -20$  dB, for a matching thickness  $< 1.75$  mm, with favorable microwave absorption properties. The nanocomposite bandwidth covered the frequency range of 1-18GHz by varying the thickness of the sample. The highest microwave absorption performance was displayed by nanocomposite with  $x = 0.3$ , at a matching thickness of 1.5mm with a bandwidth of 4.59 GHz and REL of -47.40 dB. Consequently, these nanocomposites exhibited high-efficiency microwave absorption capabilities despite their lightweight and thin structure, making them suitable for various applications as microwave absorbers [123].

**Aggarwal N. et al. (2021)** investigated the absorption characteristics of sol-gel citrate precursor synthesized  $Ni_{0.6}Zn_{0.4}(MgZr)_xFe_{2-2x}O_4$  ferrites. The microwave properties were evaluated using a VNA concluded that the insertion of Mg and Zr ions increased the dielectric/magnetic loss and a maximum REL of 35.10 dB had been obtained at 10.52 GHz of 4 mm thickness sample at  $x = 0.10$  [124].

**Widanarto W. et al. (2020)** revealed the effect of neodymium ions on barium ferrite composites by analyzing the morphology and magnetic properties of composites. The change in grain size, shapes, and grain distribution of NdBFCs was observed by substituting  $Nd^{3+}$  ions. As we increased the concentration of  $Nd^{3+}$  level, the average size of NdBFCs grains and porosity were decreased and increased, respectively. The saturation magnetization ( $M_s$ ) showed an increment when adding 2% of  $Nd_2O_3$  in to NdBFCs composites. Nicholson-Ross-Weir (NRW) method was used to examine microwave characteristics by calculating permittivity/permeability values in the frequency regime of 8.2-12.4 GHz. Addition of  $Nd^{3+}$  ascribed a widening of bandwidth in the 9-10 GHz frequency regime. With the achievement of minimum reflection loss and maximum absorption at various frequencies, NdBFCs were accomplished for microwave X-band absorber application [125].

**Feng G. et al. (2020)** reported the impacts of La doping in  $Ba_{0.4}Ca_{0.6}Fe_{11.4}Co_{0.6}O_{19}$  ferrites for analyzing absorption properties. XRD pattern showed the formation of a standard pattern of hexagonal  $BaFe_{12}O_{19}$  crystalline phases. Magnetic properties like saturation magnetization ( $M_s$ ), remnant magnetization ( $M_r$ ), coercivity ( $H_c$ ) were determined from hysteresis loops. As we raised the concentration of La in  $Ba_{0.4}Ca_{0.6}Fe_{11.4}Co_{0.6}O_{19}$  ferrites the value of  $M_s$  was decreased (80 emu/g to 50 emu/g), and a gradual increment in  $H_c$  and  $H_a$

was also observed. By using VNA, complex permittivity and permeability values were calculated which showed that La substituted ceramics have more  $\epsilon'$  and  $\epsilon''$  values than  $Ba_{0.4}Ca_{0.6}Fe_{11.4}Co_{0.6}O_{19}$  ceramics in the frequency regime of 21.5 - 34.9 and 6.6 - 44.3, respectively. The minimum REL of -5 dB at 8.6-12.9 GHz with a thickness of 1.5 mm and maximum reflection loss of -28.3 dB at 10.6 GHz were attributed to lanthanum substitution in  $Ba_{0.4}Ca_{0.6}Fe_{11.4}Co_{0.6}O_{19}$  ceramics [126].

**Phan T. L. et al. (2020)** investigated the effect of Co-Mn ions on the magnetic and crystalline structure of Ba-hexaferrite with the composition of  $BaCo_{1-x}Mn_xFe_{11}O_{19}$  which were synthesized via the co-precipitation method. XRD and SEM analysis show that the size of the particle rises with the increase of x. XAS spectra revealed that  $Co^{+2}$ ,  $Fe^{+3}$  and  $Mn^{+3,+4}$  ions exist concurrently in composition  $BaCo_{1-x}Mn_xFe_{11}O_{19}$ . M-H curves demonstrated that saturation magnetization shows decline behavior whereas coercivity increases gradually from x = 0 to 1. Such results make this composite a promising material for hard magnetic materials [127].

**Feng G. et al. (2020)** explored the impact of temperature on the magnetic, structural, and electrical properties of indium doped SrM hexaferrite. The analysis of hexaferrite structure was performed considering both non-centrosymmetric and centrosymmetric space groups. The total magnetic moment decreased with increasing the ambient temperature [128].

**Guan G. et al. (2020)** examined the absorption characteristics of a double-layer designed microwave absorber composed of carbon nanofibers and hollow  $Ba_2Co_2Fe_{12}O_{22}$ , over the frequency range of 2 to 18 GHz. Investigators observed that absorption results of double-layer structures were far better than single-layer absorbers with higher absorption intensity and a broader effective bandwidth. When 5 wt% of carbon nanofibers filled the absorbing layer of 1.15 mm thickness and 67 wt% of  $Ba_2Co_2Fe_{12}O_{22}$  microfibres filled the matching layer of 0.85 mm thickness, a minimal reflection loss = 85.5 dB at 16.1 GHz frequency was achieved, while REL less than -10 dB was found in the frequency regime 10.4 to 18 GHz [129].

**Anand S. et al. (2020)** reported structural, magnetic, morphological, and EM absorption characteristics of the PVDF/RGO/BaZrFe<sub>11</sub>O<sub>19</sub> composite. The shielding effectiveness (40.98

dB) was prominently due to higher magnetic (0.41) and dielectric (1.67) loss. An excellent shielding effectiveness of 48.59 dB was shown by 10 wt% BaZrFe<sub>11</sub>O<sub>19</sub>/polymer of small thickness 0.2 mm at 11.1 GHz [130].

**Liu C. et al. (2020)** enquired about the structured and magnetic properties of Eu-doped SrM hexaferrite nanoparticles. Using XRD analysis, investigators examined that a single-phase Sr<sub>1-x</sub>Eu<sub>x</sub>Fe<sub>12</sub>O<sub>19</sub> hexaferrite obtained up to x = 0.10 dopant content of Eu and a shift in peak was observed due to smaller ionic radii of Eu (0.95 Å) than Sr (1.13 Å). A VSM technique was used to carry out magnetic parameters at 5 K and 300 K, separately. Analysis showed that the value of saturation magnetization ( $M_s$ ) was considerably higher for 5 K than 300 K and overall, there was a continuous increment in  $M_s$  value up to x = 0.20 and hereafter a considerable decrease in  $M_s$  was observed [131].

**Jing Z. et al. (2020)** investigated the FeCo/SrM/PANI composite to evaluate its magnetic and microwave absorption characteristics. The hysteresis graphs of the composite were determined through VSM. Investigators reported a minimum value of  $M_s$  and  $H_c$  of 15.8 emu/g and 329.4 Oe for Fe@Sr@PANI composite, respectively. The transmission theory was employed to calculate the absorption properties through a vector network analyzer. The REL<sub>max</sub> of -22.1 dB at 8.5 GHz and bandwidth of 2.6 GHz under -10 dB at 2 mm thickness [132].

**Tran N. et al. (2019)** and his co-workers explored the absorption, structural, and magnetic properties of BaFe<sub>12-x</sub>Co<sub>x</sub>O<sub>19</sub> hexagonal ferrite synthesis via co-precipitation technique. XRD affirmed the existence of the secondary phase Ba<sub>2</sub>Co<sub>2</sub>Fe<sub>12</sub>O<sub>22</sub>. XAS results showed the coexistence of Fe<sup>3+</sup> and Co<sup>2+</sup> ions in BaFe<sub>12-x</sub>Co<sub>x</sub>O<sub>19</sub>. By VSM, it was investigated that the prepared sample showed the properties of the hard magnet due to the presence of the Y-type hexaferrite phase. The saturation magnetization ( $M_s$ ) and coercivity ( $H_c$ ) values plotted with temperature, and revealed that  $M_s$  decreased with increasing the concentration of x and dropped with the temperature increment from 15 to 300 K, while  $H_c$  declined with the increment of both T and x. Investigators analyzed the frequency-dependent parameters which showed that  $\epsilon''$  values were negative at x = 1 and 2 and maximum reflection loss (> -5 dB) at frequency 0.1 to 15 GHz were observed. So, the prepared composite enhanced the EMA properties at a frequency above 15 GHz [133].

**Barakat M. M. E. et al. (2020)** analyzed  $\text{Hg}^{2+}$  doped barium hexaferrite in terms of magnetic, structural, and electron paramagnetic resonance characteristics. The investigated samples were synthesized via the co-precipitation technique. XRD revealed the existence of a pure M-type phase and minor traces of  $\text{Fe}_2\text{O}_3$ , which further decreased with the increment of substitution. The hysteresis loop technique was utilized to determine magnetic properties. Authors reported a non-linear decrease in coercivity (4943 to 4345 Oe) and, an increase in saturation magnetization (56.38 to 62.33 emu/g), as the content of  $\text{Hg}^{2+}$  ions increased [134].

**Handoko E. et al. (2019)** employed a conventional ceramic method and planetary ball mill method to synthesize Barium hexaferrite (BHF)  $\text{BaFe}_{12}\text{O}_{19}$  and  $\text{Fe}_3\text{O}_4$  powder, respectively for investigating the capabilities of multilayer absorbers in the X band frequency region. XRD pattern showed a single phase of  $\text{BaFe}_{12}\text{O}_{19}$  and  $\text{Fe}_3\text{O}_4$ . The hysteresis loop technique was utilized to determine magnetic properties which represent the value of saturation magnetization ( $M_s$ ) for both the samples was about 0.25 Tesla. On the other side the value of the coercive field ( $H_c$ ) of  $\text{BaFe}_{12}\text{O}_{19}$  was remarkably bigger than the coercive field ( $H_c$ ) of  $\text{Fe}_3\text{O}_4$ . The transmission line theory method was deployed to measure absorption parameters, and the efficient reflection loss was observed at a thickness of 10 mm with effective bandwidth below -10 dB. Hence, results show that the sum of layers and thickness of samples are inevitable factors for increasing the capacity of the EM absorber [135].

**Shoostary Veisi S. et al. (2019)** explored  $\text{Ba}_{0.5}\text{Sr}_{0.5}\text{Cu}_x\text{Zr}_x\text{Fe}_{12-2x}\text{O}_{19}$  hexaferrites nanoparticles for analyzing microwave and magnetic characteristics. The magnetic properties were evaluated by using the VSM technique. Investigators observed an inclination in values of saturation magnetization from  $x = 0.0$  to  $x = 0.4$  and then declined to the minimum value of 48.6 emu/g in  $x = 0.8$ . The decline in coercivity was also observed from 5010 Oe to 301.180 Oe by increasing the doping content of Cu – Zr in Ba/Sr hexaferrite. The microwave properties were evaluated using a VNA (vector network analysis) method. The study concluded that REL (Reflection loss) values show non-linear behavior and showed a maximum REL of -15.2 dB in  $x = 0.4$  at 11.1 GHz after that there is a gradual decline in REL value. Investigators conclude that  $\text{Ba}_{0.5}\text{Sr}_{0.5}\text{Cu}_{0.4}\text{Zr}_{0.4}\text{Fe}_{12-2(0.4)}\text{O}_{19}$  can play an important role in microwave absorption [136].

**Handoko E. et al. (2019)** synthesized  $BaFe_{12}O_{19}$  and  $BaFe_{10}CoZnO_{19}$  double-layer composite via solid-state reaction methodology for investigating absorption characteristics in X-band frequencies. VNA results revealed that the prepared absorber of 5 mm thickness exhibited a REL of -5 dB [137].

**Khandani M. et al. (2019)** comprehensively analyzed the magnetic and structural properties of  $Sr(CeNd)_{x/2}Fe_{12-x}O_{19}$  hexaferrites doped with Ce-Nd ions. The sample was prepared through the co-precipitation methodology and characterized by various techniques. By using the VSM method it was demonstrated that remnant magnetization,  $M_s$ , and  $H_c$  values fall gradually with the increment of dopant ions. The absorption properties of samples were analyzed by two methods. The simulation method and direct calculation of REL values using  $S_{11}$  parameters and results conclude that absorption was a maximum of -37.18 dB at 9.62 GHz at  $d = 2.5$  mm was obtained due to the second method. Hence, the prepared composites were a promising material as microwave absorbers to operate in-X band [138].

**Gunanto Y. et al. (2019)** employed a solid-state reaction methodology to prepare  $Ba_{0.6}Sr_{0.4}Fe_{10}MnTiO_{19}$  composite paint and investigated microwave absorption characteristics. VNA technique was utilized to determine the absorption characteristics of samples. The ability of microwave absorbers was better in the sample with spray times 10, with a REL nearly -4.02 dB at 9.7 GHz [139].

**Peymanfar R. et al. (2019)** analyzed the microwave absorption properties of  $BaFe_{12}O_{19} / La_{0.5}Sr_{0.5}MnO_3$  nanocomposites by adding graphene oxide (GO) with several mass fractions using a freeze dryer. VSM was deployed to determine the magnetic properties of prepared nanocomposites at an applied magnetic field of 15 kOe. The transmission line theory was used to determine the REL value of nanocomposites with several mass fractions of GO. Results revealed that the saturation magnetization ( $M_s$ ) of  $BaFe_{12}O_{19} / La_{0.5}Sr_{0.5}MnO_3$  nanocomposites were diminished from 54.86 to 22.55 (emu  $g^{-1}$ ) and a considerable increase in  $M_s$  value (decrease in  $H_c$ ) was obtained by adding graphene oxide (GO) in these nanocomposites. The highest REL of  $GO_{2.5\%} / BaFe_{12}O_{19} / La_{0.5}Sr_{0.5}MnO_3$  nanocomposites was 67.10 dB at 11.6 GHz with a thickness of 2.25 mm. Interestingly, the composite shows metamaterial properties [140].

**Mohammed J. et al. (2019)** investigated microwave absorption, EM shielding, and optical sensing characteristics of  $\text{Ba}_{1-x}\text{Co}_x\text{Fe}_{12-x-y}\text{Dy}_x\text{La}_y\text{O}_{19}/\text{Ca}_{1-x}\text{Er}_x\text{Cu}_3\text{Ti}_{4-y}\text{Mn}_y\text{O}_{12}$  composites. Morphology analysis revealed hexagonal and cubic-like structures of BaM and CCTO particles, respectively. Composite  $\text{Ba}_{0.7}\text{Co}_{0.3}\text{Fe}_{11.1}\text{Dy}_{0.3}\text{La}_{0.6}\text{O}_{19}/\text{Ca}_{0.7}\text{Er}_{0.3}\text{Cu}_3\text{Ti}_{3.4}\text{Mn}_{0.6}\text{O}_{12}$  showed maximum REL = -27.9 dB of 3 mm thickness at 16.5 GHz with an effective bandwidth (REL < -10 dB) 1.7 GHz. Whereas the same composite exhibited a shielding effectiveness of 41.8 dB at 16.5 GHz [141].

**Singh C. et al. (2019)** fabricated  $\text{Ba}_{0.5}\text{Sr}_{0.5}\text{Co}_x\text{Ti}_x\text{Fe}_{12-2x}\text{O}_{19}/\text{PANI}$  composites with a volume fraction of 70: 30. The good electrical conductivity of PANI and substitution of Co-Ti ions enhanced the attenuation of the microwave signal. The maximum attenuation of -40.9 dB at 12.4 GHz had been observed in the  $x = 0.8$  composition [142].

**Mansour S. et al. (2018)** explored nanocomposites comprising  $\text{BaFe}_{11.7}\text{Al}_{0.15}\text{Zn}_{0.15}\text{O}_{19}$  (M-type hexaferrite) and  $\text{Mn}_{0.8}\text{Mg}_{0.2}\text{Fe}_2\text{O}_4$  (spinel ferrite) were prepared through the citrate combustion method, following the formula  $[(x) (\text{BaFe}_{11.7}\text{Al}_{0.15}\text{Zn}_{0.15}\text{O}_{19}) + (1-x) (\text{Mn}_{0.8}\text{Mg}_{0.2}\text{Fe}_2\text{O}_4)]$ ; where  $x = 0.3, 0.4, \text{ and } 0.5$ . Upon the addition of the  $\text{BaFe}_{11.7}\text{Al}_{0.15}\text{Zn}_{0.15}\text{O}_{19}$  phase,  $M_r$  and  $H_c$  of the nanoparticles increased significantly, and showed enhancement of 2 and 2.5 times, respectively. In the case of the nanocomposites with  $x = 0.4$ , the Cole-Cole plots exhibited two successive semicircles at different temperatures. At low frequencies, the first semicircle indicated the contribution of grain boundaries, while with second semicircle at higher frequencies attributed to the grain conduction process [143].

**Tyagi S. et al. (2018)** fabricated  $\text{BaFe}_{12}\text{O}_{19}/\text{ZnFe}_2\text{O}_4$  nanoparticle to investigate RADAR absorbing characteristics in its wave band. The VSM analysis revealed that an increment in heat treatment led to an increase in  $M_s$  from 24.10 to 53.49 emu/g. When 20 % by weight CNTs were combined with  $\text{BaFe}_{12}\text{O}_{19}/\text{ZnFe}_2\text{O}_4$  to form a 2 mm thickness composite, the  $\text{REL}_{\text{max}}$  of -43. 22 dB were obtained at 10.30 GHz and bandwidth reaches 2.95 GHz for REL = -10 dB [144].

**Sai R. et al. (2018)** enquired about the effect of Co-Ti ions on SrM hexaferrite for EM noise suppression above 6 GHz. The hysteresis results revealed as the Co-Ti content increased, a fall observed in  $H_c$  from 710 to 40 Oe. The power loss ratio in the magnetic element to the input power when placed on top of a microstrip line was measured to assess EM noise



suppression. EM noise suppression of up to 20% was accomplished using a 500 nm thick composite sheet [145].

**Patel C. K. *et al.* (2017)** synthesized  $\text{CoFe}_2\text{O}_4/\text{Sr}_2\text{Co}_2\text{Fe}_{12}\text{O}_{22}$  composite by chemical coprecipitation methodology. They explored structural, magnetic, and dielectric characteristics of synthesized composites with changing ratios (1:0, 3:7, 4:6, 6:4, 7:3, 0:1). The VSM analysis revealed the  $M_s$  ranged from 50.44 to 31.21 emu/g, whereas  $M_r$  varies from 11.18 to 3.70 emu/g. The general dielectric behavior was shown by all synthesized composites [146].

**Nikmanesh H. *et al.* (2016)** examined magnetic, structural, and absorption characteristics of  $\text{BaCu}_x\text{Mg}_x\text{Zr}_{2x}\text{Fe}_{12-2x}\text{O}_{19}/\text{MWCNTs}$  over the frequency regime of 1 GHz to 18 GHz. Investigators observed that a decrease in  $M_s$  value and  $H_c$  varied non-linearly from 4689 to 256 G. It could be seen that with increasing the level of substitution the REL values of  $\text{BaCu}_x\text{Mg}_x\text{Zr}_{2x}\text{Fe}_{12-2x}\text{O}_{19}/\text{MWCNTs}$  composite increased and  $x=0.5$  exhibited large REL of -23.1 dB at 6 GHz for 2.1 mm thickness. The investigation concluded that the reflection loss of synthesized composites depends on the thickness of the absorber [147].

**Seyed Dorraji M. S. *et al.* (2016)** successfully synthesized polypyrrole- $\text{SrFe}_{12}\text{O}_{19}$ - $\text{TiO}_2$ -epoxy resin nanocomposites and investigated absorption performance within the X-band range. The contribution of both magnetic and dielectric loss resulted REL of -15 dB in the frequency range of 9.2 to 10.8 GHz [148].

**Ren X. *et al.* (2016)** explored Co-Zn doped barium hexaferrite/carbonyl iron composite at 1 to 14 GHz for investigating microwave absorption characteristics. A vector network analyzer evaluated the microwave absorption regarding REL through  $\epsilon_r/\mu_r$ . Authors observed absorption characteristics of double-layer absorbers are far better than those of single-layer due to coupling interactions between absorption and matching layers. REL of -55.4 dB at 2.7 mm and a maximum bandwidth of 10.8 GHz for REL < -10 dB was reported at 1.4 mm [149].

**Durmus Z. *et al.* (2015)** prepared graphene sheet (EGO) decorated SrM hexaferrite via sol-gel citrate combustion methodology. A VSM was deployed to determine the magnetic

properties of prepared nanocomposites at an applied magnetic field of 15 KOe. Investigators reported addition of EGO layers diminished the  $M_s$  of composites [150].

**Singh L. et al. (2015)** investigated electrical and microwave characteristics of  $\text{Ba}_{0.5}\text{Sr}_{0.5}\text{Co}_x\text{Zr}_x\text{Fe}_{(12-2x)}\text{O}_{19}$  hexaferrite as a function of composition and frequency. VNA results showed that the maximum REL of -13.91 dB (3.5 mm) was observed in  $\text{Ba}_{0.5}\text{Sr}_{0.5}\text{Co}_{0.8}\text{Zr}_{0.8}\text{Fe}_{10.4}\text{O}_{19}$  composition at 9 GHz due to an increase in grain connectivity and reduction in grain boundaries [151].

**Hosseini S. et al. (2015)** fabricated core-shell structure  $\text{SrTiO}_3/\text{SrFe}_{12}\text{O}_{19}/\text{PANI}$  composites which were nanometer in size. TEM, XRD, VSM, and VNA were deployed to examine the morphology, structure, magnetic, and absorption characteristics of synthesized composites. The addition of PANI results decreased in magnetic properties and an increase in conductivity (helps in dielectric loss). A minimum REL of -15 dB with 1 mm thickness at 9.2 GHz had been observed [152].

**Hazra S. et al. (2015)** reported magnetic and microwave characteristics of  $(\text{Ni}_{0.65}\text{Zn}_{0.35}\text{Fe}_2\text{O}_4)_x - (\text{BaFe}_{12}\text{O}_{19})_{1-x}$  composites by one-pot and physical mixing method. XRD, TEM, and SEM affirmed the existence of both hard/soft phases. Synthesis through the one-pot method improved the saturation magnetization and coercivity because of well exchange coupling in hard/soft ferrite. Composition  $x = 0.85$  exhibited REL of -21 dB for 3.5 mm thickness at 9.86 GHz [153].

## 2.2 Research Gaps

After the literature review, there are some research gaps which are mentioned below:

(a) The literature reported that the best-performing hard magnetic materials contained a certain amount of rare-earth materials. Unfortunately, the high cost of rare earth materials makes them less accessible and viable for commercial use. In contrast, soft magnetic materials are more economical and less reactive. Therefore, achieving the optimal blend of these hard and soft magnetic materials can improve chemical and physical properties while being cost-effective. The addition of a spinel phase might improve the material's magnetic,

electrical, and absorption characteristics, enhancing the technological significance of the composite.

(b) Very few researchers have conducted analyses that correlate the morphology of substituted M-type hexaferrites and their composites with their electrical, magnetic, and absorption characteristics.

(c) To enhance the microwave absorption of M-type hexaferrite material, several composites containing spinel ferrite and conducting polymer can be formulated. However, microwave-absorbing composites of rare-earth/transition metal substituted M-type hexaferrite with a fixed ratio of spinel ferrite, and PANI composites have received limited exploration.

The purpose of the present research is to synthesize an economical and tunable absorption bandwidth microwave absorber with REL > -10 dB (90% absorption) to suppress electromagnetic interference. The prime objective of preparing hexaferrite composites is to mold them in any shape because pure strontium hexaferrite is mechanically hard and thus difficult to machine. To overcome this problem, composites are made by selecting the optimal weight ratio of the matrix (ferrite), and filler material and REL must remain  $\geq$  -10 dB. The composites of hexaferrite may or may not dilute the magnetic and dielectric characteristics due to their different crystal structures. Thus, we tested samples for different microwave frequency ranges X -band (8.2 to 12.4 GHz) and K<sub>u</sub> -band (12-18 GHz). We are reporting results of samples wherein REL  $\geq$  -10 dB at the mentioned bands.

### **2.3 Objective of this study**

This research aims to synthesize divalent/trivalent substituted M-type hexaferrite material and their composite which will be able to absorb EM radiation in the GHz frequency spectra. The main objectives are to:

- i. To investigate structural, electrical, and magnetic properties of rare-earth/transition metal-doped hexaferrite composite.
- ii. To study and enhance microwave absorption of hexaferrite composites.
- iii. To correlate hysteresis and absorption properties.

---

# CHAPTER 3

## RESEARCH METHODOLOGY AND CHARACTERIZATION

---

In the present study, our objective is to utilize the sol-gel method for the synthesis of pure strontium hexaferrite and doped strontium hexaferrite. The synthesis methodology significantly influences various important properties of hexaferrite, including its structure, morphology, and electrical, and magnetic behavior. However, these properties are also heavily influenced by the composition, dopant type, doping concentration, and calcination temperature of the synthesized material. Furthermore, we prepared hexaferrite composites with spinel ferrite ( $\text{CoFe}_2\text{O}_4$ ), Polyaniline (PANI), and Magnetite ( $\text{Fe}_3\text{O}_4$ ). Substituted M-type hexaferrite and spinel ferrite ( $\text{CoFe}_2\text{O}_4$ ) are successfully synthesized using the sol-gel technique and polyaniline (PANI) which is a conducting polymer will be synthesized via chemical oxidative polymerization. To prepare PANI, it is essential to carefully select the dopant, oxidant, and synthesis techniques. Moreover, we directly purchased Magnetite ( $\text{Fe}_3\text{O}_4$ ) from Sigma-Aldrich company. For the preparation of strontium hexaferrite composites, it is important to choose a quick and facile synthesis procedure to ensure excellent entanglement of composite material with strontium hexaferrite.

### 3.1 Method of Synthesis

#### 3.1.1 Sol-gel Auto combustion Methodology

It is a wet chemical technique widely utilized for synthesizing nanomaterials. There are several methodologies for synthesizing hexaferrites including chemical co-precipitation, a solid-state reaction route, a ceramic method, sol-gel auto combustion, and microemulsion, etc. However, this method has gained popularity and widespread acceptance due to its significant advantages over other synthesis methods. The benefits of the sol-gel auto-combustion method include desirable particle size, formulation of nano-size particles, low cost, and high homogeneity. In this method (Fig. 3.1), the raw materials, typically metal nitrates or alkoxides, are dissolved in a liquid medium such as water, ethylene glycol, or a suitable acid to form a colloidal suspension known as “sol”. The sol is then subjected to

aging, followed by heating to form a solid network called the “gel”. Further heating or drying of the gel at higher temperatures causes the liquid medium to evaporate, transforming the gel into a “precursor”. It is worth noting that a sol refers to a colloid suspended in a liquid, while a gel is a suspension that maintains its shape, thus giving to the name “sol-gel” [154].

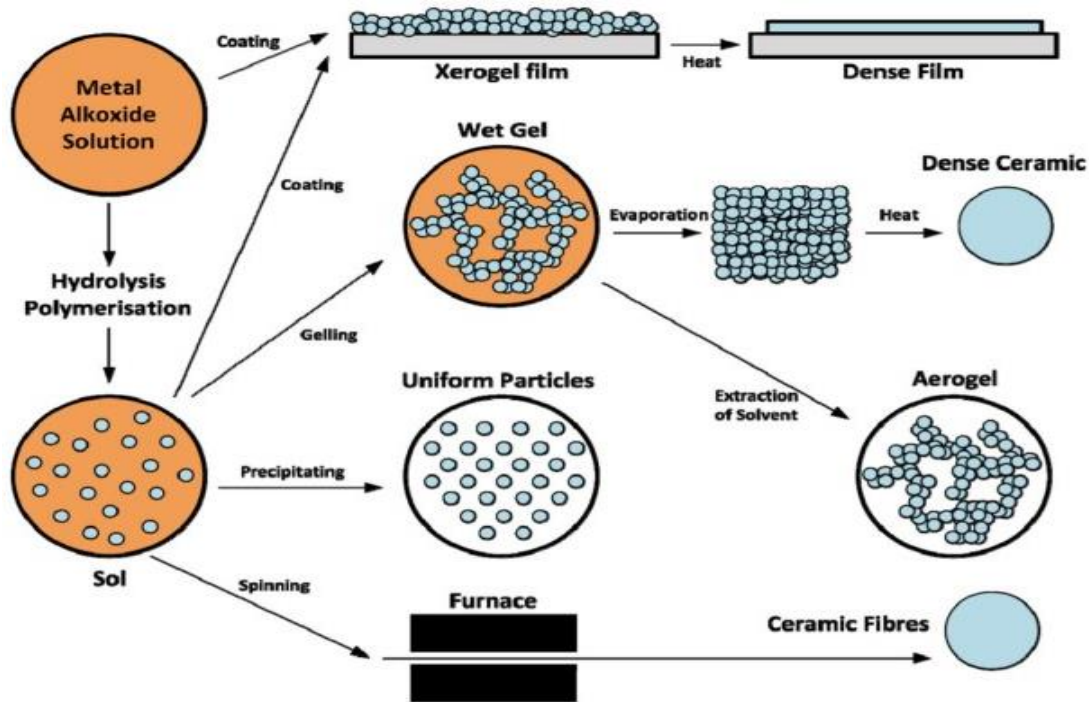


**Fig. 3.1.** Sol-gel auto combustion process

The sol-gel auto-combustion method primarily involves the hydrolysis, condensation, and polymerization of monomers, leading to the formation of particles that subsequently agglomerate. This process is followed by the development of networks that spread throughout the liquid medium, resulting in the formation of a gel-like solution [155]. Hydrolysis refers to the chemical decomposition of a compound due to its reaction with water, while condensation is the conversion of a gas vapor into a liquid state [156].

Fig. 3.2 illustrates the Schematic procedure of sol-gel auto combustion methodology followed in the present manuscript. The incorporated nitrates were of analytical reagent grade and  $C_6H_8O_7$  (citric acid) was employed as a chelating agent. All the precursors were weighed according to the stoichiometric calculations and cation to citric acid was retained at 1:1.5 ratios. The aqueous solution was prepared by mixing nitrates of all the cations with de-ionized water and preserved on a magnetic stirrer for some time. Ammonia solution was gradually added to maintain the pH 7-8 of an aqueous solution. Furthermore, the prepared aqueous solution was placed on a magnetic stirrer for about 8-9 h at  $70^\circ C - 80^\circ C$ , which resulted in a viscous solution and later formed a brownish gel. The gel gets burnt with the

progressive temperature and results in the formation of powder. Thereafter, the powdered sample was pre-sintered for 2 hours at 550 °C and sintered at 1100 °C/5 h with an increasing rate of the temperature of 12 °C/ min.

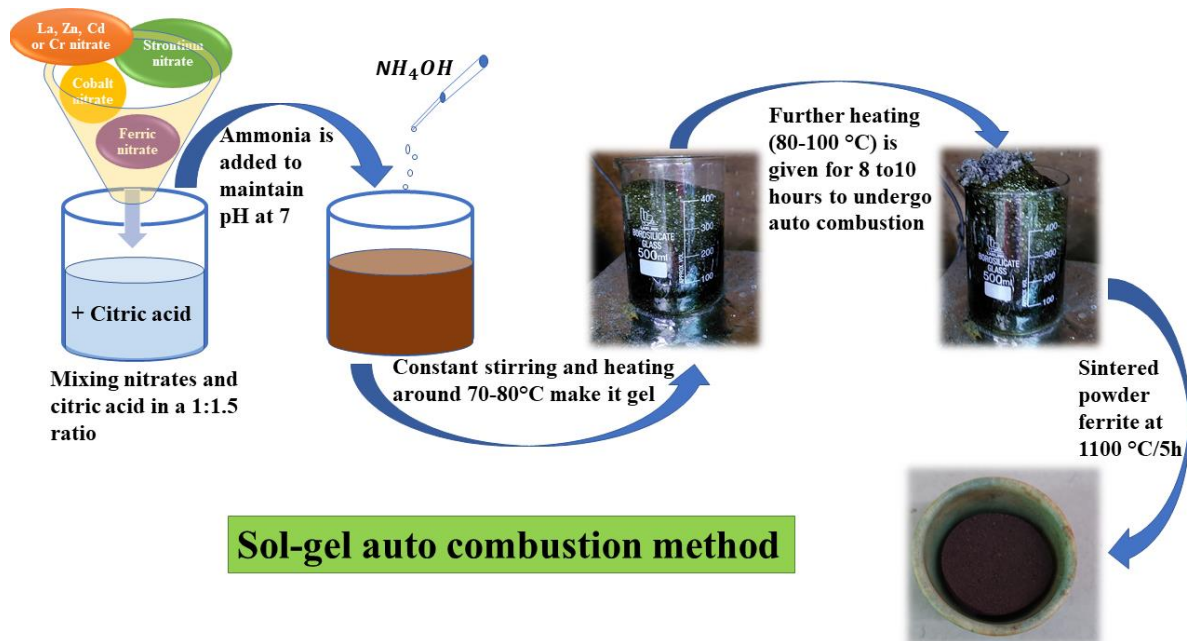


Fig. 3.2. Schematic procedure of Sol-gel combustion

### 3.1.2 Polyaniline (PANI) synthesis method

The Chemical oxidative polymerization (COP) technique involves three main components: aniline (monomer), ammonium persulphate (oxidant), and hydrochloric acid (dopant or acidic medium). To prepare PANI, aniline (2 ml) was dispersed in 50 ml of HCl (0.1 M). In an ice bath, the mixture was stirred to form a homogeneous suspension and it was continuous for 2 hours until anilinium ions were formed. Meanwhile, a solution of ammonium persulphate (APS) was prepared by combining 5 g of ammonium persulphate with 50 ml of HCl (1 M). After that, the APS solution was added dropwise to the aforementioned aniline-HCl mixture while constantly stirring in an ice bath. This stirring process continued for 5-6 hours until the solution turned dark green, indicating the formation of the conducting form of PANI, known as emeraldine salt (ES). Overnight, the solution was placed in an ice bath, and the subsequent precipitates were filtered under a vacuum. To remove any remaining residues, the PANI precipitates were washed multiple times with HCl and distilled water. In the end, PANI green precipitates were dried for 12 hours in a hot air oven at 70 °C and subsequently ground into a fine powder using a mortar pestle. The schematic diagram of the synthesis of PANI is illustrated in Fig. 3.3.

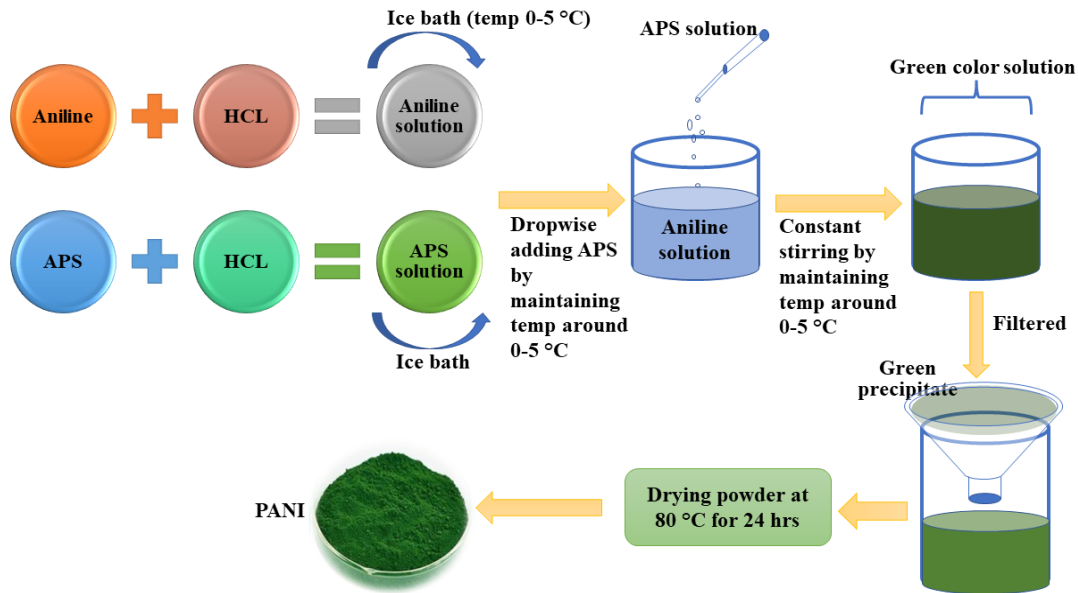


Fig. 3.3. Schematic procedure of preparing PANI.

### 3.1.3 Synthesis of ferrite composites

Blending, sometimes called direct compounding, is a quick and efficient process for preparing ferrite composites. Within the realm, there are several ways involved in blending procedures such as solution, emulsion, mechanical, physical, and melt. These blending procedures facilitate the direct incorporation of filler and matrix material in precise proportions. The process entails separate filler and matrix material preparation, subsequently combined to yield the composite.

### 3.1.4 Synthesis of $\text{Co}^{2+}$ and $\text{La}^{3+}$ substituted SrM hexaferrite with composition $\text{SrCo}_{1.5z}\text{La}_{0.5z}\text{Fe}_{12-2z}\text{O}_{19}$

The equation of the combustion reaction is as follows:

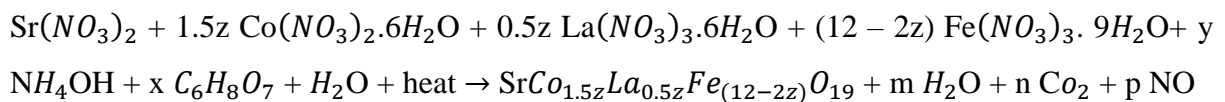
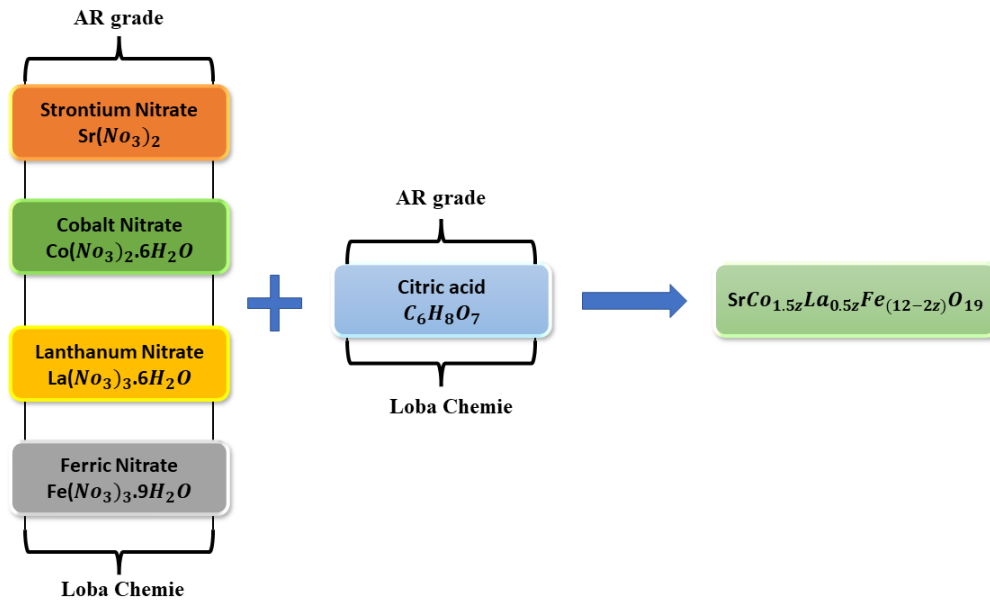


Fig. 3.4 illustrates the chemicals (AR grade) with the company name employed for the preparation of  $\text{SrCo}_{1.5z}\text{La}_{0.5z}\text{Fe}_{12-2z}\text{O}_{19}$  ( $0.0 \leq z \leq 0.5$ ) hexaferrite. The detailed description of chemicals used in quantity (g), as well as their properties studied using different characterization techniques, are mentioned in Table 3.1.



**Fig. 3.4.** Chemicals along with their company for the preparation of  $\text{SrCo}_{1.5z}\text{La}_{0.5z}\text{Fe}_{12-2z}\text{O}_{19}$ .

**Table 3.1** Detailed description of chemicals used in quantity (g) and performed characterization of  $\text{SrCo}_{1.5z}\text{La}_{0.5z}\text{Fe}_{12-2z}\text{O}_{19}$ .

Synthesis Material: Cobalt and Lanthanum doped Strontium hexaferrite ( $\text{SrCo}_{1.5z}\text{La}_{0.5z}\text{Fe}_{12-2z}\text{O}_{19}$ )						
Method of Synthesis: Sol-gel Method						
Doping Concentration: $z = 0.0, 0.1, 0.2, 0.3, 0.4, 0.5$						
Cations to citric acid ratio: 1:1.5						
Chemicals used with Mol. Wt. (g)	$\text{Sr}(\text{NO}_3)_2$	$\text{Co}(\text{NO}_3)_2 \cdot 6\text{H}_2\text{O}$	$\text{La}(\text{NO}_3)_3 \cdot 6\text{H}_2\text{O}$	$\text{Fe}(\text{NO}_3)_3 \cdot 9\text{H}_2\text{O}$	$\text{C}_6\text{H}_8\text{O}_7$	
Amount of chemicals used (In g)	$z = 0.0$	2.11	-	-	48.48	37.46
	$z = 0.1$	2.11	0.43	0.21	47.67	37.46
	$z = 0.2$	2.11	0.87	0.43	46.86	37.46
	$z = 0.3$	2.11	1.30	0.64	46.05	37.46
	$z = 0.4$	2.11	1.74	0.86	45.24	37.46
	$z = 0.5$	2.11	2.18	1.08	44.44	37.46
Characterization studied: Structural, Morphology, Magnetic, Electrical, and Microwave absorption						



### 3.1.5 Synthesis of $\text{Co}^{2+}$ and $\text{Cr}^{3+}$ substituted $\text{SrM}$ hexaferrite with composition $\text{Sr}(\text{CoCr})_x\text{Fe}_{(12-2x)}\text{O}_{19}$

The equation of the combustion reaction is as follows:

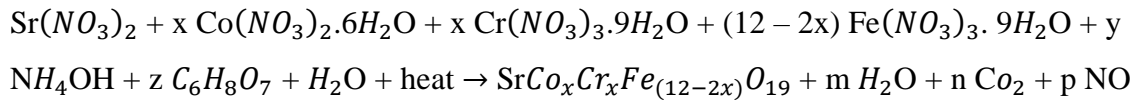


Fig. 3.5 illustrates the AR grade chemicals with the company name utilized for the preparation of  $\text{Sr}(\text{CoCr})_x\text{Fe}_{(12-2x)}\text{O}_{19}$  ( $0.0 \leq x \leq 1.0$ ) hexaferrite. The detailed description of chemicals used in quantity (g), as well as their properties studied using different characterization techniques, are mentioned in Table 3.2.

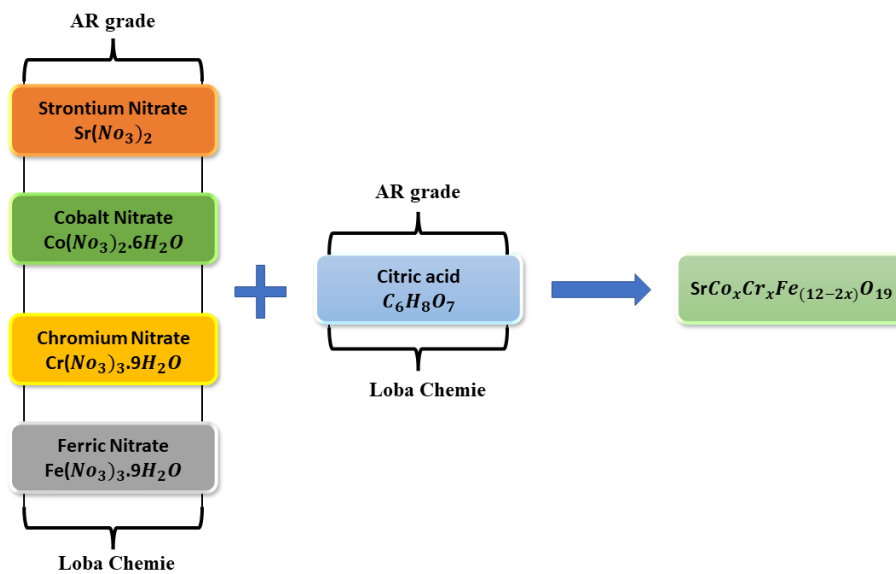


Fig. 3.5. Chemicals along with their company for the preparation of  $\text{Sr}(\text{CoCr})_x\text{Fe}_{(12-2x)}\text{O}_{19}$ .

Table 3.2 Detailed description of chemicals used in quantity (g) and performed characterization of  $\text{Sr}(\text{CoCr})_x\text{Fe}_{(12-2x)}\text{O}_{19}$ .

Synthesis Material: Cobalt and Chromium doped Strontium hexaferrite ( $\text{Sr}(\text{CoCr})_x\text{Fe}_{(12-2x)}\text{O}_{19}$ )						
Method of Synthesis: Sol-gel combustion Method						
Doping Concentration: $x = 0.0, 0.2, 0.4, 0.6, 0.8, 1.0$						
Cations to citric acid ratio: 1:1.5						
Chemicals used with Mol.	$\text{Sr}(\text{NO}_3)_2$	$\text{Co}(\text{NO}_3)_2 \cdot 6\text{H}_2\text{O}$	$\text{Cr}(\text{NO}_3)_3 \cdot 9\text{H}_2\text{O}$	$\text{Fe}(\text{NO}_3)_3 \cdot 9\text{H}_2\text{O}$	$\text{C}_6\text{H}_8\text{O}_7$	
Wt. (g)						
Amount of	$x = 0.0$	2.11	-	-	48.48	37.46

<b>chemicals used (In g)</b>	x = 0.2	2.11	0.58	0.80	46.86	37.46
	x = 0.4	2.11	1.16	1.60	45.24	37.46
	x = 0.6	2.11	1.74	2.40	43.63	37.46
	x = 0.8	2.11	2.32	3.20	42.01	37.46
	x = 1.0	2.11	2.91	4	40.4	37.46
<b>Characterization studied: Structural, Morphology, Magnetic, Electrical, and Microwave absorption</b>						

### 3.1.6 Synthesis of $\text{Co}^{2+}$ and $\text{Zn}^{2+}$ substituted SrM hexaferrite with composition $\text{SrCo}_x\text{Zn}_x\text{Fe}_{12-2x}\text{O}_{19}$

The equation of the combustion reaction is as follows:

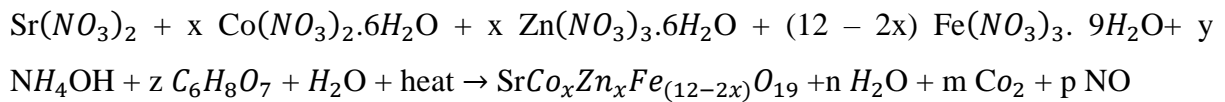
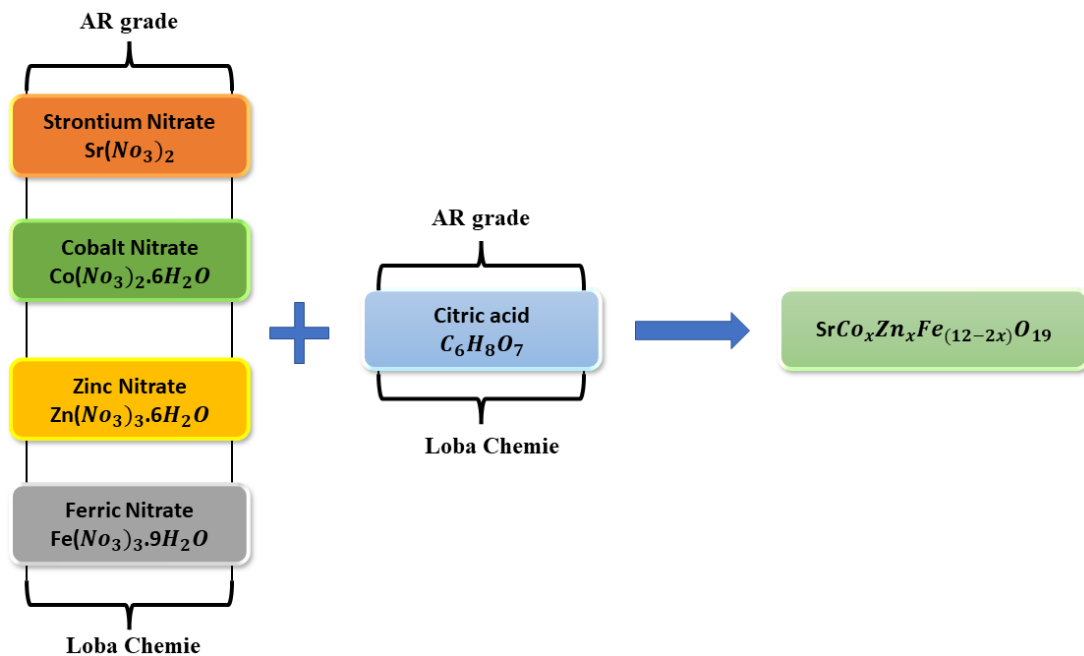


Fig. 3.6 illustrates the chemicals (AR grade) with the company name employed for the preparation of  $\text{SrCo}_x\text{Zn}_x\text{Fe}_{(12-2x)}\text{O}_{19}$  ( $0.4 \leq x \leq 2.0$ ) hexaferrite. The detailed description of chemicals used in quantity (g), as well as their properties studied using different characterization techniques, are mentioned in Table 3.3.



**Fig. 3.6.** Chemicals along with their company for the preparation of  $\text{SrCo}_x\text{Zn}_x\text{Fe}_{(12-2x)}\text{O}_{19}$ .

**Table 3.3** Detailed description of chemicals used in quantity (g) and performed characterization of  $SrCo_xZn_xFe_{(12-2x)}O_{19}$ .

Synthesis Material: Cobalt and Lanthanum doped Strontium hexaferrite ( $SrCo_xZn_xFe_{12-2z}O_{19}$ )						
Method of Synthesis: Sol-gel Method						
Doping Concentration: x = 0.4, 0.8, 1.2, 1.6, 2.0						
Cations to citric acid ratio: 1:1.5						
Chemicals used with Mol. Wt. (g)		$Sr(NO_3)_2$	$Co(NO_3)_2 \cdot 6H_2O$	$Zn(NO_3)_2 \cdot 6H_2O$	$Fe(NO_3)_3 \cdot 9H_2O$	$C_6H_8O_7$
Amount of chemicals used (In g)	x = 0.4	2.11	1.16	1.18	45.24	37.46
	x = 0.8	2.11	2.32	2.37	42.01	37.46
	x = 1.2	2.11	3.49	3.56	38.77	37.46
	x = 1.6	2.11	4.65	4.75	35.55	37.46
	x = 2.0	2.11	5.82	5.94	32.32	37.46
Characterization studied: Structural, Morphology, Magnetic, Electrical, and Microwave absorption						

### 3.1.7 Synthesis of $Co^{2+}$ and $Cd^{2+}$ substituted SrM hexaferrite with composition $SrCo_{1.5z}Cd_{0.5z}Fe_{12-2z}O_{19}$

The equation of the combustion reaction is as follows:

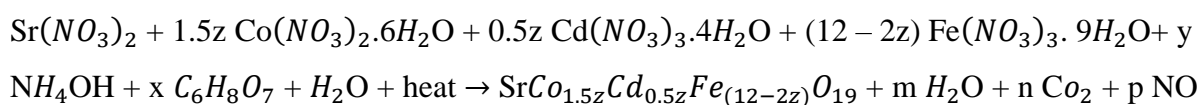
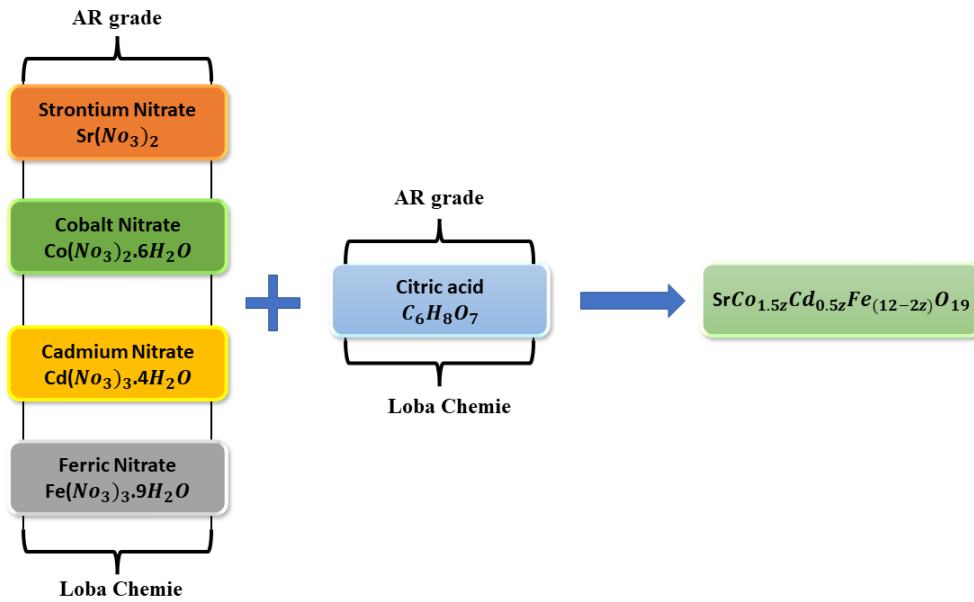


Fig. 3.7 illustrates the chemicals (AR grade) with the company name employed for the preparation of  $SrCo_{1.5z}Cd_{0.5z}Fe_{12-2z}O_{19}$  ( $0.2 \leq x \leq 1.0$ ) hexaferrite. The detailed description of chemicals used in quantity (g), as well as their properties studied using different characterization techniques, are mentioned in Table 3.4.



**Fig. 3.7.** Chemicals along with their company for the preparation of  $\text{SrCo}_{1.5z}\text{Cd}_{0.5z}\text{Fe}_{12-2z}\text{O}_{19}$ .

**Table 3.4** Detailed description of chemicals used in quantity (g) and performed characterization of  $\text{SrCo}_{1.5z}\text{Cd}_{0.5z}\text{Fe}_{12-2z}\text{O}_{19}$ .

Synthesis Material: Cobalt and Lanthanum doped Strontium hexaferrite ( $\text{SrCo}_{1.5z}\text{Cd}_{0.5z}\text{Fe}_{12-2z}\text{O}_{19}$ )						
Method of Synthesis: Sol-gel Method						
Doping Concentration: $x = 0.2, 0.4, 0.6, 0.8, 1.0$						
Cations to citric acid ratio: 1:1.5						
Chemicals used with Mol. Wt. (g)		$\text{Sr}(\text{NO}_3)_2$	$\text{Co}(\text{NO}_3)_{2.6}\text{H}_2\text{O}$	$\text{Cd}(\text{NO}_3)_{3.4}\text{H}_2\text{O}$	$\text{Fe}(\text{NO}_3)_3 \cdot 9\text{H}_2\text{O}$	$\text{C}_6\text{H}_8\text{O}_7$
Amount of chemicals used (In g)	$x = 0.2$	2.11	0.87	0.30	46.86	37.46
	$x = 0.4$	2.11	1.74	0.61	45.24	37.46
	$x = 0.6$	2.11	2.61	0.92	43.63	37.46
	$x = 0.8$	2.11	3.49	1.23	42.01	37.46
	$x = 1.0$	2.11	4.36	1.54	40.40	37.46
Characterization studied: Structural, Morphology, Magnetic, Electrical, and Microwave absorption						

### 3.1.8 Synthesis of $\text{SrCo}_{1.5z}\text{La}_{0.5z}\text{Fe}_{12-2z}\text{O}_{19}$ (80%) + $\text{Fe}_3\text{O}_4$ (20%) ferrite composites

As we have already discussed (Fig. 3.2) synthesis procedure of the  $\text{SrCo}_{1.5z}\text{La}_{0.5z}\text{Fe}_{12-2z}\text{O}_{19}$  hexagonal ferrite and  $\text{Fe}_3\text{O}_4$  (Magnetite) are directly purchased from Sigma Aldrich company. For the synthesis of hard/soft ( $\text{SrCo}_{1.5z}\text{La}_{0.5z}\text{Fe}_{12-2z}\text{O}_{19}$

(80%) + Fe<sub>3</sub>O<sub>4</sub> (20%)) ferrite composites, a physical blending method was utilized. To obtain a homogeneous mixture of the ferrite composites, the weight ratio of SrCo<sub>1.5z</sub>La<sub>0.5z</sub>Fe<sub>12-2z</sub>O<sub>19</sub>: Fe<sub>3</sub>O<sub>4</sub> was taken to be 1:5.

### **3.1.9 Synthesis of SrCo<sub>x</sub>Zn<sub>x</sub>Fe<sub>(12-2x)</sub>O<sub>19</sub> (80%) + PANI (20%) ferrite composites.**

As we have already discussed (Fig. 3.2) synthesis procedure of the SrCo<sub>x</sub>Zn<sub>x</sub>Fe<sub>(12-2x)</sub>O<sub>19</sub> hexagonal ferrite and Fig. 3.3 demonstrated the detailed synthesis procedure of PANI. For the synthesis of SrCo<sub>x</sub>Zn<sub>x</sub>Fe<sub>(12-2x)</sub>O<sub>19</sub> (80%) + PANI (20%) a physical blending method was utilized. To obtain a homogeneous mixture of the ferrite composites, the weight ratio of SrCo<sub>x</sub>Zn<sub>x</sub>Fe<sub>(12-2x)</sub>O<sub>19</sub>: PANI was taken to be 1:5.

### **3.1.10 Synthesis of Sr(CoCr)<sub>x</sub>Fe<sub>(12-2x)</sub>O<sub>19</sub> (80%) + CoFe<sub>2</sub>O<sub>4</sub> (20%) ferrite composites**

As we had already discussed (Fig. 3.2) synthesis procedure of Sr(CoCr)<sub>x</sub>Fe<sub>(12-2x)</sub>O<sub>19</sub> hexagonal ferrite, while CoFe<sub>2</sub>O<sub>4</sub> (spinel ferrite) has also been synthesized using sol-gel combustion methodology by utilizing analytical grade starting materials, including like Co(NO<sub>3</sub>)<sub>2</sub>.6H<sub>2</sub>O, and Fe(NO<sub>3</sub>)<sub>3</sub>.9H<sub>2</sub>O. During the spinel ferrite synthesis the ratio of all nitrates and citric acid (C<sub>6</sub>H<sub>8</sub>O<sub>7</sub>) was 1: 1. The prepared powder was calcined at 1100 °C/2h with a rate of heating of 12°C/ min. For the synthesis of hard/soft (Sr(CoCr)<sub>x</sub>Fe<sub>(12-2x)</sub>O<sub>19</sub> (80%) + CoFe<sub>2</sub>O<sub>4</sub> (20%)) ferrite composites, a physical blending method was utilized. The weight ratio of Sr(CoCr)<sub>x</sub>Fe<sub>(12-2x)</sub>O<sub>19</sub>: CoFe<sub>2</sub>O<sub>4</sub> was 1:5 to obtain a homogeneous mixture of the ferrite composites.

### **3.1.11 Synthesis of SrCo<sub>1.5z</sub>Cd<sub>0.5z</sub>Fe<sub>12-2z</sub>O<sub>19</sub> (80%) +20% PANI ferrite composites.**

As we have already discussed (Fig. 3.2) synthesis procedure of SrCo<sub>1.5z</sub>Cd<sub>0.5z</sub>Fe<sub>12-2z</sub>O<sub>19</sub> hexagonal ferrite and Fig. 3.3 demonstrated the detailed synthesis procedure of PANI. For the synthesis of SrCo<sub>1.5z</sub>Cd<sub>0.5z</sub>Fe<sub>12-2z</sub>O<sub>19</sub> +20% PANI a physical blending method was utilized. To obtain a homogeneous mixture of the ferrite composites, the weight ratio of SrCo<sub>1.5z</sub>Cd<sub>0.5z</sub>Fe<sub>12-2z</sub>O<sub>19</sub>: PANI was taken to be 1:5.

## 3.2 Characterization Technique

To determine the impact of cation substitution on the properties of prepared samples, an extensive array of characterization techniques has been utilized such as X-ray diffraction technique (XRD), Field emission scanning electron microscopy (FESEM), Fourier transform-infrared spectroscopy (FTIR), Mössbauer analysis, Vibrating sample magnetometer (VSM), Impedance analyzer, and Vector network analyzer (VNA).

### 3.2.1 X-ray diffraction technique (XRD)

XRD is a non-destructive and widely utilized technique for determining the phase purity and crystalline structure of synthesized materials at an atomic level. It is a long-range order technique that enunciates the strain, preferred orientation, impurity phases, lattice parameters, grain size, and structural defect within the crystal [157]. The wavelength of X-rays, which are EM waves, is roughly 0.1 nm, or about the same size as the distance between atoms. Fig. 3.8 depicts the snapshot of the Bruker D8 advanced X-ray diffractometer. Powder XRD works on the principle of constructive interference of cathode ray tube-generated monochromatic X-rays, as shown in Fig. 3.9. In multilayer structures, the arrangement of atoms at interfaces is precisely assessed through intensity measurements in XRD. It is essential to comprehend that this characterization method only works on materials that have a crystallization or are partially crystallized.

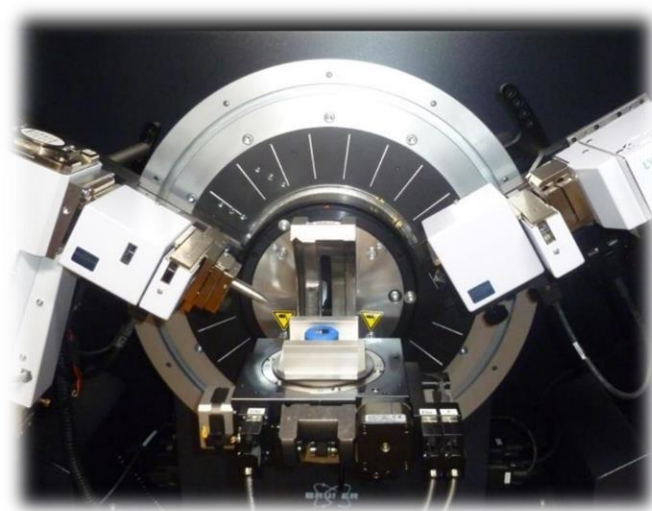


**Fig. 3.8. Snapshot of Bruker D8 advance [158].**

When the monochromatic beam of X-ray interacts with the specimen, it diffracts the incoming ray in arbitrary directions of  $2\theta$ , and a movable detector as a function of  $2\theta$  is deployed to measure the intensity of diffracted radiations. Thus, if the sample to be analyzed

acquires a regular arrangement of atoms, the scattered light is oriented in particular directions. For constructive interference, the diffracted X-rays should satisfy Bragg's law mentioned below [159]:

$$n\lambda = 2d_{hkl}\sin\theta$$

where  $n$ ,  $d_{hkl}$ ,  $\lambda$  and  $\theta$  signify the order of reflection, interplanar spacing, wavelength of X-ray (1.54 Å), and diffraction angle, respectively. The diffracted X-ray beam at different angles with different intensities is recorded by a detector. Afterward, the first step is indexing XRD peaks, which entails assigning the correct Miller indices to each peak in the diffraction pattern [160]. The indexing of peaks can be done by three methods: Analytical method, graphical method, and by comparing the measured XRD pattern with standard reference ICDD-cards.

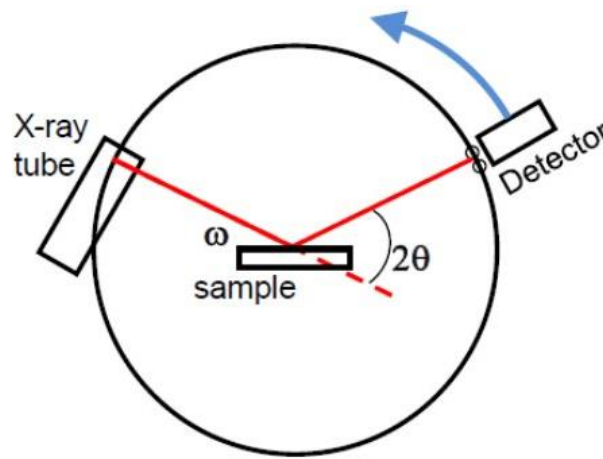


**Fig. 3.9. Schematic diagram of X-ray diffractometer [161].**

### 3.2.2 Parameters derived from XRD data

XRD analysis helps us to determine some useful structural parameters of M-type hexagonal ferrite samples. Some of them are discussed below. The structural parameter ( $a$ ,  $c$ , and  $c/a$ ), the volume of the unit cell ( $V$ ) has been estimated from the following expression [162]:

$$\frac{1}{d_{hkl}^2} = \frac{4}{3} \left( \frac{h^2 + hk + k^2}{a^2} \right) + \frac{l^2}{c^2} \quad (3.1)$$

In hexagonal ferrites  $\alpha = \beta = 90^\circ$ ,  $\gamma = 120^\circ$  and  $b = a \neq c$

$$V_{cell} = \frac{\sqrt{3}}{2} a^2 c \quad (3.2)$$

Where  $d_{(hkl)}$  displays interplanar distance which has been calculated from the relation  $2d_{hkl}\sin\theta = n\lambda$  and (hkl) implies Miller indices. We can calculate the crystallite size ( $D$ )

using the Debye-Scherrer equation, dislocation density ( $\delta$ ), and microstrain ( $\epsilon$ ) of the sintered samples using the following equation [163]:

$$D = \frac{k\lambda}{\beta_{hkl}\cos\theta} \quad (3.3)$$

$$\delta = \frac{1}{D^2} \quad (3.4)$$

$$\epsilon = \frac{\beta_{hkl}}{4\tan\theta} \quad (3.5)$$

Where  $\beta$  is displayed as the full width at half maxima (in radians),  $k = 0.9$  denotes as Scherrer constant,  $\theta$  implies Bragg's angle (radians),  $\rho_x$ =X-ray density, and  $\lambda$  (1.540 Å) x-ray wavelength. The spacing between magnetic ions denotes a hopping length and could be estimated using the following expression for octahedral and tetrahedral sites.

$$L_A = (a\sqrt{3})/4 \quad (3.6)$$

$$L_B = (a\sqrt{2})/4 \quad (3.7)$$

Here  $L_A$  and  $L_B$  represent hopping length for tetrahedral and octahedral sites, respectively. The bulk density ( $\rho_{bulk}$ ) can be calculated with the help of a pellet having thickness ( $h$ ), radius ( $r$ ), and mass of pellet ( $m$ ) using the following expression:

$$\rho_{bulk} = \frac{m}{\pi r^2 h} \quad (3.8)$$

The XRD density ( $\rho_x$ ) and porosity ( $P$ ) of the prepared specimen can be estimated using the below expression [164]:

$$\rho_x = \frac{zM}{N_A V} \quad (3.9)$$

$$P \% = \left(1 - \frac{\rho_{bulk}}{\rho_x}\right) \times 100 \quad (3.10)$$

$$S = \frac{6000}{D\rho_x} \quad (3.11)$$

Where  $N_A$  represent as Avogadro's number, M implies molecular weight and z, and V implies the no. of molecules per unit cell, and volume per unit cell, respectively.

### 3.2.3 Fourier Transform Infrared Spectroscopy (FTIR)

FTIR spectroscopy aids as a valuable tool for obtaining quantitative and qualitative insights into molecular band position, existing chemical bonds, and attached functional groups. FTIR is a versatile technique used to distinguish between inorganic and organic compounds [165]. The principle of FTIR spectroscopy is illustrated in Fig. 3.10. The infrared spectrum (IR) is typically categorized into three distinct regions by its wavelength range. The first one low-energy far-infrared encompasses the range of 400 to 10  $\text{cm}^{-1}$ , indicating



rotational and fundamental vibrations. The mid-infrared lies ranging from  $4000$  to  $400\text{ cm}^{-1}$ , are leveraged to explore associated rotations combined with vibrational structures [166]. Conversely, the near-infrared spanning from  $14000$ - $4000\text{ cm}^{-1}$  focuses on studying excite harmonic vibrations or overtone in experiments. The Perkin Elmer company FTIR spectrometer ( $4000$  to  $400\text{ cm}^{-1}$ ) has been employed for characterization purposes. This FTIR instrument boasts an impressive capability to swiftly measure the  $4000 - 400\text{ cm}^{-1}$  frequency spectrum in mere seconds. It incorporates a beam splitter that divides the incoming IR radiation into two components, one component remains at a fixed path length to introduce a path difference, while the second component varies with the position of a moving mirror. These two components of the beam undergo interference and culminate in a composite beam known as an interferogram, which is emitted from the interferometer. This interferogram entails comprehensive data of the entire signal that comes from the interferometer. Indeed, this comprehensive data is extracted at individual frequencies and decoded via software that employs a mathematical technique known as Fourier transformation.

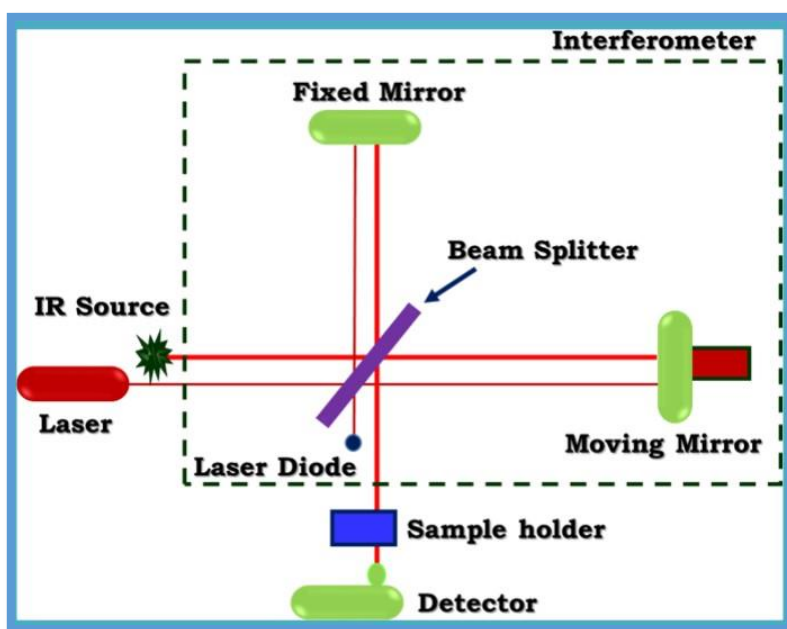


Fig. 3.10 Ray diagram of FTIR-spectrometer [167].

### 3.3.4 Field Emission Scanning Electron Microscopy

FESEM serves as a powerful and widely utilized technique for producing high-resolution images of the sample surface. In this technique, when electrons are incident on atoms, they produce signals that give insights into the elemental analysis, grain size, surface topology, particle size, etc. of the material. This enables the investigation of samples with a

spatial resolution of  $\sim 1$  nm (3 to 6 times better resolution than SEM images) and low electrostatic distortion [168].

FESEM is composed of an electromagnetic lens system and an electron gun to examine the morphology and surface structure of solids. In FESEM electrons are generated in vacuum by a field emission source and accelerated via a field gradient. A well-defined beam of electrons strikes the specimen and results in a variety of emissions depending on energies including secondary electrons, absorbed electrons, characteristics X-rays, backscattered electrons, etc., as seen in Fig. 3.11. A suitable detector is deployed to detect secondary electrons and produce electrical signals which are further converted into scan images and appear as a digital image of the sample on the monitor. The characteristic X-rays generated are utilized for the estimation and identification of different elements that exist in the sample by energy dispersive spectrometer (EDS) [169]. In this research, Field emission scanning electron microscopy (FESEM) (SIGMA 500VP) was used to study the morphology and elemental analysis.

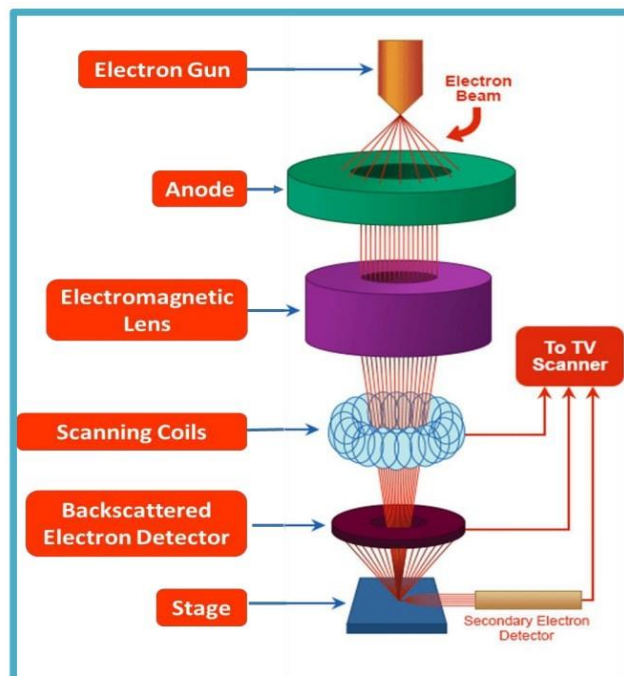


**Fig. 3.11 Ray diagram of FESEM [170].**

### **3.3.5 Vibrating Sample Magnetometer (VSM)**

A magnetic sample undergoing oscillatory motions generates a time-varying magnetic field in its surroundings because of its magnetization. When a coil is positioned near the sample, this phenomenon induces a voltage. This fundamental principle is harnessed in a vibrating sample magnetometer to examine the magnetic response of the sample [171]. This

involves placing the sample within the sample holder, which is then positioned between two sets of pick-up coils affixed to an electromagnet, as depicted in Fig. 3.12. A coherent magnetic field generated by the electromagnet causes the sample to experience induced magnetization. The sample holder, along with the sample inside, undergoes mechanical sinusoidal vibrations. When this vibrational component induces alterations in the magnetic field surrounding the sample, Faraday's principle of electromagnetic induction produces an electric field corresponding to this magnetization change [172]. The change in magnetic flux results in a voltage being induced in the pickup coils, which is directly proportional to the sample's magnetization. The software running on a computer connected to a VSM apparatus converts these changes into a graphical representation of magnetization (M) as a function of the applied magnetic field (H) [173].

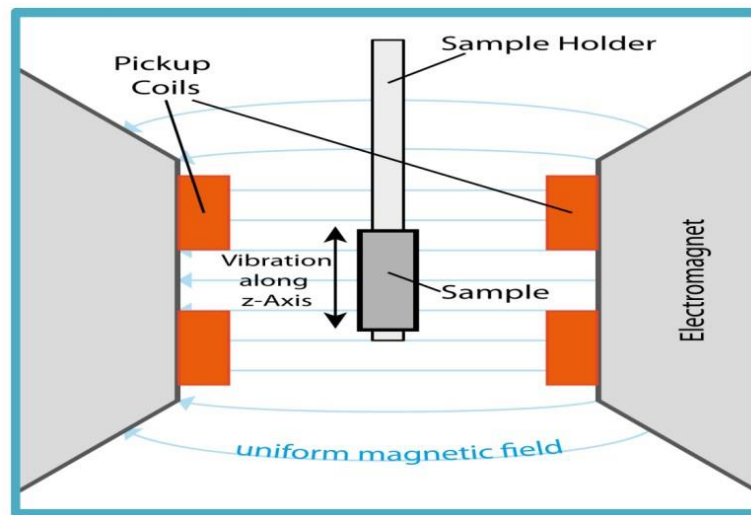


**Fig. 3.12 Schematic diagram of VSM [174].**

### 3.3.6 Parameters Derived from M-H loops

The VSM analysis provides us data in the form of M-H loops, wherein magnetization (M) is along the y-axis in terms of emu/g and the applied field (H) is along the x-axis in units of oersted (Oe). We can easily determine the magnetic parameters from M-H loops such as coercivity ( $H_c$ ), saturation magnetization ( $M_s$ ), anisotropy field ( $H_a$ ), squareness ratio (SQR), remanent magnetization ( $M_r$ ), Bohr-magneton ( $n_B$ ), and magnetic susceptibility ( $dM/dH$ ). The saturation law is used to derive the  $M_s$  and  $H_a$  of prepared specimens using the below equation [175]:

$$M = M_s(1 - A/H - B/H^2) + \chi_p H \quad (3.12)$$

Here  $M_s$  imply as saturation magnetization,  $\chi_p$  illustrates susceptibility at high field, A represents an inhomogeneity parameter, and B represents the anisotropy parameter

In the hexagonal symmetry of the crystal, we can calculate B using the below expression [176]:

$$B = H_a^2 / 15 = 4K_1^2 / 15M_s^2 \quad (3.13)$$

Here  $K_1$  denotes a constant of anisotropy and  $H_a$  implies an anisotropy field. Afterward, substituting the value of B in equation 4.13, we can easily estimate the value of  $H_a$ . The Bohr magneton ( $n_B$ ) shows a significant role in investigating the magnetic characteristics of the material, which is widely used in microwave and high-frequency applications and calculated using the following expression [177]:

$$n_B = \frac{M_s \times M.W}{5585} \quad (3.14)$$

Here M.W – Molecular weight,  $M_s$  – Saturation magnetization.

### (a) Squareness Ratio (SQR)

The squareness ratio (SQR) is described as the ratio of remanent to saturation magnetization ( $M_r/M_s$ ). It is a crucial parameter for determining the hardness of magnetic material and the existence of inter-grain groups in the synthesized samples. In M-type hexaferrite, the value of  $M_r/M_s$  is usually high and lies in the range of 0 and 1. The materials with a large squareness ratio ( $0.5 < M_r/M_s < 1$ ) are more anisotropic, single domain, and hard while those with  $0.05 < M_r/M_s < 0.5$  have randomly oriented multi-magnetic domains. The Stoner-Wohlfarth model of ferromagnetism is considered a basic model capable of explaining the magnetic behavior of grains that are sufficiently small enough to contain a single domain [178].

### (b) Switching Field Distribution ( $dM/dH$ )

The expression  $dM/dH$  symbolizes the magnetic susceptibility ( $\chi$ ) of the material and is used to estimate the effect of grains on magnetic characteristics and the magnitude of  $dM/dH$  elaborates the existence of switching or inversion field distribution. The hysteresis loop with infinite ( $\infty$ ) susceptibility ( $dM/dH$ ) at  $H_c$  and zero susceptibility at  $H \sim 0$  indicates the case of an ideal single domain [179]. The small peak height at  $H_m$  with narrow separation owes to the existence of large no. of unstable superparamagnetic domains along with an amorphous phase in the crystal structure. Alternatively, the wide separation between peaks with large peak heights at  $H_m$  specifies a magnetically stable state, higher grain size along with the well-crystalline structure of hexaferrite.

The investigation of  $dM/dH$  against  $H$ , known as switching field distribution, is often used for assessing the exchange-coupling effect between hard/soft ferrite composites. If the sample exhibits a single narrower peak in the switching field distribution attributed to a strong exchange coupling between soft/hard magnetic phases [180]. Conversely, the single peak with a shoulder peak suggests the weak coupling between them. The first single peak is attributed to reversible susceptibility and is the result of reversible domain wall movement, whereas the shoulder peak is ascribed to the involvement of an irreversible component or a contribution of the switching field [181].

### 3.3.7 Mössbauer Spectroscopy

Mössbauer spectroscopy is a spectroscopic method based on the Mössbauer effect, which involves the absorption and emission of gamma rays by atomic nuclei in a solid sample without any recoil. When the gamma-ray energy precisely matches the energy difference between the ground state and the excited state of a nucleus, resonance absorption occurs. This is feasible because atomic nuclei exist in specific, well-defined energy levels.

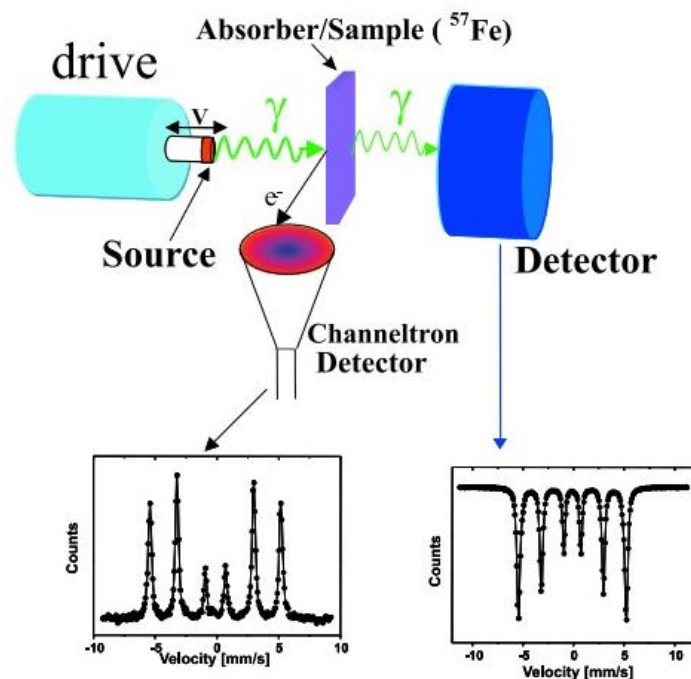


**Fig. 3.13. Schematic diagram Mössbauer spectroscopy [182].**

This spectroscopy configuration includes three major components: a gamma source, a detector, and a sample (as illustrated in Fig. 3.13). Typically, the gamma-ray source is  $^{57}\text{Co}$  (cobalt nuclei), which is inherently unstable. These cobalt nuclei typically decay into  $^{57}\text{Fe}$  (iron nuclei), ultimately reaching the ground state by emitting a gamma ray that is absorbed by the sample in a resonant manner. To achieve this, the gamma-ray source is often subjected

to acceleration through varying velocities, typically accomplished using a linear motor. This manipulation introduces the Doppler effect. When the velocity of the source aligns with the resonant energy level of the sample, a portion of the gamma ray is absorbed. This phenomenon results in a reduction in the intensity of the gamma-ray, an observable dip that is observable in the Mössbauer spectrum. Subsequently, the gamma-ray, generated in this process, is systematically scanned across a specified range of velocities for  $^{57}\text{Fe}$  and is subsequently detected by a specialized detector. A computer, connected to the detector, then generates a plot illustrating the relationship between gamma-ray intensity and the velocity of the source.

### 3.3.8 Impedance Analyzer

An impedance analyzer is an electronic device employed for assessing admittance and impedance. Fig. 3.14 displays a snapshot of the universal impedance analyzer. When a periodic current (AC test signal) and voltage are given to the circuit or device then the overall resistance offered to the flow of current is termed impedance. This periodic current is composed of both real and imaginary components. When the connection is done in series, the impedance can be expressed as follows [183]:

$$Z = R + jX$$

$$Z^* = Z' - jZ''; (j = -1) \quad (3.15)$$

Where  $j$  = imaginary number,  $Z'$  (real part of impedance) =  $R$  (resistance) and  $Z''$  (imaginary part of impedance) =  $X$  (reactance). The measurement plane of impedance can be taken as resistance on the x-axis and reactance on the y-axis. Additionally, the obtained parameters can be utilized to determine dielectric parameters such as loss tangent ( $\tan\delta$ ), dielectric constant ( $\epsilon'$ ), ac conductivity ( $\sigma$ ), and complex electric modulus ( $M^*$ ) of the material [184]. The impedance measurements of incorporated samples are carried out at room temperature within the frequency range 20 Hz to 2 MHz using Agilent E4980A, Precision LCR meter. To make disc-shaped specimens, the powder was granulated with a 4 wt% PVA (polyvinyl alcohol) binder and uniaxially pressed by applying a pressure of 2 tons. For measuring electrical characteristics, the neighboring surfaces of the pellets were thoroughly polished with silver paste to form a parallel plate capacitor, with measurements taken for both thickness and diameter. The sample was then carefully placed into the cell and the electrodes were gently brought into contact with the sample, avoiding any excessive pressure. The

micrometer was adjusted with a light touch, and the corresponding electrometer settings were recorded.

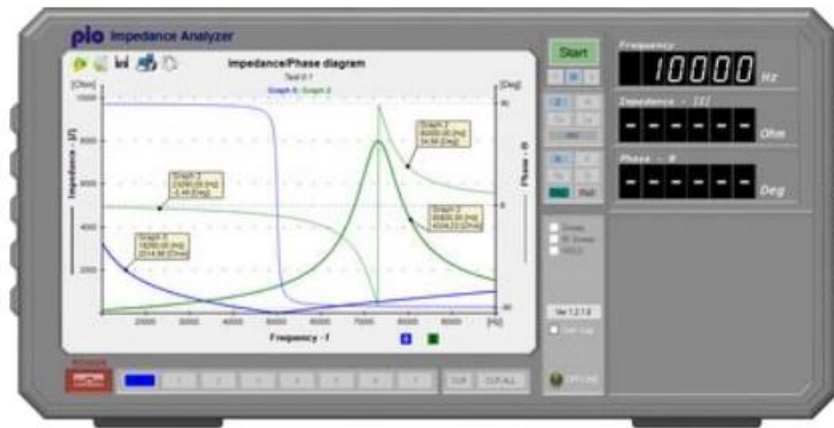


**Fig. 3.14.** Universal impedance analyzer [185]

### 3.3.9 Parameters derived from Impedance measurements

#### (a) Dielectric Analysis

The complex dielectric constant consists of two components one is the real part ( $\epsilon'$ ), and the other is the imaginary part ( $\epsilon''$ ), and it has been calculated from the following equations [186]:

$$\epsilon' = \frac{Cd}{\epsilon_0 A} \quad (3.16)$$

Here  $C$  implies as capacitance (F) of the circular pellet,  $A$  = cross-sectional area of the circular pellet,  $d$  suggests the thickness (m) of the circular pellet and  $\epsilon_0$  = permittivity constant (free space).

The below relation can be used to estimate dielectric loss tangent:

$$\tan \delta = \frac{1}{2\pi f C_p R_p} \quad (3.17)$$

where  $\delta$  represents as loss angle,  $f$  implies frequency,  $C_p$  and  $R_p$  are its equivalent parallel capacitance and resistance, respectively.

The dielectric loss is derived from the following expression:

$$\epsilon'' = \epsilon' \tan \delta \quad (3.18)$$

The following expression is used to estimate AC conductivity:

$$\sigma = 2\pi f \epsilon_0 \epsilon'' \quad (3.19)$$



### (b) Complex Electric Modulus

Electric modulus spectroscopy provides a comprehensive understanding of charge transport mechanisms such as the dynamics of ions, conductivity relaxation, and the mechanism of electrical transport. It can also be utilized to differentiate grain boundary conduction and electrode polarization processes. The electric Modulus could be formulated through [187]:

$$\begin{aligned} M^* &= (\varepsilon^*)^{-1} = (\varepsilon' - i\varepsilon'')^{-1} \\ &= \frac{\varepsilon'}{\varepsilon'^2 + \varepsilon''^2} + i \frac{\varepsilon''}{\varepsilon'^2 + \varepsilon''^2} \\ &= M' + iM'' \end{aligned} \quad (3.20)$$

Here  $M'$  - real and  $M''$  - imaginary parts of the complex modulus.

### 3.3.10 Vector Network Analyzer

A vector network analyzer (VNA) is an essential tool to measure and analyze the performance of high-frequency electrical components and networks in the field of radio frequency (RF) and microwave engineering [188]. Fig. 3.15 represents the Agilent (E8361C) Vector Network Analyzer broadband measurement setup. The primary function of VNA is to provide insights into how the material behaves at different frequencies. It works on the principle of measurement of reflected and transmitted waves when a signal passes through a device under test (DUT) [189]. Based on transmission line theory, the normalized input impedance ( $Z_{in}$ ) at the interference can be expressed as [190]:

$$Z_{in} = Z_0(\mu_r/\varepsilon_r)^{1/2} \tanh\left[j \frac{2\pi f t (\mu_r \varepsilon_r)^{1/2}}{c}\right] \quad (3.21)$$

Where  $Z_0$  implies as characteristic impedance with value  $377\Omega$ ,  $f$  represents EM wave frequency,  $t$  denotes the thickness of the pellet,  $c$  is the velocity of the EM wave (Vaccum) and  $\varepsilon_0 = 8.854 \times 10^{-7}$  F/m /  $\mu_0 = 4\pi \times 10^{-7}$  H/m is the permittivity/permeability of the vacuum, respectively.

According to the theory of absorbing walls, the reflection loss can be written as [191]:

$$\text{REL (dB)} = 20 \log \left| \frac{Z_{in} - Z_0}{Z_{in} + Z_0} \right| \quad (3.22)$$

### (a) Eddy Current Loss

The resonance peaks observed in the magnetic loss ( $\tan\delta_\mu$ ) shows the effect of eddy current and is expressed by the relation:

$$C_o = \mu''(\mu')^{-2} f^{-1} = 2\pi\mu_0\sigma t \quad (3.23)$$

Where  $\sigma$  implies conductivity.



### (b) Quarter Wavelength Mechanism

The mathematical representation for the occurrence of a quarter-wavelength ( $\lambda/4$ ) mechanism can be defined as follows [192]:

$$d_m = \frac{n \cdot c}{4 f_m \sqrt{|\mu_r \epsilon_r|}} \quad , \text{ Here } n = 1, 3, 5, \dots \quad (3.24)$$

### (c) Bandwidth to Thickness Ratio (BTR)/Percentage Bandwidth Ratio (PBW)

$$\text{BTR} = \frac{\lambda_2 - \lambda_1}{d_m} \quad (3.25)$$

$$\text{PBW} = \frac{f_2 - f_1}{f_0} \quad (3.26)$$

Here,  $\lambda_2$  (wavelength at frequency  $f_2$ ) =  $c/f_2$ ,  $\lambda_1$  (wavelength at frequency  $f_1$ ) =  $c/f_1$ ,  $f_2$  = upper frequency,  $f_1$  = lower frequency,  $f_0$  = center frequency, and  $d_m$  = thickness at the REL dip of interest



**Fig. 3.15. Vector network analyzer (VNA).**

---

# CHAPTER 4

## RESULTS AND DISCUSSION

---

### 4.1 $\text{Co}^{2+}$ - $\text{La}^{3+}$ substituted $\text{SrCo}_{1.5z}\text{La}_{0.5z}\text{Fe}_{12-2z}\text{O}_{19}$ hexaferrite

In the present section, we intend to use the sol-gel combustion method to synthesize Co-La substituted  $\text{SrFe}_{12}\text{O}_{19}$  hexaferrite, having a composition of  $\text{SrCo}_{1.5z}\text{La}_{0.5z}\text{Fe}_{12-2z}\text{O}_{19}$ . Table 4.1 displays the assignment of sample names/codes for a different level of substitution for  $\text{SrCo}_{1.5z}\text{La}_{0.5z}\text{Fe}_{12-2z}\text{O}_{19}$  hexaferrite.

**Table 4.1** Assignment of sample name for a different level of substitution of  $\text{SrCo}_{1.5z}\text{La}_{0.5z}\text{Fe}_{12-2z}\text{O}_{19}$  hexaferrite.

Sample Composition $\text{SrCo}_{1.5z}\text{La}_{0.5z}\text{Fe}_{12-2z}\text{O}_{19}$	Sample Code (D-series)
$z = 0.0$	D1
$z = 0.1$	D2
$z = 0.2$	D3
$z = 0.3$	D4
$z = 0.4$	D5
$z = 0.5$	D6

#### 4.1.1 Structural Analysis

##### 4.1.1.1 X-ray Analysis

Figure 4.1 illustrates the XRD pattern of the prepared D-series hexaferrite samples, demonstrating the reflection planes within the  $2\theta$  range of  $20^\circ$ - $70^\circ$  agreed with the ICDD-801197 reference of M-type hexaferrite. This affirms the successful synthesis of single-phase  $\text{SrFe}_{12}\text{O}_{19}$  (SrM) hexaferrite [193]. The high-intensity peak (107) displays a subtle shift of  $2\theta$  toward the right side of the Bragg angle. The observed changes in peak intensity and lattice sizes as we transition from D1 to D6 indicate the successful substitution of  $\text{Co}^{2+}$  -  $\text{La}^{3+}$  ions

at distinct crystallographic sites [194]. Table 4.2 lists lattice parameters (c, a, and c/a) and unit cell volume (V) estimated using equation 3.1 and equation 3.2 [195].

Table 4.2 presents the observed value of the lattice constant ‘c’ ranges from 22.9518 to 22.9048 Å, ‘a’ varies from 5.8545 to 5.8644 Å, and the unit cell volume ranges from 681.26 – 679.86 Å<sup>3</sup>. These findings indicate that the expansion of the lattice parameter ‘a’ is smaller than that of the parameter ‘c’ and is consistent with the conventional behavior of M-type hexaferrites[196]. The slight change observed in the lattice parameter ascribed to larger ionic radii of  $Co^{2+}$ (0.72 Å) and  $La^{3+}$ (1.15 Å) ions as compared to the host ion  $Fe^{3+}$ (0.645 Å). For the M-phase, the height-to-width ratio (c/a) should be around 3.98 and the observed values lie in the range of 3.92 to 3.91, which is close to the predicted values [197].

**Table 4.2** Various structural parameters at different levels of substitution.

Sample Name	2θ (°)	FWHM M	c (Å)	a (Å)	V (Å <sup>3</sup> )	c/a	Crystallite size (nm)	ε
D1	32.4806	0.169	22.9518	5.8545	681.26	3.92	48.94	0.0514
D2	32.4806	0.186	22.9518	5.8545	681.26	3.92	44.46	0.0210
D3	32.4806	0.209	22.9518	5.8545	681.26	3.92	39.57	0.0420
D4	32.5290	0.218	22.9048	5.8545	679.86	3.91	37.94	0.0300
D5	32.4806	0.254	22.9518	5.8545	681.26	3.92	32.56	0.0500
D6	32.4806	0.287	22.9357	5.8644	683.08	3.91	28.82	0.0070

**Table 4.3** Density, porosity, and surface area values of all D-series hexaferrite samples.

Sample name	Density(g/cm <sup>3</sup> )		Porosity(P) (%)	S × 10 <sup>7</sup> (cm <sup>2</sup> /g)
	XRD ( $\rho_x$ )	bulk ( $\rho_{bulk}$ )		
D1	5.18	3.03	41.50	23.37
D2	5.20	2.75	47.11	25.73
D3	5.22	2.52	51.72	26.97
D4	5.25	2.20	58.09	27.90
D5	5.27	2.95	44.02	28.44
D6	5.27	2.90	44.97	29.88

### 4.1.1.2 Crystallite size and Density measurement

The calculated values of full-width half maxima (FWHM) and crystallite size from equation 3.3 are listed in Table 4.2. From D1 to D6, the FWHM value of the high-intensity peak becomes broader and consequently declines the crystallite size. The average crystallite size of the high-intensity peak decreases from 48.94 nm (D1) to 28.82 nm (D6) with increasing the level of substitution [198][199]. The William- Hall equation  $\beta \cos \theta = k\lambda/D + 4\varepsilon \sin\theta$  is used to determine the degree of deformation in the crystal lattice[200]. Its measurement is based on the lattice parameters of the crystals and their changes concerning the applied stress or strain. The average lattice strain of all prepared specimens lies between D1 (0.0514) – D6 (0.0070). Table 4.3 enlist the value of bulk density ( $\rho_{\text{bulk}}$ ), Porosity (P), X-ray density ( $\rho_x$ ), and surface area (S). The surface area (S) of a prepared specimen is inversely linked to the crystallite size (equation 3.11), and the value of the surface area (Table 4.3) gradually increases from D1 to D6 ( $23.37 - 29.88 \times 10^7 \text{ cm}^2/\text{g}$ ). Substitution causes an increment in XRD density ( $\rho_x$ ) (calculated using equation 3.9) from D1 ( $5.17 \text{ g/cm}^3$ ) to D6 ( $5.28 \text{ g/cm}^3$ ), which may be due to the lesser atomic mass of host  $\text{Fe}^{3+}$  (55.84 amu) ion than substituted  $\text{Co}^{2+}$  (58.93 amu) and  $\text{La}^{3+}$  (138.90 amu) ions, as presented in Table 4.3 [199]. Moreover, the value of  $\rho_x$  surpasses  $\rho_{\text{bulk}}$  (calculated using equation 3.8), suggesting the existence of pores during the sample preparation and attributed to irregular grain shape [201]. The porosity (P) (calculated using equation 3.10) shows an irregular trend with substitution and is minimal for the D1 sample [202].

Figure 4.2 illustrates the Rietveld refinement of D1 to D6 samples was carried out using the Fullprof program and was employed to calculate lattice parameters as listed in Table 4.4. The fitting was assessed by the goodness of fit and the low values of the reliable factor as included in Table 4.4. It is noteworthy, that the lattice parameter decreased non-linearly comparatively to undoped SrM hexaferrite. Typically, the insertion of larger ionic radii elements in the host lattice causes the crystal lattice to expand. However, contrary to this general trend, the current study reveals a reduction in lattice parameters. This unusual behavior can be attributed to various factors. Notably, the low solubility of the rare earth substitution in SrM may induce the formation of secondary phases, which may be observed in D5 and D6 samples. The introduction of small quantities of larger rare earth elements can lead to strong interactions between neighboring atoms, inducing stress on the crystal lattice resulting from a cationic redistribution of ions within the host lattice. Consequently, the crystal lattice diminishes in size, resulting in a decrease in lattice parameters [203].

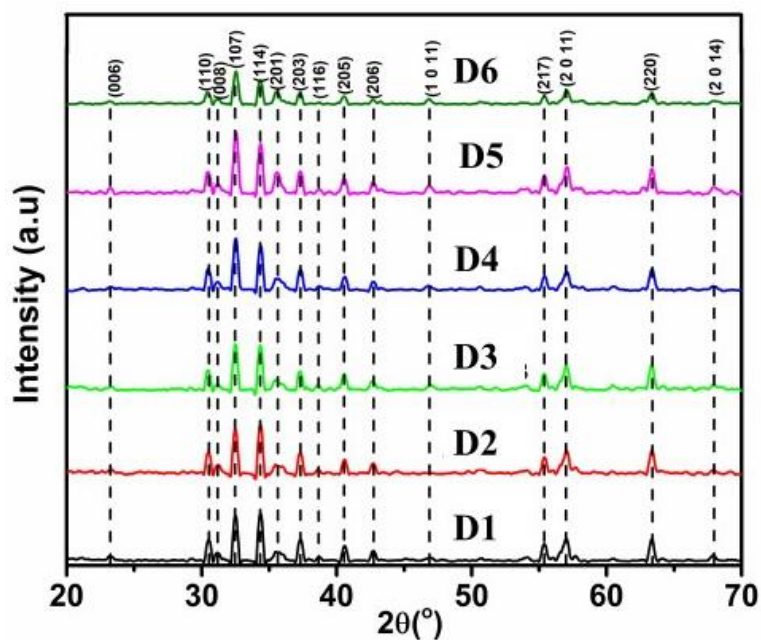
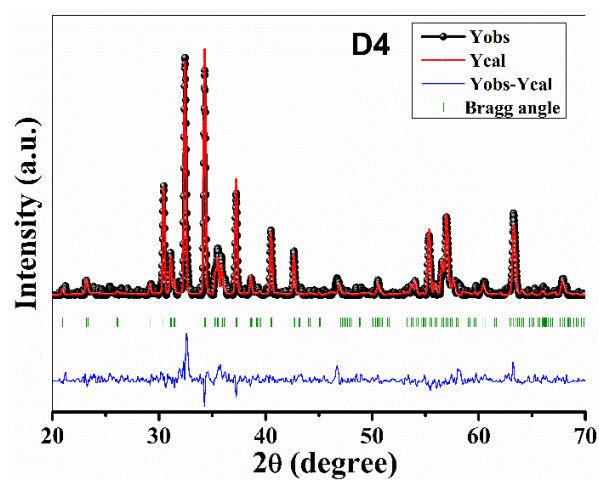
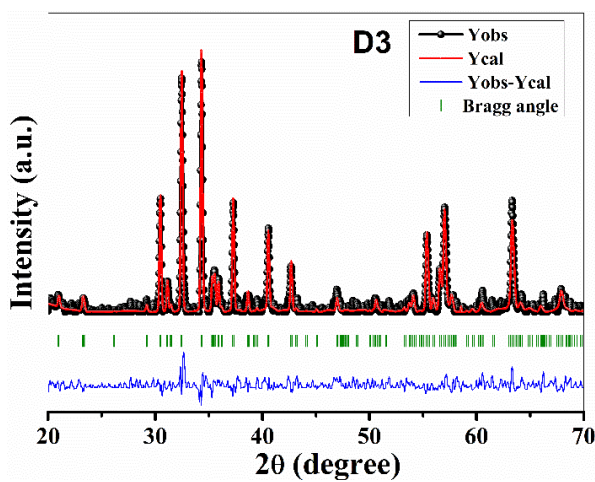
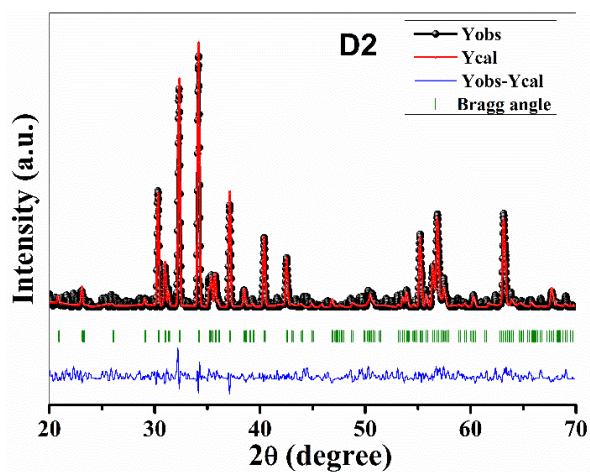
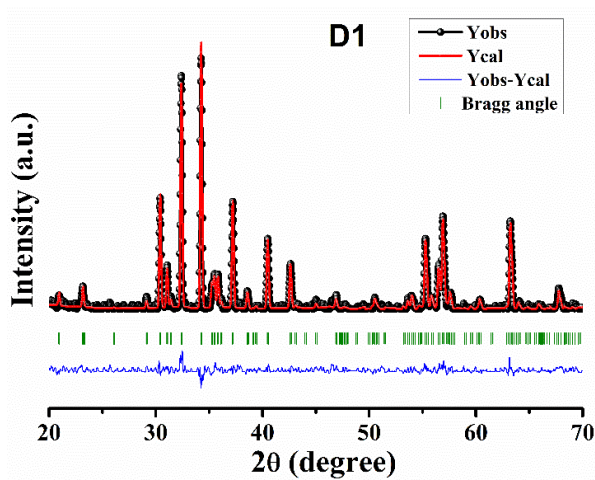


Fig. 4.1. XRD pattern of D-series hexaferrite.



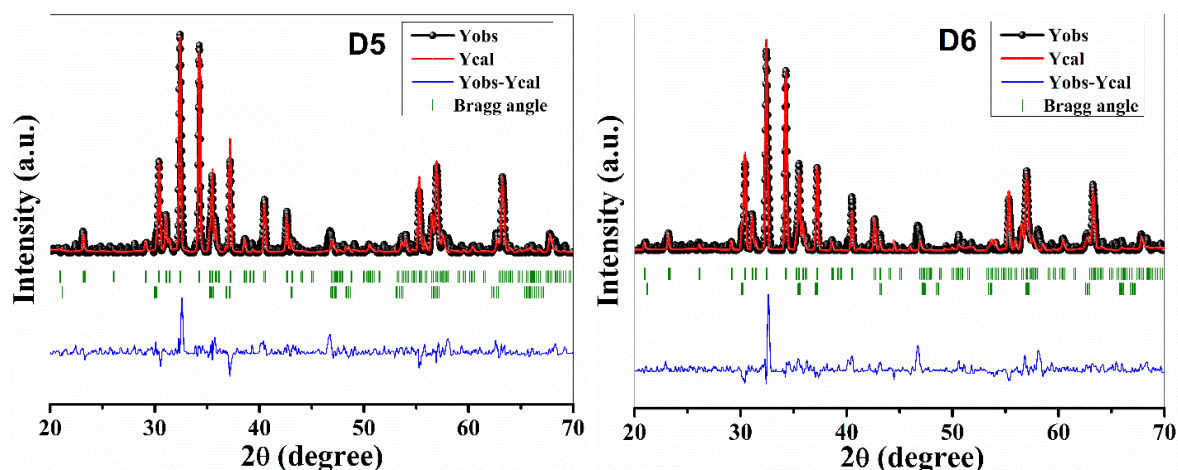


Fig. 4.5. Rietveld refinement of synthesized samples.

Table 4.4 Lattice parameters obtained from Rietveld refinement.

Sample codes	D1	D2	D3	D4	D5	D6
a (Å)	5.878404	5.885925	5.870990	5.873567	5.878076	5.875697
c (Å)	23.034563	23.052750	22.994368	23.005497	23.018208	22.997269
c/a	3.9185	3.9165	3.9166	3.91678	3.9159	3.9139
V <sub>cell</sub> (Å <sup>3</sup> )	689.334	691.644	686.396	687.331	688.767	687.584
R <sub>p</sub> (%)	22.4	31.0	31.6	31.6	31.4	35.3
R <sub>wp</sub> (%)	36.5	46.0	46.1	46.4	44.2	48.5
GoF	2.0	2.6	2.8	2.8	2.8	3.0
Percentage of phases	SrM:100%	SrM:100 %	SrM:100 %	SrM:100 %	SrM:89.67 % CoFe <sub>2</sub> O <sub>4</sub> : 10.33 %	SrM:80.64 % CoFe <sub>2</sub> O <sub>4</sub> : 19.36 %

#### 4.1.1.3 FTIR Analysis

FTIR spectroscopy serves as a valuable tool for obtaining both quantitative and qualitative insights into molecular band position, existing chemical bonds, and attached functional groups. It aids in determining the structural changes resulting from the substitution of  $Co^{2+}$ - $La^{3+}$  ions in SrM hexaferrites [204]. IR spectra of the prepared specimen were examined in the infrared range from 3000 to 400  $cm^{-1}$ , as seen in Fig. 4.3. Table 4.5 explains the position of absorption bands obtained in the IR range of 600 to 400  $cm^{-1}$  for a different level of substitution. There are no broad absorption bands near 1385  $cm^{-1}$ , 2750  $cm^{-1}$ , and 3000  $cm^{-1}$ , indicating the nonexistence of  $NO_3^-$ , C-H bending vibration, and vibrations due



to the hydroxyl group (O-H), respectively[205][206]. The observed bands lie in the range of 500-600  $cm^{-1}$  representing mode  $\nu''$  and are owed to stretching vibrations of  $Fe^{3+}-O^{2-}$  at tetrahedral sites. Other absorption bands from 400-450  $cm^{-1}$  represent mode  $\nu'$  and are due to vibrations of  $Fe^{3+}-O^{2-}$  at octahedral crystallographic sites of crystal structure[207]. Furthermore, the substitution of  $Co^{2+}$  and  $La^{3+}$  ions alter the band position of tetrahedral and octahedral sites towards a higher frequency side. This may be attributed to the substitution of  $Co^{2+}-La^{3+}$  ions in crystallographic sites of hexagonal crystal structure [208].

**Table 4.5** FTIR spectra details of D-series samples.

Sample name	Fe – O vibrations at		
	Octahedral sites (400-450 $cm^{-1}$ )	Tetrahedral sites (500-600 $cm^{-1}$ )	
D1	422.35	541.92	582.42
D2	430.06	555.42	584.35
D3	426.20	547.70	588.20
D4	426.20	547.70	586.27
D5	433.92	551.26	593.99
D6	433.92	-	590.13

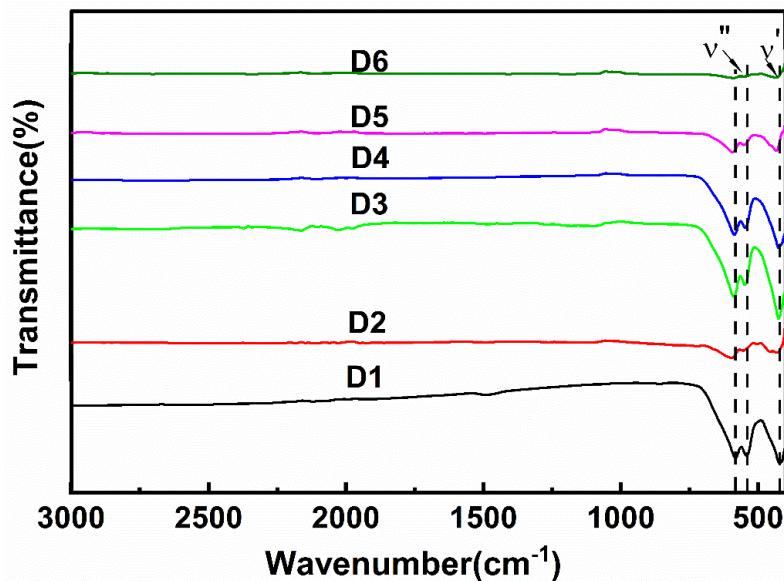


**Fig. 4.6.** FTIR spectra of D-series

#### 4.1.1.4 Morphology Analysis

Figure 4.4 shows micrographs of all prepared D-series hexaferrite samples. The formation of grains exhibiting diverse sizes and shapes can be attributed to the aggregation of crystallites caused by dipolar attractive interaction among magnetic particles. It is evident from Fig. 4.4 that the substitution of  $Co^{2+} - La^{3+}$  ions improve the inter-grain connectivity of particles. All the compositions obtained display a porous morphology and consist of micron-sized agglomerates containing a substantial number of nanometer-sized particles[209]. As the proportion of substituents increases in the composition of the synthesized samples, there is no significant change in morphology, which is associated with the same synthesis conditions in all D-series samples. It should be noted that, in comparison with traditional methods of obtaining hexaferrite, this sol-gel technique made it possible to obtain samples with a more developed morphology.

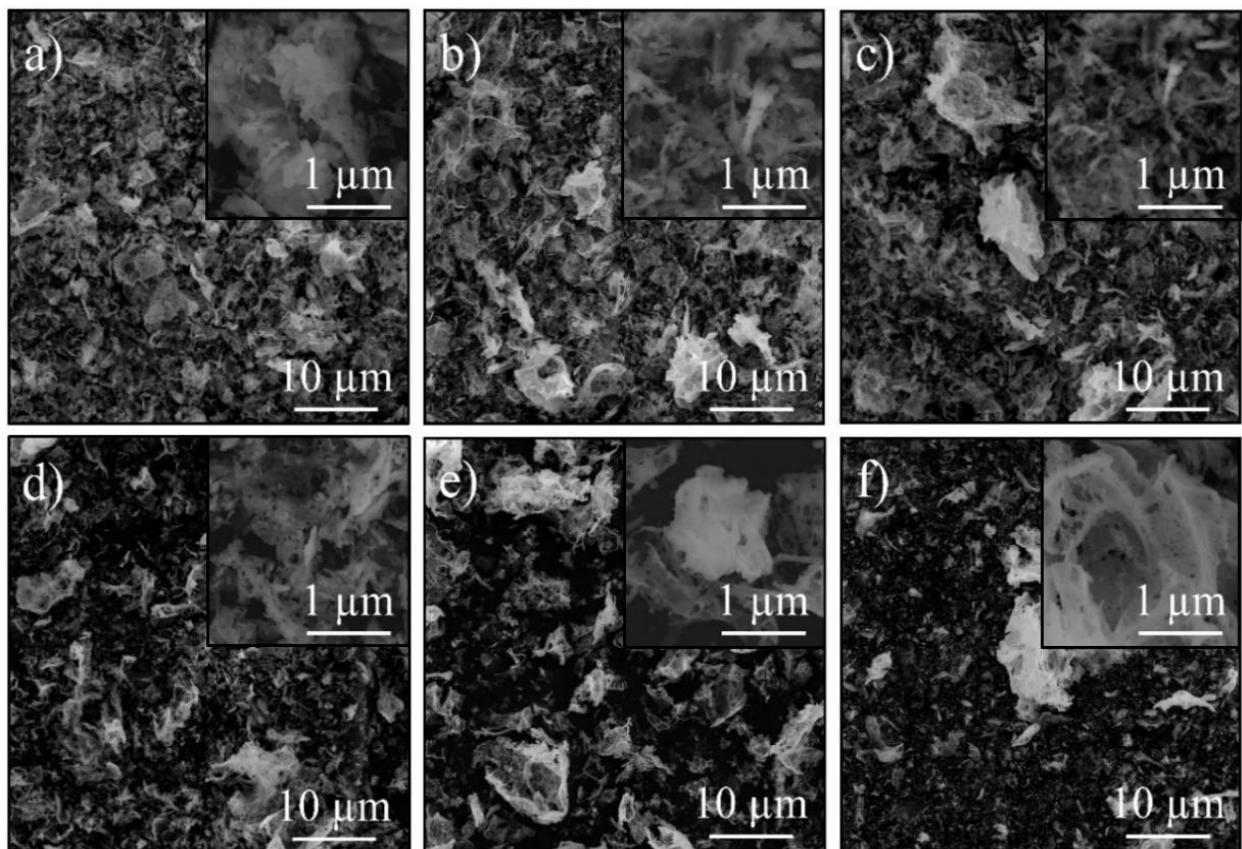
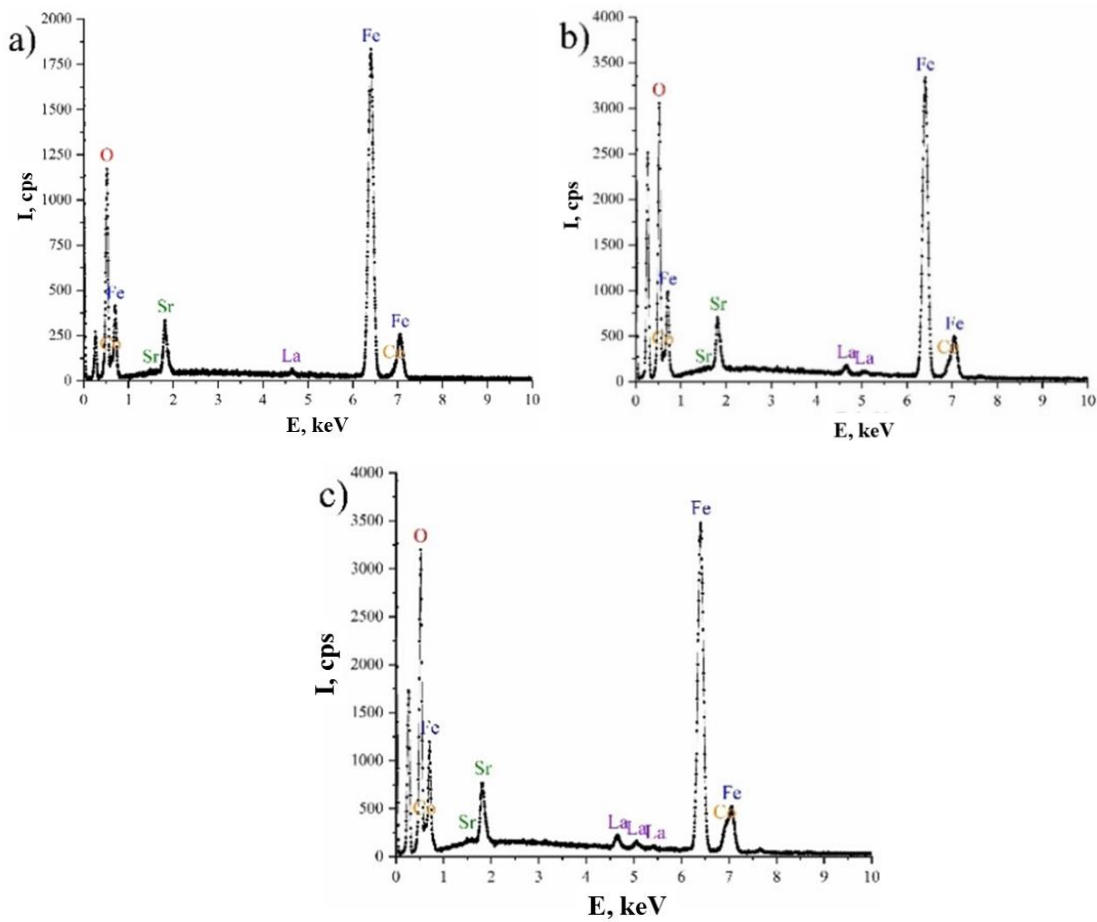


Fig. 4.7. SEM micrographs of D-series from D1 to D6 (a-f) samples.

Elemental analysis performed by the method of energy-dispersive analysis (Fig. 4.5) confirms that all obtained powders correspond in their composition to the calculated values within the error of the determination method. In addition, it was found that all the main chemical elements are evenly distributed over the entire area of the samples, which indirectly



confirms the XRD phase analysis data on the homogeneous nature of the compositions obtained.



**Fig. 4.8.** EDX spectra of the (a) D2, (b) D4 (b), and (c) D6 samples.

## 4.1.2 Electrical Analysis

### 4.1.2.1 Dielectric Constant

It has been noted that among all samples of the D-series only D1, D2, and D4 exhibit the electrical characteristics due to uncertainty observed in the rest of the samples of the D-series [210]. The variation of frequency-dependent  $\epsilon'$  (calculated using equation 3.16) of D1, D2, and D4 samples in the frequency range 20Hz to 2MHz are shown in Fig. 4.6(a). The dielectric constant of D1, D2, and D4 generally decreases as frequency increases but the rate of dispersion is different for all. This is the normal frequency-dependent behavior shown by all hexaferrites [17]. The value of  $\epsilon'$  for D1 is 953.374 at 100 Hz and decreases to 79.61 at 1 MHz, while the value of  $\epsilon'$  for D2 is 485.833 at 100 Hz and decreases to 87.957 at 1 MHz. The same trend is observed for D4, where  $\epsilon'$  is 561.257 at 100 Hz and 77.07 at 1 MHz. This

dielectric mechanism could be explained by Koop's theory which agrees with the two-layer model proposed by Maxwell and Wagner. The high value of a  $\epsilon'$  in low-frequency regions is caused by space charge polarization, which occurs when higher conductivity phases (i.e., grains) create a local accumulation of charge in the insulating matrix (i.e., grain boundary) under the influence of an electric field. The space charge carriers take some time to align their axes parallel to an alternating field. As the field reversal frequency increases, the space charge carriers can no longer keep their direction in step with the field causing a delay in changing their direction relative to the field. This delay is attributed to the fall observed in the material's dielectric constant [18]. In ferrites, polarization can be considered a similar process to conduction and is caused primarily by the hopping conduction mechanism. The Verwey-de-Boer [19] explains the electrical conduction mechanism in hexaferrite is caused by electrons hopping between ions of the same element that are formed during sintering and exist in multiple valence states. The concentration of  $Fe^{2+}$  ions are characteristic of ferrite materials and dependent on factors such as atmosphere, grain structure, and sintering time/temperature. The presence of  $Fe^{2+}$  ions lead to electrons hopping between  $Fe^{2+} - Fe^{3+}$  ions and causing a local shift of charges towards the electric field, resulting in polarization in hexaferrite. The extent of the exchange depends on the concentration of  $Fe^{2+}/Fe^{3+}$  ion pairs on the octahedral position. Indeed, the large value of  $\epsilon'$  in the lower-frequency region can also be explained through the domains of species such as  $Fe^{2+}$ , defects in the grain boundary, oxygen vacancies, and voids. The value of  $\epsilon'$  decreases non-linearly with substitution from D1 to D4, which can be explained by the availability of  $Fe^{2+}$  ions at octahedral sites. As we increase the substitution, the Co-La ions may tend to occupy the octahedral sites which lessen the no. of Fe ions responsible for polarization, thus resulting in a decrease in the dielectric constant.

#### 4.1.2.2 Dielectric Loss and Loss tangent

Figure 4.6(b) depicts that the imaginary part ( $\epsilon''$ ) (calculated using equation 3.18) of the dielectric constant decreases as the applied frequency increases. It is observed that  $\epsilon''$  decreases more rapidly than  $\epsilon'$  at a lower frequency, while the variation is similar to that of  $\epsilon'$  at a higher frequency region. The increment in interfacial polarization of the Maxwell-Wagner type results in maximum  $\epsilon''$  at low frequency. The contribution of bound charges to the conduction mechanism is responsible for the decrease in  $\epsilon''$  at high- frequency.

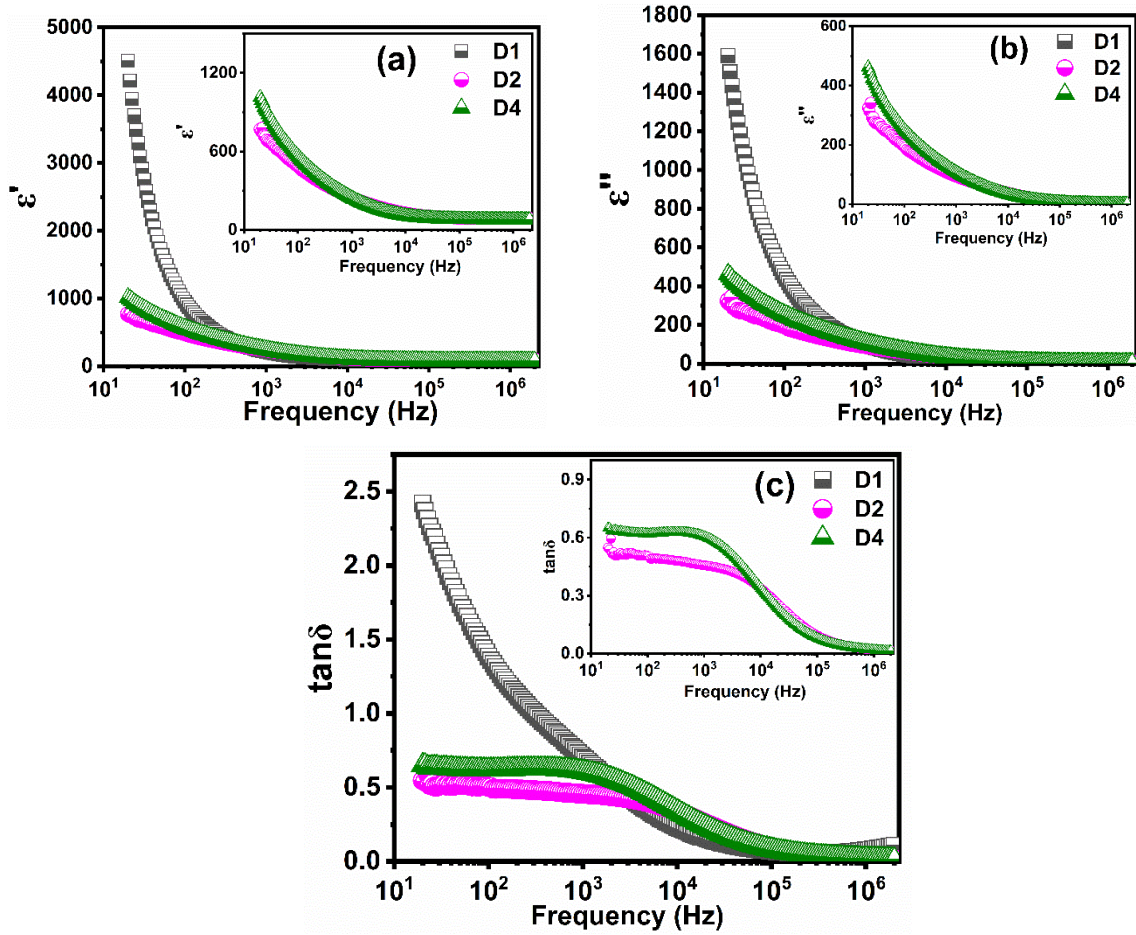


**Fig. 4.9.** (a)  $\epsilon'$  and (b)  $\epsilon''$  (c)  $\tan \delta$  variation with frequency of D-series samples.

The value of  $\tan \delta$  (calculated using equation 3.17) is influenced by various factors involving the sintering temperature and composition of the samples, as well as the stoichiometry and  $Fe^{2+}$  content, which affects the structural homogeneity. Fig. 4.6(c) indicates that the value of  $\tan \delta$  is high at a low applied frequency and it subsequently decreases as the applied frequency increases. The high value of  $\tan \delta$  at lower frequencies is due to the impediment caused by grain boundaries. Moreover, this emanating behavior shows that more energy is required for exchanging electrons between  $Fe^{3+}$  and  $Fe^{2+}$  ions which lead to a high energy loss. In contrast, a small amount of energy is sufficient for transferring electrons between these ions at higher frequencies. The grains assist conductivity at high-frequency which results in low energy loss. Substitution of Co-La ions causes heterogeneity in the prepared samples and results in more interface polarization. A relatively strong relaxation is observed in the D4 sample than in the D2 sample, which can be explained by the Rezlescu model. According to this model, a strong relaxation is observed in  $\tan \delta$  plots, when the hopping frequency of charges between  $Fe^{2+} \rightleftharpoons Fe^{3+}$  cations at the octahedral position matches with the applied frequency. Substitution causes a shift in peak towards the lower

frequencies from D2 to D4. This could be explained through the availability of large no. of grain boundaries in D4 with substitution, which acts as scattering centers within the material. These scattering centers cause charge carriers to lose energy more frequently, increasing energy dissipation at lower frequencies.

#### 4.1.2.3 AC conductivity

In ferrites, the primary mode of conduction is determined by the electrons hopping at octahedral positions between  $Fe^{2+}$  and  $Fe^{3+}$  ions, as proposed by Verwey et al [19]. As the frequency increases, the frequency of hopping between  $Fe^{2+}$  and  $Fe^{3+}$  ions also increase, which further causes an increment in conductivity. The frequency-dependent conductivity could also be estimated through the polaron hopping model. Fig. 4.7 displays the increase in ac conductivity ( $\sigma$ ) of D1, D2, and D4 samples as the applied frequency increases. It also reveals that  $\sigma$  (calculated using equation 3.19) exhibits frequency-independent behavior at a lower-frequency region and sharply increases at a higher-frequency region ( $>10^4$  Hz). This ubiquitous rise in  $\sigma$  value with increasing frequency is the general behavior of hexaferrite explained by Verwey's hopping mechanism. According to this mechanism, at higher frequencies, the electronic conduction is due to the successful electrons hopping between  $Fe^{2+}$  and  $Fe^{3+}$  ions. While at lower frequencies, grain boundaries are active which hinders the electron exchange between two valence states of the same element at octahedral position. The minimal charge hopping at lower frequencies is evidently due to the high polarization [Fig. 4.6(a)] caused by the entrapment of charge carriers at different trapping sites at grain boundaries. However, at higher frequencies, the active conductive grains promote electrons hopping and releasing the trapped charge carriers. The replacement of  $Fe^{3+}$  ions with Co-La ions causes a reduction in conductivity value and this reduction elucidates a decrement in the concentration of  $Fe^{3+}$  ions at an octahedral position, which restricts the probability of hopping between  $Fe^{2+}$  and  $Fe^{3+}$  ions. The AC conductivity of prepared samples may also be affected by grain distribution and porosity in the material. The material with heterogeneous morphology, such as a large no. of grain boundaries and porosity impedes the movement of charge carriers, resulting in a lower conductivity value.

#### 4.1.2.4 Complex Electric Modulus

The complex electric modulus framework was utilized to determine the transport dynamics in electronic or ionic materials vary with their microstructure (including grain and

grain boundaries) with various factors like the hopping rate of charge carriers, dispersion of relaxation times which further related to the suppression of electrode polarization.

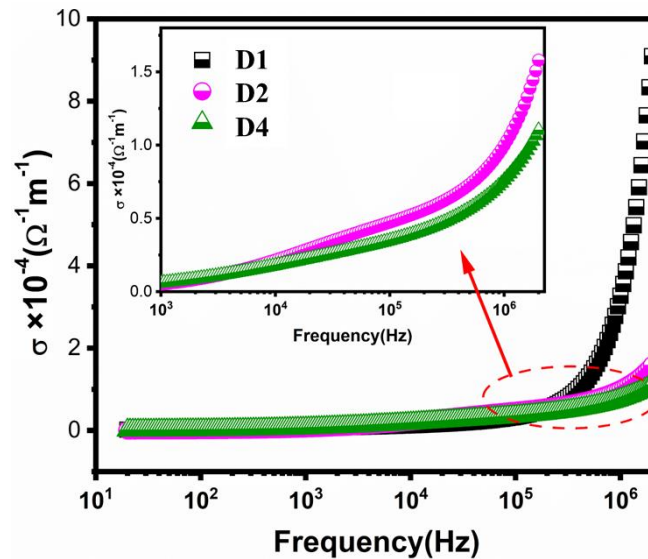


**Fig. 4.10.**  $\sigma$  variation with frequency for D-series samples.

The modulus can be expressed in terms of both resistive (real) and reactive(imaginary) components and is calculated using equation 3.20. Fig. 4.8(a) displays the changes in  $M'$  with frequency and the plot shows a very low value of  $M'$  at lower frequencies approaching zero implying no contribution of electrode polarization. With increasing frequency,  $M'$  varies continuously and reaches an asymptotic value ( $M'$ ) which is maximum at the high-frequency range for all sintered hexaferrite. This pattern suggests that there is a lack of a restoring force controlling the movement of charge carriers in response to an induced electric field [25]. Also, it supports the concept that charge carriers have long-range mobility. Moreover, the value of  $M'$  increases sigmoidally with increased frequency, eventually reaching a value ( $M_\infty$ ) for all sintered hexaferrite. This increment may be ascribed to the conduction phenomena resulting from the short-range mobility of carriers, especially ions. This variation is similar to the behavior observed in  $\sigma_{ac}$ , discussed in the previous section. However, substitution causes the minimum value of  $M'$  for D2 at a high frequency.

Figure 4.8(b) illustrates the variation of  $M''$  with frequency. The value of  $M''$  is related to the dissipation of energy during an irreversible conduction process. The nature of  $M''$  spectrum of D1, D2, and D4 can be discussed via (i) an appearance of an asymmetrical peak at a certain frequency, (ii) a shift in the peaks toward a higher frequency with the substitution of Co-La, (iii) a broadening peak of D2 and narrowing peak of D1 and D4. The lower frequency side of the peak suggests the range of frequencies where ions could hop from one site to the neighboring site over long distances. Conversely, the high-frequency side

of the peak indicates the range of frequencies where the motion of ions is localized within the potential wells. The frequency region at which the peak is observed, affirms a transition of charge carriers from long-range to short-range mobility. The pattern of the modulus spectrum reveals that the electrical conduction mechanism in the samples is of the hopping type for all levels of substitution. The peak frequency enunciates information about the conduction relaxation time and the forward shift in the peak frequency implies a reduction in relaxation time (substituents have less relaxation than  $\text{Fe}^{3+}$ ) with Co-La substitution. The asymmetric shape of the plot for the peak maxima and the width of the peaks on either side of the maxima indicate a non-Debye behavior of the material, caused by the distribution of relaxation time [26], [27]. Substitution of Co-La ions causes a non-linear variation in the relaxation frequency and is the minimum for the D2 sample.

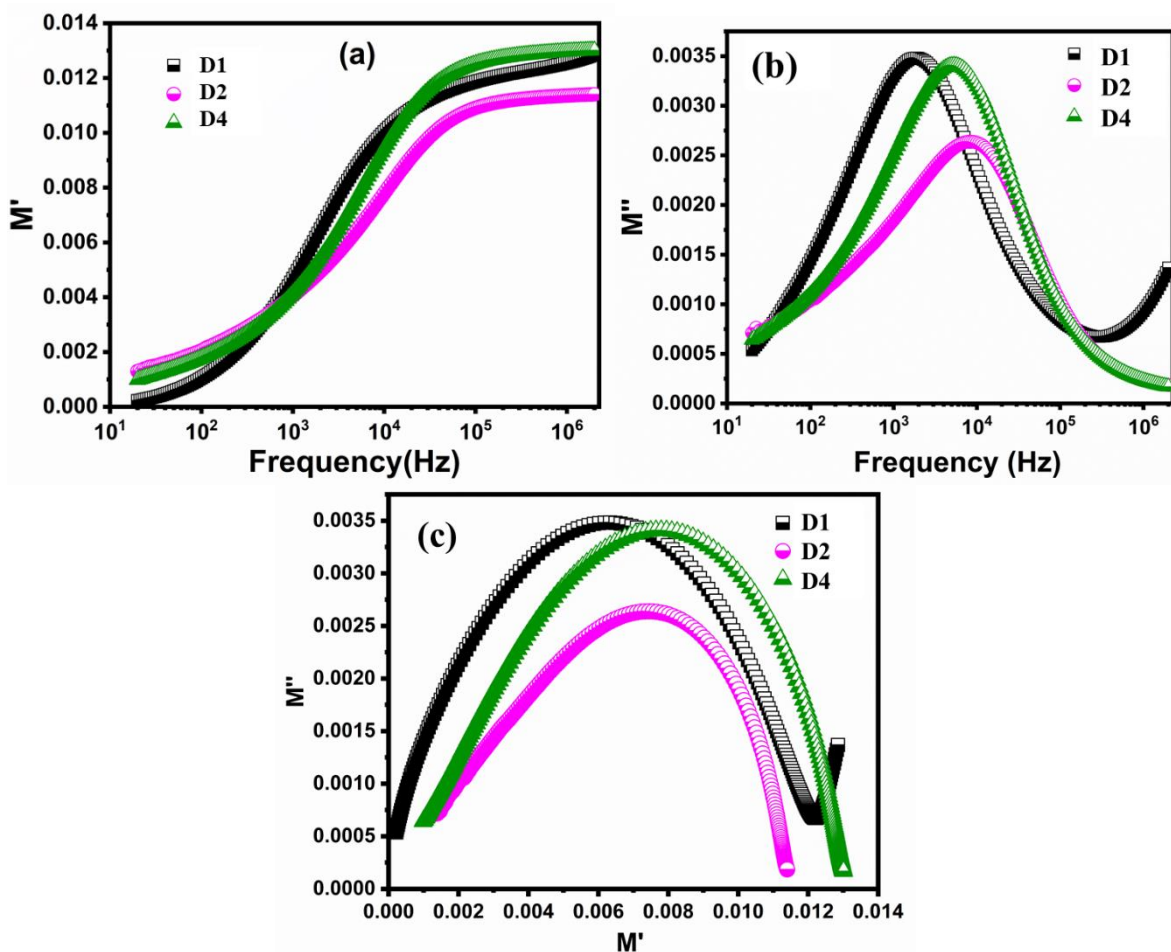


**Fig. 4.11.** (a)  $M'$  (b)  $M''$  (c) Cole-Cole plots ( $M''$  vs  $M'$ ) variation with frequency of D1, D2, and D4 hexaferrite

Figure 4.8(c) illustrates the Cole-Cole plot ( $M''$  vs  $M'$ ) of D1, D2, and D4 sintered hexaferrite. The obtained curves demonstrate a deformed semicircle instead of a perfect semicircle with the center lying below the x-axis. This signifies that the relaxation is



distributed over different time constants and is not of the Debye-type. The semicircular arc reflected at a low frequency is attributed to charge carrier relaxation due to grain boundaries, while the semicircular arc at a high frequency is caused by charge carrier relaxation associated with grains. Moreover, it is seen in Fig. 4.8(c) that the semi-circular arc of the D2 and D4 samples begin almost at the same point in the low-frequency region due to minimum conductivity. While the curve distribution ( $M''$  vs  $M'$ ) of D2 and D4 samples are different in the higher frequency region. This could be due to the maximum conductivity caused by different grain size distributions in D2 and D4 samples as seen in the magnified view of SEM micrographs (Fig. 4.9).

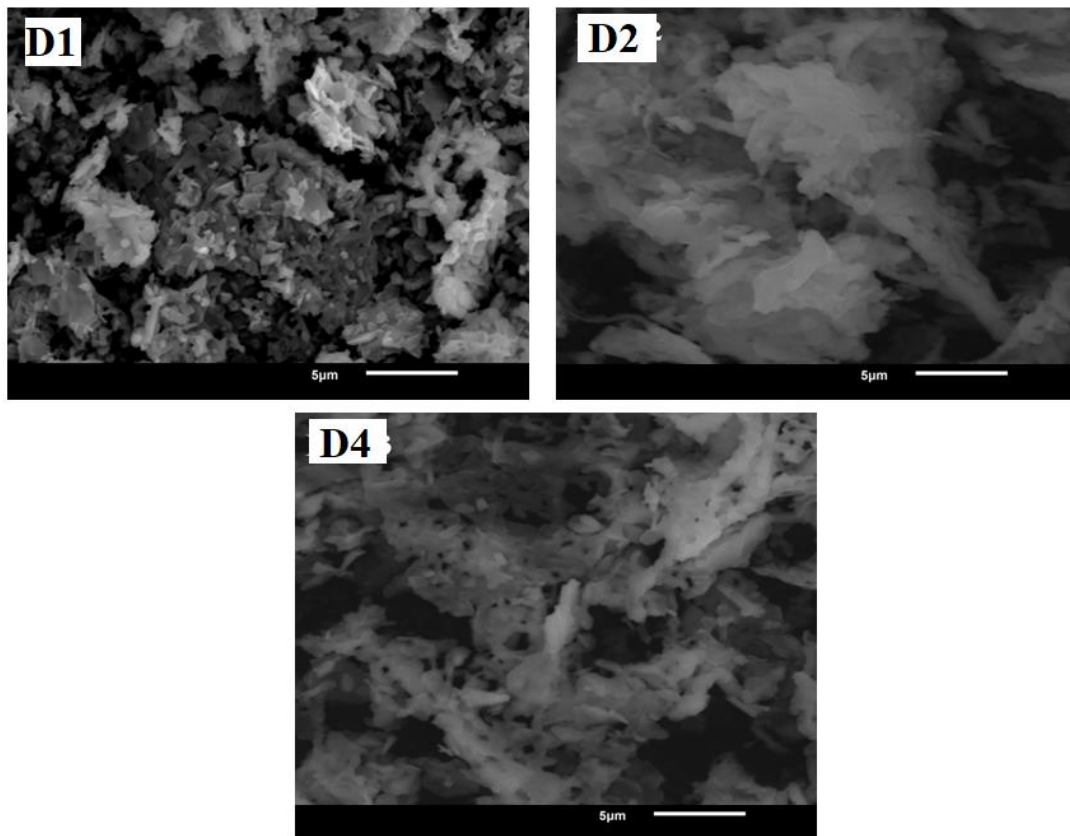


**Fig. 4.12.** A magnified view of SEM micrographs of D1, D2, and D4 samples.

#### 4.1.2.5 Impedance Analysis

Impedance spectroscopy is an indispensable tool for determining the response of dielectric material against an applied AC in the combined form of resistance and reactance in a circuit. Impedance analysis differentiates the charge relaxation of the dielectric material based on its microstructure [28]. This analysis considered the contributions of grain boundaries, grains, and stray charges at the electrode to understand the conduction behavior

within the polycrystalline material, which possesses multi-grain orientations. The complex impedance at any applied frequency can be calculated using equation 3.15. The decrease observed in both  $Z'$  and  $Z''$  with increasing frequencies is shown in Fig. 4.10(a) and 4.10(b), respectively. As the frequency increases, both  $Z'$  and  $Z''$  decreases, suggesting an increment in the material's conductivity due to the increase in electron hopping between the localized ions [29]. At higher frequencies, the reduction in  $Z'$  could be explained through the Maxwell-Wagner model [30]. However, the investigation of  $Z''$  led to a better understanding of the relaxation process and space charge effect. This space charge effect dominates the impedance response at low frequencies and results in a larger value of  $Z''$ . However, the charge carriers may not be able to respond rapidly to the alternating applied field at high frequencies, leading to a decrement in the  $Z''$ . A weak dielectric relaxation at the low-frequency region in the D1 sample can be described by the weak grain connectivity (due to the occurrence of individual grains with porosity) as seen in SEM micrographs (Fig. 4.9), which hindered the flow of charge carriers.

Fig. 4.10(c) shows the Cole-Cole plots ( $Z''$  vs  $Z'$ ) of D1, D2, and D4 sintered hexaferrite at room temperature. These plots are commonly used to analyze impedance spectroscopic data and are particularly useful in understanding electrical properties about changes in microstructure. In the Cole-Cole distribution, the semi-circular arc reflects at a lower-frequency regime corresponding to the resistance caused by the grain boundary, whilst the semi-circular arc at a high-frequency region is attributed to the grain's resistance [27], [31]. The behavior of the observed Cole-Cole plots can also be explained through grain size and distributions. Instead of a complete semicircular arc, only a segment of a semicircular arc has been observed for all. It is also noted that as the substitution increases, the depression of the arc decreases from D1 to D2, and then increases for D4. This depression suggests that the impedance mechanism at low frequency explicitly depends on the dielectric polarization that occurs at grain boundaries, also referred to as the Maxwell-Wagner effect. Additionally, the fitted circle in a cole-cole plot for D1 represents the predicted relaxation.

### 4.1.3 Magnetic Analysis

The magnetic characteristics of the prepared specimens can be tailored by substituting cations with varying electronegativity, magnetic moment, and d-configuration[222]. It has been reported that ions with higher electronegativity generally occupy octahedral sites more than tetrahedral positions of the crystal lattice [223]. The electronegativity of  $La^{3+}(1.1)$  ions



are lower than that of  $Co^{2+}$  (1.88) ions, so the former ions tend to occupy the tetrahedral site  $4f_i$  ( $\downarrow$ ) [224].

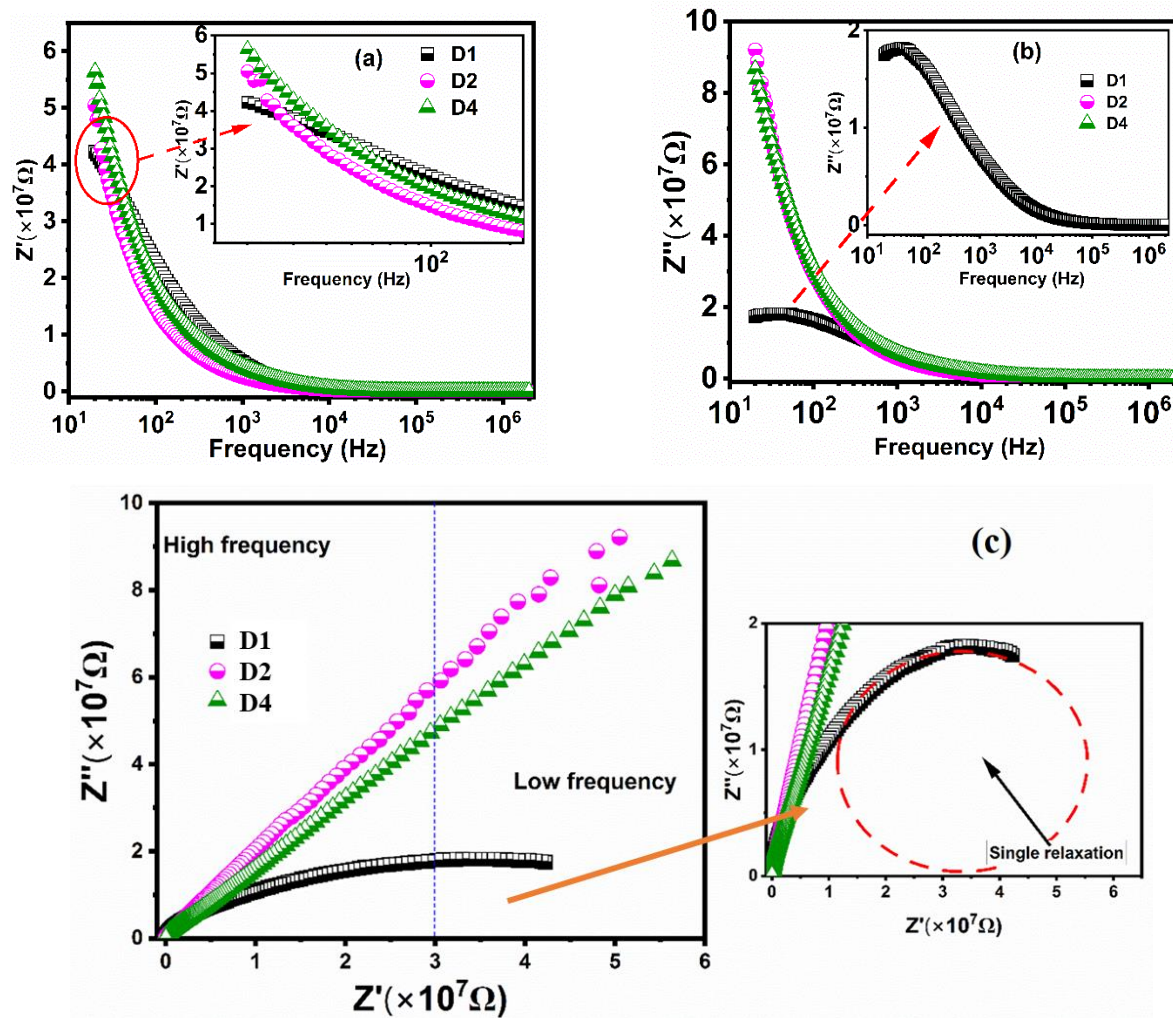


**Fig. 4.13.** (a)  $Z'$  (b)  $Z''$  (c) Cole-Cole plots ( $Z''$  vs  $Z'$ ) variation with frequency of D1, D2, and D4 hexaferrite.

According to ligand field theory,  $La^{3+}$  ions have no site preference due to  $d^0$  configuration and  $Co^{2+}$  ions with  $d^7$  configuration preferably choose to occupy octahedral sites  $12k$  ( $\uparrow$ ),  $2a$  ( $\uparrow$ ),  $4f_2$  ( $\downarrow$ ) [225][226]. When the substituted ion has larger ionic radii than the host ion, it preferentially occupies octahedral sites at the edges of the unit cell. From previous reports  $Co^{2+}$  ( $3\mu_B$ ) ions can occupy both the octahedral ( $4f_2$ ) and tetrahedral ( $4f_i$ ) crystallographic sites [227][47] while  $La^{3+}$  ( $0\mu_B$ ) behaves as a non-magnetic ion and can occupy more octahedral spin-up positions ( $12k$  and  $2a$ ) than tetrahedral sites [229].

The saturation magnetization ( $M_s$ ), remanence magnetization ( $M_r$ ), coercivity ( $H_c$ ), anisotropy field ( $H_a$ ) (calculated using equation 3.13), remanence ratio ( $M_r/M_s$ ) and magnetic moment ( $n_B$ ) values derived from the M-H loop are listed in Table 4.6. Fig. 4.11

demonstrates the hysteresis loops of all D-series samples at room temperature. The values of  $M_s$  and  $H_a$  parameters decrease from D1 to D4 samples, followed by a gradual increase.

The magnetic moment of the incorporated specimen can be explained through the distribution of host and substituted cations over five crystallographic sites of hexagonal crystal structure using the following expression[230]:

$$M_s = M_a(2a + 12k + 2b) (\uparrow) - M_b (4f_1 + 4f_2) (\downarrow) \quad (4.1)$$

The total magnetization increases by substituting non-magnetic ions or less magnetic at the  $(4f_1\downarrow + 4f_2\downarrow)$  lattice site, while magnetization shows decline behavior with the substitution of these ions at  $(2a\uparrow + 12k\uparrow + 2b\uparrow)$  lattice sites[231]. Table 4.6 shows that  $M_s$  decreases non-monotonically with increasing the level of substitution from D1 to D6. The decrease in  $M_s$  can be described by various factors, such as spin canting, change of valence state from high to low spin, site occupancy, and exchange interaction[232]. For lower levels of substitution (D1 to D3), a 14% decrease in the  $M_s$  value is evident. This decrease can be attributed to the replacement of  $Fe^{3+}$  ( $5 \mu_B$ ) ions by non-magnetic ( $La^{3+}$ ) and weakly magnetic ( $Co^{2+}$ ) cations, which reduces the no. of  $Fe^{3+}$  ions on spin-up positions. This resulted in the conversion of  $Fe^{3+}$  ions to  $Fe^{2+}$  ions to maintain electrical neutrality, which reduces the strength of the super exchange interactions and leads to a decline in magnetic moment. Moreover, the decrease in  $M_s$  from D3 to D4 is about 23%, which is consistent with the 21% decrease observed in the relative area of the 12k-2a sites in the Mössbauer analysis (discussed in the next section 4.1.4). This indicates that the  $Co^{2+}$ - $La^{3+}$  ions replace more no. of  $Fe^{3+}$  ions of 12k and 2a sites than other positions[233]. Thereafter an increase of 37% in  $M_s$  from D4 to D6, can be ascribed as a reduction in porosity. The Porosity acts as a non-magnetic void, which depresses magnetization and simultaneously induces demagnetizing fields. However, the increase in  $M_s$  is not as substantial as the decrease in porosity. This can be explained by the fact that the increase in  $M_s$  also depends on the occupation of  $4f_2$  and  $4f_1$  positions of crystallographic sites [234]. Furthermore, the substitution of a rare-earth element in the ferrite attributes to cationic vacancies disturbs the collinear ferromagnetic order and causes environmental distortions[50]. In this context, doping with rare-earth cations often leads to incomplete substitution[236][237], which may indirectly explain the significant change in the intensity of the diffraction peaks of the D6 sample and the absence of a large difference between the Mössbauer spectra of the D5 and D6 samples [238].

**Table 4.6** Magnetic parameters  $M_s$ ,  $H_c$ ,  $H_a$ ,  $M_r$  and  $M_r/M_s$  value of D-series samples.

Sample Name	$M_s$ (emu/g)	$H_c$ (Oe)	$H_a$ (kOe)	$M_r$ (emu/g)	$n_B$	$M_r/M_s$
D1	103.290	5026.54	23.98	52.68	7.27	0.510
D2	101.812	4379.59	26.69	49.18	19.43	0.483
D3	88.614	3826.72	19.18	43.14	16.99	0.486
D4	67.969	2728.33	19.31	34.57	13.08	0.508
D5	87.454	1741.77	24.12	31.61	16.91	0.361
D6	92.939	862.47	24.87	32.27	18.05	0.347

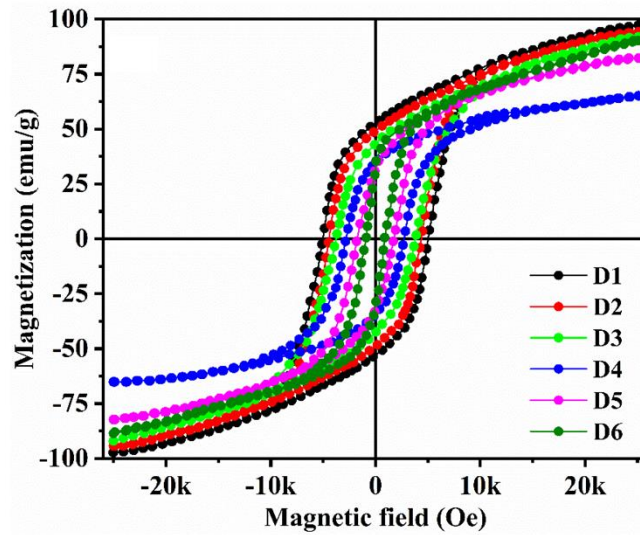


**Fig. 4.14.** Hysteresis loops of all D-series hexaferrites.

The highest values of the coercivity (5026 Oe), and remanent magnetization (52.68 emu/g) are observed in a pure sample of strontium hexaferrite (D1), which is associated with the absence of substitution cations in the crystal lattice. The behavior of  $H_c$  can be easily explained by intrinsic and extrinsic factors. Intrinsic factors are those that are inherent to the material, such as the crystal structure, chemical composition, and anisotropy field ( $H_a$ )[238]. External factors are those that are external to the material such as temperature, magnetic field, and grain size[239]. The initial fall observed in  $H_c$  from D1 (5026 Oe) to D4 (2730 Oe) with increasing the level of substitution, is caused by  $H_a$ . The anisotropy field ( $H_a$ ) depends primarily on the magnetic moments of the iron ions at the  $4f_2$  and  $2b$  sites. A larger anisotropy field leads to a higher coercivity, i.e., more energy is required to reverse the magnetic moment of the hexaferrite. However, with further substitution at D5 and D6,  $H_c$  gradually decreases to 839 Oe and  $H_a$  remains relatively constant. This envisaged behavior can be explained through the existence of inter-grain connectivity in D5 and D6 samples as

seen in SEM images. The remanent magnetization ( $M_r$ ) depends on the orientation of the magnetic moments and decreases from D1 (52.68 emu/g) to D6 (32.27 emu/g) with increasing the level of substitution. The remanence ratio ( $M_r/M_s$ ) is a measure of the retention of magnetization after removing an applied field, and it's usually high in M-type hexaferrite, indicating high remanence. This ratio is also used to determine the formation of the inter-grain group and magnetic hardness of the material and its value should be in the range of 0 to 1[240]. The magnetic material whose values lie within 0.05 to 0.5 is randomly oriented multi-domain particles[241]. It is seen in [Table 4.6](#) that the remanence value of all prepared specimens comes out to be less than or equal to 0.5 which proves the formation of multi-domain particles in all D-series samples[242]. The Bohr magneton ( $n_B$ ) shows a significant role in investigating the magnetic characteristics of the material, which is widely used in microwave and high-frequency applications and calculated using equation 3.14. The Bohr magneton is closely related to saturation magnetization and molecular weight (M.W). As the level of substitution increases, the value of the Bohr magneton decreases, potentially weakening the magnetic interactions within the hexaferrite, as seen in [Table 4.6](#).

#### 4.1.4 Mössbauer Spectra Analysis

[Fig.4.12](#) shows the  $^{57}\text{Fe}$  Mössbauer spectra obtained at room temperature of strontium hexaferrite doped with various amounts of cobalt and lanthanum cations. All spectra show five well-defined sextets of iron cations, which ascribed the structural positions of magnetoplumbite, i.e., octahedral, tetrahedral, and trigonal bipyramidal iron positions. The parameters of the quadrupole splitting, isometric shift, and hyperfine field are listed in [Table 4.7](#). The obtained values are in harmony with the results of earlier published works on strontium hexaferrite [243].

It is known that in pure strontium hexaferrite, the area of the sextet is directly related to the  $\text{Fe}^{3+}$  cations in the corresponding sites and is equal to the ratio  $12k - 50, 4f_1 - 16.7, 4f_2 - 16.7, 2a - 8.3, 2b - 8.3$  [244][245]. Based on the relative area of D1 (pure SrM), the positions of  $4f_2, 12k,$  and  $2a$  are quite close to their predicted values, while the  $4f_1$  site is heavily populated and the  $2b$  site has less occupancy, as seen in [Table 4.7](#). The relative area of D-series samples changes from D1 (48.7:21.5:17.7:6.1:3.3) to D6 (43.5:27.5:17.5:3.6:3.5) and is ascribed to the substitution  $\text{Co}^{2+}$  and  $\text{La}^{3+}$  ions over five crystallographic sites. Moreover, from D3 to D4, the total relative area of  $12k$  and  $2a$  sites decreases by 21.86 % and that of the  $4f_2$  site by 19 %, signifying the tendency of the substituents to occupy these sites. On the

other hand, the relative area of  $4f_1$  increases by 34 %, indicating that some of the Fe ions migrated towards the  $4f_1$  site from D3 to D4.

According to equation 4.1,  $M_a$  decreases with the occupancy of weak magnetic  $Co^{2+}$  ( $3 \mu_B$ ) and diamagnetic  $La^{3+}$  ( $0 \mu_B$ ) ions on 12k and 2a sites, while  $M_b$  increases with the increases in area/occupancy of  $4f_1$  site by  $Fe^{3+}$  ions. However, the decrease in the net area observed at 12k-2a spin-up sites is greater than the increase in the net area of the  $4f_1$  and  $4f_2$  spin-down sites, which may indicate that relatively large no. of  $Co^{2+} - La^{3+}$  ions occupy the 12k-2a sites from D3 to D4. Therefore, the net magnetic moment or  $M = M_a - M_b$  decreases considerably in D4.

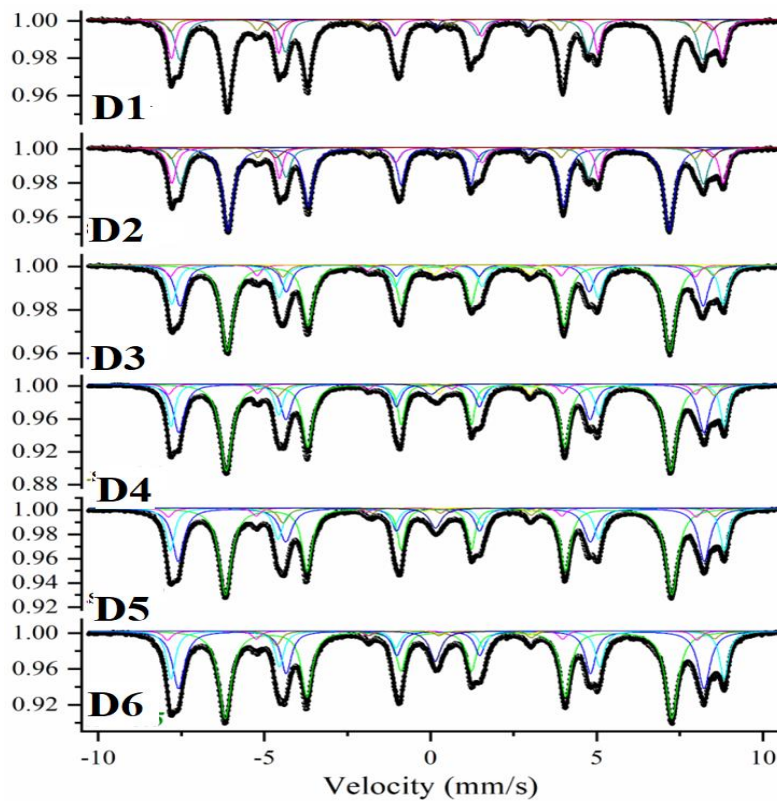


**Fig. 4.15.**  $^{57}Fe$  Mössbauer spectra of all D-series hexaferrite samples.

The isomer shift (IS) provides information about the chemical bonding, including the valence state of  $Fe^{3+}$  ions in magnetically ordered materials. From the previous reports, the value of isomer shift for  $Fe^{2+}$ ,  $Fe^{3+}$ , and  $Fe^{4+}$  ions should lie between 0.6 to 1.7 mm/s, 0.05 to 0.5 mm/s, and 0.15 to 0.05 mm/s respectively. Table 4.7 displays the value of isomer shift ranges from 0.27 to 0.38 mm/s, identifying that samples consist of  $Fe^{3+}$  high spin valence state. With substitution, the isomer shift value remains relatively constant for all crystallographic sites, suggesting little impact on the s electron density of  $Fe^{3+}$  ions. The quadrupole splitting gives knowledge about the local distortion and symmetry of the crystal



lattice. Substitution of Co-La ions causes a feeble reduction in the QS value of 4f<sub>1</sub> and 4f<sub>2</sub>, implying a minor perturbation of the symmetry in the vicinity of these sites.

**Table 4.7** Isometric shift, hyperfine field, and quadrupole splitting of spectral components of all D-series hexaferrite samples.

Sample name	Site	IS (mm/s)	QS (mm/s)	H <sub>eff</sub> (mm/s)	Area (%)
<b>D1</b>	12k	0.34(9)	0.38(3)	41.17(1)	48.7(3)
	4f1	0.27(2)	0.13(7)	48.85(4)	21.5(3)
	4f2	0.38(1)	0.26(4)	51.45(3)	17.7(4)
	2a	0.28(2)	0.73(1)	48.93(5)	6.1(8)
	2b	0.60(4)	2.60(3)	40.80(0)	3.3(7)
	Doublet	1.56(8)	2.75(5)	-	1.1(5)
<b>D2</b>	12k	0.35(3)	0.38(2)	41.22(7)	49.2(6)
	4f1	0.27(4)	0.13(4)	48.85(7)	22.0(0)
	4f2	0.38(2)	0.26(0)	51.50(0)	17.9(2)
	2a	0.27(8)	0.72(0)	48.96(2)	6.3(0)
	2b	0.62(6)	2.59(1)	40.86(7)	3.2(7)
	Doublet	1.57(8)	2.76(1)	-	1.2(5)
<b>D3</b>	12k	0.35(5)	0.37(2)	41.35(1)	48.3(0)
	4f1	0.27(4)	0.11(7)	48.86(9)	19.5(6)
	4f2	0.37(7)	0.27(1)	51.53(3)	21.3(3)
	2a	0.28(8)	0.70(5)	49.09(1)	5.6(1)
	2b	0.66(7)	2.73(3)	40.22(2)	2.9(6)
	Doublet	1.54(1)	2.85(5)	-	2.2(4)
<b>D4</b>	12k	0.35(6)	0.36(8)	41.53(8)	45.5(0)
	4f1	0.27(5)	0.10(5)	49.06(2)	26.2(5)
	4f2	0.38(2)	0.26(4)	51.67(6)	17.2(0)
	2a	0.28(6)	0.65(3)	49.23(6)	4.7(5)
	2b	0.68(0)	2.57(3)	40.85(5)	3.0(5)
	Doublet	1.61(7)	2.73(9)	-	1.6(2)
	Singlet	0.01(8)	-	-	1.6(4)
<b>D5</b>	12k	0.35(7)	0.37(0)	41.71(6)	43.6(7)
	4f1	0.27(3)	0.09(4)	49.14(9)	27.6(9)
	4f2	0.36(9)	0.26(9)	51.76(0)	17.5(7)

	2a	0.29(6)	0.70(0)	49.32(4)	3.8(0)
	2b	0.67(8)	2.80(2)	40.26(3)	4.0(2)
	Doublet	1.39(2)	3.15(3)	-	0.5(9)
	Singlet	0.14(6)	-	-	2.6(6)
<b>D6</b>	12k	0.35(5)	0.37(0)	41.73(9)	43.5(7)
	4f1	0.27(7)	0.08(9)	49.09(8)	27.5(5)
	4f2	0.38(9)	0.23(8)	51.68(0)	17.5(4)
	2a	0.29(1)	0.68(5)	49.48(1)	3.6(3)
	2b	0.57(4)	2.73(0)	41.05(1)	3.5(1)
	Doublet	1.63(7)	2.65(8)	-	0.7(4)
	Singlet	0.14(2)	-	-	3.4(6)

It can be noted that the values of the hyperfine field (ranging from 40.2 to 41.05 mm/s) and quadrupole splitting (in the order of 2.5 – 2.8 mm/s) for site 2b may indicate a strong deformation of the local lattice medium with  $Co^{2+} - La^{3+}$  substitution[246]. The above discussion highlights that the magnetic parameters of all the D-series samples are strongly associated with the arrangement of substituents across five crystallographic sites. The vacancies resulting in the replacement of  $Fe^{3+}$  ions by  $Co^{2+} - La^{3+}$  ions may serve as effective pinning centers for domain walls. This magnetic dilution is demonstrated by the decrease observed in  $H_c$  and  $M_s$  values as shown in [Table 4.6](#).

#### 4.1.5 Electromagnetic Analysis

To comprehend the intrinsic factors influencing microwave absorption characteristics, we have investigated the complex permittivity/permeability of synthesized samples. The magnetic and electric energy storage ability of the synthesized samples are respectively determined by the nature of  $\mu'$  and  $\epsilon'$ , while the ability to dissipate magnetic and electric energy is respectively determined by  $\mu''$  and  $\epsilon''$  values. [Fig.4.13\(a\)](#) illustrates the variation of dielectric constant ( $\epsilon'$ )/loss ( $\epsilon''$ ) as a function of frequency, in the frequency ranges 8.2-12.4 GHz. Introducing Co-La ions causes a gradual decrement in  $\epsilon'/\epsilon''$  values from D1 to D6. This phenomenon is likely attributed to the occupancy of Co-La ions in octahedral positions, reducing the number of Fe ions responsible for polarization, thus leading to a decrease in  $\epsilon'/\epsilon''$ . Among all samples, the  $\epsilon'$  for the D6 sample is lowest, indicating that the electric storage capacity decreases with substitution. The dielectric constant ( $\epsilon'$ )/loss ( $\epsilon''$ ) remains relatively constant over the entire frequency region for D3, D4, D5, and D6 samples.

Among these samples, the D1 sample exhibit the highest value of  $\epsilon'/\epsilon''$  in low and high-frequency regime, while D2 owes relaxation peaks around 8.5 GHz and 11 GHz and attain the minimum value of  $\epsilon''$  in high-frequency regime. Fig. 4.13(b) depicts the variation of permeability ( $\mu'$ )/ magnetic loss ( $\mu''$ ) as a function of frequency, indicating that all the samples remain relatively constant over the entire frequency range, except D2 (resonance around 11.25 GHz)- the magnetic loss emanating from eddy current losses, natural resonance, and domain wall displacement. The domain wall displacement is usually observed in 1 to 2GHz frequency windows, while eddy current losses are shown by low-resistive materials. Thus, magnetic loss observed in this GHz window is significantly attributed to the natural resonance properties of the synthesized samples. It is very well known that  $\mu''$  is proportional to  $M_S$  and  $H_a$  via  $\mu'' = M_S/(2 H_a\alpha)$ , where  $H_a$  and  $\alpha$  are the magneto crystalline anisotropy field and extinction coefficient, respectively. When Co-La ions are introduced,  $\mu''$  fall owing to the decrease in  $M_S$  as indicated above. In contrast, from 10.75 – 11.25 GHz the  $\epsilon''$  rises and  $\mu''$  decreases, while from 11.25 GHz to 11.5 GHz  $\epsilon''$  decreases  $\mu''$  rises, evidently decreasing the difference between  $\mu''$  and  $\epsilon''$  and so enhancing the impedance match [247].

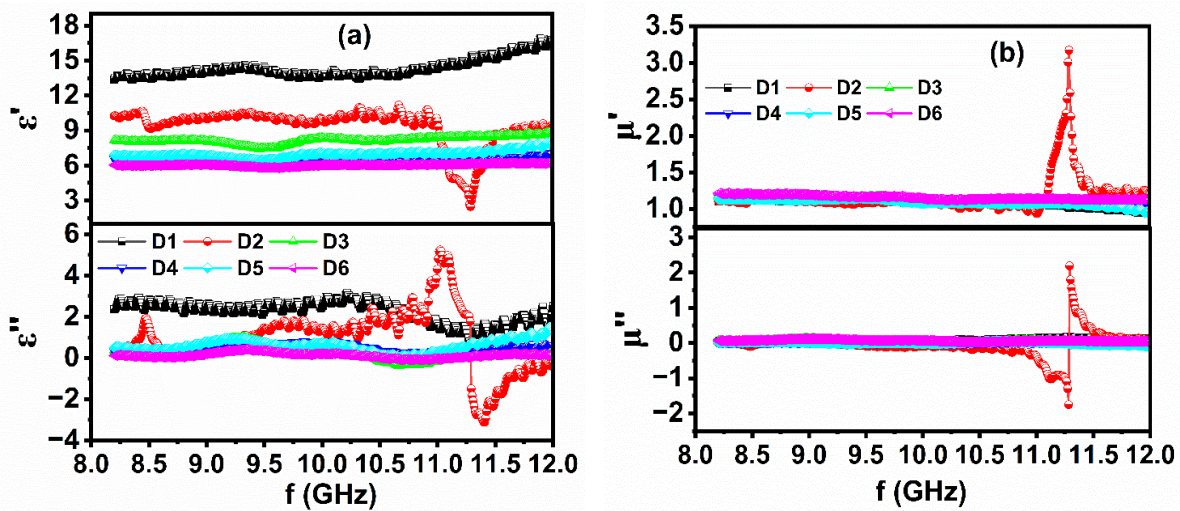


**Fig. 4.16.** (a) Complex permittivity and (b) permeability plots of D-series samples in 8-12 GHz.

The microwave absorption phenomena are investigated by examining REL plots as a function of frequency for different simulated thicknesses. Fig. 4.14(a, c, e), 4.15(a), 4.16(a, c), 4.17(a), 4.18(a, c) and 4.19(a) illustrate the REL plots of all synthesized samples and can be utilized to deduce parameters such as bandwidth/frequency range for REL of -10 dB (90% absorption) /-20 dB and matching frequency/thickness, as listed in Table 4.8. For better

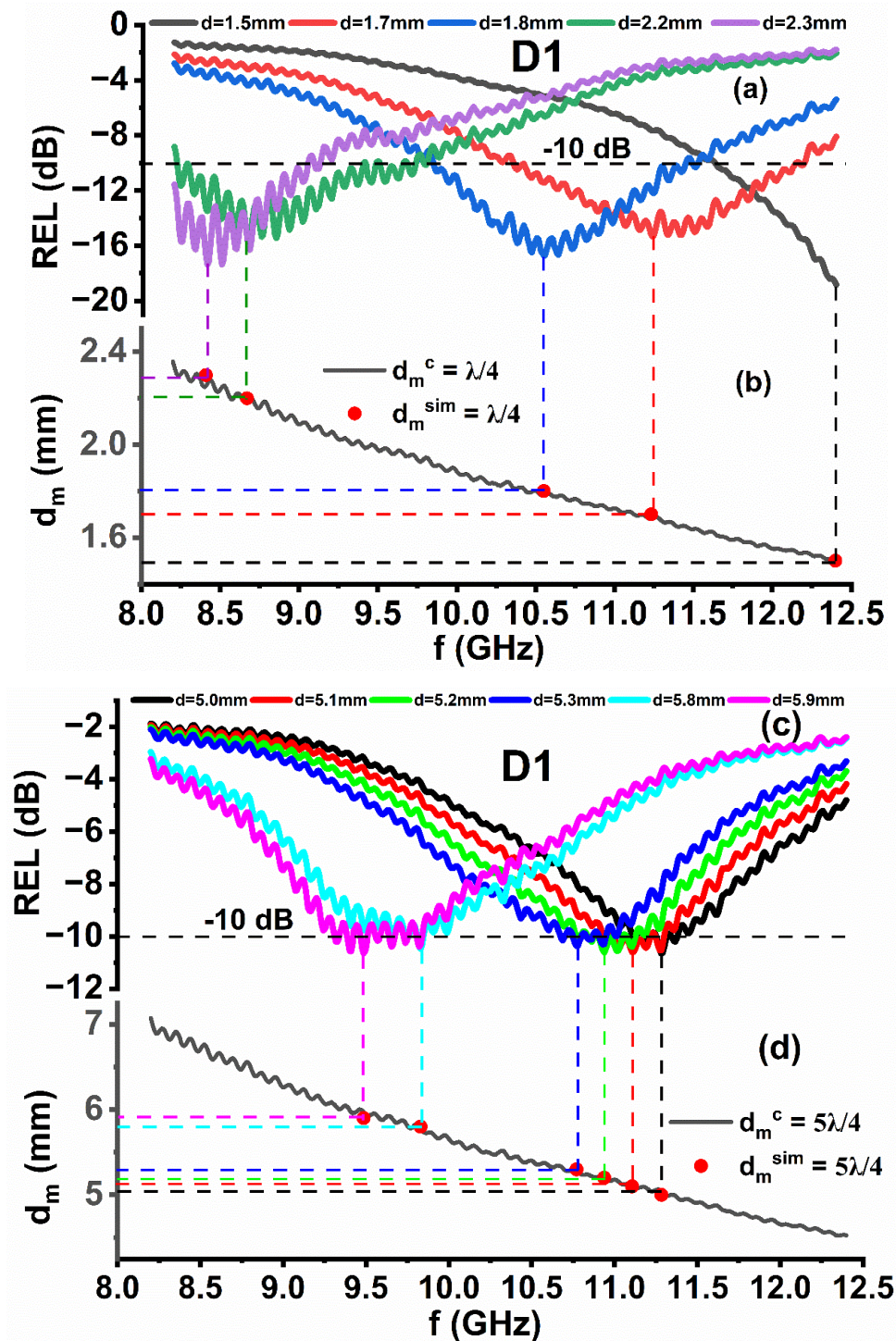


visualization Fig. 4.20 displays three-dimensional (3D) plots of REL of synthesized samples at various thicknesses and frequencies. The reflection loss dip shows in the form of color transformation, as the value of REL dip increases color gets transformed based on VIBGYOR from red to violet. The 3D plot of D1 outlined that REL dip is pronounced more at low thicknesses and it exhibits multiple REL dip  $> -10$  dB. Substitution of Co-La ions improves the microwave absorption properties of the synthesized sample. The highest dip in REL, measuring  $-45.61$  dB ( $> 99$  % absorption), is observed in the D3 sample [Fig. 4.16(a,b)], occurring at a frequency of 8.98 GHz and a thickness of 8.1 mm. Additionally, it shows multiple REL peaks with values greater than  $-10$  dB  $-20$  dB over a frequency range of 9.0 to 10 GHz with thickness 7.9 mm, 8.0 mm, and 8.1 mm. In Table 4.8, the remaining compositions exhibit REL values ranging from  $-10$  to  $-18.70$  dB, spanning frequencies between 8 and 12.4 GHz, and thicknesses between 5.0 and 10 mm. The plots illustrate the shift of REL peaks towards lower frequency ranges as the thickness increases. This trend aligns with the quarter wavelength mechanism described by equation 3.24, in which frequency and thickness are inversely related.

Fig. 4.14(a, c, e) demonstrated the absorption characteristics of the D1 sample within the examined frequency range. Reflection loss remains at or above  $-10$  dB, with REL peaks spanning the 8.2 to 12.4 GHz frequency spectrum from 1.5 to 7.0 mm thickness. For D2 and D4 samples, Fig. 4.15(a) and 4.17(a) reveal REL peaks with values  $> -10$  dB across thickness ranging from 7.8 to 8.1 mm and 8.0 to 8.5 mm, by covering a small frequency range of 8.46 to 8.47 GHz and 9.83 to 10.09 GHz, respectively. Fig. 4.18(a, c) is notable for the D5 sample, as it exhibits multiple REL peaks with values greater than  $-10$  dB over a wide range of frequency from 8.2 to 12.4 GHz and a thickness ranging from 6.6 to 10 mm. Fig. 4.19(a) for D6 sample display peaks with REL  $\geq -10$  dB across thickness ranging from 8.6 to 9.2 mm, covering the frequency range from 9 to 10 GHz.

Using equation 3.22, Reflection loss (REL) is computed using both the simulated thickness ( $d_m^{\text{sim}}$ ) and the calculated thickness ( $d_m^{\text{c}}$ ), which is determined through equation 3.24 by substituting values of  $n = 1, 3, 5$ , and so forth. The purpose is to establish a relationship between the quarter wavelength mechanism and REL peaks. Fig 4.14(b, d, f), 4.15(b), 4.16(b, d), 4.17(b), 4.18(b, d), and 4.19(b) depicts plots of a calculated thickness ( $n\lambda/4$ ) within the frequency range. To compare the simulated thickness ( $d_m^{\text{sim}}$ ) with the calculated thickness ( $n\lambda/4$ ), vertical lines are drawn from REL peaks to the thickness-frequency plots. Results indicate that the quarter wavelength mechanism is envisaged in D4,

D5, and D6 samples where the calculated thickness is  $5\lambda/4$  with  $n = 5$ . Conversely, D1 shows the occurrence of both  $\lambda/4$  and  $5\lambda/4$ , while D3 exhibits the presence of both  $5\lambda/4$  and  $9\lambda/4$  values. The existence of the  $\lambda/4$  mechanism in D1 results in  $REL \geq -10$  dB with maximum bandwidth ranging from 1.2 to 1.79 GHz and thickness between 1.5 and 7.0 mm, as detailed in Table 4.8. For all other substituted samples, REL peaks are observed within the thickness range of 6.5 to 10 mm.



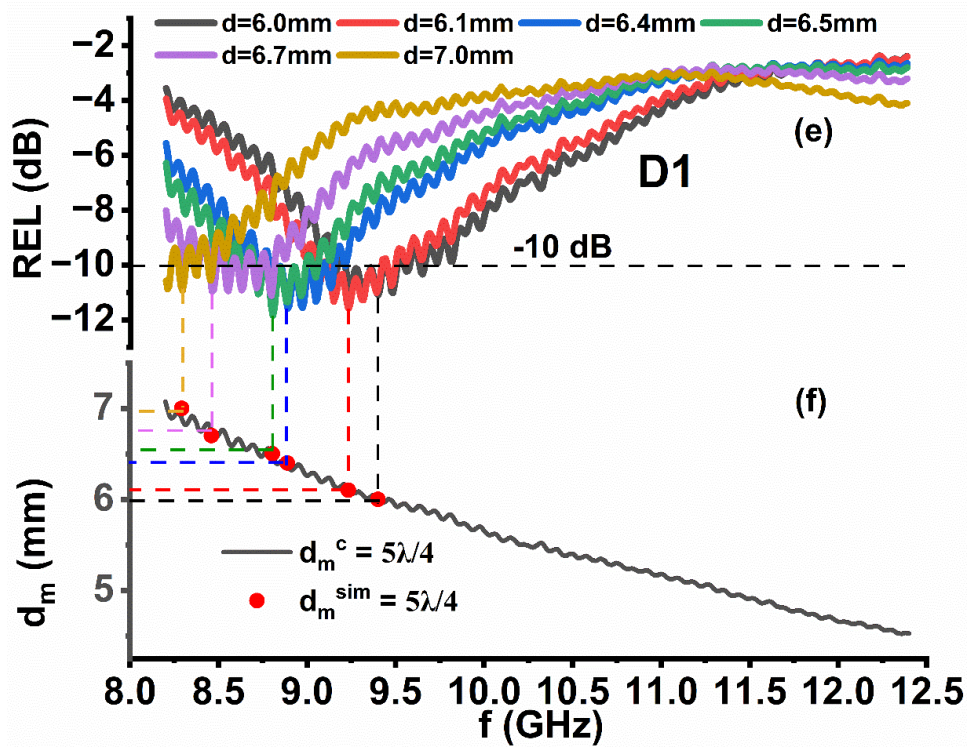


Fig. 4.17. (a, c, e) Dependence of REL on frequency in D1 sample. (b, d, f)  $d_m^{sim}$  and  $d_m^c$  versus frequency for  $\lambda$  and  $5\lambda/4$  in the D1 sample.

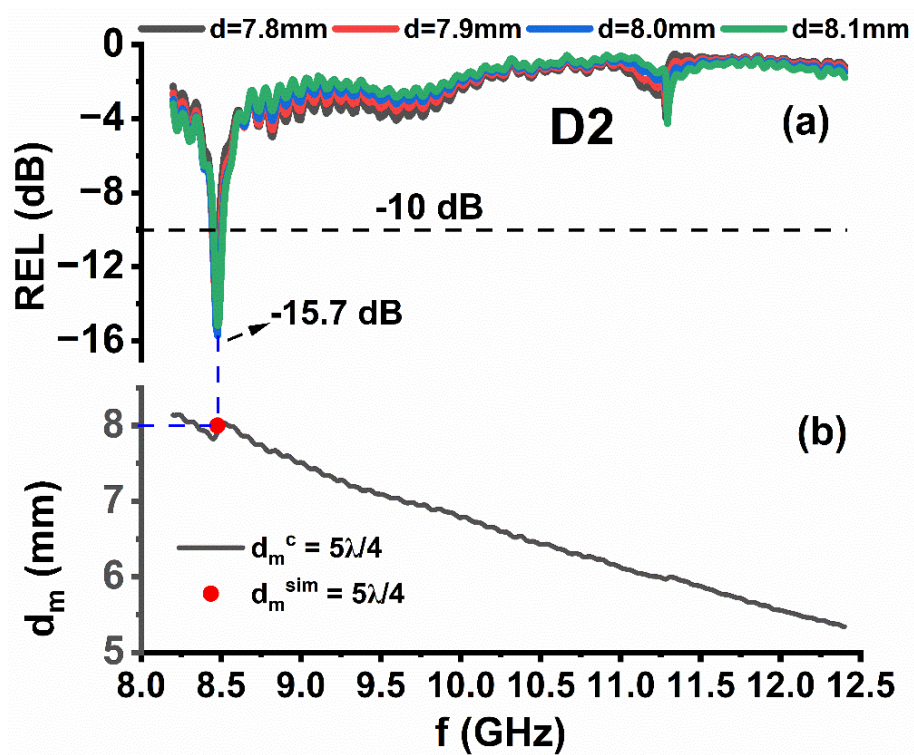


Fig. 4.18. (a) Dependence of REL on frequency in D2 sample. (b)  $d_m^{sim}$  and  $d_m^c$  versus frequency for  $5\lambda/4$  in the D2 sample.



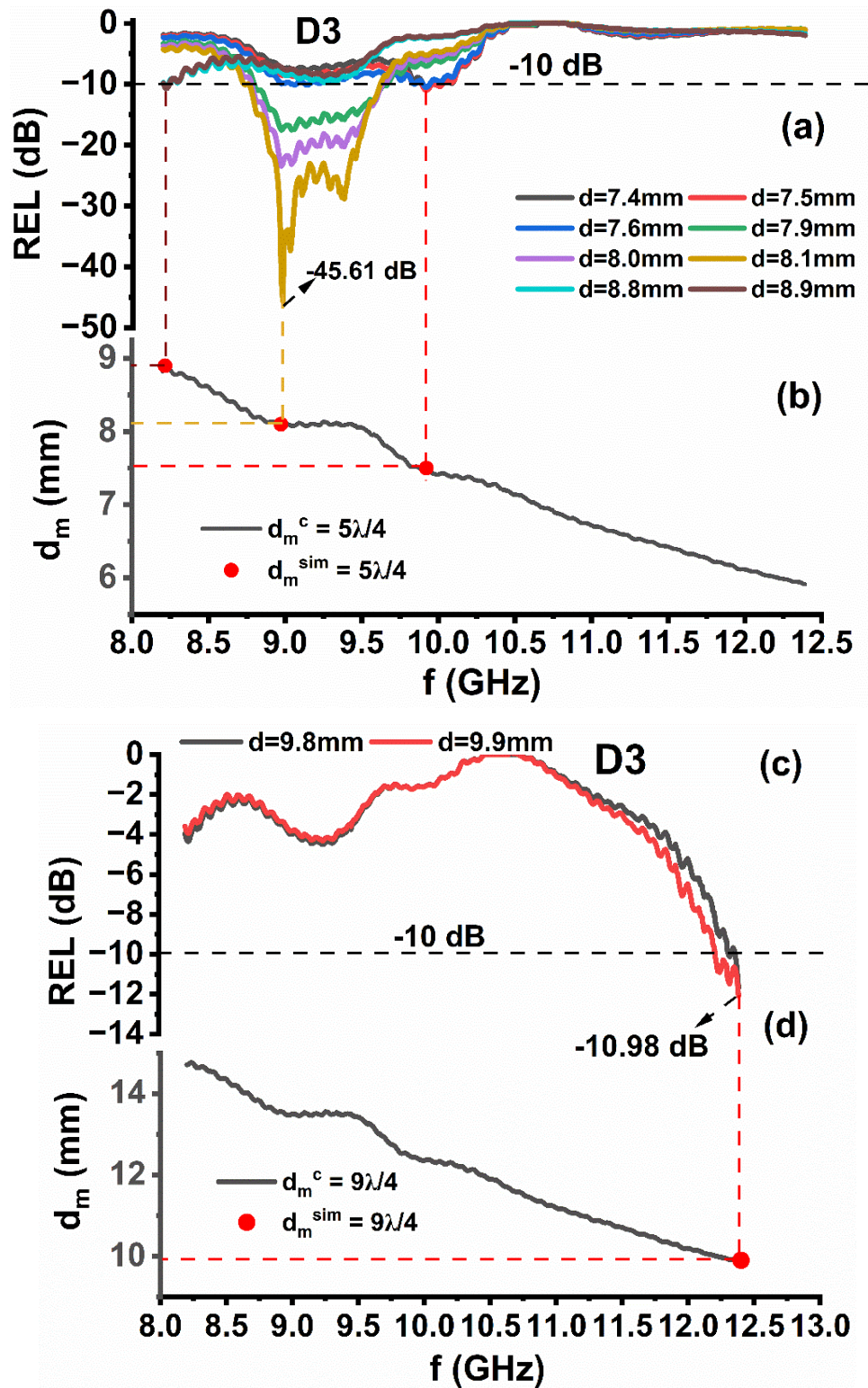


Fig. 4.19. (a, c) Dependence of REL on frequency in D3 sample. (b, d)  $d_m^{\text{sim}}$  and  $d_m^c$  versus frequency for  $5\lambda/4$  and  $9\lambda/4$  in D3 sample.

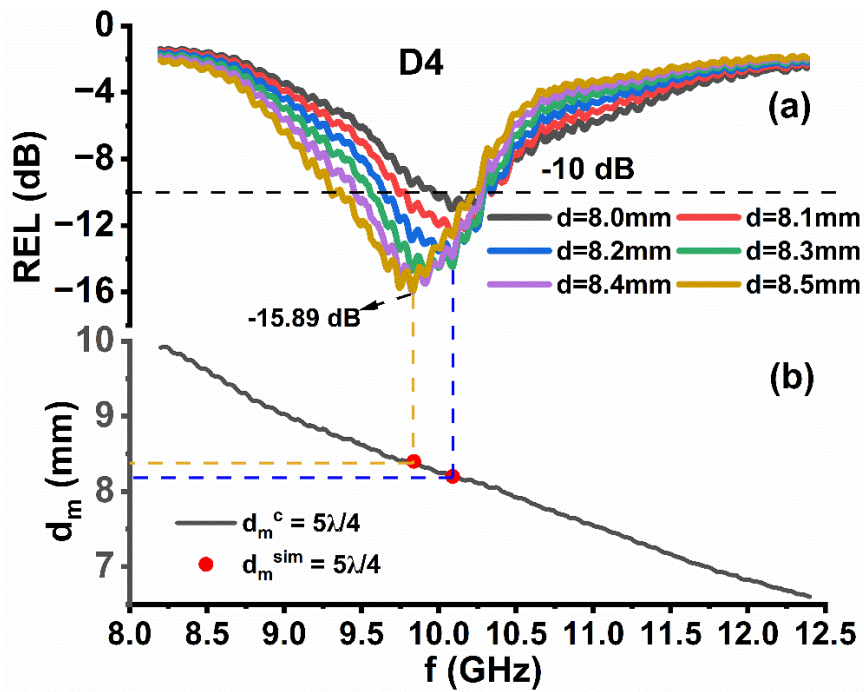
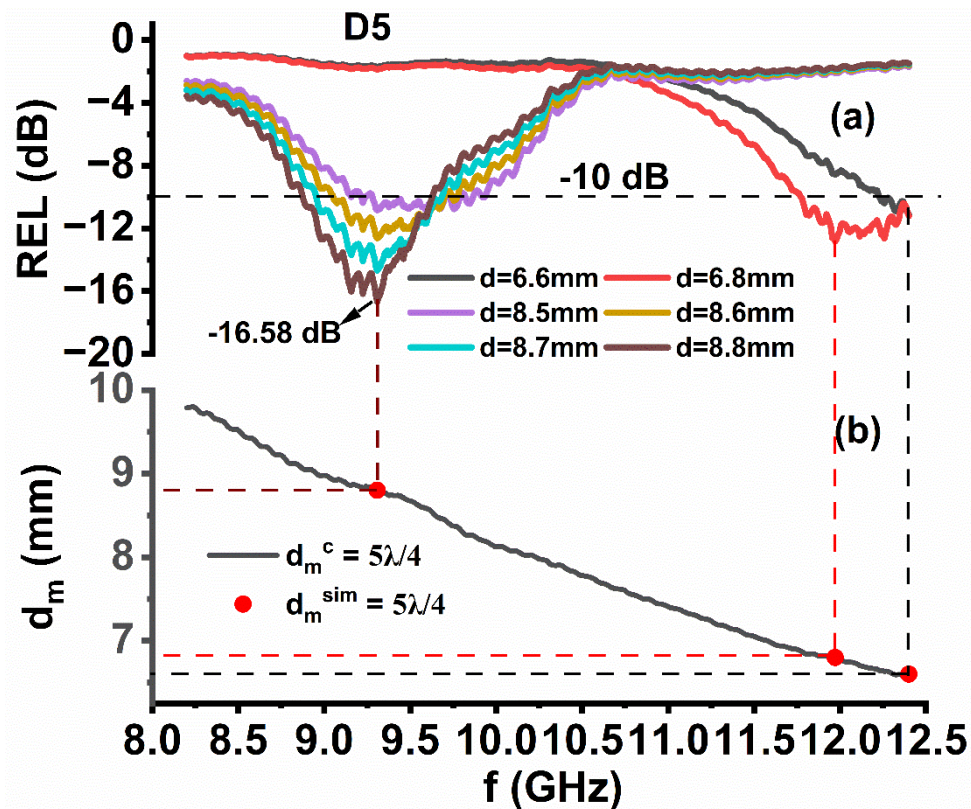


Fig. 4.20. (a) Dependence of REL on frequency in D4 sample. (b)  $d_m^{sim}$  and  $d_m^c$  versus frequency for  $5\lambda/4$  in the D4 sample.





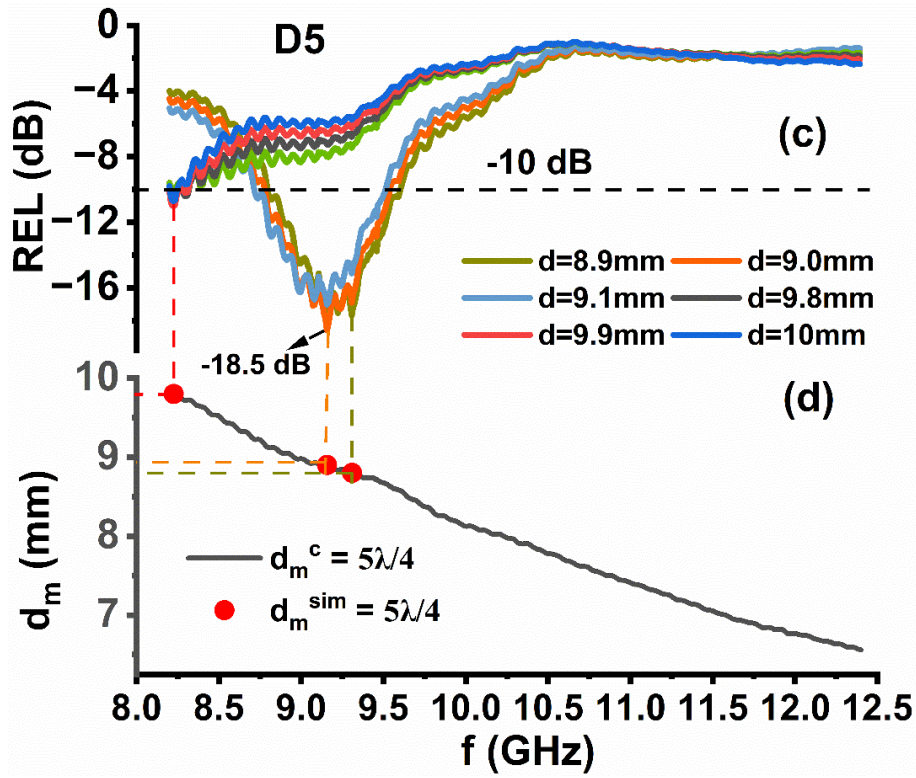


Fig. 4.21. (a, c) Dependence of REL on frequency in D5 sample. (b, d)  $d_m^{sim}$  and  $d_m^c$  versus frequency for  $5\lambda/4$  in the D5 sample.

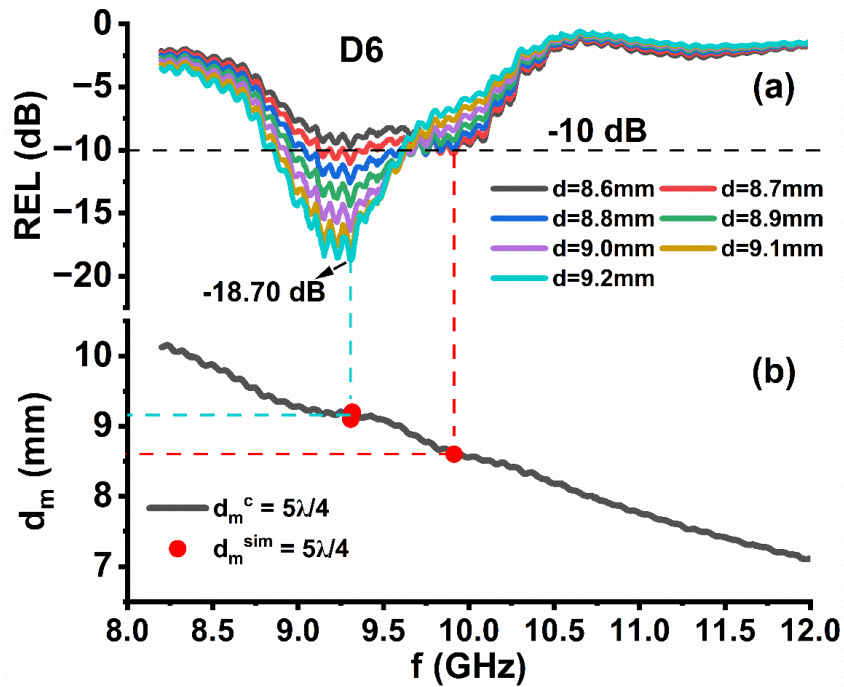


Fig. 4.22. (a) Dependence of REL on frequency in D5 sample. (b)  $d_m^{sim}$  and  $d_m^c$  versus frequency for  $5\lambda/4$  in the D5 sample.

**Table 4.8** Absorption parameters (REL > -10/-20 dB).

Sample Name	Matching Thickness (mm)	Maximum REL (dB)	Matching frequency (GHz)	Frequency Band for REL > -10 dB (GHz)	Bandwidth for REL > -10 dB (GHz)	Frequency Band REL > -20 dB (GHz)	Bandwidth for REL > -20 dB (GHz)	BTR	PBW (%)
<b>D1</b>	1.5	-18.83	12.4	--	--	--	--		
	1.7	-15.32	11.23	10.36-12.15	1.79	--	--	2.5E-03	15.9
	1.8	-15.98	10.55	9.85-11.44	1.59	--	--	2.3E-03	15
	2.2	-15.71	8.67	8.20-9.40	1.20	--	--	2.1E-03	13.8
	2.3	-17.38	8.41	--	--	--	--		
	5.0	-10.66	11.28	--	--	--	--		
	5.1	-10.60	11.10	--	--	--	--		
	5.2	-10.61	10.93	--	--	--	--		
	5.3	-10.36	10.77	--	--	--	--		
	5.8	-10.47	9.82	--	--	--	--		
	5.9	-10.64	9.48	--	--	--	--		
	6.0	-11.09	9.40	--	--	--	--		
	6.1	-11.59	9.23	--	--	--	--		
	6.4	-11.59	8.88	--	--	--	--		
	6.5	-11.34	8.80	--	--	--	--		
6.7	-10.96	8.46	--	--	--	--			
7.0	-10.92	8.29	--	--	--	--			
<b>D2</b>	7.8	-12.09	8.46	8.45-8.48	0.04	--	--	1.6E-05	0.4
	7.9	-14.44	8.46	8.44-8.49	0.05	--	--	2.6E-05	0.5
	8.0	-15.70	8.47	8.44-8.50	0.06	--	--	3.1E-05	0.7
	8.1	-15.17	8.47	8.45-8.50	0.05	--	--	2.6E-05	0.5
<b>D3</b>	7.4	-10.53	9.92	--	--	--	--		
	7.5	-10.98	9.92	--	--	--	--		
	7.6	-10.49	9.92	--	--	--	--		
	7.9	-17.52	8.97	8.79-9.66	0.87	--	--	3.9E-04	9
	8.0	-23.45	8.97	--	--	8.78-9.63	0.85	3.8E-04	9
	8.1	-45.61	8.98	--	--	8.76-9.62	0.86	3.8E-04	9
	8.8	-10.49	8.21	--	--	--	--		
8.9	-10.71	8.21	--	--	--	--			

	9.8	-11.68	12.4	--	--	--	--		
	9.9	-12.08	12.4	--	--	--	--		
<b>D4</b>	8.0	-11.02	10.09	--	--	--	--		
	8.1	-12.62	10.09	9.98-10.27	0.29	--	--	1E-04	2
	8.2	-13.95	10.09	9.79-10.29	0.50	--	--	1.8E-04	4
	8.3	-14.68	9.83	9.65-10.3	0.65	--	--	2.4E-04	6
	8.4	-15.96	9.83	9.56-10.29	0.73	--	--	2.7E-04	7
	8.5	-15.89	9.83	9.46-10.28	0.82	--	--	3E-04	8
<b>D5</b>	6.6	-11.12	12.4	12.23-12.4	0.17	--	--	5.1E-05	1
	6.8	-12.82	11.97	11.77-12.4	0.63	--	--	1.9E-04	5
	8.5	-10.84	9.30	--	--	--	--		
	8.6	-12.63	9.30	9.06-9.71	0.65	--	--	2.6E-04	6
	8.7	-14.67	9.30	8.95-9.68	0.73	--	--	2.9E-04	7
	8.8	-16.67	9.30	8.87-9.62	0.75	--	--	3E-04	8
	8.9	-18.12	9.15	8.80-9.60	0.80	--	--	3.2E-04	8
	9.0	-18.59	9.15	8.78-9.54	0.76	--	--	3E-04	8
	9.1	-17.02	9.15	8.71-9.51	0.80	--	--	3.2E-04	8
	9.7	-10.32	8.22	--	--	--	--		
	9.8	-10.871	8.22	--	--	--	--		
	9.9	-11.01	8.22	--	--	--	--		
	10	-10.77	8.22	--	--	--	--		
<b>D6</b>	8.6	-10.29	9.91	--	--	--	--		
	8.7	-11.06	9.30	--	--	--	--		
	8.8	-12.59	9.30	9.04-9.54	0.50	--	--	2E-04	5
	8.9	-14.39	9.30	8.95-9.63	0.68	--	--	2.7E-04	7
	9.0	-16.38	9.30	8.92-9.62	0.70	--	--	2.7E-04	7
	9.1	-18.13	9.30	8.88-9.64	0.76	--	--	2.9E-04	8
	9.2	-18.70	9.30	8.86-9.61	0.75	--	--	2.9E-04	8

For several matching thicknesses, D2 has REL > -10 dB along with a narrow bandwidth of 0.05 GHz from 8.45-8.50 GHz with matching thicknesses of 7.8 to 8.1 mm. The highest value of REL is elucidated for the D3 sample at -45.61 dB and a thickness of 8.1 mm. Additionally, D3 exhibits REL values greater than -10 dB /-20 with effective broad bandwidths of 0.87 GHz and 0.86GHz from 8.79-9.66 GHz and 8.76-9.62 GHz with matching thicknesses of 7.9 mm and 8.1 mm, respectively. It can be depicted from [Table 4.8](#), that D4 owes REL> -10 dB with a wide absorption bandwidth of 0.82 GHz and narrow



bandwidth of 0.29 GHz from 9.46-10.28 GHz and 9.98-10.27 GHz with matching thicknesses of 8.5 and 8.1 mm, respectively. In the case of the D5 sample, REL  $\geq$  -10 dB narrow (0.17 GHz) and wide (0.80 GHz) absorption bandwidth is observed from 12.23-12.4 GHz and 8.80-9.60 GHz at 6.6 and 8.9 mm, respectively. For the D6 sample, a -10 dB broad bandwidth of 0.76 GHz is observed over the 8.88-9.64 GHz frequency range at 9.1 mm thickness.

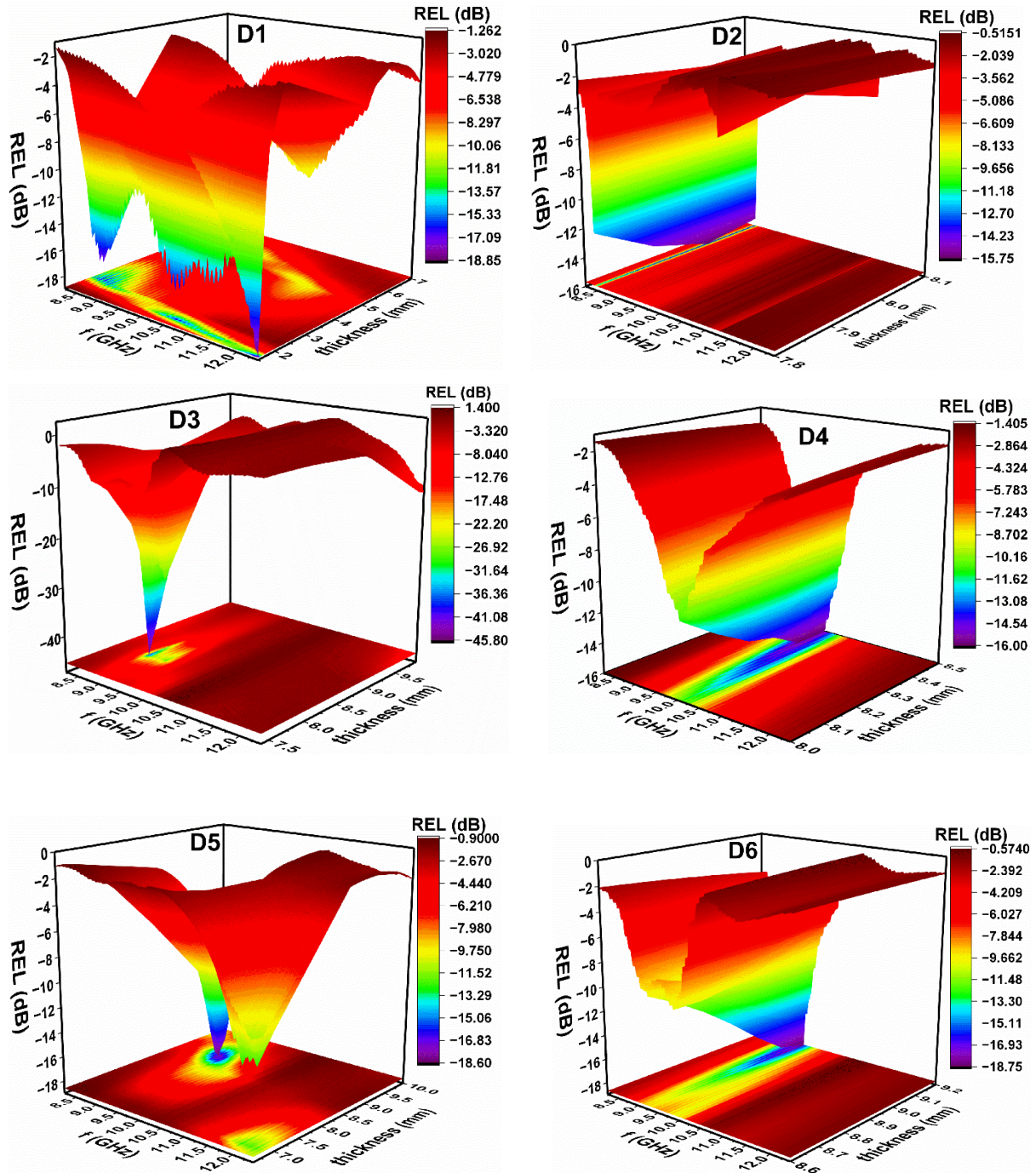


Fig. 4.23. Three-dimensional (3D) plots of reflection loss at various frequencies and thicknesses for all samples of D-series.

The significant factor in designing and evaluating absorber performance, apart from achieving, an REL value of at least -10 dB, is the ample bandwidth to be obtained at a minimal thickness for a standard REL or absorption dip. Once you reach this REL limit, it becomes important to prioritize a thinner material thickness rather than solely thriving to improve the REL value. [Table 4.8](#) enumerates the value of BTR and PBW of all synthesized samples calculated using equations [3.25](#) and [3.26](#). The BTR is highest in the D1 sample with values of 2.5E-03 and PBW (15.3 %) at 11.23 GHz and REL = -15.9 dB at 1.7 mm thickness. Notably, the D3 sample owes a considerably high REL of -45.61 dB, has a lower BTR than the D1 sample, where REL doesn't exceed -18 dB.

The characteristic impedance of free space, denoted as  $Z_0 = 377 \Omega$ , is calculated as the square root of the ratio of permeability to permittivity values for free space. In contrast, the impedance of the absorber is called  $Z_{in}$  and it differs from the impedance of free space due to differences in their permeability and permittivity characteristics. When a microwave signal propagates through free space and encounters an absorber, a portion of the signal is reflected from the absorber's surface. The extent of this reflection depends on the near and far value of  $Z_{in}/Z_0 \cong 1$ . The farther the  $Z_{in}/Z_0$  value from 1, the greater the level of signal reflection. When  $Z_{in}/Z_0$  differs significantly from 1, only a small part of the microwave signal manages to penetrate the absorber material, while most is reflected. Consequently, even though the absorber material exhibits maximum dielectric and magnetic loss properties, the actual attenuation or absorption of the signal inside the absorber is minimal and lacks practical significance due to the dominance of signal reflection. Therefore, it is important to consider the impedance matching between the absorber and free space, resulting in  $Z_{in}/Z_0 \cong 1$  when designing the absorber material and its application in microwave systems. [Fig. 4.21\(a\)](#), [4.22\(a\)](#), [4.23\(a\)](#), [4.24\(a\)](#), [4.25\(a, c\)](#), and [4.26\(a, c\)](#) illustrate the graphs of reflection loss and  $Z_{in}/Z_0$  as a function of frequency for some considerable thicknesses of samples. Impedance matching may manifest as REL peaks with  $Z_{in}/Z_0 \cong 1$  at specific frequencies, corresponding to different thicknesses of matching materials. [Table 4.10](#) enumerates the  $Z_{in}/Z_0$  values for these samples, obtained from  $Z_{in}/Z_0$  plots illustrated in the mentioned figures. The values of  $Z_{in}/Z_0$  ([Table 4.9](#)) are from 0.9 to 1.45 for all synthesized samples.

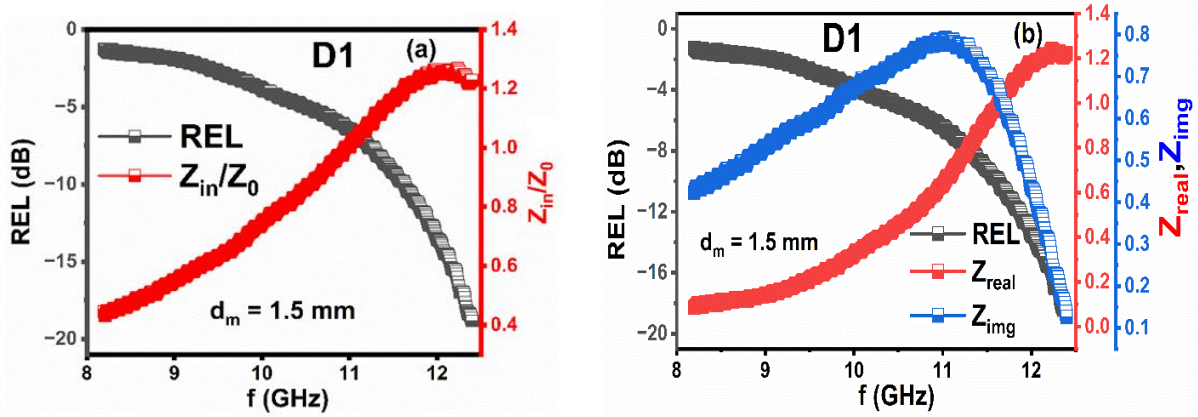
The problem is found in the D5 sample, wherein REL -10.84 dB at 9.30 GHz frequency 8.5 mm thickness with  $Z_{in}/Z_0 = 1.192$  ([Table 4.9](#)) which is close to 1. Conversely, at 9.15 GHz and a thickness of 9.0 mm, a relatively higher REL -18.59 dB with  $Z_{in}/Z_0 = 1.242$  [[Fig. 4.25\(a, c\)](#) and [Table 4.9](#)] which is far away from 1. A similar situation arises in

the D6 sample owes REL -11.06 dB at 9.30 GHz and 8.7 mm thickness with  $Z_{in}/Z_0 = 1.071$  (closer to 1) (Table 4.9), whereas at 9.30 GHz and 9.2 mm thickness, a relatively large REL = -18.70 dB is observed, but  $Z_{in}/Z_0 = 1.258$ , which is farther from 1 [Fig. 4.26 (a, c)]. This behavior may elucidate the complex nature of  $|Z_{in}|$  (Equation 3.21) including real/imaginary terms  $Z_{real}/Z_{img}$ . The  $Z_{real}/Z_{img}$  values for maximum REL are estimated from plots displayed in Fig. 4.21(b), 4.22(b), 4.23(b), 4.24(b), 4.25(b, d), and 4.26(b, d) and listed in Table 4.9. It can be observed from Table 4.9 that D3 exhibits maximum REL value (-45.61 dB at 8.98 GHz) and has  $Z_{real} = 0.997$  and  $Z_{img} = 0.010$  which are respectively close to 1 ( $Z_{real}$ ) and 0 ( $Z_{img}$ ) than other samples. Due to more offset values of  $Z_{real}/Z_{img}$  from 1 and/or 0, sample D1, D2, D4, and D5 owes a relatively lower REL value than the D3 sample. Substitution of Co-La ions changes the  $Z_{in}$  ( $Z_{real}$  and  $Z_{img}$ ) of the synthesized samples. Table 4.9 depicts that the impedance mechanism quantifies more in the D3 sample, while the quarter wavelength mechanism is satisfied by all synthesized samples, except D6. Fig. 4.27 displays the dependence of  $C_o$  on frequency for all samples of D-series, suggesting no contribution of eddy current in absorption characteristics.

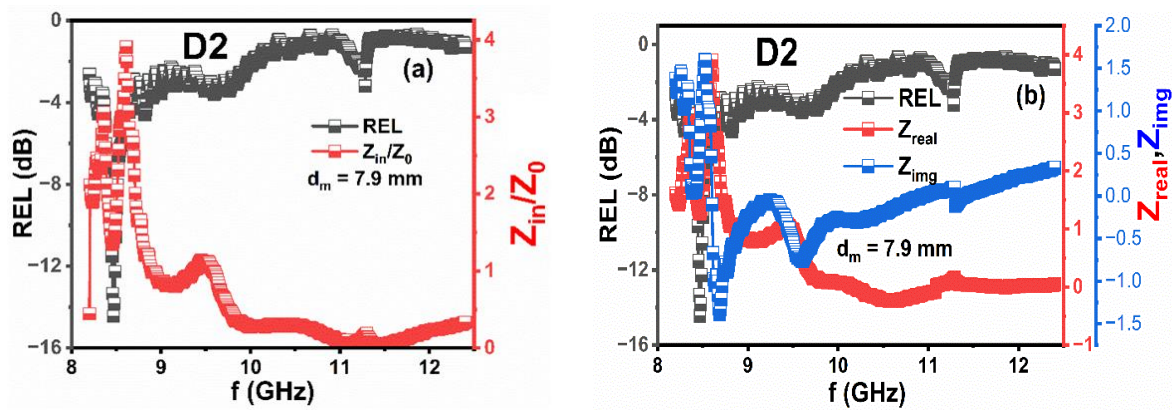
**Table 4.9** Reflection loss peak's impedance parameters at different thicknesses.

Sample Name	Thickness (mm)	Max. REL (dB)	Matching frequency (GHz)	$Z_{in}/Z_0$	$Z_{real}$	$Z_{img}$
<b>D1</b>	1.5	-18.83	12.4	1.227	1.220	0.125
	2.3	-17.38	8.41	1.312	1.312	-0.004
<b>D2</b>	7.9	-14.44	8.46	1.430	1.267	0.661
	8.0	-15.70	8.47	1.656	1.560	0.536
<b>D3</b>	7.9	-17.52	8.97	0.986	0.951	0.257
	8.0	-23.45	8.97	1.012	1.003	0.134
	8.1	-45.61	8.98	0.997	0.997	0.010
<b>D4</b>	8.4	-15.96	9.83	1.378	1.378	0.014
	8.5	-15.89	9.83	1.329	1.313	-0.200
<b>D5</b>	8.5	-10.84	9.30	1.192	1.026	0.606
	8.6	-12.63	9.30	1.264	1.164	0.491
	8.9	-18.12	9.15	1.276	1.274	0.066
	9.0	-18.59	9.15	1.242	1.236	-0.115
<b>D6</b>	9.1	-17.02	9.15	1.181	1.151	-0.265
	8.7	-11.06	9.30	1.071	0.918	0.552

	8.9	-14.39	9.30	1.202	1.137	0.390
	9.0	-16.38	9.30	1.245	1.218	0.258
	9.1	-18.13	9.30	1.265	1.260	0.103
	9.2	-18.70	9.30	1.258	1.256	-0.057

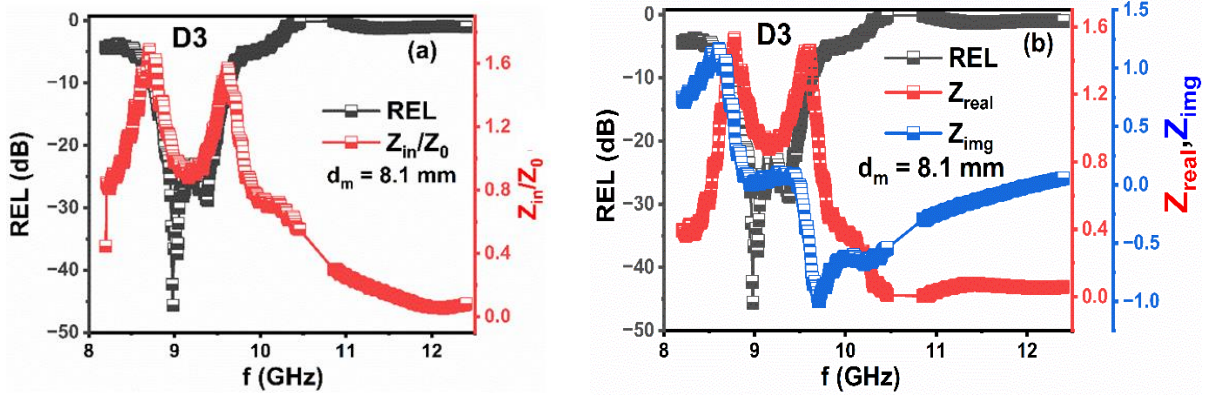


**Fig. 4.24.** (a) Dependence of  $Z_{in}$  and REL in frequency (b) Dependence of REL,  $Z_{real}$ , and  $Z_{img}$  on frequency for D1 sample.

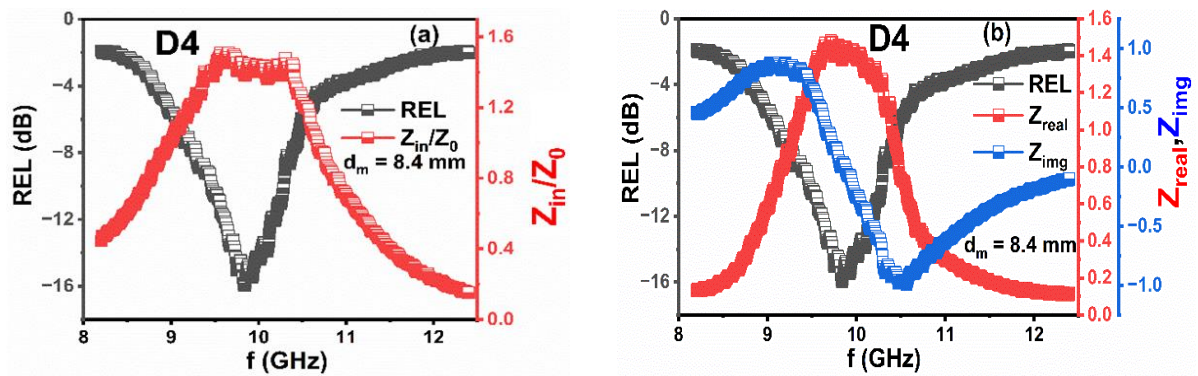


**Fig. 4.25.** (a) Dependence of  $Z_{in}$  and REL in frequency (b) Dependence of REL,  $Z_{real}$ , and  $Z_{img}$  on frequency for D2 sample.



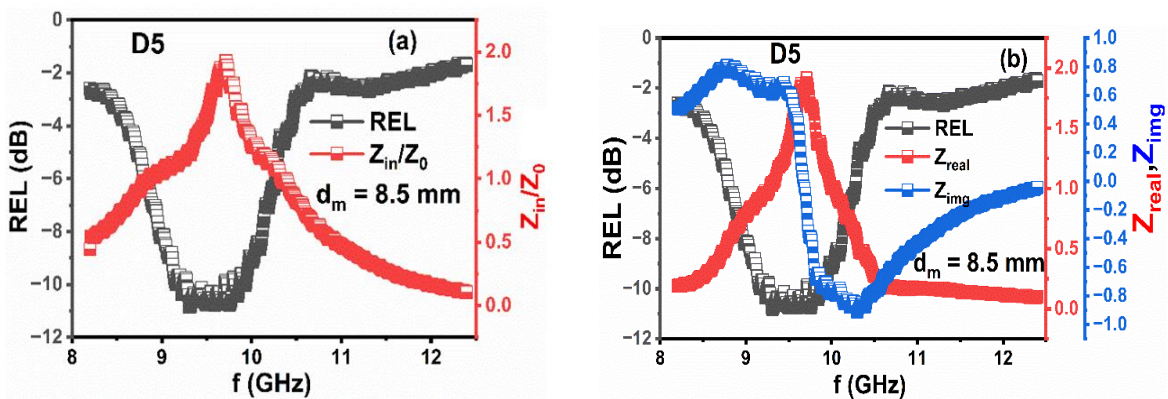


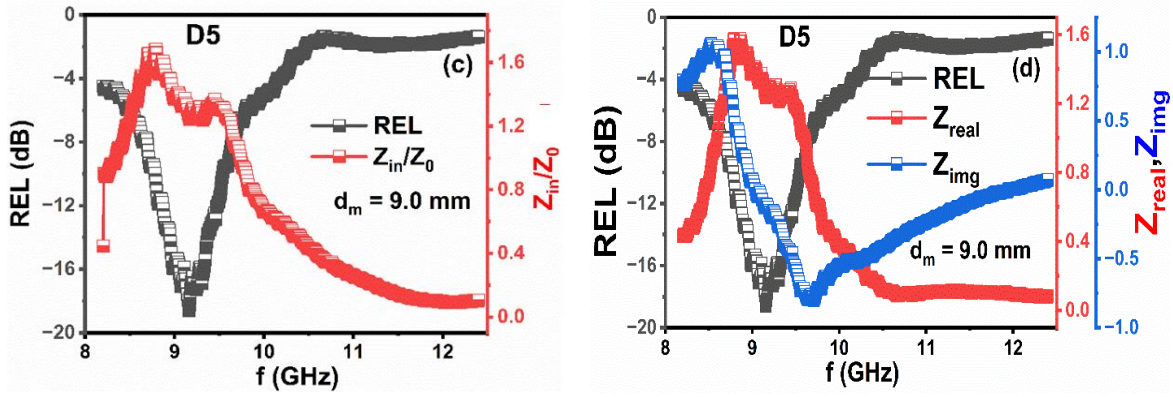
**Fig. 4.26.** (a) Dependence of  $Z_{in}$  and REL in frequency (b) Dependence of REL,  $Z_{real}$ , and  $Z_{img}$  on frequency for D3 sample.



**Fig. 4.27.** (a) Dependence of  $Z_{in}$  and REL in frequency (b) Dependence of REL,  $Z_{real}$ , and  $Z_{img}$  on frequency for D4 sample.

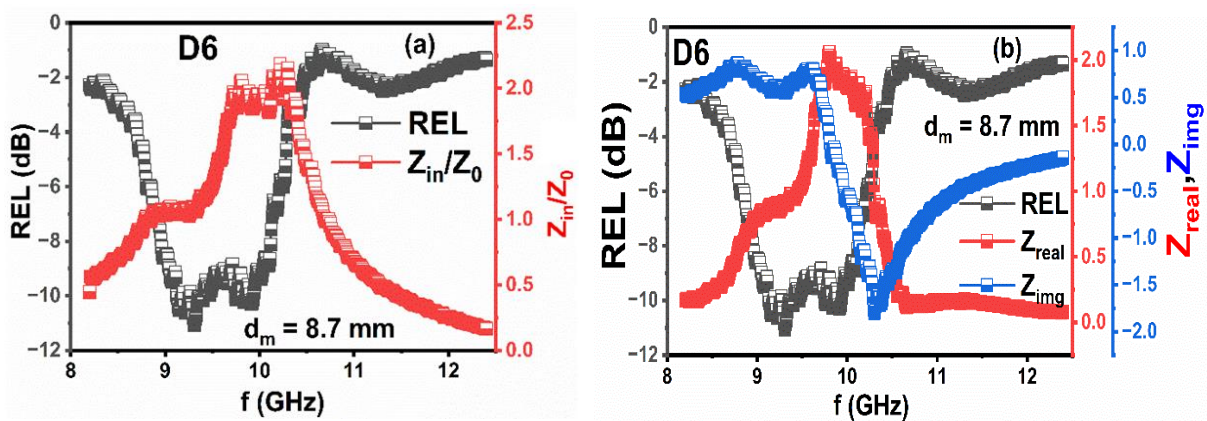
The single-phase magnetoplumbite structure and morphology of the D-series significantly influence their electrical, magnetic, and microwave characteristics. A magnetoplumbite structure consists of five distinct layers within the unit cell, which contribute to the material's magnetic properties whereas, grain size and grain boundaries influence the electrical analysis.





**Fig. 4.28.** (a, c) Dependence of  $Z_{in}$  and REL in frequency (b, d) Dependence of REL,  $Z_{real}$ , and  $Z_{img}$  on frequency for D5 sample.

The alignment of spins in the magnetoplumbite structure results in high saturation magnetization as observed in D1 (103.29 emu/g), which leads to high hysteresis loss. The presence of pores, or non-magnetic voids obstructs the flow of magnetic flux due to poor inter-grain connectivity, leads to high coercivity (5026.54 Oe). Consequently, a higher magnetic field is required for magnetizing and demagnetizing the ferrite, thereby increasing hysteresis loss. The substitution of Co-La ions decreases the saturation magnetization ( $M_s$ ) from 103.29 emu/g to 67.96 emu/g, and the coercivity ( $H_c$ ) from 5026.54 Oe to 862.47 Oe. The introduction of Co-La ions causes a gradual decrease in dielectric loss  $\epsilon''$ , which results in less reflection loss. Another critical parameter contributing to the performance of absorber material is impedance matching  $Z_{in}/Z_0 \cong 1$  i.e.  $Z_{real} = 1$  and  $Z_{img} = 0$ . For sample D3,  $Z_{real} = 0.997$  and  $Z_{img} = 0.010$ , is very close to the ideal values 1 ( $Z_{real}$ ) and 0 ( $Z_{img}$ ), compared to other samples. This results in D3 maximum REL of -45.61 dB at 8.1 mm thickness.



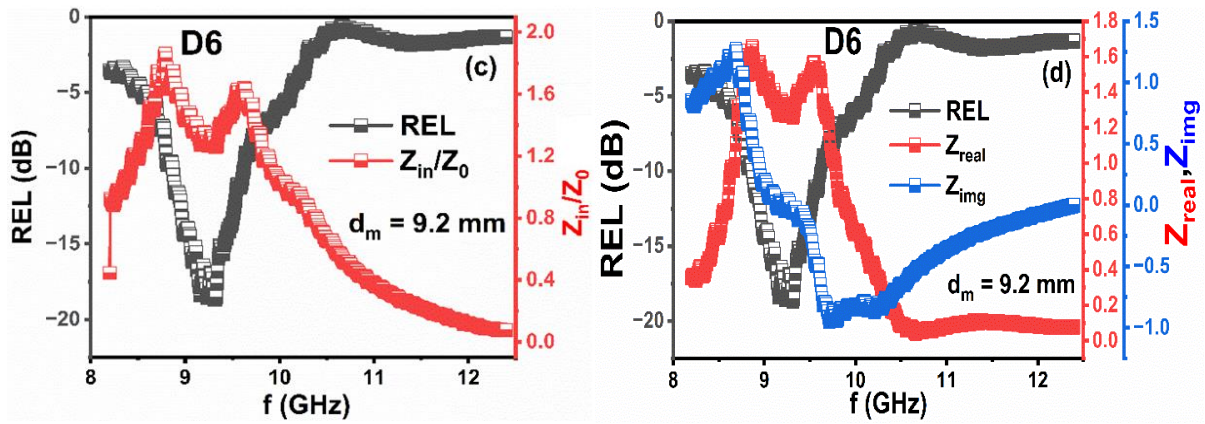


Fig. 4.29. (a) Dependence of  $Z_{in}$  and REL in frequency (b) Dependence of REL,  $Z_{real}$ , and  $Z_{img}$  on frequency for D6 sample.

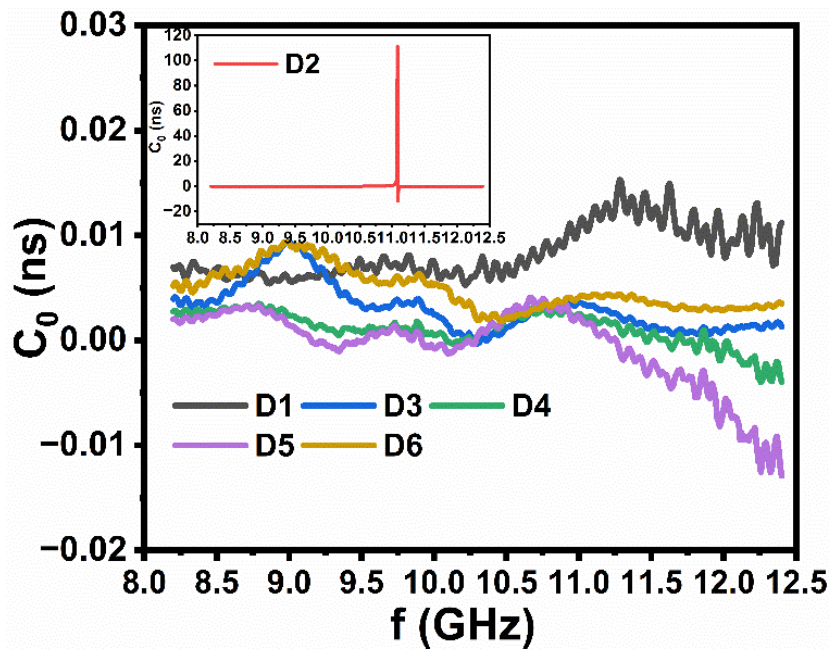


Fig. 4.30. Dependence of  $C_0$  on the frequency of D-series samples.



## 4.2 Co<sup>2+</sup>- Cr<sup>3+</sup> substituted Sr(CoCr)<sub>x</sub>Fe<sub>12-2x</sub>O<sub>19</sub> hexaferrite.

In the present section, we intend to use the sol-gel combustion method to synthesize Co and Cr substituted SrFe<sub>12</sub>O<sub>19</sub> hexaferrite, having composition Sr(CoCr)<sub>x</sub>Fe<sub>12-2x</sub>O<sub>19</sub> Table 4.10 displays the assignment of sample names/codes for a different level of substitution for Sr(CoCr)<sub>x</sub>Fe<sub>12-2x</sub>O<sub>19</sub>.

**Table 4.10** Assignment of sample name for a different level of substitution of Sr(CoCr)<sub>x</sub>Fe<sub>12-2x</sub>O<sub>19</sub> hexaferrite.

Sample Composition Sr(CoCr) <sub>x</sub> Fe <sub>(12-2x)</sub> O <sub>19</sub>	Sample Code (B-series)
x = 0.0	B1
x = 0.2	B2
x = 0.4	B3
x = 0.6	B4
x = 0.8	B5
x = 1.0	B6

### 4.2.1 Structural Analysis

#### 4.2.1.1 X-ray Diffraction Analysis

The phase purity and the crystalline structure of B-series hexagonal ferrites are matched with JCPDS file # 80-1197 (Xp powder software) of M-type hexaferrite as seen in Fig. 4.28. The reflection plane of sintered samples is as (006), (110), (112), (107), (114), (108), (203), (205), (206), (217), (2011) and (220) depicts the establishment of magnetoplumbite structure of space group P63/*mmc* (194) [248]. The confirmation of the successful replacement of Co<sup>2+</sup> and Cr<sup>3+</sup> ions in Fe<sup>3+</sup> is attributed to no secondary peak/phase of substituted ions in SrFe<sub>12</sub>O<sub>19</sub>. The relative shift occurs towards the right side in the Bragg angle of the high-intensity peak (114) due to Co<sup>2+</sup>- Cr<sup>3+</sup> substitution. The relative change in the intensity of peaks with the increment of Co<sup>2+</sup> – Cr<sup>3+</sup> ions is an indicator of the fact that substituted ions have occupied crystallographic sites. It is further associated with different ionic radii of Co<sup>2+</sup> (0.72 Å) and Cr<sup>3+</sup> (0.62 Å) ions than Fe<sup>3+</sup> (0.64 Å) ions. Table 4.11 list the structural parameters of substituted samples calculated using equation 3.1 and



3.2. The structural parameters ‘ $a$ ’, ‘ $c$ ’,  $V_{cell}$ , and  $c/a$  of prepared samples, are in good agreement with a standard JCPDS file # 80-1197. It is noted from Table 4.11 that the lattice parameter ‘ $a$ ’ value observes a meager change, and in contrast, the lattice constant ‘ $c$ ’ displays considerable variation with substitution. This can be attributed that the  $c$ -axis which gets easily magnetized undergoes more expansion than the  $a$ -axis. Moreover, Table 4.11 also reveals that the cell volume of substituted sintered samples comes out to be less than undoped samples due to, unlike ionic radii of substituted ions than host ion. It has been analyzed from Table 4.11 that the height to width i.e.  $c/a$  ratio of hexagonal ferrite falls below 3.98 which describes the sintered sample forming the hexagonal structure. Table 4.12 enlist the value of bulk density ( $\rho_{bulk}$ ), X-ray density ( $\rho_x$ ), Porosity (P), crystallite size ( $D$ ), surface area (S), and lattice strain ( $\epsilon$ ). The value of crystallite size (nm) was estimated from the Scherrer formula (using equation 3.3) indicating an irregular trend with the random increment of  $Co^{2+} - Cr^{3+}$  ions. The calculated values of  $D$  are perceived to be in the range 40 – 36 nm as seen in Table 4.12. The diversity in crystallite size owes to variable lattice strain in the magnetoplumbite crystal structure as seen in Table 4.12.

As from equation 3.9,  $\rho_x$  is directly and inversely correlated to the molar mass and  $V_{cell}$ , respectively. Furthermore, the value of  $\rho_{bulk}$  is less than  $\rho_x$  which could be due to the presence of pores that appeared during the process of sintering as seen in SEM. Another important factor is the higher atomic mass of the substituted ion than the host ion. While there is a non-linear pattern apparent in seen in the porosity parameter of the sintered samples with substitutions. The surface area value falls within the range of 29-30  $cm^2/g$ , which correlates with the crystallite size, as seen in equation 3.11. As the crystallite size increases, the surface area decreases, resulting in a lower no. of atoms on the surface.

**Table 4.11** Structural parameters  $V_{cell}$ ,  $a$ ,  $c$  and  $c/a$  ratio of B-series sintered hexaferrite.

Sample name	$a$ (Å)	$c$ (Å)	$V_{cell}$ (Å <sup>3</sup> )	$c/a$
B1	5.888	23.173	693.83	3.9409
B2	5.884	23.046	690.96	3.9167
B3	5.884	22.951	688.12	3.9005
B4	5.883	23.014	689.77	3.9119
B5	5.869	23.027	686.88	3.9234
B6	5.879	23.128	692.24	3.9340

**Table 4.12** Various parameters such as Xrd density ( $\rho_x$ ), bulk density ( $\rho_{bulk}$ ), porosity (P), the crystallite size (D), lattice strain ( $\epsilon$ ) and surface area (S) of B-series samples.

Sample name	Density(g/cm <sup>3</sup> )		Porosity(P) (%)	D (nm)	Lattice strain ( $\epsilon$ )	S × 10 <sup>7</sup> (cm <sup>2</sup> /g)
	XRD ( $\rho_x$ )	bulk ( $\rho_{bulk}$ )				
B1	5.09	3.03	40.48	40	0.0029	29.66
B2	5.11	2.62	48.72	39	0.0030	30.13
B3	5.13	2.90	43.46	36	0.0033	32.70
B4	5.12	2.68	47.65	38	0.0031	30.84
B5	5.15	2.38	53.78	38	0.0030	30.35
B6	5.11	2.48	51.46	37	0.0032	31.99

#### 4.2.1.2 FTIR Spectroscopy Analysis

The FTIR spectroscopy comprehensively analyzed the ferrite phase formation, molecular bands, and attached functional groups. The measurements of B-series sintered hexaferrite was noted in Fig. 4.29 in the IR range from 4000 - 400 cm<sup>-1</sup>. Table 4.13 lists the allocation of several absorption bands detected in Fourier transform infrared spectroscopy. Generally, M-type hexagonal ferrite constitutes metal-oxygen ions that are distributed across 5 different sublattices. The noticeable absorption peaks around 400-600 cm<sup>-1</sup> determines the stretching and bending vibration of metal-oxygen at tetrahedral as well as octahedral sites, providing insights into the formation of M-type hexaferrites. The absorption bands within the 550-600 cm<sup>-1</sup> ( $\nu_1$ ) and 400-450 ( $\nu_2$ ) ranges attributed to Fe – O stretching through Fe - O<sub>4</sub> and Fe – O bending due to Fe - O<sub>4</sub> and Fe - O<sub>6</sub>, respectively. Fig. 4.29 illustrates that substitution causes a slight gradual shift in  $\nu_1$  and  $\nu_2$  toward the lower frequency side. A weak absorption peak of CO<sub>2</sub> occurs at 2354 cm<sup>-1</sup>, while there is no other absorption peak in the range 4000 - 1000 cm<sup>-1</sup>. This indicates the nonexistence of metal carbonates (in the form of remaining carbon), NO<sub>3</sub> stretching vibrations and residual water in all sintered hexaferrite. It is attributed to completely burnt-off carbon, nitrates, and residual water through the self-ignition process during the preparation of ferrite.

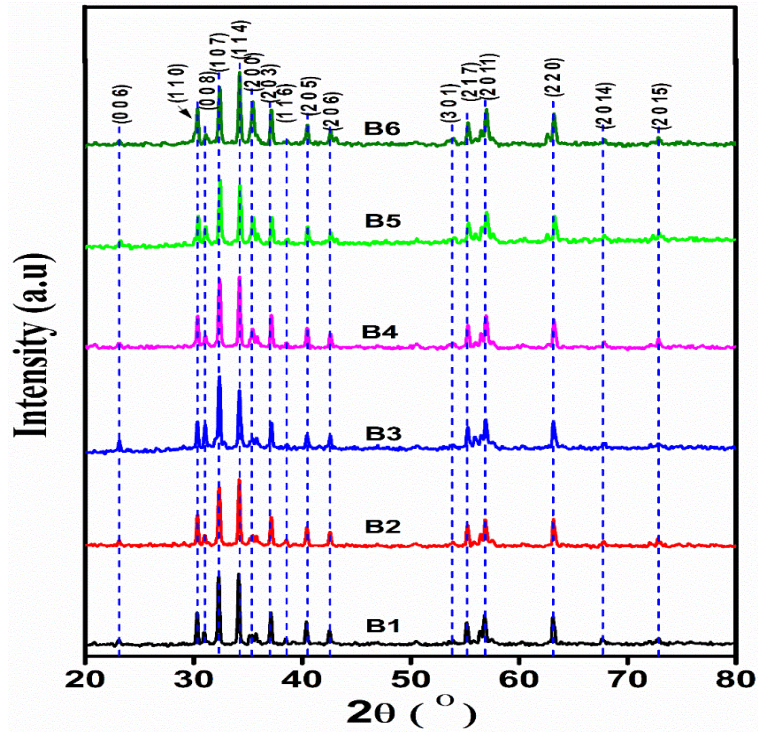


Fig. 4.31. X-ray diffraction pattern of B-series sintered hexaferrite.

Table 4.13 FTIR spectra details of B-series sample.

Peak position ( $cm^{-1}$ )	Assignments	References
400 – 450	Fe–O vibrations (octahedral site)	[249]
550 – 600	Fe–O stretching vibrations (tetrahedral site)	''
2354	O=C=O vibrations	''

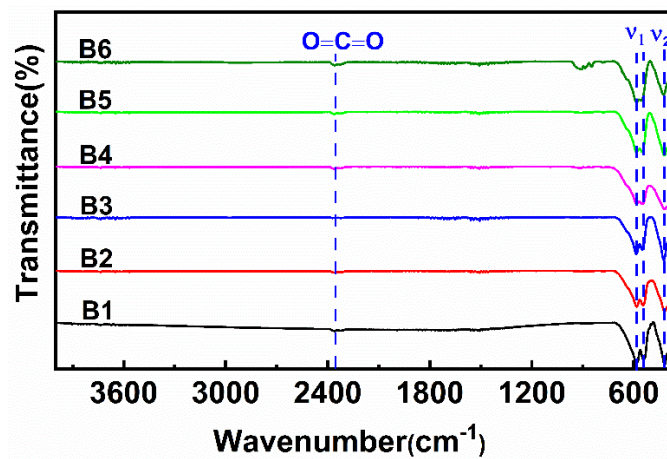
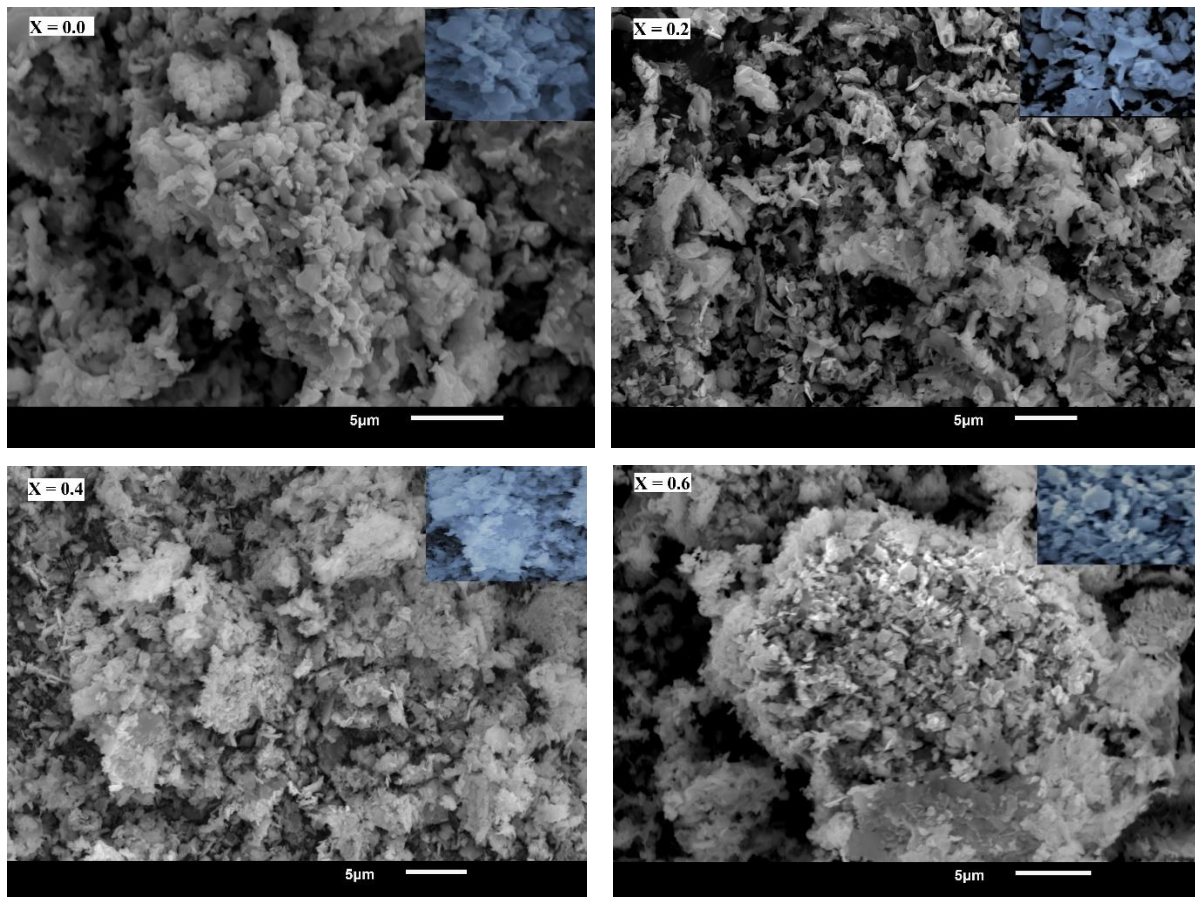


Fig. 4.32. FTIR spectra of B-series samples.

### 4.2.1.3 SEM Analysis

Fig. 4.30 reveals SEM micrographs ( $\mu\text{m}$ ) of all sintered hexaferrite samples. The grain size involves a lack of linearity with the substitution of  $\text{Co}^{2+}\text{-Cr}^{3+}$  ions. Most of the grains of substituted samples are distributed non-uniformly over the surface and are of different shapes and sizes. The hexagonal platelet-like structure is observable in B1, B2, and B4 samples. The grain size of all substituted samples comes out to be more than that of the average crystallite size estimated from Debye Scherrer Eq. (3.3). It is due to the aggregation (due to dipolar attractive interaction between magnetic particles) of crystallites and form grains of numerous sizes and shapes. SEM images provide the mean physical size of the grain, while mean crystallite size gives the mean structural coherence length. When the grains consist of polycrystalline particles, then the mean crystallite size is not equal to the mean physical grain size and equality comes in the case of a single crystal. A large number of grain boundaries along with some platelet-type grains have been formed at B2. It causes an impediment to the applied field, thus causing an increase in coercivity at the B2 sample.





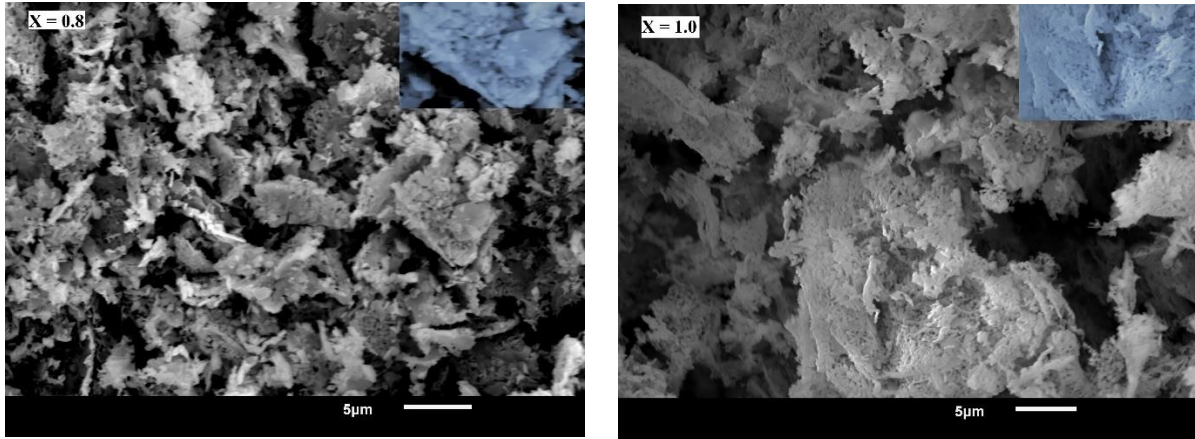


**Fig. 4.33.** Scanned Electron Micrographs of  $x=0.0$  (B1) to  $x=1.0$  (B6) samples.

## 4.2.2 Electrical Analysis

### 4.2.2.1 Dielectric Analysis

It has been noted that among all samples of the B-series only B1, B2, B3, and B4 exhibit the electrical characteristics due to uncertainty observed in the rest of the samples of the B-series. Fig. 4.31(a) and (b) reveal the variation of  $\epsilon'$ -real and  $\epsilon''$ -imaginary part of the complex dielectric constant of B1, B2, B3, and B4 sintered hexaferrite in the frequency range 20 Hz – 2 MHz, respectively. It can be noticed that both parameters are larger (at low frequency), and it decreases with increasing frequency [250]. This is the normal frequency-dependent behavior shown by all hexaferrites. In the low-frequency region, it is observed that the  $\epsilon''$  decreases more rapidly than  $\epsilon'$ , while the variation is similar to that of  $\epsilon'$  at a higher frequency region [211]. At higher frequencies, the value of both parameters becomes small and nearly constant with no dependence on frequency. The high value of a  $\epsilon'$  in low-frequency regions is caused by space charge polarization, which occurs when higher conductivity phases (i.e., grains) create a local accumulation of charge in the insulating matrix (i.e., grain boundary) under the influence of an electric field. The space charge carriers take some time to align their axes parallel to an alternating field. As the field reversal frequency increases, the space charge carriers can no longer keep their direction in step with the field causing a delay in changing their direction relative to the field. This delay is attributed to the fall observed in the material's dielectric constant.

The non-linear increment in  $\epsilon'$  is observed with the increment of *Cr-Co* ions in SrM hexaferrite, as seen in Fig. 4.31(a). The lowest frequency dependence of the dielectric dispersion is observed in B1 and B2 samples. As we substituted *Cr-Co* ions at B2 it may occupy the octahedral positions which lessen the no. of Fe ions responsible for polarization,

thus decreasing the dielectric constant. With the further substitution of *Cr-Co* ions, it may occupy tetrahedral sites, resulting in an equal no. of ions migrating to an octahedral position which causes an increment in  $\epsilon'$  [248]. In the B4 sample, the substitution of *Cr-Co* ions in place of  $Fe^{3+}$  ions causes charge imbalance, so to maintain the electrical neutrality  $Fe^{3+}$  ions convert into  $Fe^{2+}$  ions and allows maximum polarization. This dielectric mechanism could be explained by Koop's theory which is in agreement with the two-layer model proposed by Maxwell and Wagner [251].

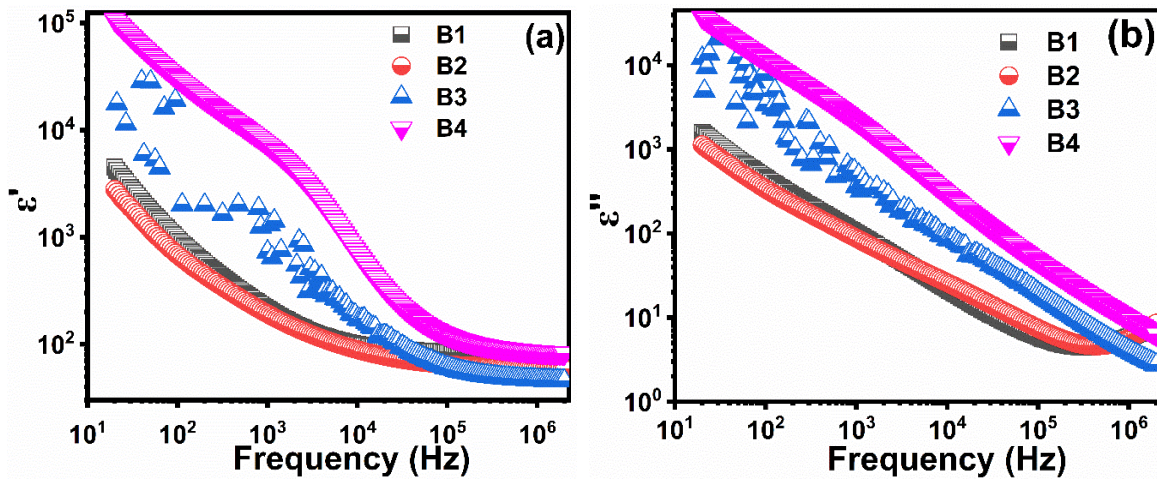
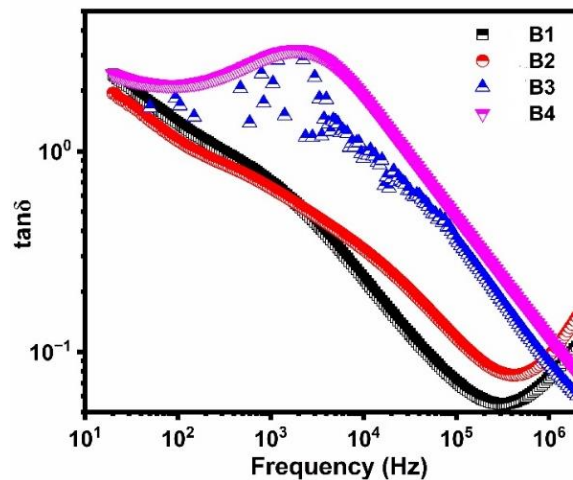


Fig. 4.34. (a)  $\epsilon'$  and (b)  $\epsilon''$  variation with frequency of B1, B2, B3, and B4 sintered hexaferrite.

#### 4.2.2.2 Loss Tangent

Fig. 4.32 illustrates the frequency-dependent variation of  $\tan\delta$  for B1, B2, B3, and B4 sintered hexaferrite at room temperature. The value of  $\tan\delta$  is influenced by various factors involving the sintering temperature and composition of the samples, as well as the stoichiometry and  $Fe^{2+}$  content, which affects the structural homogeneity [252]. When the frequency is low,  $\tan\delta$  is high and declines as the frequency increases. The high value of  $\tan\delta$  at lower frequencies is due to the impediment caused by grain boundaries. Moreover, this emanating behavior shows that more energy is required for exchanging electrons between  $Fe^{3+}$  and  $Fe^{2+}$  ions which lead to a high energy loss. In contrast, a small amount of energy is sufficient for transferring electrons between these ions at higher frequencies. The grains assist conductivity at high frequency which results in low energy loss [253]. Substitution of *Cr-Co* ions causes heterogeneity in the synthesized samples and results in more interface polarization. A weak relaxation is observed in B1 and B2, and further substitution causes strong relaxation in B3 and B4. Furthermore, the B4 sample shows a broad peak at certain frequencies, and it appears when the applied frequency of an alternating field coincides with

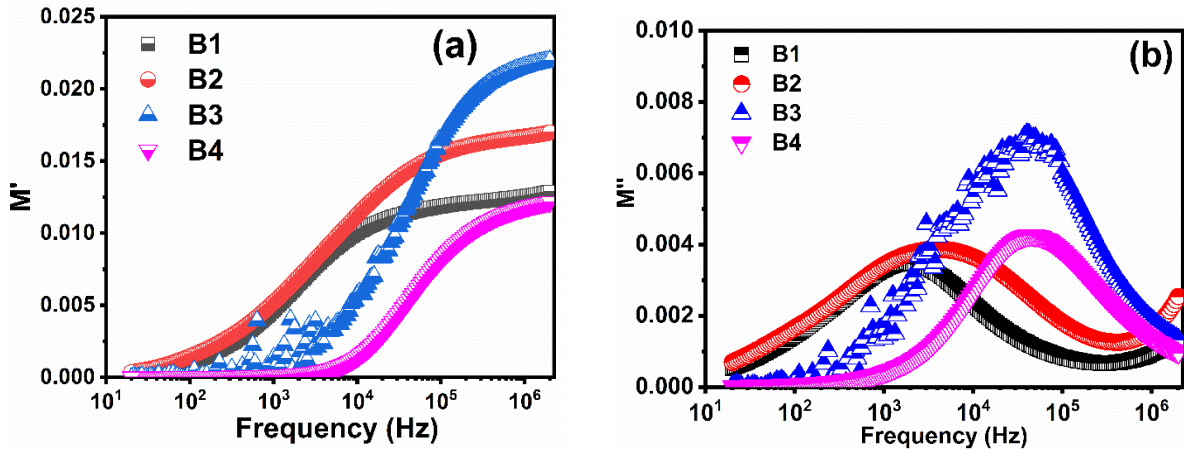
the hopping frequency of charge carriers [254]. This suggests the existence of interfaces and traps, that cause interfacial polarization during the sintering process of M-type hexaferrite. This polarization creates an electric field in which the charge carriers are trapped. When the AC signal is applied, the electric field at the interfaces of the hexaferrite changes, causing the charge carriers to move away from the trapped region. As the frequency of the AC signal increases, this rapidly changing electric field exerts a strong force on the charge carriers, causing them to move away from the traps. This results in an increase in the density of charge carriers, but the grain boundaries impede their movement, requiring more energy for electron exchange and resulting in greater loss of energy, which contributes to the high value of  $\tan\delta$ .



**Fig. 4.35.** Loss tangent variation with frequency of B1, B2, B3, and B4 sintered hexaferrite.

### 4.2.2.3 Complex Electric Modulus Analysis

Fig. 4.33(a) displays the changes in  $M'$  with frequency. The plot shows a very low value of  $M'$  at lower frequencies, approaching zero implying no contribution of electrode polarization. With increasing frequency,  $M'$  varies continuously and reaches an asymptotic value ( $M'$ ) which is maximum at the high-frequency range for all sintered hexaferrite. This pattern suggests that there is a lack of a restoring force controlling the movement of charge carriers in response to an induced electric field [255]. Also, it supports the concept that charge carriers have long-range mobility. Moreover, the value of  $M'$  increases sigmoidally with increased frequency, eventually reaching a value ( $M_\infty$ ) for all sintered hexaferrite. This increment may be ascribed to the conduction phenomena resulting from the short-range mobility of carriers, especially ions[256]. In addition, the substitution increases the value of  $M'$  from B1 to B3 and it is minimum for B4.



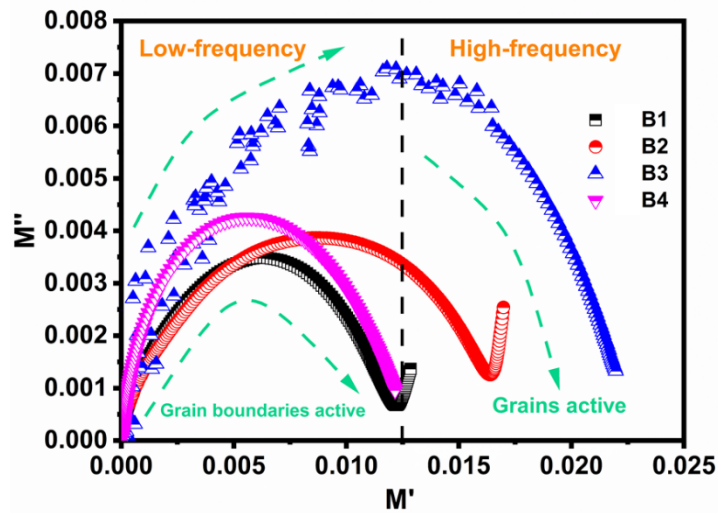
**Fig. 4.36.** (a)  $M'$  and (b)  $M''$  variation with frequency of B1, B2, B3, and B4 sintered hexaferrite.

Fig. 4.33(b) illustrates the plots of  $M''$  versus frequency. The peak frequency enunciates information about the conduction relaxation time and the forward shift in the peak frequency implies a reduction in relaxation time with *Cr-Co* substitution. The asymmetric shape of the plot for the peak maxima and the width of the peaks on either side of the maxima indicate a non-Debye behavior of the material, caused by the distribution of relaxation time. Substitution of *Cr-Co* ions causes an increment in the relaxation frequency and is the maximum for B3. This can be explained by the densely/closely packed small grains with uniform distribution as seen in SEM [257].

Fig. 4.34 illustrates the Cole-Cole plot ( $M''$  vs  $M'$ ) of B1, B2, B3, and B4 sintered hexaferrite. The obtained curves demonstrate a deformed semicircle instead of a perfect semicircle with centers lying below the x-axis. This signifies that the relaxation is distributed over different time constants, and is not of the Debye-type. The semicircular arc reflected at a low frequency is associated to grain boundary relaxation, while at a high frequency it is caused by grain relaxation. It is clear (Fig. 4.34) that both B1 and B4 samples exhibit small diameter curves, but B4 shows a larger peak height than B1. This variation in the B4 sample supports the micrographs which show the existence of small-sized grains having good intergrain connectivity compared to the B1 sample. The second semicircular arc begins in B2 samples, possibly due to the action of grains/grain boundaries. This could be claimed through the obtained SEM micrographs where substitution causes aggregation of grains. Furthermore, a maximum peak height with a larger diameter is observed for the B3 sample. This may elucidate the existence of a wide range of dense/closely packed grain clusters (large-sized



grain) as seen in SEM, which contribute to different relaxation processes with a wide distribution of relaxation times, leading to a larger diameter and peak height in B3.



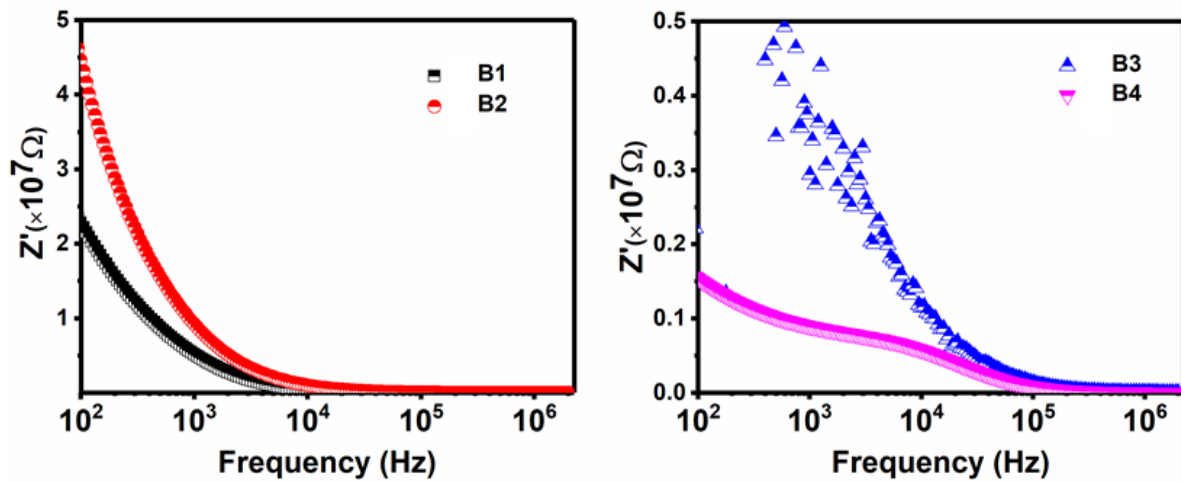
**Fig. 4.37.** Cole-Cole plots ( $M''$  vs  $M'$ ) of B1, B2, B3, and B4 sintered hexaferrite.

#### 4.2.2.4 Complex Impedance Analysis

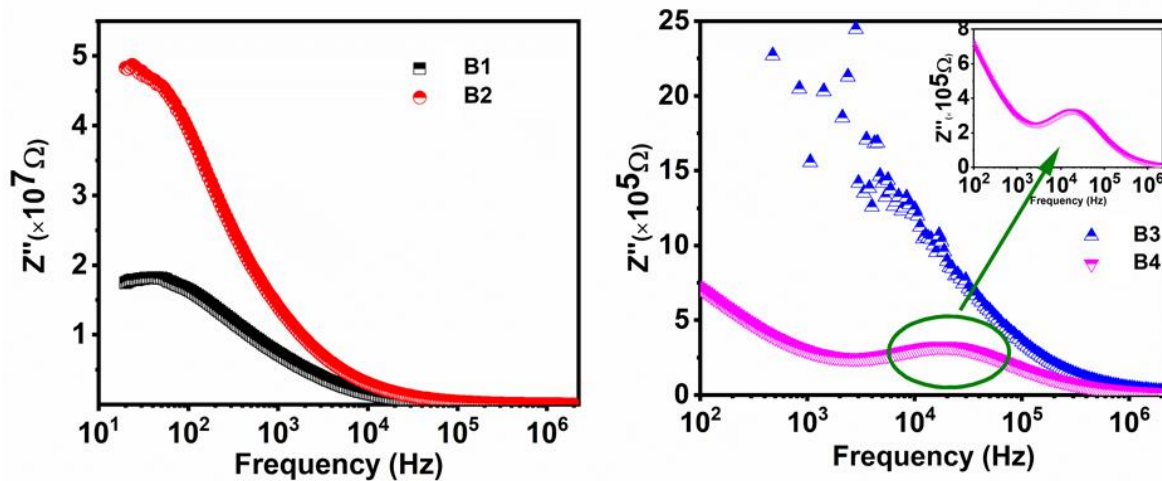
Complex impedance spectroscopy includes the separate involvements of different processes, such as electrode effects, bulk effects, and electrode interfaces in the frequency domain [258]. The decrease observed in both  $Z'$  and  $Z''$  with increasing frequencies is shown in Fig. 4.35 and 4.36, respectively. As the frequency increases,  $Z'$  decreases, suggesting an increment in the material's conductivity caused by an increase in electron hopping between the localized ions. At higher frequencies, the reduction in  $Z'$  could be described through the Maxwell-Wagner model. The space charge effect dominates the impedance response at low frequencies and results in a larger value of  $Z''$ . However, the charge carriers may not be able to respond rapidly to the alternating applied field at high frequencies, leading to a decrement in the  $Z''$ . A peak observed in the B4 sample, when the frequency of localized hopping electrons matches the applied frequency of an AC field. The merging of all the curves above  $10^5$  Hz suggests the possibility of space charge release.

Fig. 4.37 shows the Cole-Cole plots ( $Z''$  vs  $Z'$ ) of B1, B2, B3, and B4 sintered hexaferrite with a weak relaxation in B1, B2, and B3 and relatively good relaxation in B4. The Cole-Cole plots are commonly used to analyze impedance spectroscopic data and are particularly useful in understanding electrical properties in terms of changes in microstructure [259]. Instead of a complete semicircular arc, only a segment of a semicircular arc has been observed for B1, B2, and B3. It is also noted that as the *Cr-Co* substitution increases, the

depression of the arc gradually decreases. This depression suggests that the impedance mechanism at low frequency explicitly depends on the dielectric polarization that occurs at grain boundaries, also referred to as the Maxwell-Wagner effect [221].



**Fig. 4.38.**  $Z'$  variation with frequency of B1, B2, B3, and B4 sintered hexaferrite.



**Fig. 4.39.**  $Z''$  variation with frequency of B1, B2, B3, and B4 sintered hexaferrite.

Moreover, in the B4 sample, a combination of an incomplete semicircle and a segment of a semi-circular arc has been observed, an arc in the lower frequency is due to the grain boundaries and an incomplete semicircle at a higher frequency accompanies the effect of bulk grain. The dielectric relaxation decreases with substitution from B1 to B4 attributing to the decrease in  $\text{Fe}^{3+}$  ions. The B1 and B2 sample shows a complete semicircle in the low-frequency region of  $M''$  vs  $M'$  plots (Fig. 4.34) and a segment of a semi-circular arc all over the frequency region of  $Z''$  vs  $Z'$  plots (Fig. 4.37). This may suggest that the conductivity relaxation dominates the material's response. Furthermore, B4 shows a complete semicircle in the low-frequency region of  $M''$  vs  $M'$  plots (Fig. 4.34) having a diameter the same as B1,

along with two dielectric relaxations in a wide frequency range of  $Z''$  vs  $Z'$  plots (Fig. 4.37). In the B4 sample, the dielectric relaxation at a higher frequency is relatively weak than at a lower frequency. This can be explained by the resonance peak observed in the loss tangent plots (Fig. 4.32) of the B4 sample at a low-frequency region. However, B3 shows a single semicircle all over the frequency range in  $M''$  vs  $M'$  plots (Fig. 4.34) and a segment of a semi-circular arc in  $Z''$  vs  $Z'$  plots (Fig. 4.37). The position of the semicircle on the real axis ( $M'$ ) at high frequency suggests the high-frequency limit of the conductivity relaxation. This indicates that in this region the conductivity relaxation is less significant, and the dielectric relaxation processes become more prominent.

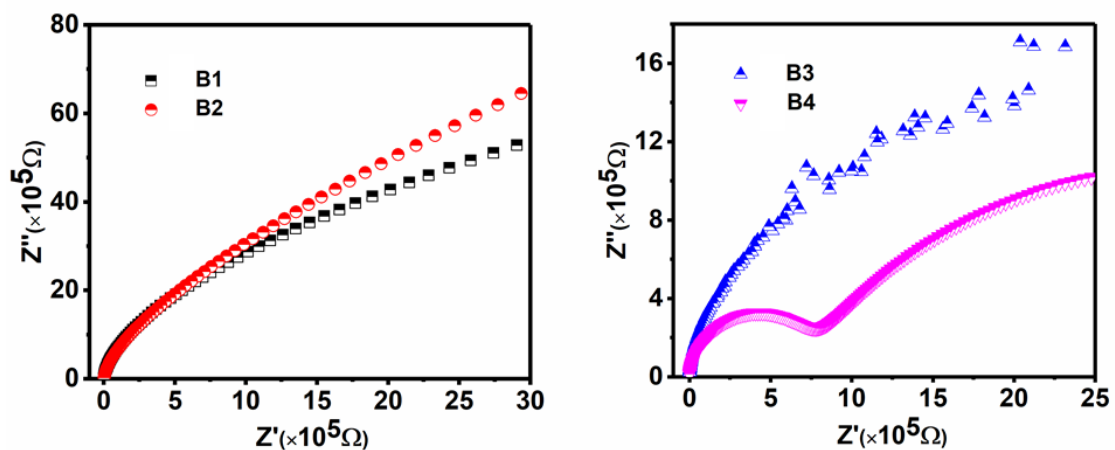


Fig. 4.40.  $Z''$  versus  $Z'$  plots of B1, B2, B3, and B4 sintered hexaferrite.

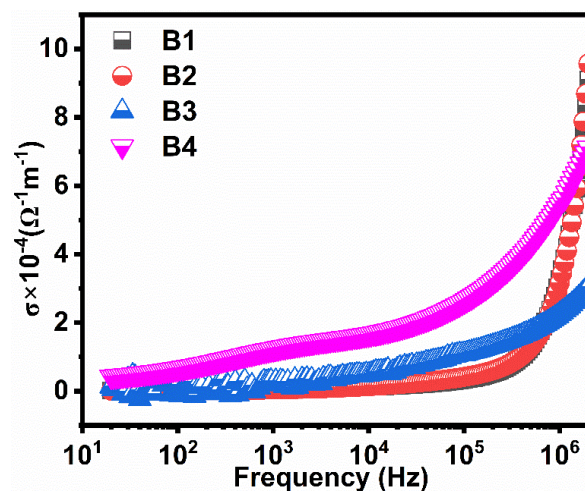
#### 4.2.2.5 Ac conductivity analysis

Fig. 4.38 displays the increase in ac conductivity ( $\sigma$ ) of B1, B2, B3, and B4 samples as the applied frequency increases. It also reveals that  $\sigma$  exhibits frequency-independent behavior for B1, B2, and B3 samples in lower-frequency regions and sharply increases in higher-frequency regions ( $>10^4$  Hz). However, the B4 sample shows a gradual increase in  $\sigma$  value from lower to higher frequency region, which is evidently due to the availability of free charge carriers increasing with increased frequency. The behavior of ac conductivity is consistent with  $M'$  the behavior is seen in Fig. 4.33(a). The small value of  $M'$  approaches to zero in the low-frequency region suggest a maximum restoring force dipolarization which results in a low value of conductivity and suppression of electrode polarization. However, in high-frequency regions the high value of  $M'$  caused by weak space charge and interfacial polarization and results in a high value of  $\sigma$ . Moreover, the results of  $\sigma$  can be explained through the  $\epsilon'$  plots with frequency (Fig. 4.31(a)). The small value of  $\sigma$  in the lower-

frequency region can be understood by the high value of  $\epsilon'$  caused by space charge polarization. Since in this region material's ability to store electric charge outweighs its ability to conduct current. A replacement of  $Fe^{3+}$  ions with  $Cr-Co$  ions cause a reduction in conductivity value. This reduction elucidates a decrement in the concentration of  $Fe^{3+}$  ions at the octahedral position, which restricts the probability of hopping between  $Fe^{2+}$  and  $Fe^{3+}$  ions.

### 4.2.3 Magnetic properties

It has been reported that the octahedral positions are occupied via more electronegative ions and  $Co^{2+}$  (1.88) ions are more electronegative than  $Cr^{3+}$  (1.66) ions. Thus, it can choose to occupy  $12k(\uparrow) - 2a(\uparrow) - 4f_2(\downarrow)$  octahedral sites. Based on ligand field theory, ions with  $d^0, d^5, d^{10}$  orbitals have no site preference,  $d^1, d^2, d^3,$  and  $d^4$  orbitals occupy tetrahedral sites and  $d^6, d^7, d^8$  and  $d^9$  orbitals choose to occupy octahedral sites.  $Cr^{3+}$  ions having  $d^3$  orbitals prefer to occupy  $4f_1(\downarrow)$  tetrahedral sites, while Cobalt ( $Co^{2+}$ ) ions with  $d^7$  orbitals can occupy octahedral sites. It has been reported that Cobalt ( $Co^{2+}$ ) ions can occupy  $4f_2(\downarrow), 4f_1(\downarrow),$  and  $2b$  sites. Fig. 4.39 demonstrates the hysteresis loop of B-series hexagonal ferrites at room temperature. The derived parameters from the hysteresis loop are listed in Table 4.14.



**Fig. 4.41.** Variation of  $\sigma$  with a frequency of B1, B2, B3, and B4 sintered hexaferrite.

It is known that the anisotropy field ( $H_a$ ) primarily depends on  $2b$  and  $4f_2$  sites.  $H_a$  increases and decreases with the replacement of  $Fe^{3+}$  ion on  $4f_2$  and  $2b$  sites with less magnetic or diamagnetic substituted ions, respectively.  $Co^{2+}-Cr^{3+}$  substitution causes an increase in  $H_a$  by 36.1% from B1 to B3 sample. It is because more no. of substituents occupies at  $4f_2(\downarrow)$  sites than alone  $2b(\uparrow)$  sites. There is a notable decrease in  $H_a$  (41.57%) as substitution continues up to the B6 sample. Consequently, it can be inferred that both  $Co^{2+}-$

$Cr^{3+}$  ions display a preference for occupying  $4f_2$  and  $2b$  lattice sites, which aligns with prior reports indicating the presence of  $Co^{2+}$  ions on  $2b$  and  $4f_2$  sites.

**Table 4.14** Magnetic parameters  $M_s$ ,  $H_c$ ,  $M_r$ ,  $M_r/M_s$  and  $H_a$  of B-series sample.

Sample name	$M_s$ (emu/g)	$H_c$ (Oe)	$M_r$ (emu/g)	$M_r/M_s$	$H_a$ (kOe)	$n_B$ ( $\mu_B$ )
B1	79.824	3426.116	40.938	0.51	20.74	7.27
B2	74.700	3767.750	36.661	0.49	20.48	6.83
B3	82.930	727.824	16.685	0.20	28.24	7.62
B4	82.140	2955.418	35.094	0.42	26.28	7.53
B5	71.851	1325.430	22.350	0.31	22.62	6.62
B6	53.961	2138.266	26.891	0.49	16.50	4.93

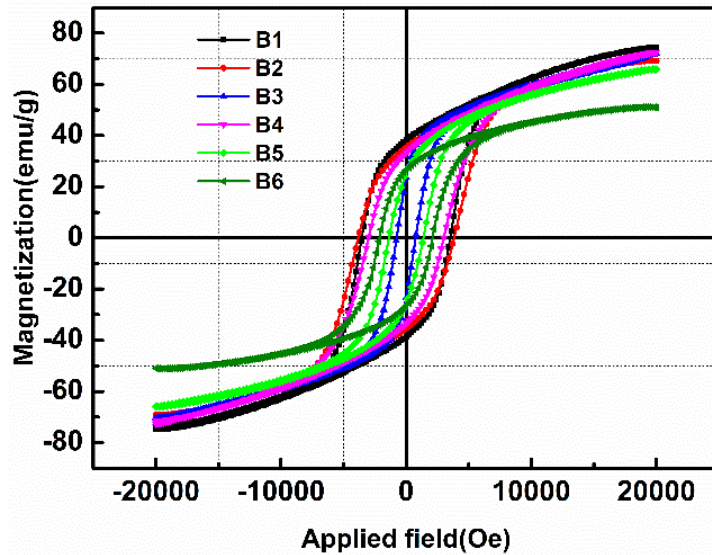


**Fig. 4.42.** Hysteresis plots of B-series sintered hexaferrite.

The lattice site occupancy and porosity contribute to the variation observed in saturation magnetization ( $M_s$ ). Table 4.14 shows the non-significant change in  $M_s$  from B1 (79.82 emu/g) to B4 (82.14 emu/g). The saturation magnetization is highest (Table 4.14) at B3 presumably due to occupancy of both substituents at spin-down sites i.e.  $M_b$ . It also correlates to electronegativity and ligand field theory parameters as discussed earlier. From B1 to B4,  $M_s$  (2.90%) doesn't show an increment to that level then the change is observed in  $H_a$  (36.1%). This may be caused by the occupancy of octahedral sites by  $Cr^{3+}$  ions for high substitution level  $x \geq 0.25$  and  $Cr^{3+}$  ions occupy  $2a$  ( $\uparrow$ ) and  $12k$  ( $\uparrow$ ) sites than

4f<sub>2</sub> (↓) sites. This would result in more no. of substituted ions to occupy spin-up sites i.e.,  $M_a$  and hence, a competition between  $M_a$  and  $M_b$  causes a slight change in  $M_s$ .

The formation of grain clusters is seen with the increase of substitution level in SEM images Fig. 4.30. This can increase the  $M_s$  due to the decreased impediment to the flow of applied field by grain clusters. However, further substitution breaks down the magnetic collinearity and weakens the superexchange interaction among octahedral and tetrahedral sites. Table 4.14 shows a considerable fall in  $M_s$  (34.30%) for  $x \geq 0.8$ . Here, the substitution of  $Cr^{3+}$  ions prevail the coupling between 12k – 2a and 12k – 2b, and results a decrement in the magnetic moment and subsequently shows the declining nature of  $M_s$ . The minimum and maximum remanence magnetization values of 16.68 and 40.93 emu/g in B3 and B1, respectively, as shown in Table 4.14.

Table 4.14 displays a  $H_c$  that decreases non-linearly from B1 (3426 Oe) to B6 (2138 Oe). Coercivity's mechanism is dependent on both intrinsic and extrinsic effects. Intrinsic effect is associated with site occupancy, where  $H_a$  is directly linked to  $H_c$ , and this relationship is primarily influenced by the 4f<sub>2</sub> and 2b sites. Extrinsic effect encompasses grain size and porosity;  $H_c$  is directly related to porosity and inversely related to grain size. It can be seen in Table 4.14 that  $H_a$  decreases from B1 (20.74 kOe) to B6 (16.50 kOe) owing to the site occupancy mechanism discussed in  $M_s$ . Also, SEM images (Fig. 4.30) indicate that sample B6 owes relatively more uniformly in grain size distribution and dense clusters as compared to sample B1. The non-linear variation of  $H_a$  and grain size distribution/clusters contribute to non-linear variation in  $H_c$ . However, the lowest value of coercivity observed in B3 needs more investigation to know the exact mechanism. The magnetic hardness and presence of an intergrain group can be assessed using the squareness ratio ( $M_r/M_s$ ), a value that falls within the range of 0 to 1. When the value falls within the range of 0.05 to 0.5, the magnetic material is regarded as containing multi-domain particles which are randomly oriented. Moreover, a material with  $0.5 < M_r/M_s < 1$  are hard, more anisotropic, and contain single-domain particles. The  $M_r/M_s$  of B-series, hexaferrite was calculated and listed in Table 4.14. The ratio comes out to be less than 0.5 in all substituted samples which proves the formation of multi-domain. Table 4.14 enlists the value of Bohr magneton ( $n_B$ ) which show declining behavior with the increment of substitution which may also weaken the magnetic interaction among different sites of hexaferrite.



#### 4.2.4 Electromagnetic Analysis

Fig. 4.40(a) illustrates the dependence of dielectric constant ( $\epsilon'$ )/loss ( $\epsilon''$ ) on frequency. Substitution of Co-Cr ions causes a non-monotonic decrease in  $\epsilon'/\epsilon''$  values from B1 to B6. This may be due to the occupancy of Co-Cr ion on octahedral positions, which lessen the no. of Fe ions responsible for polarization, thus decreasing  $\epsilon'/\epsilon''$ . The dielectric constant ( $\epsilon'$ )/loss ( $\epsilon''$ ) remains relatively constant with increasing frequency for all samples, except B4. Sample B1 acquires the highest value of  $\epsilon'/\epsilon''$  overall frequency range, and B4 exhibits relaxation peaks around 9 GHz and 11 GHz. This relaxation indicates a specific dipolar polarization mechanism active at the measurement frequency. In detail, the  $\epsilon'$  curve of B4 is stable at 8.2 -9 GHz, then it decreased, it suddenly increased to higher values than those of B2, B3, B5, and B6 around 11 GHz and then decreased to lower values. Notably, the behavior of  $\epsilon''$  in sample B4 is unusual. It becomes negative in the 10-11 GHz frequency range, exhibits a broad minimum, and then returns to positive. This negative behavior is attributed to plasma oscillation and dielectric resonance, as explained by Drude model [260]. Generally, dielectric resonance occurs when the natural vibrating frequency of atoms or charge carriers matches the applied electric field. In contrast, plasma oscillation results from the repetitive motion of electrons in an alternating applied field. During plasma oscillation, free electrons accelerate with the fluctuation of the external electric field, and the columbic force generated by positive ion cores pull them back, resulting in oscillation. This plasma behavior leads to negative dielectric parameters, making lossy plasmas effective RADAR absorbers. This phenomenon is an artificial behavior in materials and is not commonly discussed for polycrystalline materials. Hussain *et al.* [261] discussed the negative behavior of  $\epsilon'$  occurs in dysprosium substituted bismuth ferrite due to plasma resonance. Domain resonance and irregular grain boundaries in the samples can also cause negative dielectric constant, as discussed by Gajula *et al.* [262]. Jones *et al.* [263] found a negative dielectric constant due to relaxation process adding more holes to the material, which recombine with free electrons, causing negative value. Mallikarjuna *et al.* [264] suggested that the alignment of charge carriers create internal electric field, opposite to the direction of the applied electric field due to some geometrical defects of the samples, resulting in negative dielectric behavior. The transition of dielectric behavior from its positive to negative is associated with a change from capacitive to inductive behavior of the material. Axelrod *et al.* [265] and Bartkowska *et al.* [266] specified negative dielectric behavior in sol-gel glasses and ceramic composites, respectively, with the concept of stored energy getting released. In the present

study, positive dielectric loss is attributed to normal relaxation processes associated with the absorption and emission of energy. However, negative dielectric loss indicates energy release exceeds absorption, which is consistent with the principle of energy conservation. This can be explained by the concept of trapped charges getting released. The charges assemble at the inner and outer surfaces of the system and their separation causes the energy to be stored, making it a meta-stable state. This state is eliminated under certain frequency and temperatures, releasing the stored energy. This energy release causes  $\epsilon''$  to be negative. Fig. 4.40(b) demonstrated variation of permeability ( $\mu'$ )/ magnetic loss ( $\mu''$ ) as a function of frequency and it does not vary too much over the entire frequency range for all samples, except B4. Substitution causes an insignificant change in the value of  $\mu'/\mu''$  in the low and high-frequency regions. The elevated  $\mu''$  values of the B4 sample within the range of 10-12.4 GHz can be attributed to an increment in the effective molecular magnetic moment (as supported by  $M_s$  value Table 4.14), thus enhancing the magnetic loss capability of the B4 sample compared to remaining samples. Furthermore, from 10 – 11 GHz the  $\epsilon''$  decreases and  $\mu''$  rises, while from 11GHz to 11.25 GHz  $\epsilon''$  rises and  $\mu''$  decreases, evidently decreasing the difference between  $\mu''$  and  $\epsilon''$  and so enhancing the impedance match.

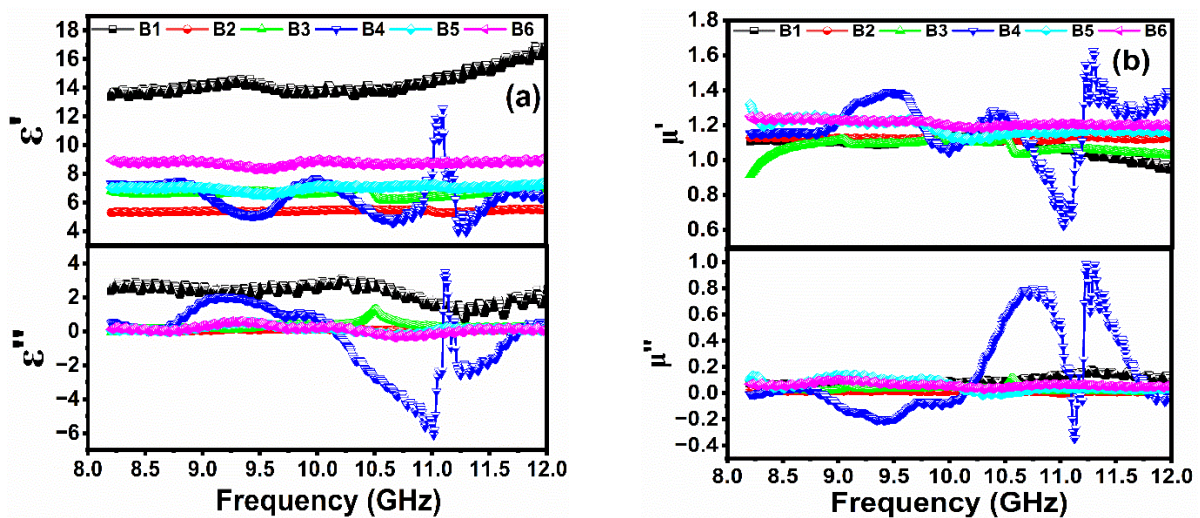


**Fig. 4.43.** (a) Complex permittivity and (b) permeability plots of D-series samples in 8-12 GHz.

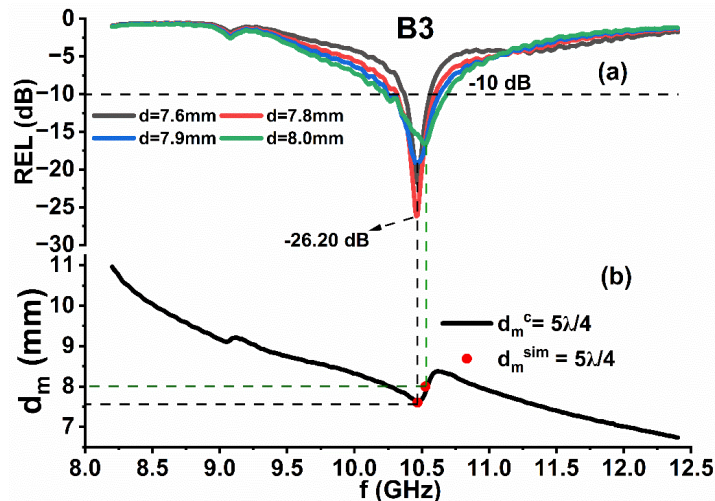
Fig. 4.41 (a, c), 4.42 (a), 4.43 (a, c) and 4.44 (a, c) illustrate the REL plots of B3, B4, B5, and B6 samples and it has been utilized to deduce parameters matching thickness/frequency, bandwidth and REL frequency range of -10 dB/-20 dB, as enlists in Table 4.15. For better visualization, 3D plots of REL at various thickness and frequency is displayed in Fig. 4.45. The discussion of pure  $\text{SrFe}_{12}\text{O}_{19}$  (B1 sample) is already done in the previous section 4.1.5 as the name of the D1 sample. The introduction of Co-Cr ions



improves the microwave absorption properties of the synthesized samples. The highest dip in REL, measuring -36.7 dB (> 99 % absorption), is observed in the B5 sample, occurring at a frequency of 9.23 GHz and a thickness of 8.4 mm. In Table 4.15, the remaining compositions exhibit REL values ranging from -10 to -36.5 dB, spanning frequencies between 8 to 12.4 GHz, and thicknesses between 7 to 10 mm. The plots illustrate the shift of REL peaks towards lower frequency ranges as the thickness increases, affirming the existence of a quarter wavelength mechanism.

Fig. 4.41(a, c) demonstrated the absorption characteristics of the B3 sample within the examined frequency range. Reflection loss remains above -20 dB, with REL peaks spanning the 8.2 to 12.4 GHz frequency spectrum from 7.6 to 8.9 mm thickness. Sample B4 shows [Fig. 4.42 (a)] REL dip greater than -10 dB/-20 dB for 8.4 to 8.8 mm thickness. For the B5 sample, Fig. 4.43(a,c) reveals REL peaks with values > -10 dB across thickness ranging from 7.7 to 9.5 mm, by covering a frequency range of 8.46 to 10.5 GHz. Fig. 4.44(a, c) is notable for the B6 sample, as it exhibits multiple REL peaks with values greater than -10 dB over a wide range of frequency from 8.2 to 12.4 GHz and a thickness ranging from 7.2 to 10 mm.

Using equation 3.22, Reflection loss (REL) is computed using both the simulated thickness ( $d_m^{sim}$ ) and the calculated thickness ( $d_m^c$ ), which is determined through equation 3.24 by substituting values of  $n = 1, 3, 5$ , and so forth. The purpose is to establish a relationship between the quarter wavelength mechanism and REL peaks. Fig 4.41(b, d), 4.42(b), 4.43 (b, d) and 4.44 (b, d) depict plots of a calculated thickness ( $n\lambda/4$ ) within the frequency range. To compare the simulated thickness ( $d_m^{sim}$ ) with calculated thickness ( $n\lambda/4$ ), vertical lines are drawn from REL peaks to the thickness-frequency plots. Results envisaged a quarter wavelength mechanism in B3, B4, and B5 samples where the calculated thickness is  $5\lambda/4$  with  $n = 5$ . Conversely, B6 shows the occurrence of both  $5\lambda/4$  and  $9\lambda/4$  values.



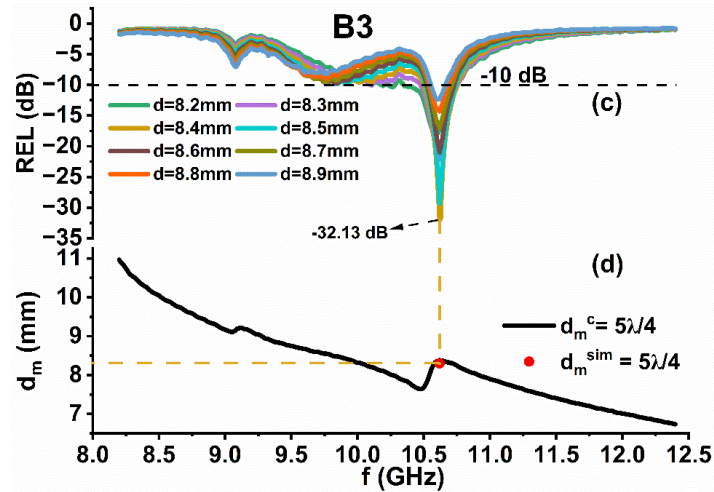


Fig. 4.44. (a, c) Dependence of REL on frequency in B3 sample. (b, d)  $d_m^{sim}$  and  $d_m^c$  versus frequency for  $5\lambda/4$  in the B3 sample.

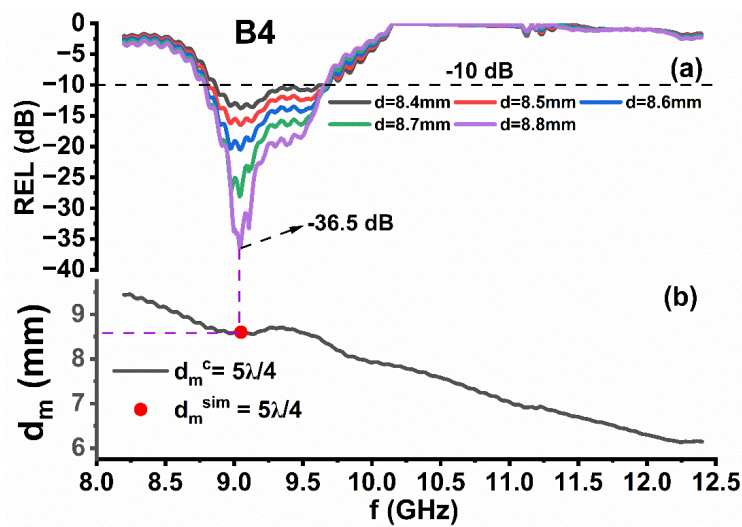
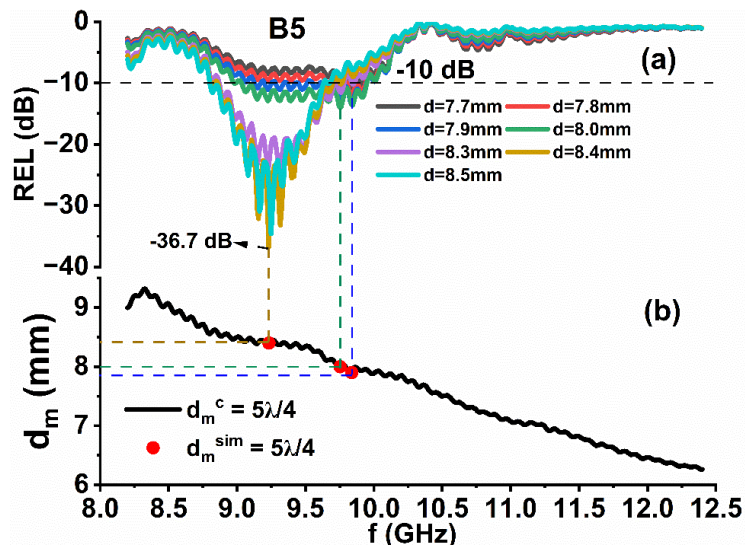
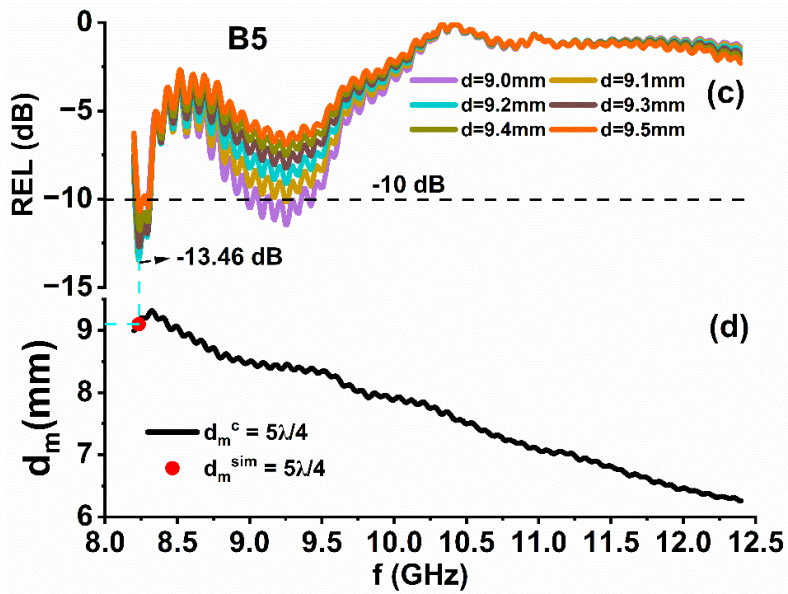


Fig. 4.45. (a) Dependence of REL on frequency in B3 sample. (b)  $d_m^{sim}$  and  $d_m^c$  versus frequency for  $5\lambda/4$  in the B3 sample.





**Fig. 4.46.** (a, c) Dependence of REL on frequency in B5 sample. (b, d)  $d_m^{\text{sim}}$  and  $d_m^c$  versus frequency for  $5\lambda/4$  in the B5 sample.

Sample B3 possesses  $\text{REL} > -10 \text{ dB}/ -20 \text{ dB}$  for several matching thicknesses, the thicknesses having  $\text{REL} > -10 \text{ dB}$  exhibit narrow bandwidth of 0.11 GHz (10.55-10.66 GHz) and wide bandwidth of 0.38 GHz (10.36-10.74 GHz) at 8.9 mm and 8.2 mm, while thicknesses having  $\text{REL} > -20 \text{ dB}$  exhibit bandwidth of 0.27 GHz (10.32-10.59 GHz) and narrow bandwidth of 0.18 GHz (10.37-10.55 GHz) at 7.8 mm and 7.6 mm. It can be depicted from Table 4.15, that B5 owes  $\text{REL} > -10 \text{ dB}/ -20 \text{ dB}$ , for thicknesses  $\text{REL} > -10 \text{ dB}$  shows a wide absorption bandwidth of 0.91 GHz and a very small bandwidth of 0.09 GHz from 9.03-9.94 GHz) and 8.21-8.31 GHz with matching thicknesses of 9.4 and 8.0 mm, respectively. Whereas, 8.3 to 8.5 mm matching thicknesses owe  $\text{REL} > -20 \text{ dB}$  with effective broad absorption bandwidth of 0.86 GHz (8.86-9.72 GHz). In the case of the B6 sample,  $\text{REL} > -10 \text{ dB}$  absorption bandwidth (0.67 GHz) is observed from 8.85-9.52 GHz at 7.7 mm, and when  $\text{REL} > -20 \text{ dB}$  broad absorption bandwidth of 0.73 GHz (8.87-9.60 GHz) at 7.5 mm. Table 4.15 enumerates the value of BTR and PBW of synthesized samples. Substitution of Co-Cr ions causes a non-monotonic increase in both parameters, with a maximum PBW value of 9.72 in sample B4. The BTR value ranges from 0.113 to 0.009 for all samples.

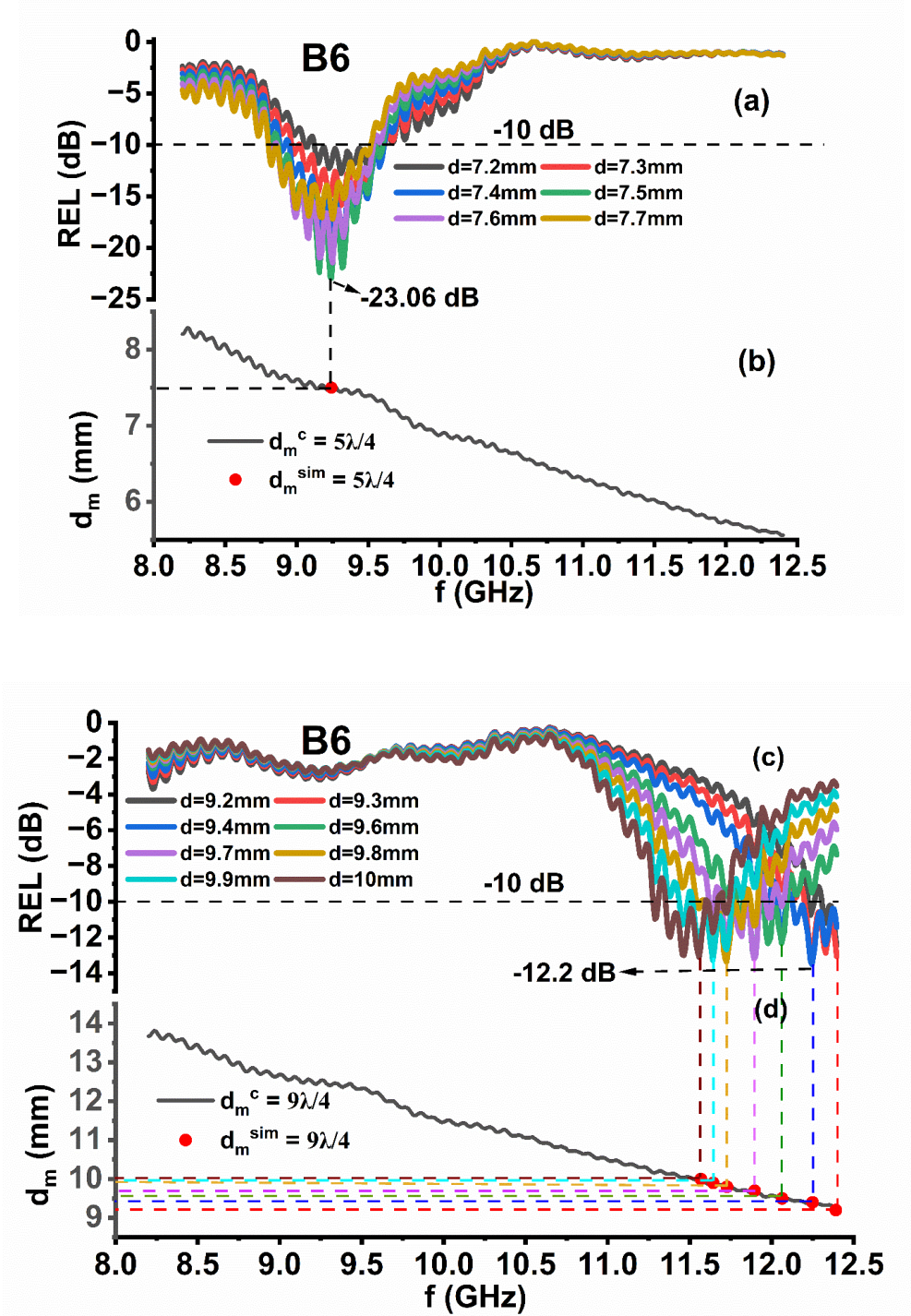


Fig. 4.47. (a, c) Dependence of REL on frequency in B6 sample. (b, d)  $d_m^{\text{sim}}$  and  $d_m^c$  versus frequency for  $5\lambda/4$  and  $9\lambda/4$  in the B6 sample.



**Table 4.15** Absorption parameters (REL > -10/-20 dB).

Sample Name	Matching Thickness (mm)	Maximum REL (dB)	Matching frequency (GHz)	Frequency Band for REL > -10 dB (GHz)	Band width for RL > -10 dB (GHz)	Frequency Band REL > -20 dB (GHz)	Bandwidth for REL > -20 dB (GHz)	BTR	PBW (%)
<b>B3</b>	7.6	-21.65	10.46	--	--	10.37-10.55	0.18	6.5E-05	1.72
	7.8	-26.20	10.45	--	--	10.32-10.59	0.27	9.5E-05	2.58
	7.9	-19.05	10.45	10.29-10.62	0.33		--	1.1E-04	3.15
	8.0	-16.63	10.52	10.31-10.68	0.37		--	1.3E-04	3.51
	8.2	-17.99	10.60	10.36-10.74	0.38		--	1.2E-04	3.58
	8.3	-22.33	10.61	--	--	10.47-10.74	0.27	8.7E-05	2.54
	8.4	-32.13	10.61	--	--	10.50-10.74	0.24	7.6E-05	2.26
	8.5	-29.12	10.61	--	--	10.51-10.73	0.22	6.9E-05	2.07
	8.6	-20.89	10.61	--	--	10.52-10.72	0.20	6.2E-05	1.88
	8.7	-16.78	10.61	10.53-10.71	0.18	--	--	5.5E-05	1.69
	8.8	-14.38	10.61	10.54-10.68	0.14	--	--	4.2E-05	1.31
	8.9	-12.42	10.61	10.55-10.66	0.11	--	--	3.3E-05	1.03
<b>B4</b>	8.4	-14.06	9.048	--	--	--	--	--	--
	8.5	-16.81	9.048	8.80-9.68	0.88	--	--	3.6E-04	9.72
	8.6	-20.92	9.048	8.78-9.66	0.88	--	--	3.6E-04	9.72
	8.7	-28.23	9.04	8.79-9.67	0.88	--	--	3.6E-04	9.72
	8.8	-36.5	9.04	8.78-9.66	0.88	--	--	3.5E-04	9.72
<b>B5</b>	7.7	-11.05	9.838	--	--	--	--	--	--
	7.8	-12.33	9.838	--	--	--	--	--	--
	7.9	-13.60	9.838	--	--	--	--	--	--
	8.0	-14.02	9.754	9.03-9.94	0.91	--	--	3.8E-04	9.32
	8.3	-24.09	9.233	--	--	8.86-9.72	0.86	3.6E-04	9.31
	8.4	-36.70	9.233	--	--	8.85-9.64	0.79	3.3E-04	8.55
	8.5	-34.60	9.233	--	--	8.80-9.63	0.83	3.5E-04	8.98
	9.0	-12.85	8.233	8.20-8.30	0.10	--	--	4.9E-05	1.21
	9.1	-13.48	8.233	8.20-8.31	0.11	--	--	5.3E-05	1.33
	9.2	-13.44	8.233	8.20-8.31	0.11	--	--	5.3E-05	1.33
	9.3	-12.69	8.233	8.20-8.31	0.11	--	--	5.2E-05	1.33
	9.4	-11.76	8.233	8.21-8.31	0.09	--	--	4.7E-05	1.09

	9.5	-10.68	8.233	8.22-8.31	0.09	--	--	4.2E-05	1.09
<b>B6</b>	7.2	-12.91	9.241	--	--	--	--	--	--
	7.3	-16.00	9.241	8.95-9.61	0.66	--	--	3.2E-04	7.14
	7.4	-19.73	9.241	8.94-9.61	0.67	--	--	3.2E-04	7.25
	7.5	-23.06	9.241	--	--	8.87-9.60	0.73	3.4E-04	7.89
	7.6	-21.56	9.241	--	--	8.85-9.53	0.68	3.2E-04	7.35
	7.7	-17.28	9.241	8.85-9.52	0.67	--	--	3.1E-04	7.25
	9.2	-12.55	12.39	--	--	--	--	--	--
	9.3	-13.00	12.39	--	--	--	--	--	--
	9.4	-13.54	12.24	--	--	--	--	--	--
	9.6	-12.32	11.89	--	--	--	--	--	--
	9.7	-13.16	11.89	--	--	--	--	--	--
	9.8	-13.33	11.72	--	--	--	--	--	--
	9.9	-13.24	11.64	--	--	--	--	--	--
	10	-13.12	11.56	--	--	--	--	--	--

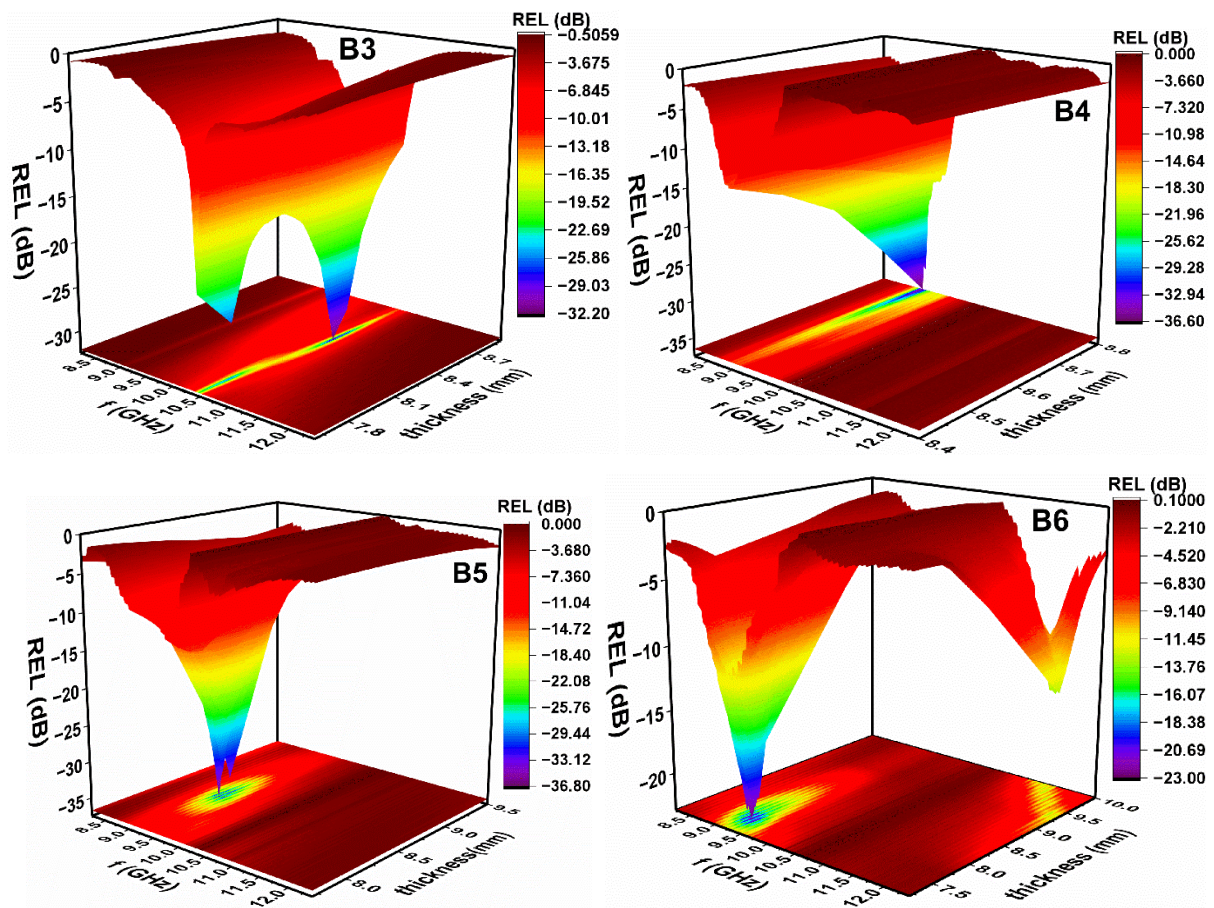
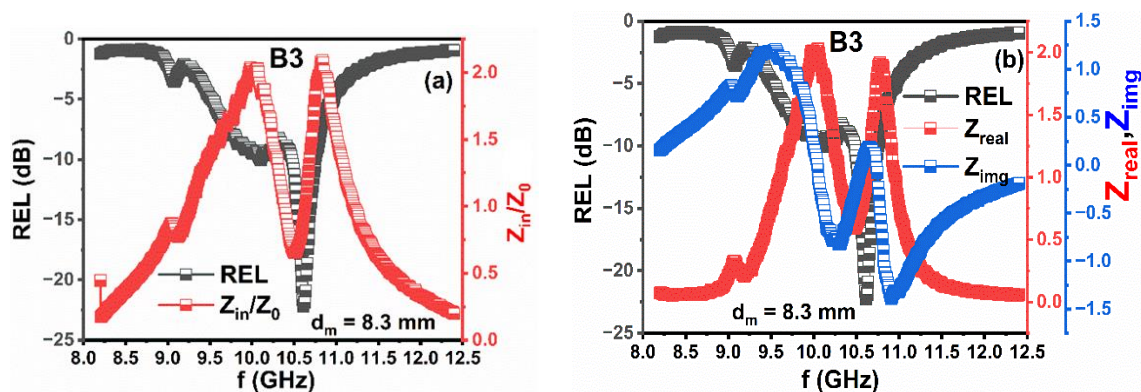


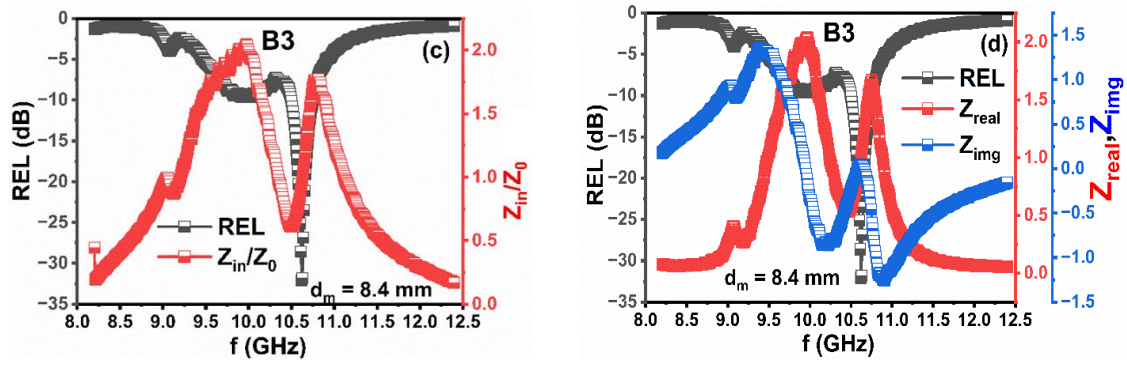
Fig. 4.48. 3D plots of REL at various thickness and frequency for B3, B4, B5 and B6 sample.

Table 4.16 enlists  $Z_{in}/Z_0$  and  $Z_{real}/Z_{img}$  values associated with the REL peak of the synthesized composite materials and these impedance values are calculated using 3.21. The significance of impedance matching between the absorber and free space, resulting in  $Z_{in}/Z_0 \cong 1$  ( $Z_{real} \cong 1$  and  $Z_{img} \cong 0$ ) when designing the absorber material and its application in microwave systems is already discussed in section 4.1.5. This can be explained because if  $Z_{in}/Z_0 \cong 1$ , then the maximum amount of incoming EM wave enters into the material. Fig. 4.46(a, c), 4.47(a), and 4.48(a, c) illustrate the graphs of reflection loss and  $Z_{in}/Z_0$  as a function of frequency for some considerable thicknesses of samples. Sample B5 exhibits the highest REL = -36.70 dB at a thickness of 8.5 mm and a frequency of 9.233 GHz with  $Z_{in}/Z_0$  value is approximately 1.022, wherein  $Z_{real} = 1.022$  and  $Z_{img} = 0.019$ . Similarly, sample B4 shows optimal REL = -36.5 dB at a thickness of 8.8 mm and a frequency of 9.04 GHz ( $Z_{real} = 0.992$  and  $Z_{img} = -0.028$ ).

There are some cases found where the  $Z_{in}/Z_0$  value is close to 1, but still, they didn't undergo high reflection loss. For example, the B3 sample at 8.3 mm and 8.4 mm thicknesses show  $Z_{in}/Z_0 = 0.936$  (close to 1) having REL dip of -22.33 dB and -32.13 dB at 10.61 GHz frequency, respectively (Table). Furthermore, at both thicknesses, the  $Z_{in}/Z_0$  values are similar, but they exhibit different REL values. A similar issue lies with the  $Z_{in}/Z_0$  value, where B6 owes REL = -19.73 dB at 9.241 GHz frequency-7.4 mm thickness with  $Z_{in}/Z_0 = 1.132$  (Table) i.e., close to 1. Whereas, relatively large REL = -23.06 dB is observed at 9.241 GHz-7.5 mm with  $Z_{in}/Z_0 = 1.148$  (more offset from 1). This can be explained through the complex nature of  $|Z_{in}|$ , it involves  $Z_{real}$  (real) and  $Z_{img}$  (imaginary). The curves of  $Z_{real}/Z_{img}$  and REL as a function of frequency are displayed in Fig. 4.46(b, d), 4.47(b) and 4.48(b, d). It is worth mentioning whether the  $Z_{in}/Z_0$  value is close to 1, but the REL<sub>max</sub> value follows  $Z_{real} \cong 1$  and  $Z_{img} \cong 0$ , which is observed B5 sample. Due to more offset  $Z_{real}/Z_{img}$  values from 1 and/or zero, the remaining samples exhibit relatively low REL values. The value of  $Z_{in}/Z_0$  changes with Co-Cr ions substitution.







**Fig. 4.49.** (a, c) Dependence of  $Z_{in}$  and REL in frequency (b, d) Dependence of REL,  $Z_{real}$ , and  $Z_{img}$  on frequency for B3 sample.

**Table 4. 16** Reflection loss peak's impedance parameters at different thicknesses.

Sample Name	Thickness (mm)	Max. REL (dB)	Matching frequency (GHz)	$Z_{in}/Z_0$	$Z_{real}$	$Z_{img}$
<b>B3</b>	7.6	-21.65	10.46	1.041	1.025	0.180
	7.8	-26.20	10.45	1.007	1.002	-0.0981
	7.9	-19.05	10.45	0.958	0.9350	-0.208
	8.3	-22.33	10.61	0.936	0.927	0.130
	8.4	-32.13	10.61	0.936	0.936	0.032
	8.5	-29.12	10.61	0.921	0.919	-0.061
<b>B4</b>	8.4	-14.06	9.048	1.018	0.936	0.400
	8.5	-16.81	9.048	1.032	0.988	0.300
	8.6	-20.92	9.048	1.029	1.012	0.190
	8.7	-28.23	9.04	1.010	1.006	0.080
	8.8	-36.5	9.04	0.993	0.992	-0.028
<b>B5</b>	8.3	-24.09	9.233	1.017	1.008	0.133
	8.4	-36.70	9.233	1.022	1.022	0.019
	8.5	-34.60	9.233	1.009	1.004	-0.093
	9.5	-10.68	8.233	1.267	1.088	-0.649
<b>B6</b>	7.2	-12.91	9.241	1.002	0.876	0.487
	7.3	-16.00	9.241	1.079	1.008	0.385
	7.4	-19.73	9.241	1.132	1.108	0.230
	7.5	-23.06	9.241	1.148	1.147	0.039
	7.6	-21.56	9.241	1.123	1.113	-0.150
	7.7	-17.28	9.241	1.065	1.021	-0.303

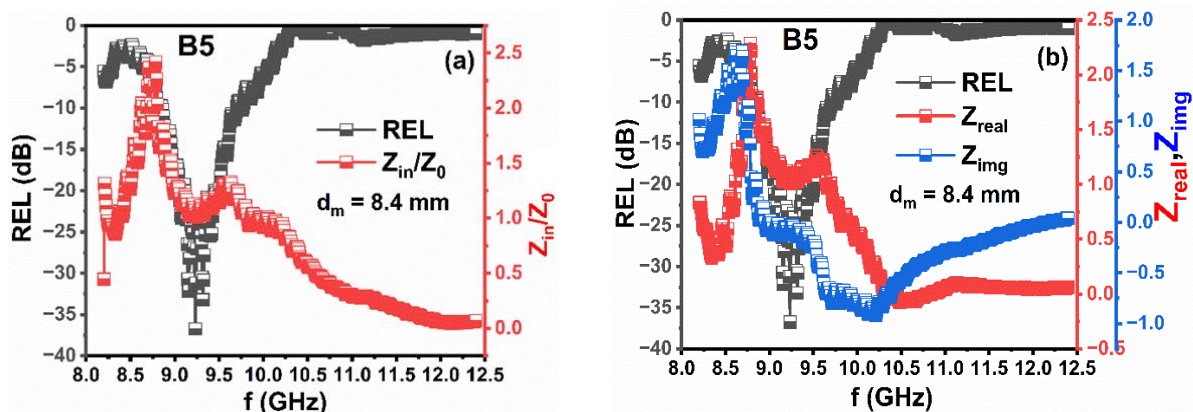


**Fig. 4.50.** (a) Dependence of  $Z_{in}$  and REL in frequency (b) Dependence of REL,  $Z_{real}$ , and  $Z_{img}$  on frequency for B5 sample.

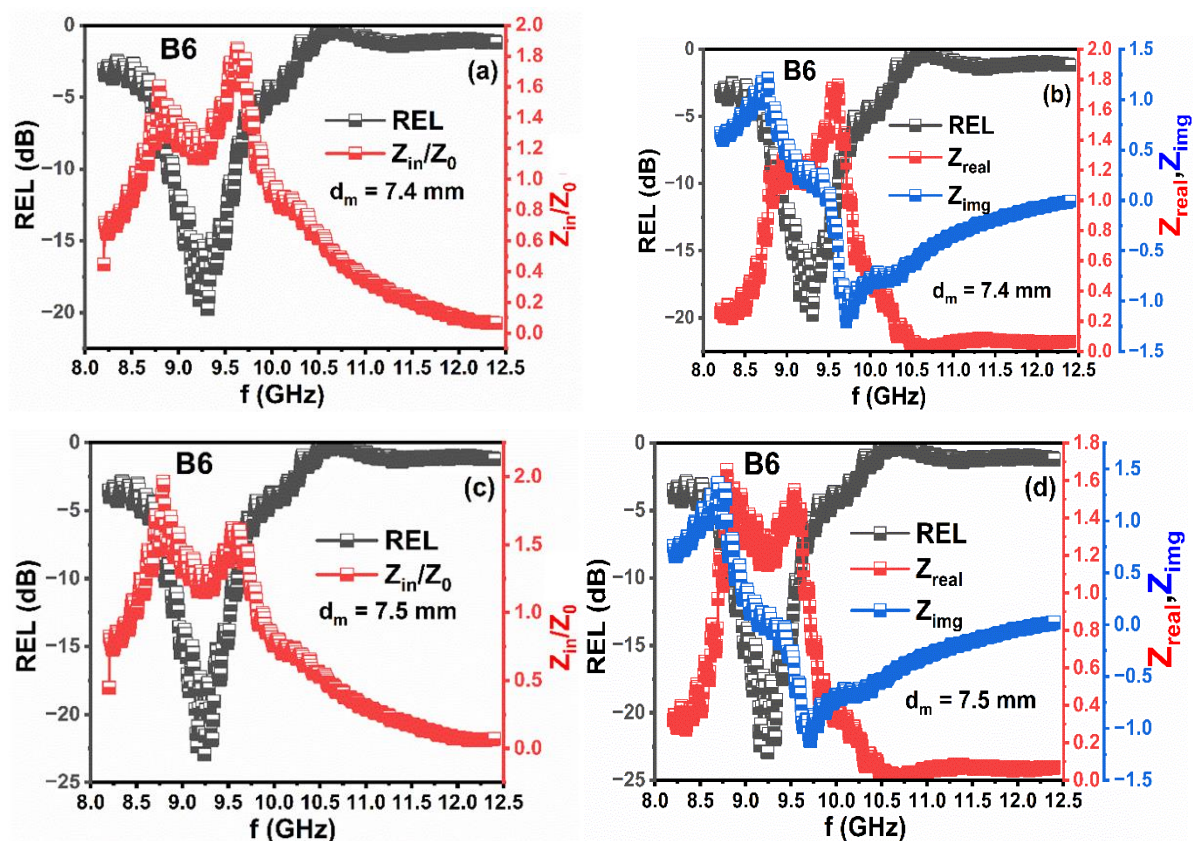


**Fig. 4.51.** (a, c) Dependence of  $Z_{in}$  and REL in frequency (b, d) Dependence of REL,  $Z_{real}$ , and  $Z_{img}$  on frequency for B6 sample.

Conclusively, the substitution of  $\text{Co}^{2+}$  and  $\text{Cr}^{3+}$  ions cause non-linear variation in dielectric and magnetic loss and is maximum for the B4 sample ( $\epsilon'' = 3.48$  at 11.11 GHz and  $\mu'' = 0.986$  at 11.23 GHz). Both B4 and B5 samples exhibit maximum reflection loss of -36.5

dB (8.8 mm) and -36.7 dB (8.4 mm) at 9.04 GHz and 9.233 GHz, respectively. In comparison to other samples, B4 and B5 have  $Z_{real}/Z_{img}$  values that are closer to 1 and 0. The resonance observed in the B4 sample is also responsible for the large value of REL. Furthermore, Fig. 4.39 demonstrates the losses due to hysteresis parameters. The contribution of impedance matching, quarter wavelength mechanism, and magnetic loss are altogether responsible for the large value of REL in B4 and B5 samples. Substitution of  $Co^{2+}$ - $Cr^{3+}$  ions improve the performance of the magnetic absorber.

### 4.3 $Co^{2+}$ - $Zn^{2+}$ substituted $SrCo_xZn_xFe_{12-2x}O_{19}$ hexaferrite.

Table 4.17 displays the assignment of sample names/codes for a different level of substitution for  $SrCo_xZn_xFe_{12-2x}O_{19}$ .

**Table 4.17** Assignment of sample name for a different level of substitution of  $SrCo_xZn_xFe_{12-2x}O_{19}$  hexaferrite.

Sample Composition $SrCo_xZn_xFe_{12-2x}O_{19}$	Sample Code (F-series)
$x = 0.4$	F1
$x = 0.8$	F2
$x = 1.2$	F3
$x = 1.6$	F4
$x = 2.0$	F5

#### 4.3.1 Structural Analysis

##### 4.3.1.1 X-ray Analysis

The crystalline structure and phase purity of the prepared F-series samples in the range of  $2\theta = 20^\circ-70^\circ$  (step scan  $0.02^\circ/\text{min}$ ) are illustrated in Fig. 4.49. X-powder software was deployed for indexing the (hkl) planes and phase identification of all peaks observed in the XRD pattern. The obtained XRD pattern was matched with a reference pattern of

magneto plumbite-  $SrFe_{12}O_{19}$  (ICDD # 80-1197) with space group  $P6_3/mmc$ . Analysis of the XRD pattern affirms the formation of the magnetoplumbite crystalline phase as the major and cobalt iron-oxide ( $CoFe_2O_4$ ) as the secondary phase (ICDD # 22-1086) for all samples, except F5 [267]. The refinement analysis using MAUD software affirms the existence of SrM hexaferrite phase and cobalt iron-oxide ( $CoFe_2O_4$ ) as a secondary phase (ICDD # 22-1086) in F2 sample, as seen in Fig. 4.50. XRD revealed that increasing the level of  $Co^{2+}$  ions increase the strength of the  $CoFe_2O_4$  peak [33], [34],[270]. It is evident from Fig. 4.49 that the replacement of  $Fe^{3+}$  ions with  $Co^{2+} - Zn^{2+}$  ions results change in intensity of peak. The slight variation observed in the diffraction angle indicates the successful substitution of  $Co^{2+} - Zn^{2+}$  ions in the crystal lattice of hexaferrite. The various structural parameters ( $a$ ,  $c$ ,  $c/a$ , and  $V$ ), the crystallite size ( $D$ ), and the lattice strain ( $\epsilon$ ) are calculated using equations 3.1, 3.2, and 3.3, and are listed in Table 4.18.

**Table 4.18** Values of structural parameters ( $a$ ,  $c$ ,  $c/a$ ,  $V$ ), the crystallite size ( $D$ ), hopping length ( $L_A$  and  $L_B$ ), dislocation density ( $\delta$ ), and lattice strain ( $\epsilon$ ) are listed below:

Sample Code	$a$ (Å)	$c$ (Å)	$c/a$	$V$ (Å <sup>3</sup> )	$D$ (nm)	$L_A$ (nm)	$L_B$ (nm)	$\delta \times 10^{-4}$ (nm <sup>-2</sup> )	$\epsilon$
F1	5.847	22.92	3.919	678.5	41.9	2.5317	2.0672	5.67	0.002947
F2	5.856	22.94	3.917	681.2	45.9	2.5356	2.0703	4.73	0.002695
F3	5.856	22.99	3.925	682.7	49.8	2.5356	2.0703	4.03	0.002491
F4	5.847	23.11	3.952	684.2	47.0	2.5317	2.0672	4.52	0.002419
F5	5.847	22.96	3.926	679.7	48.0	2.5317	2.0672	4.32	0.002575

Table 4.18 the value of the ‘ $c$ ’ parameter ranges from 22.92 to 23.11 Å, while the lattice parameter ‘ $a$ ’ varies from 5.847 to 5.856 Å as the degree of substitution increases. These results clearly show that the expansion of the lattice parameter ‘ $a$ ’ is lesser than that of the parameter ‘ $c$ ’ which is consistent with the conventional behavior of SrM hexaferrite[163] Due to the easily magnetized axis i.e., the  $c$ -axis is more responsive to the substitution process than the  $a$ -axis. The slight change observed in the lattice parameter is caused by the larger ionic radii of  $Co^{2+}$  ion (0.72Å) and  $Zn^{2+}$  ion (0.82Å) than host  $Fe^{3+}$  ion (0.645 Å)[194]. The value of unit cell volume ( $V$ ) calculated using equation 3.2

increases from 678.5 Å<sup>3</sup> (F1) – 684.2 Å<sup>3</sup> (F4) and then decreases to 679.7 Å<sup>3</sup>(F5). For M-phase, the height-to-width or *c/a* ratio should be around 3.98 and the observed values lie in the range of 3.917 to 3.952, which is close to the predicted values [194], [197].

**Table 4.19** Calculated values of bulk density ( $\rho_{bulk}$ ), XRD density ( $\rho_x$ ), porosity (P) and surface area (S) are listed below:

Sample Code	Density (g/cm <sup>3</sup> )		Porosity (%)	$S \times 10^7$ (cm <sup>2</sup> /g)
	Bulk density ( $\rho_{bulk}$ )	XRD density ( $\rho_x$ )		
<b>F1</b>	2.93	5.22	43.78	27.37
<b>F2</b>	2.79	5.23	46.64	24.96
<b>F3</b>	2.70	5.24	48.33	22.98
<b>F4</b>	3.03	5.26	42.24	24.25
<b>F5</b>	2.92	5.31	44.97	23.49

The calculated crystallite size and microstrain values from equations (3.3) and (3.5), respectively are enlisted in Table 4.18. The insertion of larger ions disrupts the regular arrangement of atoms in the crystalline structure and leads to the formation of lattice defects and strain within the crystal. The non-linear decrease observed in the values of the microstrain corresponds to the non-linear increment in the crystallite size from F1 (41.99 nm) to F5 (48.09 nm). Moreover, it's worth mentioning that the microstrain value is higher in the F1 sample, which contributes to its smaller crystallite size results in the F1 sample. The dislocation density calculated using equation 3.4 varies non-linearly with the substitution of Co<sup>2+</sup> and Zn<sup>2+</sup> ions. Table 4.18 depicts that the slight variation observed in  $L_A$  and  $L_B$  values [calculated using equations (3.6) and (3.7)] may be attributed to small ionic radii of Fe<sup>3+</sup> ions compared to Co<sup>2+</sup> and Zn<sup>2+</sup> ions. The XRD density ( $\rho_x$ ) increases from 5.22 g/cm<sup>3</sup> (F1) to 5.31 g/cm<sup>3</sup> (F6) with substitution which may be due to the lesser atomic mass of Fe<sup>3+</sup> (55.84 amu) ion than both Co<sup>2+</sup> (58.93 amu) and Zn<sup>2+</sup> (65.38 amu) ions as seen in Table 4.19. Moreover,  $\rho_x$  value [calculated using equation (3.9)] turns out to be greater than  $\rho_{bulk}$  [calculated using equation (3.8)], which suggests the existence of pores that can form during sample preparation and cause the irregular shape of grains. The porosity (P) [calculated using equation (3.10)] shows an irregular trend with substitution and is minimum for the F4 sample.



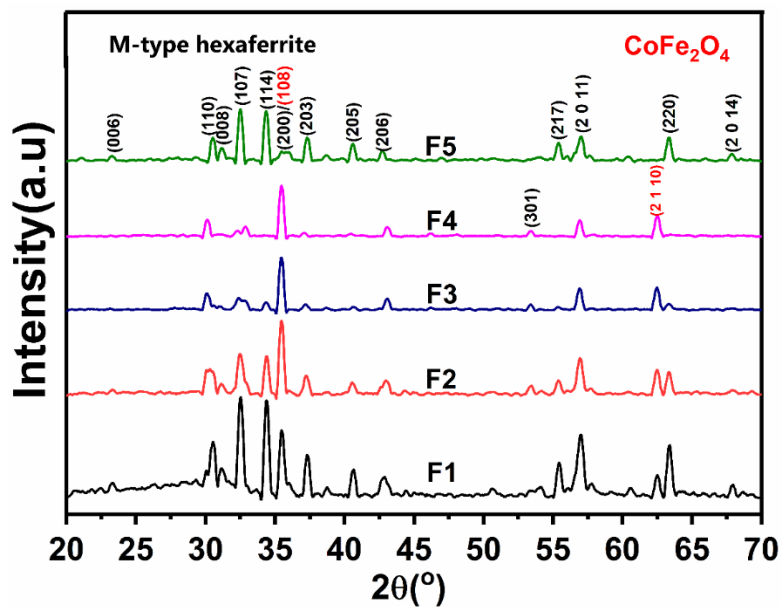


Fig. 4.52. XRD pattern of prepared specimen F1 to F5 hexaferrite.

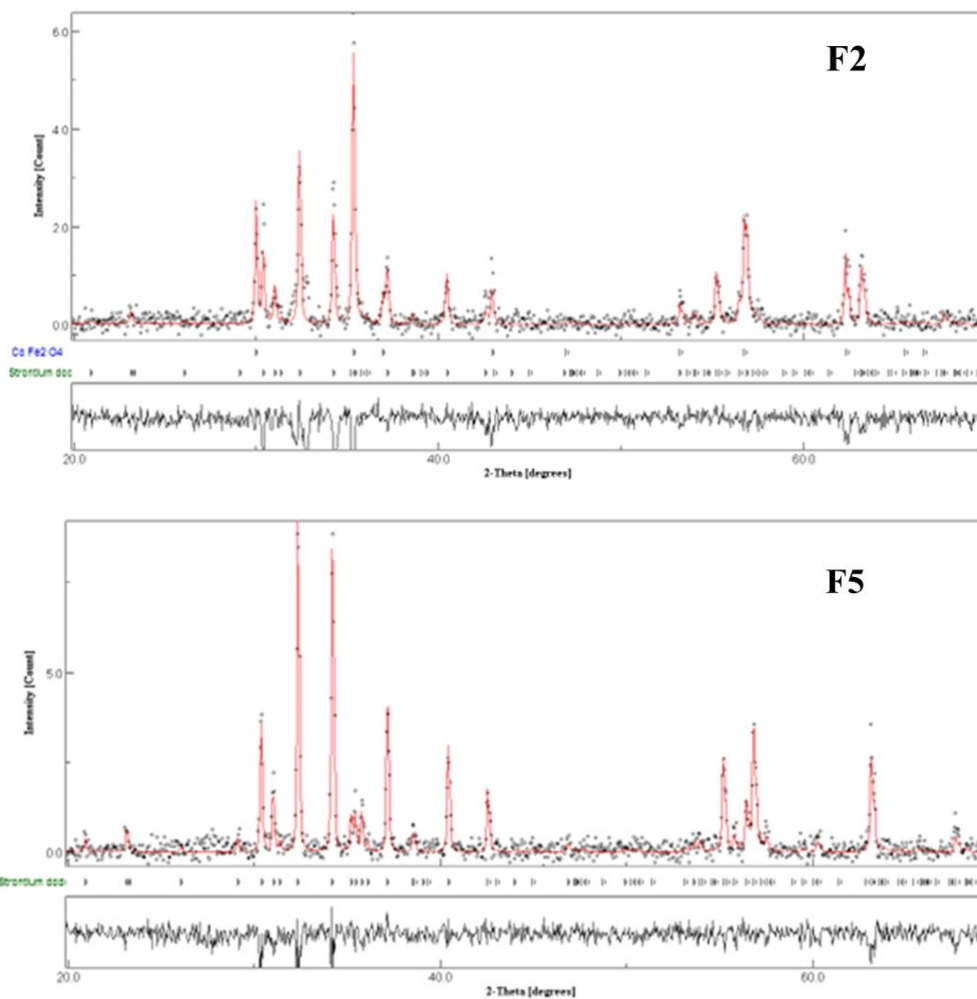


Fig. 4.53. Refinement analysis of F2 and F5 sample.

### 4.3.1.2 FTIR spectroscopy analysis

The FTIR spectra F-series samples were measured in the wavenumber range of 4000 – 380  $\text{cm}^{-1}$ . The FTIR spectra displayed in Fig. 4.51 are used to identify the position of the different bands and to study the structural changes caused by the substitution of  $\text{Co}^{2+}$  and  $\text{Zn}^{2+}$  in  $\text{SrFe}_{12}\text{O}_{19}$  hexaferrite [271]. The observed absorption bands are found to be in nearly the same position for all, but their relative intensities vary [272]. The band at 435.15  $\text{cm}^{-1}$  is assigned to Fe-O bending by  $\text{Fe-O}_4$  and Fe-O stretching by  $\text{Fe-O}_6$ , while the band at 597.98  $\text{cm}^{-1}$  is assigned to Fe-O stretching by  $\text{Fe-O}_4$ [249]. When the content of  $\text{Co}^{2+}$  -  $\text{Zn}^{2+}$  ions increase, and these bands shift slightly toward the low-frequency side. This could be due to the substitution of  $\text{Co}^{2+}$  -  $\text{Zn}^{2+}$  ions, which changes the distribution of  $\text{Fe}^{3+}$  ions.

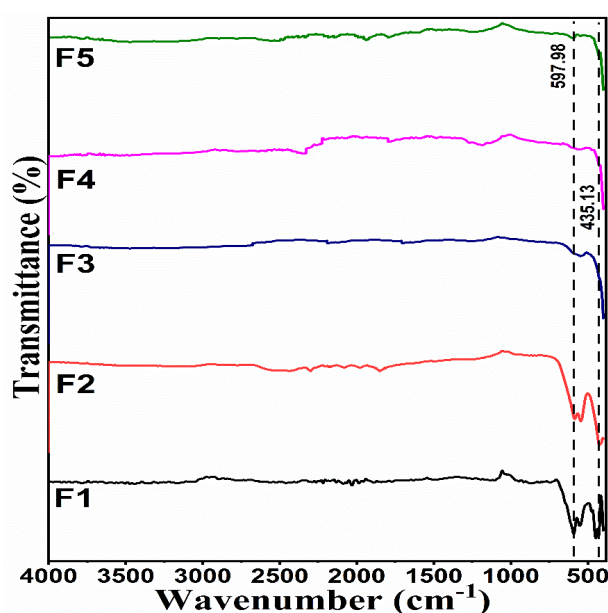


Fig. 4.54. FTIR spectra in 400-4000  $\text{cm}^{-1}$  range of F-series hexaferrite samples.

### 4.3.1.3 SEM and EDX Analysis

Fig. 4.52 displays the micrographs of the F-series samples. The micrographs illustrate that all samples of micrometer sizes consist of an agglomeration of several nanometer-sized particles[273]. Moreover, it is observed in all samples that the composition of the resulting grain clusters contains hexagonal, platelet-shaped particles with distinct geometric shapes, which could be due to the high combustion temperature during synthesis[274]. The agglomerations observed in the form of grain clusters are likely due to magnetic interaction among the molecules of ferric, cobalt, zinc, and strontium ions. Substitution causes agglomeration of grains in the form of fused grains with uneven size distribution.



Furthermore, the non-porous small pits can be visualized in micrographs. In non-porous regions, there are fewer disruptions to the magnetic domains and atomic alignment within the material. This can lead to enhanced magnetic response, including higher magnetization levels and improved magnetic efficiency. Moreover, an increment in the degree of substitution from F2 to F5 causes densification in grains. It refers to a reduction in porosity and an increase in interparticle contact, resulting in a more compact and closely packed grain structure. This behavior is consistent with the calculated bulk density and porosity as seen in [Table 4.18](#).

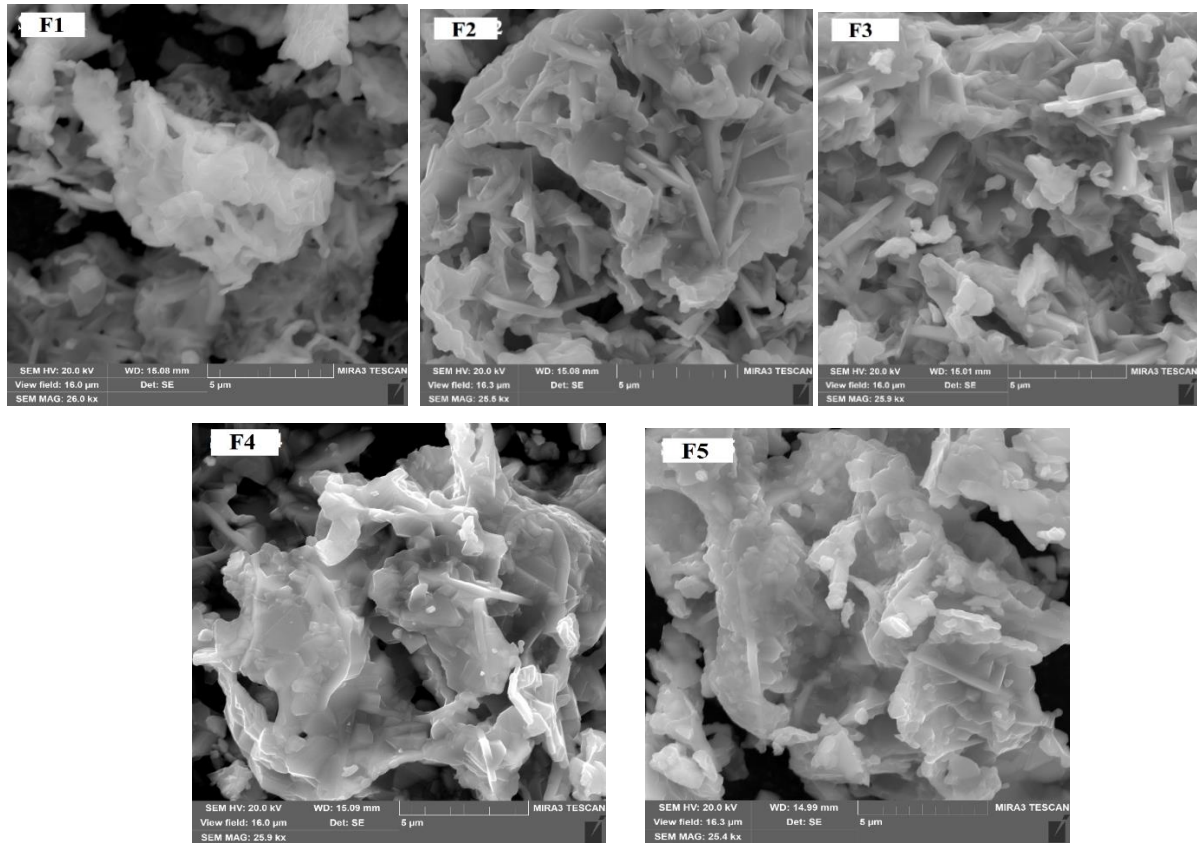


**Fig. 4.55.** SEM micrographs of F-series hexaferrite samples.

## 4.3.2 Electrical Analysis

### 4.3.2.1 Dielectric Analysis

It has been noted that among all samples of the F-series only F2, and F5 exhibit the electrical characteristics due to uncertainty observed in the rest of the samples of the F-series. [Fig. 4.53\(a\)](#) and [4.53\(b\)](#) shows the frequency-dependent real ( $\epsilon'$ ) and imaginary ( $\epsilon''$ ) part of the dielectric constant, which decreases as frequency increases from 20 Hz to 2 MHz, respectively. This is the general frequency-dependent behavior of ferrites. The dielectric characteristics of hexaferrite materials are affected by various factors such as method of

preparation, grain size, cation distribution, structural homogeneity, density, porosity, etc. The dispersion rate is different for F2, and F5 samples. The value of  $\epsilon'$  for the F2 is 16.41 at 20 Hz and decreases to 9.381 at 2 MHz. The same trend is observed for F5, wherein  $\epsilon'$  is 22.73 at 20 Hz and falls to 19.51 at 2 MHz. As the substitution level increases, the dispersion rate decreases and is found to be maximum for F2. The observed dispersion is due to interfacial polarization which can be explained through the Maxwell-Wagner model [275]. In polycrystalline ferrites, the polarization mechanisms involve electron hopping between Fe ions having different oxidation states at the octahedral site [276]. When the AC field is applied, electrons flow through hopping within the grain in the direction of the field and accumulate at the boundaries of grains to generate polarization. However, as the frequency increases, the electrons can't follow up with the field, and their change of direction lags behind the field. This dilutes the probability of electrons reaching the grain boundaries, which diminishes the polarization and consequently the dielectric constant. It has been reported that the polarization in ferrites resembles that of the conduction mechanism, which is further interlinked with the dielectric behavior of the ferrites [214]. The value of  $\epsilon'$  and  $\epsilon''$  decreases with substitution from F2 to F5, which can be explained by the availability of  $\text{Fe}^{2+}$  ions at octahedral sites. As we increase the substitution, the Co-Zn ions may tend to occupy the octahedral sites, which lessen the no. of Fe ions responsible for polarization, thus resulting in a decrease in the dielectric constant [277].

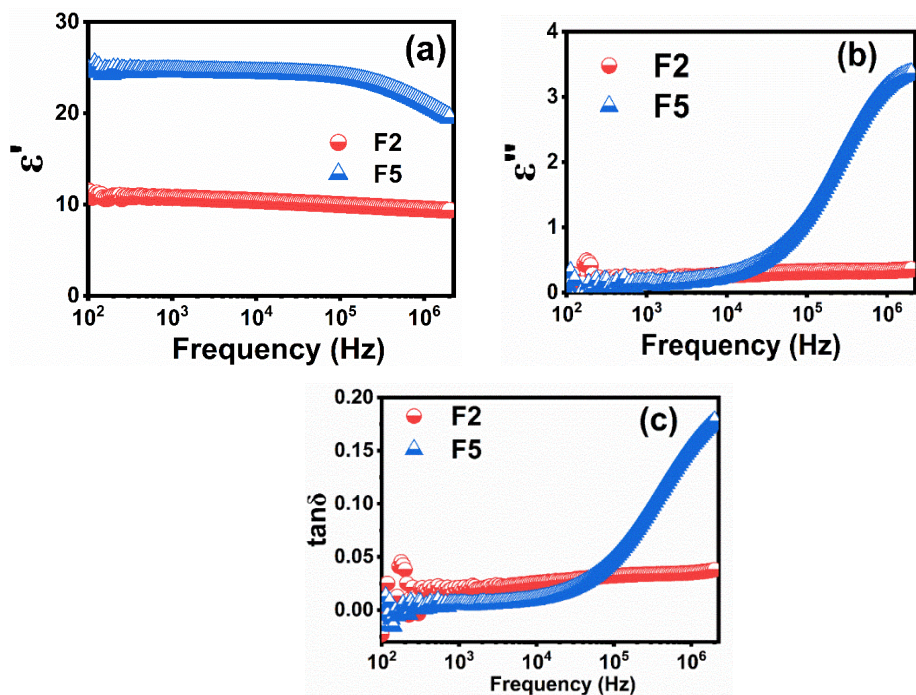


**Fig. 4.56.** (a)  $\epsilon'$  (b)  $\epsilon''$  (c) dielectric loss tangent variation with frequency of F2, and F5 hexaferrite.

The dielectric loss tangent ( $\tan\delta$ ) is affected by various factors, such as interfacial polarization, interface traps,  $Fe^{2+}/Fe^{3+}$  content, sample stoichiometry, and structural integrity, all of which ultimately depend on the sintering temperature. Fig. 4.53(c) shows the frequency-dependent variation of  $\tan\delta$  for F2 and F5 samples at room temperature. It is observed that the value of  $\tan\delta$  is high at the low-frequencies region and it decreases with increasing frequency. This trend can be explained through Koop's phenomenological theory of dielectrics [276]. Additionally, the  $\tan\delta$  of the F5 sample begins to exhibit a peak at a specific frequency in the high-frequency region. This can be ascribed to the occurrence of a relaxation phenomenon in the F5 sample. When an externally applied field of varying frequency is given to the material, a resonance occurs because the frequency of charge hopping between cations  $Fe^{3+}$  and  $Fe^{2+}$  at the octahedral sites matches the applied frequency.

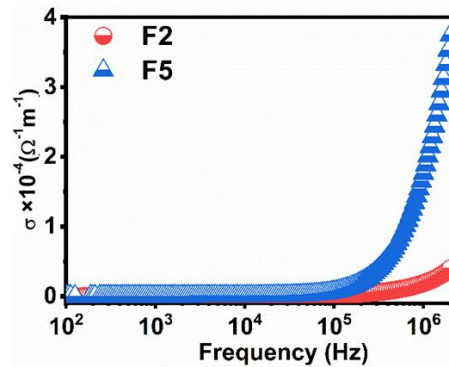
#### 4.3.2.2 AC conductivity

Fig. 4.54 illustrates the variation of  $\sigma$  with increasing frequency. It depicts the frequency-independent behavior of  $\sigma$  at lower frequencies and sharply increases in the higher frequency region ( $>10^4$  Hz). Verwey's hopping mechanism explains the consistent increment in ac values as frequency increases in hexaferrites. At higher frequencies, electrical conduction in hexaferrite is likely attributed to electrons successfully hopping between two valence states of the same element ( $Fe^{2+}/Fe^{3+}$ ). The effect of grain boundaries is more prominent in lower frequencies, where it impedes the free movement of electrons between ions at octahedral sites. This results in high polarization and lower charge hopping due to charge carriers getting trapped at multiple trapping sites on grain boundaries. On the other hand, the conductive grains facilitate electron hopping and releasing the stored charge carriers at high frequency. The replacement of  $Fe^{3+}$  ions with Co-Zn ions causes a reduction in conductivity value and this reduction elucidates a decrement in the concentration of  $Fe^{3+}$  ions at an octahedral position, which restricts the probability of hopping between  $Fe^{2+}$  and  $Fe^{3+}$  ions.

#### 4.3.2.3 Complex Electric Modulus

Fig. 4.55(a) illustrates that  $M'$  values are low in the lower frequency range and it increases with increasing frequency. At lower frequencies, the  $M'$  values for all synthesized samples tend to approach zero, indicating maximum restoring force depolarization and consequently the lowest conductivity and minimal electrode polarization. The low  $M'$  value

observed in the low-frequency region for F5, suggests the suppression of electrode polarization phenomena. Substitution causes a decrease in the electrode polarization effect, as evident from the increment in  $M'$  values at low frequencies.



**Fig. 4.57.**  $\sigma$  variation with frequency of F2 and F5 hexaferrite.

The electrode polarization phenomenon arises due to the long-range mobility of charge carriers, governed by the restoring force under the influence of an induced electric field [278]. Moreover, the value of  $M'$  increases with increasing frequency, showing that the conduction can be attributed to the short-range mobility of charge carriers. This variation is like the behavior observed in  $\sigma$ , discussed in the previous section.

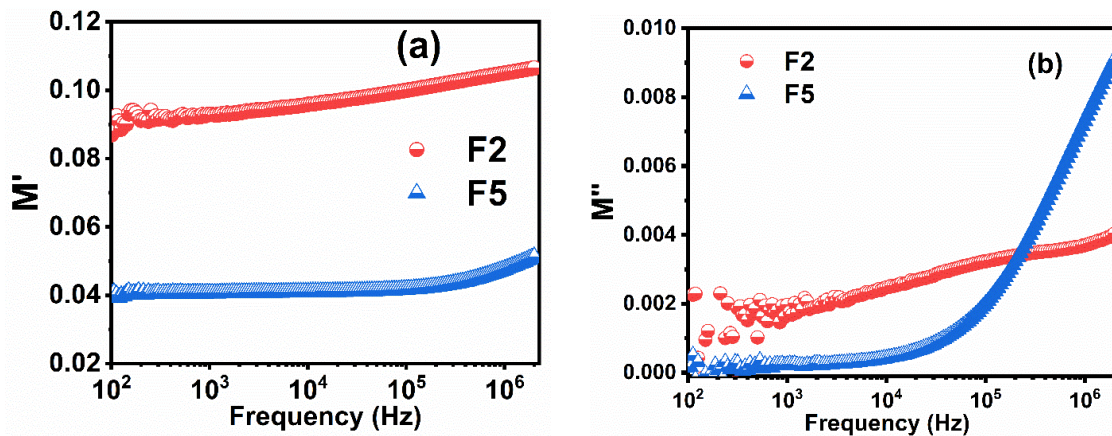


**Fig. 4.58.** (a)  $M'$  (b)  $M''$  variation with frequency of F2 and F5 hexaferrite.

Fig. 4.55(b) displays the frequency-dependent behavior of  $M''$  for F2 and F5 at room temperature. This parameter is directly linked to the energy dissipation in the irreversible conduction process. The high-frequency tail of the peak corresponds to the frequency range where ions are confined to their potential well, allowing only localized motion within those walls. Conversely, the low-frequency tail of the peak represents the frequency range where ions can move over long distances, enabling successful hopping from one to a neighboring site in the crystal [186]. The observed peak signifies the transition of charge carriers from long-range to short-range mobility. The broadening of the peak implies the propagation of



relaxation time with various time constants, indicating a non-exponential behavior. The asymmetric shape of the plot for the peak maxima suggests non-Debye relaxation but rather exhibits characteristics of Cole-Cole relaxation [279]. As the substitution level of Co-Zn ions increases, a noticeable shift is observed in the peak towards the higher frequencies.

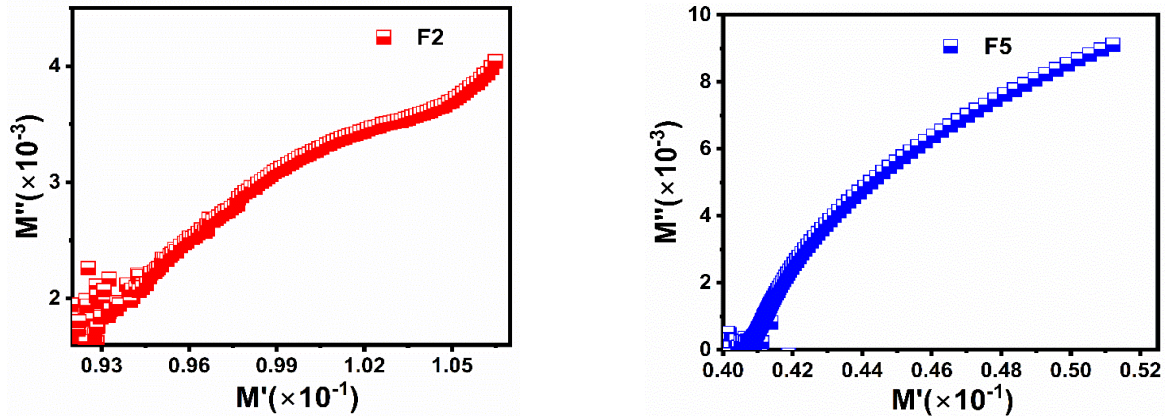


Fig. 4.59. Cole-Cole plots ( $M''$  vs  $M'$ ) variation with frequency of F2 and F5 hexaferrite

Fig. 4.56 depicts the Cole- Cole plots ( $M''$  versus  $M'$ ) for F2 and F5 samples at room temperature. The obtained curves demonstrate that their centers are situated below  $M'$ -axis. This suggests that the observed relaxations are of non-Debye type and distributed over different time constants [280]. The semicircular arc reflected at a low frequency is attributed to charge carrier relaxation due to grain boundaries, while the semicircular arc at a high frequency is caused by charge carrier relaxation associated with grains. It can be seen (Fig. 4.52) that due to the different size distribution of grains, the curve distribution ( $M''$  versus  $M'$ ) of all samples is also distinct. Both F2 and F5 samples show a segment of an arc instead of perfect semicircles. This suggests that the grain boundary effect decreases, and the effect of grains increases as frequency increases. Substitution causes the formation of grain clusters, and this can also be visualized in the SEM micrographs.

#### 4.3.2.4 Complex Impedance Analysis

Fig. 4.57(a) and 4.57(b) illustrate the decreasing trend observed in both  $Z'$  and  $Z''$  with increasing the frequency of an applied field, respectively. The declining behavior of both  $Z''$  and  $Z'$  with increasing frequency, suggests an increment in the electron hopping between localized ions and results a rise in ac conductivity. The reduction observed in  $Z'$  could be explained through the Maxwell-Wagner model at higher frequencies. The investigation of  $Z''$  led to a better understanding of the relaxation process and space charge effect [281]. At low frequencies, the space charge effect dominates the impedance response

and results in a larger value of  $Z''$ . However, at higher frequencies the charge carriers may not be able to respond rapidly to the alternating applied, leading to a decrement in the  $Z''$  [282].

The Cole-Cole plot reveals the effect of morphology and polarization process on dielectric relaxation. Fig. 4.57(c) illustrates the Cole-Cole plot of F2 and F5 samples at room temperature. Instead of obtaining a complete semicircular arc, a segment of an arc is observed for all samples. It is also noted that as the substitution increases, the depression of the arc decreases from F2 to F5. This depression suggests that the impedance mechanism at low frequency explicitly depends on the dielectric polarization that occurs at grain boundaries, also referred to as the Maxwell-Wagner effect [283].

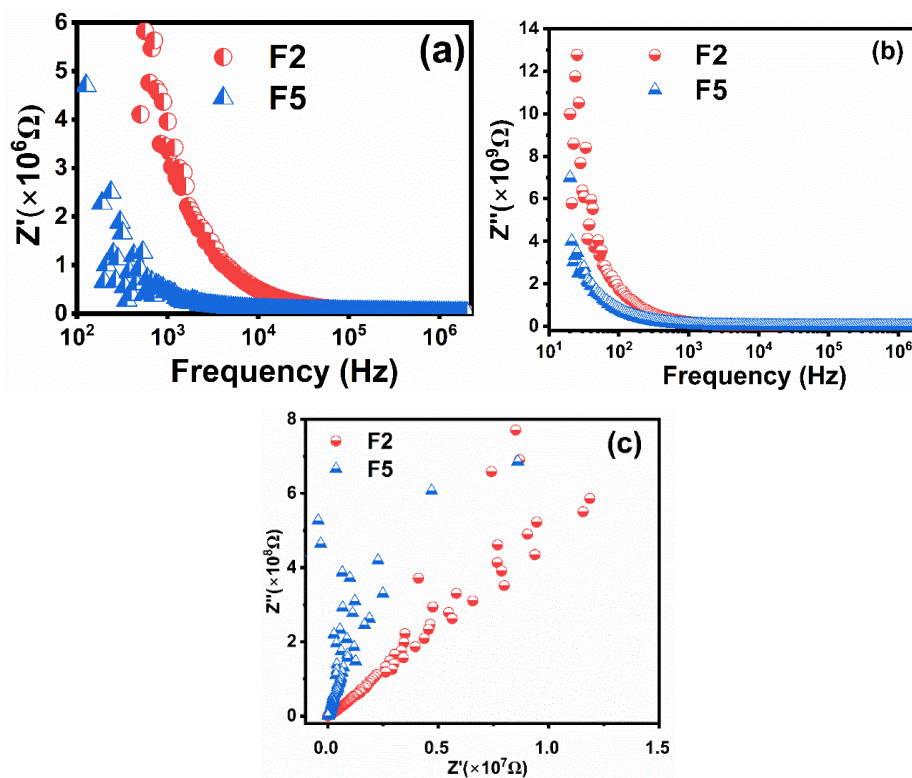


**Fig. 4.60.** (a)  $Z''$  (b)  $Z'''$  (c) Cole-Cole plots ( $Z'''$  vs  $Z'$ ) variation with frequency of F2 and F5 hexaferrite

### 4.3.3 Magnetic Analysis

The magnetic characteristics of the prepared specimens can be tailored by replacing  $\text{Fe}^{3+}$  ions with cations of different electronegativity, magnetic moment, and d-configuration [284]. It is reported that the more electronegative ions generally occupy more octahedral sites than tetrahedral positions in the crystal structure. The electronegativity of  $\text{Zn}^{2+}$  (1.65) ions is lower than that of  $\text{Co}^{2+}$  (1.88) ions, so the former ions can occupy the

tetrahedral site  $4f_1$  ( $\downarrow$ ) [285]. According to ligand field theory,  $Zn^{2+}$  ions have no site preference due to  $d^0$  configuration, and  $Co^{2+}$  ions with  $d^7$  configuration preferably choose to occupy octahedral sites  $12k$  ( $\uparrow$ ),  $2a$  ( $\uparrow$ ),  $4f_2$  ( $\downarrow$ ) [286]. When the substituted ion has larger ionic radii than the host ion, it preferentially occupies octahedral sites at the edges of the unit cell. From previous reports,  $Co^{2+}$  ( $3 \mu_B$ ) ions can occupy both the octahedral ( $4f_2$ ) and tetrahedral ( $4f_1$ ) crystallographic sites, while  $Zn^{2+}$  ( $0 \mu_B$ ) tends to replace  $Fe^{3+}$  ions at the  $4f_1$  site [287]. The saturation magnetization ( $M_s$ ), remanence magnetization ( $M_r$ ), coercivity ( $H_c$ ), anisotropy field ( $H_a$ ), remanence ratio ( $M_r/M_s$ ) and magnetic moment ( $n_B$ ) values derived from the hysteresis loop are enumerated in Table 4.20. Fig. 4.58 shows the M-H loops of F-series samples.

The magnetic moment of the incorporated specimen could be determined through the distribution of host and substituted cations over five crystallographic sites of hexagonal crystal structure using the following expression[288]:

$$M_s = M_a (2a + 12k + 2b) (\uparrow) - M_b (4f_1 + 4f_2) (\downarrow)$$

The total magnetization increases by substituting non-magnetic ions or less magnetic at the ( $4f_1\downarrow + 4f_2\downarrow$ ) lattice site, while magnetization shows decline behavior with the substitution of these ions at ( $2a\uparrow + 12k\uparrow + 2b\uparrow$ ) lattice sites[231]. Table 4.20 and Fig. 4.58 show that the value of  $M_s$  remains almost constant from F1 (75.26 emu/g) to F3 (75.71 emu/g) with the substitution of both  $Zn^{2+}$  and  $Co^{2+}$  ions. This could be ascribed to the simultaneous replacement of  $Fe^{3+}$  ions by Co and Zn ions at spin-up and spin-down sites. This can also be confirmed through the Mössbauer spectroscopy results (explained in the next section), where significant change is not observed in the net  $R_A$  of spin-up ( $2a + 12k + 2b$ ) and spin-down ( $4f_1 + 4f_2$ ) sites with Co-Zn substitution. Furthermore, a small increase of 6.2% in  $M_s$  from F3 to F5 could be understood through the 6.7% reduction in porosity calculated from XRD data. Moreover, the remanence magnetization ( $M_r$ ) is found to gradually increase with substitution from F1 (26.95 emu/g) to F5 (59.12 emu/g). The calculated value of  $M_r/M_s$  is enlisted in Table 4.20 and it turns out to be less than 0.5 for F1, F2, and F3 samples, which depicts the multi-domain nature of particles within the material. On the other hand, F4 and F5 indicate the existence of a single domain in the material.

The anisotropy field ( $H_a$ ) mainly depends on the 2b and  $4f_2$  sites of magnetoplumbite structure, but the  $4f_2$  site prominently affects  $H_a$  more than the alone 2b site. It is clear from Table 4.20 that  $H_a$  increases by 11.58% from F1 to F2 and is caused by the increment in the total relative area of both 2b and  $4f_2$  sites. Further substitution causes a decrement in  $H_a$  from



F2 to F5. This can be explained through the Mössbauer spectra (discussed in the next section), where the net change in the relative area of the 2b site is more than the relative area of the 4f<sub>2</sub> site. But, the contribution of the 2b site is less than the 4f<sub>2</sub> site, therefore despite the large change in 2b site occupancy, the overall  $H_a$  doesn't decrease by the same amount. The high coercivity ( $H_c$ ) value is the pre-requisite of material to be used for recording media application and substitution of Co-Zn ions causes a non-linear increment in  $H_c$ . The nature of this variation can be explained by the support of intrinsic and extrinsic factors. The initial increment observed in  $H_c$  from F1 (2035 Oe) to F2 (3035 Oe), is caused by  $H_a$ . The  $H_a$  is mainly determined by the magnetic moments of the Fe<sup>3+</sup> ions at the 2b and 4f<sub>2</sub> sites as discussed before.

**Table 4.20** Magnetic parameters  $M_s$ ,  $H_c$ ,  $H_a$ ,  $M_r$ ,  $n_B$  and  $M_r/M_s$  value of all hexaferrite samples.

Sample Name	$M_s$ (emu/g)	$H_c$ (Oe)	$H_a$ (kOe)	$M_r$ (emu/g)	$n_B$ ( $\mu_B$ )	$M_r/M_s$
<b>F1</b>	75.26	2035	28.55	26.95	14.37	0.358
<b>F2</b>	75.36	3035	32.29	31.83	14.46	0.422
<b>F3</b>	75.71	2028	26.60	34.00	14.59	0.449
<b>F4</b>	77.57	3511	26.90	48.98	15.02	0.631
<b>F5</b>	80.72	4159	22.65	59.12	15.70	0.732

A larger anisotropy field results in a higher coercivity value, indicating a large amount of energy is needed to reverse the magnetic moment of hexaferrite. Furthermore, a decrease in  $H_c$  from F2 (3035 Oe) to F3 (2028 Oe) may be predicted to be caused by good shape anisotropy as shown in the micrograph (Fig. 4.52). The coercivity is influenced by shape anisotropy and magnetocrystalline anisotropy (Fig. 4.52). Sample F3 exhibited a significant no. of platelet-shaped hexagonal grains compared to F2. This causes enhancement in shape anisotropy of the F3 sample due to the high diameter/thickness ratio and is ascribed to the reduction in coercivity as seen in SEM micrographs of F3 (Fig. 4.52) [274]. Further substitution of Co-Zn ions at F4 and F5 decreases  $H_a$ , whilst  $H_c$  gradually increases to 4159 Oe. This predicted behavior can be ascribed to the existence of grain clusters (aggregation of small grains) along with large non-porous pits that cause demagnetizing fields as seen in SEM micrographs of F5 (figure 13). As a result, it requires more field to get magnetized and causes high coercivity. The Bohr magneton [calculated from equation (3.14)] is closely

related to saturation magnetization and molecular weight (M.W). As the level of substitution increases, the value of the Bohr magneton increases and it can be observed in [Table 4.20](#).

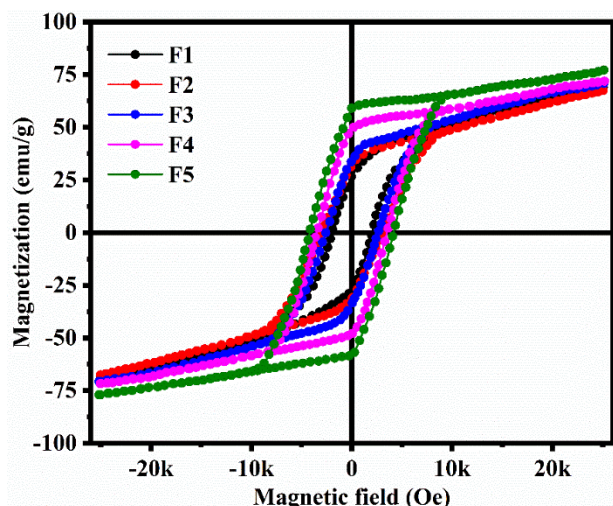


**Fig. 4.61.** Hysteresis loops of all F-series hexaferrite.

#### 4.3.4 Mössbauer analysis

[Fig. 4.59](#) presents the analysis of the Mössbauer spectra of F-series synthesized samples of SrM hexaferrite substituted with cobalt and zinc cations at room temperature. The summarized values of the quadrupole splitting relative area, isometric shift, and hyperfine field are presented in [Table 4.21](#). The observed spectra were fitted to 5 distinct sextets corresponding to trigonal-bipyramidal (2b), tetrahedral ( $4f_1$ ), octahedral (12k,  $4f_2$ , and 2a) sites, which are linked to the existence of  $Fe^{3+}$  ions in different lattice sites of hexaferrite. The Mössbauer spectra of F1 and F2 samples exhibit a sixth sextet, which is evident by the parameters of isomer shift and quadrupole splitting, belonging to the hematite impurity phase. The content of the impurity phase does not exceed 5% and does not significantly affect the structural and functional properties of these samples. This impurity phase has been not observed in XRD. On the contrary, the spectra of F3 and F4 samples expressed five sextets of iron cations clearly which makes it possible to attribute them to structural positions of  $Fe^{3+}$  in magnetoplumbite structure. The absence of one of the sextets in the F5 sample is apparently due to the broadening of spectral lines and the inability to separate some of them properly. In addition, a doublet is present in all spectra, which is characteristic of strontium hexaferrite and was repeatedly encountered in previously published works [289], [290].

The isomer shift determined in the synthesized samples can be attributed to factors such as variation in nuclear radius, chemical environment, and the interaction between the surrounding s-electron cloud and charge density. It has been observed that the value of

isomer shift remains relatively constant with Co-Zn substitution for all lattice sites, except for the 2a site. This may indicate that the substitution of Co-Zn ions causes more impact on the s-electron density of  $Fe^{3+}$  ions on the 2a site than others. Quadrupole splitting provides valuable information about crystal symmetry and local distortion in the synthesized samples. The appearance of quadrupole is due to the interaction between the electric quadrupole moment of  $Fe^{3+}$  ion and the electric gradient field. The small variation observed in the value of quadrupole splitting of 4f<sub>1</sub> and 2a lattice sites indicates a small perturbation in the vicinity of these sites with Co-Zn substitution. The hyperfine field is a result of the interaction between the nucleus and the internal magnetic field of the synthesized sample, which arises from its dipole properties. The value of the hyperfine field is observed to be relatively constant across all lattice sites from F1 to F5. The Mössbauer spectra of samples can assess the site occupancy of Co-Zn ions [244]. In the F1 sample, the relative area of 12k, 4f<sub>1</sub>, and 2b sites are quite close to the predicted relative area of SrM hexaferrite [245], while the 4f<sub>2</sub> is populated and 2a has less occupancy as seen in Table 4.21. It has been determined from Fig. 4.59 that no significant change is observed in the total relative area of 12k-2a-2b (spin-up) and 4f<sub>1</sub>-4f<sub>2</sub> (spin-down) sites, which validates that the substituents tend to concurrently occupy both spin-up and down sites from F1 to F5 samples. This result supports a feeble change observed in the value of  $M_S$  with Co-Zn substitution [291].

**Table 4.21** Isometric shift, hyperfine field, and quadrupole splitting of spectral components of all F-series hexaferrite samples

Sample	Site	IS (mm/s)	QS (mm/s)	Heff (mm/s)	R <sub>A</sub> (%)
F1	12k	0.35(9)	-0.37(5)	41.44(9)	48.7(2)
	4f1	0.36(0)	-0.30(2)	51.81(9)	15.1(4)
	4f2	0.25(1)	0.01(5)	49.95(4)	11.0(5)
	2a	0.19(3)	-0.16(2)	48.91(8)	11.9(8)
	2b	0.33(9)	-0.45(9)	35.93(5)	4.7(4)
	Hematite	0.51(3)	0.00(2)	49.71(2)	6.7(6)
	Doublet	-0.02(7)	0.54(3)	-	1.6(2)
F2	12k	0.35(4)	-0.37(8)	41.53(4)	18.6(7)
	4f1	0.36(2)	-0.30(2)	51.85(3)	7.9(9)
	4f2	0.23(3)	-0.19(8)	49.08(2)	11.8(2)
	2a	0.11(6)	0.44(1)	31.56(1)	1.1(9)
	2b	0.40(3)	-0.26(9)	39.68(1)	53.8(7)
	Hematite	0.38(4)	0.00(7)	50.77(8)	4.6(2)
	Doublet	1.56(3)	2.80(3)	-	1.8(4)

<b>F3</b>	12k	0.36(6)	-0.32(9)	41.59(1)	15.6(9)
	4f1	0.38(8)	-0.23(2)	51.83(0)	5.2(1)
	4f2	-0.20(8)	-0.74(6)	48.33(9)	1.3(7)
	2a	0.25(7)	-0.17(6)	49.51(8)	6.5(2)
	2b	0.32(2)	0.00(1)	39.21(2)	62.8(2)
	Doublet	0.31(9)	1.22(4)	-	8.3(8)
<b>F4</b>	12k	0.31(0)	0.30(4)	38.88(4)	4.5(7)
	4f1	-0.40(1)	-0.34(0)	47.20(0)	0.8(1)
	4f2	0.29(6)	0.07(2)	43.37(4)	9.5(4)
	2a	0.25(2)	-0.11(0)	40.97(3)	15.5(1)
	2b	0.01(8)	34.84(7)	64.2(2)	0.31(9)
	Doublet	0.35(9)	-0.37(5)	-	48.7(2)
<b>F5</b>	12k	0.35(7)	-0.34(4)	41.54(1)	13.0(3)
	4f1	0.38(2)	-0.19(7)	51.56(1)	5.6(5)
	2a	0.14(4)	-0.40(4)	49.49(0)	5.3(1)
	2b	0.33(4)	0.06(7)	35.80(1)	62.5(4)
	Doublet	0.30(5)	0.96(2)	-	13.4(8)

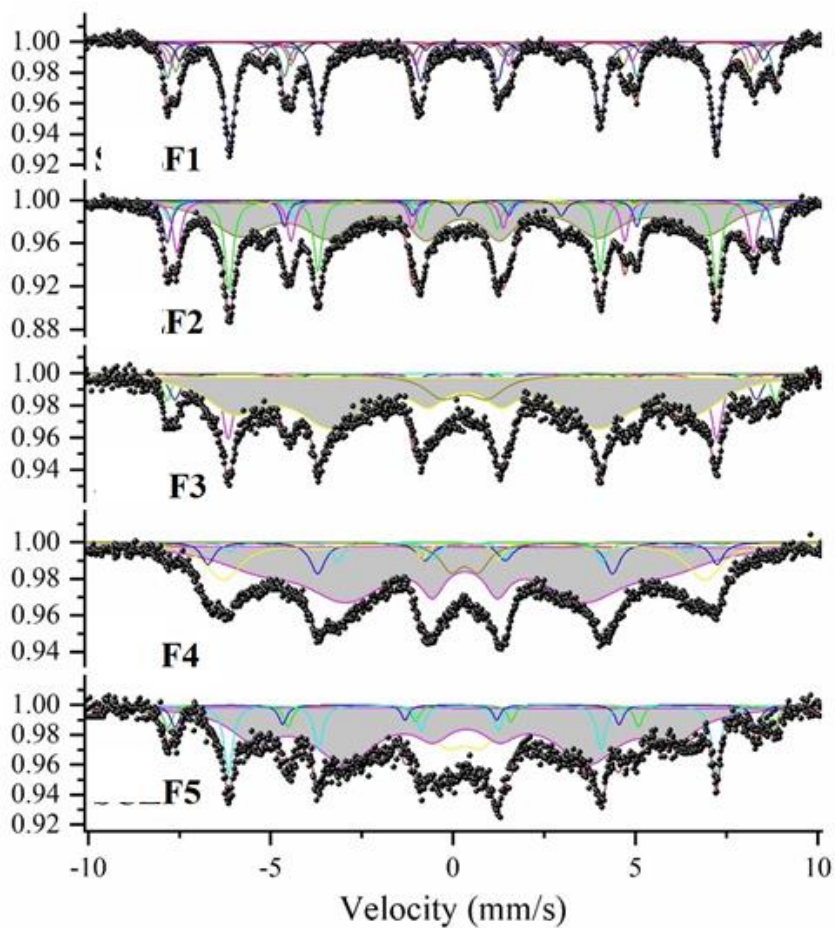


**Fig. 4.62.**  $^{57}\text{Fe}$  Mössbauer spectra of all F-series hexaferrite samples.

### 4.3.5 Electromagnetic Analysis

Fig. 4.60(a) and 4.60(b) illustrated the curves of dielectric constant ( $\epsilon'$ )/loss ( $\epsilon''$ ) and permeability ( $\mu'$ )/ magnetic loss ( $\mu''$ ) of all synthesized samples, respectively. All four parameters stay stable over the entire frequency range of 12.4 – 18 GHz. The substitution of Co-Zn ions causes (i) a non-monotonic decrease in  $\epsilon'$  and  $\mu'$ , (ii) a non-linear increment in  $\epsilon''$  values (iii) a non-linear decrease in  $\mu''$  at high-frequency region. Sample F5 reflects the maximum  $\epsilon'/\epsilon''$  value over the entire frequency range. This can be explained through the microstructure of the F5 sample (Fig. 4.52), wherein substitution causes the agglomeration of grains (results in large size grain) which offers less hindrance to the applied field, leading to increment in  $\epsilon'/\epsilon''$ .

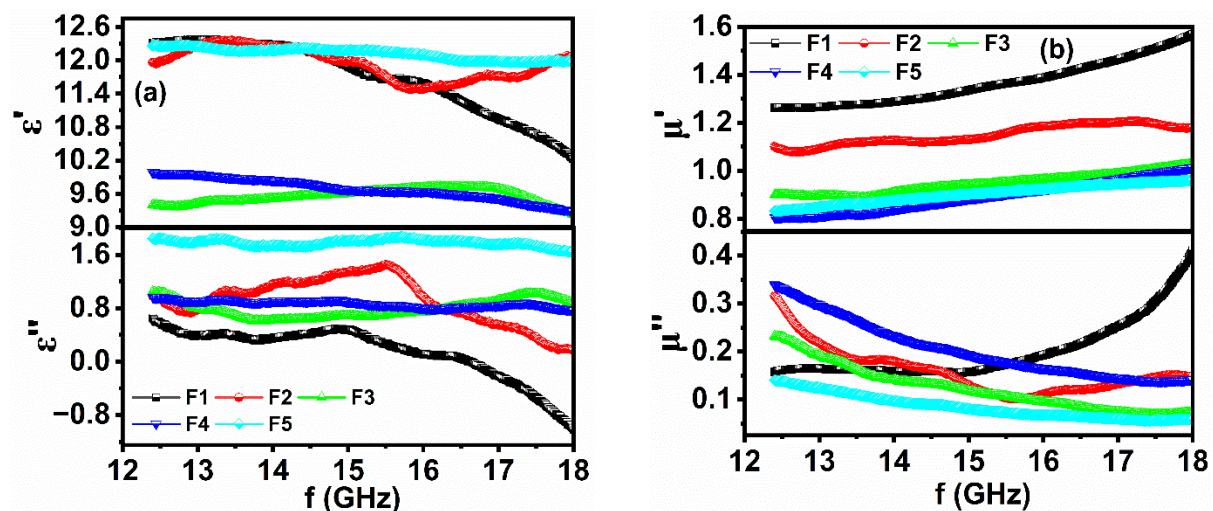
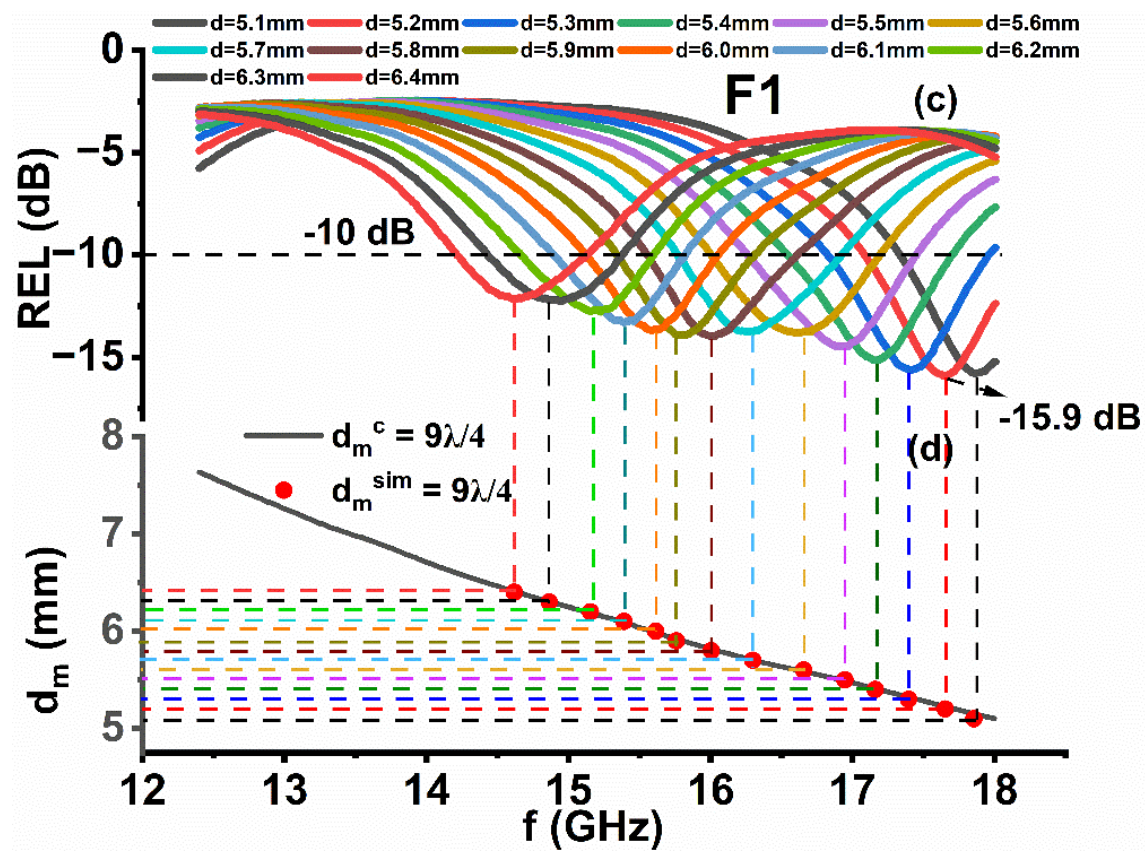
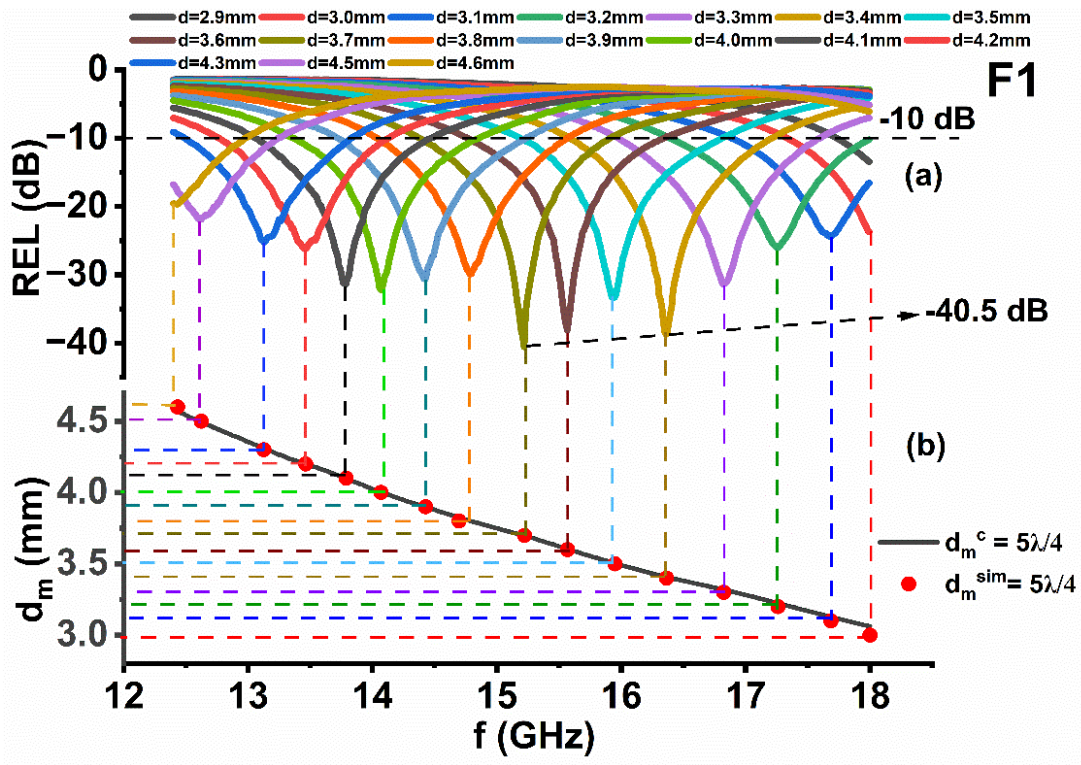


Fig. 4.63. (a) Complex permittivity and (b) permeability plots of F-series samples in 12 to 18 GHz.

The microwave absorption phenomena are investigated by examining REL plots as a function of frequency for different simulated thicknesses. Fig. 4.61(a, c, e), 4.62(a, c, e), 4.63(a, c), 4.64(a, c) and 4.65(a, c) illustrate the REL plots of all synthesized samples and can be utilized to deduce parameters such as bandwidth/frequency range for REL of -10 dB (90% absorption) /-20 dB and matching frequency/thickness, as listed in Table 4.22. For better visualization 3D REL plots are depicted in Fig. 4.66. Substitution of Co-Zn ions improves the microwave absorption properties of the synthesized sample from F1 to F3 and then decreases. The highest dip in REL, measuring -47.2 dB (> 99 % absorption), is observed in the F2 sample [Fig. 4.62(c)], occurring at a frequency of 18 GHz and a thickness of 3.3 mm. The plots illustrate the shift of REL peaks towards lower frequency ranges as the thickness increases, affirming the existence of a quarter wavelength mechanism.







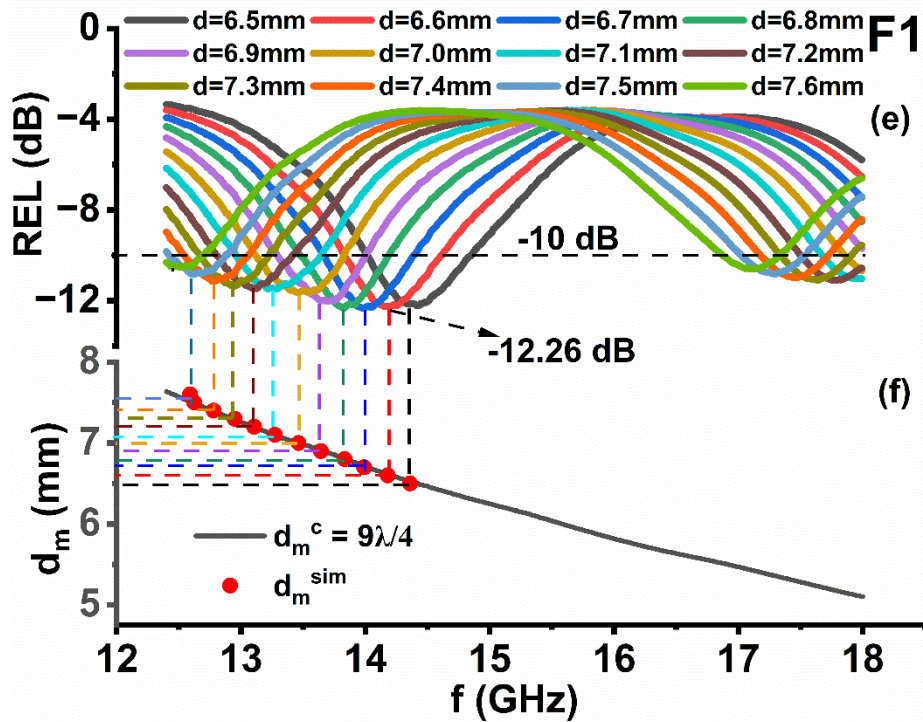
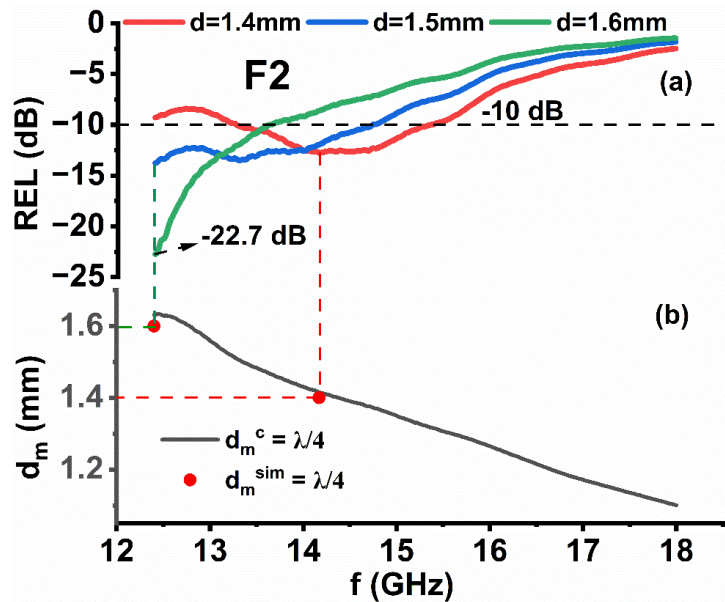


Fig. 4.64. (a, c, e) Dependence of REL on frequency in F1 sample. (b, d, f)  $d_m^{sim}$  and  $d_m^c$  versus frequency for  $5\lambda/4$  and  $9\lambda/4$  in the F1 sample.

Using equation 3.22, Reflection loss (REL) is computed using both the simulated thickness ( $d_m^{sim}$ ) and the calculated thickness ( $d_m^c$ ), which is determined through equation 3.24 by substituting values of  $n = 1, 3, 5$ , and so forth. The purpose is to establish a relationship between the quarter wavelength mechanism and REL peaks. Fig 4.61(a, c, e), 4.62(a, c, e), 4.63(b, d), 4.64(b, d) and 4.65(b, d) depicts plots of a calculated thickness ( $n\lambda/4$ ) within the frequency range. To compare the simulated thickness ( $d_m^{sim}$ ) with the calculated thickness ( $n\lambda/4$ ), vertical lines are drawn from REL peaks to the thickness-frequency plots.



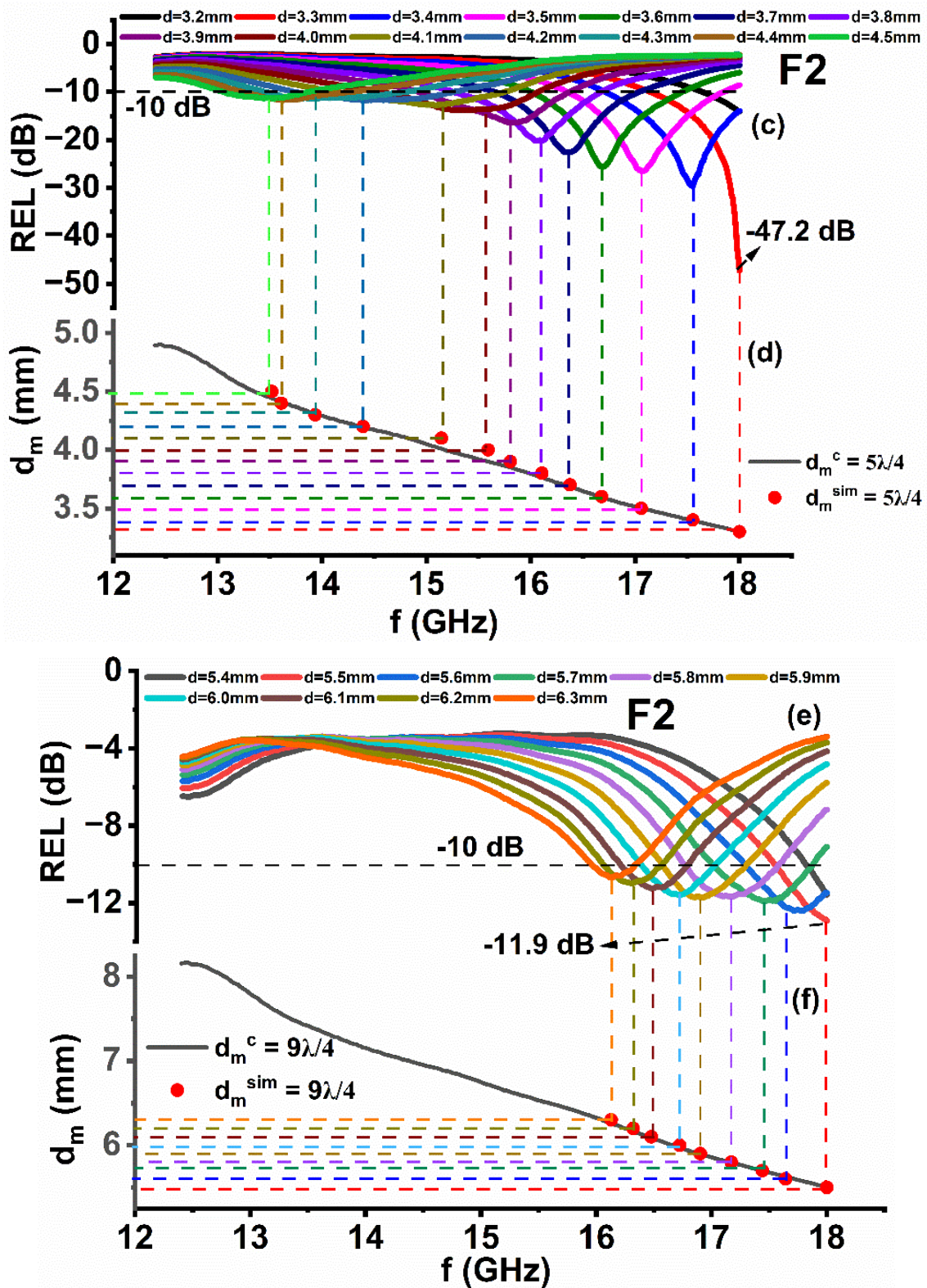


Fig. 4.65. (a, c, e) REL dependence on frequency in the F5 sample. (b, d, f)  $d_m^{sim}$  and  $d_m^c$  versus frequency for  $\lambda/4$ ,  $5\lambda/4$  and  $9\lambda/4$  in the F5 sample.



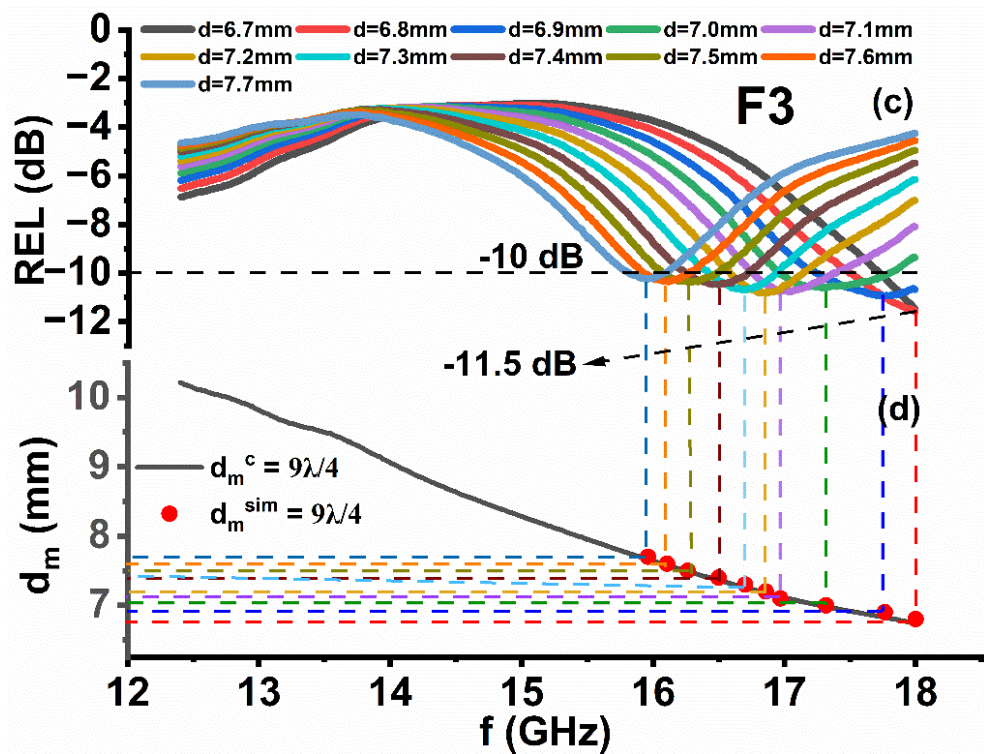
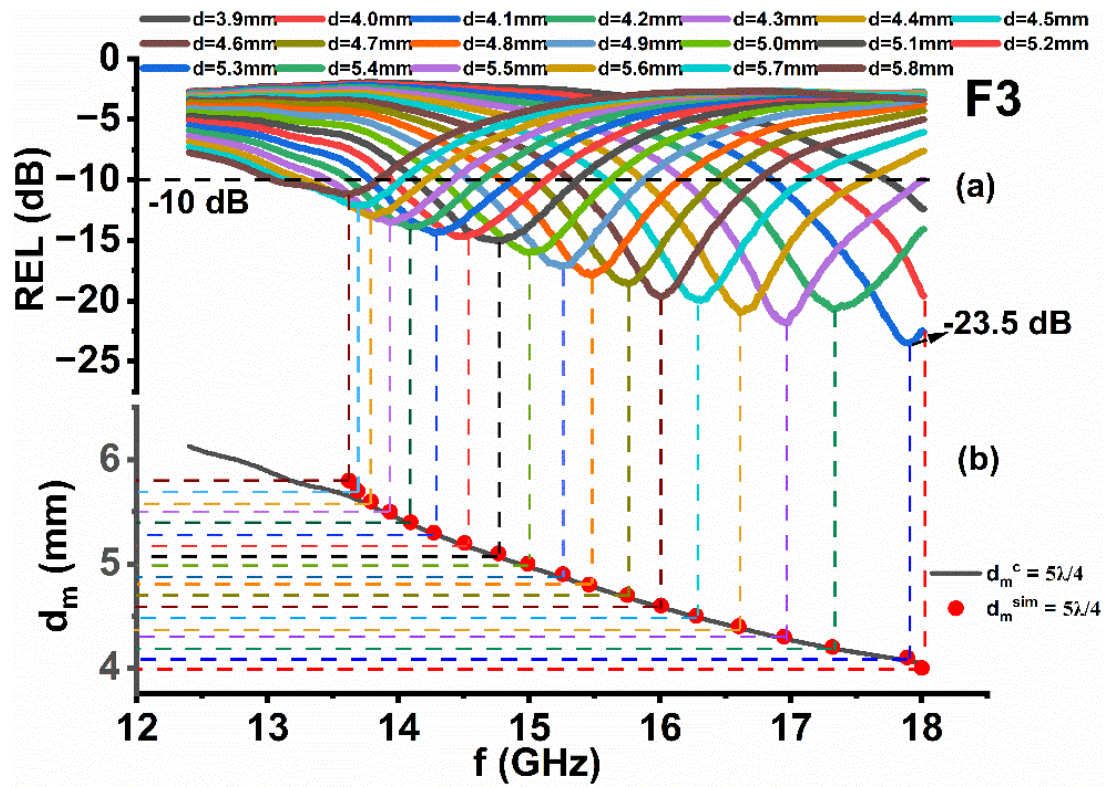


Fig. 4.66. (a, c) REL dependence on frequency in the F3 sample. (b, d)  $d_m^{sim}$  and  $d_m^c$  versus frequency for  $5\lambda/4$  and  $9\lambda/4$  in the F3 sample.

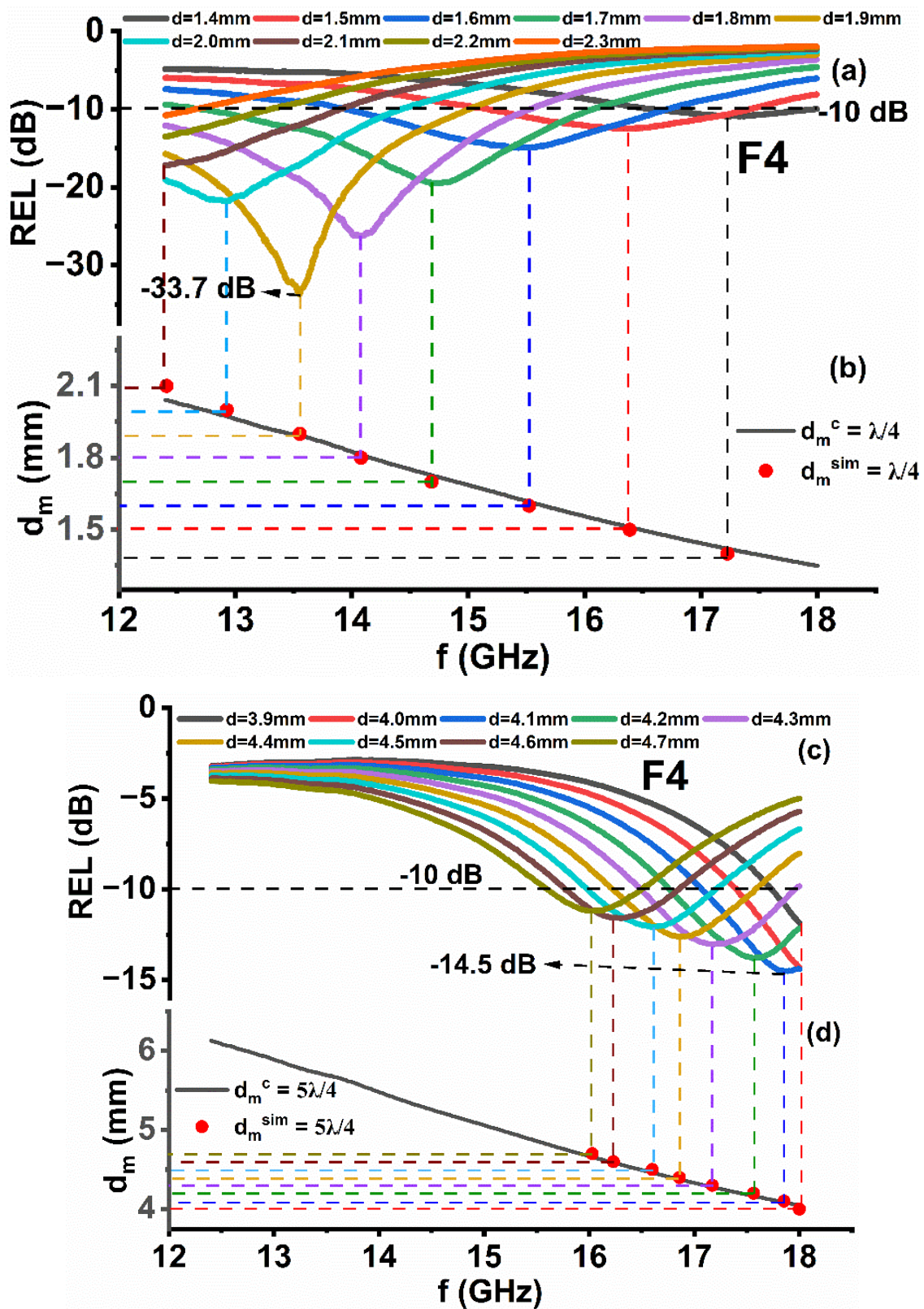


Fig. 4.67. (a, c) REL dependence on frequency in the F4 sample. (b, d)  $d_m^{sim}$  and  $d_m^c$  versus frequency for  $\lambda/4$  and  $5\lambda/4$  in the F4 sample.

(ii) For the F2 sample, REL values vary from -10.70 dB to -47.26 dB and thickness ranges from 1.4 mm to 6.3 mm, over the entire frequency region. The value of REL increases



for 1.4 mm to 3.3 mm thickness and reaches a  $REL_{\max} = -47.2$  dB observed at 3.3mm of frequency 18 GHz, and afterward, it gradually decreases. The plots display quarter-wavelength mechanism ( $n\lambda/4$ ) for  $n=1, 5,$  and  $9$  values, with a narrow (0.36 GHz) and a wide (2.99 GHz) at 6.3 mm and 1.4 mm thickness, respectively, as shown in Table 4.21.

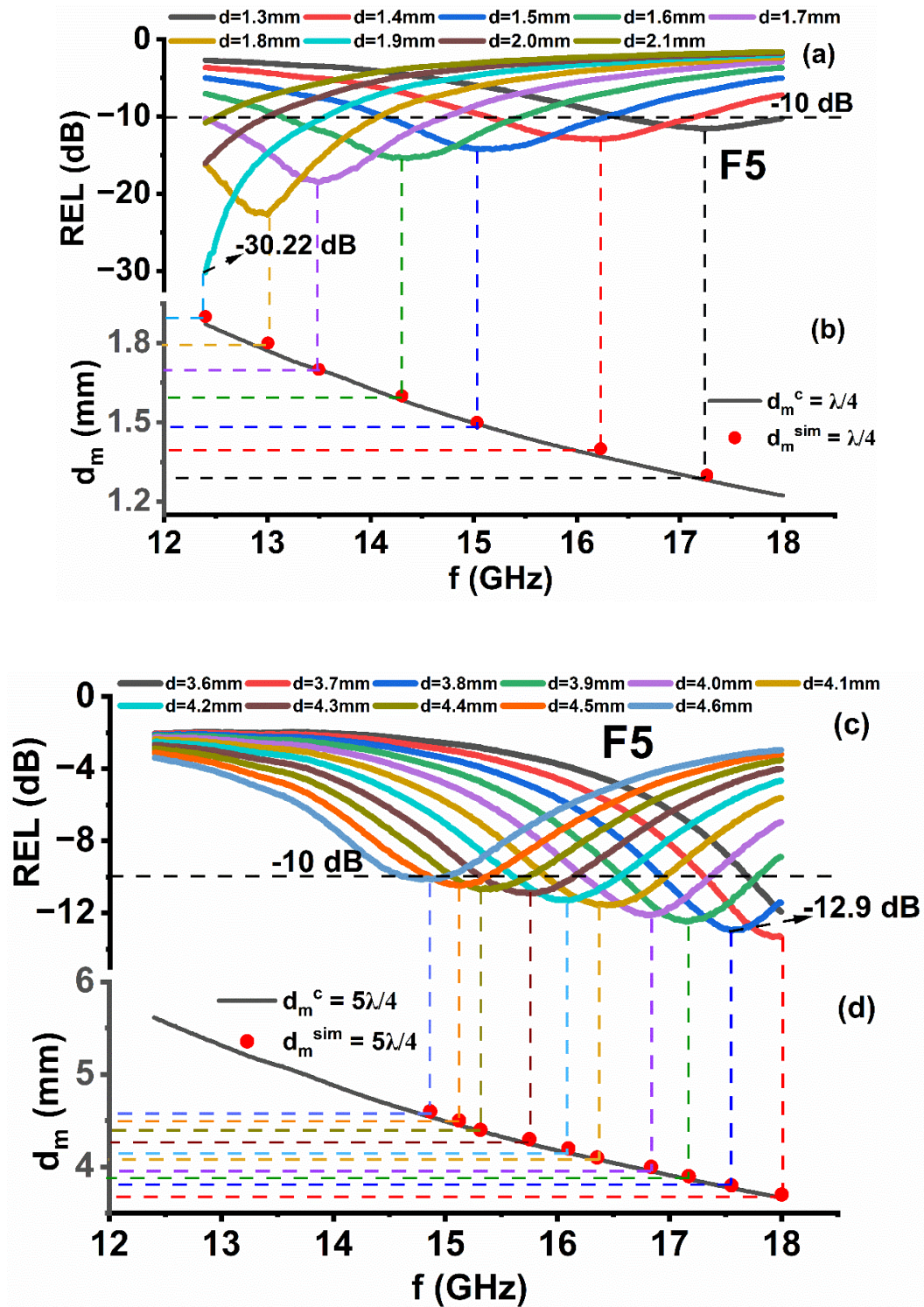


Fig. 4.68. (a, c) REL dependence on frequency in the F5 sample. (b, d)  $d_m^{sim}$  and  $d_m^c$  versus frequency for  $\lambda/4$  and  $5\lambda/4$  in the F5 sample.

(iii) For the F3 sample, REL is maximum (-23.51 dB) at 4.1 mm thickness of frequency 17.88 GHz. The value of REL varies from -10.23 dB to -21.84 dB for the remaining thickness of 3.9 mm to 7.6 mm over the frequency range of 12.4 to 18 GHz. The plots satisfy the quarter-wavelength mechanism ( $n\lambda/4$ ) for  $n= 5$  and  $9$  values, with a narrow (0.34 GHz) and a wide (1.84 GHz) at 7.6 mm and 4.3 mm thickness, respectively, as shown in Table 4.21.

(iv) For the F4 and F5 samples, several thicknesses ranging from 1.3 mm to 4.7 mm exhibit  $REL > -10$  dB /  $-20$  dB over a frequency range of 12.4 to 18 GHz. As the thickness increases, REL reaches a maximum value of -33.7 dB and -30.2 dB both at 1.9 mm of frequency 13.55 GHz and 12.4 GHz for F4 and F5 samples, respectively. The plots indicate that the quarter wavelength mechanism is envisaged in F4 and F5 samples where the calculated thickness is  $\lambda/4$  and  $5\lambda/4$  with  $n = 1$  and  $5$ . In the F4 sample, both -10 dB and -20 dB broad bandwidth of 3.3 GHz and narrow bandwidth of 0.91 GHz are observed from 12.78-16.08 GHz and 15.58-16.49 GHz with a matching thickness of 1.6 mm and 4.7 mm, respectively. Conversely, F5 shows a narrow bandwidth of 0.53 GHz from 14.84-15.37 GHz and a broad bandwidth of 2.29 GHz from 12.40-14.69 GHz with a matching thickness of 4.5 mm and 1.7 mm, respectively.

**Table 4.22** Absorption Parameters ( $REL > -10/-20$  dB).

Sample Name	Matching Thickness (mm)	Maximum REL (dB)	Matching frequency (GHz)	Frequency Band for $REL > -10$ dB (GHz)	Bandwidth for $REL > -10$ dB (GHz)	Frequency Band $REL > -20$ dB (GHz)	Bandwidth for $REL > -20$ dB (GHz)	BTR	PBW (%)
F1	2.9	-13.46	18	--	--	--	--	--	--
	3.0	-23.72	18	--	--	--	--	--	--
	3.1	-24.27	17.68	--	--	--	--	--	--
	3.2	-26.07	17.26	--	--	16.41-18	1.59	5E-04	9.21
	3.3	-31.37	16.82	--	--	15.95-17.61	1.66	5.37E-04	9.86
	3.4	-38.70	16.36	--	--	15.58-17.19	1.61	5.3E-04	9.84
	3.5	-33.29	15.95	--	--	15.22-16.81	1.59	5.32E-04	9.96
	3.6	-38.10	15.56	--	--	14.76-16.35	1.59	5.49E-04	10.21
	3.7	-40.53	15.22	--	--	14.40-15.80	1.4	4.98E-04	9.19
	3.8	-29.87	14.69	--	--	14.05-15.55	1.5	5.42E-04	10.21



								04	
	3.9	-30.58	14.42	--	--	13.72-15.22	1.5	5.52E-04	10.40
	4.0	-32.19	14.06	--	--	13.37-14.84	1.47	5.55E-04	10.45
	4.1	-31.33	13.78	--	--	13.06-14.46	1.4	2E-03	10.15
	4.2	-26.21	13.46	--	--	12.75-14.11	1.36	5.39E-04	10.10
	4.3	-25.23	13.12	--	--	12.48-13.79	1.31	5.31E-04	9.98
	4.4	-23.88	12.87	--	--	--	--	--	--
	4.5	-21.89	12.62	--	--	--	--	--	--
	4.6	-19.65	12.43	--	--	--	--	--	--
	5.1	-15.78	17.85	--	--	--	--	--	--
	5.2	-15.93	17.65	--	--	--	--	--	--
	5.3	-15.63	17.39	16.82-17.96	1.14	--	--	2.13E-04	6.55
	5.4	-15.14	17.16	16.54-17.69	1.15	--	--	2.18E-04	6.70
	5.5	-14.48	16.94	16.27-17.49	1.22	--	--	2.33E-04	7.20
	5.6	-13.81	16.6	16.01-17.18	1.17	--	--	2.27E-04	7.04
	5.7	-13.72	16.29	15.73-16.91	1.18	--	--	2.33E-04	7.24
	5.8	-13.98	16.00	15.55-16.60	1.05	--	--	2.10E-04	6.56
	5.9	-13.89	15.76	15.34-16.30	0.96	--	--	1.95E-04	6.09
	6.0	-13.67	15.61	15.12-16.04	0.92	--	--	1.89E-04	5.89
	6.1	-13.29	16.39	14.87-15.79	0.92	--	--	1.92E-04	5.61
	6.2	-12.74	15.15	14.66-15.60	0.94	--	--	1.98E-04	6.20
	6.3	-12.20	14.86	14.41-15.36	0.95	--	--	2.04E-04	6.39
	6.4	-12.16	14.61	14.21-15.13	0.92	--	--	2E-04	6.29
	6.5	-12.15	14.36	14.02-14.84	0.82	--	--	1.81E-04	5.71
	6.6	-12.26	14.18	13.83-14.60	0.77	--	--	1.73E-04	5.43
	6.7	-12.33	13.99	13.66-14.39	0.73	--	--	1.66E-04	5.21

	6.8	-12.33	13.83	13.84-14.17	0.33	--	--	7.4E-05	2.38
	6.9	-12.01	13.64	13.30-14.00	0.7	--	--	1.6E-04	5.13
	7.0	-11.35	13.46	13.12-13.81	0.69	--	--	1.6E-04	5.12
	7.1	-11.49	13.27	12.97-13.63	0.66	--	--	1.57E-04	4.97
	7.2	-11.48	13.10	12.80-13.41	0.61	--	--	1.48E-04	4.65
	7.3	-11.37	12.94	12.66-13.23	0.57	--	--	1.39E-04	4.40
	7.4	-11.15	12.78	12.54-13.06	0.52	--	--	1.28E-04	4.06
	7.5	-10.85	12.62	12.07-12.43	0.36	--	--	9.59E-05	2.85
	7.6	-10.52	12.59	--	--	--	--	--	--
<b>F2</b>	1.4	-12.77	14.16	13.25-15.34	2.99	--	--	2.2E-03	21.11
	1.5	-13.77	12.4	--	--	--	--	--	--
	1.6	-22.74	12.4	--	--	--	--	--	--
	1.7	-18.70	12.43	--	--	--	--	--	--
	1.8	-12.23	12.43	--	--	--	--	--	--
	3.2	-14.07	18	--	--	--	--	--	--
	3.3	-47.26	18	--	--	--	--	--	--
	3.4	-29.68	17.55	--	--	--	--	--	--
	3.5	-26.52	17.05	--	--	16.30-17.83	1.53	4.51E-04	8.97
	3.6	-25.62	16.67	--	--	15.99-17.47	1.48	4.41E-04	8.87
	3.7	-22.59	16.37	--	--	15.66-17.03	1.37	4.16E-04	8.36
	3.8	-20.16	16.10	--	--	15.33-16.67	1.34	4.13E-04	8.32
	3.9	-16.43	15.80	14.93-16.37	1.44	--	--	4.53E-04	9.11
	4.0	-13.59	15.59	14.59-16.07	1.48	--	--	4.73E-04	9.49
	4.1	-12.68	15.14	14.14-15.73	1.59	--	--	5.23E-04	10.5
	4.2	-11.74	14.39	13.86-15.20	1.34	--	--	4.54E-04	9.31
	4.3	-11.37	13.93	--	--	--	--	--	--
	4.4	-11.71	13.60	--	--	--	--	--	--

	4.5	-11.34	13.52	--	--	--	--	--	--
	5.4	-11.56	18	--	--	--	--	--	--
	5.5	-12.91	18	--	--	--	--	--	--
	5.6	-12.38	17.76	--	--	--	--	--	--
	5.7	-11.90	17.44	17.01-17.87	0.8	--	--	1.48E-04	4.58
	5.8	-11.68	17.17	16.75-17.57	0.82	--	--	1.44E-04	4.77
	5.9	-11.72	16.90	16.57-17.30	0.73	--	--	1.29E-04	4.31
	6.0	-11.56	16.72	16.40-17.02	0.62	--	--	1.1E-04	3.70
	6.1	-11.24	16.47	16.22-16.76	0.54	--	--	9.76E-05	3.27
	6.2	-10.96	16.32	16.07-16.55	0.48	--	--	8.73E-05	2.94
	6.3	-10.70	16.12	15.97-16.33	0.36	--	--	6.57E-05	2.23
<b>F3</b>	3.9	-12.41	18	--	--	--	--	--	--
	4.0	-19.60	18	--	--	--	--	--	--
	4.1	-23.51	17.88	--	--	--	--	--	--
	4.2	-20.75	17.31	--	--	--	--	--	--
	4.3	-21.84	16.94	--	--	16.15-17.99	1.84	4.4E-04	10.86
	4.4	-21.01	16.60	--	--	15.85-17.55	1.7	4.1E-04	10.24
	4.5	-19.93	16.27	15.57-17.06	1.49	--	--	3.7E-04	9.15
	4.6	-19.66	16.00	15.30-16.75	1.45	--	--	3.6E-04	9.06
	4.7	-18.63	15.74	15.04-16.43	1.39	--	--	3.59E-04	8.83
	4.8	-17.88	15.45	14.77-16.13	1.36	--	--	3.56E-04	8.80
	4.9	-17.11	15.25	14.53-15.85	1.32	--	--	3.50E-04	8.65
	5.0	-16.01	14.98	14.32-15.60	1.28	--	--	3.4E-04	8.54
	5.1	-15.04	14.76	14.11-15.34	1.23	--	--	3.3E-04	8.33
	5.2	-14.71	14.50	13.95-15.12	1.17	--	--	3.2E-04	8.06
	5.3	-14.37	14.27	13.77-14.87	1.1	--	--	3E-04	7.70
	5.4	-13.92	14.09	13.61-14.62	1.01	--	--	2.81E-04	7.16

								04	
	5.5	-13.55	13.93	13.46-14.39	0.93	--	--	2.6E-04	6.67
	5.6	-12.96	13.78	13.31-14.19	0.88	--	--	2.49E-04	6.38
	5.7	-12.14	13.68	13.14-13.99	0.85	--	--	2.43E-04	6.21
	5.8	-11.20	13.62	13.11-13.84	0.73	--	--	2.08E-04	5.35
	6.7	-11.46	18	--	--	--	--	--	--
	6.8	-11.57	18	--	--	--	--	--	--
	6.9	-10.92	17.76	--	--	--	--	--	--
	7.0	-10.61	17.31	16.94-17.78	0.84	--	--	1.19E-04	4.85
	7.1	-10.76	16.96	16.77-17.40	0.63	--	--	9.12E-05	3.71
	7.2	-10.82	16.85	16.59-17.14	0.55	--	--	8.05E-05	3.26
	7.3	-10.70	16.70	16.41-16.93	0.52	--	--	7.69E-05	3.11
	7.4	-10.47	16.49	16.26-16.72	0.46	--	--	6.85E-05	2.78
	7.5	-10.36	16.26	16.04-16.46	0.42	--	--	6.3E-05	2.58
	7.6	-10.32	16.10	15.92-16.26	0.34	--	--	5.18E-05	2.11
	7.7	-10.23	15.96	--	--	--	--	--	--
<b>F4</b>	1.4	-10.89	17.22	15.15-17.43	2.28	--	--	1.8E-03	13.24
	1.5	-12.49	16.38	13.97-16.71	2.74	--	--	2.3E-03	16.72
	1.6	-14.93	15.52	12.78-16.08	3.3	--	--	3E-03	21.26
	1.7	-19.54	14.68	--	--	--	--	--	--
	1.8	-26.25	14.08	--	--	--	--	--	--
	1.9	-33.74	13.55	--	--	--	--	--	--
	2.0	-21.83	12.92	--	--	--	--	--	--
	2.1	-17.77	12.41	--	--	--	--	--	--
	2.2	-13.50	12.4	--	--	--	--	--	--
	2.3	-10.77	12.4	--	--	--	--	--	--
	3.9	-11.86	18	--	--	--	--	--	--
	4.0	-14.30	18	--	--	--	--	--	--
	4.1	-14.53	17.85	--	--	--	--	--	--
	4.2	-13.82	17.56	--	--	--	--	--	--

	4.3	-13.06	17.17	16.48-17.95	1.47	--	--	3.4E-04	8.56
	4.4	-12.64	16.85	16.21-17.57	1.36		--	3.2E-04	8.07
	4.5	-12.09	16.6	15.99-17.19	1.2	--	--	2.9E-04	7.22
	4.6	-11.57	16.23	15.75-16.85	1.1	--	--	2.7E-04	6.77
	4.7	-11.20	16.02	15.58-16.49	0.91	--	--	2.2E-04	5.68
<b>F5</b>	1.3	-11.60	17.26	16.39-17.98	1.59	--	--	1.2E-03	7.06
	1.4	-12.93	16.23	15.20-17.22	2.02	--	--	1.6E-03	12.44
	1.5	-14.25	15.03	14.14-16.27	2.13	--	--	1.8E-03	14.17
	1.6	-15.39	14.30	13.13-15.39	2.26	--	--	2E-03	15.80
	1.7	-18.52	13.49	12.40-14.69	2.29	--	--	2.2E-03	16.97
	1.8	-22.78	13.00	--	--	--	--	--	--
	1.9	-30.22	12.4	--	--	--	--	--	--
	2.0	-16.05	12.4	--	--	--	--	--	--
	2.1	-10.82	12.4	--	--	--	--	--	--
	3.6	-11.92	18	--	--	--	--	--	--
	3.7	-13.34	18	--	--	--	--	--	--
	3.8	-12.97	17.55	--	--	--	--	--	--
	3.9	-12.46	17.17	16.58-17.78	1.2	--	--	3.1E-04	6.98
	4.0	-12.10	16.83	16.22-17.36	1.14	--	--	3E-04	6.77
	4.1	-11.53	16.35	15.89-16.97	1.08	--	--	2.9E-04	6.60
	4.2	-11.28	16.09	15.59-16.55	0.96	--	--	2.6E-04	5.96
	4.3	-10.91	15.74	15.31-16.14	0.83	--	--	2.3E-04	5.27
	4.4	-10.70	15.31	15.05-15.71	0.66	--	--	1.9E-04	4.31
	4.5	-10.48	15.12	14.84-15.37	0.53	--	--	1.5E-04	3
	4.6	-10.64	14.86	--	--	--	--	--	--

Table 4.22 enumerates the value of BTR and PBW for various thicknesses in different compositions and both parameters increase non-monotonically with Co-Zn substitution. F2

and F4 samples exhibit maximum BTR values of 2.13 and 2.06, respectively. The PBW values range from 2.23 to 21.11 for all samples and is a maximum of 21.26 in the F4 sample.

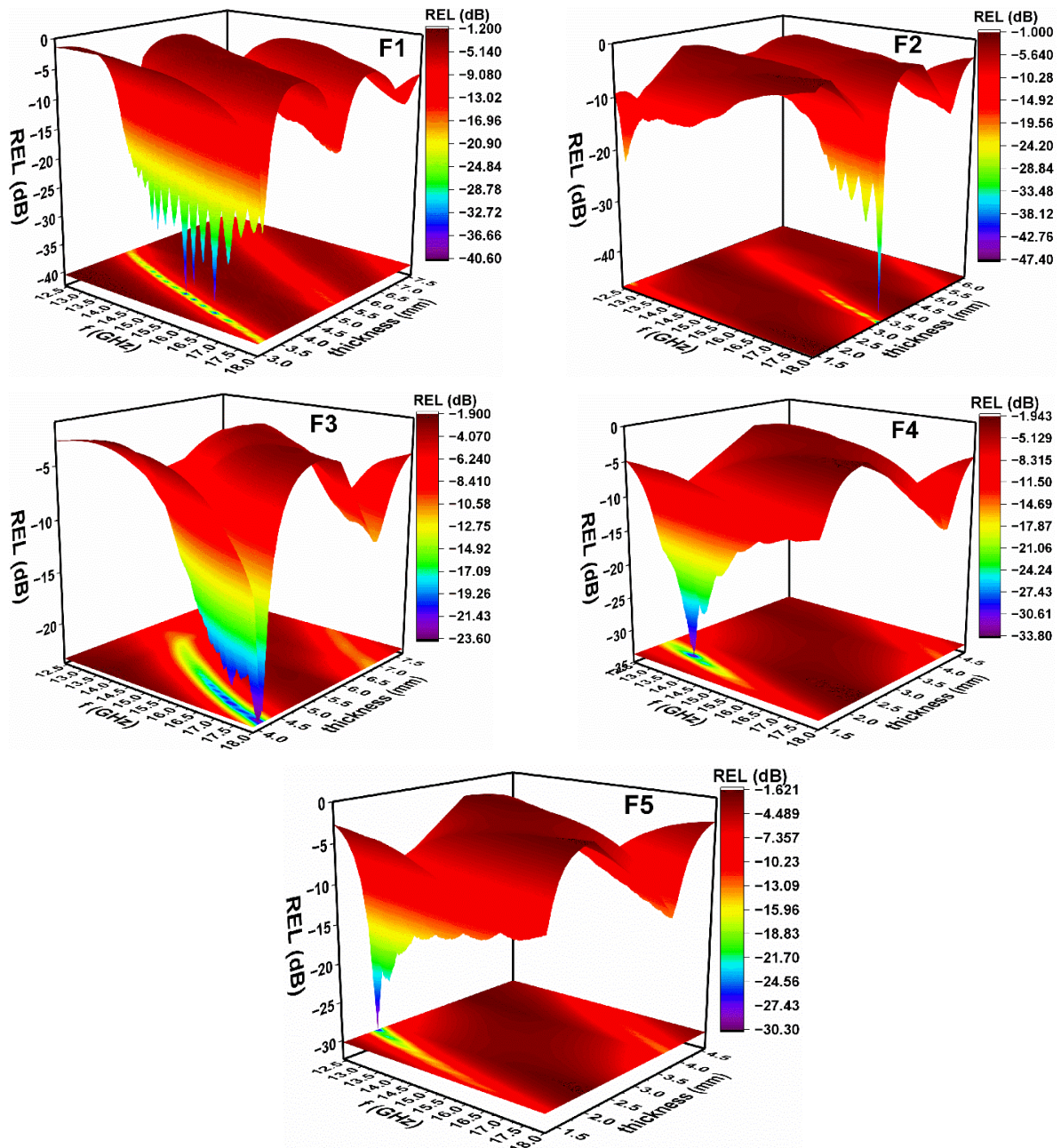


**Fig. 4.69.** 3D representation of REL plots over the entire range of frequency at various thicknesses.

Table 4.23 enlists  $Z_{in}/Z_0$  and  $Z_{real}/Z_{img}$  values associated with the REL peak of the synthesized composite materials and these impedance values are determined using equation 3.21. The significance of impedance matching between the absorber and free space, resulting in  $Z_{in}/Z_0 \cong 1$  ( $Z_{real} \cong 1$  and  $Z_{img} \cong 0$ ), has been extensively discussed in section 4.1.5. When the impedance of MAMs does not align with that of free space, incoming EM waves are strongly reflected at the interface. Therefore, regardless of their intrinsic attenuation



capabilities, they fail to deliver appropriate MWA performance. Sample F2 stands out, achieving the highest REL= -47.2 dB at a thickness of 3.3 mm and a frequency of 18 GHz with a  $Z_{in}/Z_0$  value is approximately 0.993, wherein  $Z_{real} = 0.993$  (close to 1) and  $Z_{img} = -0.005$  (nearly 0). It is notable in all synthesized samples, that optimal REL is exhibited by those thicknesses where  $Z_{real} \cong 1$  and  $Z_{img} \cong 0$ . Due to more offset  $Z_{real}/Z_{img}$  values from 1 and/or zero, the remaining thickness of all synthesized samples exhibits relatively low REL values. The value of  $Z_{in}/Z_0$  changes with Co-Zn ions substitution. Fig. 4.67 presents that  $C_o$  varies as the frequency increases, indicating the non-existence of eddy current loss.

**Table 4.23** Reflection loss peak's impedance parameters at different thicknesses.

Sample Name	Thickness (mm)	Max. REL (dB)	Matching frequency (GHz)	$Z_{in}/Z_0$	$Z_{real}$	$Z_{img}$
<b>F1</b>	3.4	-38.70	16.36	1.023	1.023	-0.004
	3.6	-38.10	15.56	1.025	1.025	0.0008
	3.7	-40.53	15.22	0.983	0.983	-0.009
	4.0	-32.19	14.06	0.952	0.952	0.0023
	4.1	-31.33	13.78	0.948	0.948	-0.0115
<b>F2</b>	3.2	-14.07	18	0.907	0.842	0.3356
	3.3	-47.26	18	0.993	0.993	-0.005
	3.4	-29.68	17.55	0.9399	0.9397	-0.0204
	3.5	-26.52	17.05	0.9104	0.9103	0.0096
	3.6	-25.62	16.67	0.9006	0.9005	0.0094
	4.0	-19.60	18	0.8987	0.8842	0.1605
<b>F3</b>	4.1	-23.51	17.88	0.8766	0.8764	-0.02
	4.2	-20.75	17.31	0.8339	0.8335	0.0237
	4.3	-21.84	16.94	0.8503	0.8503	0.0043
	4.4	-21.01	16.60	0.8345	0.8343	-0.017
	4.5	-19.93	16.27	0.8175	0.8174	0.0129
	1.7	-19.54	14.68	1.202	1.195	0.124
	1.8	-26.25	14.08	1.093	1.093	0.041
<b>F4</b>	1.9	-33.74	13.55	0.9706	0.9703	-0.0275
	2.0	-21.83	12.92	0.868	0.865	-0.0691
	2.1	-17.77	12.41	0.7875	0.7796	-0.111
	1.7	-18.52	13.49	1.253	1.250	0.092

	1.8	-22.78	13.00	1.151	1.150	-0.041
	1.9	-30.22	12.4	1.059	1.058	-0.023
	2.0	-16.05	12.4	0.956	0.909	-0.291

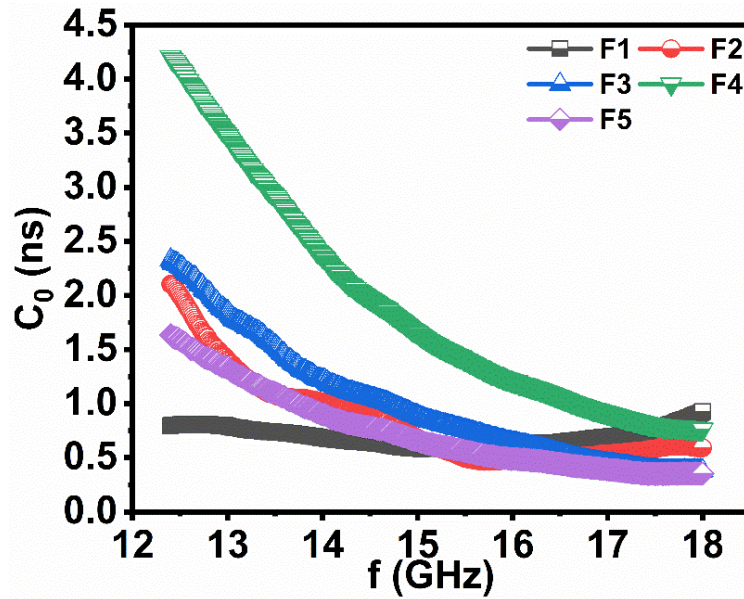


**Fig. 4.70.**  $C_0$ -dependence on frequency for all samples.

Conclusively, the unlike ionic radii of substituted  $\text{Co}^{2+}$  (0.72 Å) and  $\text{Zn}^{2+}$  (0.84 Å) ions than host  $\text{Fe}^{3+}$  (0.64 Å) ions and atomic mass of Co, Zn, and Fe 58.93, 65.38 and 55.84 amu, respectively, attributed to heterogeneity in the crystal structure. This heterogeneity causes a non-linear trend in complex permittivity/permeability values with substitution. It can be observed in the SEM micrographs (Fig. 4.52) that substitution leads to grain agglomeration along with porosity between them, which results in a reduction in permittivity/permeability, as consistent with porosity calculated from XRD (Table 4.19). The porosity, analogous to non-magnetic pores, induces a demagnetizing field, hindering the field and discouraging polarization. All these factors lead to  $\text{REL} > -20$  dB (more than 99% absorption) in all synthesized samples.

## 4.4 Co<sup>2+</sup>-Cd<sup>2+</sup> substituted SrCo<sub>z</sub>Cd<sub>0.5z</sub>Fe<sub>12-2z</sub>O<sub>19</sub> hexaferrite.

Table 4.24 displays the assignment of sample names/codes for a different level of substitution for SrCo<sub>z</sub>Cd<sub>0.5z</sub>Fe<sub>12-2z</sub>O<sub>19</sub>.

**Table 4.24** Assignment of sample name for a different level of substitution of SrCo<sub>z</sub>Cd<sub>0.5z</sub>Fe<sub>12-2z</sub>O<sub>19</sub> hexaferrite.

SrCo <sub>z</sub> Cd <sub>0.5z</sub> Fe <sub>12-2z</sub> O <sub>19</sub>	Sample Name
<b>z = 0.2</b>	C1
<b>z = 0.4</b>	C2
<b>z = 0.6</b>	C3
<b>z = 0.8</b>	C4
<b>z = 1.0</b>	C5

### 4.4.1 Structural Analysis

#### 4.4.1.1 X-ray Analysis

The XRD pattern of Co-Cd doped SrM hexaferrite powder calcined at 1100°C for 5h has been presented in Fig. 4.68. The diffraction peaks observed in all synthesized samples are indexed to the magnetoplumbite structure of SrFe<sub>12</sub>O<sub>19</sub> - P6<sub>3</sub>/mmc (ICDD# 80-1197). These synthesized samples manifest a composite phase with the M-type hexaferrite as the major phase and spinel ferrite, namely CdFe<sub>2</sub>O<sub>4</sub> - Fd-3m:1 (ICDD# 001-1087) and CoFe<sub>2</sub>O<sub>4</sub> - R-3m: H (ICDD# 22-1086), serving as secondary phases [268] [269]. The XRD patterns were subjected to Rietveld refinement using MAUD software for all samples (Fig. 4.69). The prominent peaks (107) and (114) of M-type hexaferrite are dominating in C1, C2, and C3 samples, whereas their intensity decreases in the remaining samples. Moreover, a successful substitution of Co-Cd ions can be explained by the slight shift and change in the intensity of peaks. The lattice constant (a, c), height-to-width ratio (c/a), the volume of the unit cell (V), FWHM (β), the crystallite size (D), and lattice strain (ε) of all incorporated specimens are calculated using equations 3.1, 3.2, 3.3, 3.4, and 3.5 listed in Table 4.25. Substitution of Co-Cd ions causes a slight change in the lattice parameter ‘a’ compared to lattice constant ‘c’. This can be elucidated that the c-axis, which is easily magnetized, expands more than the a-axis [163]. The value of unit cell volume (V) ranges from 690.91 Å<sup>3</sup> – 689.55 Å<sup>3</sup>.

Furthermore, the height-to-width or  $c/a$  ratio of all incorporated samples is found to be less than 3.98, which affirms the formation of the magneto plumbite structure of hexaferrite [126].

Table 4.25 depicts that the slight variation observed in  $L_A$  and  $L_B$  values [calculated using Equations (3.5) and (3.6)] may be attributed to small ionic radii of  $Fe^{3+}$  ions compared to  $Co^{2+}$  and  $Cd^{2+}$  ions. The greater atomic masses of Co (58.93 u) and Cd (112.411 u) than Fe (55.84 u) may account for the increase in X-ray density with substitution. The bulk density and porosity (Table 4.26) exhibit a non-monotonic trend with the  $Co^{2+}$  and  $Cd^{2+}$  ions substitution.

**Table 4.25** Values of structural parameters ( $a$ ,  $c$ ,  $c/a$ ,  $V$ ), the crystallite size ( $D$ ), hopping length ( $L_A$  and  $L_B$ ), dislocation density ( $\delta$ ), and lattice strain ( $\epsilon$ ) are listed below:

Sample name	C1	C2	C3	C4	C5
$a$ (Å)	5.882	5.880	5.881	5.881	5.879
$c$ (Å)	23.06	23.03	23.04	23.06	23.06
$c/a$	3.920	3.916	3.917	3.921	3.922
$V$ (Å <sup>3</sup> )	690.91	689.55	690.08	690.68	690.21
$D$ (nm)	124.4	143.3	132.8	117.6	111.4
$L_A$ (nm)	2.547	2.546	2.546	2.546	2.545
$L_B$ (nm)	2.079	2.078	2.078	2.078	2.078
$\chi^2$	0.315	0.310	0.289	0.318	0.383

**Table 4.26** Calculated values of bulk density ( $\rho_{bulk}$ ), XRD density ( $\rho_x$ ), porosity (P) and surface area (S) are listed below:

Sample Name	Density (g/cm <sup>3</sup> )		Porosity (%)
	Bulk density ( $\rho_{bulk}$ )	XRD density ( $\rho_x$ )	
C1	2.72	5.13	46.9
C2	2.26	5.17	56.2
C3	3.05	5.20	41.3
C4	2.63	5.23	49.7
C5	2.50	5.26	47.5

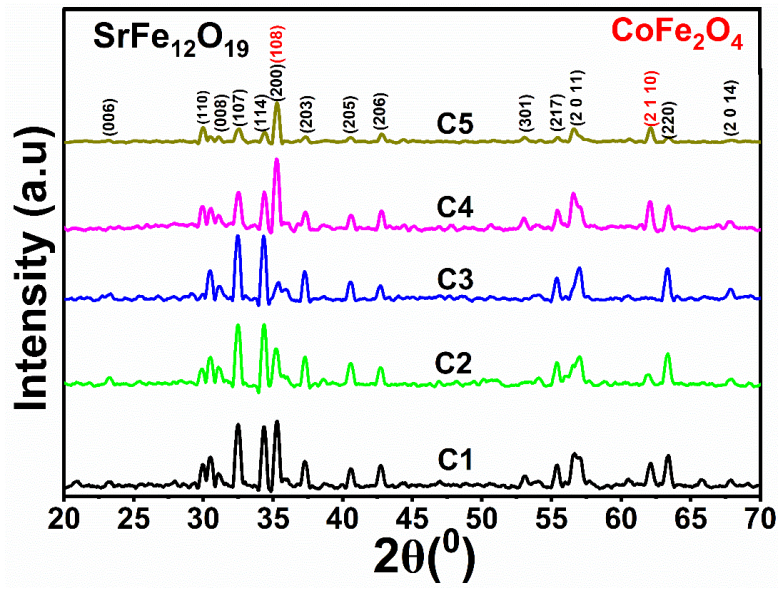
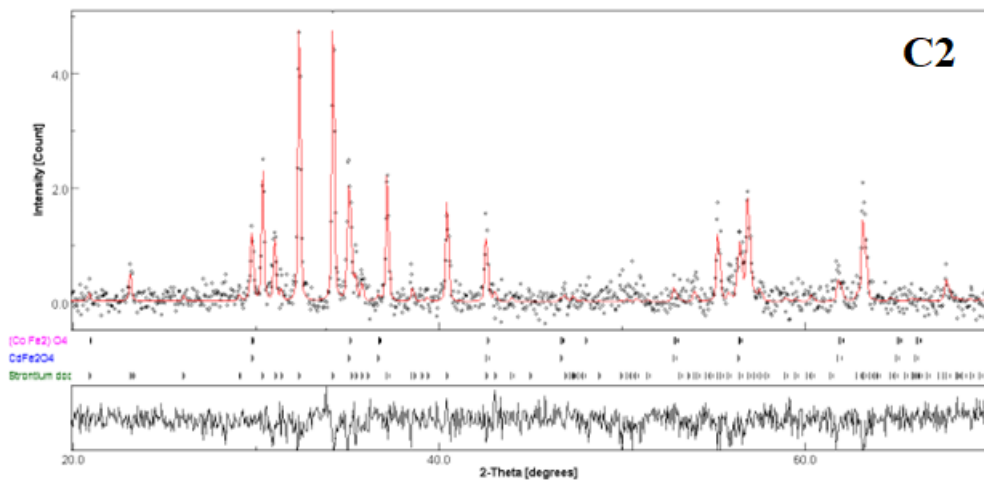
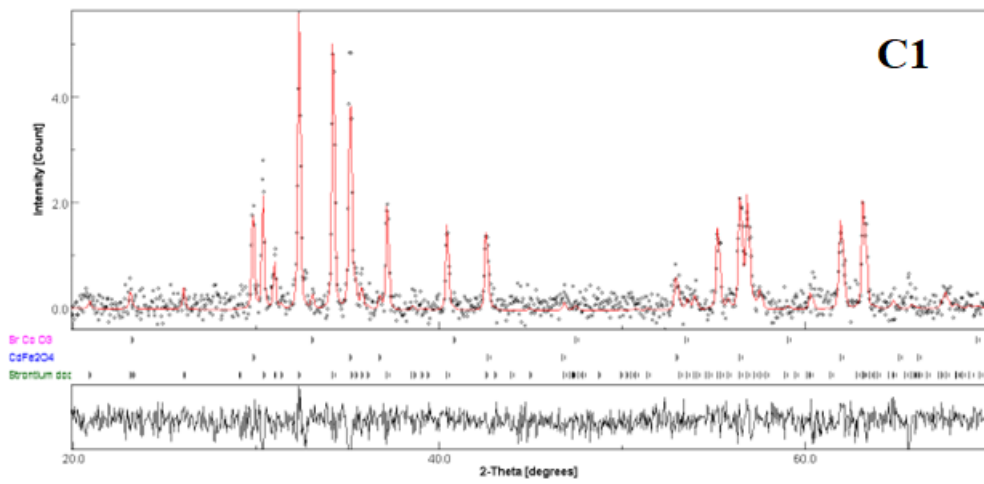


Fig. 4.71. XRD pattern of prepared specimen C1 to C5 hexaferrite.



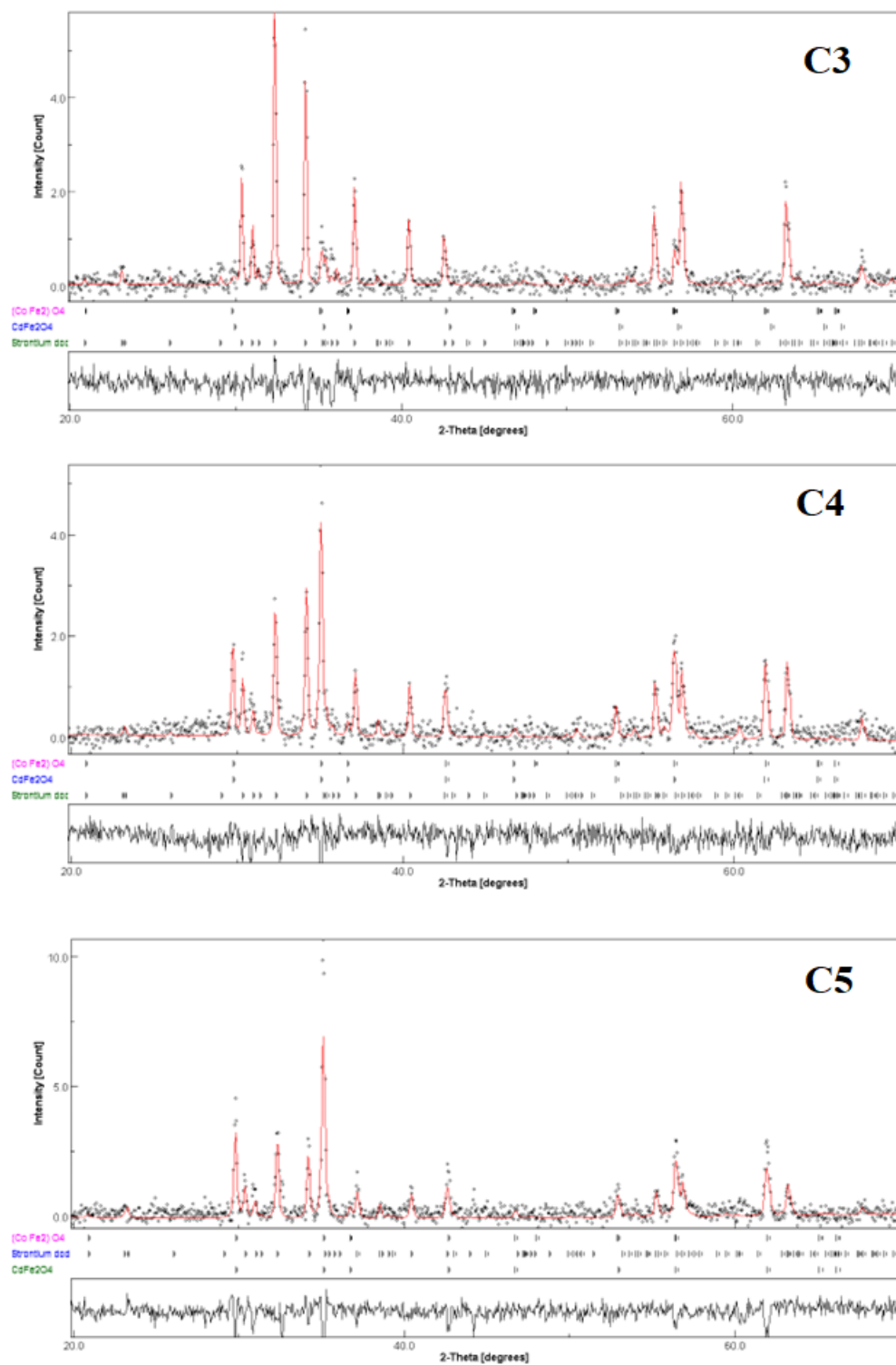


Fig. 4.72. Refinement of C1, C2, C3, C4, and C5 samples.

#### 4.4.1.2 FTIR analysis

The mid-region infrared spectroscopy comprehensively analyzed the attached functional groups, located molecular bands, and identified the existing chemical bonds. The FTIR spectra of incorporated specimen  $\text{SrCo}_{1.5z}\text{Cd}_{0.5z}\text{Fe}_{12-2z}\text{O}_{19}$  ( $z = 0.2, 0.4, 0.6, 0.8,$  and



1.0) were measured in the IR range from 400-4000  $cm^{-1}$  at room temperature as shown in Fig. 4.70. Two distinct absorption peaks were observed in the 400-600  $cm^{-1}$  a range that depicts the stretching vibration of Fe-O in tetrahedral and octahedral sites [292]. The two characteristics absorption band obtained near 582.42 $cm^{-1}$  ( $\nu''$ ) and 422.35  $cm^{-1}$  ( $\nu'$ ) undergo a gradual blue shift with increasing the level of substitution. The frequency band at 1038.83  $cm^{-1}$  is assigned to the Fe-O-Fe stretching vibrations which may be caused by the Fe-O anti-symmetric stretching vibration and Fe-O stretching vibration. The intensity of this band decreases from C1 to C5 sample with Co-Cd substitution. Moreover, FTIR spectra of the incorporated specimen (Fig. 4.70) exhibit a weak broad absorption band in the range of 2000-2500  $cm^{-1}$ , which may give us a suggestion of the existence of CO<sub>2</sub> [293]. There is no absorption band in the 2500-4000  $cm^{-1}$  range, indicating the non-existence of the citric acid hydroxyl group (O-H) [294].

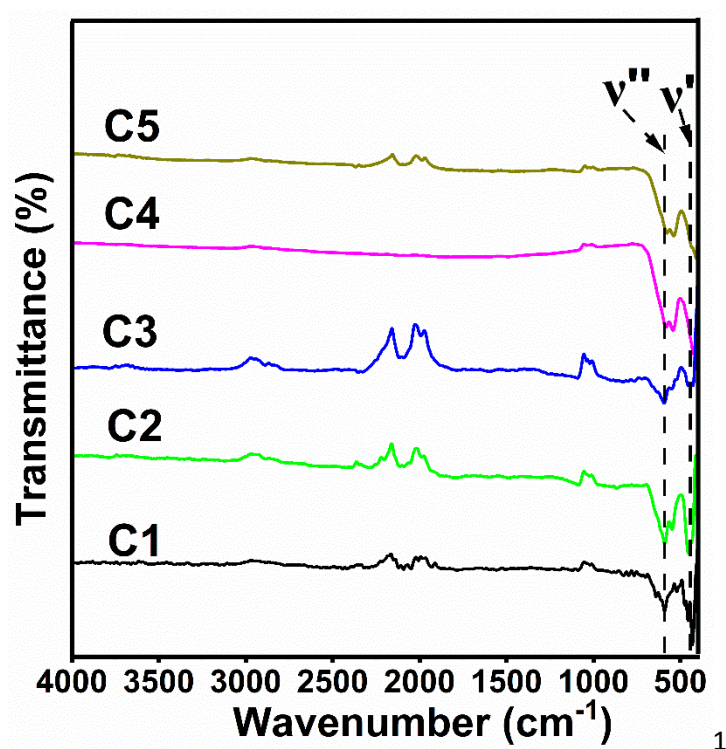
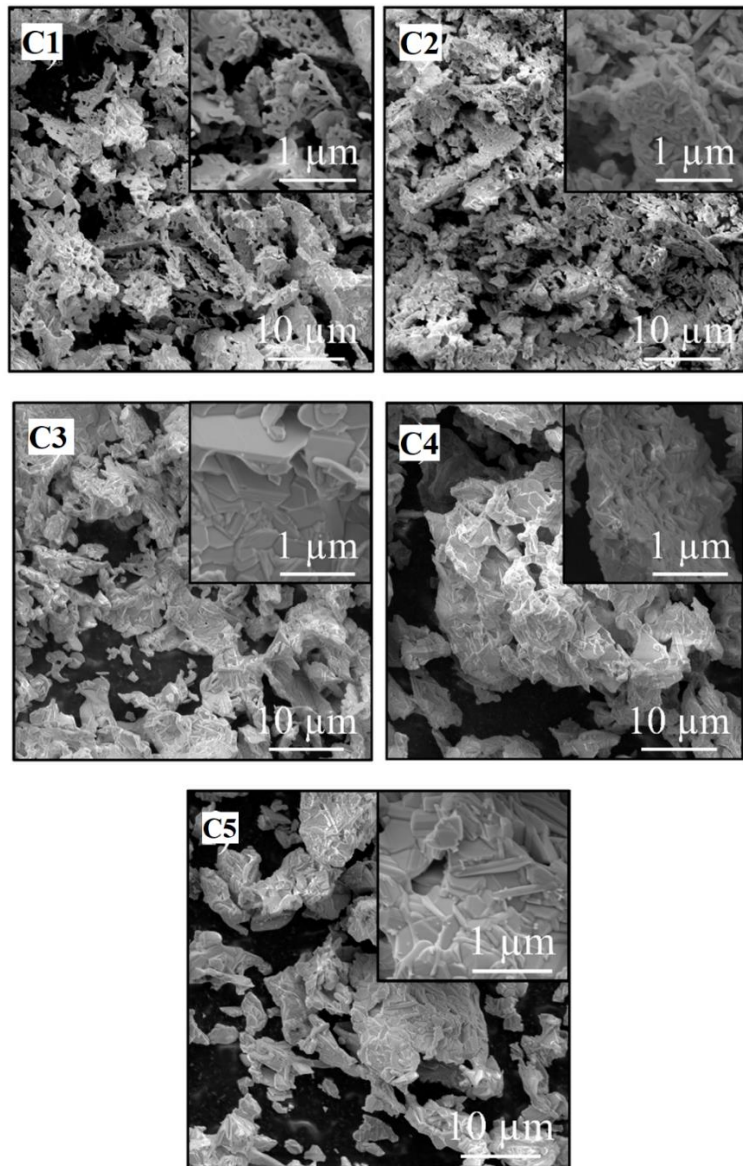


Fig. 4.73. FTIR spectra in 400-4000  $cm^{-1}$  range of all hexaferrite samples.

#### 4.4.1.3 SEM analysis

The change in the morphology of strontium hexaferrite powders synthesized with various additions of cobalt and cadmium substitute cations is shown in Fig. 4.71. All synthesized samples are micron agglomerates with tens of microns in size, consisting of nanoparticles, the size of which varies depending on the chemical composition of the final product [295]. It should be noted that the entire synthesized series can be conditionally

divided into two groups according to the features of their morphology. The first group includes C1 and C2 samples, wherein large no. of small grains is engaged with one another over long distances by involving several voids, as seen in Fig. 4.72. For C3, C4, and C5 samples, substitution causes agglomeration of grains in the form of large-sized grains with uneven size distribution. Furthermore, an increment in the degree of substitution from C3 to C5 causes densification in grains. It refers to an increment in interparticle contact, resulting in a more compact and closely packed grain structure. This variation affects the functional properties of the synthesized samples [296].



**Fig. 4.74.** SEM micrographs of C1, C2, C3, C4, and C5 hexaferrite samples.

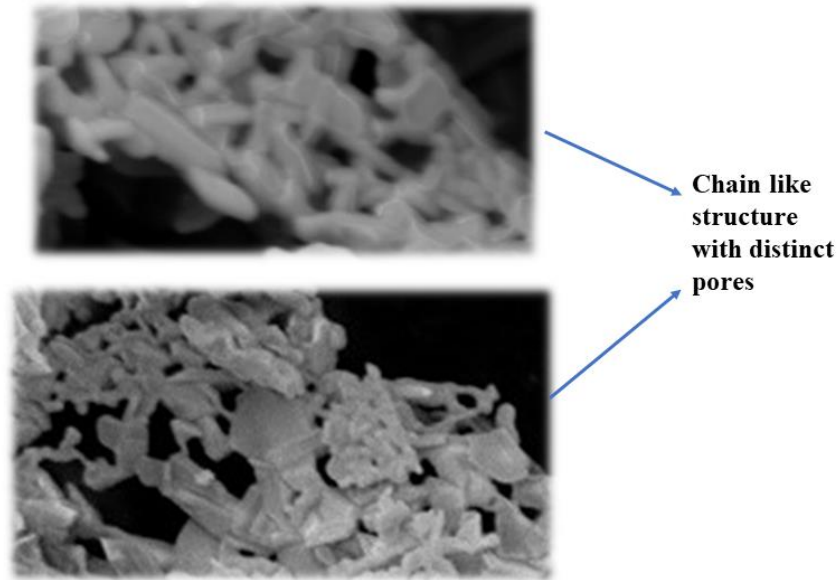


**Fig. 4.75.** Enlarged view of C1 sample

Energy-dispersive spectra (EDX) of synthesized doped strontium hexaferrite are shown in Fig. 4.73. According to the data obtained, all synthesized compositions correspond to the calculated composition within the error of the determination method. In the C4 sample, there is an insignificant deviation of the actual content of cobalt and chromium from the calculated one, which, can be associated with the presence of an impurity phase of cobalt ferrite in these samples.

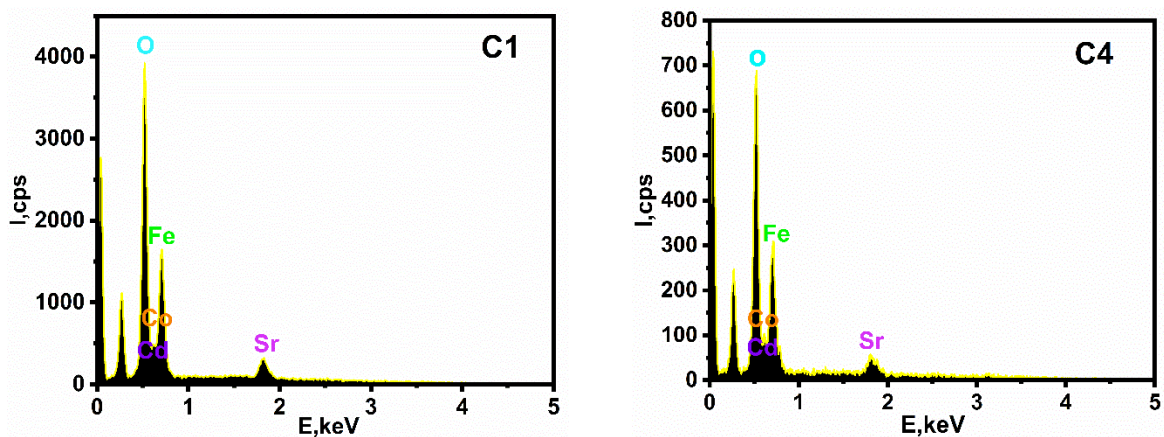


**Fig. 4.76.** EDX spectra of the C1 and C4 samples.

## 4.4.2 Electrical Analysis

### 4.4.2.1 Dielectric study

It has been noted that among all samples of the C-series only C1, C3, C4 and C5 exhibit the electrical characteristics due to uncertainty observed in the rest of the samples of

the C-series. Fig. 4.74(a) and 4.74(b) reveals the variation of dielectric constant ( $\epsilon'$ ) and loss ( $\epsilon''$ ) of C1, C3, C4 and C5 as a function of frequency at room temperature. It can be seen [Fig. 4.74(a)] that the value of  $\epsilon'$  is high at low applied frequencies, which gradually decreases and is constant at higher frequencies. This dispersion shows a normal behavior of dielectric materials, caused by interfacial polarization. Samples C1, C3, and C4 exhibit the lowest frequency dependence dielectric dispersion as compared to sample C5. This behavior can be attributed to the availability of ferrous ions at octahedral sites. Due to the availability of multiple  $\text{Fe}^{2+}$  ions at octahedral sites, the value of  $\epsilon'$  increases with Co-Cd substitution from C1 to C5. This could be due to the tendency of Co-Cd ions to occupy tetrahedral sites, which enhances the no. of Fe ions responsible for polarization, thus increasing the dielectric constant [297].

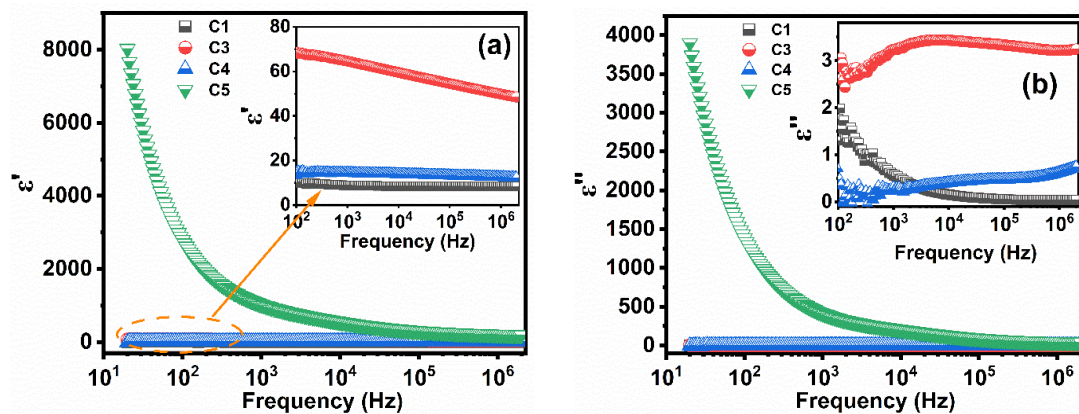


**Fig. 4.77.** (a)  $\epsilon'$  (b)  $\epsilon''$  variation with frequency of C1, C3, C4 and C5 hexaferrite.

Fig. 4.75 illustrates how the dielectric loss tangent ( $\tan\delta$ ) changes in response to the frequency at room temperature. It can be seen (Fig. 4.75) that as the frequency of the alternating field increases, the value of the  $\tan\delta$  decreases. The initial drop in  $\tan\delta$  with increasing frequency can be explained by Koop's phenomenological theory of dielectrics. At lower frequencies, the resistivity of the material is higher due to the presence of grain boundaries. Substitution of Co-Cd ions introduces heterogeneity in the synthesized samples and results in more interface polarization. The  $\tan\delta$  value linearly decreases from C1 to C4, and afterward, a sudden increment. A relatively weak broad relaxation in the C5 sample suggests the hopping frequency of charges between  $\text{Fe}^{2+} \rightleftharpoons \text{Fe}^{3+}$  cations at the octahedral position matches with the applied frequency.



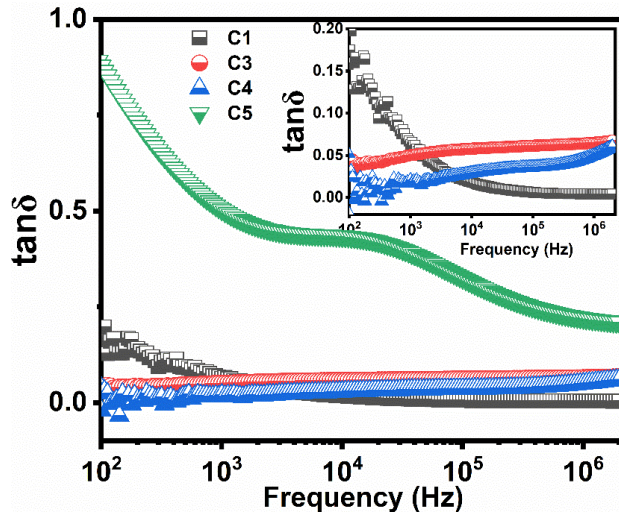


**Fig. 4.78.** Loss tangent variation with frequency of C1, C3, C4 and C5 hexaferrite.

#### 4.4.2.2 AC conductivity

Fig. 4.76 displays the increase in ac conductivity ( $\sigma$ ) of C1, C3, C4, and C5 samples as the applied frequency increases. It also reveals that at low-frequency,  $\sigma$  shows frequency-independent behavior and sharply increases at a higher-frequency region ( $>10^4$  Hz). This ubiquitous rise in  $\sigma$  value with increasing frequency is the general behavior of hexaferrite explained by Verway's hopping mechanism. The introduction of Co-Cd ions causes an increment in conductivity value and this elucidates an enrichment in the concentration of  $\text{Fe}^{3+}$  ions at the octahedral sites, which facilitates the probability of hopping between  $\text{Fe}^{2+}$  and  $\text{Fe}^{3+}$  ions. The AC conductivity of prepared samples may also be affected by grain distribution and porosity in the material. The material with heterogeneous morphology, such as a large number of voids in a chain-like structure as seen in SEM of the C1 sample (Fig. 4.72) impedes the movement of charge carriers, resulting in a lower conductivity value.

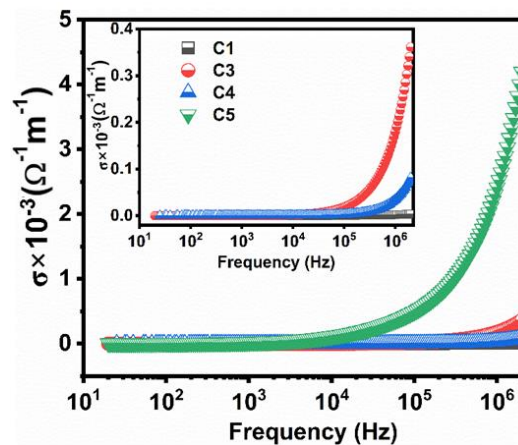


**Fig. 4.79.**  $\sigma$  variation with frequency of C1, C3, C4 and C5 hexaferrite.

### 4.4.2.3 Electric modulus

Fig. 4.77(a) displays the changes in  $M'$  with frequency and the plot shows a very low value of  $M'$  at lower frequencies approaching zero implying no contribution of electrode polarization. With increasing frequency,  $M'$  varies continuously and reaches an asymptotic value ( $M'$ ) which is maximum at the high-frequency range for all sintered hexaferrite. This pattern suggests that there is a lack of a restoring force controlling the movement of charge carriers in response to an induced electric field [25]. Also, it supports the concept that charge carriers have long-range mobility. Moreover, the value of  $M'$  increases sigmoidally with increased frequency, eventually reaching a value ( $M_\infty$ ) for all sintered hexaferrite. This increment may be ascribed to the conduction phenomena resulting from the short-range mobility of carriers, especially ions. This variation is similar to the behavior observed in  $\sigma$ , discussed in the previous section. However, the substitution of Co-Cd ions decreases the value of  $M'$  at high-frequency range.

Fig. 4.77(b) illustrates the variation of  $M''$  with frequency. The value of  $M''$  is related to the dissipation of energy during an irreversible conduction process. The nature of  $M''$  spectrum can be discussed via (i) an appearance of an asymmetrical peak at a certain frequency, (ii) a shift in the peaks toward a higher frequency with the substitution of Co-La, (iii) a broadening and narrowing peak. As the substitution level of Co-Cd ions increases, a noticeable shift is observed in the peak towards the higher frequencies. The asymmetric shape of the plot for the peak maxima and the width of the peaks on either side of the maxima indicate a non-Debye behavior of the material, caused by the distribution of relaxation time [26], [27].

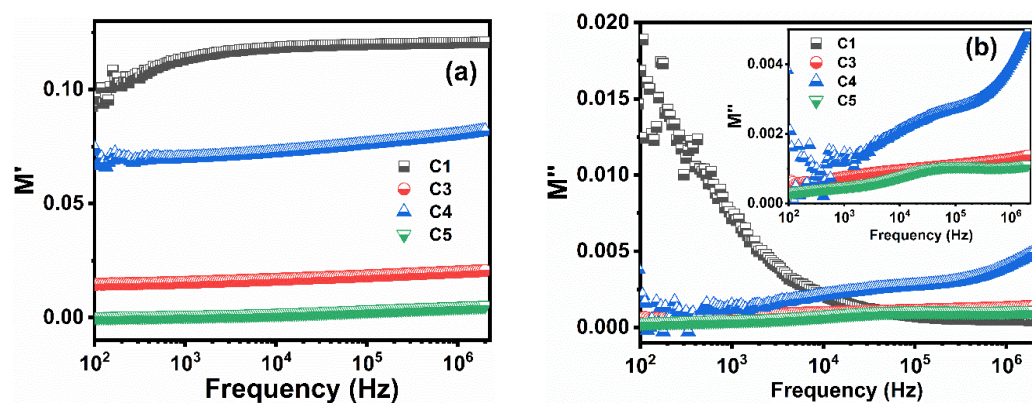


**Fig. 4.80.** (a)  $M'$  (b)  $M''$  variation with frequency of C1, C3, C4 and C5 hexaferrite

Fig. 4.77 illustrates the Cole-Cole plot ( $M''$  vs  $M'$ ) of C1, C3, C4, and C5 sintered hexaferrite. The obtained curves demonstrate a deformed semicircle instead of a perfect semicircle with the center lying below the x-axis. This signifies that the relaxation is



distributed over different time constants and is not of the Debye-type. The existence of a single semicircle in the C1 sample confirms the relaxation due to grain boundaries alone. This variation is consistent with SEM micrographs (Fig. 4.72) of the C1 sample, wherein a large no. grains boundaries can be visualized and interlinked with one another over long distances. However, C3, C4, and C5 samples show a segment of an arc instead of perfect semicircles. This suggests that the grain boundary effect decreases, and the effect of grains increases as frequency increases. Substitution causes the formation of grain clusters, and this can also be visualized in the SEM micrographs (Fig. 4.71).

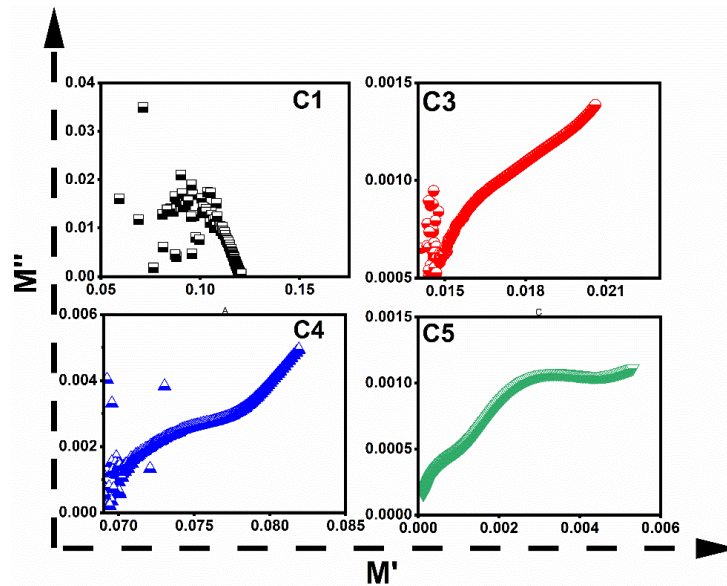


**Fig. 4.81.** Cole-Cole plots ( $M''$  vs  $M'$ ) variation with frequency of C1, C3, C4 and C5 hexaferrite.

#### 4.4.2.4 Complex impedance analysis

The fall observed in both  $Z'$  and  $Z''$  with increasing frequencies is shown in Fig. 4.79(a) and Fig. 4.79(b), respectively. As the frequency increases, both  $Z'$  and  $Z''$  decreases, suggesting an increment in the material's conductivity due to the increase in electron hopping between the localized ions [29] At higher frequencies, the reduction in  $Z'$  could be explained through the Maxwell-Wagner model [30].

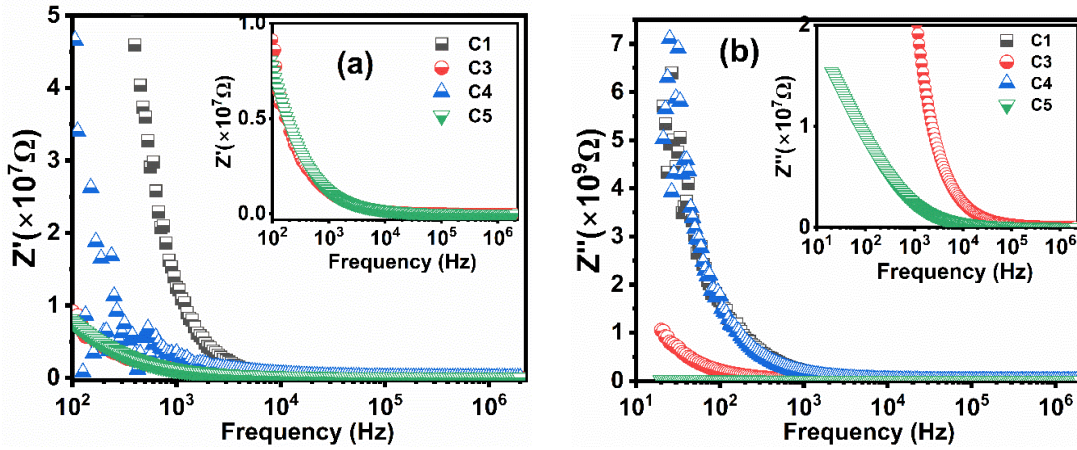


**Fig. 4.82.** (a)  $Z'$  (b)  $Z''$  variation with frequency of C1, C3, C4 and C5 hexaferrite.

Fig. 4.80 shows the Cole-Cole plots ( $Z''$  vs  $Z'$ ) of C1, C3, C4, and C5 sintered hexaferrite at room temperature. Instead of a complete semicircular arc, only a segment of a semicircular arc has been observed for all. It is also noted that as the substitution increases, the depression of the arc decreases from C1 to C4, and then increases for C5. This depression suggests that the impedance mechanism at low frequency explicitly depends on the dielectric polarization that occurs at grain boundaries, also referred to as the Maxwell-Wagner effect.

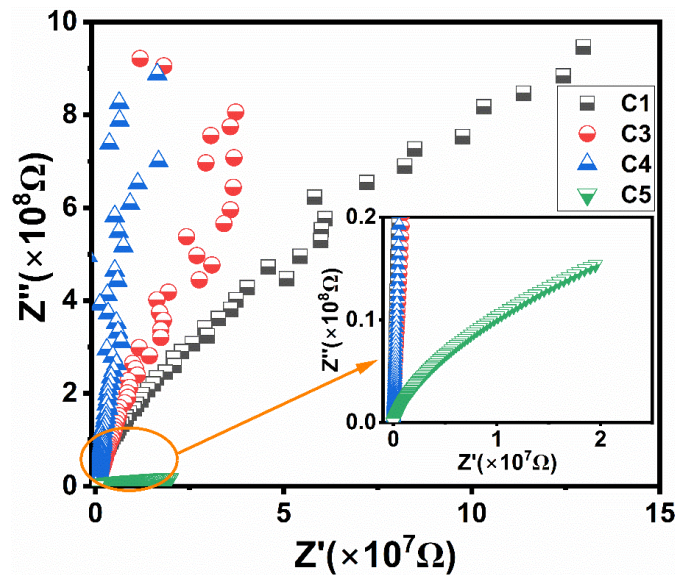


**Fig. 4.83.** Cole-Cole plots ( $Z''$  vs  $Z'$ ) variation with frequency of MC1, MC2, MC3 and MC4 hexaferrite.

#### 4.4.3 Magnetic analysis

The electronegativity of cations influences their occupancy in the crystallographic sites, with more electronegative ions preferring octahedral sites which are larger than tetrahedral positions. Thus,  $\text{Cd}^{2+}$  (1.69) being less electronegative than  $\text{Co}^{2+}$  (1.88) preferably

choose to occupy tetrahedral sites [298]. The site occupancy of cations can also be ascribed by d-configuration and the nature of the cations involved.  $\text{Co}^{2+}$  ions tend to occupy octahedral sites with a  $d^7$  configuration, and  $\text{Cd}^{2+}$  have no site preference due to their  $d^0$  configuration. It has been reported that  $\text{Co}^{2+}$  ions preferentially occupy the  $4f_1$ ,  $4f_2$ , and  $2b$  sites. Additionally, both  $\text{Cd}^{2+}$  ( $0.96 \text{ \AA}$ ) and  $\text{Co}^{2+}$  ( $0.72 \text{ \AA}$ ) ions have larger ionic radii than host  $\text{Fe}^{3+}$  ( $0.64 \text{ \AA}$ ) ions, so former both ions can occupy octahedral positions at the edges of the unit cell [299]. Fig. 4.81 illustrates the recorded M-H curves of C1, C2, C3, C4, and C5 hexagonal ferrites by applying a field of 25kOe at room temperature. The derived magnetic parameters from M-H curves are enumerated in Table 4.27.

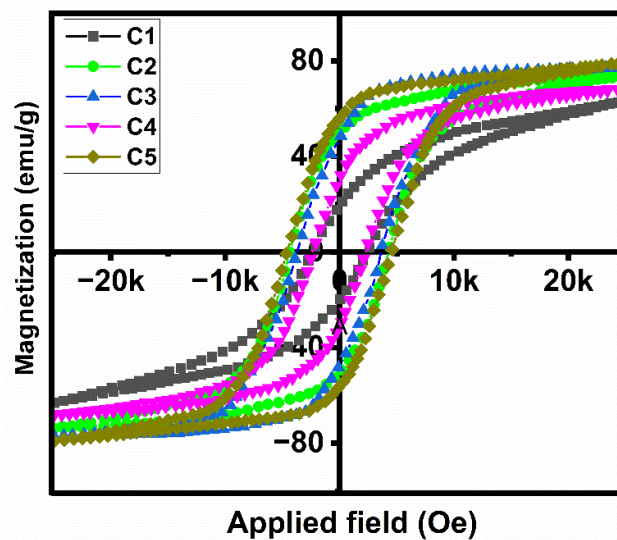


**Fig. 4.84.** Hysteresis loops of C1, C2, C3, C4, and C5 hexaferrite.

The variation in saturation magnetization ( $M_s$ ) can be explained through the distribution of both substituents on crystallographic sites. The replacement of  $\text{Fe}^{3+}$  ions with diamagnetic ion ( $\text{Zn}^{2+}$ ) and weakly magnetic ion ( $\text{Co}^{2+}$ ) in the spin-up state results in a decrease in magnetization, while substituting in the spin-down state leads to an increase in net magnetization.

$$M_s = M_a (2a + 12k + 2b) (\uparrow) - M_b (4f_1 + 4f_2) (\downarrow)$$

The remanence ratio ( $M_r/M_s$ ) is a measure of the retention of magnetization after removing an applied field, and it's usually high in M-type hexaferrite, indicating high remanence. In the present work,  $M_r/M_s$  value of C2, C3, and C5 samples turns out to be greater than 0.5, which depicts the single-domain nature of particles within the material. On the other hand, C1 and C4 indicate the existence of multi-domains in the material with  $M_r/M_s < 0.5$ . Table 4.27 and Fig.4.81 show that the value of  $M_s$  gradually increases from C1 to C3 samples with the substitution of Co-Cd ions [297]. This could be attributed to the

occupancy of spin-down sites by these substituents. This can also be confirmed through the Mössbauer spectroscopy results (discussed in the next section), wherein a significant decrease is observed in the net  $R_A$  of spin-down ( $4f_1 + 4f_2$ ) sites with Co-Cd substitution. Furthermore, the value of  $M_s$  decreases from C3 to C4 and thereafter is found to be maximum for C5. This behavior of saturation magnetization can be explained through the SEM micrographs (Fig. 4.71) and squareness ratio ( $M_r/M_s$ ). SEM micrograph of the C4 sample depicts the existence of a large number of grain boundaries between individual crystalline grains. These grain boundaries impede the movement and alignment of magnetic domains, resulting in lower saturation magnetization. Moreover, in the C5 sample, the densification of grains reduces the defects and grain boundaries within the material. It improves the alignment of magnetic moments of atoms present within the grains.

**Table 4.27** Magnetic parameters  $M_s$ ,  $H_c$ ,  $H_a$ ,  $M_r$  and  $M_r/M_s$  value of all hexaferrite samples.

Sample name	C1	C2	C3	C4	C5
$M_s$ (emu/g)	67.51	74.58	77.69	69.83	82.13
$H_c$ (Oe)	2379.98	4273.50	3612.63	2255.13	4551.28
$H_a$ (kOe)	27.24	13.50	8.99	15.90	19.61
$M_r$ (emu/g)	19.2	50.15	47.73	30.95	55.96
$M_r/M_s$	0.290	0.669	0.614	0.443	0.681
$n_B$ ( $\mu_B$ )	12.91	14.31	15.04	13.60	16.09

So, when a field is applied to the material then a large number of magnetic moments easily align itself in a particular direction strengthening the overall magnetization of the material, thus resulting in high  $M_s$ . However, in the low-applied field, a slow rise in magnetization is observed in the C1 sample (Fig. 4.81). This can be explained with SEM micrographs (Fig. 4.72) and anisotropy field (Table 4.27) of the C1 sample, wherein a small grain forms a chain-like structure with distinct pores and causes shape anisotropy. Such grains take a longer time to reorient themselves in response to a low-applied field with pronounced  $H_a$ .

The anisotropy field ( $H_a$ ) mainly depends on the 2b and 4f<sub>2</sub> sites of magnetoplumbite structure, but the 4f<sub>2</sub> site prominently affects  $H_a$  more than the alone 2b site [300]. It is clear from the table that  $H_a$  decreases by 28 % from C1 to C5 and this can be explained through the Mössbauer spectra, where the net change in the relative area of the 2b site is more than the relative area of the 4f<sub>2</sub> site. But, the contribution of the 2b site is less than the 4f<sub>2</sub> site,

therefore despite the large change in 2b site occupancy, the overall  $H_a$  decreased by the same amount of 29%.

The non-linear increase observed in the value of  $H_c$ , with Co-Cd substitution, can be estimated through grain size distribution and the occurrence of porosity in the synthesized samples. In the present studies, the  $H_c$  value of C2, C3, and C5 samples is quite higher than C1 and C4. The increment in  $H_c$  can be understood with the porosity value calculated from XRD data (Table 4.25), wherein largely porous samples lead to higher values of  $H_c$ . The Bohr magneton (calculated from equation 3.14) is closely related to saturation magnetization and molecular weight (M.W). As the level of substitution increases, the value of the Bohr magneton increases, and it can be observed in Table 4.27.

#### 4.4.4 Mössbauer analysis

Mössbauer spectroscopy was employed to determine the impact of Co-Cd substitution on the local chemical structure of SrM hexaferrite, by varying the level of substitution. Fig. 4.82 illustrates the Mössbauer spectra of synthesized samples and Table 4.28 enlists the quadrupole splitting (QS), isomer shift (IS), hyperfine field ( $H_{\text{eff}}$ ), and relative areas values obtained from fitting of the Mössbauer spectra of SrM hexaferrite substituted with cobalt and cadmium cations at room temperature. All the obtained spectra show five main sextets of iron cations related to the structural positions of magnetoplumbite (12k, 4f<sub>1</sub>, 4f<sub>2</sub>, 2a, 2b) and one sextet, the appearance of which, is associated with the presence of the cobalt ferrite phase in the samples. The content of the impurity phase varies depending on the chosen ratio x and is in the range of values from 5 to 10%.

The isomer shift (IS) provides information about the chemical bonding, including the valence state of  $Fe^{3+}$  ions in magnetically ordered materials. From the previous reports, the value of isomer shift for  $Fe^{2+}$ ,  $Fe^{3+}$ , and  $Fe^{4+}$  ions should lie between 0.6 to 1.7 mm/s, 0.05 to 0.5 mm/s, and 0.15 to 0.05 mm/s respectively [301]. In this case of the prepared samples, the observed isomer shift values for all sites fall within the range of 0.246 to 0.461, indicating that the Fe ions are in a '+3' oxidation state. Furthermore, the isomer shift values of 4f<sub>2</sub>, 4f<sub>1</sub>, and 12k sites relatively remain constant, while 2b and 2a sites slightly vary with substitution. This may suggest the variation in the s-electron density around the  $Fe^{3+}$  ions at the 2b and 2a sites. The quadrupole splitting gives knowledge about the local distortion and symmetry of the crystal lattice. As the  $^{57}Fe$  atom has transitioned from 3/2 to 1/2 states, it is expected to exhibit quadrupole splitting. All the sextets exhibit QS values ranging from 0 to 1 mm/s which indicates a spherical charge distribution, except the C1 sample. Throughout the



substitution of Co-Cd ions, the QS values of the 12k site remain nearly constant, indicating an insignificant change in the distribution of charges at these sites upon substitution. For the  $4f_1$  and  $4f_2$  sites, the QS slightly increases, reaching a maximum at the C3 sample, and then decreases slightly. However, the QS for the 2a and 2b sites reduces at C3 and then slightly increases. This paradoxical behavior can be described as follows: the Co-Cd substitution leads to an increase in the density of cations around the  $4f_1$  and  $4f_2$  sites and results in slight distortion [302]. The decrement in QS value for the 2b and 2a sites at the C3 sample indicates that the octahedra becomes more symmetric with Co-Cd ions substitution at these particular sites [303]. The hyperfine field is observed to be relatively constant across all lattice sites from C1 to C5, except the 2b site.

In the C1 sample, the relative area of 12k and 2b sites are quite close to the predicted relative area of SrM hexaferrite, while the  $4f_1$ ,  $4f_2$ , and 2a have less occupancy as seen in Table 4.28. From C1 to C5, the total relative area of  $4f_1$  and  $4f_2$  sites decreases by 37.38%, which signifies that Co-Cd ions tend to occupy these sites. Whilst, the total relative area of 12k-2a-2b sites increases by 31%, suggesting that some of the Fe ions migrated towards these sites. The obtained results assured that Co-Cd ions tend to occupy  $4f_1 - 4f_2$  spin-down sites.

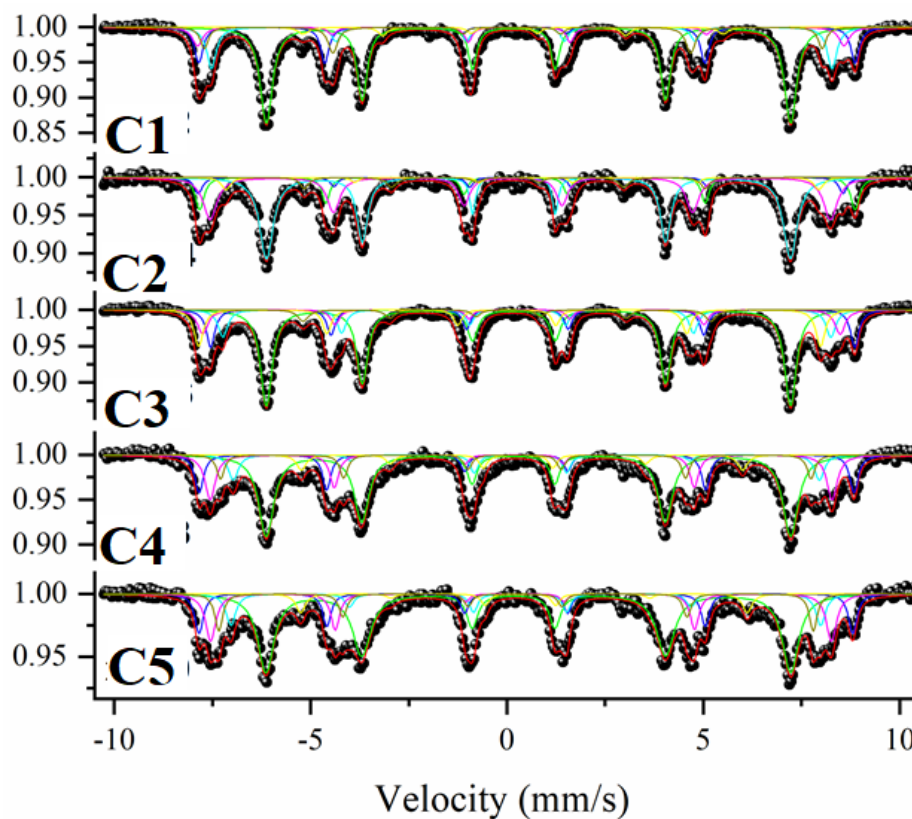


**Fig. 4.85.**  $^{57}\text{Fe}$  Mössbauer spectra of C1, C2, C3, C4, and C5 hexaferrite samples.



**Table 4.28** Isometric shift, hyperfine field, and quadrupole splitting of spectral components of all hexaferrite samples.

Sample	Site	IS (mm/s)	QS (mm/s)	Heff (mm/s)	Area (%)
<b>C1</b>	12k	0.362	-0.370	41.464	49.67
	4f1	0.355	-0.308	51.912	13.94
	4f2	0.299	-0.156	49.080	13.80
	2a	0.046	-0.222	33.218	4.36
	2b	0.333	-0.038	51.126	8.08
	Ferrite?	0.140	-0.037	48.870	10.15
<b>C2</b>	12k	0.361	0.366	41.443	43.57
	4f1	0.369	0.299	51.838	12.81
	4f2	0.246	0.183	49.063	28.57
	2a	0.441	0.073	46.875	4.13
	2b	0.017	0.098	31.703	5.14
	Ferrite?	0.348	0.001	50.996	5.79
<b>C3</b>	12k	0.362	0.368	41.460	46.11
	4f1	0.461	0.387	50.945	13.70
	4f2	0.389	0.236	48.079	12.01
	2a	0.343	0.047	50.411	9.20
	2b	0.032	0.068	49.178	13.49
	Ferrite?	0.016	0.025	32.248	5.49
<b>C4</b>	12k	0.355	0.379	41.477	47.08
	4f1	0.367	0.262	51.794	13.86
	4f2	0.418	0.148	46.348	8.26
	2a	0.273	0.175	49.191	15.37
	2b	0.333	0.100	34.894	6.24
	Ferrite?	0.210	0.030	46.709	9.19
<b>C5</b>	12k	0.355	0.372	41.505	47.58
	4f1	0.358	0.248	51.698	12.83
	4f2	0.407	0.144	46.651	9.74
	2a	0.280	0.155	49.103	14.72
	2b	0.388	0.091	35.328	5.31
	Ferrite?	0.217	0.027	47.018	9.82

#### 4.4.5 Electromagnetic Analysis

Fig. 4.83(a, b) demonstrated the variation of dielectric constant ( $\epsilon'$ )/loss ( $\epsilon''$ ) of C1, C2, C4, and C5 samples in the frequency range of 8.2 to 12 GHz, and C3 from 12.4 to 18 GHz. The introduction of Co-Cd ions causes a feeble change in  $\epsilon'/\epsilon''$  values. In frequency spectra (8.2 -12.4 GHz), sample C1 remain constant, while C2, C4, and C5 show resonance peak from 8.5 to 9.5 GHz and does not vary too much in the remaining frequency spectra. Conversely, the C3 sample exhibits small fluctuation from the 12 to 18 GHz frequency regime. Whenever the applied frequency of the microwave coincides with the hopping frequency of electrons, the phenomena of dielectric resonance occur. Fig. 4.84(a, b) depicts the plots of permeability ( $\mu'$ )/ magnetic loss ( $\mu''$ ) of C1, C2, C4, and C5 samples in a frequency range of 8.2 to 12 GHz, and C3 from 12.4 to 18 GHz. The maximum value of  $\mu''$  as observed at resonance frequencies are 0.30 at 10.26 GHz for C1, 0.33 at 10.28 GHz for C2, 0.20 at 14.01 GHz for C3, 2.06 at 10.57 GHz for C4, and 1.31 at 10.29 GHz for C5. The introduction of the weak magnetic moment of Co and Cd ions than Fe ions ascribed the non-linearly increase in  $\mu''$  values. Fig. 4.81 contributes to magnetic loss in synthesized samples.

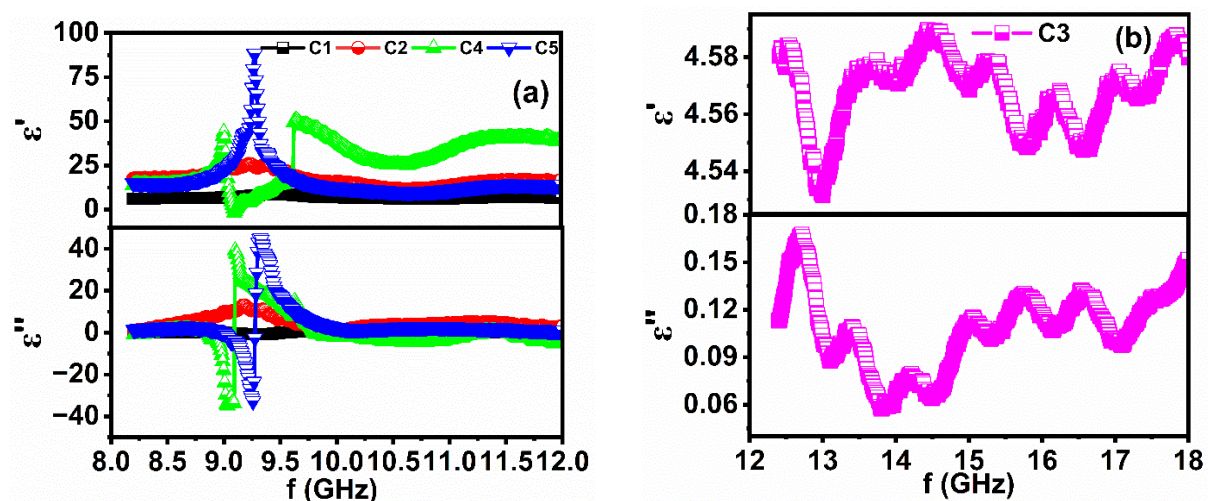
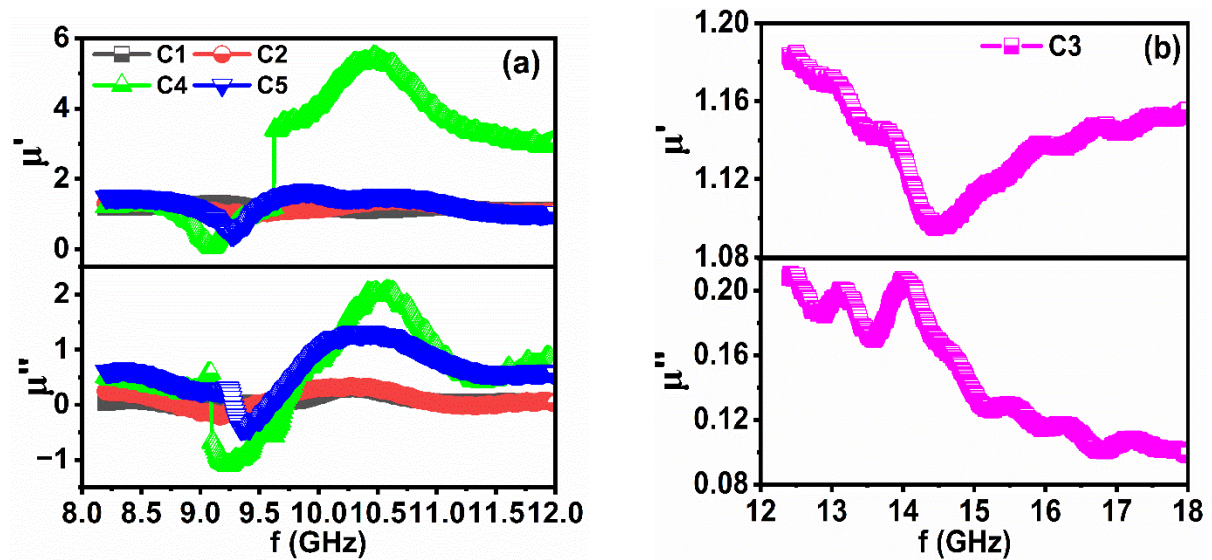


Fig. 4.86. (a) Complex permittivity of C1, C2, C4, and C5 samples (b) Complex permittivity of C3 sample.

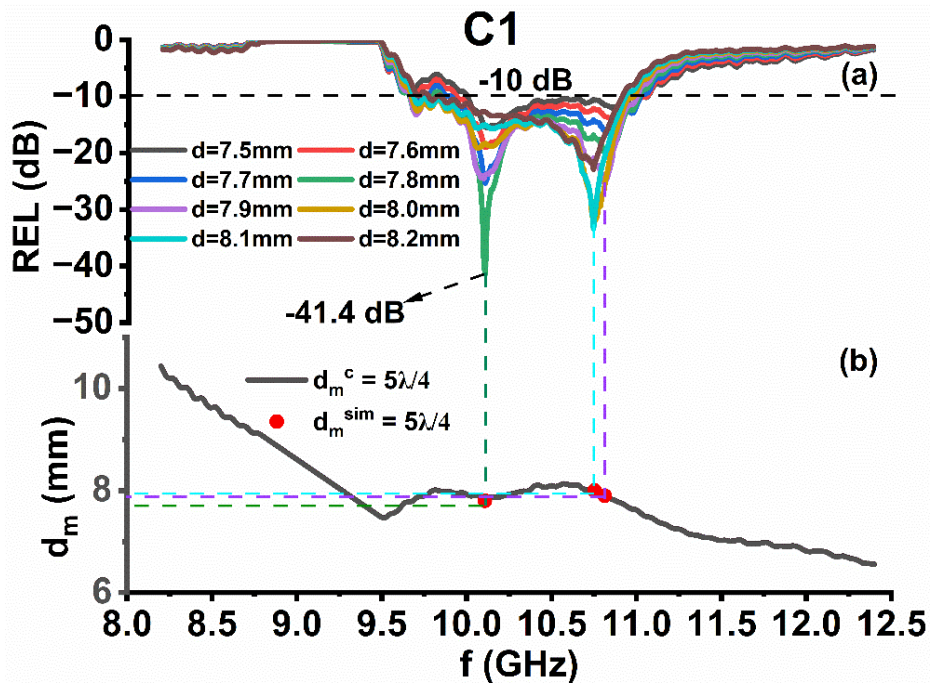
The microwave absorption phenomena are investigated by examining REL vs frequency plots for different simulated thicknesses. Fig. 4.85(a), 4.86(a, c), 4.87(a, c, e), 4.88(a, c), and 4.89(a, c, e, g) illustrate the REL plots of all synthesized samples and can be utilized to deduce parameters such as bandwidth/frequency range for REL of -10 dB (90% absorption) /-20 dB and matching frequency/thickness, as listed in Table 4.29. For better visualization 3D REL plots are depicted in Fig. 4.90. The insertion of Co-Cd ions initially

increases the microwave absorption of the synthesized sample from C1 to C2 and further substitution decreases it non-linearly.



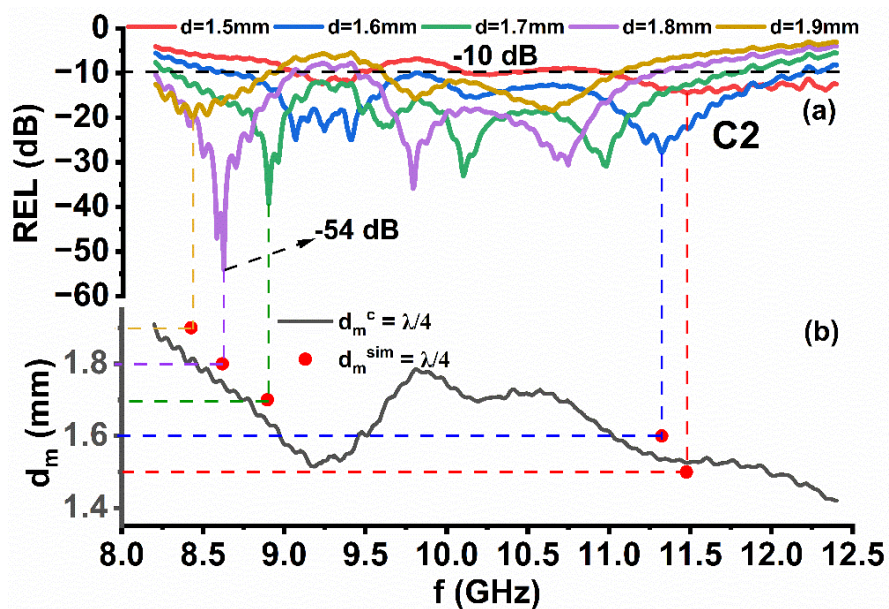
**Fig. 4.87.** (a) Complex permeability of C1, C2, C4, and C5 samples (b) Complex permeability of C3 sample.

The highest dip in REL, measuring -54.04 dB (> 99 % absorption), is observed in the C2 sample [Fig. 4.86(a, c)], occurring at a frequency of 8.62 GHz and a thickness of 1.8 mm. The plots illustrate the shift of REL peaks towards lower frequency ranges as the thickness increases, affirming the existence of quarter wavelength mechanism described by equation 3.24. Using equation 3.22, Reflection loss (REL) is computed using both the simulated thickness ( $d_m^{\text{sim}}$ ) and the calculated thickness ( $d_m^c$ ), which is determined through equation 3.24 by substituting values of  $n = 1, 3, 5$ , and so forth. The purpose is to establish a relationship between the quarter wavelength mechanism and REL peaks. Fig. 4.85(b), 4.86(b, d), 4.87(b, d, f), 4.88(b, d), and 4.89(b, d, f, g) depicts plots of a calculated thickness ( $n\lambda/4$ ) within the frequency range. To compare the simulated thickness ( $d_m^{\text{sim}}$ ) with the calculated thickness ( $n\lambda/4$ ), vertical lines are drawn from REL peaks to the thickness-frequency plots.

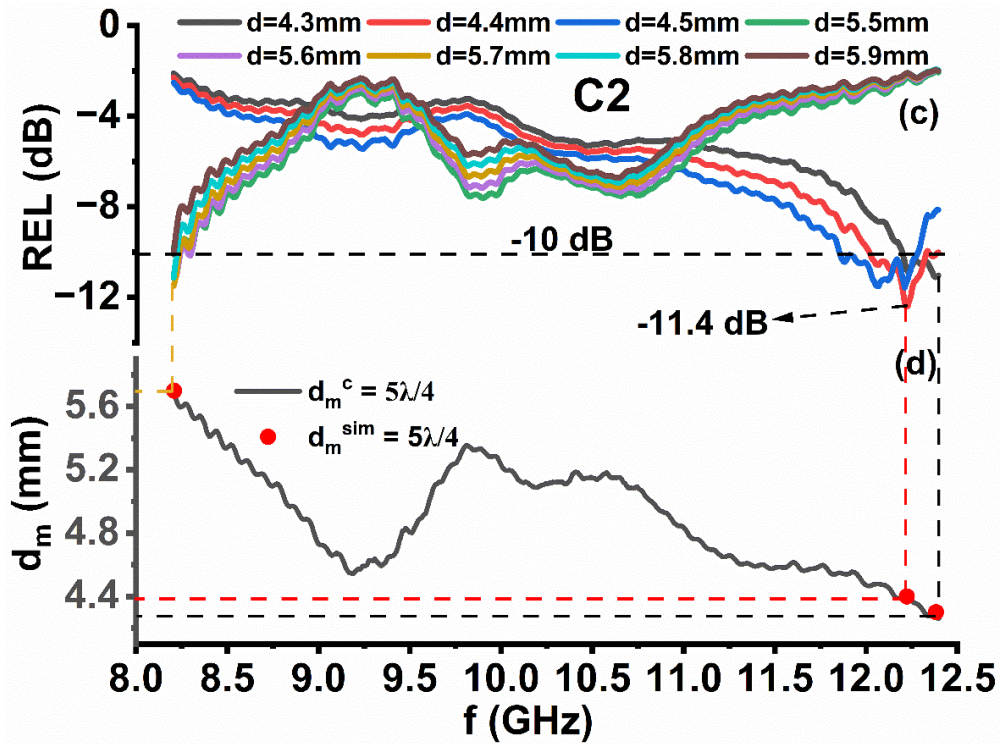


**Fig. 4.88.** (a) Dependence of REL on frequency in C1 sample. (b)  $d_m^{sim}$  and  $d_m^c$  versus frequency for  $5\lambda/4$  in the C1 sample.

(i) For the C1 sample, REL values vary from -15.49 dB to -41.42 dB, and thickness ranges from 7.5 mm to 8.2 mm, and the plots display quarter-wavelength mechanism ( $n\lambda/4$ ) for  $n=5$  values over the 8.2 to 12.4 frequency region. In C1, an optimal REL = -41.42 dB is observed at 10.10 GHz with an effective bandwidth of 1.18 GHz with a matching thickness of 7.8 mm Table 4.29. Furthermore, a dual REL peak ( $>-10$  dB) is observed for all thicknesses of the C1 sample.



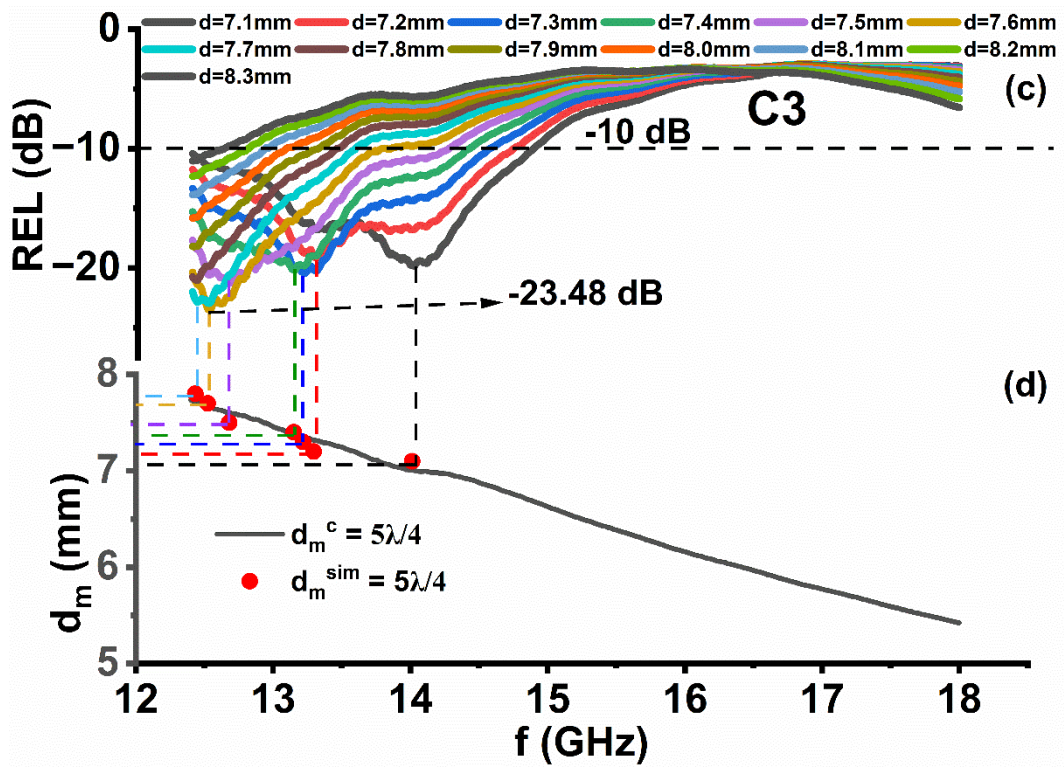
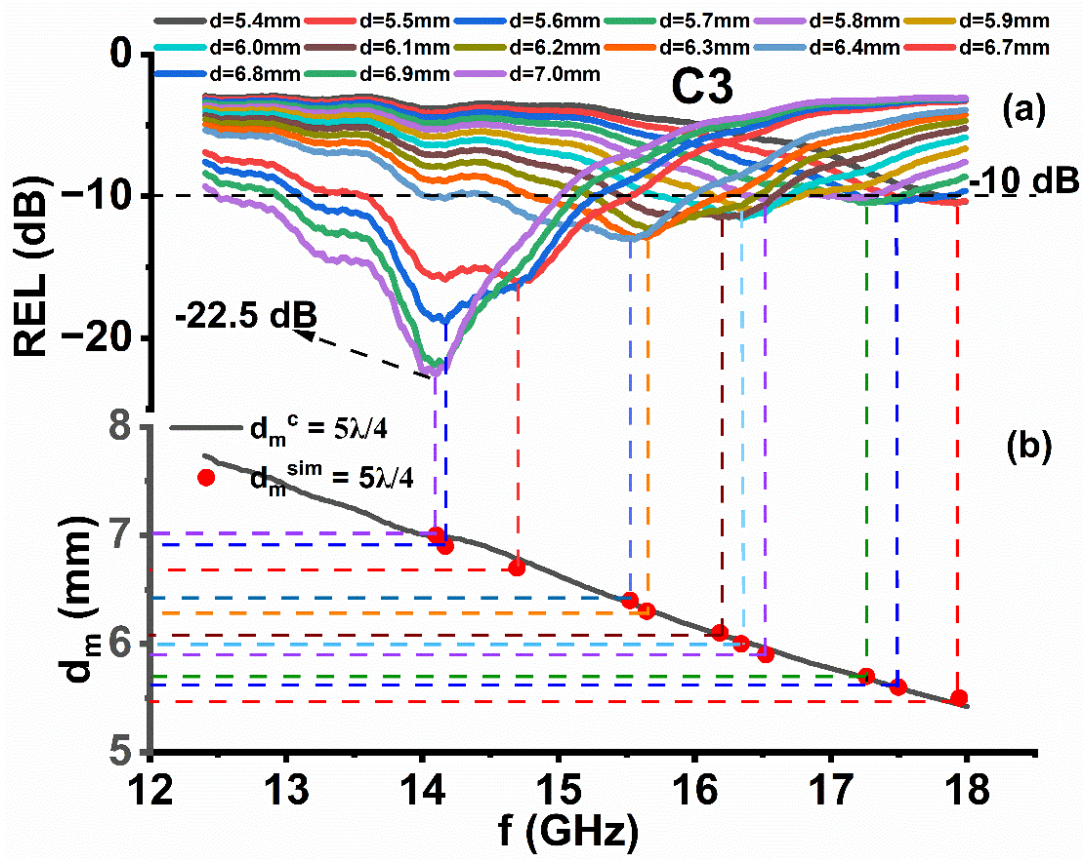




**Fig. 4.89.** (a, c) Dependence of REL on frequency in C2 sample. (b, d)  $d_m^{\text{sim}}$  and  $d_m^c$  versus frequency for  $5\lambda/4$  in the C2 sample.

(ii) For the C2 sample, a maximum REL of -54.04 dB was observed at 1.8 mm thickness of frequency 8.62 GHz and for 1.5 to 1.9 mm thickness multiple REL dip (>-10 dB) over the 8.2 to 12.4 GHz frequency spectra. As the thickness increases decrease from 4.3 mm to 5.9 mm, reflection loss decreases. The obtained plots exhibit quarter-wavelength mechanism ( $n\lambda/4$ ) for  $n=1$  and 5, with a narrow (0.29 GHz) and a wide (3.41 GHz) at 4.4 mm and 1.7 mm thickness, respectively, as shown in Table 4.29.

(iii) For the C3 sample, several thicknesses exhibit REL > -10 dB /-20 dB over a frequency range of 12.4 to 18 GHz. As the thickness increases from 5.4 mm to 10 mm, REL increases non-linearly from -10.42 dB to -27.17 dB. The plots exhibit a quarter-wavelength mechanism ( $n\lambda/4$ ) for  $n=5$  and 9 values, with bandwidth ranges from 0.65 GHz to 2.53 GHz, as shown in Table 4.29. In the C3 sample, for REL > -10 dB broad bandwidth of 2.17 GHz and a narrow bandwidth of 0.65 GHz is observed from 13.09-15.28 GHz and 15.93-16.58 GHz with a matching thickness of 6.8 mm and 6.1 mm, respectively. Furthermore, for REL > -20 dB a wide bandwidth of 2.53 GHz from 12.48-15.01 at 7.0 mm thickness.





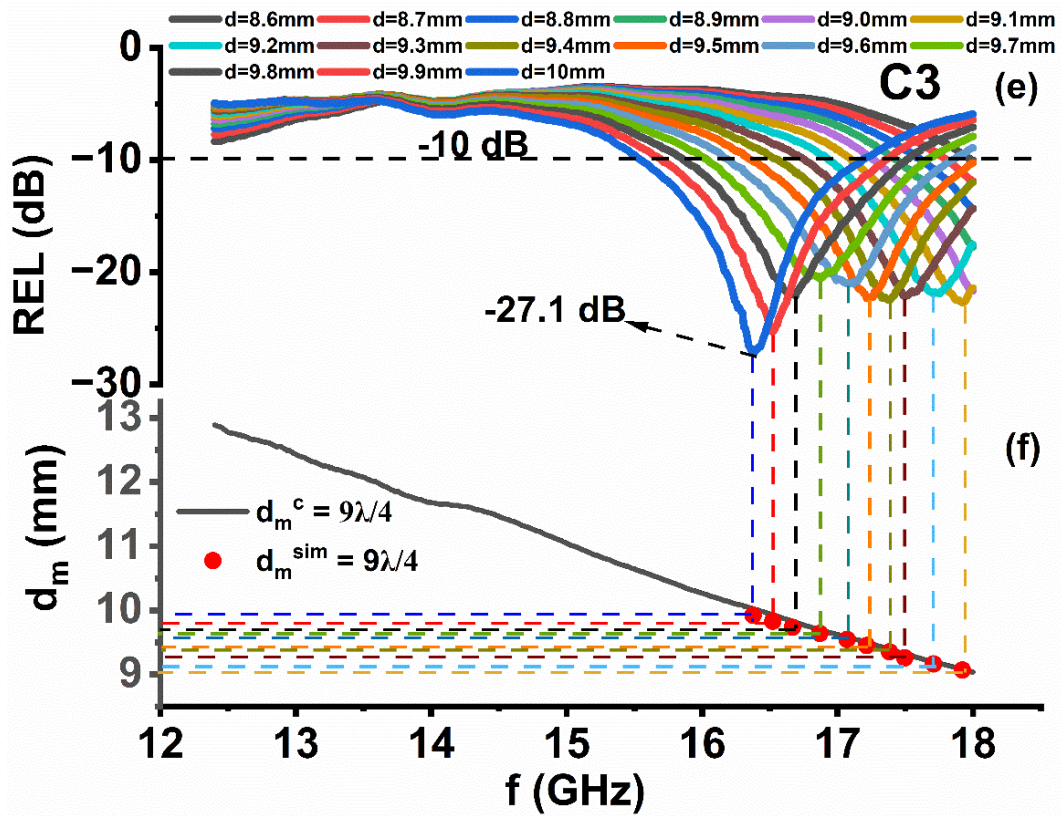
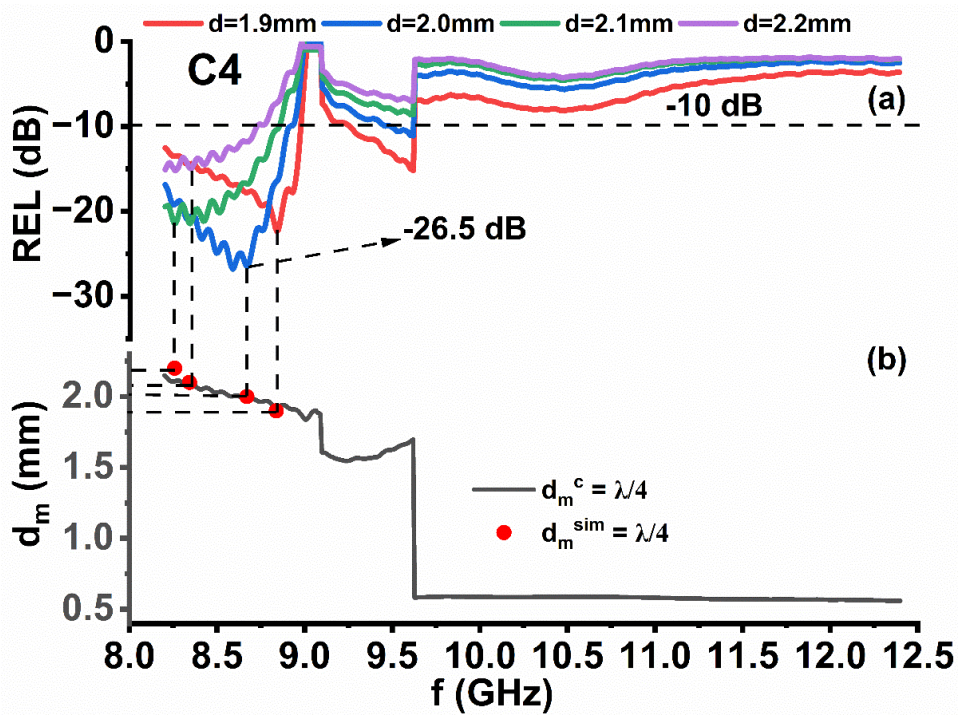


Fig. 4.90. (a, c, e) Dependence of REL on frequency in C3 sample. (b, d, f)  $d_m^{sim}$  and  $d_m^c$  versus frequency for  $5\lambda/4$  and  $9\lambda/4$  in the C3 sample.



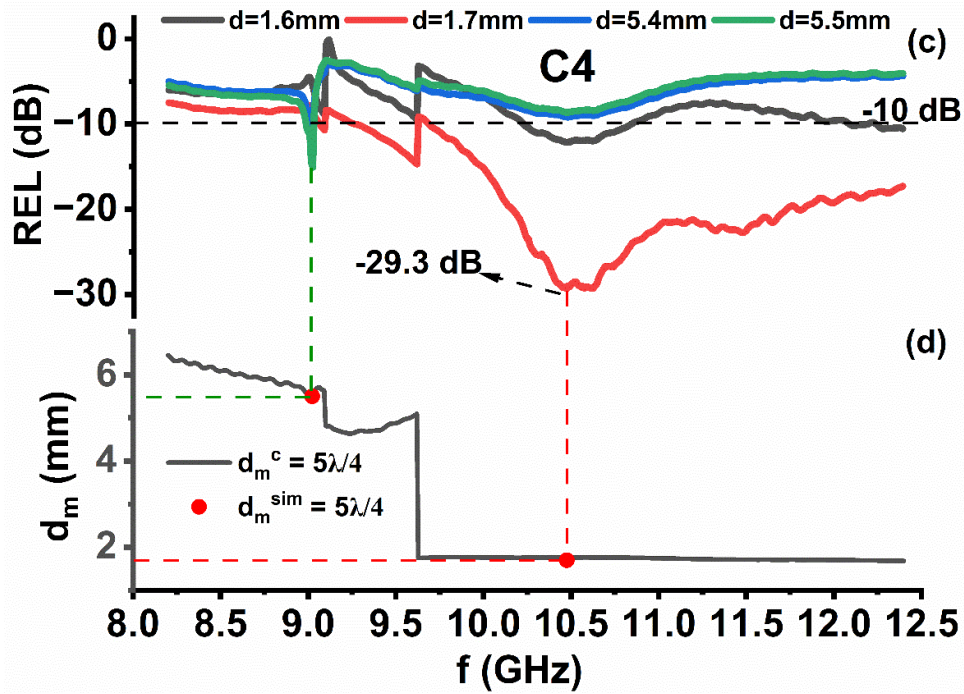
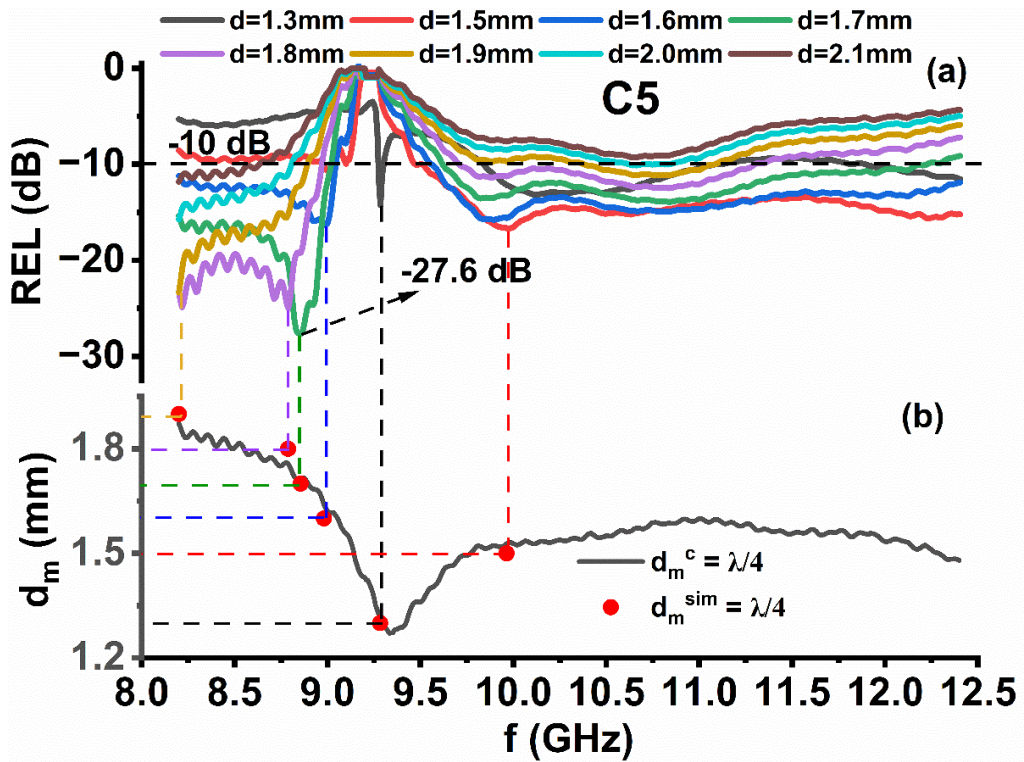
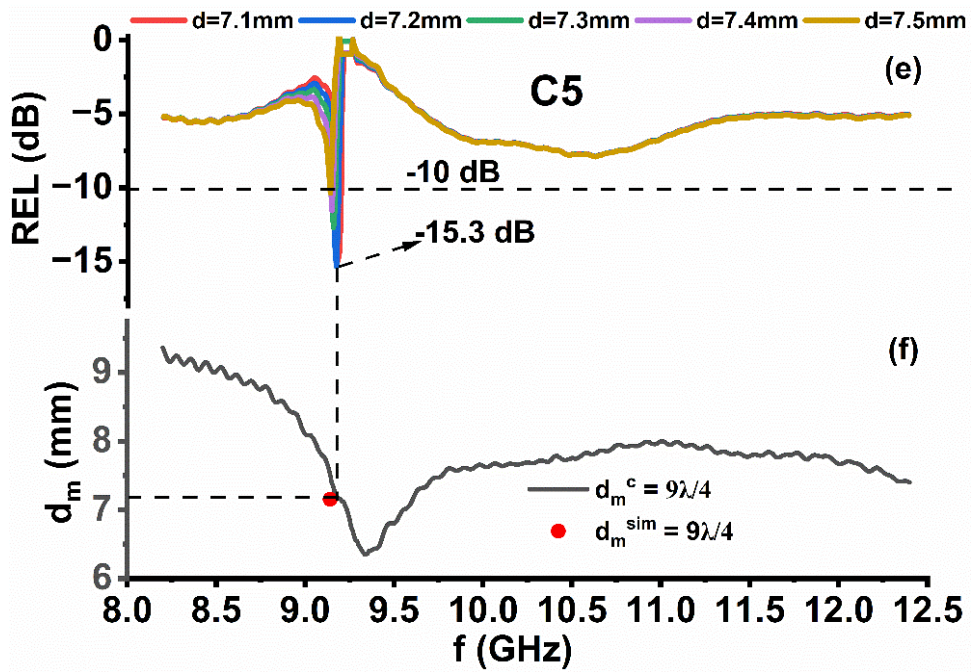
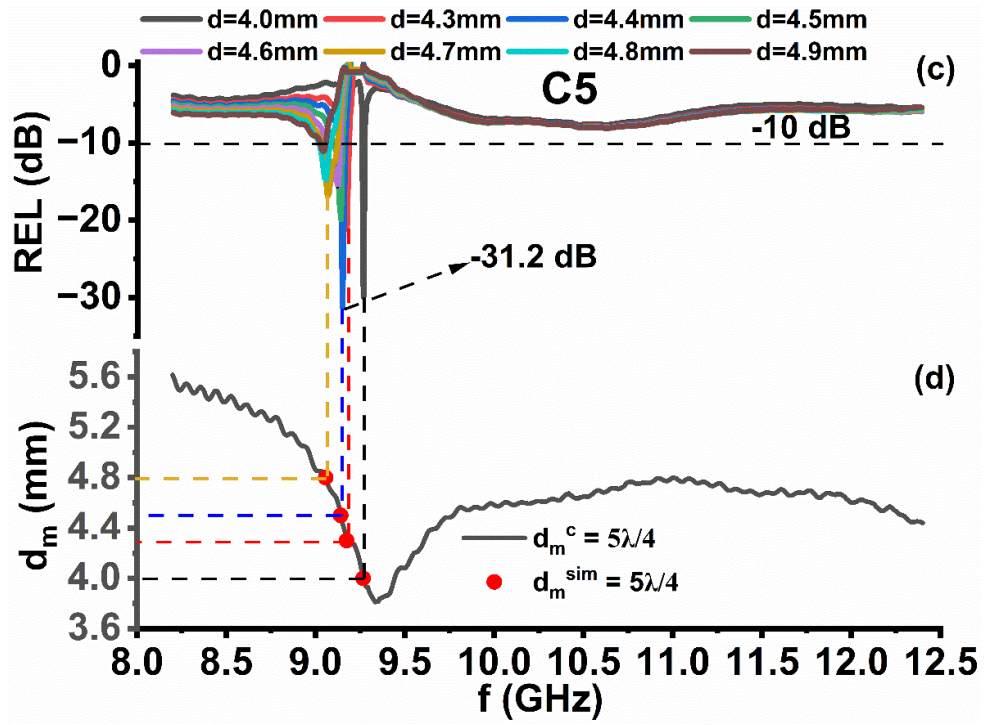
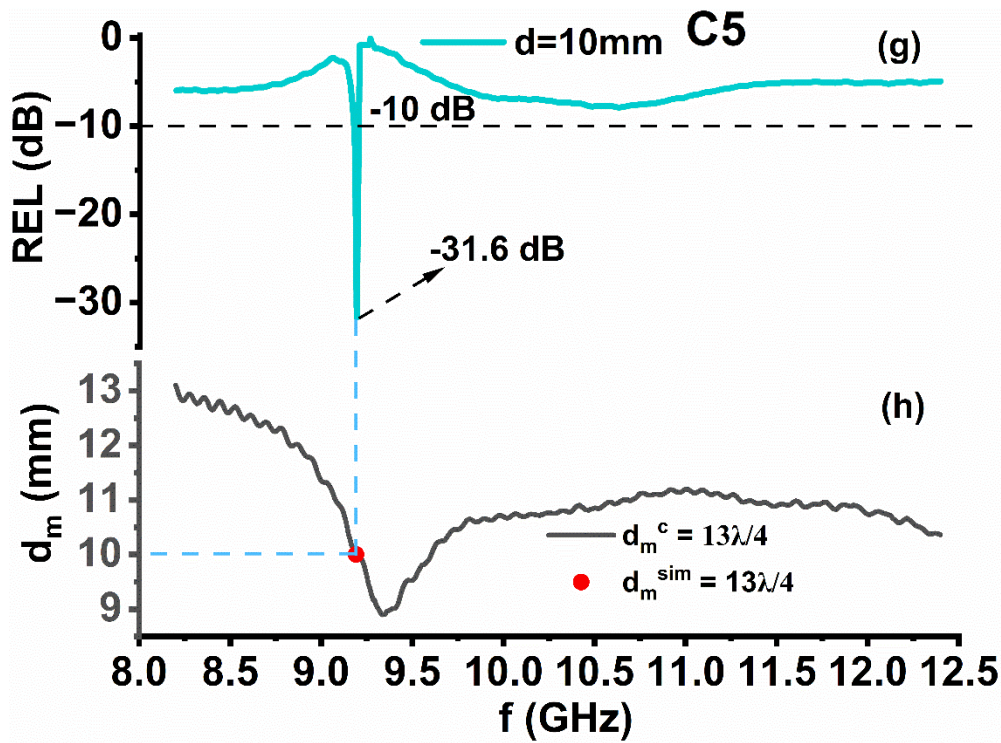


Fig. 4.91. (a, c) Dependence of REL on frequency in C4 sample. (b, d)  $d_m^{sim}$  and  $d_m^c$  versus frequency for  $\lambda/4$  and  $5\lambda/4$  in the C4 sample.









**Fig. 4.92.** (a, c, e, g) Dependence of REL on frequency in C5 sample. (b, d, f, h)  $d_m^{\text{sim}}$  and  $d_m^c$  versus frequency for  $\lambda/4$ ,  $5\lambda/4$ ,  $9\lambda/4$  and  $13\lambda/4$  in the C5 sample.

(iv) For the C4 sample, an optimal REL ( $-29.32\text{ dB}$ ) is observed in a low thickness of  $1.7\text{ mm}$  at  $10.47\text{ GHz}$ . The remaining thickness from  $1.6\text{ mm}$  to  $5.5\text{ mm}$  exhibits  $\text{REL} > -10\text{ dB}/-20\text{ dB}$  over the  $8.2$  to  $10.5\text{ GHz}$  frequency spectra. The obtained REL plots satisfy the quarter-wavelength mechanism ( $n\lambda/4$ ) for  $n=1$  and  $5$  values. Moreover, in the C5 sample REL non-linearly increases from  $-11.07\text{ dB}$  to  $-31.68\text{ dB}$  for  $1.3\text{ mm}$  to  $10\text{ mm}$  thickness. The obtained REL plots satisfy the quarter-wavelength mechanism ( $n\lambda/4$ ) for  $n=5, 9$ , and  $13$  values.

**Table 4.29** Absorption Parameters ( $\text{REL} > -10/-20\text{ dB}$ ).

Sample Name	Matching Thickness (mm)	Maximum REL (dB)	Matching frequency (GHz)	Frequency Band for REL $> -10\text{ dB}$ (GHz)	Bandwidth for REL $> -10\text{ dB}$ (GHz)	Frequency Band REL $> -20\text{ dB}$ (GHz)	Bandwidth for REL $> -20\text{ dB}$ (GHz)	BTR	PBW (%)
C1	7.5	-15.49	10.11	9.98-11.03	1.05	--	--	$3.8\text{E}-03$	10.38
	7.6	-19	10.10	9.94-11.04	1.10	--	--	$3.9\text{E}-04$	10.89
	7.7	-25.32	10.10	--	--	9.87-11.02	1.15	$4.1\text{E}-04$	11.38
	7.8	-41.42	10.10	--	--	9.84-11.02	1.18	$4.1\text{E}-04$	11.68

	7.9	-25.41	10.81	--	--	9.82-11.00	1.18	4.1E-04	10.91
	8.0	-31.93	10.75	--	--	9.83-10.97	1.14	3.9E-04	10.60
	8.1	-33.40	10.74	--	--	9.82-10.92	1.10	3.7E-04	10.24
	8.2	-22.90	10.74	--	--	9.83-10.92	1.09	3.7E-04	10.14
<b>C2</b>	1.5	-14.46	11.47	--	--	--	--	--	--
	1.6	-27.75	11.32	--	--	--	--	--	--
	1.7	-39.29	8.89	--	--	8.30-11.71	3.41	6.1E-03	38.35
	1.8	-54.04	8.62	--	--	--	--	--	--
	1.9	-20.04	8.42	--	--	--	--	--	--
	4.3	-11.10	12.38	--	--	--	--	--	--
	4.4	-12.4	12.22	12.03-12.32	0.29	--	--	1.3E-04	2.37
	4.5	-11.57	12.22	11.92-12.27	0.35	--	--	1.5E-04	2.86
	5.5	-10.30	8.21	--	--	--	--	--	--
	5.6	-11.03	8.21	--	--	--	--	--	--
	5.7	-11.49	8.2	--	--	--	--	--	--
	5.8	-11.12	8.2	--	--	--	--	--	--
	5.9	-10.89	8.2	--	--	--	--	--	--
<b>C3</b>	5.4	-10.42	17.94	--	--	--	--	--	--
	5.5	-10.50	17.94	--	--	--	--	--	--
	5.6	-10.44	17.49	--	--	--	--	--	--
	5.7	-10.47	17.26	--	--	--	--	--	--
	5.8	-10.26	16.52	--	--	--	--	--	--
	5.9	-11.03	16.52	--	--	--	--	--	--
	6.0	-11.53	16.34	15.72-16.68	0.96	--	--	1.8E-04	0.97
	6.1	-11.47	16.18	15.93-16.58	0.65	--	--	1.2E-04	0.61
	6.2	-12.27	15.64	15.23-16.45	1.22	--	--	2.3E-04	1.21
	6.3	-12.91	15.64	14.77-16.19	1.42	--	--	2.8E-04	1.40
	6.4	-13.01	15.52	14.48-16.01	1.53	--	--	3E-04	1.48
	6.7	-16.10	14.69	13.57-15.51	1.94	--	--	4.1E-04	1.90
	6.8	-18.89	14.16	13.09-15.28	2.19	--	--	4.8E-04	2.25
	6.9	-22.05	14.16	--	--	12.90-15.12	2.22	4.9E-04	2.25
	7.0	-22.53	14.10	--	--	12.48-15.01	2.53	5.7E-04	2.55
	7.1	-19.82	14.10	--	--	--	--	--	--
	7.2	-19.12	13.29	--	--	--	--	--	--
	7.3	-20.46	13.21	--	--	--	--	--	--
	7.4	-20.15	13.15	--	--	--	--	--	--
	7.5	-21.14	12.68	--	--	--	--	--	--

	7.6	-23.48	12.52	--	--	--	--	--	--
	7.7	-22.95	12.52	--	--	--	--	--	--
	7.8	-21.03	12.43	--	--	--	--	--	--
	7.9	-18.21	12.41	--	--	--	--	--	--
	8.0	-15.81	12.4	--	--	--	--	--	--
	8.1	-13.87	12.4	--	--	--	--	--	--
	8.2	-12.30	12.4	--	--	--	--	--	--
	8.3	-11.02	12.4	--	--	--	--	--	--
	8.6	-10.02	18	--	--	--	--	--	--
	8.7	-11.89	18	--	--	--	--	--	--
	8.8	-14.37	18	--	--	--	--	--	--
	8.9	-17.75	18	--	--	--	--	--	--
	9.0	-21.67	18	--	--	--	--	--	--
	9.1	-22.70	17.92	--	--	--	--	--	--
	9.2	-21.92	17.70	--	--	--	--	--	--
	9.3	-22.16	17.49	--	--	--	--	--	--
	9.4	-22.51	17.38	--	--	--	--	--	--
	9.5	-22.35	17.21	--	--	16.37-17.99	1.62	1.7E-04	0.98
	9.6	-21.04	17.07	--	--	16.16-17.85	1.69	1.8E-04	0.99
	9.7	-20.42	16.86	--	--	16.00-17.68	1.68	1.8E-04	1.00
	9.8	-21.99	16.66	--	--	15.87-17.44	1.57	1.7E-04	0.96
	9.9	-25.32	16.52	--	--	15.69-17.35	1.66	1.8E-04	0.96
	10	-27.17	16.37	--	--	15.53-17.17	1.64	1.8E-04	0.90
<b>C4</b>	1.6	-12.15	10.47	10.23-10.84	0.61	--	--	1E-03	5.82
	1.7	-29.32	10.47	--	--	--	--	--	--
	1.9	-22.34	8.83	--	--	--	--	--	--
	2.0	-26.52	8.67	--	--	--	--	--	--
	2.1	-21.44	8.34	--	--	--	--	--	--
	2.2	-15.18	8.25	--	--	--	--	--	--
	5.4	-11.94	9.01	--	--	--	--	--	--
	5.5	-15.08	9.02	--	--	--	--	--	--
<b>C5</b>	1.3	-14.26	9.28	--	--	--	--	--	--
	1.5	-16.71	9.96	--	--	--	--	--	--
	1.6	-16.32	8.98	--	--	--	--	--	--
	1.7	-27.67	8.85	--	--	--	--	--	--
	1.8	-24.98	8.78	--	--	--	--	--	--
	1.9	-23.36	8.2	--	--	--	--	--	--



	2.0	-15.75	8.2	--	--	--	--	--	--
	2.1	-11.83	8.2	--	--	--	--	--	--
	4.0	-29.95	9.26	--	--	--	--	--	--
	4.3	-21.14	9.17	--	--	--	--	--	--
	4.4	-31.23	9.14	--	--	--	--	--	--
	4.5	-19.90	9.14	--	--	--	--	--	--
	4.6	-15.6	9.14	--	--	--	--	--	--
	4.7	-16.89	9.06	--	--	--	--	--	--
	4.8	-14.74	9.11	--	--	--	--	--	--
	4.9	-11.07	9.11	--	--	--	--	--	--
	7.1	-14.92	9.18	--	--	--	--	--	--
	7.2	-15.31	9.17	--	--	--	--	--	--
	7.3	-12.69	9.15	--	--	--	--	--	--
	7.4	-11.55	9.14	--	--	--	--	--	--
	7.5	-10.36	9.14	--	--	--	--	--	--
	10	-31.68	9.19	--	--	--	--	--	--

Table 4.29 enumerates the value of BTR and PBW of all synthesized samples calculated using equations 3.25 and 3.26. The BTR is highest in the C2 sample with values of 6.1E-03 and PBW (38.3 %) at 8.89 GHz and REL = -39.2 dB at 1.7 mm thickness.

Table 4.30 presents the  $Z_{in}/Z_0$  and  $Z_{real}/Z_{img}$  values corresponding to the REL peak of the synthesized composite materials. These impedance values are calculated using equation 3.21. Impedance matching plays an indispensable role of absorbing the incoming EM waves. When  $Z_{in}/Z_0 \cong 1$  i.e.,  $Z_{real} \cong 1$  and  $Z_{img} \cong 0$ , the incoming EM wave can effectively penetrate the absorbing material and be attenuated by dielectric and magnetic losses. Sample C2 demonstrates the highest REL= -54.04 dB at a thickness of 1.8 mm and a frequency of 8.62 GHz, with a  $Z_{in}/Z_0$  value is approximately 1.003, wherein  $Z_{real} = 1.003$  (close to 1) and  $Z_{img} = 2E-05$  (nearly 0). On the contrary, when the value of  $Z_{in}/Z_0$  deviates significantly from 1; a substantial portion of the incoming waves is reflected, regardless of their intrinsic attenuation capability, they fail to provide appropriate MWA performance. It is essential to note that while  $Z_{in}/Z_0 \cong 1$  may be the case,  $Z_{real}/Z_{img}$  is far away from 1 and or/0, and an effective reflection loss is not observed. As the  $Z_{real}/Z_{img}$  values deviate further from 1 and/or zero, the remaining thickness of all synthesized samples exhibits relatively low REL values. The value of  $Z_{in}/Z_0$  changes with Co-Cd ions substitution.

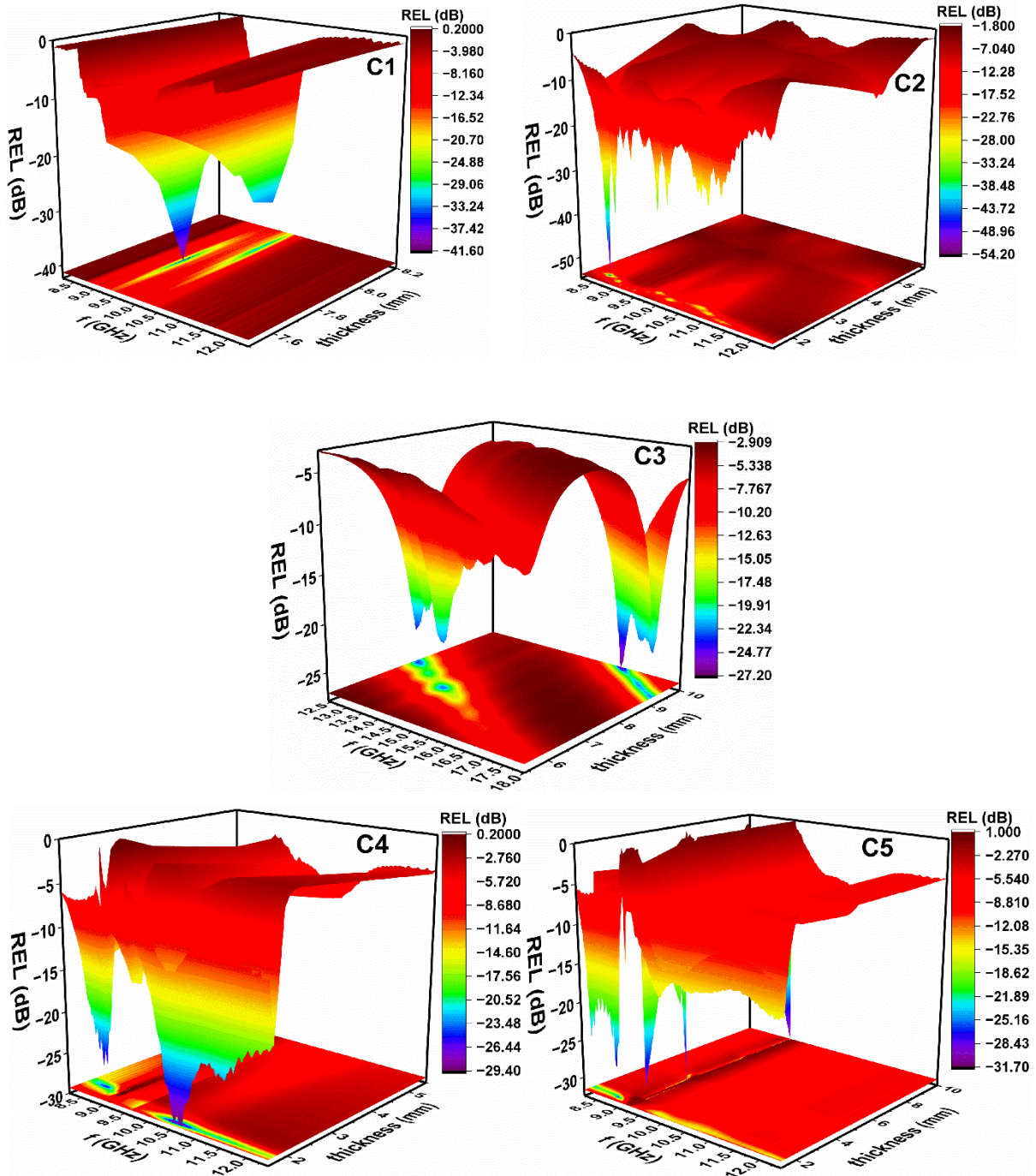


Fig. 4.93. 3D plots of REL at various thicknesses and frequencies for all samples.

**Table 4.30** Reflection loss peak's impedance parameters at different thicknesses.

Sample Name	Thickness (mm)	Max. REL (dB)	Matching frequency (GHz)	$Z_{in}/Z_0$	$Z_{real}$	$Z_{img}$
<b>C1</b>	7.7	-25.32	10.10	0.970	0.965	0.100
	7.8	-41.42	10.10	0.987	0.987	-0.010
	7.9	-25.41	10.81	1.096	1.094	0.060
	8.0	-31.93	10.75	1.009	1.008	0.050
	8.1	-33.40	10.74	0.973	0.973	-0.032
	8.2	-22.90	10.74	0.951	0.943	-0.127
<b>C2</b>	1.5	-14.46	11.47	1.194	1.129	0.389
	1.6	-27.75	11.32	1.081	1.081	-0.026
	1.7	-39.29	8.89	0.988	0.988	0.018
	1.8	-54.04	8.62	1.003	1.003	2E-05
	1.9	-20.04	8.42	1.055	1.035	-0.200
<b>C3</b>	6.9	-22.05	14.16	1.152	1.149	0.080
	7.0	-22.53	14.10	1.154	1.153	-0.048
	7.6	-23.48	12.52	1.135	1.134	0.047
	7.7	-22.95	12.52	1.133	1.131	-0.076
	9.3	-22.16	17.49	1.163	1.162	0.043
	9.4	-22.51	17.38	1.161	1.161	-0.012
<b>C4</b>	9.5	-22.35	17.21	1.164	1.164	-0.016
	1.7	-29.32	10.47	1.002	1.000	0.068
	1.9	-22.34	8.83	1.142	1.137	0.102
	2.0	-26.52	8.67	1.096	1.095	-0.036
	2.1	-21.44	8.34	1.135	1.128	-0.127
<b>C5</b>	2.2	-15.18	8.25	1.102	1.039	-0.365
	1.7	-27.67	8.85	1.002	0.998	0.082
	1.8	-24.98	8.78	0.921	0.9168	-0.071
	1.9	-23.36	8.2	0.911	0.907	-0.090
	4.0	-29.95	9.26	0.956	0.955	0.043
	4.3	-21.14	9.17	1.191	1.191	0.009
	4.4	-31.23	9.14	0.761	0.723	0.238
10	-31.68	9.19	1.018	1.017	-0.049	

Conclusively, in all Co- Cd substituted samples more than 99 % absorption has been observed such as REL = -41.4 dB, -54 dB, -27.17 dB, -29.32 dB, and -31.68 dB of C1, C2, C3, C4, and C5 samples, respectively. Several factors are responsible for the adequate absorption performance of synthesized samples, such as atomic mass and ionic radii of substituted and host ions, porosity, magnetic loss, and dipole polarization. It can be seen (Fig. 4.72) in the C2 sample, wherein large no. of small grains are engaged with one another over long distances by involving several voids. These voids contribute to demagnetizing the field and impediment to the applied field, resulting in a dilution in permeability. For C3, C4, and C5 samples, substitution causes agglomeration of grains in the form of large-sized grains with uneven size distribution. Furthermore, an increment in the degree of substitution and the existence of secondary phase from C3 to C5 causes densification in grains, which enhances the complex permeability/permittivity parameters at a certain frequency. Substitution enhances the dielectric/ magnetic loss in C4 and C5 samples around 9-10 GHz, but  $REL_{max}$  is observed in the C2 sample, and this behavior can be well understood with impedance matching and quarter wavelength mechanism.

#### 4.5 $SrCo_{1.5z}La_{0.5z}Fe_{12-2z}O_{19}$ (80%) + $Fe_3O_4$ (20%) ferrite composites

A physical blending method has been utilized to synthesize hexaferrite composites. In this study, we comprehensively analyzed structural, morphological, magnetic, electrical, and microwave absorption properties. Table 4.31 displays the assignment of sample names/codes for a different level of substitution for  $Fe_3O_4/SrCo_{1.5z}La_{0.5z}Fe_{12-2z}O_{19}$ .

**Table 4.31** Assignment of sample name for a different level of substitution of  $Fe_3O_4/SrCo_{1.5z}La_{0.5z}Fe_{12-2z}O_{19}$  ferrite composites.

Sample Composition $Fe_3O_4/SrCo_{1.5z}La_{0.5z}Fe_{12-2z}O_{19}$	Sample Code (DM-series)
$z = 0.0$	DM1
$z = 0.1$	DM2
$z = 0.2$	DM3
$z = 0.3$	DM4
$z = 0.4$	DM5
$z = 0.5$	DM6

## 4.5.1 Structural Analysis

### 4.5.1.1 X-ray Analysis

The diffraction pattern of the synthesized composites as a function of Co-La ions is presented in Fig. 4.91. XRD affirms the co-existence of both SrM hexaferrite (ICDD# 80-1197) and Fe<sub>3</sub>O<sub>4</sub> (ICDD# 65-3107) in the vicinity of each other. The refinement analysis using MAUD software affirms the existence of both SrM hexaferrite (ICDD# 80-1197) and Fe<sub>3</sub>O<sub>4</sub> (ICDD# 65-3107) in the vicinity of each other, as seen in Fig. 4.92 [304]. It also indicates an insignificant impurity phase (minor phase) of hematite ( $\alpha$ -Fe<sub>2</sub>O<sub>3</sub>) in the DM1 sample and this phase disappears as the content of Co-La increases. This gives evidence that blending in mortar pestle is an appropriate approach for preparing composite without any distortion in the intrinsic structure. The crystallite size and lattice parameters of both hexaferrite and spinel ferrite have been calculated by Rietveld refinement analysis and tableted in Table 4.32 [305]. The change observed in the intensity of the peaks and the lattice size at the transition from DM1 to DM6 indicates the successful substitution of  $Co^{2+} - La^{3+}$  ions at crystallographic sites [306] [126].

**Table 4.32** Values of the lattice constant of M-type hexagonal and spinel ferrite

Sample name	$\chi^2$ (Goodness of fit)	M-type Hexaferrite			Spinel ferrite	
		a=b (Å)	c (Å)	D (nm)	a=b=c (Å)	D (nm)
DM1	0.711	5.884	23.059	49.39	8.398	11.82
DM2	1.816	5.880	23.040	31.54	8.395	12.25
DM3	0.812	5.882	23.045	21.75	8.396	14.34
DM4	1.075	5.882	23.039	18.55	8.396	10.42
DM5	1.028	5.883	22.039	20.97	8.395	18.44
DM6	0.757	5.883	23.036	11.09	8.396	10.03

The value of the 'c' parameter ranges from 23.05 to 23.03 Å, while the lattice parameter 'a' varies from 5.884 to 5.880 Å as the degree of substitution increases. These results clearly show that the expansion in the lattice parameter 'a' is lesser than that of the parameter 'c' which is consistent with the conventional behavior of SrM hexaferrite[307]. This can be elucidated that the c-axis, which is easily magnetized, expands more than the a-

axis. Whereas the lattice parameter of spinel ferrite feebly changes with Co-La substitution. The average crystallite size has been calculated using Scherrer's Eq. 3.3. and it ranges from 49.39 to 11.09 nm for M-type hexaferrite, while the crystallite size of spinel ferrite is in the range of 18.34 to 10.03 nm.

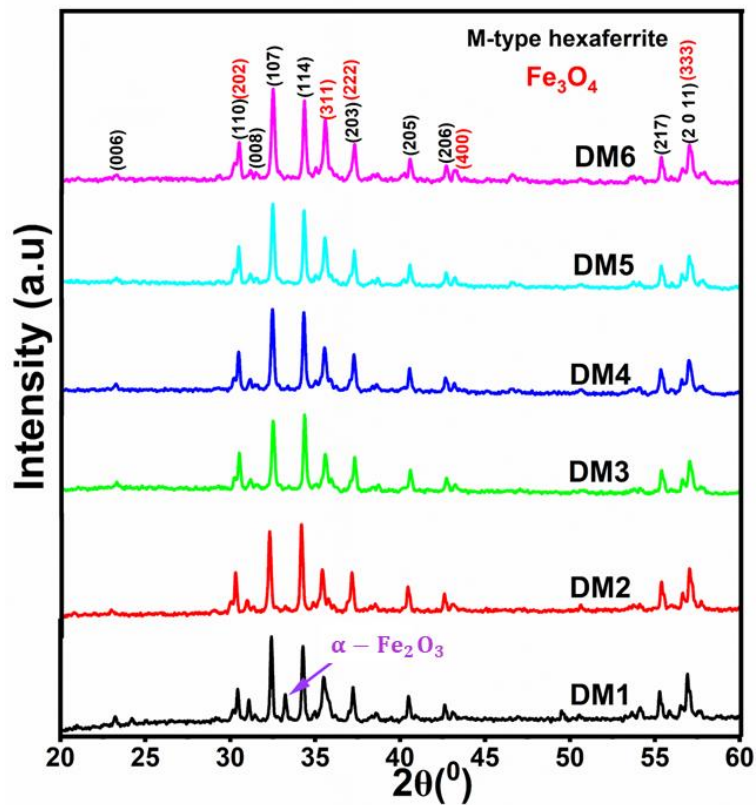
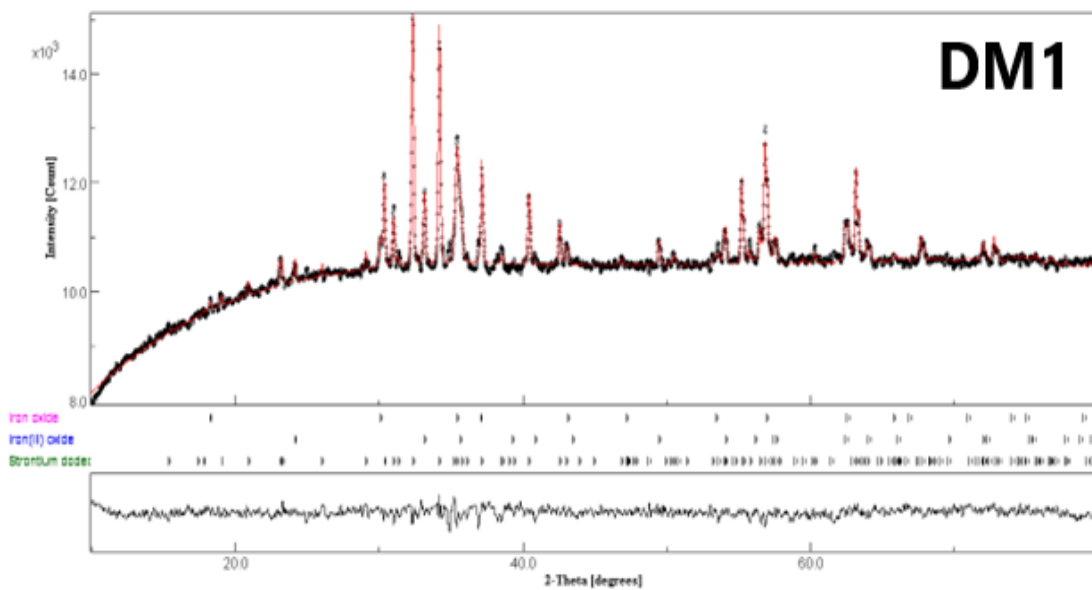
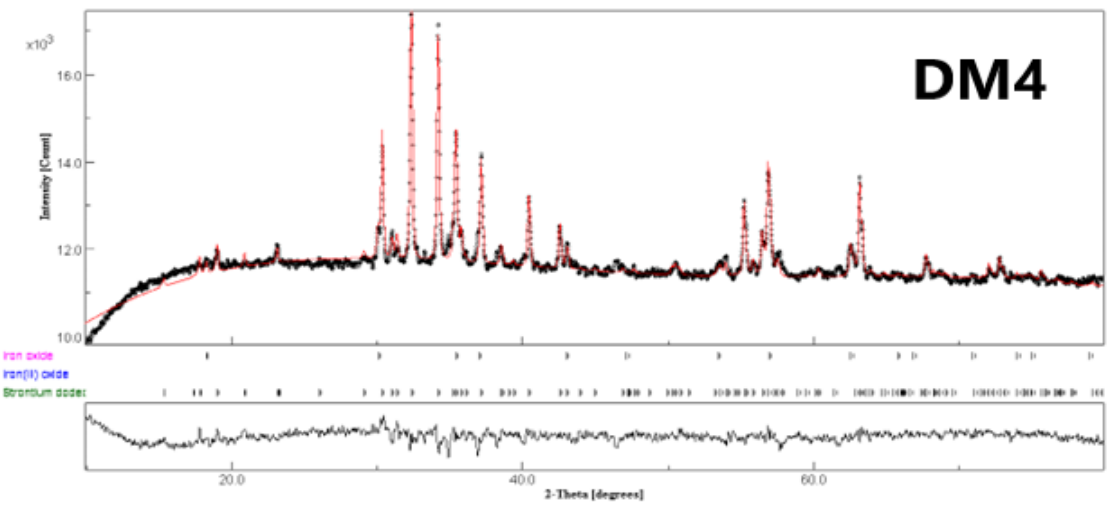
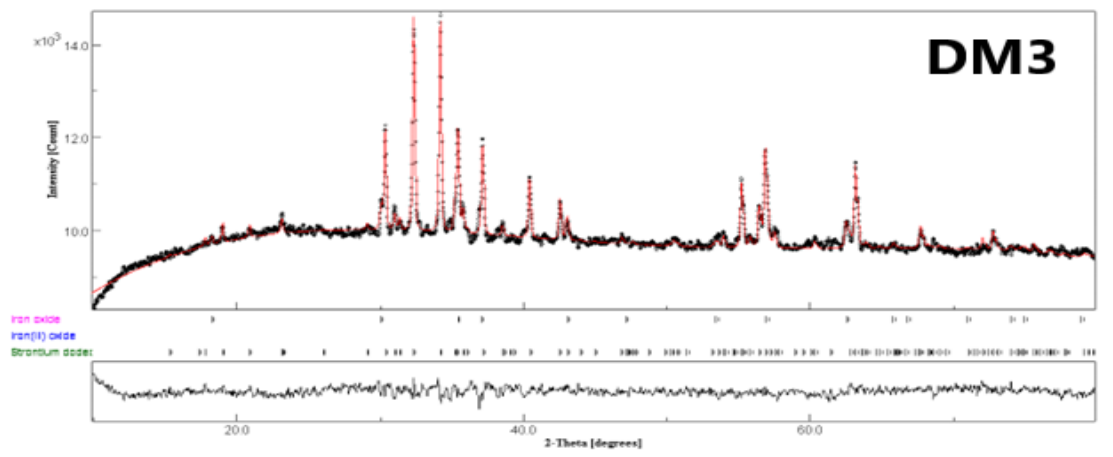
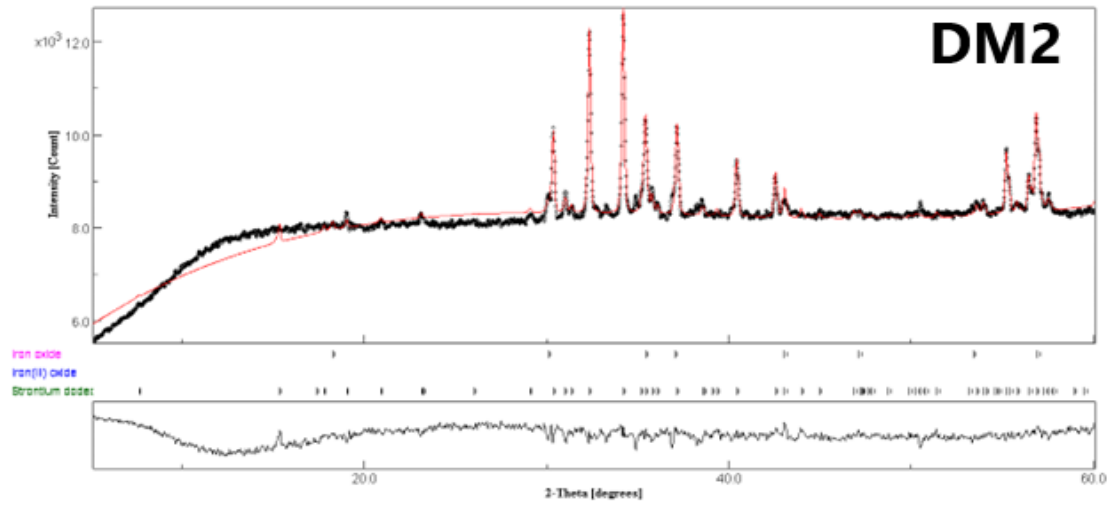
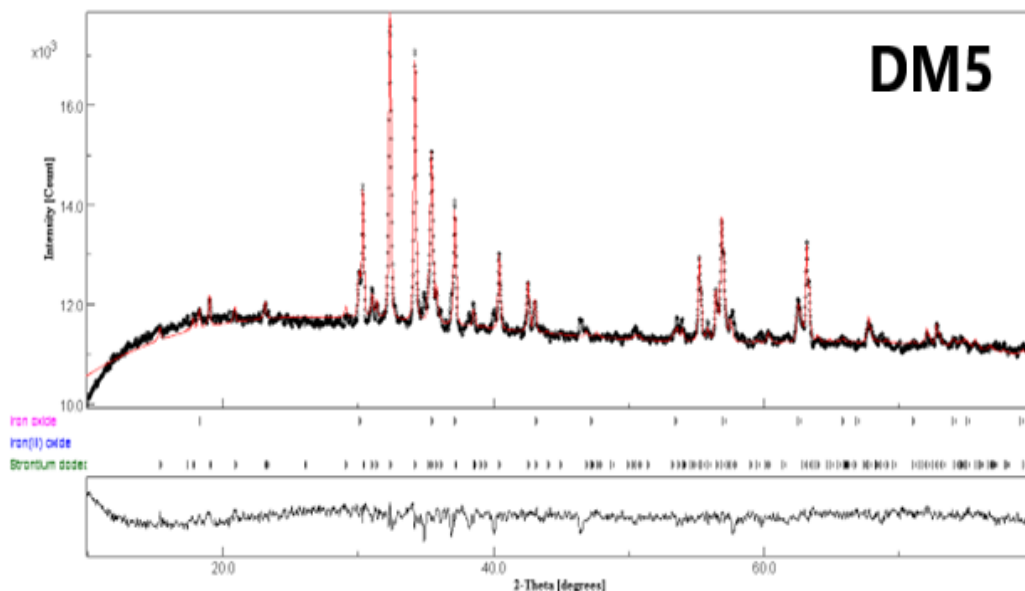


Fig. 4.94. XRD pattern of DM1, DM2, DM3, DM4, DM5 and DM6 ferrite composites.









**Fig. 4.95.** Rietveld refinement of all DM-series samples.

#### 4.5.1.2 FTIR analysis

The FTIR spectra of prepared DM-series samples were meticulously examined across the IR range, spanning from 3000 to 400  $\text{cm}^{-1}$ , as illustrated in Fig. 4.93. To elucidate the position of absorption bands achieved in the IR spectrum within the 600-400  $\text{cm}^{-1}$  range, for different levels of substitution refer to Table 4.33. Notable there are no absorption bands in between 1300 to 3000  $\text{cm}^{-1}$  range, signifying the absence of nitrates, C-H bending vibration, and O-H vibrations. Within the range of 400-800  $\text{cm}^{-1}$ , a distinctive set of resolved absorption bands is observed as listed in Table 4.33. The observed bands lie in the range of 500-600  $\text{cm}^{-1}$  representing mode  $\nu''$  and are owed to stretching vibrations of  $\text{Fe}^{3+}$ - $\text{O}^{2-}$  at tetrahedral sites. Other absorption bands from 400-450  $\text{cm}^{-1}$  represent mode  $\nu'$  and are due to vibrations of  $\text{Fe}^{3+}$ - $\text{O}^{2-}$  at octahedral crystallographic sites of crystal structure. Furthermore, the substitution of  $\text{Co}^{2+}$  and  $\text{La}^{3+}$  ions alter the band position of tetrahedral and octahedral sites towards a higher frequency side and confirm the successful substitution of  $\text{Co}^{2+}$  - $\text{La}^{3+}$  ions in crystallographic sites.

**Table 4.33** FTIR spectra details of DM1, DM2, DM3, DM4, DM5 and DM6 ferrite composites.

Sample name	Fe – O vibrations at		
	Octahedral sites (400-450 $cm^{-1}$ )	Tetrahedral sites (500-600 $cm^{-1}$ )	
DM1	420	539	580
DM2	422	542	584
DM3	421	545	583
DM4	420	545	582
DM5	421	546	582
DM6	422	547	583

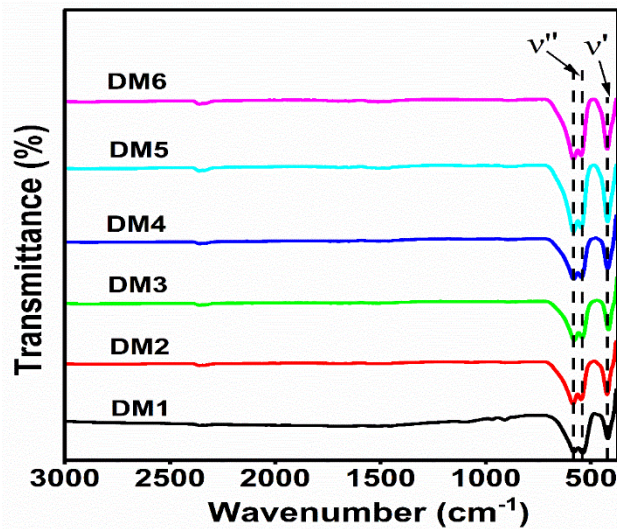


**Fig. 4.96.** FTIR spectra of DM-series ferrite composites.

#### 4.5.1.3 FESEM analysis

The FESEM micrographs in Fig. 4.94 exhibit hexagonal platelet-shaped particles along with randomly oriented and small cubical-shaped grains for all samples [308]. In the DM1 sample, fine particles with well-defined grain boundaries in the form of local clusters are observed, while larger particles display soft agglomeration due to interactions between neighboring particles [309]. This result is consistent with the crystallized size obtained from XRD, wherein the crystallite size of M-type hexaferrite is larger than spinel ferrite, as seen in Table 4.32. The insertion of Co-La ions into ferrite composites leads to an insignificant difference in the morphology of M-type hexagonal and spinel ferrites. This can also be confirmed through the crystallite size calculated from XRD data. The magnetic

agglomeration causes tiny crystals to merge and form larger particles. Substitution of Co-La ions improves the inter-grain connectivity and also increases the porosity. A magnified view of FESEM images affirms the formation of stacking layers of grains. Due to the finite separation between the layers, they do not significantly contribute to the polarization and conductivity phenomena of the synthesized samples. The EDX spectra and elemental mapping envisaged the stoichiometry of hard/soft (20%  $\text{Fe}_3\text{O}_4$  of  $\text{SrCo}_{0.3}\text{La}_{0.1}\text{Fe}_{11.6}\text{O}_{19}$ ) hexaferrite composite is shown in Fig. 4.95. The preparation method pertinent to synthesized hard/soft hexaferrite composite is worthwhile due to the existence of Sr, La, Co, Fe, and O elements in EDX spectra. Fig. 4.96 shows the schematic diagram of changing the individual phase to the composite phase.

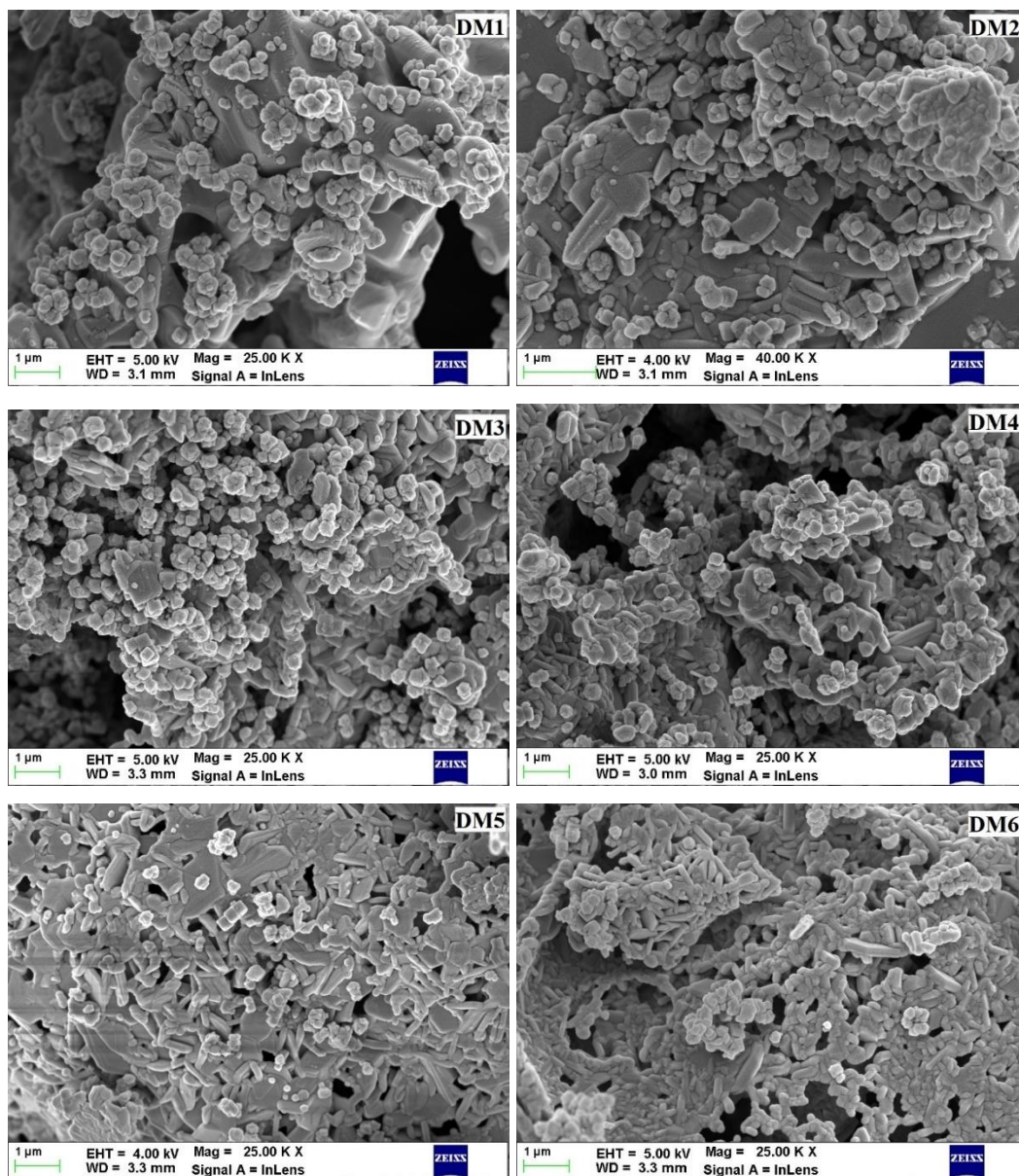


**Fig. 4.97.** FESEM micrographs of DM1, DM2, DM3, DM4, DM5 and DM6 ferrite composites.



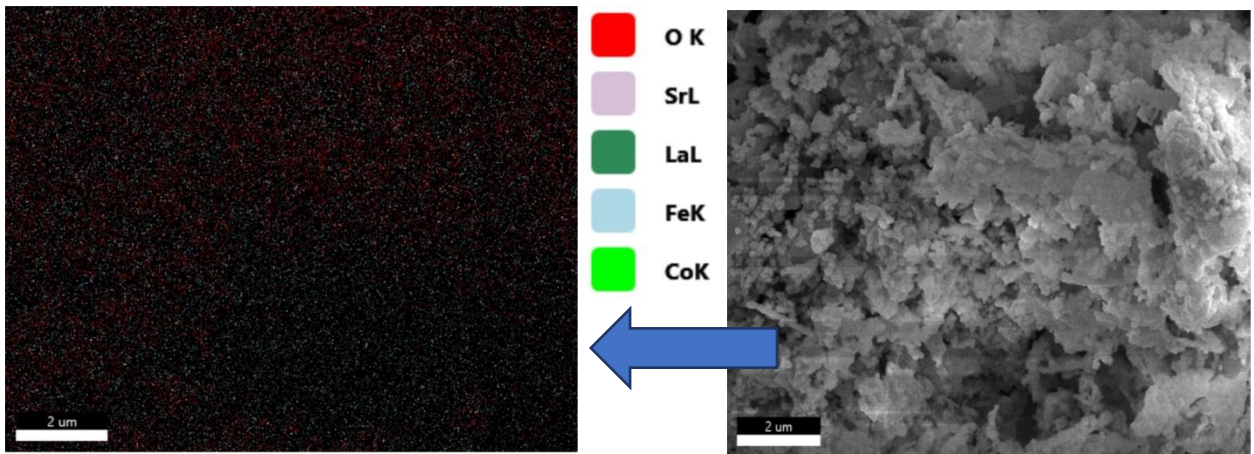
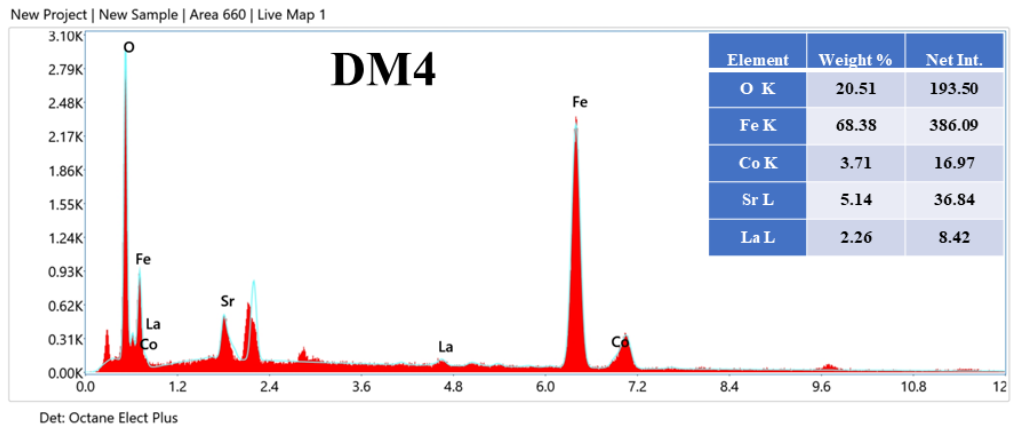


Fig. 4.98. EDX spectra and elemental mapping of DM3 ferrite composite.

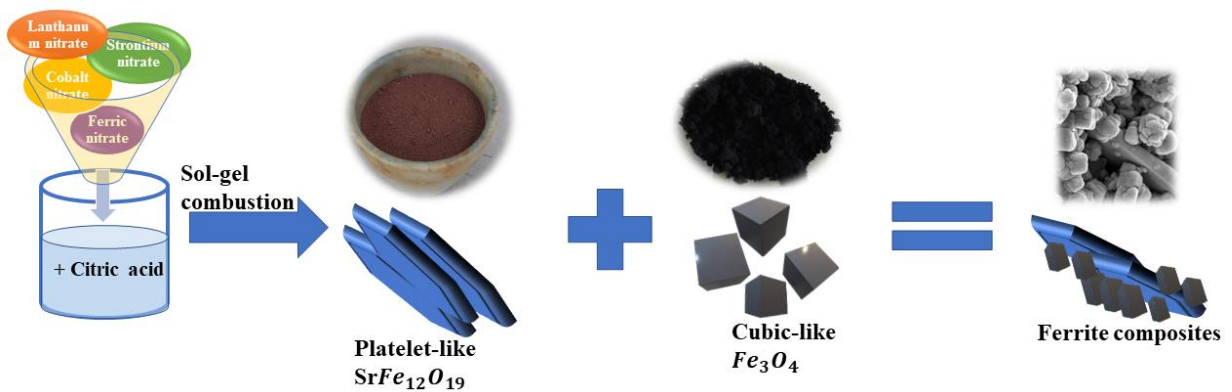


Fig. 4.99. Schematic showing morphology changes from individual hard and soft phases to composites.

## 4.5.2 Electrical Analysis

### 4.5.2.1 Dielectric constant

Fig. 4.97(a) illustrates the dispersion of  $\epsilon'$ , as a function of frequency and composition in the frequency range 100Hz to 2MHz. At lower frequencies, the relative dielectric constant changes with a frequency that affirms the existence of electrode interfacial polarization processes, and it becomes frequency-independent at higher frequencies ( $>10^5$  Hz). It can be well explained with Koop's phenomenological and Maxwell-Wagner models (discussed in section 4.1.2.1). Fig. 4.97(a) illustrates a non-linear increment in  $\epsilon'$  value of synthesized hexaferrite composites from DM1 to DM6 samples. The lowest frequency dependence of dielectric dispersion is observed in DM4 and DM6 samples. This can be determined by the availability of  $\text{Fe}^{2+}$  ions at octahedral sites. The increment in  $\epsilon'$  value of DM2, DM3, and DM5 with  $\text{Co}^{2+}$  and  $\text{La}^{3+}$  substitution can be explained by the electrons hopping between octahedral positions. However, due to larger ionic radii of  $\text{Co}^{2+}$  and  $\text{La}^{3+}$  ions than  $\text{Fe}^{3+}$  ions, and diamagnetic behavior of  $\text{La}^{3+}$  (due to  $0\mu_B$  magnetic moment), they tend to occupy octahedral lattice sites, which indicates a reduction in electron hopping. While large no. of  $\text{Fe}^{3+}$  ions are relocating at octahedral from a tetrahedral position due to the substitution of  $\text{Co}^{2+}$  ions (tendency to occupy both tetrahedral and octahedral lattice sites),  $\text{La}^{3+}$  ions can also occupy tetrahedral sites (due to less electronegativity). Hence, the Co-La substitution observes an overall non-linear variation in  $\epsilon'$  values. The behavior of  $\epsilon''$  as a function of frequency is depicted in Fig. 4.97(b). The plotted curves of DM3, DM4, and DM5 samples show a similar profile to that of  $\epsilon'$ , with lower  $\epsilon''$  values observed in the lower frequency range, which become frequency-independent beyond a specific limiting frequency [310]. On the other hand, DM1, DM2, and DM6 samples exhibit a peak in a certain frequency range, which indicates the presence of a resonance or relaxation phenomenon in the material. Materials with heterogeneous structures or interfaces, such as composites or materials with layered structures, can exhibit peaks in the  $\epsilon''$  plots with frequency. These peaks are related to interfacial polarization effects, where energy is dissipated as charges redistribute across the interfaces.



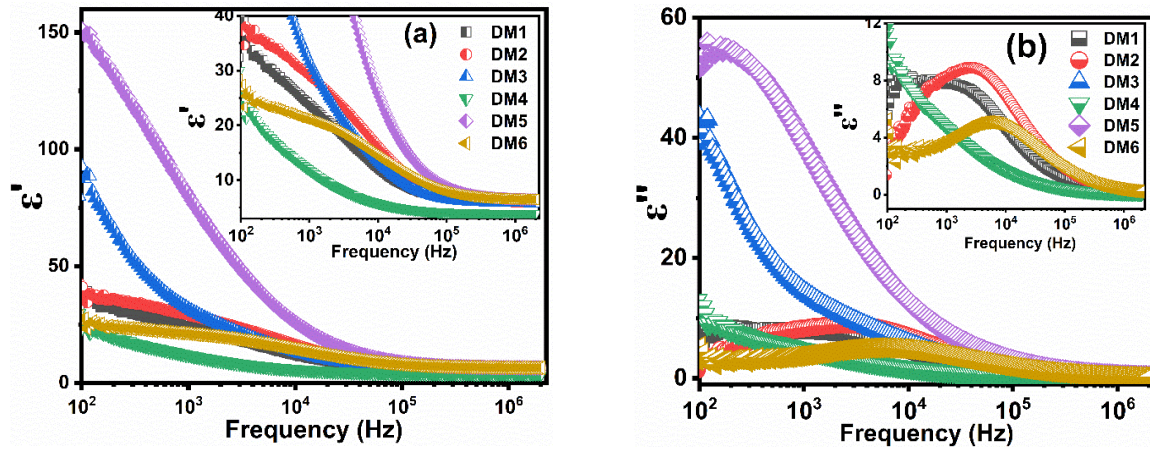


**Fig. 4.100.** (a)  $\epsilon'$  variation and (b)  $\epsilon''$  variation with frequency of DM1, DM2, DM3, DM4, DM5 and DM6 ferrite composites.

#### 4.5.2.2 Loss tangent

Fig. 4.98 displays the frequency-dependent  $\tan\delta$  curves for the synthesized hexaferrite composites. The substitution of Co-La ions contributes to a non-linear change in  $\tan\delta$  values. This could be explained by the site occupancy of Co-La ions in crystallographic lattice sites, which increase or decrease the no. of  $\text{Fe}^{3+}$  ions at the octahedral position [283]. A dielectric relaxation peak in a certain frequency range is observed for all, indicating a distribution of relaxation times. Substitution promotes heterogeneity in the synthesized composites, which results in multi-interfacial relaxation in DM3 and DM4 samples. The relative change in the peak height and peak broadening is attributed to oxygen vacancies created during substitution. The synthesized ferrite composites contain both hard/soft ferrite (20%  $\text{Fe}_3\text{O}_4$  of  $\text{SrCo}_{1.5z}\text{La}_{0.5z}\text{Fe}_{12-2z}\text{O}_{19}$ ), the exchange coupling between these two phases can alter the overall dielectric constant and loss tangent of the individual ferrite phases. Depending on the ratio of these phases, the overall dielectric constant can be higher or lower than that of the constituent materials. The addition of  $\text{Fe}_3\text{O}_4$  ferrite offers both  $\text{Fe}^{2+}$  and  $\text{Fe}^{3+}$  ions in the synthesized samples. Indeed,  $\text{Fe}^{2+}$  ions are highly polarizable which promotes polarization and plausibly enhances dielectric constant and loss tangent.

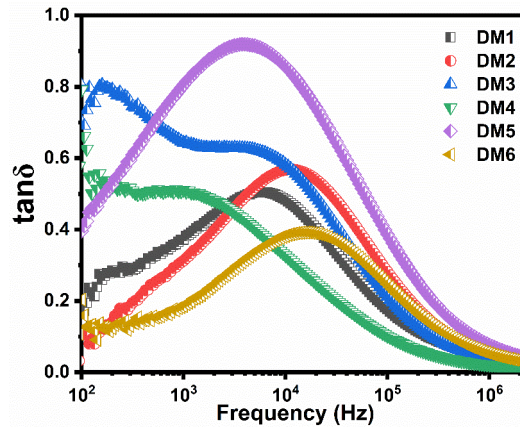


**Fig. 4.101.**  $\tan \delta$  variation with frequency of DM1, DM2, DM3, DM4, DM5 and DM6 ferrite composites.

### 4.5.2.3 AC conductivity

Fig. 4.99 displays the increase in ac conductivity ( $\sigma$ ) of hexaferrite composites as the applied frequency increases. The replacement of  $\text{Fe}^{3+}$  ions with Co-La ions causes a reduction in conductivity value and is maximum for the DM5 sample. This reduction elucidates a decrement in the concentration of  $\text{Fe}^{3+}$  ions at an octahedral position, which restricts the probability of hopping between  $\text{Fe}^{2+}$  and  $\text{Fe}^{3+}$  ions [311]. The decrement observed in the value of  $\sigma_{ac}$  at higher frequency region with substitution of Co-La ions can be easily explained through the FESEM micrographs of synthesized composites (Fig. 4.94). The maximum value of  $\sigma$  in the DM5 sample is due to the good inter-grain connectivity between large and small-sized grains, over other substituted composites. It can also be due to the synergistic effect caused by adding  $\text{Fe}_3\text{O}_4$ , which is suppressed at DM6 (due to the substitution of Co-La ions) despite the same concentration of  $\text{Fe}_3\text{O}_4$ .

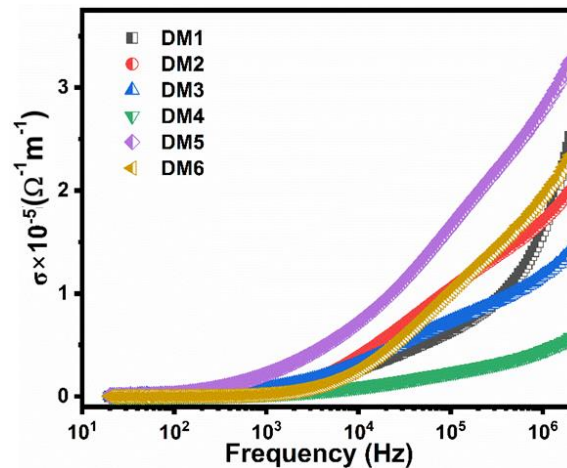


**Fig. 4.102.**  $\sigma$  variation with frequency of DM1, DM2, DM3, DM4, DM5 and DM6 ferrite composites.

#### 4.5.2.4 Complex electric modulus analysis

Fig. 4.100(a) delineates the variation of  $M'$  as a function of frequency. The  $M'$  values of all synthesized hexaferrite composites approach zero at lower frequencies, indicating a maximum dipolar polarization force and minimal electrode polarization distribution and conductivity [187]. However, as the frequency increases, the  $M'$  values gradually increase and eventually level off at a saturation point (represented by  $M_\infty$ ). This suggests increased conduction and short-range mobility of charge carriers, with less restoring force acting on them [312]. This behavior aligns with the AC conductivity described in the previous section 4.2.2.3, wherein conductivity is lowest and highest in low and high-frequency regions, respectively. The addition of  $\text{Fe}_3\text{O}_4$  promotes a synergistic effect in the DM5 sample, as seen (Fig. 4.99), resulting in the maximum value of AC-conductivity, but the value of  $M'$  is maximum for DM4. Since AC-conductivity involves the real part (R) of the impedance ( $Z = R + jX$ ), the electric modulus owes the effect of polarization. So, this causes a difference between  $\sigma_{ac}$  and  $M'$ . This maximum value of  $M'$  in DM4 can be also explained by the densely/closely packed small grains with uniform distribution as seen in FESEM (Fig. 4.94). Fig. 4.100(b) illustrates the variation of the imaginary component of electric modulus ( $M''$ ) with frequency. The broad nature of peaks is associated with a wide distribution of relaxation times and it is attributed to an increase in heterogeneity accompanied by more interfaces with substitution and  $\text{Fe}_3\text{O}_4$ . Substitution of Co-La ions causes a non-linear variation in the relaxation frequency and is the minimum for the DM6 sample. It is clear [Fig. 4.100(c)] that all hexaferrite composites exhibit small diameter curves, except the DM4 sample. Among all synthesized composites, the DM6 sample shows a smaller peak height which is attributed to the weak inter-grain connectivity, occurrence of porosity (Fig. 4.94), and effect of grain boundaries due to substitution. In the DM4 sample, a maximum peak height with a larger diameter elucidates the existence of dense/closely packed grain clusters, as seen in FESEM (Fig. 4.94). These wide-range dense grain clusters contribute to different relaxation processes with a wide distribution of relaxation times, leading to a larger diameter and peak height in DM4. Moreover, the behavior of the DM4 sample can also be explained due to the synergistic effect caused by the insertion of  $\text{Fe}_3\text{O}_4$  [278]. Substitution of Co-La ions suppressed this effect despite the same concentration of  $\text{Fe}_3\text{O}_4$  in DM5 and DM6. As a result, the DM4 sample turns out to be the optimum composite for conductivity relaxation, among all.

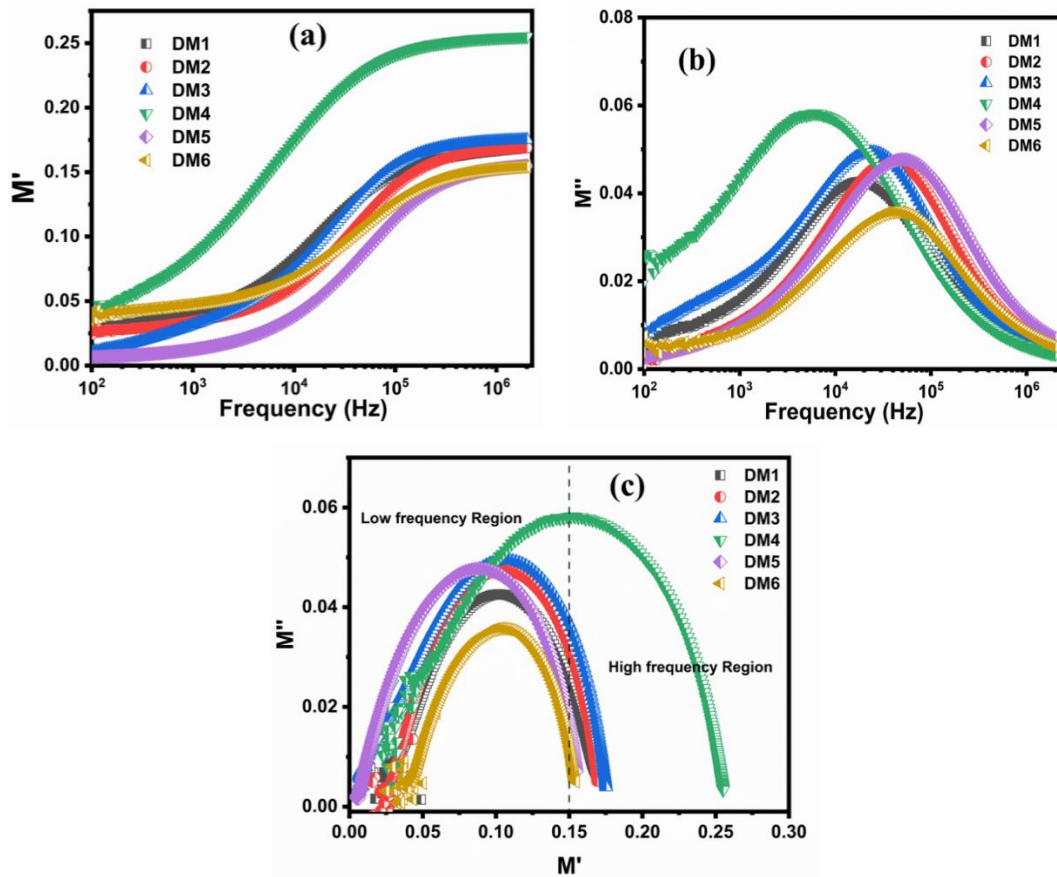


**Fig. 4.103.** (a)  $M'$ , (b)  $M''$ , and (c) Cole-Cole plot ( $M''$  vs  $M'$ ) variation with frequency of DM1, DM2, DM3, DM4, DM5 and DM6 ferrite composites.

#### 4.5.2.5 Complex impedance analysis

The frequency-dependent behavior of  $Z'$  and  $Z''$  of synthesized hexaferrite composites are shown in Fig. 4.101(a) and 4.101(b). As the frequency increases, both  $Z'$  and  $Z''$  decreases, suggesting an increment in the material's conductivity due to the increment in electron hopping between the localized ions. The curves demonstrated a fall in  $Z''$  values with increasing Co-La substitution due to a decrease in polarization.

Fig. 4.101(c) displays the Cole-Cole ( $Z''$  vs  $Z'$ ) plots of synthesized hexaferrite composites. These plots demonstrate that the relaxation is of the non-Debye-type having incomplete semi-circular arcs with the center not located on the real axis. It is also noted that with Co-La ion substitution, the depression of the arc DM1, DM3, DM4, and DM5 decreases, and it can be ascribed to the distribution of grains. An increment in the arc depression owes to the contribution of grains, which can be visualized in FESEM (Fig. 4.94) of DM2 and DM6 samples. The depression of arcs in the high-frequency region is associated with large-size grains, which promotes conductivity and reduces reactance. Moreover, the DM4 sample exhibits maximum dielectric relaxation in the high-frequency region and is caused by the



synergistic effect due to the insertion of  $\text{Fe}_3\text{O}_4$ . As the substitution level increases, the substitution phenomena dominate over the synergistic effect (due to the same concentration of  $\text{Fe}_3\text{O}_4$ ), and this results in a decrease in the dielectric relaxation of DM5 and DM6 in the high-frequency region.

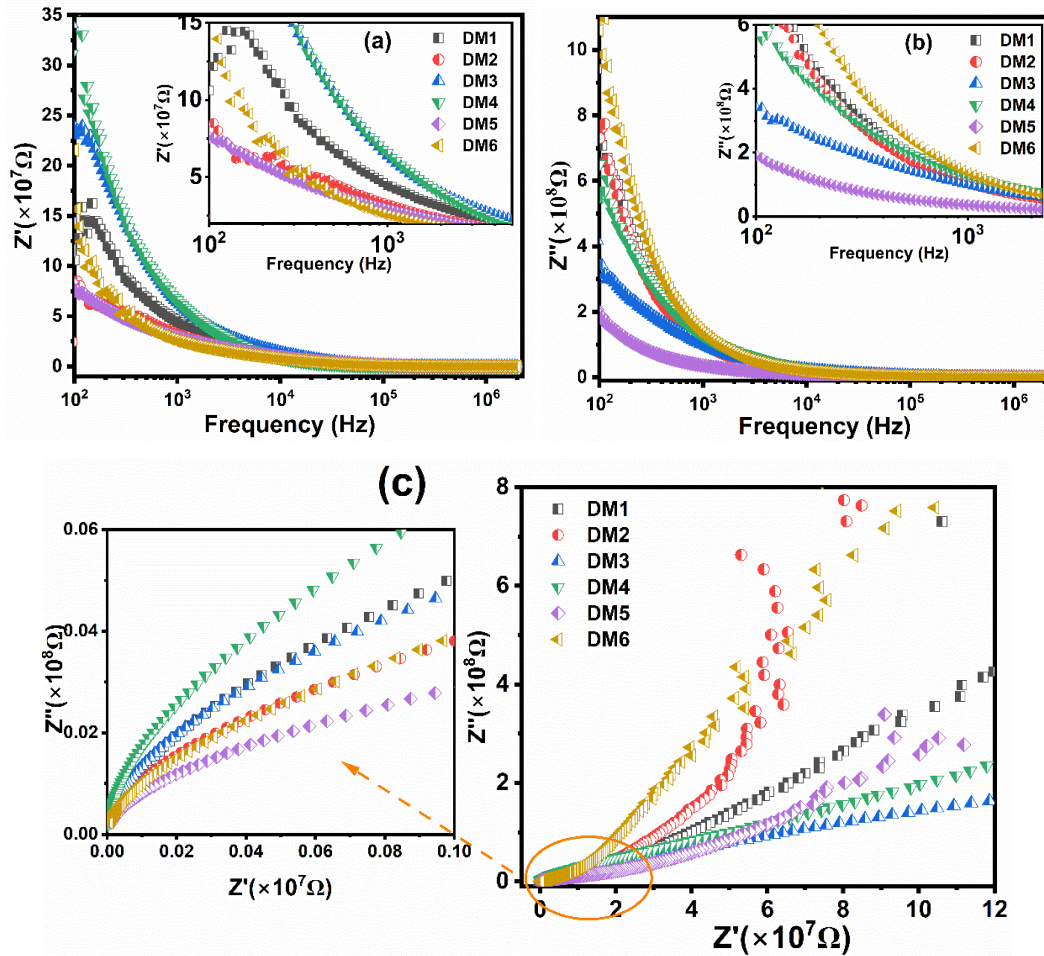


**Fig. 4.104.** (a)  $Z'$ , (b)  $Z''$ , and (c) ( $Z''$  vs  $Z'$ ) variation with frequency of DM1, DM2, DM3, DM4, DM5 and DM6 hexaferrite composites.

### 4.5.3 Magnetic Analysis

Fig. 4.102(a) shows the hysteresis loops of all synthesized composites at room temperature. The saturation magnetization ( $M_s$ ), anisotropy field ( $H_a$ ), remanence magnetization ( $M_r$ ), remanence ratio ( $M_r/M_s$ ), coercivity ( $H_c$ ), and maximum energy product  $(BH)_{\max}$  values derived from the M-H loop are enumerated in Table 4.34. It can be deduced that with an increase in the level of substitution, the value of  $M_s$  first increases from DM1 to DM2 samples and is followed by a decrement thereafter [312].

Table 4.34 shows that  $M_s$  initially increases from DM1 (55.41 emu/g) to DM2 (73.29 emu/g) and is followed by a gradual decrease to DM6 (47.74 emu/g). The initial 32% increment in  $M_s$  is plausibly due to the replacement of both Co-La ions with Fe ions at spin-

down sites. As discussed earlier (section 4.1.3), this envisaged behavior can also be explained with ligand field theory and electronegativity parameters. From DM3 to the DM4 sample, an insignificant change in  $M_s$  value indicates a feeble effect of Co-La ions on saturation magnetization. However, the further substitution of Co-La ions disrupts the magnetic collinearity and debilitates the superexchange interaction among various crystallographic sites. A gradual decrease in  $M_s$  value (DM4 to DM6) could be explained by the fact of replacing  $Fe^{3+}$  ( $5\mu_B$ ) ions with non-magnetic ( $La^{3+}$ ) and weakly magnetic ( $Co^{2+}$ ) cations at octahedral sites. This replacement reduces the no. of  $Fe^{3+}$  ions on spin-up positions, which results in the conversion of  $Fe^{3+}$  ions to  $Fe^{2+}$  ions to maintain electrical neutrality. It reduces the strength of the superexchange interactions and leads to a decline in magnetic moment, thus resulting in a decrease in  $M_s$ . It is clear from Fig. 4.102(b), that the M-H curve of the DM1 sample is smooth and convex-shaped, whereas other samples show a stepped loops indicating uncoupled behavior of hard and soft phases. This is attributed to incomplete exchange coupling between soft and hard ferrite phases [308], [313].

The remanent magnetization ( $M_r$ ) endows a similar trend of  $M_s$ , increasing from 16.55 emu/g (DM1) to 27.78 emu/g (DM2) and decreasing to 17.15 emu/g (DM6), as seen in Table 4.34. The lowest value of Coercivity (607.79 Oe), and remanent magnetization (16.55 emu/g) are observed in the DM1 sample, which is associated with the absence of substituent cations in the crystal lattice. The increment observed in  $H_c$  from DM1 (607.79 Oe) to DM3 (3084.73 Oe) followed by a decrease, thereafter to DM6 (1589.40 Oe), is caused by  $H_a$ . A larger anisotropy field leads to higher coercivity, i.e., more energy is required to reverse the magnetic moment of the hexaferrite. Due to the inverse nature of  $H_c$  with grain size, the reduction observed in  $H_c$  at a higher level of substitution can be accompanied by the increment in grain size (as seen in Fig. 4.94). The calculated value of  $M_r/M_s$  is enlisted in Table 4.34 and it turns out to be less than 0.5 for all synthesized ferrite composites, which depicts the multi-domain nature of particles within the material. However, the DM3 sample shows the largest  $H_c$  of 3084.73 Oe, resulting in a significant enhancement of 90% of  $(BH)_{max}$  from DM1, suggesting the maximum amount of energy stored by the magnet per unit volume.

**Table 4.34** Values of various magnetic parameters of ferrite composites.

Sample Name	DM1	DM2	DM3	DM4	DM5	DM6
$M_s$ (emu/g)	55.41	73.29	63.73	63.47	53.79	47.74
$H_c$ (Oe)	607.79	2414.87	3084.73	2916.79	1697.60	1589.40
$H_a$ (kOe)	12.56	16.36	16.61	16.80	15.46	14.75



$M_r$ (emu/g)	16.55	27.78	26.50	25.72	19.46	17.15
$M_r/M_s$	0.298	0.379	0.415	0.405	0.361	0.359
(BH)max (kGOe)	17.48	128.3	193.47	171.79	72.40	61.17

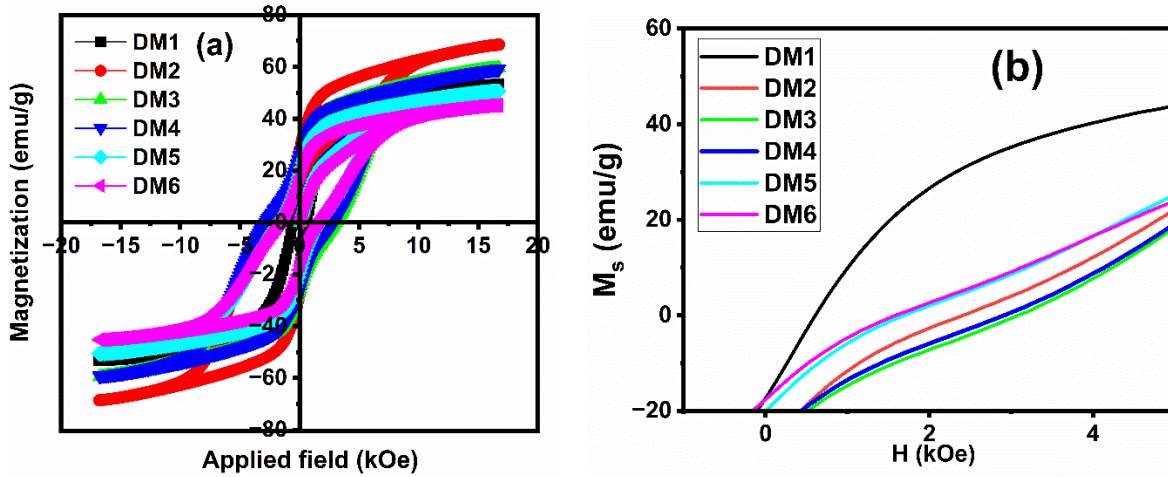


**Fig. 4.105.** (a) M-H plots (b) Enlarged view of M-H plots of DM1, DM2, DM3, DM4, DM5 and DM6 ferrite composites.

The investigation of switching field distribution ( $dM/dH$  against  $H$ ) plots is often used to determine the exchange-coupling effect between hard/soft ferrite composites [179], as seen in Fig. 4.103. The inset of Fig. 4.103 depicts that the DM1 sample exhibits a single narrower peak in the switching field distribution attributed to a strong exchange coupling between M-type (hard) and spinel (soft) magnetic phases. On the contrary, DM2, DM3, DM4, DM5, and DM6 samples exhibit a single peak with a shoulder peak, and the intensity of the shoulder peak decreases with Co-La substitution. The first single peak attributed to reversible susceptibility results from the movement of domain walls in a reversible manner, while the shoulder peak ascribed the involvement of an irreversible part or a contribution from the switching field [314]. This concludes that a strong exchange coupling is assessed in the DM1 sample. From DM2 to DM6, the insertion of Co-La ions dilutes the effect of exchange coupling between hard/soft phases [315].

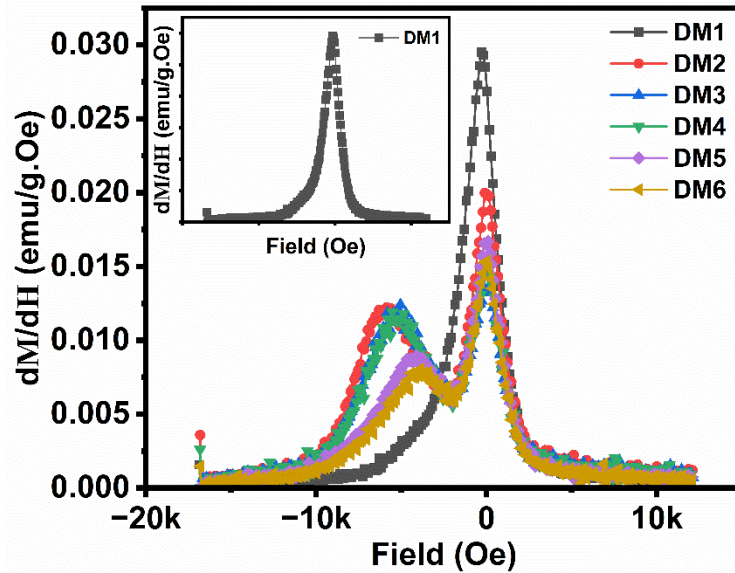


**Fig. 4.106.** dM/dH against H plots of DM1, DM2, DM3, DM4, DM5 and DM6 ferrite composites.

#### 4.5.4 Electromagnetic analysis

Fig. 4.104(a, b) demonstrated the variation of dielectric constant ( $\epsilon'$ )/loss ( $\epsilon''$ ) of DM1, DM2, DM3, DM4, and DM6 samples in a frequency range of 8.2 to 12 GHz, and DM5 from 12.4 to 18 GHz. The values of  $\epsilon'/\epsilon''$  slightly increase with increasing frequency and non-monotonically increase with Co-La substitution, despite the same concentration of  $\text{Fe}_3\text{O}_4$ . The behavior of  $\epsilon''$  is relatively similar for DM1, DM2, DM3, DM4, and DM6 samples, while it shows broad resonance around 9.5 and 11.5 GHz. In contrast, DM5 exhibits resonance around 16 GHz and remains relatively constant over the remaining frequency spectra. The resonance peaks are mainly due to the interfaces between  $\text{Fe}_3\text{O}_4$  and substituted SrM hexaferrite. The intrinsic resonance peak of substituted SrM hexaferrite and  $\text{Fe}_3\text{O}_4$  move towards one another and eventually merge into a broad peak around 9.5 GHz for all samples in the frequency spectra 8.2 to 12.4 GHz.

Fig. 4.105(a, b) displays the variation of permeability ( $\mu'$ )/ magnetic loss ( $\mu''$ ) of DM1, DM2, DM3, DM4, and DM6 samples in the frequency range of 8.2 to 12 GHz, and DM5 from 12.4 to 18 GHz. It is found that  $\mu'$  values of DM2, DM3, DM4, and DM6 slightly decrease with increasing frequency. The  $\mu''$  values of DM1 suddenly increase to 0.6 around 8.25 GHz and it decreases within 8.5 to 12.4 GHz. This behavior may be attributed to the natural resonance of  $\text{Fe}_3\text{O}_4$ , which occurs at approximately 2-8 GHz. In DM1, the value of  $\mu''$  barely changes at higher frequencies, suggesting that the natural resonance frequency of SrM hexaferrite occurs greater than 12 GHz. There is no such type of resonance observed in the substituted SrM/ $\text{Fe}_3\text{O}_4$  composites, which may be due to the introduction of Co-La ions

(suppressed the exchange coupling effect). Furthermore, the  $\mu''$  and  $\epsilon''$  values of DM1 are maximum of 0.6 and 0.5, respectively. Thus, the contribution of magnetic loss is somewhat more than dielectric loss and results in large microwave absorption in the DM1 sample. In contrast, from 8.2 – 8.5 GHz the  $\epsilon''$  decreases  $\mu''$  rises, evidently decreasing the difference between  $\mu''$  and  $\epsilon''$  and so enhancing the impedance match. Further substitution of Co-La ions enhanced the dielectric loss ( $\epsilon''$  increases with Co-La content) and decreased the magnetic loss of composites [119].

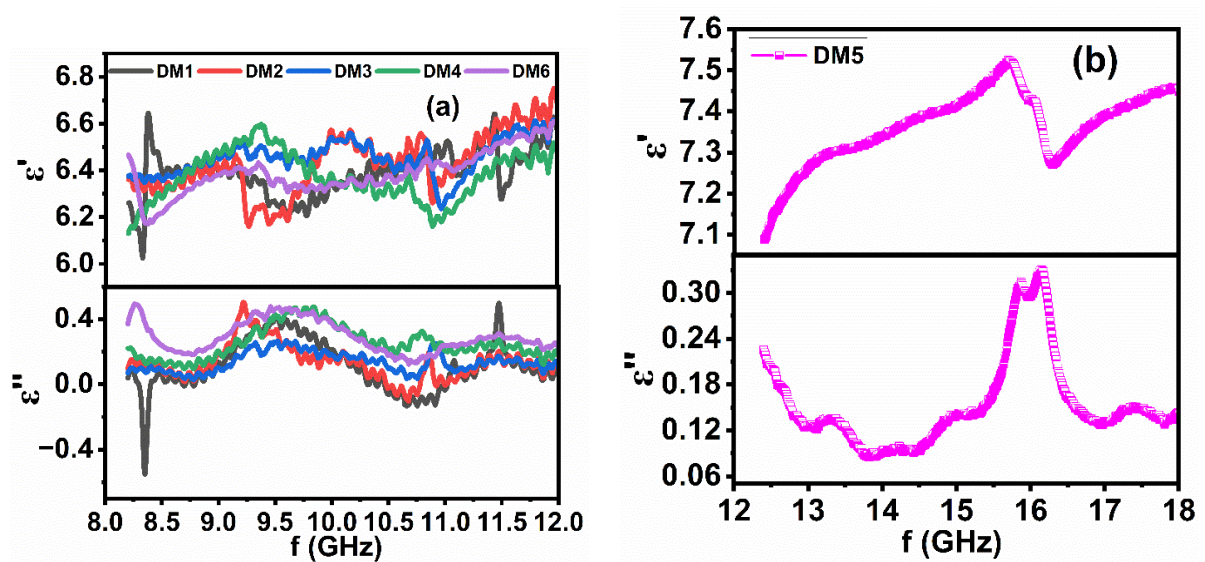


Fig. 4.107. (a) Complex permittivity of DM1, DM2, DM3, DM4, and DM6 samples (b) Complex permittivity of DM5 sample.

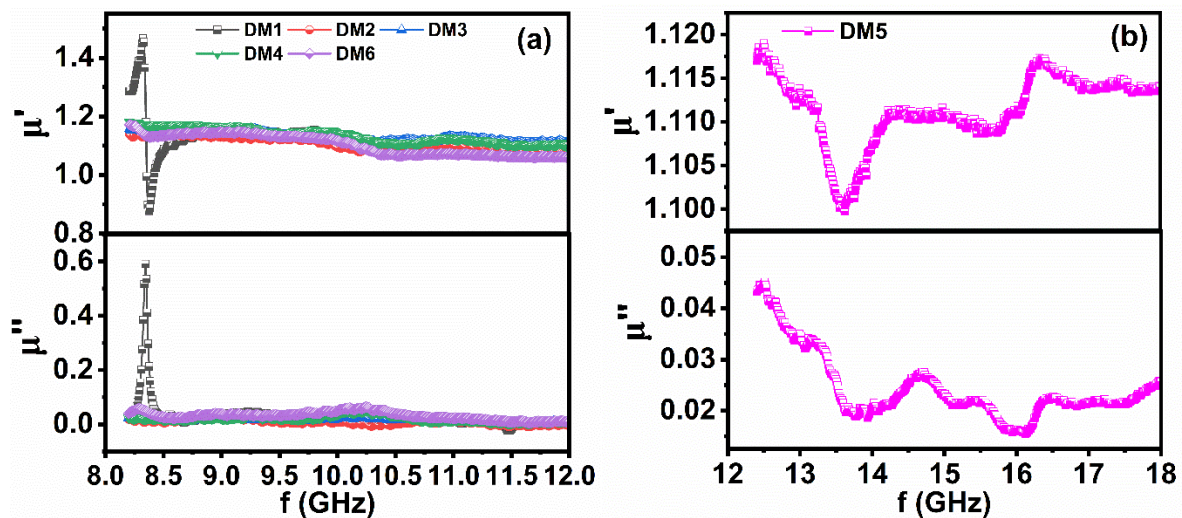


Fig. 4.108. (a) Complex permeability of of DM1, DM2, DM3, DM4, and DM6 samples (b) Complex permittivity of DM5 sample.

Fig. 4.106(a, c), 4.107(a), 4.108(a), 4.109(a), and 4.110(a) illustrate REL peaks of all investigated samples. For better visualization, 3D plots of REL as a function of frequency and thickness are illustrated in Fig. 111. The measurements revealed that samples DM1, DM2, DM4, and DM6 absorb EM radiation ( $REL \geq -10$  dB) in the 8.2-12.4 GHz frequency range, whereas DM5 exhibits  $REL \geq -10$  dB in 12.4-18.5 GHz. There is no REL dip less than -10 dB (90% absorption) for the DM3 sample. The REL is higher in the DM1 sample (-32.96 dB) of thickness 8.9 mm at 8.32 GHz. The remaining samples owe  $REL \geq -10$  dB (90 % absorption) frequency ranges from 8.2 to 12 GHz and 12.4 to 18 GHz from 8 to 10 mm thicknesses, as shown in Table 4.35. For the DM5 sample, dual  $REL \geq -10$  dB peak is observed at 16.16 and 15.82 GHz of thickness 8.1 mm. The REL plots exhibit the shift towards lower frequency region as the thickness increases. This trend reflects the quarter wavelength mechanism described by Eq. 3.24, where frequency and thickness are inversely related.

Fig. 4.106(a, c) demonstrated the absorption properties of the DM1 sample with a layer of thickness of 2.6 -10 mm in the 8.2-8.4 GHz frequency range. The REL of the DM1 sample greater than -10 dB/-20 dB within the thickness ranges from 2.6-10 mm. The  $REL_{max}$  (-32.96 dB) is observed for 8.9 mm thickness, while the remaining thicknesses of this sample show  $REL \geq -10$  dB/-20 dB at 8.32 GHz. For DM2 and DM4 samples, Fig. 4.107(a) and 4.108(a) reveal  $REL \geq -10$  dB across thickness ranging from 9.1-9.4 mm and 8.2-8.4 mm, respectively, by covering a frequency range of 9.2 to 10.1 GHz. Fig. 4.109(a) and Table 4.35 are notable for the DM5 sample, as it exhibits  $REL > -10$  dB (more than 90% absorption) with a wide (0.48 GHz) and narrow (0.18 GHz) absorption bandwidth from 15.76-16.24 GHz and 15.76-15.94 GHz with matching thicknesses 8.2 and 8.3 mm, respectively. In the DM6 sample [Fig. 4.110(a)], an effective  $REL \geq -10$  dB was observed from 8.3 to 10 mm thicknesses with a broad absorption bandwidth of 0.60 GHz (9.57-10.14 GHz) and narrow bandwidth of 0.15 GHz (8.19-8.34 GHz) at 8.6 mm and 9.9mm, respectively.



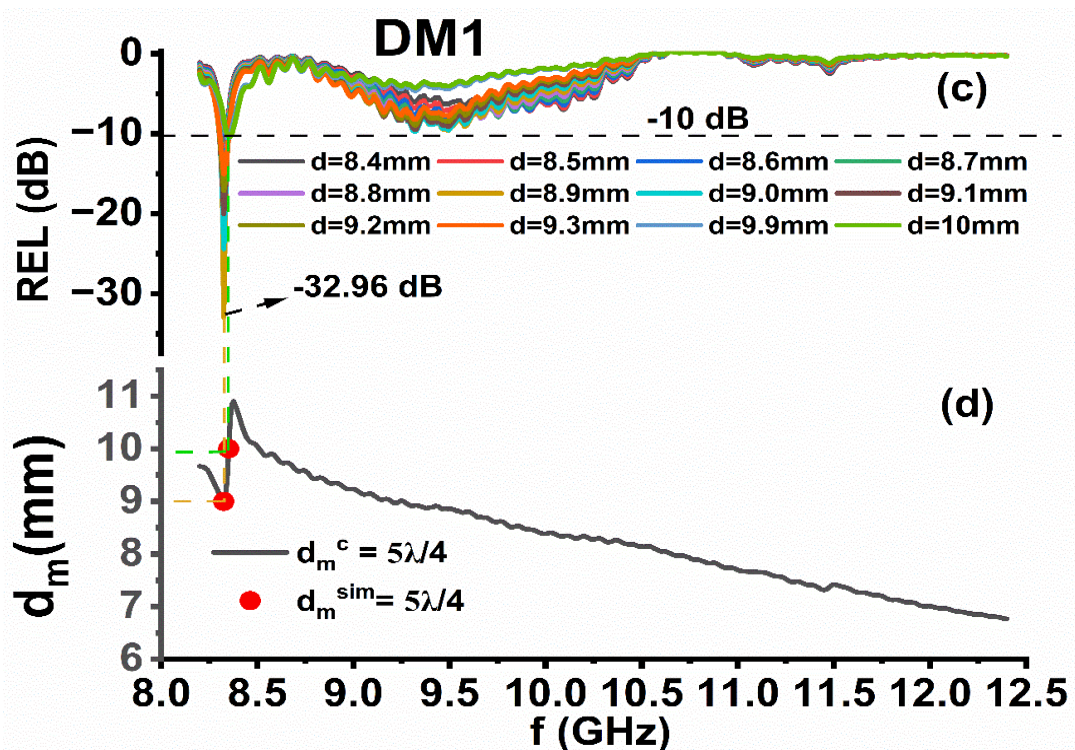
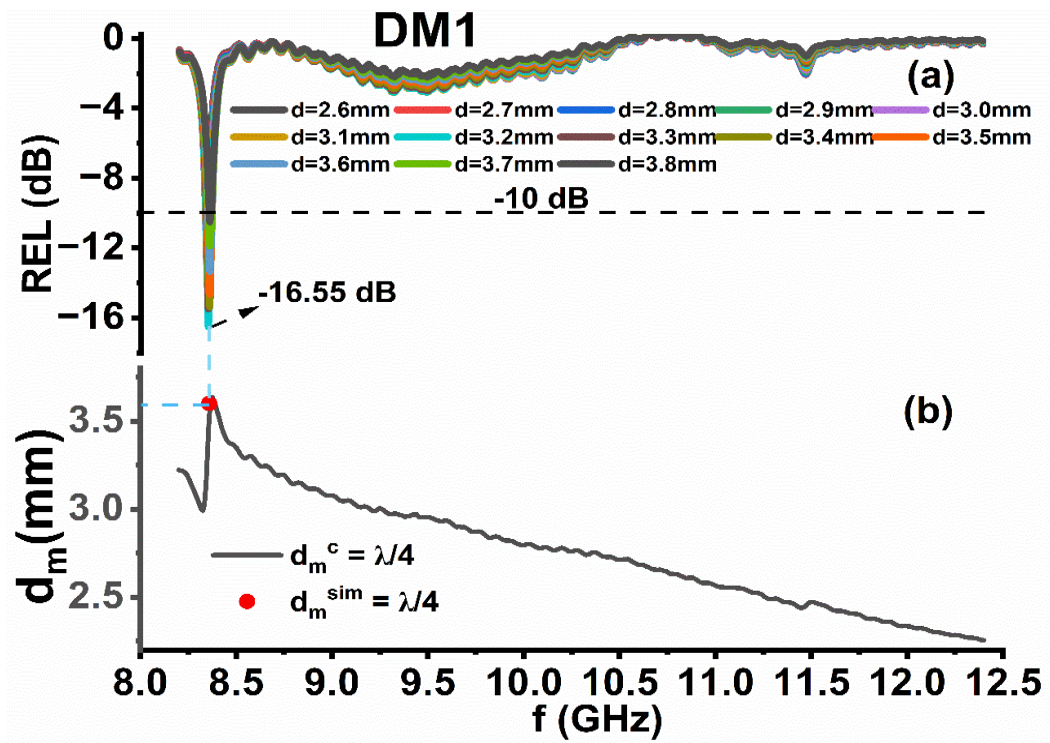


Fig. 4.109. (a, c) Dependence of REL on frequency in DM1 sample. (b, d)  $d_m^{sim}$  and  $d_m^c$  versus frequency for  $\lambda/4$  and  $5\lambda/4$  in DM1 sample.

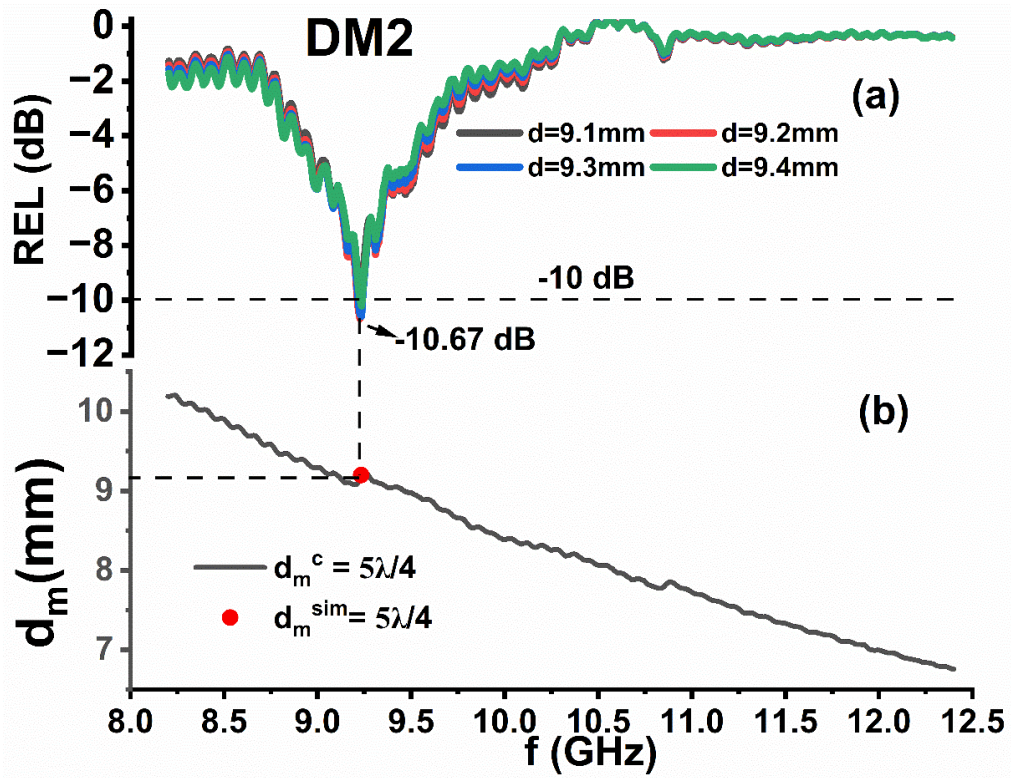


Fig. 4.110. (a) Dependence of REL on frequency in DM2 sample. (b)  $d_m^{sim}$  and  $d_m^c$  versus frequency for  $5\lambda/4$  in the DM2 sample.

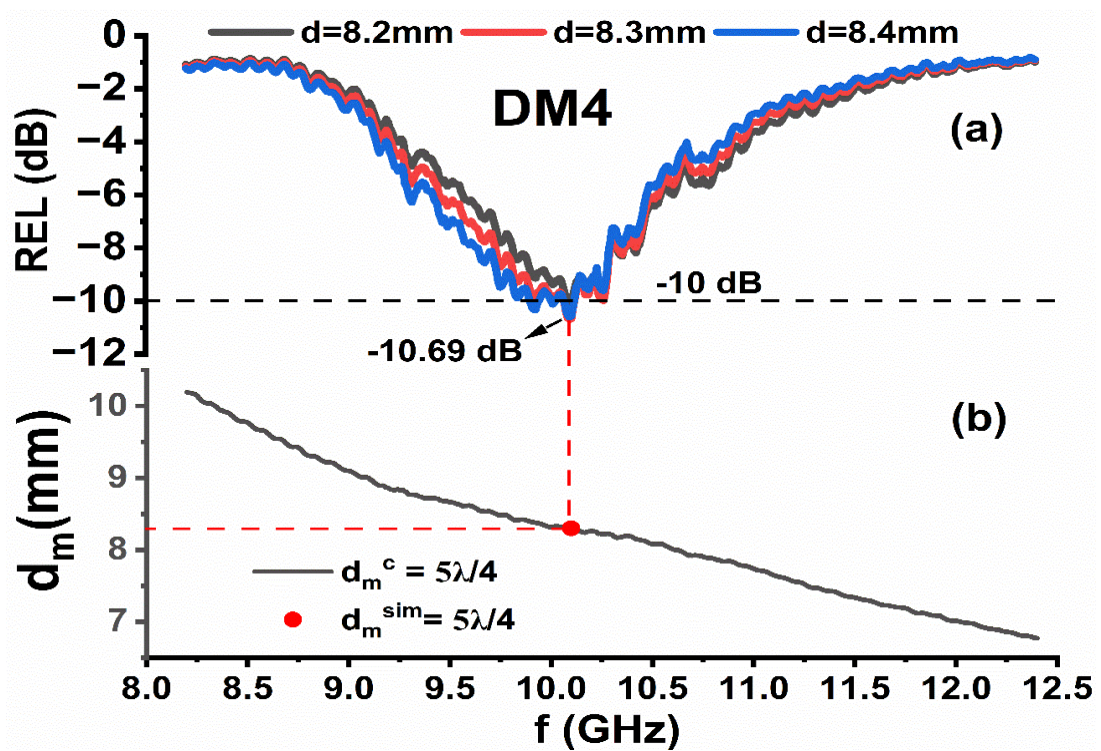


Fig. 4.111. (a) Dependence of REL on frequency in DM4 sample. (b)  $d_m^{sim}$  and  $d_m^c$  versus frequency for  $5\lambda/4$  in the DM4 sample.



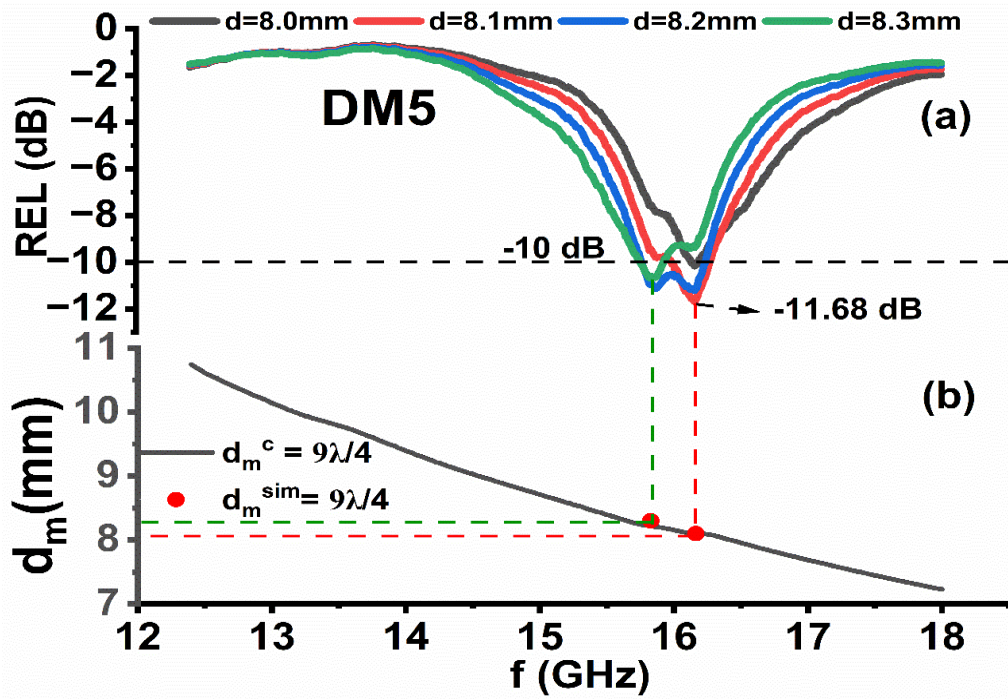


Fig. 4.112. (a) Dependence of REL on frequency in DM5 sample. (b)  $d_m^{sim}$  and  $d_m^c$  versus frequency for  $9\lambda/4$  in the DM5 sample.

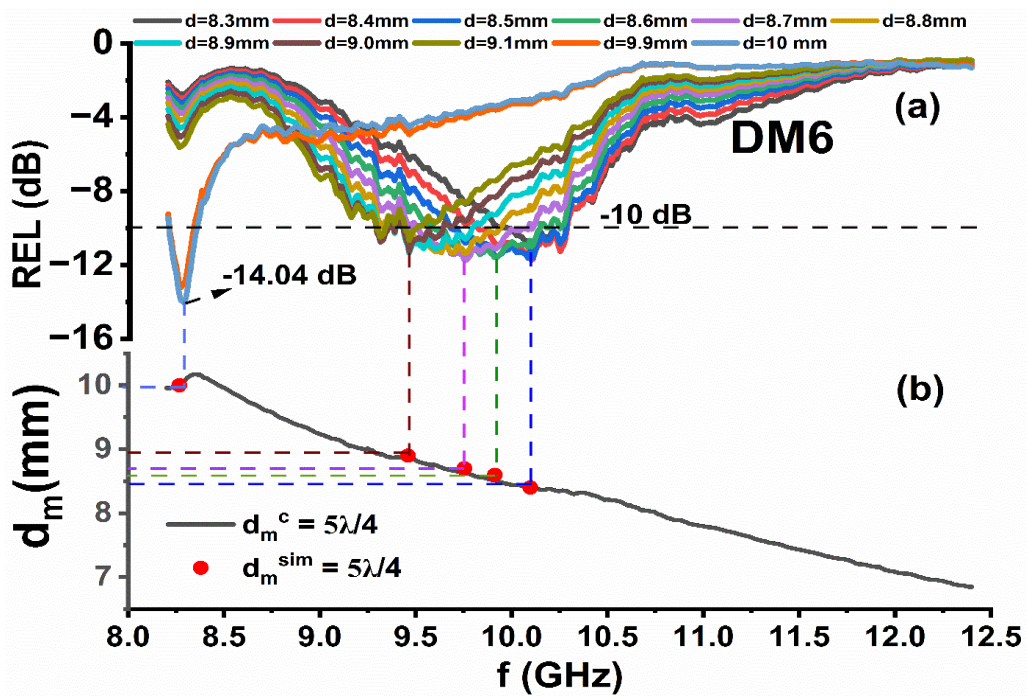


Fig. 4.113. (a) Dependence of REL on frequency in DM6 sample. (b)  $d_m^{sim}$  and  $d_m^c$  versus frequency for  $5\lambda/4$  in the DM6 sample.

**Table 4.35** Absorption Parameters (REL> -10/-20 dB).

Sample Name	Matching Thickness (mm)	Maximum REL (dB)	Matching frequency (GHz)	Frequency Band for REL > -10 dB (GHz)	Bandwidth for REL > -10 dB (GHz)	Frequency Band REL > -20 dB (GHz)	Bandwidth for REL > -20 dB (GHz)	BTR	PBW (%)
<b>DM1</b>	2.6	-10.53	8.342	--	--	--	--	--	--
	2.7	-11.53	8.342	--	--	--	--	--	--
	2.8	-12.40	8.342	--	--	--	--	--	--
	2.9	-13.77	8.351	--	--	--	--	--	--
	3.0	-15.32	8.351	--	--	--	--	--	--
	3.1	-16.45	8.351	--	--	--	--	--	--
	3.2	-16.52	8.351	--	--	--	--	--	--
	3.3	-15.49	8.351	--	--	--	--	--	--
	3.4	-15.36	8.359	--	--	--	--	--	--
	3.5	-14.66	8.359	--	--	--	--	--	--
	3.6	-13.34	8.359	--	--	--	--	--	--
	3.7	-11.88	8.359	--	--	--	--	--	--
	3.8	-10.50	8.359	--	--	--	--	--	--
	8.4	-14.69	8.326	--	--	--	--	--	--
	8.5	-16.75	8.326	--	--	--	--	--	--
	8.6	-19.53	8.326	--	--	--	--	--	--
	8.7	-23.68	8.326	--	--	--	--	--	--
	8.8	-31.47	8.326	--	--	--	--	--	--
	8.9	-32.96	8.326	--	--	--	--	--	--
	9.0	-24.39	8.326	--	--	--	--	--	--
	9.1	-20.01	8.326	--	--	--	--	--	--
	9.2	-17.14	8.326	--	--	--	--	--	--
	9.3	-15.04	8.326	--	--	--	--	--	--
	9.9	-10.55	8.351	--	--	--	--	--	--
	10	-10.43	8.351	--	--	--	--	--	--
<b>DM2</b>	9.1	-10.40	9.224	--	--	--	--	--	--
	9.2	-10.67	9.224	--	--	--	--	--	--
	9.3	-10.59	9.233	--	--	--	--	--	--
	9.4	-10.21	9.233	--	--	--	--	--	--
<b>DM4</b>	8.2	-10.26	10.09	--	--	--	--	--	--

	8.3	-10.69	10.09	--	--	--	--	--	--
	8.4	-10.60	10.09	--	--	--	--	--	--
<b>DM5</b>	8.0	-10.17	16.163	--	--	--	--	--	--
	8.1	-11.68	16.163	15.99-16.27	0.28	--	--	4E-05	1.73
	8.2	-11.21	16.163	15.76-16.24	0.48	--	--	6.9E-05	2.96
	8.3	-10.66	15.827	15.76-15.94	0.18	--	--	2.7E-05	1.13
<b>DM6</b>	8.3	-11.81	10.098	9.93-10.28	0.35	--	--	1.2E-04	3.46
	8.4	-11.74	10.098	9.82-10.27	0.45	--	--	1.6E-03	4.45
	8.5	-11.67	10.098	9.68-10.27	0.59	--	--	2.1E-04	5.84
	8.6	-11.61	9.913	9.57-10.14	0.60	--	--	2E-04	0.69
	8.7	-11.76	9.754	9.49-9.98	0.49	--	--	1.8E-04	5.02
	8.8	-11.39	9.754	9.45-9.93	0.48	--	--	1.7E-04	4.91
	8.9	-11.35	9.846	9.43-9.79	0.36	--	--	1.3E-04	3.65
	9.0	-11.24	9.846	--	--	--	--	--	--
	9.1	-10.67	9.846	--	--	--	--	--	--
	9.9	-13.21	8.284	8.19-8.34	0.15	--	--	6.6E-05	1.81
	10	-14.04	8.284	8.19-8.34	0.15	--	--	6.6E-05	1.81

For effective absorption, impedance matching is essential which can be estimated by evaluating the relationship between reflection loss and quarter wavelength mechanism (discussed in section 4.1.5). Fig. 4.106(b, d), 4.107(b), 4.108(b), 4.109(b), and 4.110(b) display the plots of the calculated thickness ( $d_m^c$ ) (calculated using Eq. 3.24) within the frequency range. To compare the calculated thickness ( $n\lambda/4$ ) with the simulated thickness ( $d_m^{sim}$ ), vertical lines are drawn from REL peaks to the thickness-frequency plots. Results indicate that the quarter wavelength mechanism is envisaged in DM2 and DM6 where the calculated thickness is  $5\lambda/4$  with  $n = 5$ . Conversely, DM1 shows the occurrence of both  $\lambda/4$  and  $5\lambda/4$ , while DM5 exhibits the presence of  $9\lambda/4$  values. Thus, synthesized samples with  $REL \geq -10$  dB/-20 dB satisfy the quarter wavelength mechanism ( $n\lambda/4$ ) at different values of  $n$ .

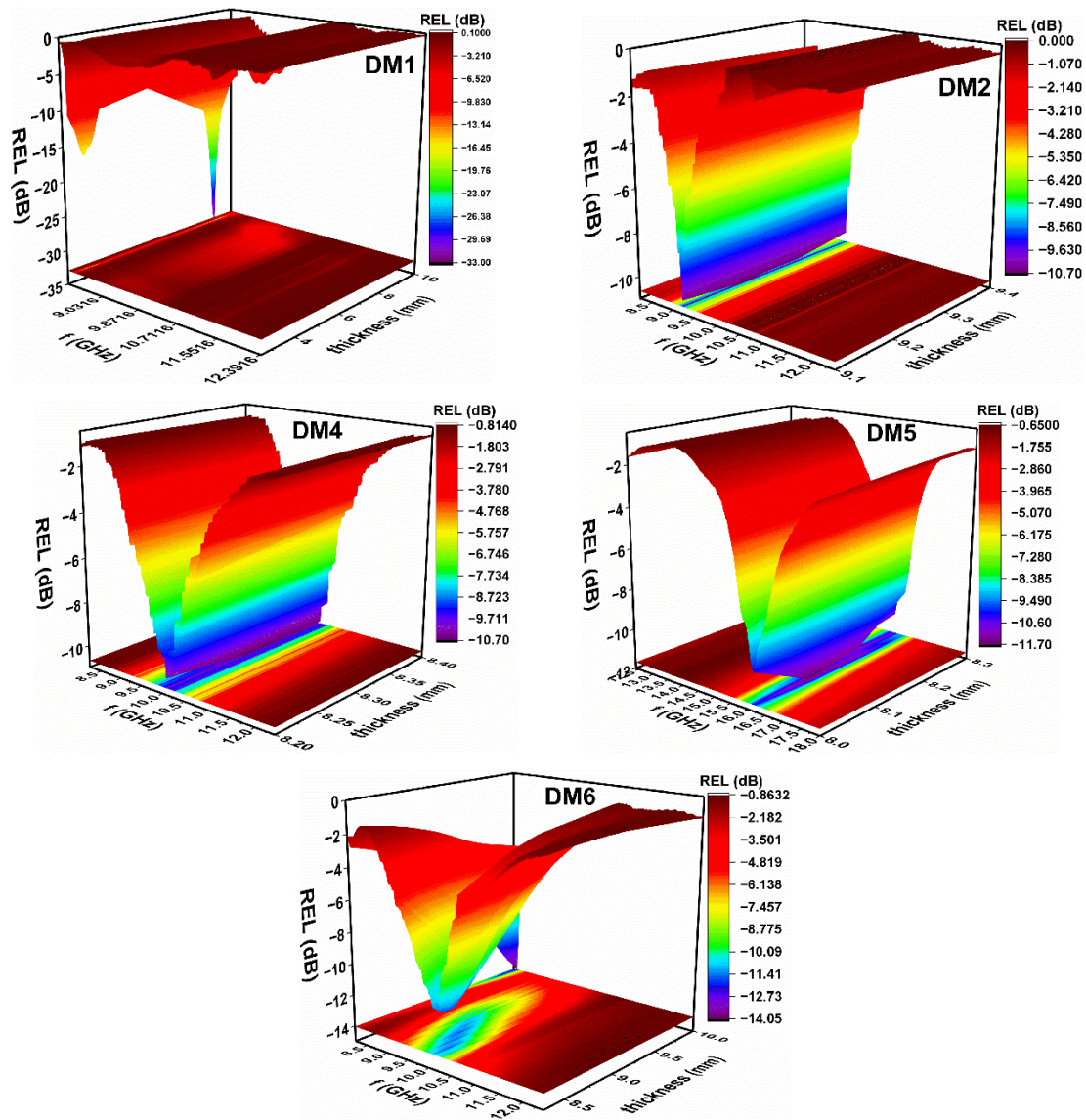


**Fig. 4.114.** 3D plots of REL as a function of thickness and frequency.

The significance of impedance matching, resulting in  $Z_{in}/Z_0 \cong 1$  when designing the absorber material and its application in microwave systems is already discussed in section 4.1.5. Fig. 4.112(a, c), 4.113(a), 4.114(a), 4.115(a), and 4.116(a, c) illustrates the graphs of reflection loss and  $Z_{in}/Z_0$  as a function of frequency for some considerable thicknesses of samples. Table 4.36 enumerates the  $Z_{in}/Z_0$  values for these samples, obtained from  $Z_{in}/Z_0$  plots illustrated in the mentioned figures. The values of  $Z_{in}/Z_0$  are from 1.562 to 1.838 for DM2, 1.747 to 1.824 for DM4, and 1.576 for DM5 which are away from the characteristic's impedance value  $Z_{in}/Z_0 = 1$ , as evident from low REL in these samples.

**Table 4.36** Reflection loss peak's impedance parameters at different thicknesses.

Sample Name	Thickness (mm)	Max. REL (dB)	Matching frequency (GHz)	$Z_{in}/Z_0$	$Z_{real}$	$Z_{img}$
<b>DM1</b>	2.7	-11.53	8.351	0.996	0.844	0.528
	8.7	-23.68	8.326	0.996	0.988	0.129
	8.8	-31.47	8.326	1.019	1.017	0.050
	8.9	-32.96	8.326	1.030	1.030	-0.034
	9.0	-24.39	8.326	1.031	1.024	-0.119
	9.2	-17.14	8.326	0.999	0.961	-0.272
<b>DM2</b>	9.1	-10.40	9.224	1.838	1.824	0.227
	9.2	-10.67	9.224	1.814	1.807	-0.157
	9.3	-10.59	9.224	1.711	1.643	-0.477
	9.4	-10.21	9.224	1.562	1.406	-0.680
<b>DM4</b>	8.2	-10.26	10.09	1.797	1.751	0.404
	8.3	-10.69	10.09	1.824	1.824	-0.006
	8.4	-10.60	10.09	1.747	1.702	-0.392
<b>DM5</b>	8.0	-10.17	16.162	1.549	1.401	0.659
	8.2	-11.21	16.162	1.576	1.498	-0.491
<b>DM6</b>	8.9	-11.35	9.846	1.096	0.803	-0.745
	9.0	-11.24	9.846	1.216	0.944	-0.760
	9.1	-10.67	9.846	1.078	0.774	-0.751
	9.9	-13.21	8.284	1.440	1.393	0.366
	10.0	-14.04	8.284	1.470	1.461	0.163

The issue lies in the DM1 sample, wherein a thickness of 9.2 mm shows REL of -17.14 dB at 8.326 GHz, and the corresponding  $Z_{in}/Z_0$  is 0.999 (as shown in Table 4.36 and Fig. 4.112(c)), which is close to 1. On the contrary, a thickness of 8.9 mm shows a maximum REL of -32.96 dB at 8.326 GHz, and the value of  $Z_{in}/Z_0$  (1.030) (Fig. 4.112(a)) is far away from characteristic value 1. Similarly, the DM6 sample exhibits  $Z_{in}/Z_0 = 1.440$  (close to 1) with REL -13.21 dB at 8.28 GHz of 9.9 mm thickness, as seen in Fig. 4.48(a). Conversely, in DM6 (Fig. 4.116(c)), at 10 mm thickness  $Z_{in}/Z_0 = 1.470$  (far from 1) exhibits REL = -14.04 dB at 8.284 GHz.



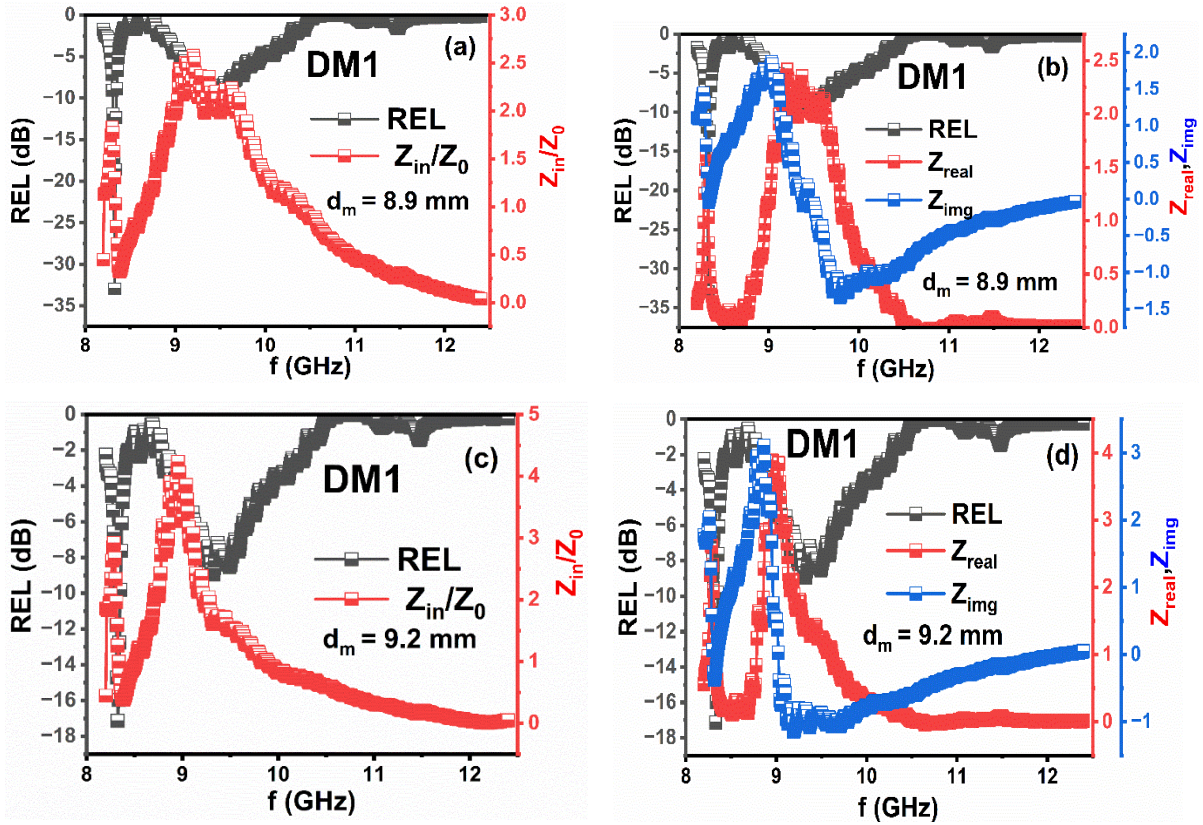


**Fig. 4.115.** (a, c) Dependence of  $Z_{in}$  and REL in frequency (b, d) Dependence of REL,  $Z_{real}$ , and  $Z_{img}$  on frequency for DM1 sample.

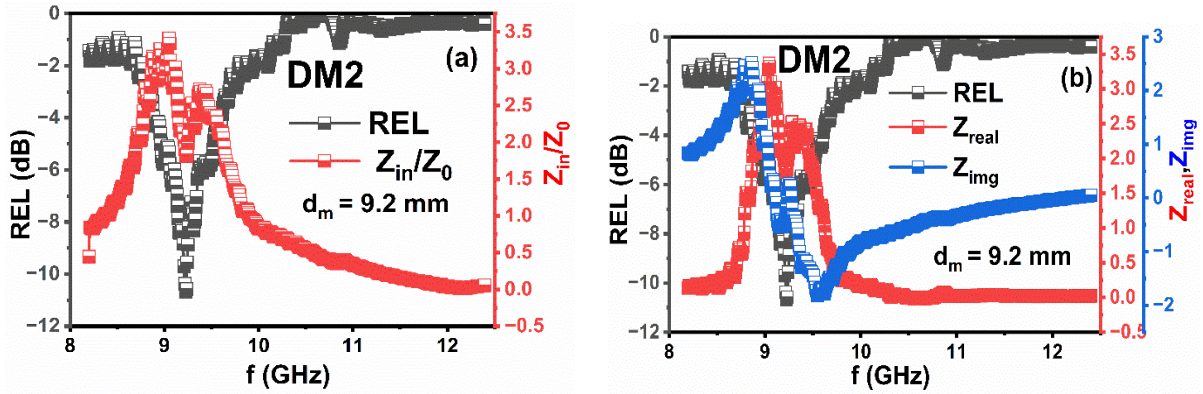


**Fig. 4.116.** (a) Dependence of  $Z_{in}$  and REL in frequency (b) Dependence of REL,  $Z_{real}$ , and  $Z_{img}$  on frequency for DM2 sample.

It is attributed to the complex nature of  $|Z_{in}|$ , it involves  $Z_{real}$  (real) and  $Z_{img}$  (imaginary). The values of  $Z_{real}/Z_{img}$  are calculated using Eq. 3.21 and the curves of  $Z_{real}/Z_{img}$  and REL as a function of frequency are displayed in Fig. 4.112(b, d), 4.113(b), 4.114(b), 4.115(b), and 4.116(b, d). It is evident from the mentioned figures that REL is the maximum for samples having  $Z_{real}/Z_{img}$  close to 1 and/or 0. Moreover, it can be seen in Table 4.36 that due to more offset of  $Z_{real}/Z_{img}$  values from 1 and/or zero, samples DM2, DM4, and DM5 exhibited relatively low REL than other samples.



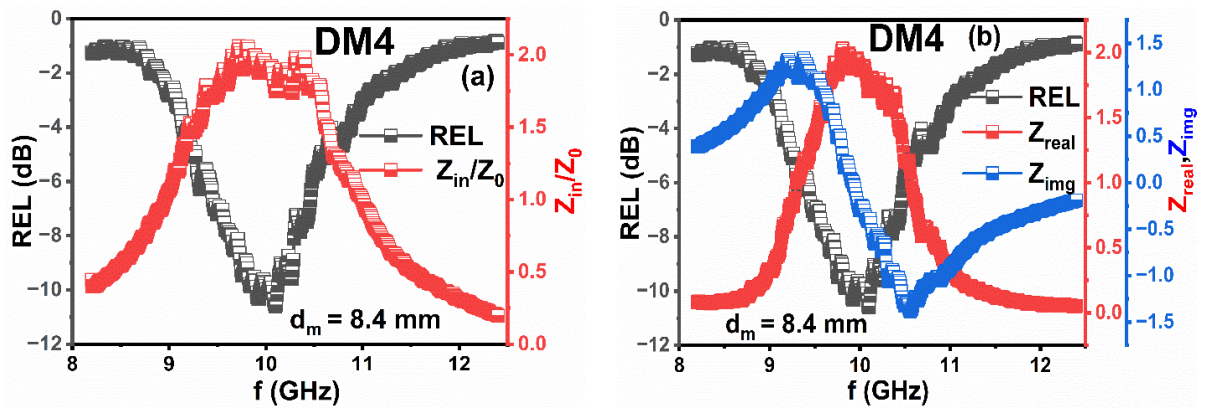


Fig. 4.117. (a) Dependence of  $Z_{in}$  and REL in frequency (b) Dependence of REL,  $Z_{real}$ , and  $Z_{img}$  on frequency for DM4 sample.

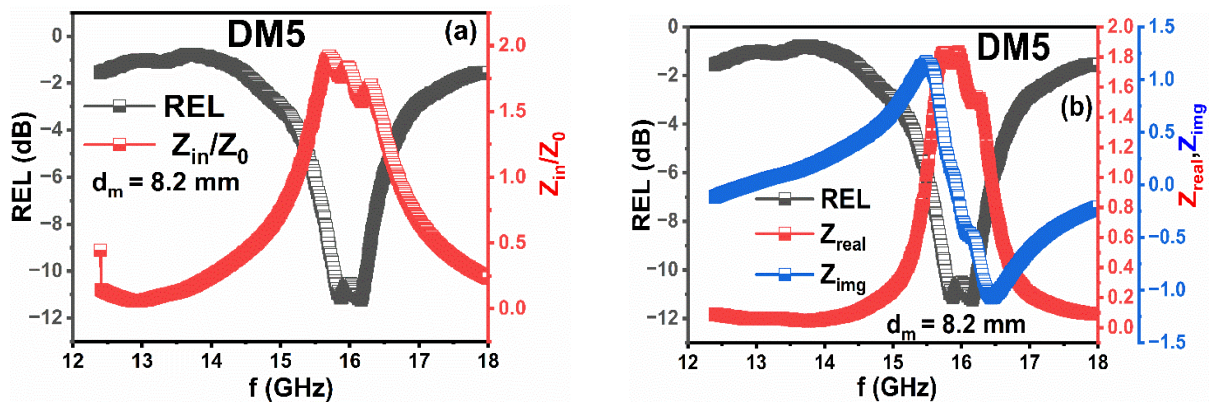
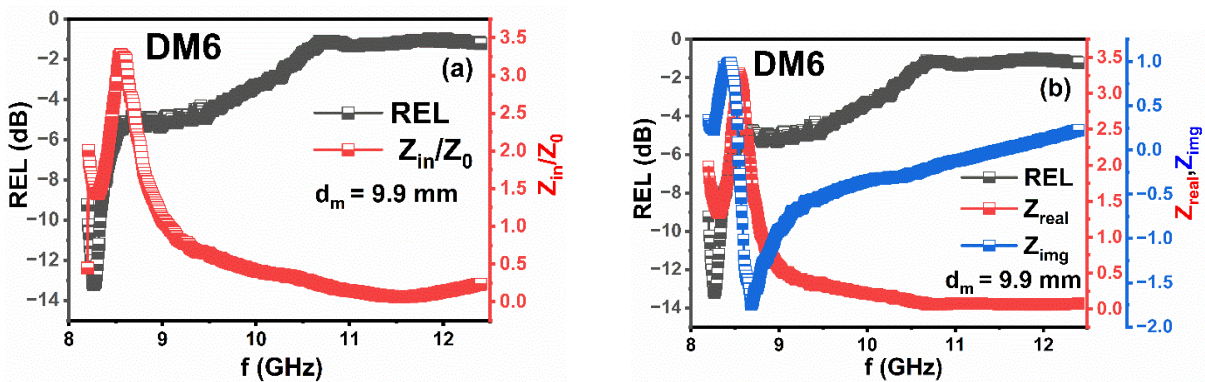
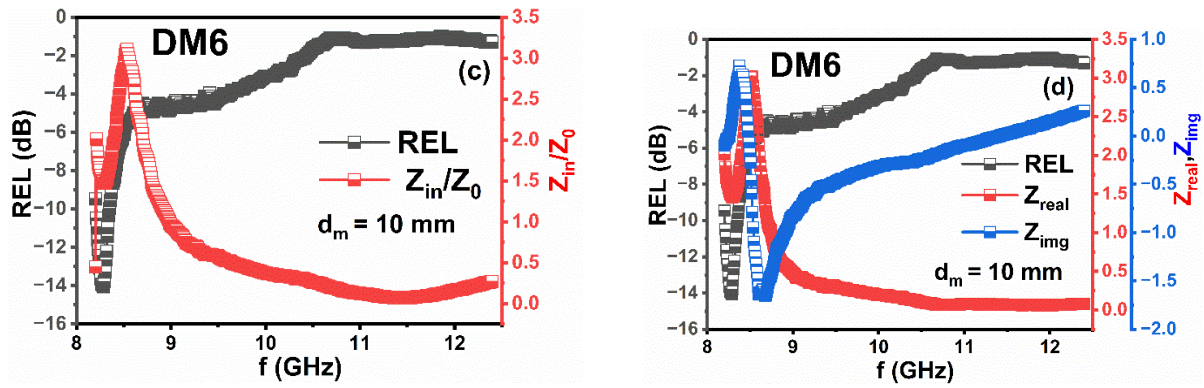


Fig. 4.118. (a) Dependence of  $Z_{in}$  and REL in frequency (b) Dependence of REL,  $Z_{real}$ , and  $Z_{img}$  on frequency for DM5 sample.





**Fig. 4.119.** (a, c) Dependence of  $Z_{in}$  and REL in frequency (b, d) Dependence of REL,  $Z_{real}$ , and  $Z_{img}$  on frequency for DM6 sample.

In conclusion, M-type hexaferrite exhibit a moderate dielectric constant and lower dielectric losses due to their ceramic nature and layered structure. In contrast,  $Fe_3O_4$  has a high dielectric constant and losses due to its semiconducting properties and the presence of  $Fe^{2+}/Fe^{3+}$  ions, which contribute to polarization mechanisms [316]. Combining Co-La substituted SrM hexaferrite with  $Fe_3O_4$  in a fixed ratio can affect the overall permittivity and permeability, thereby improving impedance matching, and resulting in effective microwave absorption. The efficacy of this combination depends on the volume fractions and interactions between SrM hexaferrite and  $Fe_3O_4$ . The maximum reflection loss ( $REL_{max}$ ) of -32.96 dB observed in the DM1 sample is attributed to polarization and conductivity losses. Dipolar polarization between  $SrFe_{12}O_{19}$  and  $Fe_3O_4$  resulting a significant reflection loss in DM1. However, the substitution of Co-La ions weakens the synergistic effect between the hard/soft ferrite phases, leading to REL of no more than -15 dB. Moreover, impedance matching and quarter wavelength mechanism also contributing to effective reflection loss. Furthermore, in all substituted hard/soft ferrite composites, the contribution of dielectric loss exceeds that of magnetic loss.

## 4.6 SrCo<sub>x</sub>Zn<sub>x</sub>Fe<sub>12-2x</sub>O<sub>19</sub> (80%) + PANI (20%) ferrite composites

A physical blending method has been utilized to synthesize hexaferrite composites. In this study, we comprehensively analyzed structural, morphological, magnetic, electrical, and microwave absorption properties. Table 4.37 displays the assignment of sample names/codes for a different level of substitution for PANI/ SrCo<sub>x</sub>Zn<sub>x</sub>Fe<sub>12-2x</sub>O<sub>19</sub>.

**Table 4.37** Assignment of sample name for a different level of substitution of PANI/

SrCo<sub>x</sub>Zn<sub>x</sub>Fe<sub>12-2x</sub>O<sub>19</sub> hexaferrite.

Sample composition 20% PANI/ SrCo <sub>x</sub> Zn <sub>x</sub> Fe <sub>12-2x</sub> O <sub>19</sub>	Sample code
x = 0.0	FP1
x = 0.4	FP2
x = 0.8	FP3
x = 1.2	FP4
x = 1.6	FP5
x = 2.0	FP6

### 4.6.1 Structural Analysis

#### 4.6.1.1 X-ray analysis

XRD technique was deployed to determine the crystalline structure and phase purity of synthesized FP hexaferrite composites. Fig. 4.117 delineates the XRD patterns of all synthesized FP hexaferrite composites, with all the reflection planes observed in the range of  $2\theta = 20^\circ$ - $60^\circ$ . The observed peaks are well matched with (ICDD# 80-1197) and affirm the formation of magnetoplumbite SrM hexaferrite and with CoFe<sub>2</sub>O<sub>4</sub> (ICDD# 22-1086) as a secondary peaks/phases [317]. A small trace of hematite ( $\alpha$ -Fe<sub>2</sub>O<sub>3</sub>) is observed in all samples, and it disappears with the increment of Co-Zn ions [318]. Instead of obtaining a sharp peak of PANI in the XRD pattern, a broad peak is observed in the range of  $2\theta = 15^\circ$ - $25^\circ$ . The Rietveld refinement of FP1 to FP6 samples was carried out using the Fullprof program (Fig. 4.118) and was employed to calculate lattice parameters as listed in Table 4.38. The fitting was assessed by the goodness of fit and the low values of the reliable factor as included in Table 4.38. The successful substitution of Co-Zn ions at crystallographic sites can be determined through the change observed in the intensity of the peaks and lattice size at the transition from FP1 to FP6. The lattice constants span from 4.914047 to 5.880236 Å, whilst

'c' changes from 23.036865 – 28.141920 Å with Co-Zn substitution. This behavior owes to the larger ionic radii of  $\text{Co}^{2+}$  ion (0.72Å) and  $\text{Zn}^{2+}$  ion (0.82Å) than host  $\text{Fe}^{3+}$  ion (0.645 Å). The average crystallite size has been calculated using (107) peak by applying Scherrer's Eq. 3.3. The crystallite size of M-type hexaferrite ranges from 29.07-67.43 nm. The volume of the unit cell ( $V_{cell}$ ) is estimated using the expression  $V_{cell} = 0.8666a^2c$ , and it ranges from 588.506 Å<sup>3</sup> to 690.169 Å<sup>3</sup>.

**Table 4.38** Values of the lattice constant of M-type hexagonal ferrite.

Sample codes	FP1	FP2	FP3	FP4	FP5	FP6
$a=b$ (Å)	5.878378	5.879609	5.880236	5.878811	4.914047	5.716410
$c$ (Å)	23.043200	23.036865	23.048105	23.042702	28.141920	23.274202
$V_{cell}$ (Å <sup>3</sup> )	689.586	689.685	690.169	689.673	588.506	658.646
$R_p$ (%)	38.2	25.8	32.2	31.9	33.3	34.9
$R_{wp}$ (%)	21.0	13.2	19.6	14.4	19.1	17.2
$GoF$	0.83	0.5	0.78	0.55	1.1	1.0

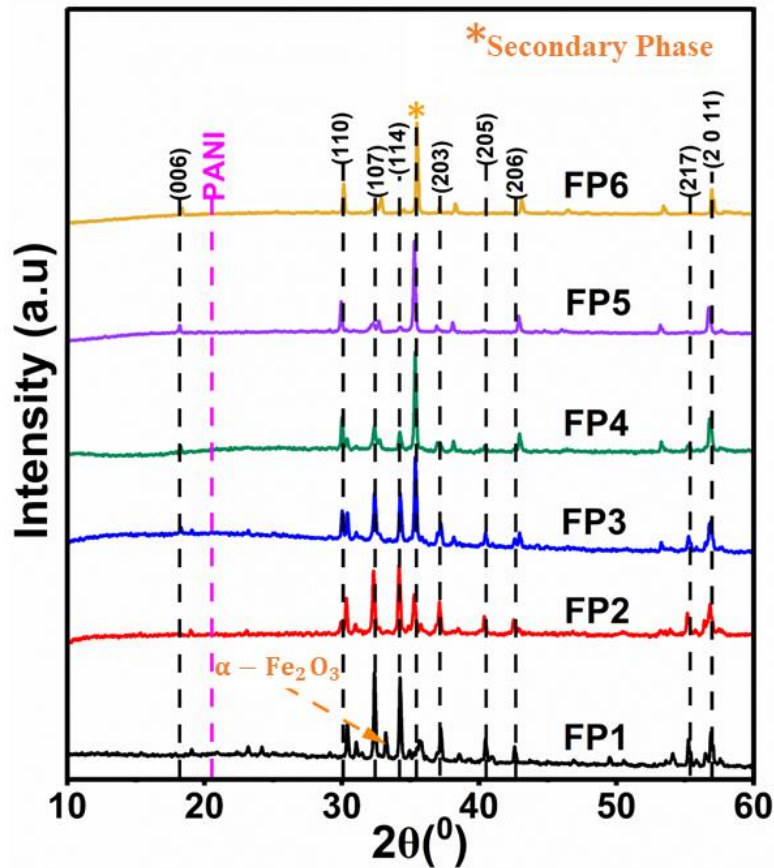


**Fig. 4.120.** XRD pattern of FP1, FP2, FP3, FP4, FP5, and FP6 ferrite composites.



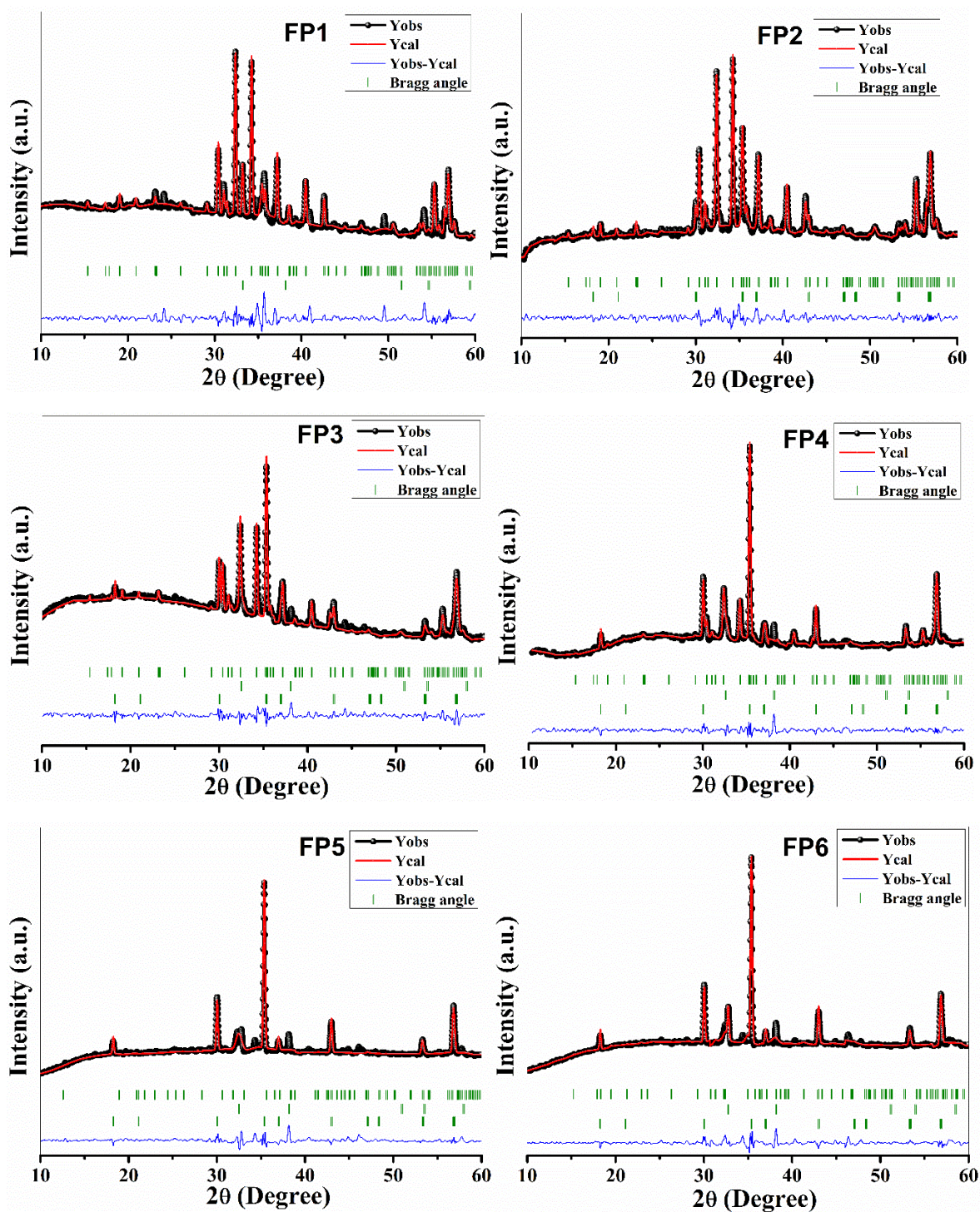
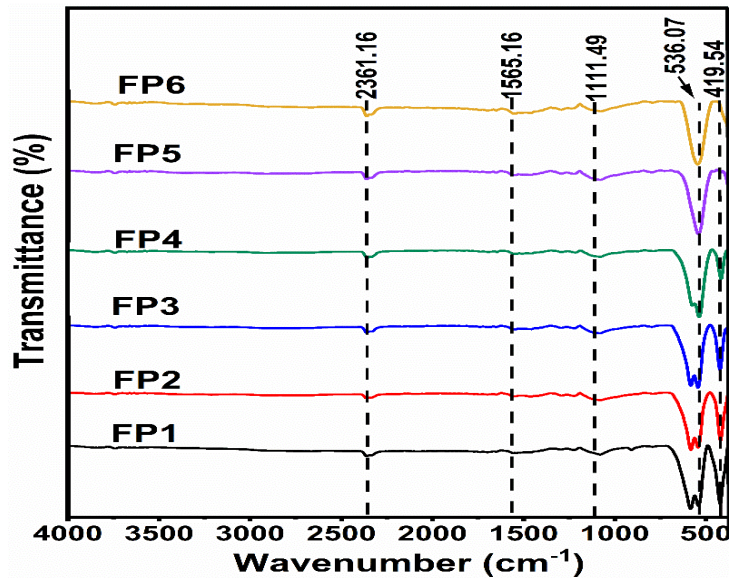


Fig. 4.121. Rietveld refinement of FP1 to FP6 samples.

#### 4.6.1.2 FTIR-analysis

Fig. 4.119 demonstrates the FTIR spectra of FP-hexaferrite composites, in the wavenumber range of 4000-380  $\text{cm}^{-1}$ , at room temperature. Two precise absorption band found near 536.07  $\text{cm}^{-1}$  and 419.54  $\text{cm}^{-1}$  owes to stretching vibrations of Fe-O at tetrahedral and octahedral sites of crystal structure, respectively. Furthermore, substitution alters the band position of crystallographic sites toward the lower frequency side. This manifests the

successful substitution of Co-Zn ions in M-type crystallographic sites. A weak absorption peak appears at  $2361\text{ cm}^{-1}$ , suggesting the occurrence of  $\text{CO}_2$ . However, bands obtained nearly at  $1111\text{ cm}^{-1}$  and  $1565\text{ cm}^{-1}$  are attributed to the weak stretching vibration in the aromatic amine (C=N) and quinoid ring (C=N), respectively, and assured the occurrence of PANI in the synthesized composites.



**Fig. 4.122.** FTIR spectra of of FP1, FP2, FP3, FP4, FP5, and FP6 ferrite composites.

#### 4.6.1.3 FESEM analysis

Surface morphology analysis of composite particles is conducted using FESEM. The FESEM micrographs of Co-Zn substituted hexaferrite-polymer composites are presented in [Fig. 4.120](#). FESEM micrographs of  $\text{SrFe}_{12}\text{O}_{19}$  display the hexagonal platelet-like structure with irregular size distribution. The morphology depicts a disk flower/small tubular-like structure of PANI, which forms a network between individual grains. The disk floret of PANI is embedded in platelet hexaferrite and affirms the encapsulation of PANI (amino group) with  $\text{SrFe}_{12}\text{O}_{19}$  (oxygen). Furthermore, an agglomerate morphology as dense/closely packed particles is due to attractive forces among the molecules of ferric, cobalt, zinc, and strontium ions, because of the same concentration of PANI (minimizing the aggregation). The insertion of Co-Zn ions into ferrite-polymer composites leads to an increment in grain size and improves inter-grain connectivity.



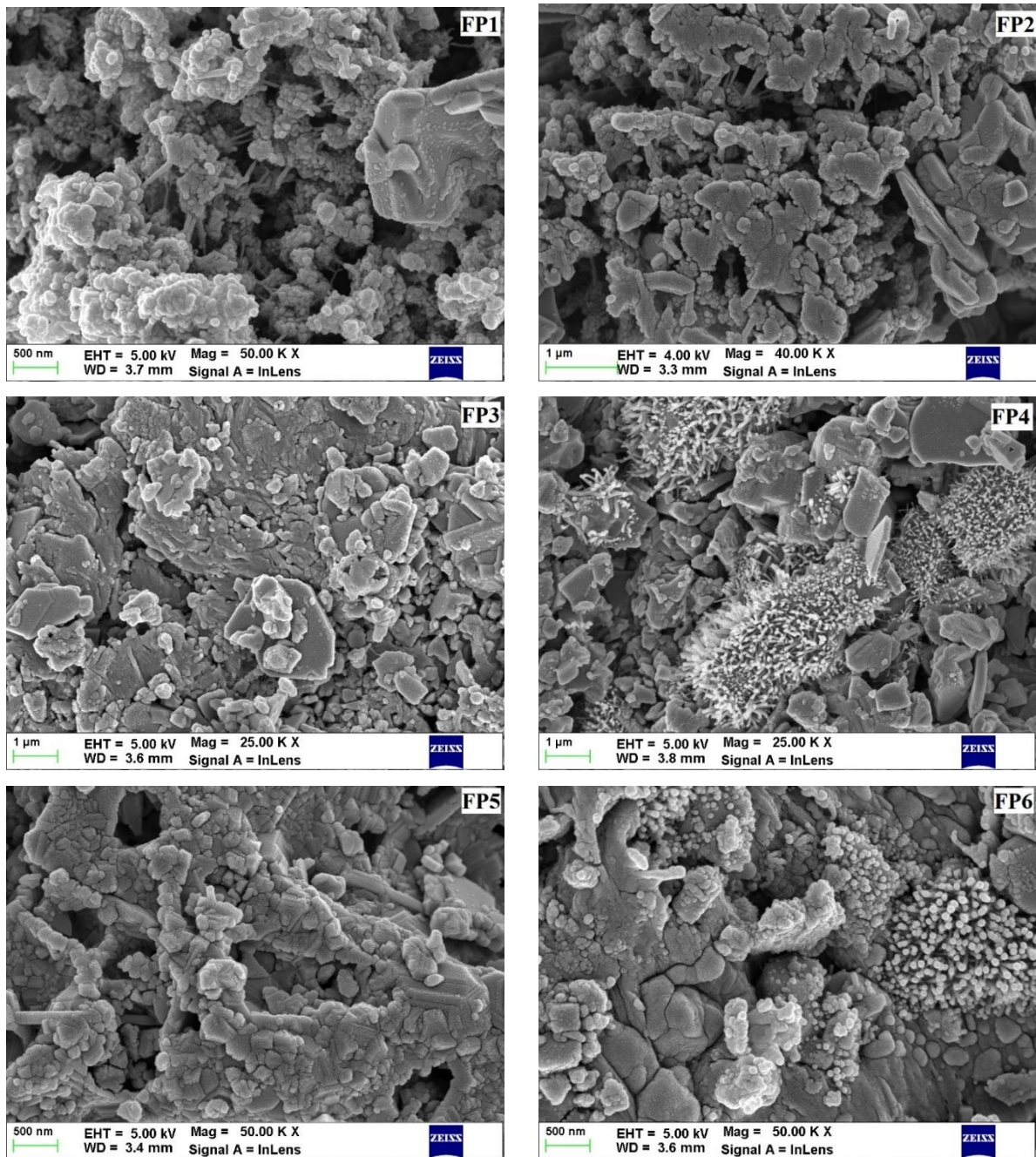


**Fig. 4.123.** FESEM micrographs of ferrite composites.

## 4.6.2 Electrical Analysis

### 4.6.2.1 Dielectric constant

Fig. 4.121 and 4.122 portrays the frequency-dependent behavior of  $\epsilon'$  and  $\epsilon''$  it decreases with increasing the frequency of an applied field. It is the general dielectric behavior exhibited by all ferrite materials. The observed dispersion can be understood through the Maxwell-Wagner model. At low-frequency region, from FP1 to FP6 a non-linear variation is observed in  $\epsilon'$  and  $\epsilon''$  value, and FP1 and FP3 samples become frequency-

independent above  $10^5$  Hz, whereas FP5 and FP6 samples show this trend above  $10^3$  Hz. The relative dielectric constant of FP2 and FP4 samples continuously varies with frequency. This significant change in the dispersion rate of all synthesized composites can be ascribed to the availability of  $Fe^{2+}$  ions at octahedral sites. From previous reports,  $Co^{2+}$  ( $3\mu_B$ ) ions can occupy both the octahedral and tetrahedral crystallographic sites, while  $Zn^{2+}$  ( $0\mu_B$ ) tends to replace  $Fe^{3+}$  ions at tetrahedral sites [286]. The non-linear nature of occupying a specific crystallographic site leads to a non-linear variation in  $\epsilon'$  and  $\epsilon''$  value at low-frequency region with substitution. The  $\epsilon'$  and  $\epsilon''$  value is found to be maximum for FP1, FP3, and FP5 samples as compared to FP2, FP4, and FP6 samples, despite the same concentration of PANI. This can be easily explained with FESEM micrographs (Fig. 4.120), where FP1, FP3, and FP5 samples exhibit small-size grains that are well interlinked with each other through grain boundaries (enhances interfacial polarization). However, Fig. 4.121 and 4.122 illustrate that the FP4 sample exhibits minimum  $\epsilon'$  and  $\epsilon''$  values at low-frequency regions, suggesting heterogeneous structures or interfaces due to large areas covered with disk flower-like structures (PANI). The addition of PANI in the FP4 sample decreases the availability of  $Fe^{2+}$  ions at octahedral sites, thus resulting in a minimum dielectric constant. Fig. 4.122 delineates a small peak in a certain range of frequencies for the FP4 sample, suggesting the existence of a resonance or absorption phenomenon in the material. Materials with heterogeneous structures or interfaces, such as composites or materials with layered structures, can exhibit peaks in the  $\epsilon''$  plots with frequency. These peaks are related to interfacial polarization effects, where energy is absorbed as charges redistribute across the interfaces. Finding the exact mechanism behind this observation needs more investigation.

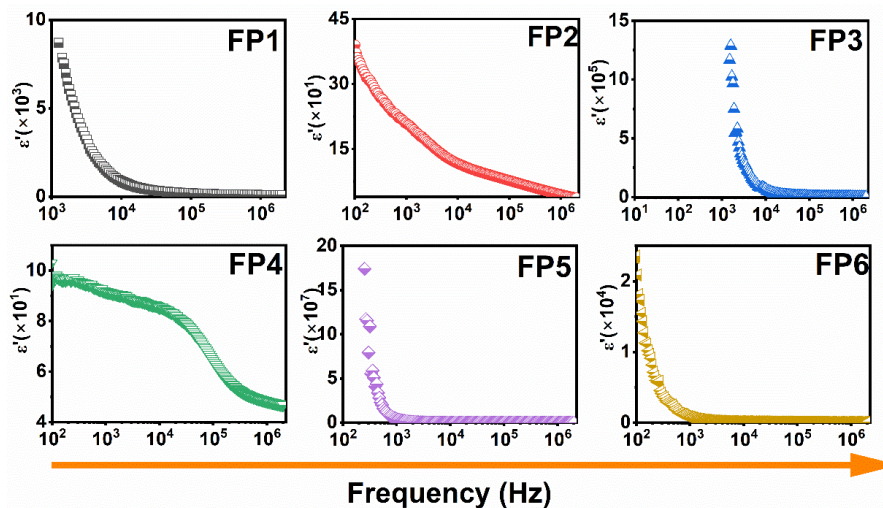
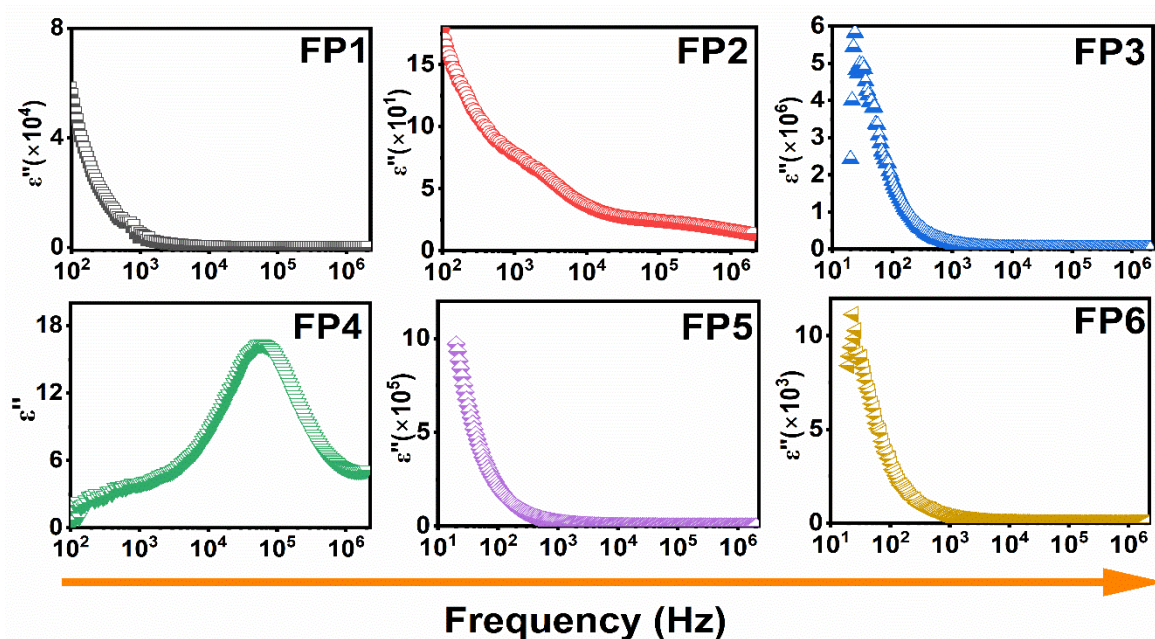


**Fig. 4.124.**  $\epsilon'$  variation with frequency of FP1, FP2, FP3, FP4, FP5, and FP6 ferrite composites.



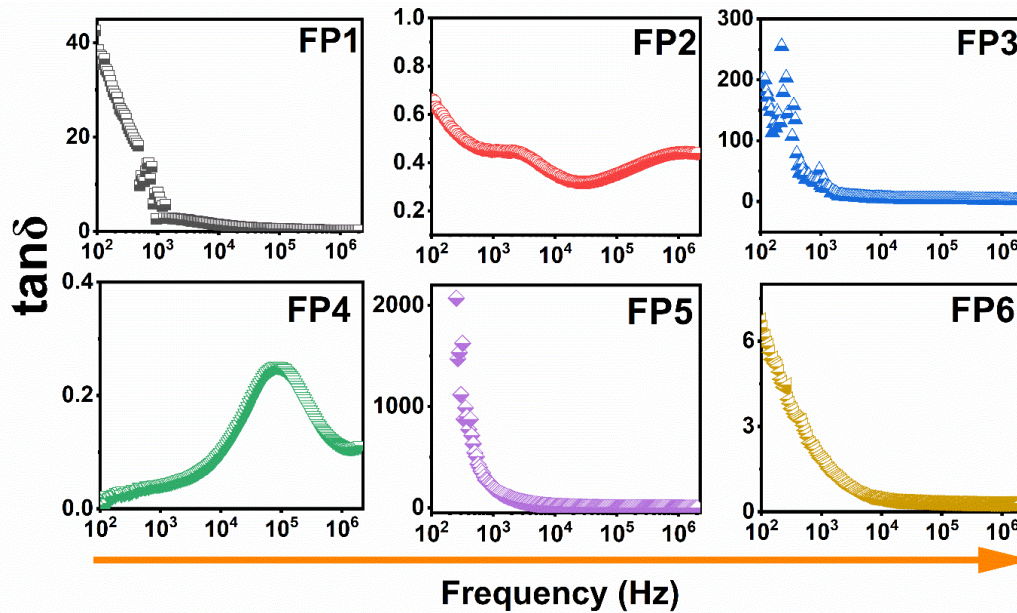
#### 4.6.2.2 Loss tangent

Fig. 4.123 depicts the frequency-dependent variation of  $\tan\delta$ , it is high at low frequencies and it declines with increasing frequency. Various features involving sample stoichiometry, interfacial polarization, interface traps, sintering temperature, and  $Fe^{2+}/Fe^{3+}$  content affected  $\tan\delta$ . This can be well understood through Koop's phenomenological theory. The  $\tan\delta$  value is found to be the maximum for the FP5 sample among all in the low-frequency region, despite the same concentration of PANI. This may be attributed to the large no. of grain boundaries in FP5, which contain crystal imperfections, impurities, dangling bonds, and porosity, which act as insulating layers causing delayed polarization and increased energy consumption. Additionally, the  $\tan\delta$  of the FP4 sample begins to exhibit a peak at a specific frequency in the high-frequency region. This can be ascribed to the occurrence of a relaxation phenomenon in the FP4 sample.



**Fig. 4.125.**  $\epsilon''$  variation with frequency of FP1, FP2, FP3, FP4, FP5, and FP6 ferrite composites.

When an externally applied field of varying frequency is given to the material, a resonance occurs because the frequency of charge hopping between cations  $Fe^{3+}$  and  $Fe^{2+}$  at the octahedral sites matches the applied frequency. It can also be elucidated through the morphology of PANI in the FP4 sample. As shown in the figure, FP4 exhibited a large area covered with a disk-flower-like structure, despite the same concentration of PANI. This morphology of PANI assessed additional interfaces that cause more energy dissipation in the sample.



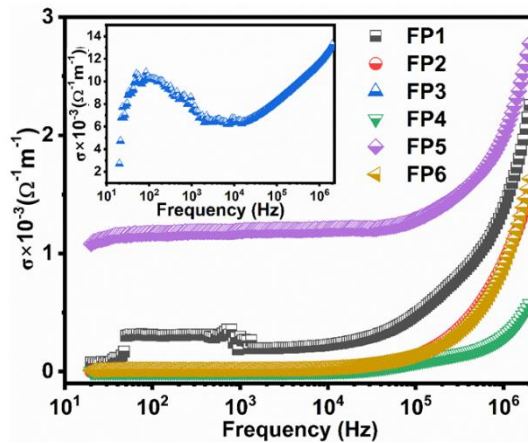
**Fig. 4.126.**  $\tan\delta$  variation with frequency of FP1, FP2, FP3, FP4, FP5, and FP6 ferrite composites

#### 4.6.2.3 AC-conductivity

Fig. 4.124 illustrates the variation of  $\sigma$  with increasing frequency. It depicts the frequency-independent behavior of  $\sigma$  at lower frequencies and sharply increases in the higher frequency region ( $>10^5$  Hz). The replacement of  $\text{Fe}^{3+}$  ions with Co-Zn ions causes a non-linear reduction in conductivity value at a higher frequency and is maximum for FP3. This reduction elucidates a decrement in the concentration of  $\text{Fe}^{3+}$  ions at an octahedral position, which restricts the probability of hopping between  $\text{Fe}^{2+}$  and  $\text{Fe}^{3+}$  ions. The maximum value of  $\sigma$  in the FP3 sample is due to the good inter-grain connectivity between large and small-sized grains, over other substituted composites, as seen in Fig. 4.120. Furthermore, the FP3 sample exhibits a broad peak in the low-frequency region, indicating the suppression of electrode polarization. This variation is consistent with  $\epsilon'$  plot obtained for the FP3 sample (Fig. 4.121).

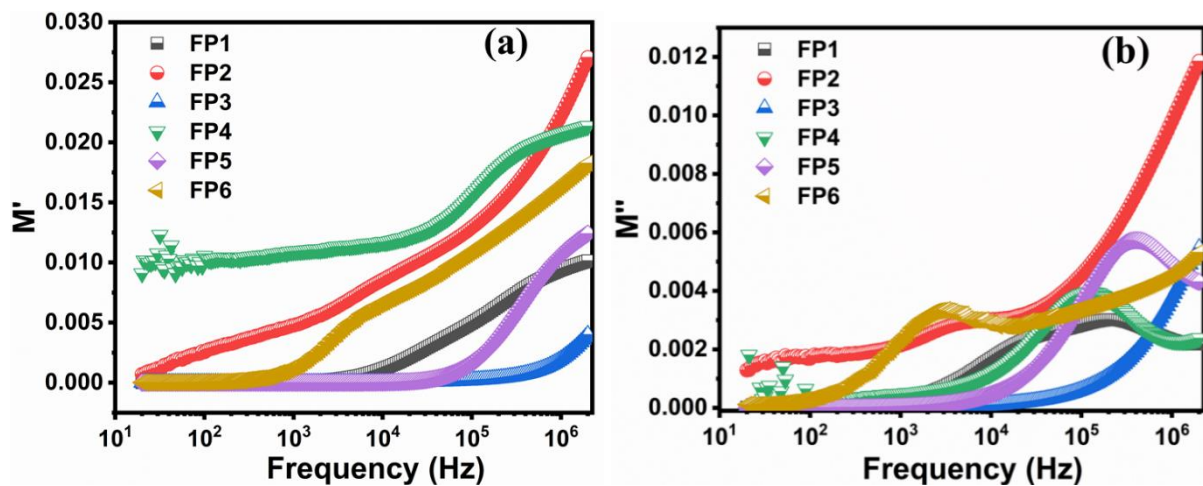
#### 4.6.2.4 Complex electric modulus

Fig. 4.125(a) illustrates that  $M'$  values are low in the lower frequency range, and it increases with increasing frequency. At lower frequencies, the  $M'$  values for all synthesized samples tend to approach zero, indicating maximum restoring force depolarization and consequently the lowest conductivity and minimal electrode polarization. The low  $M'$  value observed in the low-frequency region for all synthesized ferrite composites (except FP4), suggests the suppression of electrode polarization phenomena.



**Fig. 4.127.**  $\sigma$  variation with frequency of FP1, FP2, FP3, FP4, FP5, and FP6 ferrite composites.

In the FP4 sample, the disk-flower-like structure enhances the electrode polarization effect, as evident from the increment in  $M'$  values at low frequencies in the FP4 sample. The electrode polarization phenomenon arises due to the long-range mobility of charge carriers, governed by the restoring force under the influence of an induced electric field [277]. Furthermore, the value of  $M'$  increases with increasing frequency, showing that the conduction can be attributed to the short-range mobility of charge carriers. This variation is similar to the behavior observed in  $\sigma$ , discussed in the previous section. However, the substitution of Co-Zn ions (forming grain clusters) causes an increment in  $M'$  values of FP2, FP4, FP5, and FP6 samples in the high-frequency region, despite the same concentration of PANI.



**Fig. 4.128.** (a)  $M'$  (b)  $M''$  variation with frequency of FP1, FP2, FP3, FP4, FP5, and FP6 ferrite composites.



Fig. 4.125(b) displays the frequency-dependent behavior of  $M''$  for all ferrite composites at room temperature. The asymmetric shape of the plot for the peak maxima suggests non-Debye relaxation but exhibits characteristics of Cole-Cole relaxation. As the substitution level of Co-Zn ions increases, a non-linear variation is observed in the relaxation frequency. Fig. 4.125(b) delineates that substituting Co-Zn ions shifts the relaxation frequency from low to high-frequency region, indicating the contribution of grains.

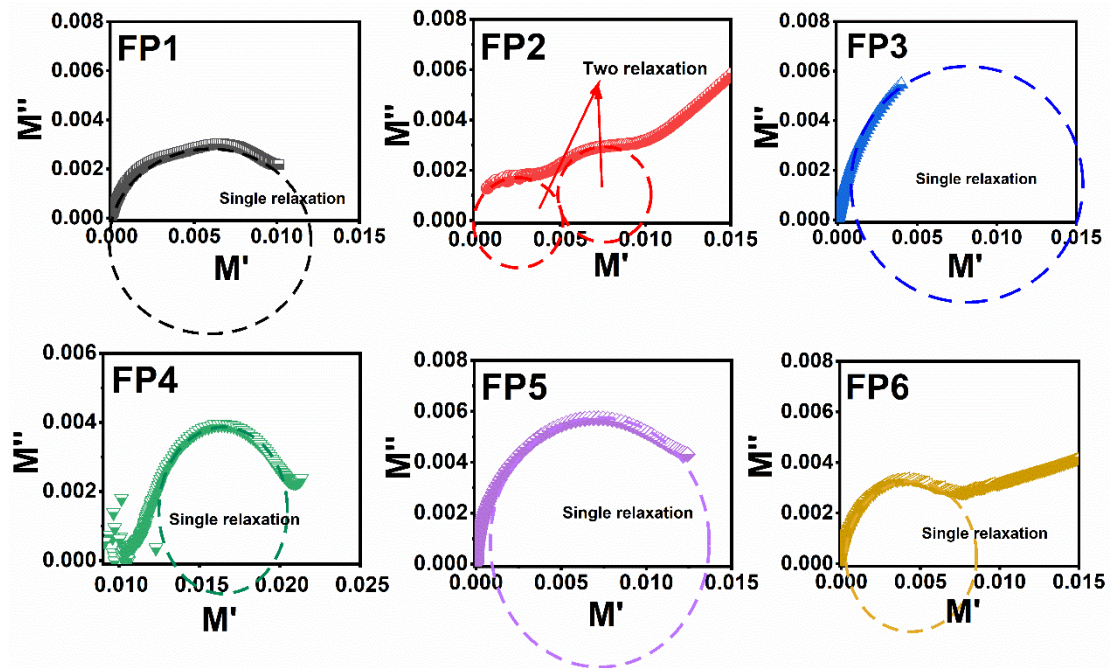


Fig. 4.129. Cole-Cole plot ( $M''$  vs  $M'$ ) variation with frequency of FP1, FP2, FP3, FP4, FP5, and FP6 ferrite composites.

Fig. 4.126 depicts the Cole- Cole plots ( $M''$  versus  $M'$ ) of all synthesized ferrite composites at room temperature. The obtained curves demonstrate that their centers are situated below  $M'$ -axis. This suggests that the observed relaxations are of non-Debye type and distributed over different time constants. It can be seen (Fig. 4.120) that due to the different grain size distribution, the curve distribution ( $M''$  versus  $M'$ ) is also found to be distinct for all samples. It is clear (Fig. 4.126) that FP1, FP4, FP5, and FP6 composites exhibit a semicircle, FP3 results in a segment of a semicircular arc, and FP2 shows two weak relaxation approaches to the high-frequency region. Among all synthesized composites, the FP1 sample shows a smaller peak height which is attributed to the weak inter-grain connectivity, occurrence of porosity (Fig. 4.120), and effect of grain boundaries. Substitution causes a shift in the semicircular arc toward the higher-frequency region from FP1 to FP6. Moreover, it is seen in the figure that semi-circular arcs of all synthesized composites (except FP4) begin almost at the same point in the low-frequency region due to minimum

conductivity. While the curve distribution ( $M''$  vs  $M'$ ) of these composites are different in the higher frequency region. This could be due to the maximum conductivity caused by different grain size distributions in all substituted composites, as seen in FESEM micrographs (Fig. 4.120)

#### 4.6.2.5 Complex impedance study

Fig. 4.127 and 4.128 illustrate the decreasing trend observed in both  $Z'$  and  $Z''$  with increasing the frequency of an applied field, respectively. The declining behavior of both  $Z'$  and  $Z''$  with increasing frequency, indicates an increment in the electron hopping between localized ions and results in an increase in ac conductivity. The reduction observed in  $Z'$  could be explained through the Maxwell-Wagner model at higher frequencies. The investigation of  $Z''$  led to a better understanding of the relaxation process and space charge effect [280]. At low frequencies, the space charge effect dominates the impedance response and results in a larger value of  $Z''$ . However, at higher frequencies the charge carriers may not be able to respond rapidly to the alternating applied, leading to a decrement in the  $Z''$ .

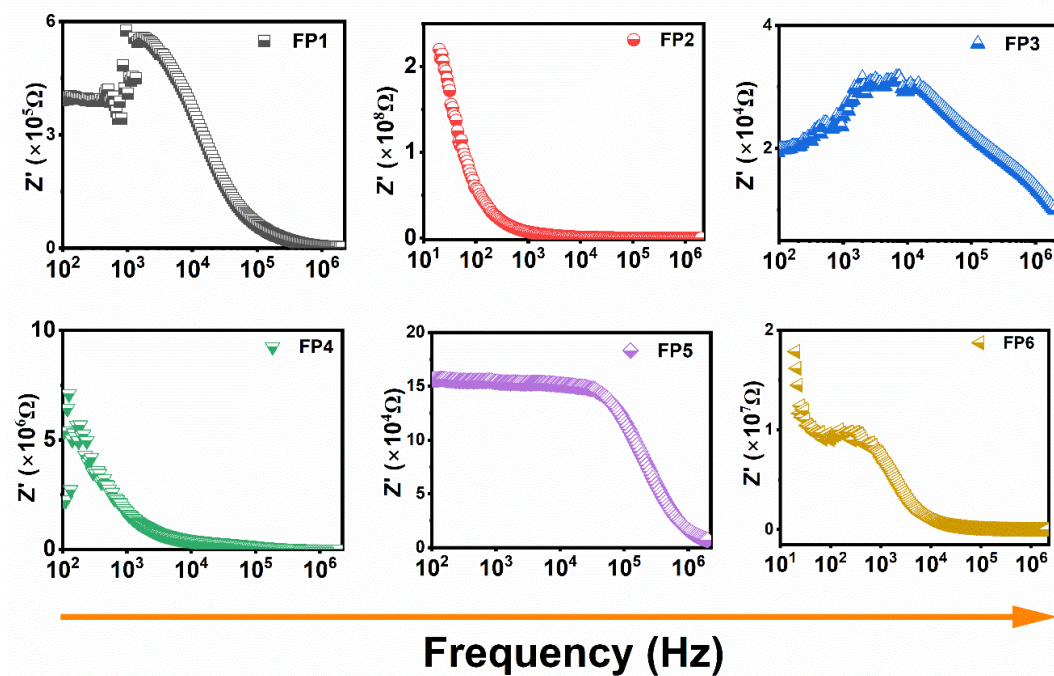
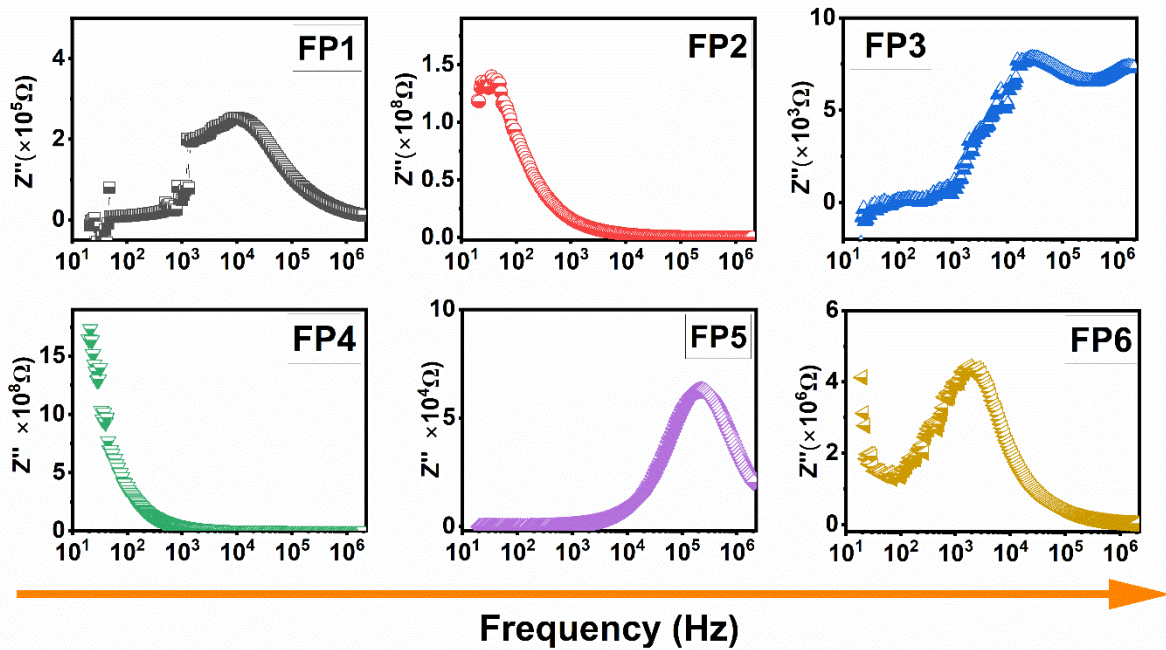
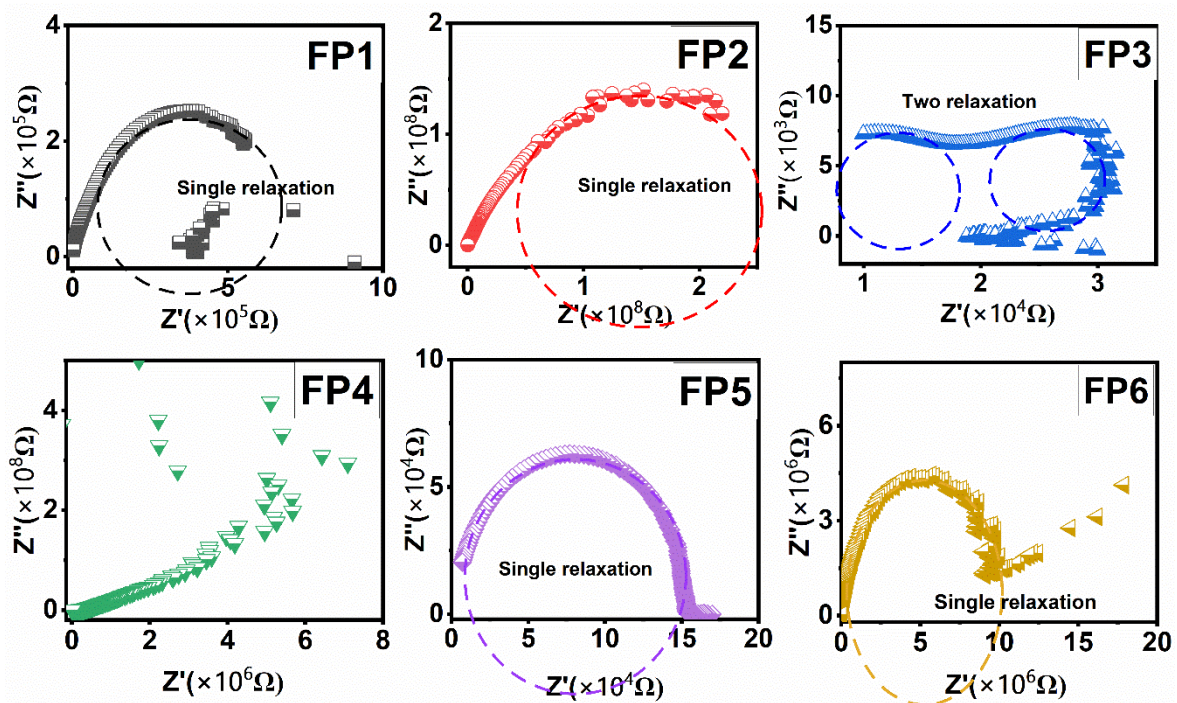


Fig. 4.130.  $Z'$  variation with frequency of FP1, FP2, FP3, FP4, FP5, and FP6 ferrite composites.





**Fig. 4.131.**  $Z''$  variation with frequency of FP1, FP2, FP3, FP4, FP5, and FP6 ferrite composites.



**Fig. 4.132.** ( $Z''$  vs  $Z'$ ) variation with frequency of FP1, FP2, FP3, FP4, FP5, and FP6 ferrite composites.

The Cole-Cole plot reveals the effect of morphology and polarization process on dielectric relaxation. Fig. 4.129 illustrates the Cole-Cole plots of all synthesized ferrite-polymer composites at room temperature. In ferrites, the conduction process involves

contributions from both the grains and the grain boundaries [319]. The grain boundaries introduce resistance, leading to a deceleration of the conduction process, which is represented by the presence of broad semi-circles. It is clear in Fig. 4.121 that FP1 and FP2 samples do not form the complete semicircle but somewhat approach the shape suggesting the relative contribution of grains. In FP3, a complete semicircle in the low-frequency region with some portion of semicircle in the high-frequency region, indicating more contribution of grain boundary resistance than grain resistance.

This behavior is analog to FESEM, wherein a large no. of small grains is distributed over large-sized grains. Further, FP4 exhibits a straight-line approach toward the low-frequency region (maximum  $Z''$ ), indicating the resistance is predominately due to the grain boundaries. This result is well consistent with FESEM micrographs, wherein a large area of the FP4 sample is covered with disk-flower structure (PANI), which promotes grain boundary resistance. Further substitution of Co-Zn ions in FP5 and FP6 samples, leads to a complete semicircle in the high-frequency region. This can be explained through the large-sized grains contributing relatively more to resistance than grain boundaries, affirmed by FESEM (Fig. 4.120).

### 4.6.3 Magnetic analysis

Fig. 4.130 shows the M-H loops of synthesized ferrite-polymer composites. From previous reports,  $Co^{2+}$  ( $3\mu_B$ ) ions can occupy both the octahedral ( $4f_2$ ) and tetrahedral ( $4f_1$ ) crystallographic sites, while  $Zn^{2+}$  ( $0\mu_B$ ) tends to replace  $Fe^{3+}$  ions at the  $4f_1$  site [286]. The insertion of PANI (non-magnetic polymer) in all ferrite-polymer composites may dilute the magnetic parameters such as  $M_s$ ,  $M_r$ ,  $H_c$ , anisotropy field ( $H_a$ ), remanence ratio ( $M_r/M_s$ ) and magnetic moment ( $n_B$ ) values derived from the hysteresis loop are enumerated in Table 4.39.

The magnetic moment of the incorporated specimen could be determined through the distribution of host and substituted cations over five crystallographic sites of hexagonal crystal structure using the following expression[287]:

$$M_s = M_a (2a + 12k + 2b) (\uparrow) - M_b (4f_1 + 4f_2) (\downarrow)$$

The total magnetization increases by substituting non-magnetic ions or less magnetic at the ( $4f_1\downarrow + 4f_2\downarrow$ ) lattice site, while magnetization shows decline behavior with the substitution of these ions at ( $2a\uparrow + 12k\uparrow + 2b\uparrow$ ) lattice sites[230]. Table and figure demonstrated a feeble change in the value of  $M_s$  from FP1 (50.53 emu/g) to FP3 (50.48 emu/g) and further substitution caused a gradual decrease of 24.30 % (FP3 to FP6). The simultaneous

replacement of Fe<sup>3+</sup> ions by Co and Zn ions at spin-up and spin-down sites signifies a minor change observed in M<sub>s</sub> (FP1 to FP3). From previous reports, Zn<sup>2+</sup> ions have a strong tendency to occupy the 4f<sub>1</sub> spin-down site and yield an increment in M<sub>s</sub>, while Co<sup>2+</sup> ions may replace Fe<sup>3+</sup> ions present at 4f<sub>2</sub> spin-down and 12k spin-up octahedral sites. A strong magnetic structure predominately depends on the arrangement of 12k sites of the crystal lattice and is disrupted by the presence of weak magnetic Co<sup>2+</sup> ions at these sites, leading to a gradual breakdown of collinear octahedral-tetrahedral superexchange interactions at a higher level of substitution. Additionally, the localization of Co<sup>2+</sup> ions in 4f<sub>2</sub> sites causes local spin canting and contributes to magnetic alteration. Moreover, the remanence magnetization (M<sub>r</sub>) is found to gradually decrease with substitution from FP1 (28.82 emu/g) to FP5 (4.62 emu/g) [320]. The calculated value of M<sub>r</sub>/M<sub>s</sub> is enlisted in the table and it turns out to be less than 0.5 for all synthesized composites, which depicts the multi-domain nature of particles within the material.

The lowest value of coercivity (50.79 Oe) is observed in the FP1 sample, which is associated with the absence of substituent cations in the crystal lattice. The initial substitution of Co-Zn ions causes a pronounced increase in H<sub>c</sub> value from FP1 (50.79 Oe) to FP2 (2293.5 Oe), and later a gradual decrement to FP6 (60.76 Oe). The nature of this variation can be explained by the support of intrinsic and extrinsic factors. Intrinsic factors primarily depend on chemical composition, anisotropy field (H<sub>a</sub>), and crystal structure[239]. On the other hand, extrinsic factors are associated with grain size, temperature, and magnetic field [238]. The increment observed in H<sub>c</sub> value from FP1 to FP2, is caused by H<sub>a</sub>. A larger anisotropy field leads to higher coercivity, i.e., more energy is required to reverse the magnetic moment of the hexaferrite. Due to the inverse nature of H<sub>c</sub> with grain size, the reduction observed in H<sub>c</sub> at a higher level of substitution can be accompanied by the increment in grain size.

**Table 4.39** Values of various magnetic parameters of ferrite composites.

Sample Name	FP1	FP2	FP3	FP4	FP5	FP6
M <sub>s</sub> (emu/g)	50.53	53.39	50.48	47.65	39.42	38.21
H <sub>c</sub> (Oe)	50.79	2293.5	1230.7	366.31	142.04	60.76
H <sub>a</sub> (kOe)	5.77	15.30	5.688	10.23	8.42	13.82
M <sub>r</sub> (emu/g)	28.82	25.12	21.19	14.30	8.487	4.622
M <sub>r</sub> /M <sub>s</sub>	0.570	0.470	0.419	0.300	0.215	0.120



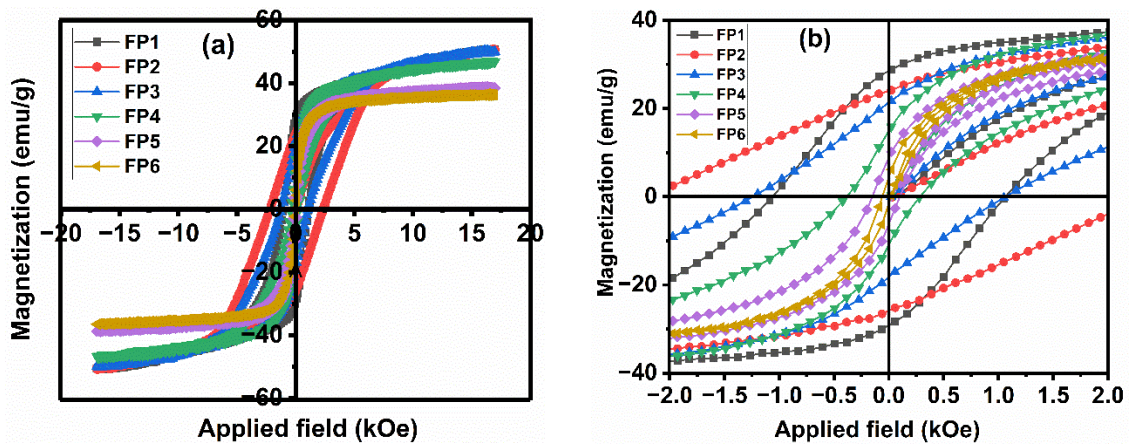


**Fig. 4.133.** (a) M-H plots (b) Enlarged view of M-H plots of FP1, FP2, FP3, FP4, FP5, and FP6 ferrite composites.

#### 4.6.4 Electromagnetic Analysis

Electromagnetic properties are often described by complex permittivity/permeability. Fig. 4.131(a, b) depicts the variation of dielectric constant ( $\epsilon'$ )/loss ( $\epsilon''$ ) of FP2, FP3, FP4 and FP6 samples in the frequency range of 8.2 to 12 GHz, FP1 and FP4 from 12.4 to 18 GHz. The inclusion of insulating hexagonal ferrite within the conductive matrix leads to the existence of additional interfaces, resulting in a heterogeneous system. This heterogeneity is due to the accumulation of space charge at these interfaces, which, in turn, contributes to enhanced microwave absorption in the composite material. A strong polarization effect occurs in PANI, due to the presence of polaron/bipolaron and other bound charges, resulting in a high  $\epsilon'/\epsilon''$ . The  $\epsilon'/\epsilon''$  values remain relatively stable for all samples. A large dispersion is observed in the FP1 sample and sample FP2 scales to the highest  $\epsilon'$  amidst all samples and with substitution it decreases. Sample FP4 exhibits a comparatively strong resonance peak around 9 GHz than FP3 and FP6 samples, despite the same concentration of PANI. This can be explained by the substitution of Co-Zn ions. Fig. 4.131(a,b) demonstrated the variation of permeability ( $\mu'$ )/ magnetic loss ( $\mu''$ ) as a function of frequency. The small dispersion observed in  $\mu''$  of the FP1 sample from 12 to 18 GHz frequency range and is maximum among all, whereas  $\mu'$  of all samples remains relatively constant over the entire frequency range. The behavior of  $\mu''$  is same for FP2, FP3, FP4, and FP6 sample and its value stays lower than 0.7. Conversely, the value of  $\mu'$  remains less than 1.5 for all samples and is maximum for FP3 (1.42 at 12 GHz). The plots illustrate that the complex permittivity is more influential than the complex permeability within the compositions. The interaction between PANI and ferrite particles at the interface reduces the magnetic characteristics of the

composites, thereby hindering the flow of magnetic field among ferrite particles. Consequently, magnetic loss (as depicted in Fig.4.130) contributes minimally to microwave attenuation.

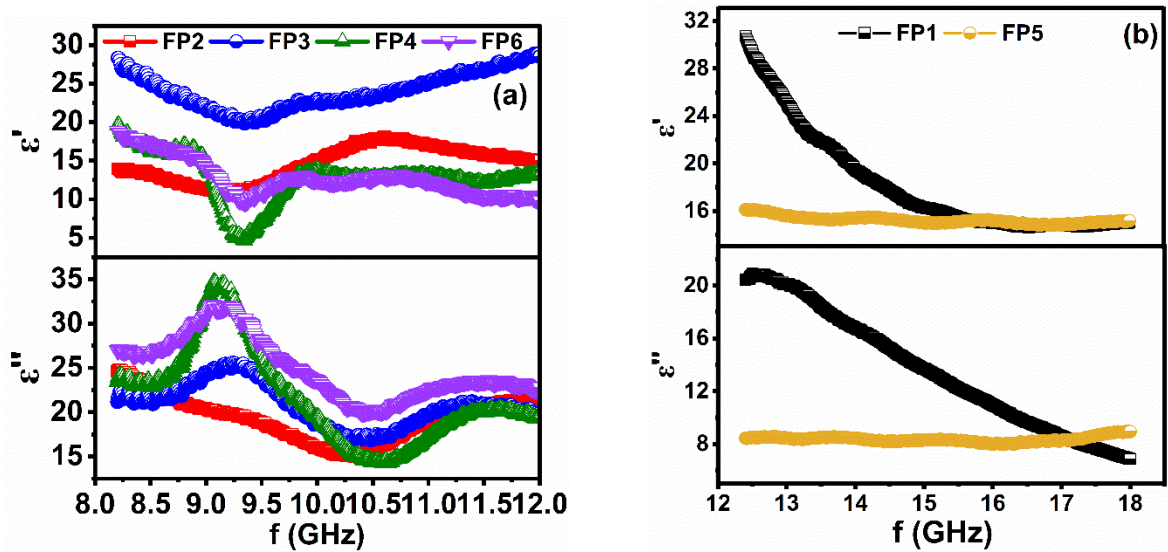


Fig. 4.134. (a) Complex permittivity of FP2, FP3, FP4, and FP6 samples (b) Complex permittivity of FP1 and FP5 samples.

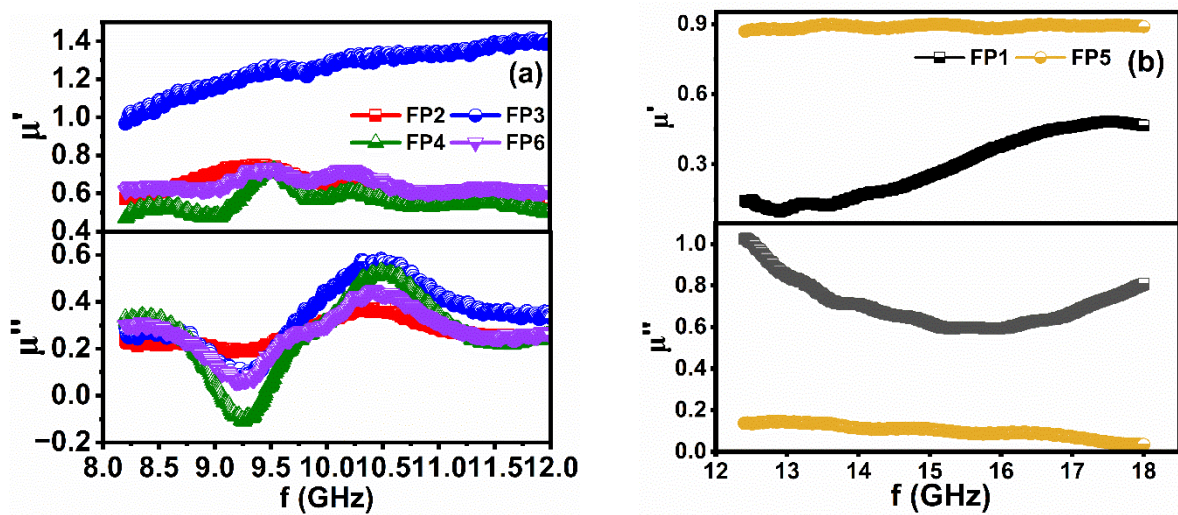


Fig. 4.135. (a) Complex permeability of FP2, FP3, FP4, and FP6 samples (b) Complex permeability of FP1 and FP5 samples.

## 4.7 Sr(CoCr)<sub>x</sub>Fe<sub>12-2x</sub>O<sub>19</sub> (80%)+ CoFe<sub>2</sub>O<sub>4</sub> (20%) ferrite composites

A physical blending method has been utilized to synthesize hexaferrite composites. In this study, we comprehensively analyzed structural, morphological, magnetic, electrical, and microwave absorption properties. Table 4.40 displays the assignment of sample names/codes for a different level of substitution for CoFe<sub>2</sub>O<sub>4</sub>/Sr(CoCr)<sub>x</sub>Fe<sub>12-2x</sub>O<sub>19</sub>.

**Table 4.40.** Assignment of sample name for a different level of substitution of CoFe<sub>2</sub>O<sub>4</sub>/Sr(CoCr)<sub>x</sub>Fe<sub>12-2x</sub>O<sub>19</sub> hexaferrite.

Sample Composition 20% CoFe <sub>2</sub> O <sub>4</sub> /Sr(CoCr) <sub>x</sub> Fe <sub>12-2x</sub> O <sub>19</sub>	Sample Code (BS-series)
x = 0.0	BS1
x = 0.2	BS2
x = 0.4	BS3
x = 0.6	BS4
x = 0.8	BS5
x = 1.0	BS6

### 4.7.1 Structural analysis

#### 4.7.1.1 X-ray analysis

Fig. 4.133 depicts the XRD pattern of the hard/soft composites as a function of Co-Cr ions. XRD study affirms the existence of both SrM hexaferrite (ICDD# 80-1197) and CoFe<sub>2</sub>O<sub>4</sub> (ICDD# 22-1086) in the vicinity of each other, without any secondary phase. This indicates that mixing in a mortar pestle is an appropriate method for synthesizing ferrite composite without disrupting the magnetoplumbite structure of M-type hexaferrite. The structural parameters 'c' and 'a' are determined using Eq. 3.1 for M-type hexaferrite and  $a = d_{hkl} (h^2 + k^2 + l^2)^{1/2}$  for spinel ferrite, involving the Miller indices  $h, k, l$ . During the transition from BS1 to BS6, the change observed in lattice size and peak intensity elaborates the successful substitution of Co-Cr ions in hard/soft ferrite composites. The lattice parameters of M-type hexaferrite and spinel ferrite are summarized in Table 4.41. The lattice constant of M-type hexagonal and spinel ferrite decreases with the substitution of large ionic radii Co<sup>2+</sup>-Cr<sup>3+</sup> ions than host Fe<sup>3+</sup> ions. Debye Scherrer's Eq. 3.3 was used to determine the average crystallite size from (M-phase, 107) and (spinel phase, 311) XRD peaks. Substitution

causes non-linear decrement in M-type hexaferrite and spinel ferrite crystallite size from 51.7 to 44.4 nm and 57.5 to 44.2 nm, respectively.

**Table 4.41** Values of the lattice constant of M-type hexagonal and spinel ferrite.

Sample name	M-type Hexaferrite			Spinel ferrite	
	a=b (Å)	c (Å)	D (nm)	a=b=c (Å)	D (nm)
<b>BS1</b>	5.892	23.086	51.7	8.395	57.5
<b>BS2</b>	5.884	23.039	45.5	8.385	48.5
<b>BS3</b>	5.888	23.033	45.7	8.399	54.8
<b>BS4</b>	5.873	22.979	44.4	8.385	44.2
<b>BS5</b>	5.881	22.987	46.2	8.395	52.5
<b>BS6</b>	5.873	22.940	45.5	8.376	48.6

#### 4.7.1.2 FTIR analysis

Fig. 4.134 displays the IR spectra of BS-series samples in the wavenumber range of 2000-380  $\text{cm}^{-1}$ . The absorption peaks around 400-600  $\text{cm}^{-1}$  determines the stretching and bending vibration of metal-oxygen at tetrahedral as well as octahedral sites. This gives us a suggestion for the formation of M-type hexagonal ferrites. The absorption band in the range of 500-600  $\text{cm}^{-1}$  and 400-450 governs the Fe – O stretching through Fe -  $O_4$  and Fe – O bending due to Fe -  $O_4$  as well as Fe -  $O_6$ , respectively [321]. The 584.1  $\text{cm}^{-1}$  absorption peak observed in all composites is attributed to Fe-O stretching/ $\text{CoFe}_2\text{O}_4$  bending modes. There is no other absorption peak in the remaining range. This indicates the nonexistence of metal carbonates (in the form of remaining carbon),  $\text{NO}_3$  stretching vibrations and residual water in all sintered hexaferrite. It is attributed to completely burnt-off carbon, nitrates, and residual water through the self-ignition process during the preparation of ferrite [35].

#### 4.7.1.3 FESEM analysis

Fig. 4.135 presents the FESEM micrographs of BS-series composites. All the micrographs disclosed the co-existence of hexagonal platelet-like particles of M-type hexaferrite and small spherical-shaped particles of spinel ferrite. A high agglomeration phenomenon is observed between M-type and spinel ferrite. The insertion of Co-Cr ions improves the inter-grain connectivity between large and small-sized grain.



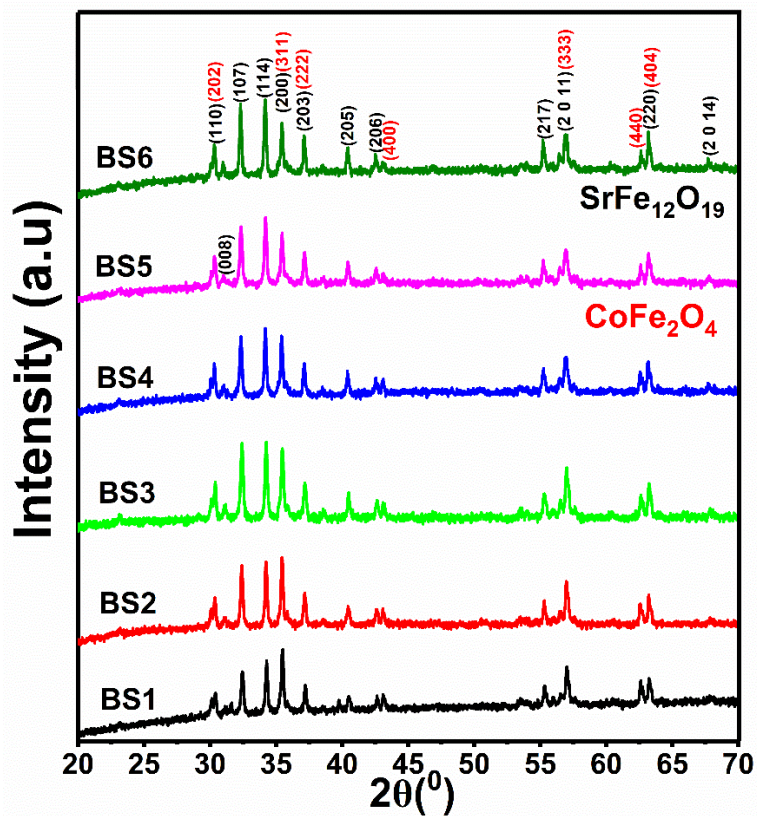


Fig. 4.136. XRD pattern of BS1, BS2, BS3, BS4, BS5, and BS6 composites.

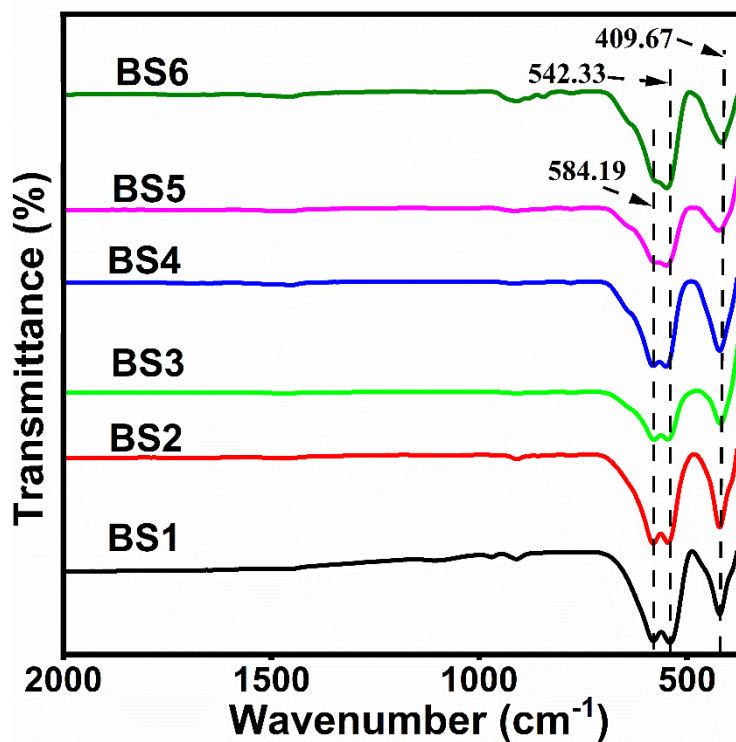
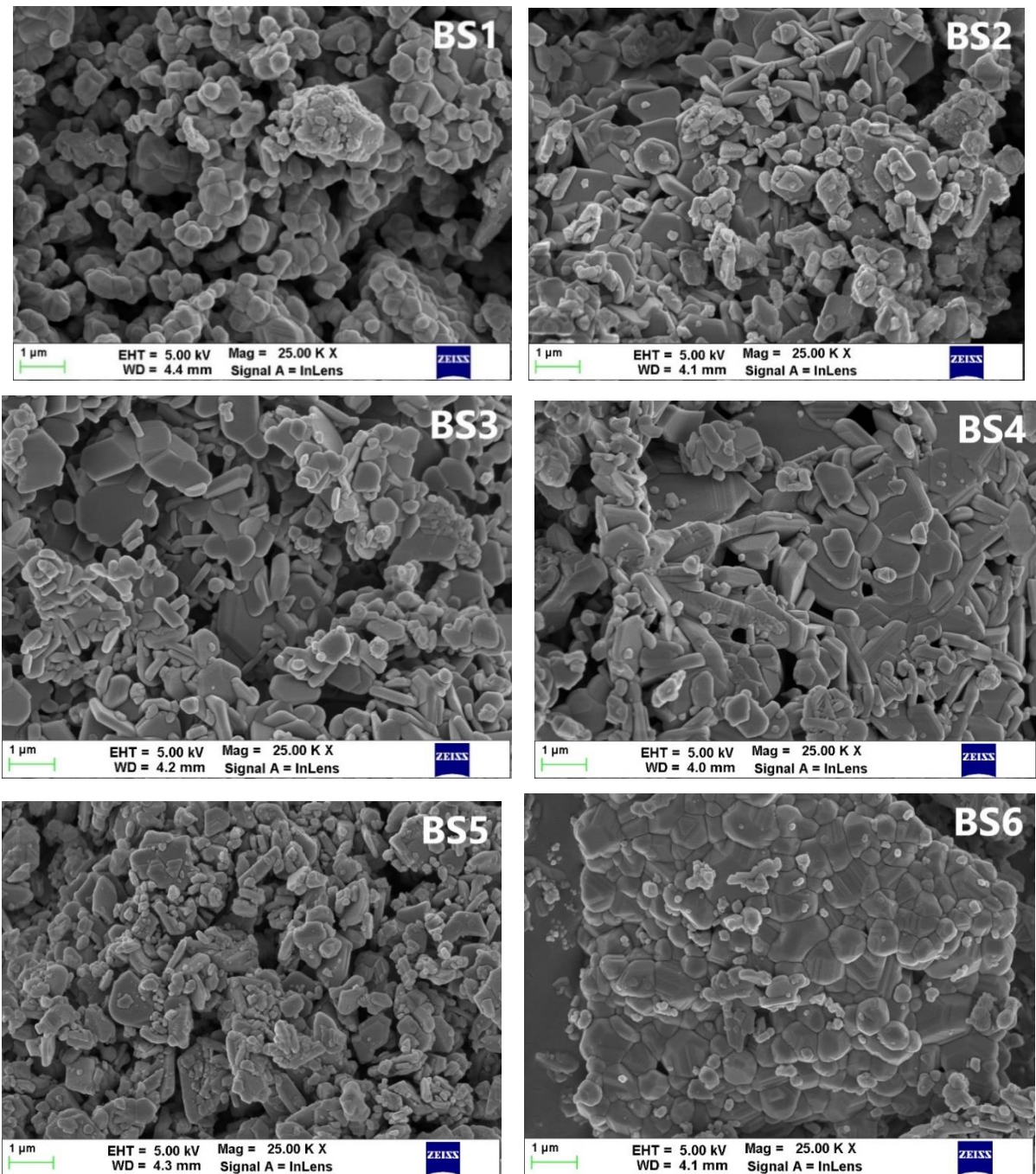


Fig. 4.137. FTIR spectra of BS1, BS2, BS3, BS4, BS5, and BS6 composites





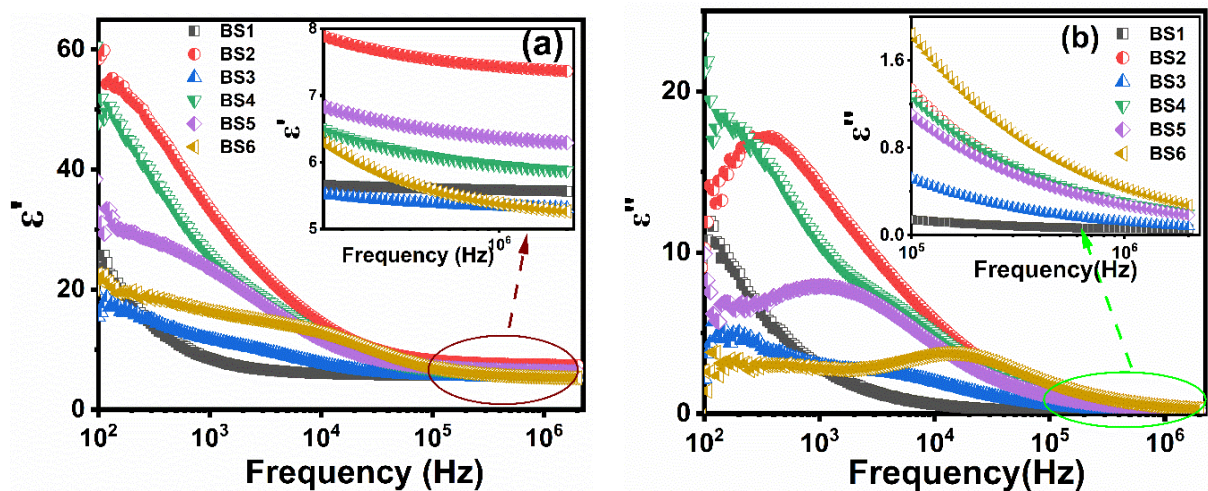
**Fig. 4.138.** FESEM micrographs of BS1, BS2, BS3, BS4, BS5, and BS6 composites.

## 4.7.2 Electrical analysis

### 4.7.2.1 Dielectric constant

In 100 Hz to 2 MHz frequency range, Fig. 4.136(a) depicts the dispersion of  $\epsilon'$  as a function of frequency/composition. Koop's phenomenological and Maxwell-Wagner models can explain it well. Fig. 4.136(a) illustrates a non-linear increment in the  $\epsilon'$  value of synthesized ferrite composites from BS1 to BS6. The lowest frequency dependence dielectric

dispersion is observed in BS3 and BS6. This can be governed by the availability of  $\text{Fe}^{2+}$  ions at octahedral sites. Substitution of Co-Cr ions causes an increment in  $\epsilon'$  value of BS2, BS4, and BS5 samples, explained by the electrons hopping between octahedral positions. Fig. 4.136(b) determines the behavior of  $\epsilon''$  as a function of frequency. The plotted curves of BS1, BS3, BS4, and BS6 samples exhibit a similar profile to that of  $\epsilon'$ , with lower values observed in the lower frequency range, and it becomes frequency independent beyond a particular limiting frequency. On the contrary, BS2 and BS5 samples show a peak in a specific frequency band, indicating the presence of a resonance or relaxation phenomena in the material. Materials with heterogeneous structures or interfaces, such as composites or materials with layered structures, can exhibit peaks in the  $\epsilon''$  plots with frequency. These peaks are related to interfacial polarization effects, where energy is dissipated as charges redistribute across the interfaces. The frequency-dependent  $\tan\delta$  curves for the synthesized ferrite composites are shown in Fig. 4.136(c). The introduction of Co-Cr ions results in a non-linear change in  $\tan\delta$  values due to the site occupancy of these ions toward the octahedral sites. All synthesized composites exhibit dielectric relaxation peaks in a certain frequency range, suggesting a distribution of relaxation times. A multi-interfacial relaxation peak observed in BS3 and BS4 samples attributed to heterogeneity caused by substitution. The relative change in peak broadening and peak height is ascribed to oxygen vacancies formed during Co-Cr substitution.



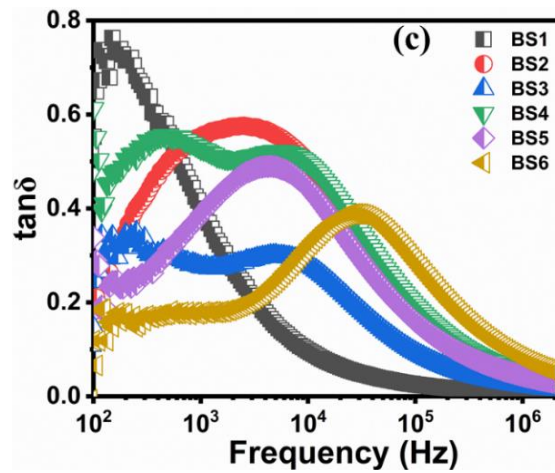


**Fig. 4.139.** (a)  $\epsilon'$  variation and (b)  $\epsilon''$  variation with frequency (c)  $\tan\delta$  of BS1, BS2, BS3, BS4, BS5, and BS6 composites.

#### 4.7.2.2 AC conductivity

Fig. 4.137 illustrates the plots of ac conductivity ( $\sigma$ ) which exhibits frequency-independent behavior up to  $10^4$  Hz and increases thereafter. The replacement of  $\text{Fe}^{3+}$  ions with Co-Cr ions causes an increment in conductivity value at high -frequency and is maximum for the BS6 sample. This increment elucidates an increase in the concentration of  $\text{Fe}^{3+}$  ions at an octahedra position, which facilitates the hopping between  $\text{Fe}^{3+}$  and  $\text{Fe}^{2+}$  ions. The rise in  $\sigma$  value can also be understood through the FESEM micrographs of synthesized composites (Fig. 4.135), wherein the inter-grain connectivity between large and small-sized grains improves with substitution, despite the same concentration of  $\text{CoFe}_2\text{O}_4$ .

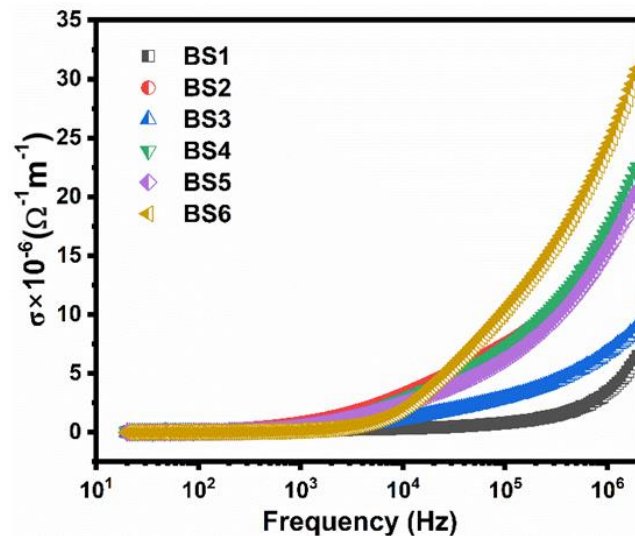


**Fig. 4.140.** variation with frequency of BS1, BS2, BS3, BS4, BS5, and BS6 composites.



### 4.7.2.3 Complex electric modulus

The frequency-dependent behavior of  $M'$  and  $M''$  are demonstrated in Fig. 4.138(a) and 4.138(b). The low value of  $M'$  in low-frequency regions suggesting maximum polarization which increases as the frequency increases. This increment may be attributed to the conduction phenomena resulting from the mobility of charge carriers of short range. Conversely, the asymmetric shape of  $M''$  plots indicate a non-Debye behavior of the material. Substitution of Co-Cr ions result a decrement in peak height and a shift toward the high-frequency side. Fig. 4.138(c) display Cole-Cole ( $M''$  vs  $M'$ ) plots of synthesized composites. Instead of obtaining a perfect semicircle, a deformed semicircle has been observed with the center lying below the axis. The semicircular arc observed at low and high-frequency regions reflected grain boundary and grain relaxation, respectively.

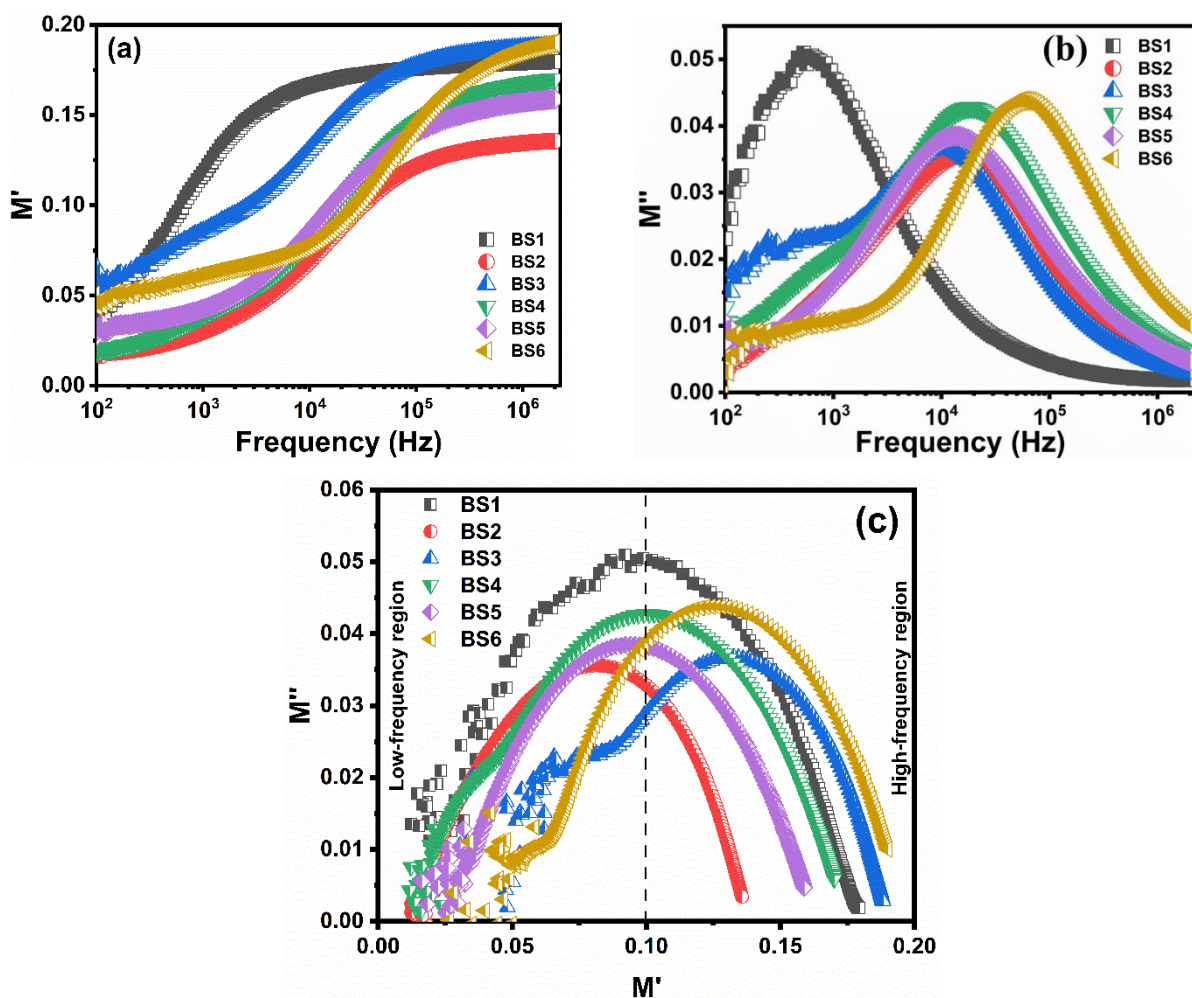


**Fig. 4.141.** (a)  $M'$ , (b)  $M''$ , and (c) Cole-Cole plot ( $M''$  vs  $M'$ ) variation with frequency of BS1, BS2, BS3, BS4, BS5, and BS6 composites.

#### 4.7.2.4 Complex impedance analysis

Frequency-dependent behavior of both  $Z'$  and  $Z''$  are depicted in Fig. 4.139(a) and 4.139(b), respectively. The decrement observed in  $Z'$  as moving from low to high frequency indicates an increase in the material's conductivity due to electron hopping between localized ions and is well explained through the Maxwell-Wagner model. However, the delayed response of charge carriers to an applied field at high frequencies leads to a decrease in  $Z''$ . Fig. 4.139(c) illustrates the Cole-Cole ( $Z''$  vs  $Z'$ ) plots of synthesized hexaferrite composites. The observed plots depict non-Debye relaxation by demonstrating incomplete semicircles with the center not located on the real axis. In the high-frequency region, the substitution of Co-Cr ions causes an increment in arc depression elucidating the contribution of grains.

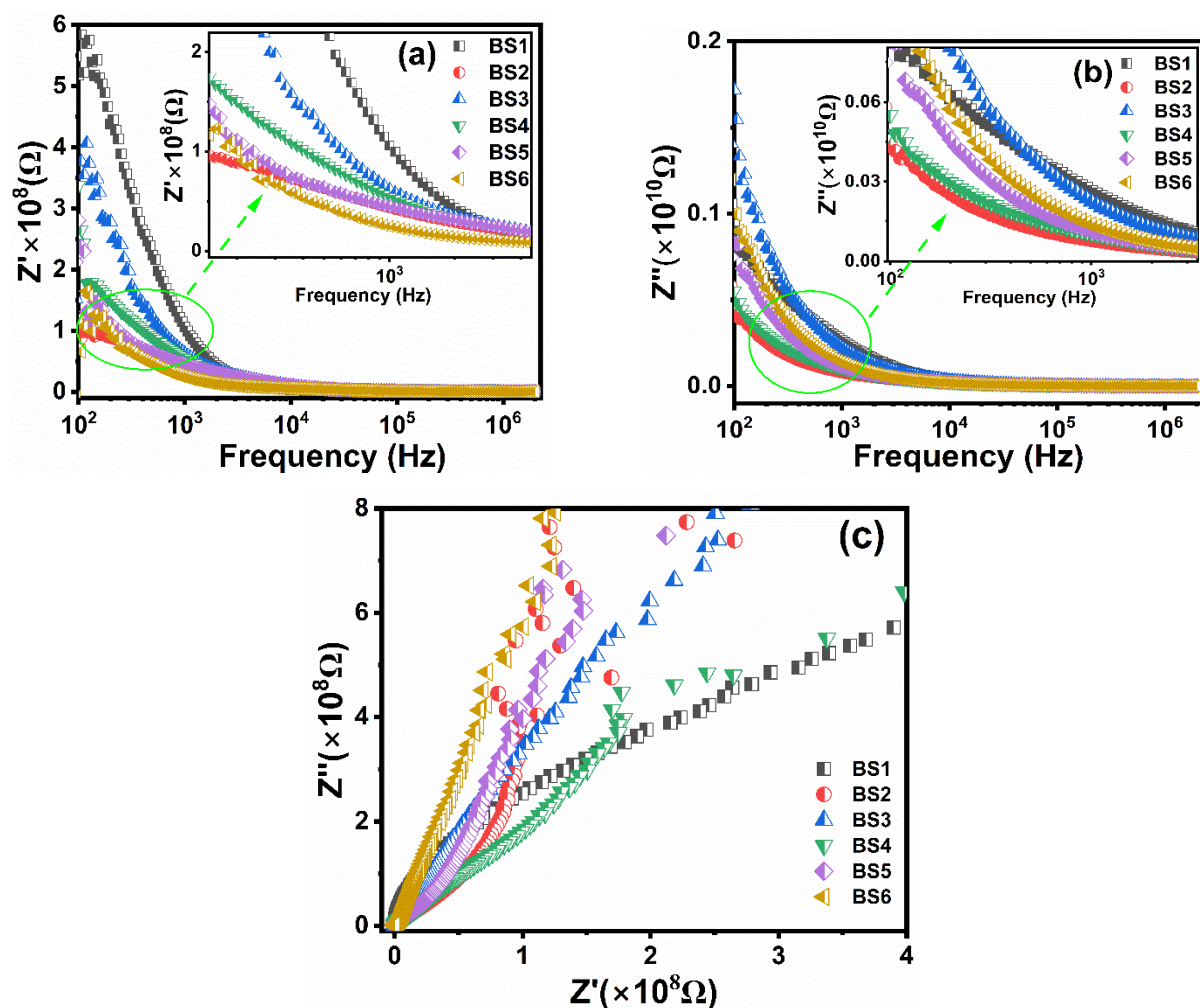


Fig. 4.142. (a)  $Z'$ , (b)  $Z''$ , and (c) ( $Z''$  vs  $Z'$ ) variation with frequency of BS1, BS2, BS3, BS4, BS5, and BS6 composites.



### 4.7.3 Magnetic analysis

Fig. 4.140 illustrates the M-H loops of BS-series composites. It affirms the exchange coupling between SrFe<sub>12</sub>O<sub>19</sub> (hard) and CoFe<sub>2</sub>O<sub>4</sub> (soft) ferrites through a smooth second quadrant of magnetization curves. Derived magnetic parameters from the M-H loop are listed in Table 4.42. The maximum value of M<sub>s</sub> (103.2 emu/g) and H<sub>c</sub> (4932 Oe) is observed for the BS1 sample and is attributed to pure SrFe<sub>12</sub>O<sub>19</sub>/CoFe<sub>2</sub>O<sub>4</sub> composites and the insertion of Co<sup>2+</sup>-Cr<sup>3+</sup> ions decrease the M<sub>s</sub> and H<sub>c</sub> of composites. This can be explained through the site occupancy of Co-Cr ions on the spin-up and down sites. It has been reported that the octahedral positions are occupied via more electronegative ions [222] and Co<sup>2+</sup> (1.88) ions are more electronegative than Cr<sup>3+</sup> (1.66) ions. Thus, it can choose to occupy 12k (↑) – 2a(↑) – 4f<sub>2</sub>(↓) octahedral sites. Based on ligand field theory, Cr<sup>3+</sup> ions having d<sup>3</sup> orbitals prefer to occupy 4f<sub>1</sub> (↓) tetrahedral sites, while Cobalt (Co<sup>2+</sup>) ions with d<sup>7</sup> orbitals can occupy octahedral sites. Furthermore, Co<sup>2+</sup> ions can occupy 4f<sub>2</sub>(↓), 4f<sub>1</sub> (↓), and 2b sites. The competition between aforementioned factors results in M<sub>s</sub> ranges from 60.92 emu/g to 68.76 emu/g. It is known that the anisotropy field (H<sub>a</sub>) primarily depends on 4f<sub>2</sub> sites and alone 2b sites. Co<sup>2+</sup>-Cr<sup>3+</sup> substitution causes a non-monotonic decrease in H<sub>a</sub> from BS1 to BS6 sample owing to the site occupancy mechanism discussed in M<sub>s</sub>. Table shows that substituted ferrite composites have lower H<sub>c</sub> than the undoped composites and the addition of Co-Cr ions results in a non-monotonic increase in H<sub>c</sub> from BS2 to BS4 and afterward it gradually decreases. An irregular variation in H<sub>c</sub> is attributed to the non-linear variation in H<sub>a</sub>, as well as the grain size distribution. Furthermore, the squareness ratio of all synthesized composites is listed in Table 4.42 and is found to be more than 0.5, indicating the existence of single-domain particles in all composites.

**Table 4.42** Magnetic parameters M<sub>s</sub>, H<sub>c</sub>, M<sub>r</sub>, M<sub>r</sub>/M<sub>s</sub> and H<sub>a</sub> of BS-series sample.

Sample name	M <sub>s</sub> (emu/g)	H <sub>c</sub> (Oe)	M <sub>r</sub> (emu/g)	M <sub>r</sub> /M <sub>s</sub>	H <sub>a</sub> (kOe)
BS1	103.28	4932	53.14	0.514	23.97
BS2	60.92	3499	36.30	0.595	24.74
BS3	61.66	2634	33.39	0.541	18.44
BS4	68.76	4326	54.85	0.797	11.16
BS5	66.78	3774	53.58	0.802	14.54
BS6	64.33	3666	45.38	0.703	14.80

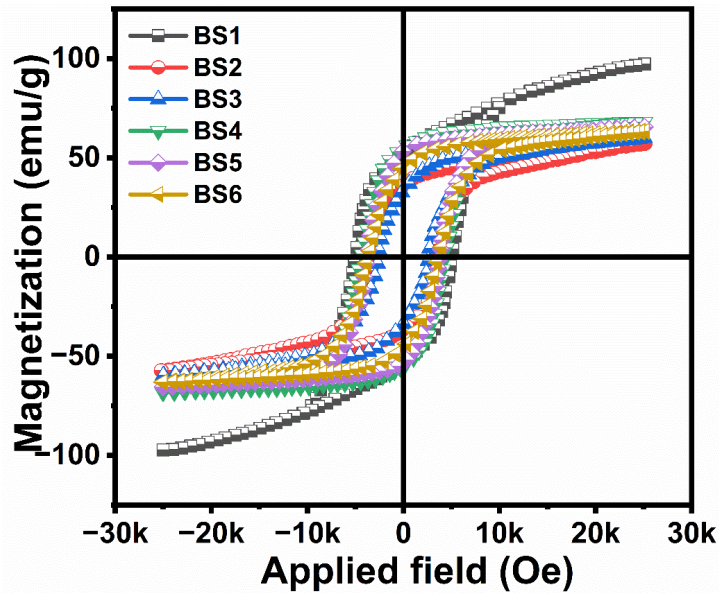


**Fig. 4.143.** M-H plots of BS1, BS2, BS3, BS4, BS5, and BS6 composites.

Fig. 4.141 demonstrates the effect of exchange coupling between hard/soft ferrites through the investigation of switching field distribution. The inset of Fig. 4.141 depicts that the BS2, BS3, and BS5 samples exhibit a single narrower peak in the switching field distribution attributed to a strong exchange coupling between M-type and spinel magnetic phases. On the contrary, BS1, BS4, and BS6 samples show a single peak with shoulder peaks, and the intensity of these peaks is less. This concludes that a strong exchange coupling is assessed in the BS2, BS3, and BS5 samples. The insertion of Co-Cr ions may or may not dilute the exchange coupling effect between hard/soft phases depending on the concentration of dopants.

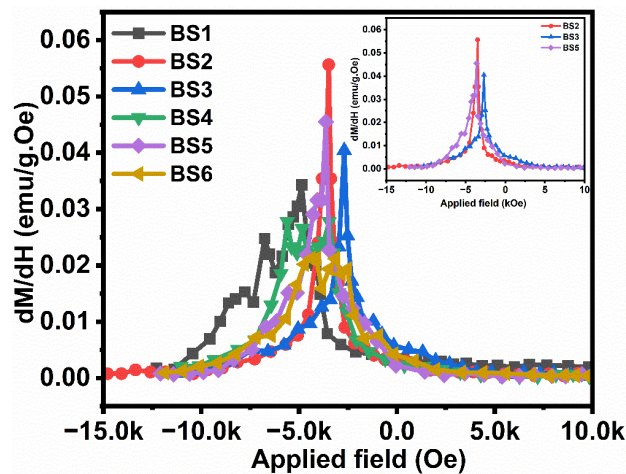


**Fig. 4.144.** dM/dH against H plots of BS1, BS2, BS3, BS4, BS5, and BS6 composites

#### 4.7.4 Electromagnetic Analysis

Fig. 4.1142(a) illustrates the dependence of dielectric constant ( $\epsilon'$ )/loss ( $\epsilon''$ ) on frequency. The introduction of Co-Cr ions causes a non-monotonic increase in  $\epsilon'$  values from BS1 to BS5 in low-frequency regions (8.2 to 10 GHz). This may be due to the occupancy of Co-Cr ions on tetrahedral positions, which moves a large no. of Fe ions responsible for polarization toward the octahedral sites, thus increasing the  $\epsilon'$ . The dielectric constant ( $\epsilon'$ )/loss ( $\epsilon''$ ) remains relatively constant with increasing frequency for BS1, BS5 and BS6 samples. Sample BS2 acquires the highest value of  $\epsilon'/\epsilon''$  over the 8.2 to 10 GHz frequency range, while BS3 and BS4 exhibit a resonance above 11 GHz. In detail, the  $\epsilon'$  curve of BS3 and BS4 is stable at 8.2 - 11 GHz, then it suddenly dispersed above 11 GHz. Fig. 4.142(b) demonstrated the dependence of permeability ( $\mu'$ )/ magnetic loss ( $\mu''$ ) as a function of frequency and it does not vary too much over the entire frequency range for BS1, BS5, and BS6 samples. Substitution causes an insignificant change in the value of  $\mu'/\mu''$  in the low-frequency regions. The  $\mu'$  value of BS2, BS3, and BS4 shows large dispersion from 10.5 to 12.4 GHz. Sample BS2 owes minimum  $\mu'$  from 8.2 to 10.5 GHz and is maximum from 10.5 to 12.4 GHz. Furthermore, from 9.5 to 11 GHz the  $\epsilon''$  rises and  $\mu''$  decreases for BS2, while in BS3 and BS4  $\epsilon''$  rises and  $\mu''$  decreases from 11GHz to 12.4 GHz, evidently decreasing the difference between  $\epsilon''$  and  $\mu''$ , enhancing the impedance match.

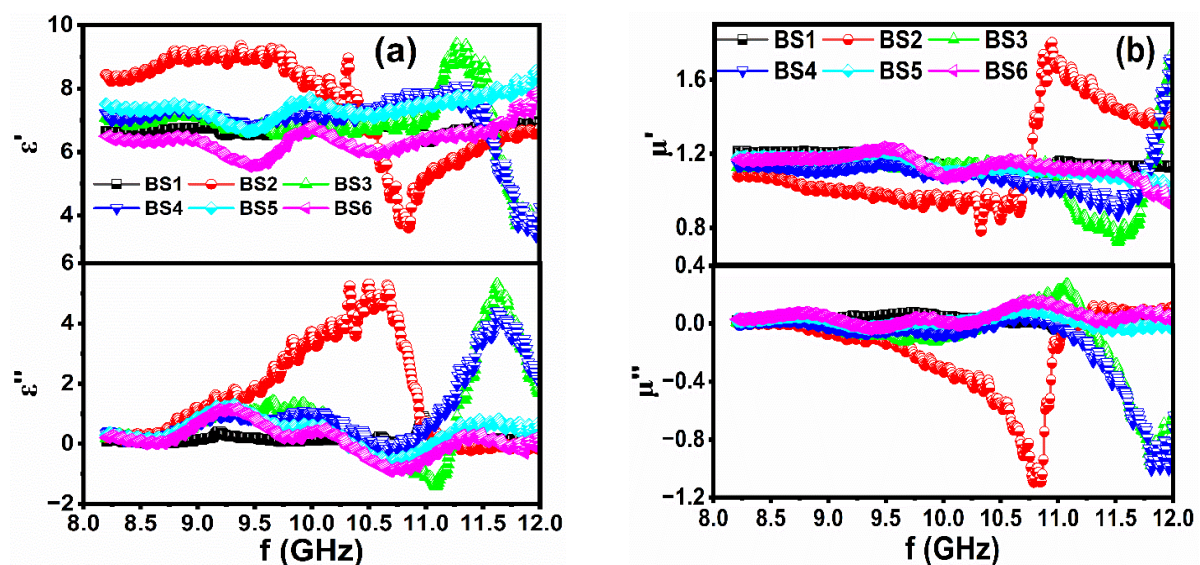


**Fig. 4.145.** (a) Complex permittivity and (b) permeability plots of BS-series samples in 8.2-12.4 GHz.

Fig. 4.143(a), 4.144(a), 4.145(a), 4.146(a), and 4.147(a) illustrate the REL plots of all synthesized samples and can be utilized to deduce parameters such as bandwidth/frequency

range for REL of -10 dB (90% absorption) /-20 dB and matching frequency/thickness, as listed in Table 4.43. For better visualization, 3D REL plots of all composites as a function of thickness and frequency are illustrated in Fig . 4.148. Substitution of Co-Cr ions improves the microwave absorption properties of the synthesized sample from BS1 to BS6. The highest dip in REL, measuring -29.9 dB (> 99 % absorption), is observed in the BS5 sample [Fig. 4.146(a)], occurring at a frequency of 9.157 GHz and a thickness of 8.5 mm. In Table 4.43, the remaining compositions exhibit REL values ranging from -10 to -29.6 dB, spanning frequencies between 8 and 12.4 GHz, and thicknesses between 7.4 and 9.5 mm. The plots of BS1 and BS5 samples illustrate the shift of REL peaks towards lower frequency ranges as the thickness increases. This trend aligns with the mechanism of quarter-wavelength described by Eq. 3.24, which states that thickness and frequency are related inversely.

Fig. 4.143(a) demonstrated the absorption characteristics of the BS1 sample within the examined frequency range. Reflection loss remains at or above -10 dB, with REL peaks spanning the 8.2 to 12.4 GHz frequency spectrum from 7.4 to 8.7 mm thickness. Sample BS2 exhibits REL < -10 dB (less than 90% absorption), which is not of interest. For BS3 and BS4 samples, Fig. 4.144(a) and 4.145(a) reveal REL peaks with values > -10 dB across thickness ranging from 8.4 to 8.7 mm and 8.5 - 8.6 mm, at 9.66 GHz and 9.32 GHz, respectively. Fig. 4.146(a) is notable for the BS5 sample, as it exhibits multiple REL peaks with values greater than -10 dB/-20 dB over a frequency range from 9 to 9.5 GHz and a thickness ranging from 8.0 to 8.5 mm. Fig. 4.147(a) for BS6 sample display peaks with REL  $\geq$  -10 dB/-20 dB across thickness ranging from 8.6 to 9.3 mm, at 9.157 GHz.

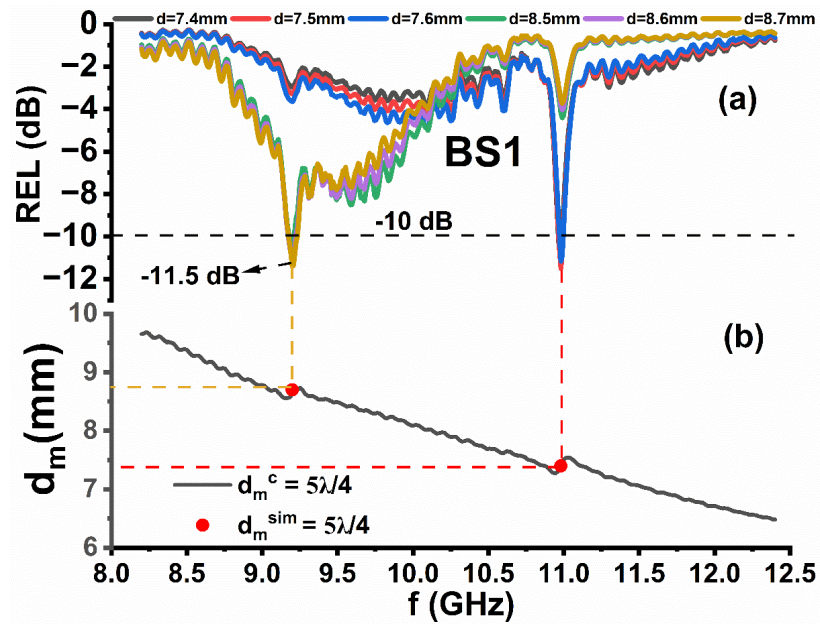


Fig. 4.146. (a) Dependence of REL on frequency in BS1 sample. (b)  $d_m^{sim}$  and  $d_m^c$  versus frequency for  $5\lambda/4$  in the BS1 sample.

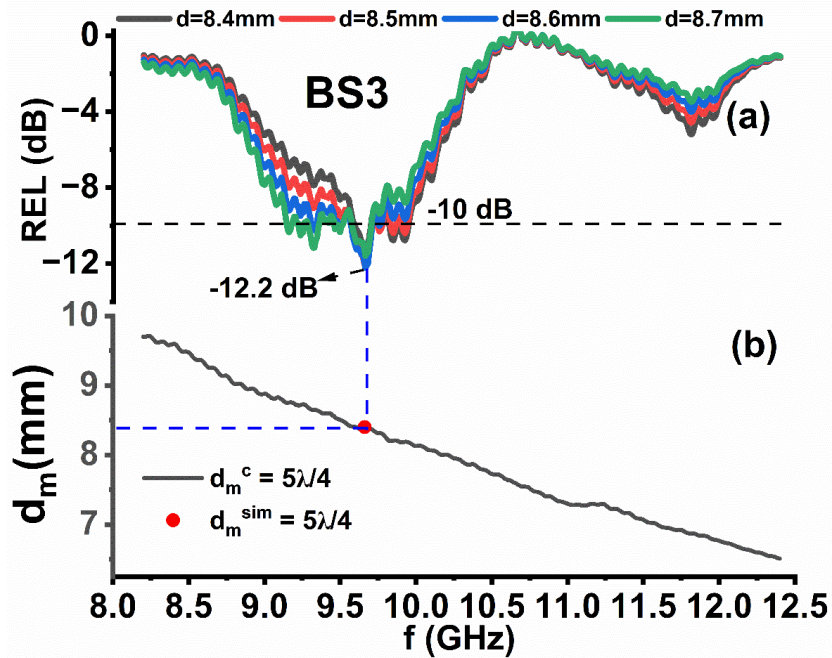


Fig. 4.147. (a) Dependence of REL on frequency in BS3 sample. (b)  $d_m^{sim}$  and  $d_m^c$  versus frequency for  $5\lambda/4$  in the BS3 sample.



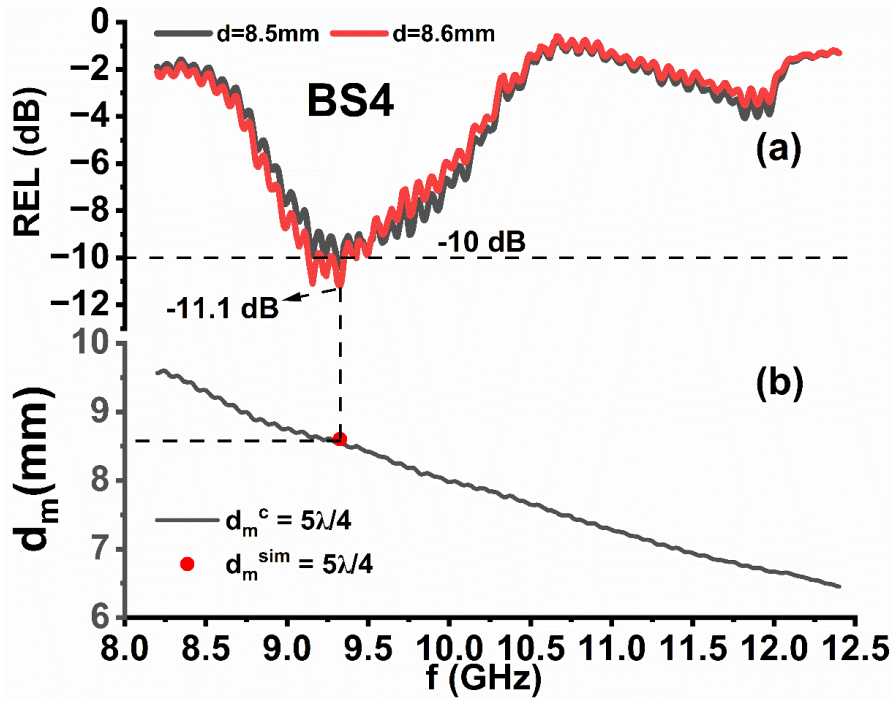


Fig. 4.148. (a) Dependence of REL on frequency in BS4 sample. (b)  $d_m^{\text{sim}}$  and  $d_m^c$  versus frequency for  $5\lambda/4$  in the BS4 sample.

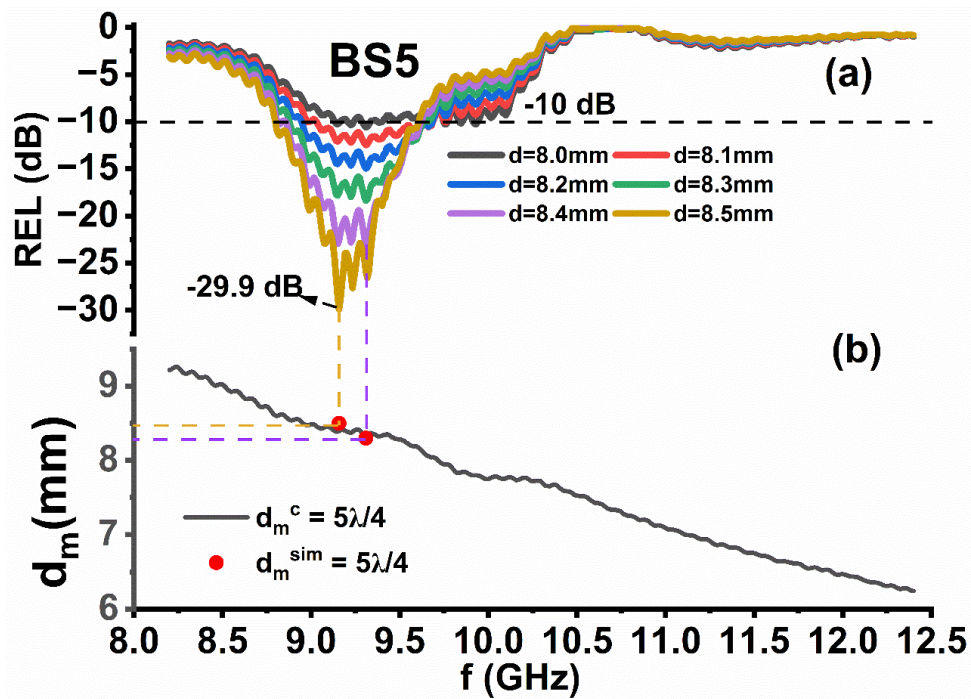


Fig. 4.149. (a) Dependence of REL on frequency in BS5 sample. (b)  $d_m^{\text{sim}}$  and  $d_m^c$  versus frequency for  $5\lambda/4$  in the BS5 sample.

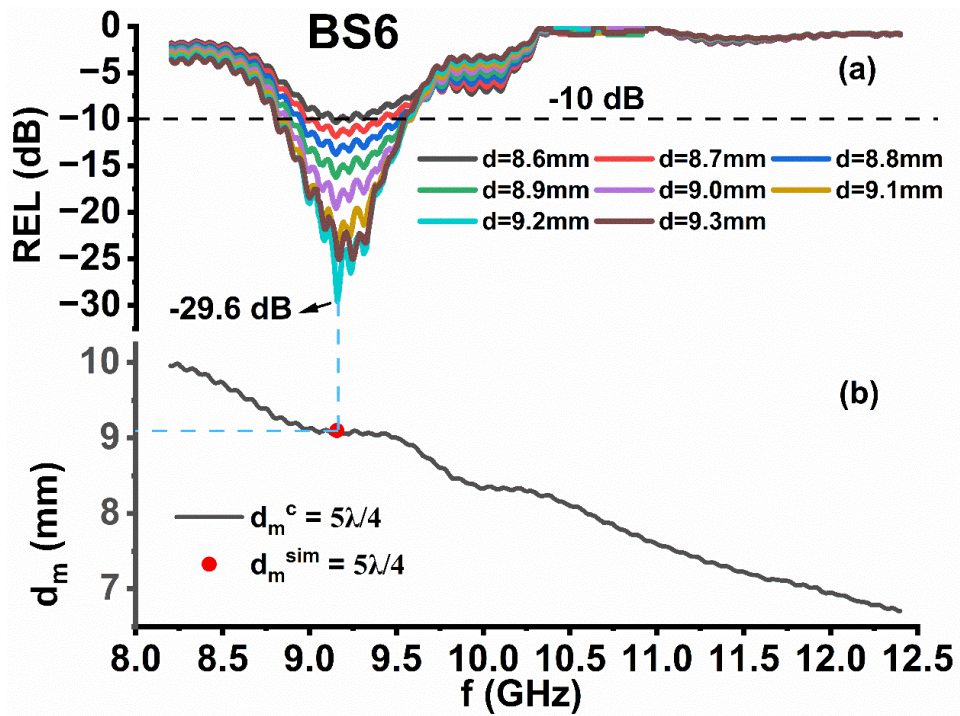


Fig. 4.150. (a) Dependence of REL on frequency in BS6 sample. (b)  $d_m^{sim}$  and  $d_m^c$  versus frequency for  $5\lambda/4$  in the BS6 sample.

Table 4.43 Parameters calculated for microwave absorption (REL more than -10/-20 dB).

Sample Name	Matching Thickness (mm)	Maximum RL (dB)	Matching frequency (GHz)	Frequency Band for RL > -10 dB (GHz)	Bandwidth for RL > -10 dB (GHz)	Frequency Band for RL > -20 dB (GHz)	Bandwidth for RL > -20 dB (GHz)	BTR	PBW (%)
BS1	7.4	-11.02	10.980	--	--	--	--	--	--
	7.5	-11.50	10.980	--	--	--	--	--	--
	7.6	-11.16	10.980	--	--	--	--	--	--
	8.5	-10.54	9.199	--	--	--	--	--	--
	8.6	-11.21	9.199	--	--	--	--	--	--
BS3	8.4	-11.43	9.661	--	--	--	--	--	--
	8.5	-12.20	9.661	--	--	--	--	--	--
	8.6	-12.22	9.661	--	--	--	--	--	--
BS4	8.5	-10.72	9.325	--	--	--	--	--	--
	8.6	-11.19	9.325	--	--	--	--	--	--

<b>BS5</b>	8.0	-10.51	9.317	--	--	--	--	--	--
	8.1	-12.47	9.308	9.01-9.67	0.66	--	--	2.8E-04	7
	8.2	-14.96	9.308	8.94-9.66	0.72	--	--	3.1E-04	7.7
	8.3	-18.38	9.308	8.88-9.64	0.76	--	--	3.2E-04	9.1
	8.4	-23.22	9.308	--	--	8.86-9.63	0.77	3.2E-05	8.2
	8.5	-29.92	9.157	--	--	8.79-9.61	0.82	3.4E-04	8.9
<b>BS6</b>	8.6	-10.34	9.157	--	--	--	--	--	--
	8.7	-11.87	9.157	9.03-9.39	0.36	--	--	1.5E-04	3.9
	8.8	-13.77	9.157	8.95-9.51	0.56	--	--	2.2E-04	6.1
	8.9	-16.23	9.157	8.88-9.55	1	--	--	2.7E-04	10.9
	9.0	-19.59	9.157	8.87-9.55	0.68	--	--	2.7E-04	7.4
	9.1	-24.41	9.157	--	--	8.80-9.58	0.78	3.1E-04	8.5
	9.2	-29.60	9.157	--	--	8.79-9.55	0.76	3E-04	8.2
	9.3	-25.06	9.157	--	--	8.80-9.55	0.75	2.9E-04	8.1

Using Eq. 3.22, Reflection loss (REL) is computed using both the simulated thickness ( $d_m^{\text{sim}}$ ) and the calculated thickness ( $d_m^c$ ), which is determined through Eq. 3.24 by substituting values of  $n = 1, 3, 5$ , and so forth. The purpose is to establish a relationship between the quarter wavelength mechanism and REL peaks. Fig. 4.143(b), 4.144(b), 4.145(b), 4.146(b), and 4.147(b) depicts plots of a calculated thickness ( $n\lambda/4$ ) within the frequency range. To compare the simulated thickness ( $d_m^{\text{sim}}$ ) with the calculated thickness ( $n\lambda/4$ ), vertical lines are drawn from REL peaks to the thickness-frequency plots. Results indicate that the quarter wavelength mechanism is envisaged in BS1 and BS6 samples where the calculated thickness is  $5\lambda/4$  with  $n = 5$ .

Furthermore, the highest value of REL is elucidated for the BS5 sample at -29.9 dB and a thickness of 8.5 mm with an EAB of 0.82 GHz from 8.79-9.61 GHz. It can be depicted from Table 4.43, that BS6 owes  $\text{REL} > -10$  dB with a wide absorption bandwidth of 1 GHz and narrow bandwidth of 0.36 GHz from 8.88-9.55 GHz and 9.03-9.39 GHz with matching thicknesses of 8.9 and 8.7 mm, respectively.

Table 4.43 enumerates the value of BTR and PBW of all synthesized samples calculated using Eq. 3.25 and 3.26. The BTR is highest in the BS5 sample with values of  $3.4E-04$  and PBW (8.9 %) at 9.15 GHz and  $\text{REL} = -29.92$  dB at 8.5 mm thickness.

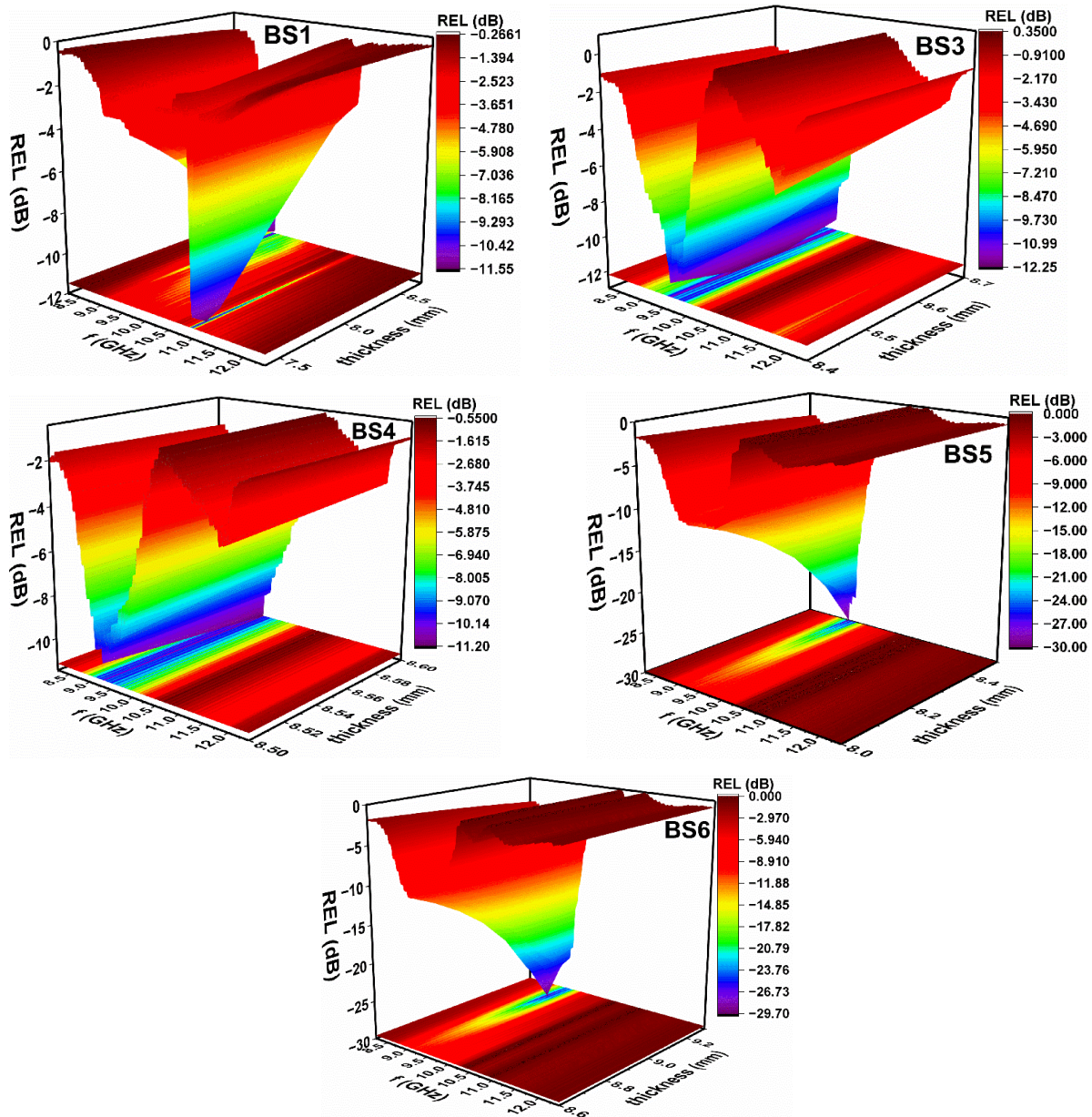


**Fig. 4.151.** 3D plots of REL at various thicknesses and frequencies.

Section 1.1.3 discusses the significance of achieving impedance matching between the absorber and free space, resulting in  $Z_{in}/Z_O \cong 1$  during the design of absorber material for microwave systems. Fig. 149(a, c) and 150(a, c) illustrate the graphs showcasing the reflection loss and  $Z_{in}/Z_O$  as a function of frequency for some considerable thicknesses of samples. Table 4.44 enumerates a comprehensive list of  $Z_{in}/Z_O$  values for these samples, derived from  $Z_{in}/Z_O$  plots in the figures. Notably, the  $Z_{in}/Z_O$  for BS1 ranges from 1.74 to 2.42, BS3 ranges from 1.33 to 1.71, while for BS4 values lie between 1.73 to 1.78. These values are far away from the characteristic impedance value of  $Z_{in}/Z_O = 1$  is evident due to the low reflection loss observed in these samples.



In some instances,  $Z_{in}/Z_0$  values come close to 1 without experiencing significant reflection loss. For instance, consider the BS5 sample with thicknesses of 8.3 mm and 8.4 mm, exhibiting  $Z_{in}/Z_0$  values of 1.12 and 1.12 (close to 1), respectively. At a frequency of 9.308 GHz, they demonstrate REL dips of -18.38 dB and -23.22 dB, respectively (Table 4.43). Interestingly, despite similar  $Z_{in}/Z_0$  values at both thicknesses, yield different REL results. A similar anomaly is observed in the BS6 case, where at respective thicknesses of 9.0 mm and 9.1 mm, REL of -19.59 dB and -24.41 dB, and  $Z_{in}/Z_0$  of 1.08 at 9.157 GHz. It can be explained by assuming the complex nature of  $|Z_{in}|$ , which comprises both the real ( $Z_{real}$ ) and imaginary ( $Z_{img}$ ) components. Fig. 144(b, d) and 145(b, d) illustrate the curves of  $Z_{real}/Z_{img}$  and REL value follows patterns where  $Z_{real} \approx 1$  and  $Z_{img} \approx 0$ , the  $Z_{real}/Z_{img}$  value of BS5 in 8.4 thickness and 9.1 mm thickness of BS6 are very close to 1 and/or zero. These variations in  $Z_{in}/Z_0$  value are attributed to the influence of Co-Cr ion substitutions.

**Table 4.44** Reflection loss peak's impedance parameters at different thicknesses.

Sample Name	Thickness (mm)	Max. REL (dB)	Matching frequency (GHz)	$Z_{in}/Z_0$	$Z_{real}$	$Z_{img}$
<b>BS1</b>	7.4	-11.02	10.980	1.762	1.751	0.1900
	7.5	-11.50	10.980	1.688	1.671	-0.239
	7.6	-11.16	10.980	2.402	0.989	-2.189
	8.5	-10.54	9.199	1.766	1.711	0.436
	8.6	-11.21	9.199	1.803	1.802	0.058
	8.7	-11.40	9.199	1.746	1.717	-0.315
<b>BS3</b>	8.4	-11.43	9.661	1.713	1.704	0.175
	8.5	-12.20	9.661	1.629	1.619	-0.176
	8.6	-12.22	9.661	1.489	1.426	-0.426
	8.7	-11.57	9.661	1.330	1.204	-0.564
<b>BS4</b>	8.5	-10.72	9.325	1.781	1.739	0.383
	8.6	-11.19	9.325	1.731	1.760	-0.023
<b>BS5</b>	8.0	-10.51	9.317	1.003	0.841	0.546
	8.1	-12.47	9.308	1.061	0.949	0.474
	8.2	-14.96	9.308	1.104	1.041	0.368
	8.3	-18.38	9.308	1.125	1.101	0.233
	8.4	-23.22	9.308	1.121	1.117	0.086



	8.5	-29.92	9.157	1.092	1.091	-0.054
<b>BS6</b>	8.6	-10.34	9.157	0.947	0.785	0.529
	8.7	-11.87	9.157	0.999	0.874	0.483
	8.8	-13.77	9.157	1.042	0.956	0.414
	8.9	-16.23	9.157	1.073	1.023	0.323
	9.0	-19.59	9.157	1.088	1.066	0.215
	9.1	-24.41	9.157	1.086	1.081	0.098
	9.2	-29.60	9.157	1.066	1.066	-0.014
	9.3	-25.06	9.157	1.033	1.026	-0.115

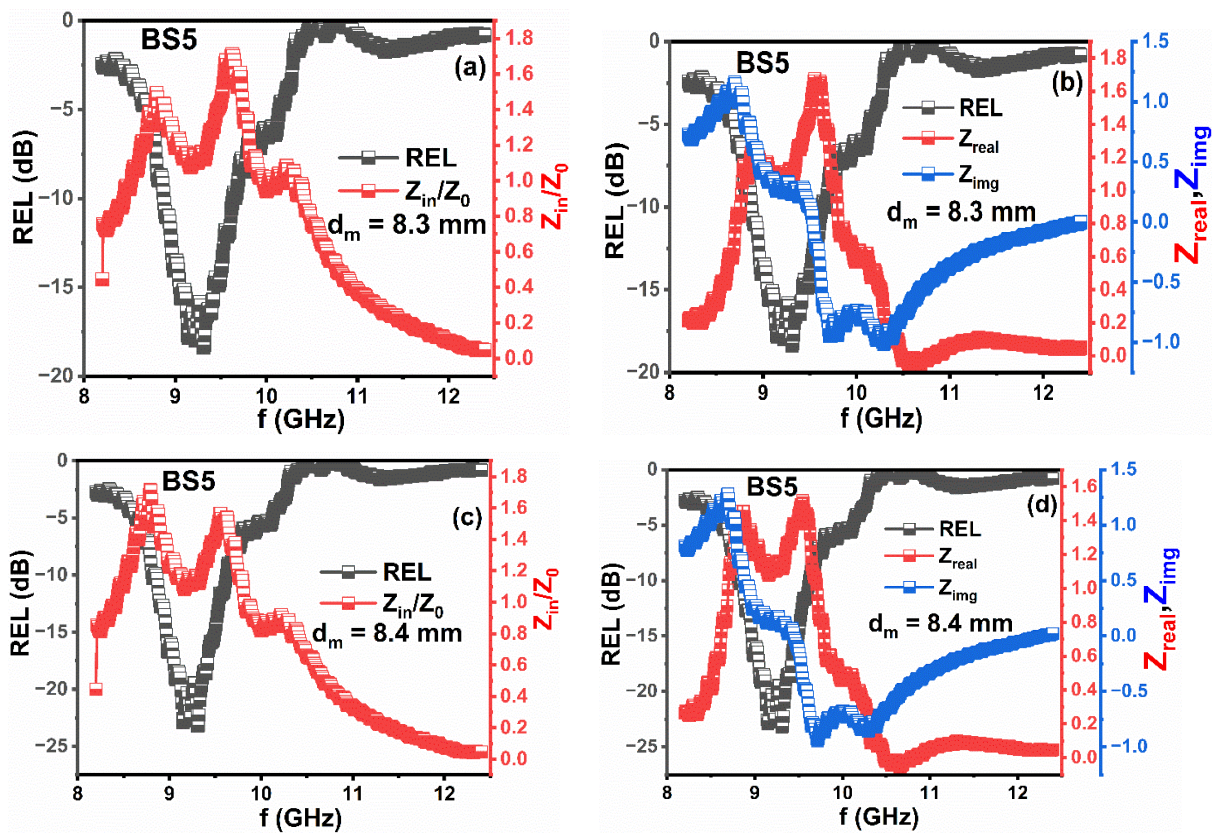


**Fig. 4.152.** (a, c) Dependence of  $Z_{in}$  and REL in frequency (b, d) Dependence of REL,  $Z_{real}$ , and  $Z_{img}$  on frequency for BS5 sample.

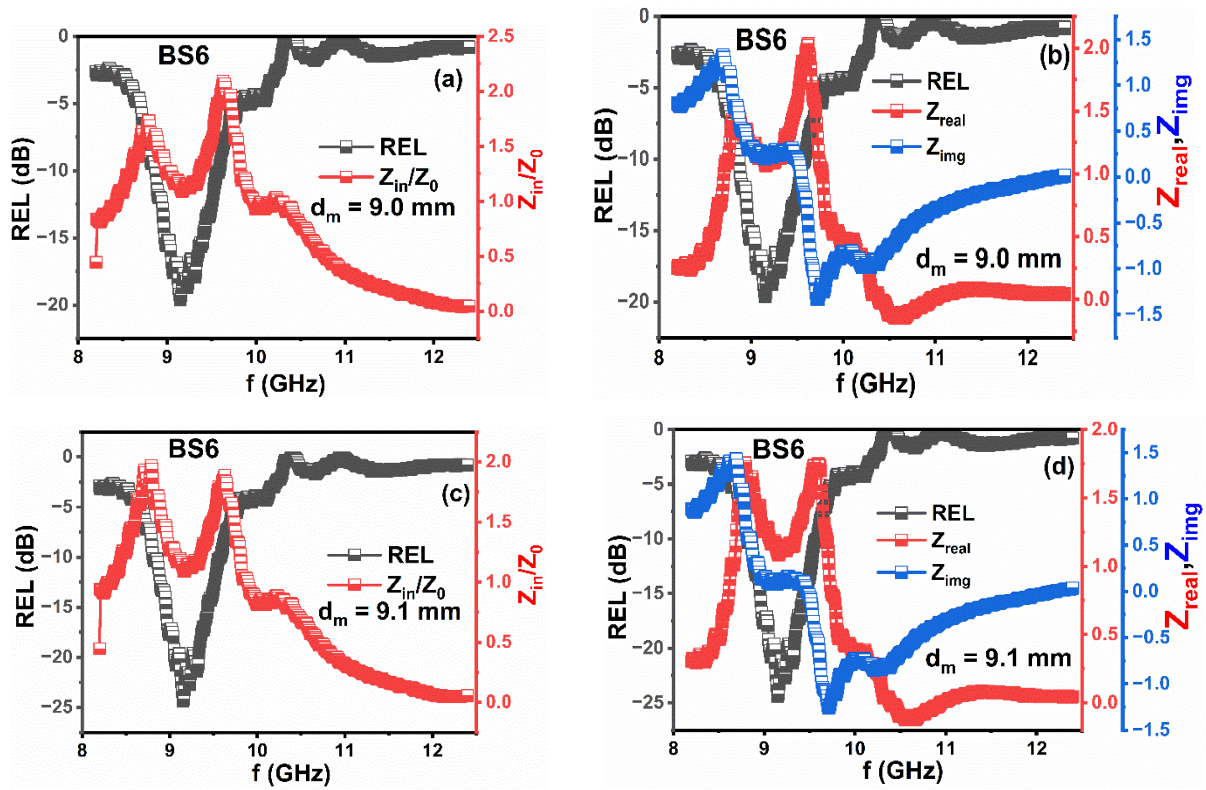


**Fig. 4.153.** (a, c) Dependence of  $Z_{in}$  and REL in frequency (b, d) Dependence of REL,  $Z_{real}$ , and  $Z_{img}$  on frequency for BS6 sample.

Conclusively, when SrM hexaferrite is combined with highly dielectric  $\text{CoFe}_2\text{O}_4$ , the overall dielectric constant of the composites increases. The efficacy of this combination depends on the volume fractions and interactions between SrM hexaferrite and  $\text{CoFe}_2\text{O}_4$ . The reflection loss dip values range from BS1 (-11.40 dB) to BS6 (29.60 dB). Several factors contribute to the more 90% absorption performance observed in all composites, including (i) high dielectric loss (Fig. 4.137) (ii) hysteresis loss (Table 4.41) (iii) defects and voids caused by substituents, as seen in micrographs (Fig.4.130). Dipolar polarization between  $\text{SrFe}_{12}\text{O}_{19}$  and  $\text{CoFe}_2\text{O}_4$  results in significant reflection loss in all synthesized composites. The Substitution of Co-Cr ions in hard/soft ferrite composites enhances the synergistic effect between the hard/soft ferrite phases, leading to effective REL values of more than -10 dB in all composites. Additionally, impedance matching and quarter wavelength mechanism also contributing to effective reflection loss. Furthermore, in all substituted hard/soft ferrite composites, the contribution of dielectric loss exceeds that of magnetic loss.

## 4.8 SrCo<sub>z</sub>Cd<sub>0.5z</sub>Fe<sub>12-2z</sub>O<sub>19</sub> (80%) + PANI (20%) ferrite composites

A physical blending method has been utilized to synthesize hexaferrite composites. In this study, we comprehensively analyzed structural, morphological, magnetic, electrical, and microwave absorption properties. Table 4.45 displays the assignment of sample names/codes for a different level of substitution for PANI/ SrCo<sub>1.5z</sub>Cd<sub>0.5z</sub>Fe<sub>12-2z</sub>O<sub>19</sub>.

**Table 4.45** Assignment of sample name for a different level of substitution of PANI/ SrCo<sub>1.5z</sub>Cd<sub>0.5z</sub>Fe<sub>12-2z</sub>O<sub>19</sub> ferrite composites.

Sample composition	Sample Name
20% PANI/SrCo <sub>1.5z</sub> Cd <sub>0.5z</sub> Fe <sub>12-2z</sub> O <sub>19</sub>	
z = 0.2	CP1
z = 0.4	CP2
z = 0.6	CP3
z = 0.8	CP4
z = 1.0	CP5

### 4.8.1 Structural Analysis

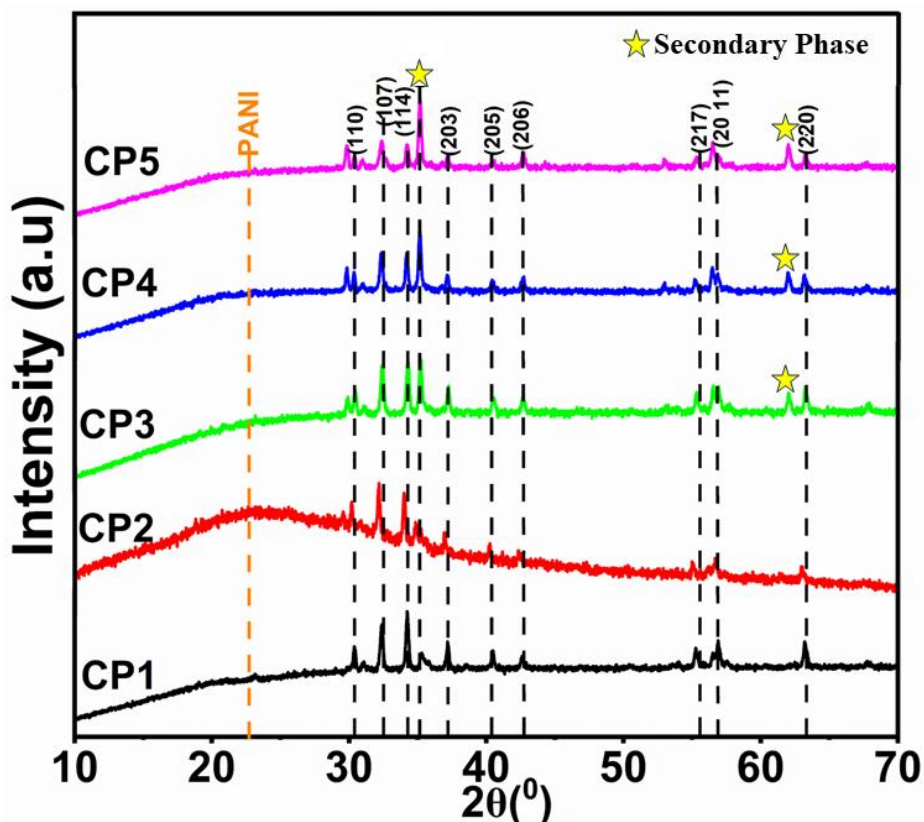
#### 4.8.1.1 XRD and FTIR Analysis

Fig. 4.151 demonstrates the XRD pattern of CP ferrite composites, wherein all reflection planes observed in the  $2\theta = 10^\circ - 70^\circ$  with a step size of  $0.02^\circ$  at room temperature. A formation of magnetoplumbite structure of M-type hexaferrite as major phase and CoFe<sub>2</sub>O<sub>4</sub> (secondary phase) has been confirmed by matching observed XRD peaks with standard reference pattern ICDD# 80-1197 and ICDD# 22-1086, respectively through PowderX software. Instead of obtaining a sharp peak of PANI in the XRD pattern, a broad peak (hump) is observed in the range of  $15^\circ - 25^\circ$ . Table 4.46 summarizes the structural parameters of Co-Cd substituted CP-series ferrite composites. The lattice constant 'c' (22.99 to 23.03 Å) exhibits more variation than lattice parameter 'a' (5.869 to 5.877 Å) with substitution and calculated using Eq. 3.1. A successful substitution of Co-Cd ions can be explained by the slight shift and change in the intensity of peaks. This could be due to the large ionic radii of substituted Cd<sup>2+</sup> ion (0.97Å) and Co<sup>2+</sup> ion (0.72Å) than host Fe<sup>3+</sup> ion (0.645 Å). The value of unit cell volume (V) decreases from 687.8 Å<sup>3</sup> (CP1) – to 684.7 Å<sup>3</sup> (CP3) and then increases to 689 Å<sup>3</sup> (CP5). The crystallite size of M-type hexaferrite was calculated using Eq. 3.3

ranges from 33.45 to 46.26 nm. Fig. 4.152 illustrates the FTIR of CP-series composites exhibit two strong absorption bands at  $425\text{ cm}^{-1}$  and  $542\text{ cm}^{-1}$ , typical Fe-O band of M-type hexaferrite. The absorption peak observed at  $587.4\text{ cm}^{-1}$  is associated with the Sr-O stretching vibrations. The additional peaks observed at  $1072\text{ cm}^{-1}$ ,  $1548\text{ cm}^{-1}$ , and  $2356\text{ cm}^{-1}$  are attributed to weak stretching vibration in the aromatic amine (C=N), quinoid ring (C=N) (due to PANI), and  $\text{CO}_2$ , respectively.

**Table 4.46** Structural parameters of CP series composites.

Sample name	$a=b$ (Å)	$c$ (Å)	$V_{cell}$ (Å <sup>3</sup> )	$c/a$	D (nm)
CP1	5.877	22.99	687.8	3.91	40.16
CP2	5.877	22.97	687.2	3.90	46.26
CP3	5.869	22.94	684.7	3.90	36.72
CP4	5.877	23.03	689.0	3.91	40.93
CP5	5.877	23.03	689.0	3.91	33.45



**Fig. 4.154.** X-ray diffraction pattern of CP series composites.



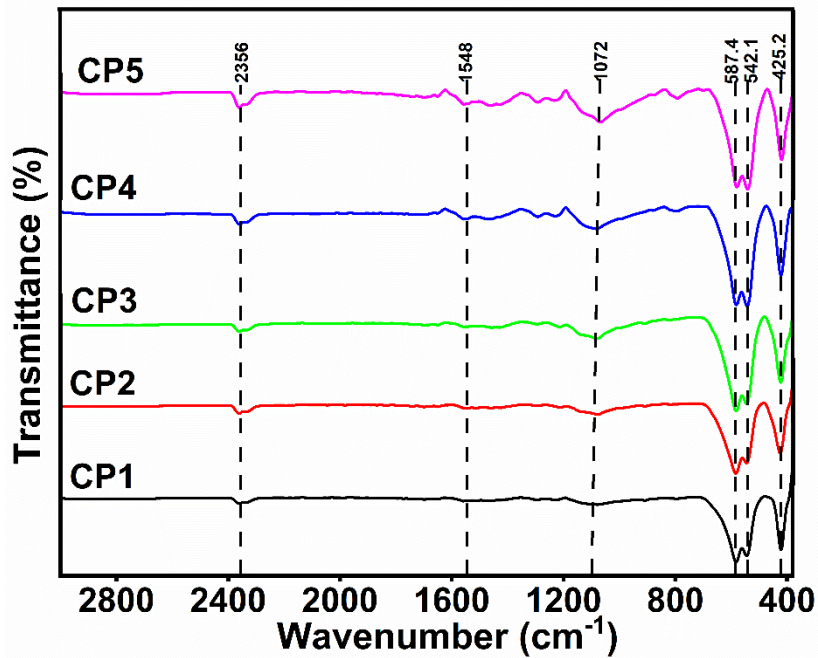
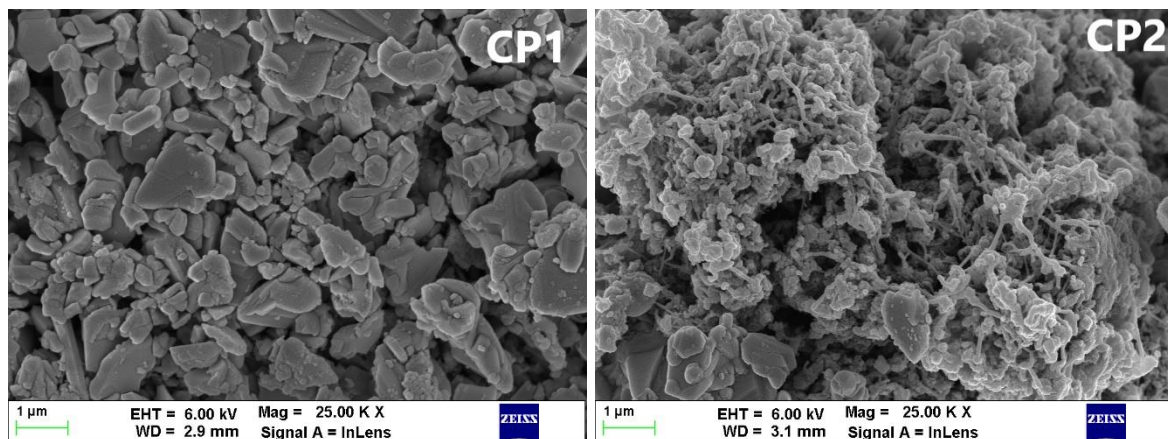


Fig. 4.155. FTIR spectra of CP series composites.

#### 4.8.1.2 FESEM analysis

FESEM micrographs of the CP-series are displayed in Fig. 4.153. Composites exhibit platelet-like hexagonal structures of M-type hexaferrite and disk flower-like structures of PANI. The entanglement between M-type hexaferrite and PANI is visualized in CP2 and CP4 composites. Substitution of Co-Cd ions cause agglomeration of grains due to interaction between magnetic elements.





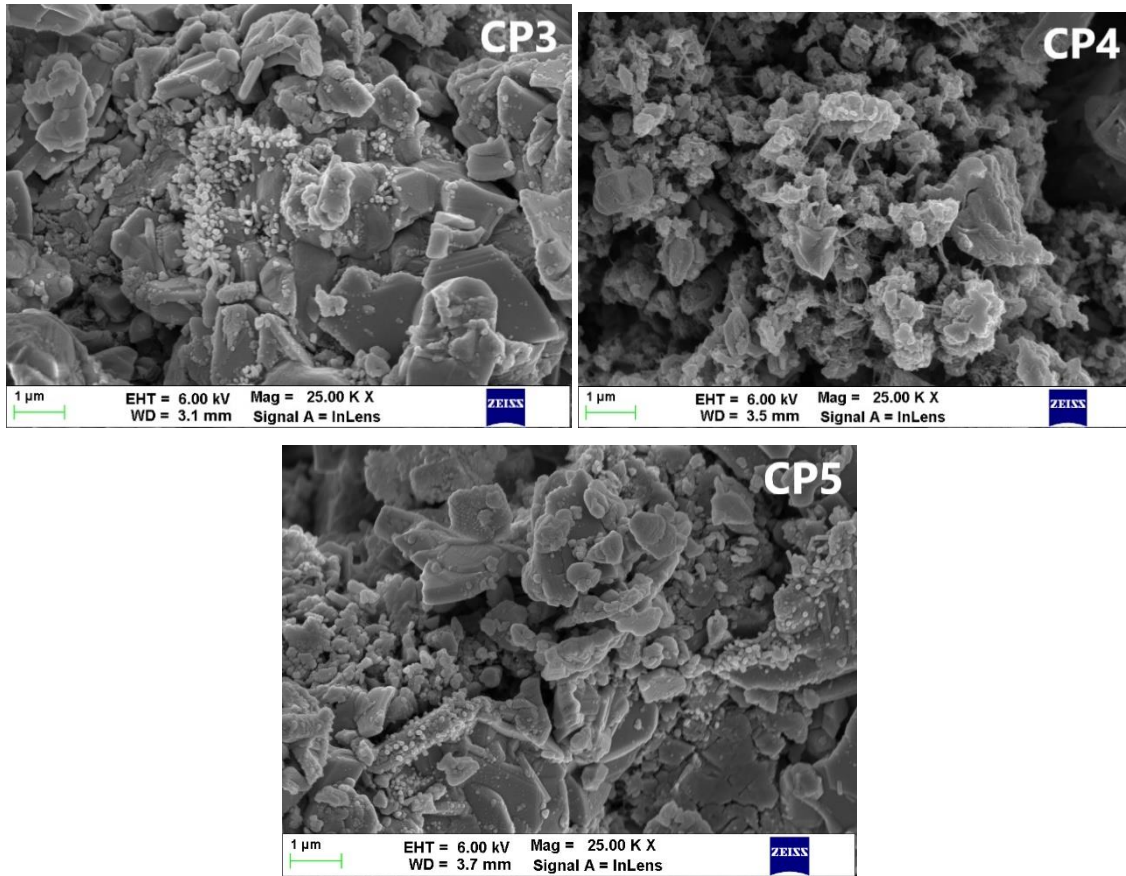


Fig. 4.156. FESEM micrographs of CP series composites.

## 4.8.2 Electrical Analysis

### 4.8.2.1 Dielectric constant and Loss tangent

It has been noted that all samples of the CP series exhibit the electrical characteristics, except CP5. Fig. 4.154 and 4.155 illustrate the dependence of  $\epsilon'$  and  $\epsilon''$  on frequency. Both  $\epsilon'$  and  $\epsilon''$  curves show dispersion with increasing frequency and become frequency-independent above  $10^3$  Hz. It is a general dielectric behavior shown by all hexaferrites and explained through the Maxwell-Wagner model. At low frequencies, both  $\epsilon'$  and  $\epsilon''$  values increase non-linearly from CP1 to CP4 and are attributed to the availability of multiple  $\text{Fe}^{2+}$  ions (responsible for polarization) on octahedral sites. It can also be explained through the site occupancy of Co-Cd ions because both substituents tend to occupy tetrahedral sites. The frequency dependent response of  $\tan\delta$  is demonstrated in Fig. 4.156 and can be well understood through Koop's phenomenological theory. According to this theory, the resistivity of material is due to grain boundaries and grains at low and high frequencies, respectively. Despite the same concentration of PANI, the substitution of Co-Cd ions introduces heterogeneity in the composites and results in more interfacial polarization. A strong broad

relaxation in CP2 and a weak relaxation in CP1 indicate that the hopping frequency of charges between  $Fe^{3+}$  and  $Fe^{2+}$  ions match with applied frequency at octahedral sites.

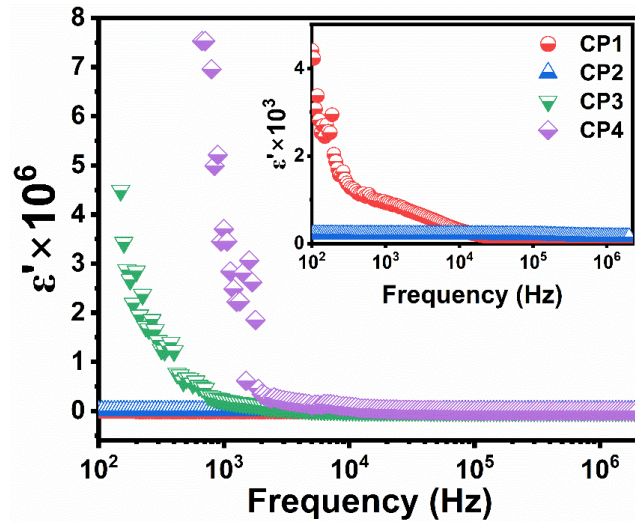


Fig. 4.157  $\epsilon'$  variation with frequency of CP1, CP2, CP3 and CP4 composites.

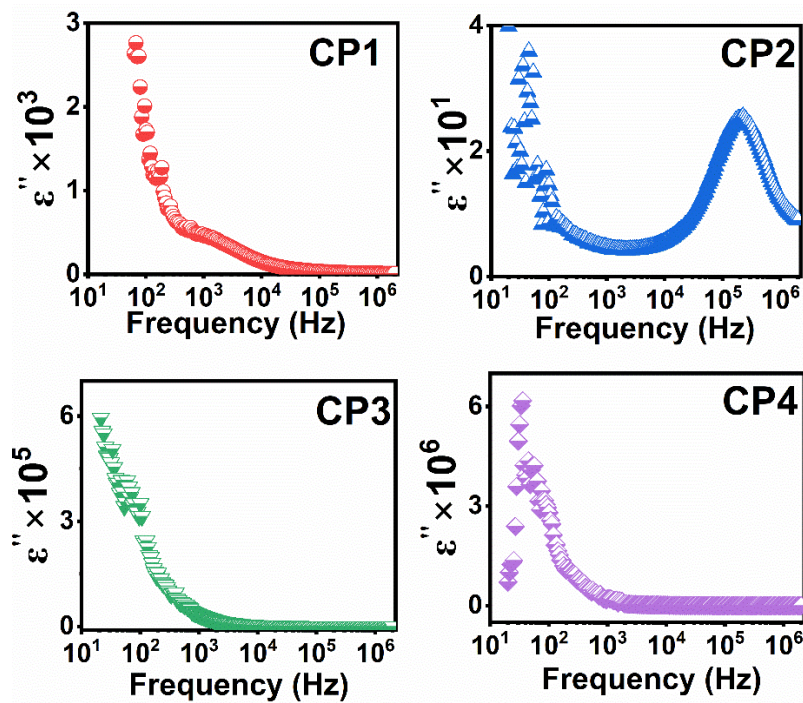


Fig. 4.158.  $\epsilon''$  variation with frequency of CP1, CP2, CP3 and CP4 composites.

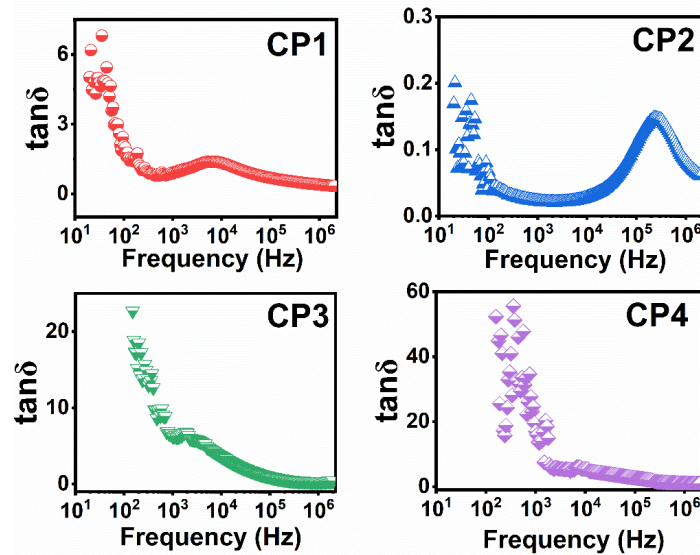


Fig. 4.159. Loss tangent variation with frequency of CP1, CP2, CP3 and CP4 composites.

#### 4.8.2.2 AC conductivity

Fig. 4.157 reveals the frequency-independent behavior of  $\sigma$  at lower-frequency regions and it sharply increases with increasing frequency. The insertion of Co-Cd ions increases the conductivity value and is ascribed to the enrichment of Fe ions at the B- sites. The maximum value of  $\sigma$  in the CP4 sample is due to the good inter-grain connectivity between large and small-sized grains, over other substituted composites.

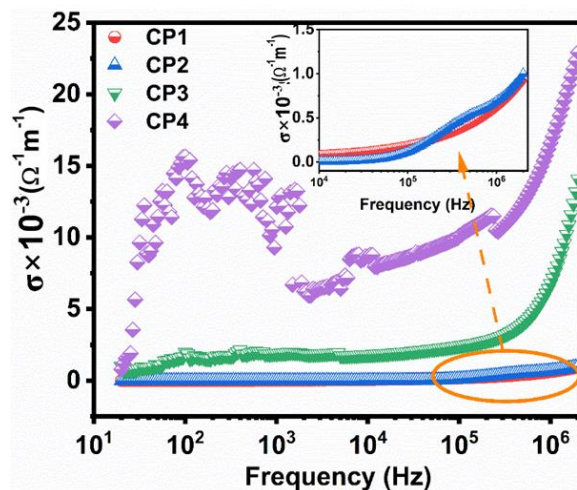


Fig. 4.160.  $\sigma$  variation with frequency of CP1, CP2, CP3 and CP4 composites.

#### 4.8.2.3 Complex Electric Modulus

Fig. 4.158(a) depicts the variation of  $M'$  with frequency for all composites. The plots show a low value of  $M'$  at low frequency and it increases continuously with increasing frequency and reaches a maximum value of  $M'$ . The variation shows that conduction is ascribed to the mobility of charge carriers of short-range. The substitution of Co-Cd ions



causes a decrease in  $M'$  values from CP1 to CP4 (high-frequency region). The  $M''$  value is related to the dissipation of energy during an irreversible conduction process and Fig. 4.158(b) illustrates the variation of  $M''$  with frequency. The Cole-Cole plot ( $M''$  vs  $M'$ ) of CP series composites are shown in Fig. 4.159. Instead of obtaining a perfect semicircle, a deformed semicircle or a segment of an arc is observed. This enunciates that the relaxation is distributed over different time constants and is not of the Debye type. The existence of a single semicircle in the CP2 and CP3 composite confirms that the relaxation is prominently due to grain boundaries. However, CP1 and CP4 composites show a segment of an arc, suggesting more contribution of grains than grain boundaries.

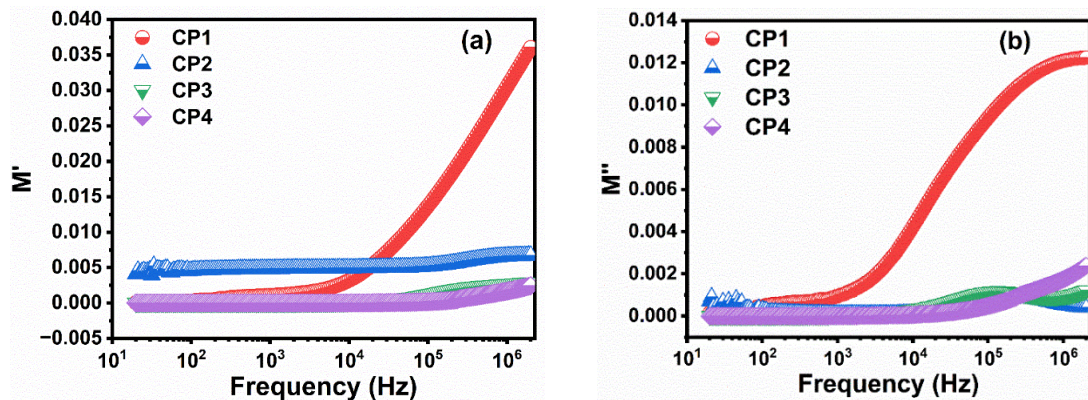


Fig. 4.161. (a)  $M'$  (b)  $M''$  variation with frequency of CP1, CP2, CP3 and CP4 composites.

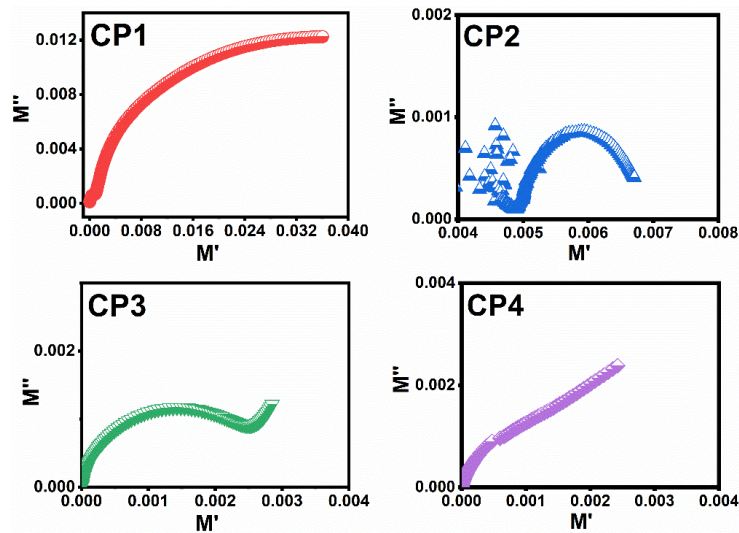


Fig. 4.162. Cole-Cole plot ( $M''$  vs  $M'$ ) variation with frequency of CP1, CP2, CP3 and CP4 composites.

#### 4.8.2.4 Complex Impedance Analysis

Fig. 4.160 and 4.161 shows the decreasing trend in  $Z'$  and  $Z''$  with increasing frequency of an applied field, respectively. With increasing frequency, the declining behavior

of both parameters suggests an increase in electron hopping between localized ions, which leads to a rise in ac conductivity. At higher frequencies, the observed decrease in  $Z'$  could be explained using the Maxwell-Wagner model. The study of  $Z''$  led to a better understanding of the relaxation process and the space charge effect. The space charge effect dominates the impedance response at low frequencies, resulting in a greater value of  $Z''$ . However, at higher frequencies, the charge carriers may be unable to respond quickly to the applied field, resulting fall in  $Z''$ . Fig. 4.162 presents the Cole-Cole plots of all CP series composites at room temperature. Sample CP1, CP2, and CP4 approaches to the shape of semicircle suggest the relative contribution of grains. Whereas, CP2 shows a straight-line approach toward the lower-frequency region indicating grain boundary resistance

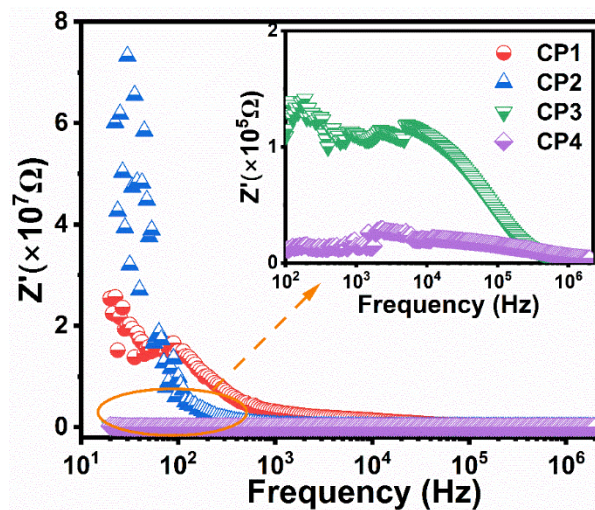


Fig. 4.163.  $Z'$  variation with frequency of CP1, CP2, CP3, and CP4 composites.

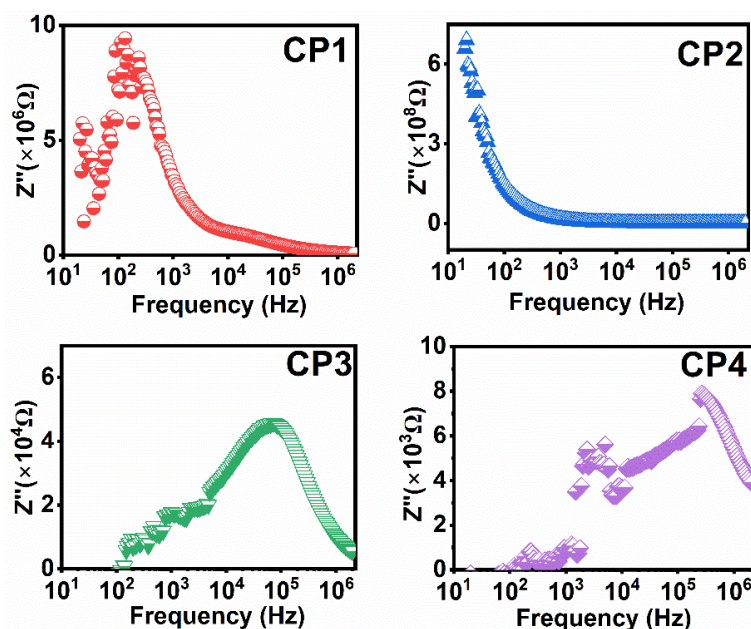
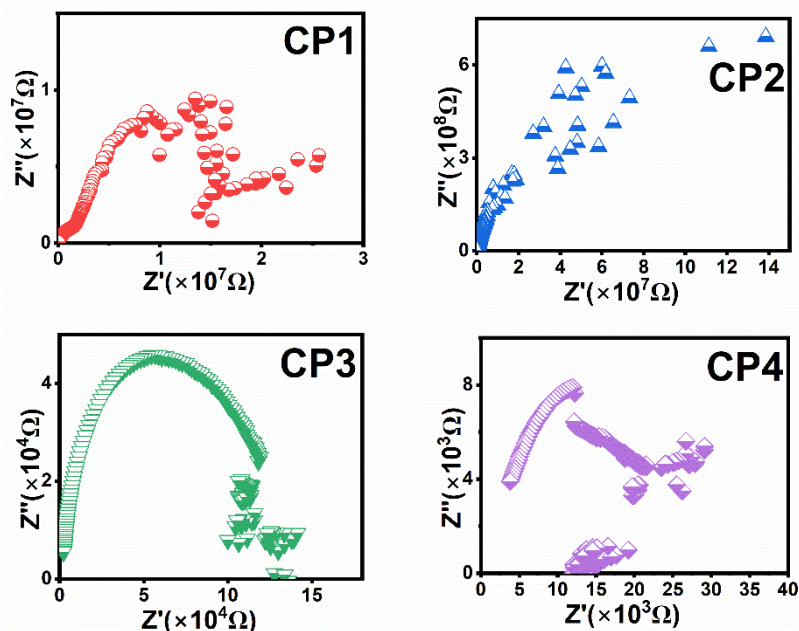


Fig. 4.164.  $Z''$  variation with frequency of CP1, CP2, CP3, and CP4 composites.





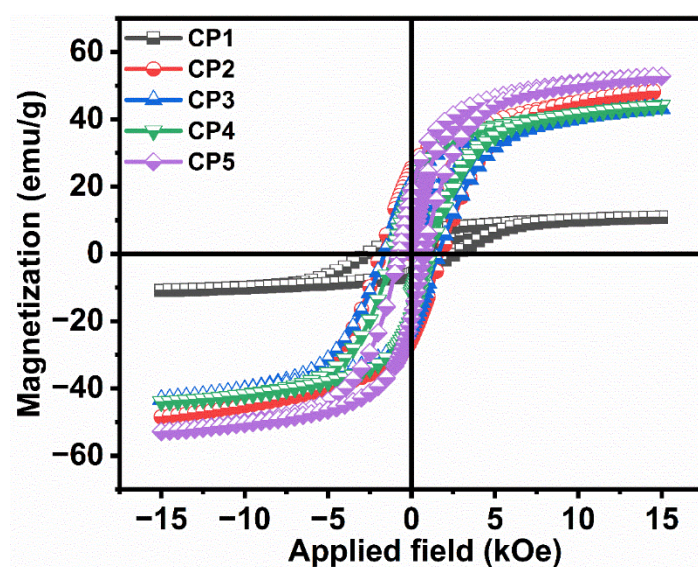
**Fig. 4.165.** ( $Z''$  vs  $Z'$ ) variation with frequency of CP1, CP2, CP3 and CP4 composites.

### 4.8.3 Magnetic Analysis

Fig. 4.163 presents the magnetic response of CP series composites by applying a field of 15kOe at room temperature and the derived parameters are listed in Table 4.47. The insertion of PANI (non-magnetic polymer) in all ferrite-polymer composites may dilute the magnetic parameters. The highest value of  $H_c$  (2620 Oe) is observed for the CP1 sample and gradually decreases with increasing the substitution. The gradual decrement observed in the coercivity values is caused by a gradual decrease in  $H_a$  ( $H_c$  is directly related to  $H_a$ ). It can also be due to the existence of secondary phase ( $CoFe_2O_4$ ), which reduces the coercivity. The occupancy of weak magnetic ions on spin-up sites (12k, 2a, and 2b) and spin-down sites ( $4f_1$  and  $4f_2$ ) results in a decrease and increase of saturation magnetization, respectively. The insertion of weak magnetic ( $Co^{2+} = 3\mu_B$ ) and diamagnetic ( $Cd^{2+} = 0\mu_B$ ) ions instead of host  $Fe^{3+}$  ( $5\mu_B$ ) ions and site occupancy of  $Co^{2+}$  (tend to occupy both octahedral and tetrahedral sites) -  $Cd^{2+}$  (occupy tetrahedral sites) ions results in a non-monotonous increase of  $M_s$  in the composites. The minimum  $M_s$  in CP1 is likely a result of an increased number of substituted ions residing on spin-up sites. Conversely, in CP5, the higher  $M_s$  is attributed to a greater occupancy of Co-Cd ions on the  $4f_1$ - $4f_2$  sites. The remanent magnetization ( $M_r$ ) displays a nonlinear increase within the composite material, ranging from 5.97 – 25.47 emu/g. The squareness ratio of CP1 (0.52) and CP2 (0.50) is close to 0.5, while the remaining composition exhibits less than 0.5 (multi-domain particles).

**Table 4.47** Hysteresis parameters derived from M-H loop.

Sample name	$M_s$ (emu/g)	$H_c$ (Oe)	$M_r$ (emu/g)	$M_r/M_s$	$H_a$ (kOe)
CP1	11.44	2620	5.97	0.521	13.50
CP2	50.87	1830	25.47	0.500	12.83
CP3	45.41	1608	21.22	0.467	12.49
CP4	45.63	1127	18.76	0.411	11.46
CP5	54.56	745	18.80	0.344	10.71

**Fig. 4.166.** M-H loop of CP series composites.

#### 4.8.4 Electromagnetic Analysis

The dependence of  $\epsilon_r/\mu_r$  as a function of frequency is shown in Fig. 4.164 (a) and 4.164(b). Introducing Co-Cd ions causes (i) a non-linear decrease in  $\mu'$  and  $\epsilon'$  (ii) non-monotonic increment in  $\mu''$  and  $\epsilon''$  values. The non-linear fashion of complex permittivity/permeability values is governed by several factors such as unlike atomic mass, ionic radii, and magnetic moments of Co-Cd ions than Fe ions, electron spin, porosity, and polarization in the microwave regime. The dielectric response of CP-series composites to an external electric field is dominantly influenced by dipolar polarization. The crystal structure SrM hexaferrite is highly complex, consisting of various positive and negative valence ions connected by bonds of differing orientations and lengths. This variation can result in dielectric dipole moments can collectively induce dipolar polarization in the SrM hexaferrites. Additionally, PANI also contribute to the overall dipolar polarization.

According to Debye dipolar mechanism, the conversion of electrical energy into the thermal energy occurs when the induced dipoles in the SrM and PANI lag behind the applied oscillating electric field. Such heterogeneity forms defects/vacancies and results in an increase in polarization.

At low frequencies, the value of  $\epsilon'$  initially increases from CP1 to CP2, then decreases non-linearly. This decrease is due to the presence of secondary phase at higher levels of Co-Cd ions substitution, which reduces the availability of  $\text{Fe}^{2+}$  ions responsible for polarization, resulting in a non-linear reduction in  $\epsilon'$  value. At higher frequencies, dipole polarizations lag behind the applied frequency, causing the incident microwave energy to be converted into heat through relaxation mechanism. Conversely,  $\epsilon''$  values increase non-linearly, due to the non-linear increment in dipolar relaxation with increasing Co-Cd substitution. Despite the high dielectric and magnetic losses, the samples did not exhibit an effective reflection loss value. This phenomenon can be understood through impedance mismatching, where  $Z_{in} / Z_0 \approx 1$ .

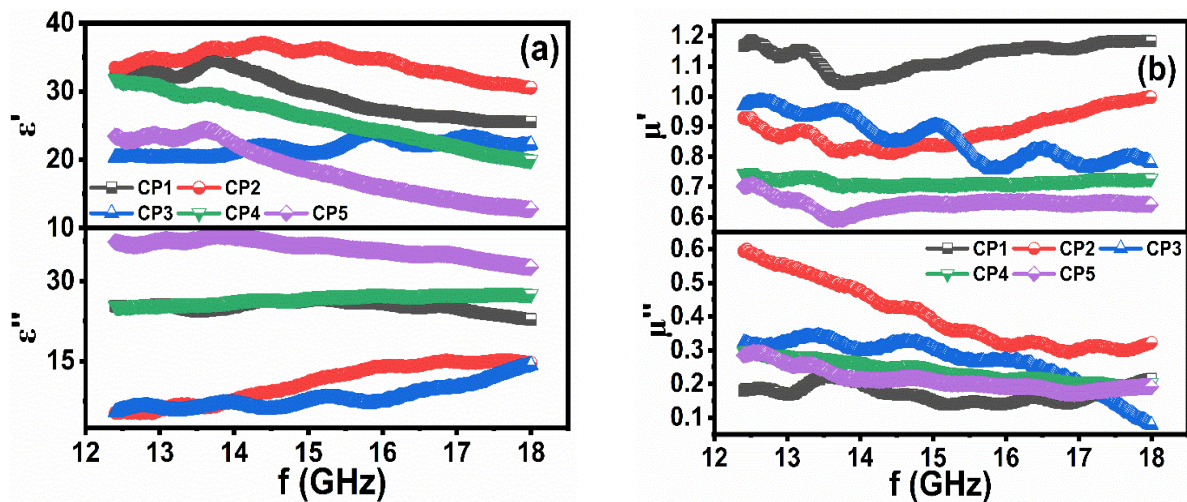


**Fig. 4.167.** (a) Complex permittivity and (b) permeability plots of CP-series samples in 12-18 GHz.

## **Correlation between substituted M-type hexaferrite and its composites.**

### A) Hard/Soft ferrite composites

The present study affirms the successful synthesis of (a) Co-La substituted SrM hexaferrite (D-series) and its composites with Fe<sub>3</sub>O<sub>4</sub> (DM-series), (b) Co-Cr substituted SrM hexaferrite (B-series) and its composites with CoFe<sub>2</sub>O<sub>4</sub> (BS-series). In the DM and BS series hard/soft ferrite composites are garnering significant technical interest. This interest arises not only from the combination of high magnetization spinel ferrite and the high coercivity of hexaferrite magnetic material but also from the exceptional exchange-coupling behavior between hard and soft magnetic phases.

- a) Fig. 4.1 demonstrates the XRD pattern of Co-La substituted SrM hexaferrite (D-series), with M-type hexaferrite as the major phase. The XRD pattern in Fig. 4.91 shows distinct diffraction peaks for both SrM hexaferrite and Fe<sub>3</sub>O<sub>4</sub> in the DM -series, indicating the successful synthesis of hard/soft ferrite composites. Similarly, the XRD pattern in Fig. 4.28 confirms the substitution of Co-Cr ions in SrM hexaferrite (B-series). The XRD analysis affirms the presence of both SrM hexaferrite and CoFe<sub>2</sub>O<sub>4</sub> in the vicinity of each other without any secondary phase as shown in Fig. 4.133.
- b) Fig. 4.4 (D-series) shows that the substitution of Co<sup>2+</sup> -La<sup>3+</sup> ions improves the inter-grain connectivity of particles. As the proportion of substituents increases in the composition of the synthesized samples, there is no significant change in morphology is observed. Fig. 4.94 exhibits hexagonal platelet-shaped particles along with randomly oriented and small cubical-shaped grains for all samples in the DM series. The particles tend to agglomerate due to magnetic dipole interactions between the magnetic hard and soft nanoparticles. The magnetic dipoles of the hard and soft particles are parallel to each other, and their mutual attraction results in the agglomeration of the particles. Besides the magnetic dipole interaction, the aggregation of particles also occurs due to the high magnetic static interaction. A magnified view of FESEM images affirms the formation of stacking layers of grains in DM composites. Due to the finite separation between the layers, they do not significantly contribute to the polarization and conductivity phenomena of the synthesized samples. Similarly, in the BS -series (Fig. 4.135), all the micrographs reveal the co-existence of hexagonal platelet-like particles of M-type hexaferrite and small spherical-shaped particles of spinel ferrite. A high degree of agglomeration is

observed between M-type and spinel ferrite particles. The insertion of Co-Cr ions improves the inter-grain connectivity between large and small-sized grains. Whereas, in B-series most of the grains of substituted samples are distributed non-uniformly over the surface and are of different shapes and sizes (Fig. 4.30).

- c) Among the various fabricated hard/soft ferrite composites, few samples exhibit decreased saturation magnetization and coercivity than substituted SrM hexaferrite. The increment in  $H_c$  value is attributed to the dominance of the exchange coupling effect over dipolar interaction in their structure. The M-H curves of the DM1 and BS3 samples are smooth and convex-shaped, whereas other samples display stepped loops, indicating the uncoupled behavior of hard and soft phases. This is due to incomplete exchange coupling between soft and hard ferrite phases. Furthermore, in the  $dM/dH$  versus  $H$  plots, a single peak with a shoulder peak indicates weak exchange coupling behavior in the samples. This demonstrates that the dipolar interaction between hard/hard and soft/soft phases significantly competes with the hard/soft exchange-coupling interaction, resulting in reduced magnetic properties.
- d) The decrease in permittivity/permeability values of hard/soft composites can be attributed to less effective polarization due to mismatched lattice structures and inadequate dipole alignment. Additionally, the presence of both hard and soft phases in composites often results in incomplete or weak exchange coupling. The interactions between hard and soft ferrite particles may lack robustness, causing a reduction in overall magnetic permeability. Dipolar interactions within each phase may dominate over the exchange interactions between phases, further diminishing the effective permeability. Despite these reductions, the composite still achieves more than 90 % absorption, an 860 MHz absorption bandwidth for  $REL > -10$  dB, and improved impedance matching. These results are highly desirable for practical applications.

#### B) Ferrite/polymer composites

In the present study, we successfully synthesized (a) Co-Zn substituted SrM hexaferrite (F-series) and its composites with polyaniline (FP-series). Co-Cd substituted SrM hexaferrite (C-series) and its composites with polyaniline (CP-series). The combination of M-type hexaferrite with PANI enhanced the overall dielectric constant/loss of the composite. The high dielectric constant of PANI enhances the polarization mechanisms within the composite, leading to improved permittivity.

- a) Fig. 4.49 demonstrates the XRD pattern of Co-Zn substituted SrM hexaferrite (F-series), whereas FP-series (Fig. 4.117) shows a broad peak (hump) due to PANI in



the range of  $15^{\circ}$ - $25^{\circ}$ . This indicates the successful synthesis of ferrite/polymer composites. Similarly, the XRD pattern in Fig. 4.68 confirms the substitution of Co-Cd ions in SrM hexaferrite (C-series). In the CP series, the presence of both SrM hexaferrite and PANI is shown in Fig. 4.151.

- b) Fig. 4.52 (F-series) shows that the substitution of Co-Zn ions results in grain clusters containing hexagonal, platelet-shaped particles with distinct geometric shapes. In contrast, the morphology of the FP-series (Fig. 4.120) depicts a disk flower/small tubular-like structure of PANI, forming a network between individual grains. The disk floret of PANI is embedded in the platelet hexaferrite, confirming the encapsulation of PANI (amino group) with SrFe<sub>12</sub>O<sub>19</sub> (oxygen). Similarly, in Co-Cd substituted hexaferrite (C-series), numerous small grains interact over long distances, involving several voids. The substitution leads to agglomeration, forming large-sized grains with uneven size distribution (Fig. 4.71). In the CP series, the entanglement between M-type hexaferrite and PANI is visualized (Fig. 4.153).
- c) The saturation magnetization and coercivity of all ferrite/polymer composites (FP and CP-series) are lower than those of substituted SrM hexaferrites (F and C-series). The diamagnetic nature of PANI can counteract the magnetic fields within the composite, leading to a net decrease in the measured magnetic parameters. Furthermore, poor dispersion can lead to agglomeration of hexaferrite particles, creating non-uniform magnetic domains and reducing the overall magnetic response. Additionally, changes in the size and shape of the hexaferrite particles during the composite formation process can also affect the magnetic parameters. Coating ferrite particles with PANI reduces magnetic anisotropy. In FP and CP series composites, the charge transfer between ferrite and PANI affects the electronic spin mechanisms, leading to decreased domain wall movement in the magnetic particles. Consequently, the coercivity of the composites is lowered.
- d) The complex permittivity value of ferrite/polymer composites (FP and CP-series) is higher than that of substituted SrM hexaferrites (F and C-series), largely due to the high dielectric constant of PANI. However, in ferrite-polymer composites, a decrease in coercivity and an increase in dielectric and magnetic loss are observed which are desirable characteristics for effective absorption. Nonetheless, these composites exhibit poor impedance-matching properties. Further investigation is required to understand the anomalous behavior of these materials.

Table 4.47 illustrates the comparison between the absorption characteristics of all synthesized samples. We must choose an optimum concentration of dopants and the weight ratio of spinel/PANI in pure strontium hexaferrite to obtain adequate absorption characteristics. All the substituted SrM hexaferrite and its composites exhibit greater than 90 % absorption. In-between substituted hexaferrite samples, the C2 sample of C-series exhibits a maximum reflection loss of -54.04 dB for a small thickness of 1.8 mm at 8.62 GHz frequency with a wide-absorption bandwidth of 3.41 GHz and better impedance matching results i.e., ( $Z_{real}$  (0.997) and  $Z_{img}$  (0.010)), very close to 1 and/or zero, respectively. However, the BS5 composite shows a REL dip of -29.92 dB for 8.5 mm thickness at 9.157 GHz frequency with an EAB of 820 MHz.

**Table 4.48** Comparison of absorption characteristics of all synthesized samples.

Sample name	REL (dB)	$d_m$	Matching frequency (GHz)	Band Width (REL > -10 dB) (GHz)	$Z_{real}/Z_{img}$
D3	-45.61	8.1	8.98	0.87	0.997/0.010
B5	-36.70	8.4	9.23	0.91	1.022/0.019
F2	-47.26	3.3	18	2.99	0.993/-0.005
C2	-54.04	1.8	8.62	3.41	1.003/2E-05
DM1	-32.96	8.9	8.32	--	1.030/-0.034
BS5	-29.92	8.5	9.15	0.82	1.091/-0.054

---

# CHAPTER 5

## SUMMARY AND CONCLUSION

---

D-series hexaferrite samples are structurally characterized using XRD and FTIR, and their morphology was assessed using SEM. The EDX checks the existence of every element in an experiment. Substitution does not alter the magneto plumbite structure, as displayed in XRD analysis. The insertion of Co-La ions improves the inter-grain connectivity of hexagonal grains and significantly affects the electrical characteristics of all prepared samples. In the low-frequency region, the value of  $\epsilon'$  and  $\tan\delta$  decreases with substitution. The VSM analysis reveals the maximum value of  $M_s$  (103.29 emu/g) and  $H_c$  (5026.24 Oe) in the D1 sample. The tendency of Co-La ions to occupy particular lattice sites of crystal structure causes a non-linear decrement in  $M_r$  from 103.29 emu/g to 67.96 emu/g and a gradual decrease in  $H_c$  from 5026.24 Oe to 862.47 Oe. The REL values below -10 dB were achieved in all samples of the D-series by carefully choosing a thickness between 1.5 to 9.9 mm within the frequency range of 8.2 to 12 GHz. Sample D1, due to its low level of Co-La substitution, demonstrated both the highest BTR (2.5E-03) and the greatest PBW (15.9 %) among all synthesized samples. Sample D1 exhibits a wide bandwidth of -10 dB with a width of 1.79 GHz at 1.7 mm thickness. All samples of the D-series, except D6, primarily followed the quarter-wavelength mechanism for various thicknesses. Sample D3 displayed the optimal values for  $Z_{real}$  (0.997) and  $Z_{img}$  (0.010), resulting in the highest REL (-45.61 dB). It's worth noting that the absorber's properties can be adjusted by fine-tuning the electromagnetic parameters and the composite thickness.

In this section, we have fabricated the single-phase B-series hexaferrite with different levels of substitution via sol-gel combustion methodology. XRD pattern confirms the establishment of the magnetoplumbite phase without the presence of any secondary phases. FTIR also signifies the substitution of cations in hexaferrite. The dielectric results exhibit an increase in dielectric constants from 79.61 to 84.77 and loss tangent from 5.85 to 9.78 with substitution at 1MHz frequency. The electric modulus spectroscopy shows maximum conductivity relaxation in the B3 sample that endorses the involvement of grain/grain boundaries in the mechanism of conduction. The substitution of  $Co^{2+}$ -  $Cr^{3+}$  ions causes a non-linear decrease in coercivity, remnant magnetization, and anisotropy field. Moreover, a large reduction in

coercivity is observed from 3767 Oe to 727 Oe which depicts the transition of ferrite from hard to soft, indicating it is suitable for various magnetic applications. The maximum REL of Co-Cr substituted SrM hexaferrite of B5 sample with 8.4 mm was -36.7 dB at 9.23 GHz with an effective absorption bandwidth (EAB) of 0.79 GHz. Moreover, altering the Co-Cr ions content and thickness improves the absorption performance of SrM hexaferrite.

Sol-gel synthesized F-series hexaferrite calcined at 1100 °C/5h led to the formation of a secondary phase (CoFe<sub>2</sub>O<sub>4</sub>) along with a magnetoplumbite structure. A structural phase transition occurs from F4 to F5 and results in rapid decrement of lattice parameters. As the Co-Zn content increased, the crystal size increased to 48 nm for the F5 sample. FTIR spectra revealed the existence of two absorption bands at 435.15 and 597.98 cm<sup>-1</sup>, which were predicted to be due to Fe-O vibrations. Hexagonal platelet-shaped particle thicknesses are in nano-scale and micro-scale in diameter and can be visualized in SEM micrographs. The F3 sample shows the minimum value of AC conductivity  $3.95 \times 10^{-5} \Omega^{-1} \text{m}^{-1}$ , which can be explained by the availability of Fe<sup>3+</sup> ions at octahedral positions. Co-Zn substitution led to a gradual increment in M<sub>s</sub> and M<sub>r</sub> from 75.26 emu/g to 80.72 emu/g and 26.95 to 59.12 emu/g, respectively, while non-monotonically in H<sub>c</sub> from 2035 Oe to 4159 Oe. The squareness ratio of F4 (0.631) and F5 (0.732) affirms the presence of single-domain particles. Substitution results in a maximum REL of -47.26 dB with 3.3 mm at 18 GHz for the F2 sample and REL ranges from -10 to -40.53 dB for remaining samples over 12 to 18 GHz. Furthermore, both F2 and F4 samples (REL > -10 dB) show maximum PBW values of 21.11 and 21.26 and BTR values of 2.06 and 2.13 with an effective absorption bandwidth of 2.99 GHz and 3.3 GHz, respectively.

C-series hexaferrites successfully synthesized via sol-gel combustion methodology. A magnetoplumbite crystal structure with a secondary phase of CoFe<sub>2</sub>O<sub>4</sub> was seen in the XRD pattern of prepared samples. The calculated crystallite size of incorporated samples decreases non-linearly from 46.46 to 40.75 nm with Co-Cd substitution. FTIR spectra corroborated the absorption band at 400- 600 cm<sup>-1</sup> supporting the formation of a magnetoplumbite structure. Substitution improves the inter-particle contact between the grains through the agglomeration of grains. Mössbauer's analysis explained the occupancy of iron cations at spin-down sites from C1 to C3. Hysteresis results exhibited a M<sub>s</sub> and H<sub>c</sub> in the range of 67.51 emu/g ≤ M<sub>s</sub> ≤ 82.13 emu/g and 2255 Oe ≤ H<sub>c</sub> ≤ 4551 Oe, respectively. According to VNA results, the

maximum REL of each sample is in the range of – 23.4 dB to -54 dB. Sample C2 reveals an optimal REL dip of -39.29 dB at a minimal thickness of 1.7 mm at 8.89 GHz frequency with a wide absorption bandwidth of 3.41 GHz (8.30-11.71 GHz), maximum BTR and PBW values of 1.84 and 38.35, respectively.

Co-La substituted hard/soft ferrite composites of DM-series with different levels of substitution were effectively prepared using the physical blending method. XRD analysis revealed the formation of a single-phase magnetoplumbite structure with peaks of spinel ferrite. This result affirms that this is the appropriate method of preparing composites. The crystallite size of M-type hexaferrite ranges from 38.70-50.54 nm, while the crystallite size of spinel ferrite is in the range of 25.80-46.94 nm. Substitution increases inter-grain connectivity and porosity in the synthesized composites. For all synthesized composites, a single peak is observed in  $\tan\delta$  plots and is attributed to electron hopping, which dissipates maximum energy. The value of  $M_s$  and  $M_r$  of ferrite composites initially increased from DM1 to DM2, and further addition of Co-La ions caused a gradual decrease in parameters. The behavior of  $H_c$  is in harmony with  $H_a$  despite the substitution of Co-La ions. The single narrow peak in the  $dM/dH$  vs.  $H$  plot is attributed to the strong exchange coupling for DM1. When  $z = 0.0$  ( $\text{SrFe}_{12}\text{O}_{19}/\text{Fe}_3\text{O}_4$ ), a maximum REL of -32.96 dB (8.9 mm) at 8.326 GHz and an absorption bandwidth of 0.60 GHz for  $\text{REL} > -10$  dB are attained. As a result, this study provides a suitable candidate for solving EM wave pollution problems.

Cobalt and Zinc substituted SrM hexaferrite and their composite with PANI (in 1:5 by wt%) are successfully synthesized. Powder XRD pattern indicates the formation of magnetoplumbite structure with PANI. This result affirms that this is the appropriate method of preparing composites. The crystallite size ranges from 29.07 to 67.5 nm. FESEM study of synthesized composites reveals that disk flower-like PANI particle is well encapsulated on platelet-shaped hexaferrite. Dielectric results show a single peak in  $\tan\delta$  plots and are attributed to maximum energy dissipation, agreed with FESEM results. The electric modulus spectroscopy shows maximum conductivity relaxation in the  $x = 0.8$  sample that endorses the involvement of grain/grain boundaries in the mechanism of conduction. The value of  $M_s$ ,  $H_c$ , and  $M_r$  of ferrite composites initially increased and reached maximum limits of 53.39 emu/g, 2293.5 Oe, and 15.3 kOe, respectively for FP2 sample, further addition of Co-Zn ions caused a gradual decrease in parameters. The insertion of Co-Zn ions into ferrite composites can



non-linearly increase the dielectric and magnetic losses, but it does not effectively contribute to reflection loss. The impedance mismatch between the  $Z_{in}$  and  $Z_o$  values of the synthesized composites results in reflection loss not exceeding -7 dB.

Composites of BS-series ferrites were produced by the physical blending method by a weight ratio of 1:5. We found that XRD shows peaks of both spinel and M-type hexagonal ferrite. The crystallite size of both M-type hexaferrite and spinel ferrite non-linearly decreases from BS1 to BS6 and it ranges from 51.7 to 44.4 Å and 57.5 to 44.2 Å, respectively. The platelet-shaped hexagonal ferrites were encapsulated with spherical-shaped spinel ferrites. As the level of substitution increases, both conductivity and dielectric relaxation endorses the involvement of grains. The value of  $M_s$  (103 emu/g) and  $H_c$  (4932 Oe) is the maximum for the BS1 sample and it falls with Co-Cr substitution. Several factors are responsible for the maximum absorption of -29.9 dB (8.5 mm) at 9.15 GHz and the effective bandwidth of 820 MHz for REL > -10 dB. Notably, the absorption performance of composites is considerably higher than previously published reports. The synthesizing materials showed promising properties for various high-frequency applications.

Composite materials comprising  $SrCo_zCd_{0.5z}Fe_{12-2z}O_{19}$  and PANI were effectively synthesized using physical blending technique. XRD analysis confirmed the existence of both the M-type phase and the PANI broad peak within the composites. FESEM shows an entanglement between platelet-shaped particles (M-type hexaferrite) and disk flower-shaped particles (PANI). Substitution of Co-Cd ions reinforces dielectric constant and loss and shifts the relaxation contribution from grain boundary to grains. VSM results gradual decrease in coercivity from 2620 Oe (CP1) to 745 Oe (CP5), a non-monotonic increase in  $M_s$  11 emu/g (CP1) to 54.5 emu/g (CP5), and linear fall in  $H_a$  13.50 kOe (CP1) to 10.71 kOe (CP5). The insertion of Co-Cd ions in ferrite/PANI composites results non-linear increase in the dielectric and magnetic losses. The impedance mismatch between the  $Z_{in}$  and  $Z_o$  values of the synthesized composites results in reflection loss not exceeding -5 dB.

## **6 Future Scope**

- Innovations in manufacturing techniques, such as advanced processing methods can impact the cost-effectiveness and scalability of M-type hexaferrite for practical applications.
- The suitable design of a multi-functional EM absorber based on M-type hexaferrite with other desirable properties, such as mechanical strength, lightweight structures, or thermal stability.
- Studies may focus on tailoring dielectric/magnetic characteristics of M-type hexaferrite composites through substitution, varying synthesis methods, or controlling grain size and morphology to achieve optimal microwave absorption performance in high-frequency regions X (8-12 GHz), Ku (12-18 GHz), K (18-26 GHz), or Ka (26-40 GHz) band.

## Bibliography

- [1] Q. Li, Z. Zhang, L. Qi, Q. Liao, Z. Kang, and Y. Zhang, "Toward the Application of High Frequency Electromagnetic Wave Absorption by Carbon Nanostructures," *Advanced Science*, vol. 6, no. 8. John Wiley and Sons Inc., Apr. 17, 2019. doi: 10.1002/advs.201801057.
- [2] S. Iqbal, H. Khatoon, R. K. Kotnala, and S. Ahmad, "Bi-doped barium ferrite decorated polythiophene nanocomposite: influence of Bi-doping on structure, morphology, thermal and EMI shielding behavior for X-band," *J Mater Sci*, vol. 55, no. 33, pp. 15894–15907, Nov. 2020, doi: 10.1007/s10853-020-05134-z.
- [3] B. Wen, H. Yang, Y. Lin, Y. Qiu, Y. cheng, and lingxiang Jin, "Novel bimetallic MOF derived hierarchical Co@C composites modified with carbon nanotubes and its excellent electromagnetic wave absorption properties," *J Colloid Interface Sci*, vol. 605, pp. 657–666, Jan. 2022, doi: 10.1016/j.jcis.2021.07.118.
- [4] S. R. Shannigrahi *et al.*, "Synthesis and electromagnetic properties of U-type hexaferrites Ba 4B 2Fe 36O 60 (B: Co, Ni, Cu)," *J Magn Magn Mater*, vol. 325, pp. 63–68, Jan. 2013, doi: 10.1016/j.jmmm.2012.08.019.
- [5] Y. Bi *et al.*, "One-dimensional Ni@Co/C@PPy composites for superior electromagnetic wave absorption," *J Colloid Interface Sci*, vol. 605, pp. 483–492, Jan. 2022, doi: 10.1016/j.jcis.2021.07.050.
- [6] S. Acharya, J. Ray, T. U. Patro, P. Alegaonkar, and S. Datar, "Microwave absorption properties of reduced graphene oxide strontium hexaferrite/poly(methyl methacrylate) composites," *Nanotechnology*, vol. 29, no. 11, Feb. 2018, doi: 10.1088/1361-6528/aaa805.
- [7] F. Meng, R. Zhao, Y. Zhan, Y. Lei, J. Zhong, and X. Liu, "Preparation and microwave absorption properties of Fe-phthalocyanine oligomer/Fe<sub>3</sub>O<sub>4</sub> hybrid microspheres," *Appl Surf Sci*, vol. 257, no. 11, pp. 5000–5006, Mar. 2011, doi: 10.1016/j.apsusc.2011.01.010.
- [8] Z. Zhang, G. H. Wang, W. Gu, Y. Zhao, S. Tang, and G. Ji, "A breathable and flexible fiber cloth based on cellulose/polyaniline cellular membrane for microwave shielding and absorbing applications," *J Colloid Interface Sci*, vol. 605, pp. 193–203, Jan. 2022, doi: 10.1016/j.jcis.2021.07.085.
- [9] S. Du, H. Chen, and R. Hong, "Preparation and electromagnetic properties characterization of reduced graphene oxide/strontium hexaferrite nanocomposites," *Nanotechnol Rev*, vol. 9, no. 1, pp. 105–114, Jan. 2020, doi: 10.1515/ntrev-2020-0010.
- [10] P. Gairola, S. P. Gairola, V. Kumar, K. Singh, and S. K. Dhawan, "Barium ferrite and graphite integrated with polyaniline as effective shield against electromagnetic interference," *Synth Met*, vol. 221, pp. 326–331, Nov. 2016, doi: 10.1016/j.synthmet.2016.09.023.
- [11] C. Zhou *et al.*, "Lightweight hollow carbon nanospheres with tunable sizes towards enhancement in microwave absorption," *Carbon N Y*, vol. 108, pp. 234–241, Nov. 2016, doi: 10.1016/j.carbon.2016.07.015.

- [12] F. Pan, L. Cai, Y. Dong, X. Zhu, Y. Shi, and W. Lu, “Mixed-dimensional hierarchical configuration of 2D Ni<sub>2</sub>P nanosheets anchored on 1D silk-derived carbon fiber for extraordinary electromagnetic wave absorption,” *J Mater Sci Technol*, vol. 101, pp. 85–94, Feb. 2022, doi: 10.1016/j.jmst.2021.05.066.
- [13] X. Zhou *et al.*, “Electromagnetic wave absorption performance of NiCo<sub>2</sub>X<sub>4</sub> (X = O, S, Se, Te) spinel structures,” *Chemical Engineering Journal*, vol. 420, Sep. 2021, doi: 10.1016/j.cej.2021.129907.
- [14] X. Liang *et al.*, “Review: Recent process in the design of carbon-based nanostructures with optimized electromagnetic properties,” *Journal of Alloys and Compounds*, vol. 749. Elsevier Ltd, pp. 887–899, Jun. 15, 2018. doi: 10.1016/j.jallcom.2018.03.344.
- [15] J. Yan, Y. Huang, Y. Yan, L. Ding, and P. Liu, “High-Performance Electromagnetic Wave Absorbers Based on Two Kinds of Nickel-Based MOF-Derived Ni@C Microspheres,” *ACS Appl Mater Interfaces*, vol. 11, no. 43, pp. 40781–40792, Oct. 2019, doi: 10.1021/acsami.9b12850.
- [16] “Electromagnetic wave.”
- [17] R. K. Kotnala and J. Shah, “Ferrite Materials: Nano to Spintronics Regime,” in *Handbook of Magnetic Materials*, vol. 23, Elsevier B.V., 2015, pp. 291–379. doi: 10.1016/B978-0-444-63528-0.00004-8.
- [18] J. Liu, Z. Zhao, and L. Zhang, “Toward the application of electromagnetic wave absorption by two-dimension materials,” *Journal of Materials Science: Materials in Electronics*, vol. 32, no. 21. Springer, pp. 25562–25576, Nov. 01, 2021. doi: 10.1007/s10854-020-03800-1.
- [19] L. B. Kong *et al.*, “Recent progress in some composite materials and structures for specific electromagnetic applications,” *International Materials Reviews*, vol. 58, no. 4. Maney Publishing, pp. 203–259, 2013. doi: 10.1179/1743280412Y.0000000011.
- [20] V. Da, R. Caffarena, J. Leixas Capitaneo, T. Ogasawara, and M. Silveira Pinho, “Microwave Absorption Properties of Co, Cu, Zn-Substituted Hexaferrite Polychloroprene Nanocomposites,” 2008.
- [21] Y. Liu, Y. Lin, and H. Yang, “Facile fabrication for core-shell BaFe<sub>12</sub>O<sub>19</sub>@C composites with excellent microwave absorption properties,” *J Alloys Compd*, vol. 805, pp. 130–137, Oct. 2019, doi: 10.1016/j.jallcom.2019.07.006.
- [22] V. Pratap, A. K. Soni, S. Dayal, S. M. Abbas, A. M. Siddiqui, and N. E. Prasad, “Electromagnetic and absorption properties of U-type barium hexaferrite-epoxy composites,” *J Magn Magn Mater*, vol. 465, pp. 540–545, Nov. 2018, doi: 10.1016/j.jmmm.2018.06.027.
- [23] S. S. S. Afghahi, A. Shokuhfar, B. Saberi, and A. Javidan, “Iron-cobalt-graphite core-shell nanoparticles as efficient electromagnetic wave absorbers at X-band frequency range,” *Micro Nano Lett*, vol. 9, no. 6, pp. 412–416, 2014, doi: 10.1049/mnl.2013.0723.

- [24] S. Singh, S. Shukla, A. Kumar, and D. Singh, "Influence of Zn dispersion in SiC on electromagnetic wave absorption characteristics," *J Alloys Compd*, vol. 738, pp. 448–460, Mar. 2018, doi: 10.1016/j.jallcom.2017.12.190.
- [25] J. Wang, B. Wang, A. Feng, Z. Jia, and G. Wu, "Design of morphology-controlled and excellent electromagnetic wave absorption performance of sheet-shaped ZnCo<sub>2</sub>O<sub>4</sub> with a special arrangement," *J Alloys Compd*, vol. 834, Sep. 2020, doi: 10.1016/j.jallcom.2020.155092.
- [26] Ali-Sharbaty and J. M. V. Khani, "Influence of Ho substitution on structural, magnetic and microwave absorption properties of PbM-type hexaferrites nanoparticles," *Journal of Materials Science: Materials in Electronics*, vol. 25, no. 1, pp. 244–248, Jan. 2014, doi: 10.1007/s10854-013-1578-3.
- [27] X. Zhou *et al.*, "Synthesis of porous carbon embedded with NiCo/CoNiO<sub>2</sub> hybrids composites for excellent electromagnetic wave absorption performance," *J Colloid Interface Sci*, vol. 575, pp. 130–139, Sep. 2020, doi: 10.1016/j.jcis.2020.04.099.
- [28] A. Arora, S. B. Narang, and K. Pubby, "Enhanced Microwave Absorption Properties of Doped M-Type Barium Hexagonal Ferrites in Ka-band Frequencies," *J Supercond Nov Magn*, vol. 32, no. 8, pp. 2705–2709, Aug. 2019, doi: 10.1007/s10948-019-5044-1.
- [29] Y. fan Wang *et al.*, "In-situ growth of magnetic nanoparticles on honeycomb-like porous carbon nanofibers as lightweight and efficient microwave absorbers," *Ceram Int*, 2023, doi: 10.1016/j.ceramint.2023.08.226.
- [30] H. Qiu, X. Zhu, P. Chen, Y. Chen, G. Chen, and W. Min, "Construction of core-shell structured ZnO/C@PPy composite as high-performance dielectric electromagnetic wave absorber," *J Magn Magn Mater*, vol. 543, Feb. 2022, doi: 10.1016/j.jmmm.2021.168604.
- [31] C. Liu *et al.*, "Graphene reinforced nanoarchitectonics of 3D interconnected magnetic-dielectric frameworks for high-efficient and anti-corrosive microwave absorbers," *J Mater Sci Technol*, vol. 168, pp. 194–207, Jan. 2024, doi: 10.1016/j.jmst.2023.06.007.
- [32] Z. Ren *et al.*, "Low-profile broadband microwave absorber based on magnetic coating and artificial electromagnetic structures," *Chemical Engineering Journal*, vol. 466, Jun. 2023, doi: 10.1016/j.cej.2023.143115.
- [33] W. Huang and Z. Zhu, "Broadband metamaterial absorbers based on magnetic composites," *J Magn Magn Mater*, vol. 576, Jun. 2023, doi: 10.1016/j.jmmm.2023.170792.
- [34] S. C. Tolani, A. R. Golhar, and K. G. Rewatkar, "A review of morphological, structural behaviour and technological applications of ferrites," in *AIP Conference Proceedings*, American Institute of Physics Inc., May 2019. doi: 10.1063/1.5100459.
- [35] S. J. Salih and W. M. Mahmood, "Review on magnetic spinel ferrite (MFe<sub>2</sub>O<sub>4</sub>) nanoparticles: From synthesis to application," *Helvion*, vol. 9, no. 6. Elsevier Ltd, Jun. 01, 2023. doi: 10.1016/j.helivon.2023.e16601.



- [36] N. R. Hulsure, A. K. Inamdar, S. S. Bandgar, and S. B. Shelke, "Oleic acid coated Mn-Zn-Sm ferrite nanoparticles for ferrofluid application," *Mater Today Proc*, May 2023, doi: 10.1016/j.matpr.2023.04.577.
- [37] G. Katoch *et al.*, "Crystal structure, synthesis, properties and potential applications of cobalt spinel ferrite: A brief review," *Mater Today Proc*, 2023, doi: 10.1016/j.matpr.2023.03.585.
- [38] J. M. Gonçalves *et al.*, "Sensing performances of spinel ferrites MFe<sub>2</sub>O<sub>4</sub> (M = Mg, Ni, Co, Mn, Cu and Zn) based electrochemical sensors: A review," *Analytica Chimica Acta*, vol. 1233. Elsevier B.V., Nov. 15, 2022. doi: 10.1016/j.aca.2022.340362.
- [39] R. C. Pullar, W. Hajjaji, J. S. Amaral, M. P. Seabra, and J. A. Labrincha, "Magnetic properties of ferrite ceramics made from wastes," *Waste Biomass Valorization*, vol. 5, no. 1, pp. 133–138, Feb. 2014, doi: 10.1007/s12649-013-9207-1.
- [40] T. F. W. Barth and E. Posnjak, "Spinel structures: with and without variate atom equipoints."
- [41] V. V. Jadhav, R. S. Mane Pritamkumar, and V. Shinde Bismuth-Ferrite-Based, "SPRINGER BRIEFS IN MATERIALS." [Online]. Available: <http://www.springer.com/series/10111>
- [42] Aakansha, B. Deka, S. Ravi, and D. Pamu, "Impedance spectroscopy and ac conductivity mechanism in Sm doped Yttrium Iron Garnet," *Ceram Int*, vol. 43, no. 13, pp. 10468–10477, 2017, doi: 10.1016/j.ceramint.2017.05.089.
- [43] Y. J. Siao and X. Qi, "Dielectric responses in polycrystalline rare-earth iron garnets," *J Alloys Compd*, vol. 691, pp. 672–682, 2017, doi: 10.1016/j.jallcom.2016.08.316.
- [44] A. I. Borhan, D. Ghercă, A. R. Iordan, and M. N. Palamaru, "Classification and types of ferrites," in *Ferrite Nanostructured Magnetic Materials: Technologies and Applications*, Elsevier, 2023, pp. 17–34. doi: 10.1016/B978-0-12-823717-5.00026-7.
- [45] "snoek1947".
- [46] K. Sharma, N. Aggarwal, N. Kumar, and A. Sharma, "A review paper: Synthesis techniques and advance application of Mn-Zn nano-ferrites," *Mater Today Proc*, 2023, doi: 10.1016/j.matpr.2022.12.088.
- [47] V. Tsakaloudi and V. T. Zaspalis, "A new Mn-Zn ferrite for high-speed data transmission applications in telecommunication networks," *J Magn Magn Mater*, vol. 310, no. 2 SUPPL. PART 3, pp. 2540–2542, Mar. 2007, doi: 10.1016/j.jmmm.2006.11.143.
- [48] I. Dumitru and O. F. Caltun, "Ferrites use in magnetic recording," in *Ferrite Nanostructured Magnetic Materials: Technologies and Applications*, Elsevier, 2023, pp. 733–745. doi: 10.1016/B978-0-12-823717-5.00017-6.
- [49] F. Wei, M. Lu, and Z. Yang, "The temperature dependence of magnetic properties of Zn-Ti substituted Ba-ferrite particles for magnetic recording," 1999.

- [50] S. Nakagawa, N. Matsushita, and M. Naoe, "Perpendicular magnetic recording media using hexagonal ferrite thin films deposited on Pt underlayers and interlayers," 2001.
- [51] C. K. Ong, H. C. Fang, Z. Yang, and Y. Li, "Magnetic relaxation in Zn}Sn-doped barium ferrite nanoparticles for recording," 2000.
- [52] S. J. Huang *et al.*, "Effects of ytterbium substitution on the structural, electrical and magnetic properties of Ni–Zn–Co ferrites for microwave equipment," *Ceram Int*, vol. 49, no. 17, pp. 28758–28763, Sep. 2023, doi: 10.1016/j.ceramint.2023.06.135.
- [53] Z. Zhang, F. Li, and Y. Zheng, "Highly sensitive resistive humidity sensor based on strontium-doped lanthanum ferrite nanofibers," *Sens Actuators A Phys*, vol. 358, Aug. 2023, doi: 10.1016/j.sna.2023.114435.
- [54] B. N. Ramakrishna, A. Pasha, S. Khasim, and S. O. Manjunatha, "LPG sensing behavior and dielectric properties of lanthanum doped cobalt-iron oxide nano ferrite sensors towards room temperature detection at ppb level," *Ceram Int*, Oct. 2023, doi: 10.1016/j.ceramint.2023.10.062.
- [55] K. Manjunatha *et al.*, "Effect of Eu<sup>3+</sup> and Sc<sup>3+</sup> on the structure, microstructure and humidity sensing properties of copper ferrites for sensor applications," *Ceram Int*, Oct. 2023, doi: 10.1016/j.ceramint.2023.09.359.
- [56] M. Rethinasabapathy *et al.*, "Cobalt ferrite microspheres as a biocompatible anode for higher power generation in microbial fuel cells," *J Power Sources*, vol. 483, Jan. 2021, doi: 10.1016/j.jpowsour.2020.229170.
- [57] N. Singh, M. K. Kansal, P. Kumar, S. Dabas, and V. Verma, "Effect of Sn doping on structural, magnetic and power loss properties of lithium ferrites for high frequency applications," *Physics Open*, vol. 16, Jul. 2023, doi: 10.1016/j.physo.2023.100155.
- [58] A. A. Ghanem and S. O. Abdellatif, "Experimentally verified numerical model for asymmetric ferrite core wireless power transfer with on-chip interfacing circuits," *e-Prime - Advances in Electrical Engineering, Electronics and Energy*, vol. 5, Sep. 2023, doi: 10.1016/j.prime.2023.100262.
- [59] J. Li *et al.*, "Enhancement of microstructure and magnetic properties of MgCd ferrite via Sm-Ga ions substitution for microwave devices," *Mater Res Bull*, vol. 142, Oct. 2021, doi: 10.1016/j.materresbull.2021.111414.
- [60] H. S. Guo *et al.*, "Effect of lanthanum substitution on structural, magnetic, and electric properties of Ni–Zn–Co ferrites for radio frequency and microwave devices," *Ceram Int*, vol. 48, no. 15, pp. 22557–22563, Aug. 2022, doi: 10.1016/j.ceramint.2022.04.275.
- [61] Q. U. A. Shahid, M. A. Khan, S. Gulbadan, G. A. Ashraf, and R. T. Rasool, "Impact of erbium substitution on structural, dielectric, spectral, and microwave absorption properties of Ba<sub>3</sub>Co<sub>2</sub>Fe<sub>24</sub>O<sub>41</sub> Z-type hexa-ferrites for microwave devices applications," *Ceram Int*, vol. 49, no. 17, pp. 27866–27877, Sep. 2023, doi: 10.1016/j.ceramint.2023.06.003.

- [62] M. Amiri, M. Salavati-Niasari, and A. Akbari, "Magnetic nanocarriers: Evolution of spinel ferrites for medical applications," *Advances in Colloid and Interface Science*, vol. 265. Elsevier B.V., pp. 29–44, Mar. 01, 2019. doi: 10.1016/j.cis.2019.01.003.
- [63] S. Amiri and H. Shokrollahi, "The role of cobalt ferrite magnetic nanoparticles in medical science," *Materials Science and Engineering C*, vol. 33, no. 1. pp. 1–8, Jan. 01, 2013. doi: 10.1016/j.msec.2012.09.003.
- [64] D. H. Kim, H. Zeng, T. C. Ng, and C. S. Brazel, "T1 and T2 relaxivities of succimer-coated MFe<sub>23</sub>O<sub>4</sub> (M=Mn<sup>2+</sup>, Fe<sup>2+</sup> and Co<sup>2+</sup>) inverse spinel ferrites for potential use as phase-contrast agents in medical MRI," *J Magn Magn Mater*, vol. 321, no. 23, pp. 3899–3904, Dec. 2009, doi: 10.1016/j.jmmm.2009.07.057.
- [65] H. C. Gomes, S. S. Teixeira, and M. P. F. Graça, "Synthesis of calcium ferrite for energy storage applications," *J Alloys Compd*, vol. 921, Nov. 2022, doi: 10.1016/j.jallcom.2022.166026.
- [66] R. Priyadharsini, C. Manoharan, M. Bououdina, S. Sagadevan, M. Venkateshwarlu, and S. Asath Bahadur, "Impact of nickel substitution on structural, dielectric, magnetic, and electrochemical properties of copper ferrite nanostructures for energy storage devices," *J Colloid Interface Sci*, vol. 653, pp. 917–929, Jan. 2024, doi: 10.1016/j.jcis.2023.09.113.
- [67] M. A. Munir *et al.*, "Testing of magnetic and dielectric traits of microwave plasma treated NiCuZn spinel ferrites for efficient energy storage and high-frequency applications," *Materials Science and Engineering: B*, vol. 291, May 2023, doi: 10.1016/j.mseb.2023.116374.
- [68] M. I. Khan *et al.*, "Magnetic behavior of Ga doped yttrium iron garnet ferrite thin films deposited by sol-gel technique," *Ceram Int*, vol. 46, no. 17, pp. 27318–27325, Dec. 2020, doi: 10.1016/j.ceramint.2020.07.217.
- [69] M. Yousaf, A. Noor, S. Xu, M. N. Akhtar, and B. Wang, "Magnetic characteristics and optical band alignments of rare earth (Sm<sup>+3</sup>, Nd<sup>+3</sup>) doped garnet ferrite nanoparticles (NPs)," *Ceram Int*, vol. 46, no. 10, pp. 16524–16532, Jul. 2020, doi: 10.1016/j.ceramint.2020.03.219.
- [70] Y. Yang *et al.*, "Construction of Ni-Zn bimetal sulfides Heterostructured-hybrids for High-performance electromagnetic wave absorption," *J Colloid Interface Sci*, vol. 606, pp. 1410–1420, Jan. 2022, doi: 10.1016/j.jcis.2021.08.095.
- [71] B. Zong and X. Niu, "Analysis of structure and magnetic behavior in M-type hexaferrite compounds Sr<sub>1-x</sub>Y<sub>x</sub>Fe<sub>10</sub>CoTiO<sub>19</sub>," *Journal of Materials Science: Materials in Electronics*, vol. 31, no. 7, pp. 5290–5297, Apr. 2020, doi: 10.1007/s10854-020-03089-0.
- [72] F. Tian *et al.*, "Effect of Mn substitution on structural, magnetic and microwave absorption properties of Co<sub>2</sub>Y hexagonal ferrite," *Journal of Magnetism and Magnetic Materials*, vol. 587. Elsevier B.V., Dec. 01, 2023. doi: 10.1016/j.jmmm.2023.171229.

- [73] A. Ramzan *et al.*, “Raveling out the effect of Pr<sup>3+</sup> ions substitution on different properties of nano-sized hexagonal ferrites,” *Materials Science and Engineering: B*, vol. 297, Nov. 2023, doi: 10.1016/j.mseb.2023.116717.
- [74] D. Gui and X. Ren, “Investigation on electromagnetic properties of La–Al co-doped Co<sub>2</sub>W hexagonal ferrites for microwave absorption,” *Ceram Int*, vol. 49, no. 9, pp. 14079–14089, May 2023, doi: 10.1016/j.ceramint.2022.12.289.
- [75] M. Junaid, H. Ahmad Jan, K. Mujasam Batoo, R. Jabeen, and S. Hussain, “Band–gap reduction of aluminum substituted M–type hexagonal ferrite to study its characteristics,” *Results Chem*, vol. 6, Dec. 2023, doi: 10.1016/j.rechem.2023.101133.
- [76] K. Kamishima, T. Sekigawa, K. Kakizaki, and K. Watanabe, “Synthesis of (Ca, Sr)-based W-type hexagonal ferrite,” *J Magn Magn Mater*, vol. 574, May 2023, doi: 10.1016/j.jmmm.2023.170670.
- [77] A. V. Trukhanov *et al.*, “Correlation of the Fe content and entropy state in multiple substituted hexagonal ferrites with magnetoplumbite structure,” *Ceram Int*, vol. 47, no. 12, pp. 17684–17692, Jun. 2021, doi: 10.1016/j.ceramint.2021.03.088.
- [78] C. Tejera-Centeno, S. Gallego, and J. I. Cerdá, “An ab initio study of the magnetic properties of strontium hexaferrite,” *Sci Rep*, vol. 11, no. 1, Dec. 2021, doi: 10.1038/s41598-021-81028-7.
- [79] P. Behera and S. Ravi, “Impedance spectroscopy and magnetic properties of Mg doped Y-type barium hexaferrite,” *Journal of Materials Science: Materials in Electronics*, vol. 29, no. 23, pp. 20206–20215, Dec. 2018, doi: 10.1007/s10854-018-0153-3.
- [80] B. B. Sahu, S. K. Patri, B. Behera, and B. Maharana, “Electrical properties of Y-type hexaferrite,” *J Adv Dielectr*, vol. 8, no. 3, Jun. 2018, doi: 10.1142/S2010135X18500224.
- [81] F. Y. Guo, G. J. Ji, J. J. Xu, H. F. Zou, S. C. Gan, and X. C. Xu, “Influence of Tb substitution on electromagnetic and microwave absorption properties of barium hexaferrites,” *Energy Materials: Materials Science and Engineering for Energy Systems*, vol. 9, no. 1, pp. 112–119, 2014, doi: 10.1179/1433075X12Y.0000000064.
- [82] M. Drogenik, M. Kristl, A. Žnidaršič, and D. Lisjak, “Barium Hexaferrite Prepared by Hydrothermal Synthesis,” *Materials Science Forum*, vol. 555, pp. 183–187, Sep. 2007, doi: 10.4028/www.scientific.net/msf.555.183.
- [83] E. Mohebbi, S. Hasani, M. Nouri-Khezrabad, and A. Ziarati, “The effect of agarose agent on the structural, magnetic and optical properties of barium hexaferrite nanoparticles synthesized by sol-gel auto-combustion method,” *Ceram Int*, vol. 49, no. 6, pp. 9757–9770, Mar. 2023, doi: 10.1016/j.ceramint.2022.11.149.
- [84] Y. Lei, W. Wang, G. Tan, X. Shang, X. Huang, and Q. Man, “Effects of dysprosium substitution on the structure, magnetic properties and microwave absorption properties of Z-type hexaferrite Ba<sub>3</sub>Co<sub>2</sub>Fe<sub>24</sub>O<sub>41</sub> synthesized by the sol-gel method,” *Journal of Materials Research and Technology*, vol. 20, pp. 1603–1615, Sep. 2022, doi: 10.1016/j.jmrt.2022.07.112.

- [85] Z. Choukchou Braham *et al.*, “Enhancing structural properties of simple perovskite materials based on zirconate and titanate prepared by sol-gel method,” *Mater Chem Phys*, p. 128460, Dec. 2023, doi: 10.1016/j.matchemphys.2023.128460.
- [86] M. A. Marjeghal, A. Sedghi, and S. Baghshahi, “The effect of the citric acid to metal nitrates molar ratio on the structural and magnetic properties of strontium hexaferrite nanoparticles synthesized by the sol-gel combustion method,” *J Alloys Compd*, vol. 968, p. 171765, Dec. 2023, doi: 10.1016/j.jallcom.2023.171765.
- [87] R. Kausar *et al.*, “Investigation into the structural and magnetic features of nickel doped U-type hexaferrites prepared through sol–gel method,” *J Magn Magn Mater*, vol. 549, May 2022, doi: 10.1016/j.jmmm.2022.169054.
- [88] M. O. Akhrame, O. S. Fatoki, B. O. Opeolu, D. I. Olorunfemi, and O. U. Oputu, “Polymeric nanocomposites (Pncs) for wastewater remediation: An overview,” *Polymer - Plastics Technology and Engineering*, vol. 57, no. 17, p. 1801-1827, 2018, doi: 10.1080/03602559.2018.1434666.
- [89] M. Beygisangchin, S. A. Rashid, S. Shafie, A. R. Sadrolhosseini, and H. N. Lim, “Preparations, properties, and applications of polyaniline and polyaniline thin films—a review,” *Polymers (Basel)*, vol. 13, no. 12, Jun. 2021, doi: 10.3390/polym13122003.
- [90] M. F. Shakir *et al.*, “EMI shielding properties of polymer blends with inclusion of graphene nano platelets,” *Results Phys*, vol. 14, Sep. 2019, doi: 10.1016/j.rinp.2019.102365.
- [91] B. Qiu, J. Wang, Z. Li, X. Wang, and X. Li, “Influence of acidity and oxidant concentration on the nanostructures and electrochemical performance of polyaniline during fast microwave-assisted chemical polymerization,” *Polymers (Basel)*, vol. 12, no. 2, Feb. 2020, doi: 10.3390/polym12020310.
- [92] C. H. B. Silva, N. A. Galiote, F. Huguenin, É. Teixeira-Neto, V. R. L. Constantino, and M. L. A. Temperini, “Spectroscopic, morphological and electrochromic characterization of layer-by-layer hybrid films of polyaniline and hexaniobate nanoscrolls,” *J Mater Chem*, vol. 22, no. 28, pp. 14052–14060, Jul. 2012, doi: 10.1039/c2jm31531a.
- [93] M. R. Saeb, P. Zarrintaj, P. Khandelwal, and N. P. S. Chauhan, “Synthetic route of polyaniline (I): Conventional oxidative polymerization,” in *Fundamentals and Emerging Applications of Polyaniline*, Elsevier, 2019, pp. 17–41. doi: 10.1016/B978-0-12-817915-4.00002-6.
- [94] U. S. Waware, R. Arukula, A. M. S. Hamouda, and P. Kasak, “Electrochemical and X-ray photoelectron spectroscopic investigations of conductive polymers,” *Ionics (Kiel)*, vol. 26, no. 2, pp. 831–838, Feb. 2020, doi: 10.1007/s11581-019-03250-8.
- [95] B. Hideki Shirakawa, E. J. Louis, A. G. Macdiarmid, C. H. W A N K Chiang, and A. J. HEEGERt, “Synthesis of Electrically Conducting Organic Polymers: Halogen Derivatives of Polyacetylene, (CH),” 1977.
- [96] J. Stejskal, I. Sapurina, J. Prokes, and J. Zemek, “In-situ polymerized polyaniline films,” 1999.



- [97] A. Khosrozadeh, M. A. Darabi, Q. Wang, and M. Xing, "Polyaniline nanoflowers grown on vibration-isolator-mimetic polyurethane nanofibers for flexible supercapacitors with prolonged cycle life," *J Mater Chem A Mater*, vol. 5, no. 17, pp. 7933–7943, 2017, doi: 10.1039/c7ta00591a.
- [98] M. Ijaz *et al.*, "Influence of ferromagnetic cobalt on microstructural and magnetic trends of sol–gel routed rare earth and aluminium based BaSr-Hexaferrites (Ba<sub>0.6</sub>Sr<sub>0.3</sub>Er<sub>0.1</sub>Fe<sub>11.5-x</sub>Al<sub>0.5</sub>CoxO<sub>19</sub>)," *Materials Science and Engineering: B*, vol. 299, Jan. 2024, doi: 10.1016/j.mseb.2023.116933.
- [99] M. Z. Khan, I. H. Gul, and F. A. Tahir, "Encapsulation of Ba–Sr hexaferrite nanoparticles and MWCNTs in conductive polymer matrix for improved dielectric spectroscopy, electromagnetic shielding and microwave absorption applications," *Ceram Int*, 2023, doi: 10.1016/j.ceramint.2023.05.266.
- [100] T. D. Thanh, N. Tran, N. Thi Viet Chinh, N. Thi Ngoc Anh, D. H. Manh, and N. Q. Tuan, "Excellent microwave absorption performances of cobalt-doped SrFe<sub>12</sub>O<sub>19</sub> hexaferrite with varying incident angles," *J Alloys Compd*, vol. 952, Aug. 2023, doi: 10.1016/j.jallcom.2023.170060.
- [101] X. Liu *et al.*, "Facilitating enhanced microwave absorption properties of barium hexaferrite/polyaniline composites based on tunable interfacial polarization by rare earth doping," *J Alloys Compd*, vol. 937, Mar. 2023, doi: 10.1016/j.jallcom.2022.168391.
- [102] K. Khan, H. Abbas, and K. Nadeem, "Magnetic exchange coupling and effect of grain and grain boundaries on conduction mechanism of (MgFe<sub>2</sub>O<sub>4</sub>)<sub>100-x</sub>/(BaFe<sub>12</sub>O<sub>19</sub>)<sub>x</sub> nanocomposites," *Ceram Int*, vol. 49, no. 9, pp. 13982–13993, May 2023, doi: 10.1016/j.ceramint.2022.12.280.
- [103] A. Gupta and P. K. Roy, "Effect of Zn<sup>2+</sup> ion substitution in Al<sup>3+</sup>-substituted rare-earth free Sr-hexaferrite for different permanent magnet applications," *Inorg Chem Commun*, p. 111114, Jul. 2023, doi: 10.1016/j.inoche.2023.111114.
- [104] M. Amini and A. Gholizadeh, "Shape control and associated magnetic and dielectric properties of MFe<sub>12</sub>O<sub>19</sub> (M = Ba, Pb, Sr) hexaferrites," *Journal of Physics and Chemistry of Solids*, vol. 147, Dec. 2020, doi: 10.1016/j.jpics.2020.109660.
- [105] S. Caliskan *et al.*, "Impact of vanadium substitution on structural, magnetic, microwave absorption features and hyperfine interactions of SrCo hexaferrites," *J Alloys Compd*, vol. 960, Oct. 2023, doi: 10.1016/j.jallcom.2023.170578.
- [106] K. Rana, S. Thakur, M. Tomar, V. Gupta, and A. Thakur, "Effect of low sintering temperature on the structural and magnetic properties of M-type strontium hexaferrite," *J Magn Magn Mater*, vol. 587, p. 171289, Dec. 2023, doi: 10.1016/j.jmmm.2023.171289.
- [107] M. F. Ramírez-Ayala *et al.*, "Study of neodymium addition on the magnetic and structural properties of strontium hexaferrite synthesized by the Pechini method," *J Magn Magn Mater*, vol. 582, p. 170985, Sep. 2023, doi: 10.1016/j.jmmm.2023.170985.

- [108] A. Yu. Mironovich, V. G. Kostishin, H. I. Al-Khafaji, A. V. Timofeev, A. I. Ril, and R. I. Shakirzyanov, "Study of structure, cation distribution and magnetic properties of Ni substituted M-type barium hexaferrite," *Materialia (Oxf)*, p. 101898, Dec. 2023, doi: 10.1016/j.mtla.2023.101898.
- [109] K. R. Nishkala, R. R. Rao, S. Mutalik, M. S. Murari, and M. D. Daivajna, "Investigations on structural, Mossbauer, dielectric, and ferroelectric properties of La doped barium hexaferrite," *Physica B Condens Matter*, vol. 664, Sep. 2023, doi: 10.1016/j.physb.2023.414954.
- [110] S. K. Fasate, P. S. Salunke, S. A. Rode, S. T. Alone, and K. M. Jadhav, "Electrical, dielectric and magnetic properties of Mn<sup>2+</sup> substitution in barium hexaferrites nanoparticles," *Mater Today Proc*, May 2023, doi: 10.1016/j.matpr.2023.04.590.
- [111] P. C. Chagas *et al.*, "Effect of Sn-substitution on the electrical conductivity of SrFe<sub>12-x</sub>Sn<sub>x</sub>O<sub>19</sub> (0.0 ≤ x ≤ 1.0) hexaferrite," *Physica B Condens Matter*, vol. 661, Jul. 2023, doi: 10.1016/j.physb.2023.414961.
- [112] Farooq Zafar MohammadFarhat HumaKashif Ali, "Magnetic and microwave absorption properties of Co and Zn co-doped barium hexaferrite nanoparticles," 2023.
- [113] V. Bilovol, M. Sikora, and K. Berent, "Exchange coupling in SrFe<sub>12</sub>O<sub>19</sub>/CoFe<sub>2</sub>O<sub>4</sub> composites: Effect of component proportions," *J Magn Magn Mater*, vol. 568, Feb. 2023, doi: 10.1016/j.jmmm.2023.170384.
- [114] M. Zareef Khan, H. Abbas, K. Nadeem, A. Iqbal, and I. L. Papst, "Concentration dependent exchange coupling in BaFe<sub>12</sub>O<sub>19</sub>/NiFe<sub>2</sub>O<sub>4</sub> nanocomposites," *J Alloys Compd*, vol. 922, Nov. 2022, doi: 10.1016/j.jallcom.2022.166105.
- [115] H. Karnajit Singh, P. P. Mohapatra, S. Sahu, and P. Dobbidi, "Dielectric and temperature dependent magnetic studies of Al<sup>3+</sup> substituted Ba<sub>0.4</sub>La<sub>0.1</sub>Sr<sub>0.5</sub>Al<sub>x</sub>Fe<sub>12-x</sub>O<sub>19</sub> hexaferrite for microwave application," *Mater Sci Eng B Solid State Mater Adv Technol*, vol. 284, Oct. 2022, doi: 10.1016/j.mseb.2022.115876.
- [116] H. F. Shakir *et al.*, "In-situ polymerization and EMI shielding property of barium hexaferrite/pyrrole nanocomposite," *J Alloys Compd*, vol. 902, May 2022, doi: 10.1016/j.jallcom.2022.163847.
- [117] C. C. Chauhan *et al.*, "Tailoring magnetic and dielectric properties of SrFe<sub>12</sub>O<sub>19</sub>/NiFe<sub>2</sub>O<sub>4</sub> ferrite nanocomposites synthesized in presence of Calotropis gigantea (crown) flower extract," *J Alloys Compd*, vol. 900, Apr. 2022, doi: 10.1016/j.jallcom.2021.163415.
- [118] S. K. Godara *et al.*, "Effect of Ca<sup>2+</sup> exchange at Ba<sup>2+</sup> site on the structural, dielectric, morphological and magnetic traits of BaM nanohexaferrites," *J Magn Magn Mater*, vol. 564, Dec. 2022, doi: 10.1016/j.jmmm.2022.170049.
- [119] M. Bozorgmehr, G. R. Gordani, A. Ghasemi, and M. Tavoosi, "An assessment of electromagnetic properties of substituted hexaferrite/SWCNTs nanocomposite," *J Magn Magn Mater*, vol. 527, Jun. 2021, doi: 10.1016/j.jmmm.2020.167709.

- [120] G. Fang, C. Liu, Y. Yang, K. Peng, G. Xu, and Y. Zhang, "Broad microwave absorption bandwidth achieved by exchange coupling interaction between hard and soft magnetic materials," *Ceram Int*, vol. 47, no. 2, pp. 2879–2883, Jan. 2021, doi: 10.1016/j.ceramint.2020.09.011.
- [121] N. Tran, M. Y. Lee, W. H. Jeong, T. L. Phan, N. Q. Tuan, and B. W. Lee, "Thickness independent microwave absorption performance of La-doped BaFe<sub>12</sub>O<sub>19</sub> and polyaniline composites," *J Magn Magn Mater*, vol. 538, Nov. 2021, doi: 10.1016/j.jmmm.2021.168299.
- [122] C. Singh *et al.*, "Controllable morphology, dielectric, magnetic and reflection loss characteristics of ferrite/wax composites for low-loss applications," *J Alloys Compd*, vol. 888, Dec. 2021, doi: 10.1016/j.jallcom.2021.161611.
- [123] M. Rostami, M. Jafarpour, and M. H. Majles Ara, "An investigation on the microwave absorption properties of Co–Al–Ti substituted barium hexaferrite-MWCNT nanocomposites," *J Alloys Compd*, vol. 872, Aug. 2021, doi: 10.1016/j.jallcom.2021.159656.
- [124] N. Aggarwal and S. B. Narang, "Microwave absorption analysis of Mg–Zr-substituted Ni–Zn spinel ferrites in the X-band," *Journal of Physics and Chemistry of Solids*, vol. 159, Dec. 2021, doi: 10.1016/j.jpics.2021.110289.
- [125] W. Widanarto *et al.*, "Neodymium ions activated barium ferrite composites for microwave X-band absorber applications: Synthesis and characterizations," *Composites Communications*, vol. 19, pp. 51–55, Jun. 2020, doi: 10.1016/j.coco.2020.02.008.
- [126] G. Feng *et al.*, "Lanthanum-substituted Ba<sub>0.4</sub>Ca<sub>0.6</sub>Fe<sub>11.4</sub>Co<sub>0.6</sub>O<sub>19</sub> ceramics with enhanced microwave absorption," *Journal of Materials Science: Materials in Electronics*, vol. 31, no. 1, pp. 621–627, Jan. 2020, doi: 10.1007/s10854-019-02567-4.
- [127] T. L. Phan, N. Tran, H. H. Nguyen, D. S. Yang, N. T. Dang, and B. W. Lee, "Crystalline and electronic structures and magnetic properties of BaCo<sub>1-x</sub>Mn<sub>x</sub>Fe<sub>11</sub>O<sub>19</sub> hexaferrites," *J Alloys Compd*, vol. 816, p. 152528, 2020, doi: 10.1016/j.jallcom.2019.152528.
- [128] V. Turchenko *et al.*, "Crystal and magnetic structures, magnetic and ferroelectric properties of strontium ferrite partially substituted with in ions," *J Alloys Compd*, vol. 821, Apr. 2020, doi: 10.1016/j.jallcom.2019.153412.
- [129] G. Guan *et al.*, "Electromagnetic wave absorption enhancement of double-layer structural absorbers based on carbon nanofibers and hollow Co<sub>2</sub>Y hexaferrite microfibers," *J Alloys Compd*, vol. 814, Jan. 2020, doi: 10.1016/j.jallcom.2019.152302.
- [130] S. Anand, S. Pauline, and C. J. Prabagar, "Zr doped Barium hexaferrite nanoplatelets and RGO fillers embedded Polyvinylidene fluoride composite films for electromagnetic interference shielding applications," *Polym Test*, vol. 86, Jun. 2020, doi: 10.1016/j.polymertesting.2020.106504.

- [131] C. Liu *et al.*, “Microstructure and magnetic properties of M-type strontium hexagonal ferrites with Y-Co substitution,” *J Magn Magn Mater*, vol. 436, pp. 126–129, Aug. 2017, doi: 10.1016/j.jmmm.2017.04.040.
- [132] Z. Jing, R. Qinghong, and Y. Atassi, “Design of ternary-component X-band microwave absorber based on FeCo/Sr hexaferrite/PANI nanocomposite in silicon resin matrix,” *J Magn Magn Mater*, vol. 512, Oct. 2020, doi: 10.1016/j.jmmm.2020.167037.
- [133] N. Tran, Y. J. Choi, T. L. Phan, D. S. Yang, and B. W. Lee, “Electronic structure and magnetic and electromagnetic wave absorption properties of BaFe<sub>12-x</sub>Co<sub>x</sub>O<sub>19</sub> M-type hexaferrites,” *Current Applied Physics*, vol. 19, no. 12, pp. 1343–1348, 2019, doi: 10.1016/j.cap.2019.08.023.
- [134] M. M. E. Barakat, D. E. S. Bakeer, and A. H. Sakr, “Structural, Magnetic Properties and Electron Paramagnetic Resonance for BaFe<sub>12-x</sub>Hg<sub>x</sub>O<sub>19</sub> Hexaferrite Nanoparticles Prepared by Co-Precipitation Method,” *Journal of Taibah University for Science*, vol. 14, no. 1, pp. 640–652, 2020, doi: 10.1080/16583655.2020.1761676.
- [135] E. Handoko *et al.*, “Enhanced microwave absorbing capabilities of multilayer absorbers based on bafe<sub>12o19</sub> and fe<sub>3o4</sub>,” in *Materials Science Forum*, Trans Tech Publications Ltd, 2019, pp. 338–343. doi: 10.4028/www.scientific.net/MSF.966.338.
- [136] S. Shoostary Veisi, M. Yousefi, M. M. Amini, A. R. Shakeri, and M. Bagherzadeh, “Magnetic and microwave absorption properties of Cu/Zr doped M-type Ba/Sr hexaferrites prepared via sol-gel auto-combustion method,” *J Alloys Compd*, vol. 773, pp. 1187–1194, 2019, doi: 10.1016/j.jallcom.2018.09.189.
- [137] E. Handoko *et al.*, “Complex permittivity, permeability and microwave absorption studies of double layer magnetic absorbers based on bafe<sub>12o19</sub> and bafe<sub>10cozno19</sub>,” in *Materials Science Forum*, Trans Tech Publications Ltd, 2019, pp. 302–307. doi: 10.4028/www.scientific.net/MSF.966.302.
- [138] M. khandani, M. Yousefi, S. S. S. Afghahi, M. M. Amini, and M. B. Torbati, “An investigation of structural and magnetic properties of Ce–Nd doped strontium hexaferrite nanoparticles as a microwave absorbent,” *Mater Chem Phys*, vol. 235, no. June, p. 121722, 2019, doi: 10.1016/j.matchemphys.2019.121722.
- [139] Y. E. Gunanto, M. P. Izaak, H. Sitompul, and W. A. Adi, “Composite paint based on barium-strontium-hexaferrite as an absorber of microwaves at X-band frequency,” *Mater Today Proc*, vol. 13, pp. 1–4, 2019, doi: 10.1016/j.matpr.2019.03.177.
- [140] R. Peymanfar, M. Ahmadi, and S. Javanshir, “Tailoring GO/BaFe<sub>12</sub>O<sub>19</sub>/La<sub>0.5</sub>Sr<sub>0.5</sub>MnO<sub>3</sub> ternary nanocomposite and investigation of its microwave characteristics,” *Mater Res Express*, vol. 6, no. 8, May 2019, doi: 10.1088/2053-1591/ab1fb3.
- [141] J. Mohammed *et al.*, “Electromagnetic interference (EMI) shielding, microwave absorption, and optical sensing properties of BaM/CCTO composites in K u -band,” *Results Phys*, vol. 13, Jun. 2019, doi: 10.1016/j.rinp.2019.102307.

- [142] C. Singh *et al.*, “Bandstop Passive Filter Characteristics of Hexagonal Ferrite Composites at X-Band,” *J Electron Mater*, vol. 48, no. 10, pp. 6189–6193, 2019, doi: 10.1007/s11664-019-07424-y.
- [143] S. F. Mansour, O. M. Hemeda, M. A. Abdo, and W. A. Nada, “Improvement on the magnetic and dielectric behavior of hard/soft ferrite nanocomposites,” *J Mol Struct*, vol. 1152, pp. 207–214, Jan. 2018, doi: 10.1016/j.molstruc.2017.09.089.
- [144] S. Tyagi *et al.*, “RADAR absorption study of BaFe<sub>12</sub>O<sub>19</sub>/ZnFe<sub>2</sub>O<sub>4</sub>/CNTs nanocomposite,” *J Alloys Compd*, vol. 731, pp. 584–590, Jan. 2018, doi: 10.1016/j.jallcom.2017.10.071.
- [145] R. Sai, M. Sato, S. Takeda, S. Yabukami, and M. Yamaguchi, “Co/Ti-substituted SrM-based composite sheets: High frequency permeability and electromagnetic noise suppression above 6 GHz,” *J Magn Magn Mater*, vol. 459, pp. 49–56, Aug. 2018, doi: 10.1016/j.jmmm.2017.12.051.
- [146] C. K. Patel *et al.*, “Structural phases, magnetic properties and Maxwell-Wagner type relaxation of CoFe<sub>2</sub>O<sub>4</sub>/Sr<sub>2</sub>Co<sub>2</sub>Fe<sub>12</sub>O<sub>22</sub> ferrite composites,” *Mater Res Express*, vol. 4, no. 7, p. aa7699, 2017, doi: 10.1088/2053-1591/aa7699.
- [147] H. Nikmanesh, M. Moradi, G. H. Bordbar, and R. S. Alam, “Synthesis of multi-walled carbon nanotube/doped barium hexaferrite nanocomposites: An investigation of structural, magnetic and microwave absorption properties,” *Ceram Int*, vol. 42, no. 13, pp. 14342–14349, Oct. 2016, doi: 10.1016/j.ceramint.2016.05.089.
- [148] M. S. Seyed Dorraji *et al.*, “Microwave absorption properties of polypyrrole-SrFe<sub>12</sub>O<sub>19</sub>-TiO<sub>2</sub>-epoxy resin nanocomposites: Optimization using response surface methodology,” *Appl Surf Sci*, vol. 383, pp. 9–18, Oct. 2016, doi: 10.1016/j.apsusc.2016.04.108.
- [149] X. Ren, H. Fan, and Y. Cheng, “Microwave absorption properties of double-layer absorber based on carbonyl iron/barium hexaferrite composites,” *Appl Phys A Mater Sci Process*, vol. 122, no. 5, May 2016, doi: 10.1007/s00339-016-0041-8.
- [150] Z. Durmus, H. Kavas, A. Durmus, and B. Aktaş, “Synthesis and micro-structural characterization of graphene/strontium hexaferrite (SrFe<sub>12</sub>O<sub>19</sub>) nanocomposites,” *Mater Chem Phys*, vol. 163, pp. 439–445, Aug. 2015, doi: 10.1016/j.matchemphys.2015.07.063.
- [151] L. Singh, J. Malhotra, C. Singh, S. B. Narang, and M. Chandra, “Investigation of microwave and electrical characteristics of Co-Zr substituted M-type Ba-Sr hexagonal ferrite,” *Materials Science- Poland*, vol. 33, no. 2, pp. 335–339, 2015, doi: 10.1515/msp-2015-0051.
- [152] S. H. Hosseini, P. Zamani, and S. Y. Mousavi, “Thermal infrared and microwave absorbing properties of SrTiO<sub>3</sub>/SrFe<sub>12</sub>O<sub>19</sub>/polyaniline nanocomposites,” *J Alloys Compd*, vol. 644, pp. 423–429, May 2015, doi: 10.1016/j.jallcom.2015.05.099.
- [153] S. Hazra, B. K. Ghosh, M. K. Patra, R. K. Jani, S. R. Vadera, and N. N. Ghosh, “A novel ‘one-pot’ synthetic method for preparation of (Ni<sub>0.65</sub>Zn<sub>0.35</sub>Fe<sub>2</sub>O<sub>4</sub>)<sub>x</sub>-(BaFe<sub>12</sub>O<sub>19</sub>)<sub>1-x</sub> nanocomposites and study of their microwave absorption and



- magnetic properties,” *Powder Technol*, vol. 279, pp. 10–17, Jul. 2015, doi: 10.1016/j.powtec.2015.03.046.
- [154] N. Fatima *et al.*, “SYNTHESIS AND CHARACTERIZATION OF COBALT SUBSTITUTED W TYPE HEXAGONAL FERRITES.”
- [155] J. Cheng, “SYNTHESIS OF LA X SR 1-X TIO 3 ANODE MATERIALS BY SOL-GEL AUTO-COMBUSTION METHOD,” 2012.
- [156] B. Dunn and J. I. Zink, “Sol-gel chemistry and materials,” *Accounts of Chemical Research*, vol. 40, no. 9. p. 729, Sep. 2007. doi: 10.1021/ar700178b.
- [157] L. D. Whittig and W. R. Allardice, “2 X-Ray Diffraction Techniques,” 1986.
- [158] “snapshot of Bruker advance X-ray .”
- [159] A. A. Bunaciu, E. gabriela Udriștioiu, and H. Y. Aboul-Enein, “X-Ray Diffraction: Instrumentation and Applications,” *Critical Reviews in Analytical Chemistry*, vol. 45, no. 4. Taylor and Francis Ltd., pp. 289–299, Oct. 02, 2015. doi: 10.1080/10408347.2014.949616.
- [160] S. V Borisov and N. V Podberezskaya, “X-RAY DIFFRACTION ANALYSIS: A BRIEF HISTORY AND ACHIEVEMENTS OF THE FIRST CENTURY,” 2012.
- [161] D. Banerjee, “X-Ray Diffraction (XRD).”
- [162] T. Tchouank Tekou Carol, J. Sharma, J. Mohammed, S. Kumar, and A. K. Srivastava, “Effect of temperature on the magnetic properties of nano-sized M-type barium hexagonal ferrites,” in *AIP Conference Proceedings*, American Institute of Physics Inc., Jul. 2017. doi: 10.1063/1.4990307.
- [163] M. Augustin and T. Balu, “Estimation of Lattice Stress and Strain in Zinc and Manganese Ferrite Nanoparticles by Williamson-Hall and Size-Strain Plot Methods,” *Int J Nanosci*, vol. 16, no. 3, Jun. 2017, doi: 10.1142/S0219581X16500356.
- [164] T. Kaur, B. Kaur, B. H. Bhat, S. Kumar, and A. K. Srivastava, “Effect of calcination temperature on microstructure, dielectric, magnetic and optical properties of Ba<sub>0.7</sub>La<sub>0.3</sub>Fe<sub>11.7</sub>Co<sub>0.3</sub>O<sub>19</sub>hexaferrites,” *Physica B Condens Matter*, vol. 456, pp. 206–212, Jan. 2015, doi: 10.1016/j.physb.2014.09.003.
- [165] I. Mohammed *et al.*, “Review on Y-type hexaferrite: Synthesis, characterization and properties,” *Applied Surface Science Advances*, vol. 16. Elsevier B.V., Aug. 01, 2023. doi: 10.1016/j.apsadv.2023.100416.
- [166] F. Faghizadeh, N. M. Anaya, L. A. Schiffman, and V. Oyanedel-Craver, “Fourier transform infrared spectroscopy to assess molecular-level changes in microorganisms exposed to nanoparticles,” *Nanotechnology for Environmental Engineering*, vol. 1, no. 1, Dec. 2016, doi: 10.1007/s41204-016-0001-8.
- [167] D. Sundeep, “Spectroscopic Investigations of MoO<sub>3</sub>/CuO Nanocomposites: Mechanical Synthesis, Spectroscopic Characterization and Thermal Analysis Nanocomposite View project ScienceDirect Spectral Investigation of Structural and Optical Properties of Mechanically Synthesized TiO<sub>2</sub>-V<sub>2</sub>O<sub>5</sub> Nanocomposite

- Powders View project,” 2017. [Online]. Available: <https://www.researchgate.net/publication/328568557>
- [168] H. Yakowitz and K. F. J. Heinrich, “Quantitative Electron Probe Microanalysis: Absorption Correction Uncertainty,” 1968.
- [169] P. D. Ngo, “Energy Dispersive Spectroscopy,” 1999.
- [170] S. Raghavan, “Comparative Studies of 6H-SiC Surface Preparation.” [Online]. Available: <https://www.researchgate.net/publication/267680691>
- [171] G. Martinek, S. Ruoho, and U. Wyss, “Magnetic Properties of Permanent Magnets & Measuring Techniques.”
- [172] W. Burgei, M. J. Pechan, and H. Jaeger, “A simple vibrating sample magnetometer for use in a materials physics course,” *Am J Phys*, vol. 71, no. 8, pp. 825–828, Aug. 2003, doi: 10.1119/1.1572149.
- [173] “Vibrating Sample Magnetometer Home Page.”
- [174] J. A. Arregi, “Vibrating sample magnetometry.”
- [175] R. Grgssinger, “CORRELATION BETWEEN THE INHOMOGENEITY AND THE MAGNETIC ANISOTROPY IN POLYCRYSTALLINE FERROMAGNETIC MATERIALS,” 1982.
- [176] S. H. Mahmood, A. A. Ghanem, I. Bsoul, A. Awadallah, and Y. Maswadeh, “Structural and magnetic properties of BaFe<sub>122x</sub>CuxMnxO<sub>19</sub> hexaferrites,” *Mater Res Express*, vol. 4, no. 3, Mar. 2017, doi: 10.1088/2053-1591/aa646c.
- [177] M. A. Gabal, A. M. Abdel-Daiem, Y. M. Al Angari, and I. M. Ismail, “Influence of Al-substitution on structural, electrical and magnetic properties of Mn-Zn ferrites nanopowders prepared via the sol-gel auto-combustion method,” *Polyhedron*, vol. 57, pp. 105–111, Jul. 2013, doi: 10.1016/j.poly.2013.04.027.
- [178] S. E. Mousavi Ghahfarokhi, F. Ranjbar, and M. Zargar Shoushtari, “A study of the properties of SrFe<sub>12-x</sub>CoxO<sub>19</sub> nanoparticles,” *J Magn Magn Mater*, vol. 349, pp. 80–87, 2014, doi: 10.1016/j.jmmm.2013.08.036.
- [179] W. Zhang, A. Sun, X. Zhao, N. Suo, L. Yu, and Z. Zuo, “Structural and magnetic properties of La 3+ ion doped Ni–Cu–Co nano ferrites prepared by sol–gel auto-combustion method,” *J Solgel Sci Technol*, vol. 90, no. 3, pp. 599–610, Jun. 2019, doi: 10.1007/s10971-019-04941-4.
- [180] V. Mahdikhah, A. Ataie, A. Babaei, S. Sheibani, C. W. Ow-Yang, and S. K. Abkenar, “CoFe<sub>2</sub>O<sub>4</sub>/Fe magnetic nanocomposite: Exchange coupling behavior and microwave absorbing property,” *Ceram Int*, vol. 46, no. 11, pp. 17903–17916, Aug. 2020, doi: 10.1016/j.ceramint.2020.04.099.
- [181] M. A. Almessiere *et al.*, “Electronic, magnetic, and microwave properties of hard/soft nanocomposites based on hexaferrite SrNi<sub>0.02</sub>Zr<sub>0.02</sub>Fe<sub>11.96</sub>O<sub>19</sub> with variable spinel phase MFe<sub>2</sub>O<sub>4</sub> (M = Mn, Co, Cu, and Zn),” *Ceram Int*, vol. 47, no. 24, pp. 35209–35223, 2021, doi: 10.1016/j.ceramint.2021.09.064.

- [182] “Spin Structure of Exchange Biased Heterostructures: Fe/MnF<sub>2</sub> and Fe/FeF<sub>2</sub>”.
- [183] S. X. Descamps, J. M. Parra, S. Ramon, and G. Calvet, “Early Proceedings of the AGACSE 2015 Conference.”
- [184] J. Long, A. Nand, and S. Ray, “Application of spectroscopy in additive manufacturing,” *Materials*, vol. 14, no. 1. MDPI AG, pp. 1–29, Jan. 01, 2021. doi: 10.3390/MA14010203.
- [185] “impedance .”
- [186] M. Nasri *et al.*, “Structural, dielectric, electrical and modulus spectroscopic characteristics of CoFeCuO<sub>4</sub> spinel ferrite nanoparticles,” *Mater Sci Eng B Solid State Mater Adv Technol*, vol. 272, Oct. 2021, doi: 10.1016/j.mseb.2021.115331.
- [187] A. K. Pradhan, T. K. Nath, and S. Saha, “Impedance spectroscopy and electric modulus behavior of Molybdenum doped Cobalt-Zinc ferrite,” *Mater Res Express*, vol. 4, no. 7, Jul. 2017, doi: 10.1088/2053-1591/aa7c8c.
- [188] M. Sayed and J. Martens, “Vector network analyzers,” in *Modern RF and Microwave Measurement Techniques*, vol. 9781107036413, Cambridge University Press, 2007, pp. 98–129. doi: 10.1017/CBO9781139567626.006.
- [189] “Design\_of\_Bowtie\_Antenna\_with\_Rounded\_Edge\_and\_Mid”.
- [190] H. Sözeri, F. Genç, B. Ünal, A. Baykal, and B. Aktaş, “Magnetic, electrical and microwave properties of Mn-Co substituted Ni<sub>x</sub>Zn<sub>0,8-x</sub>Fe<sub>2</sub>O<sub>4</sub> nanoparticles,” *J Alloys Compd*, vol. 660, pp. 324–335, Mar. 2016, doi: 10.1016/j.jallcom.2015.11.123.
- [191] Y. Zhang, F. Xu, G. Tan, J. Zhang, T. Wang, and F. Li, “Improvement of microwave-absorbing properties of Co<sub>2</sub>Z barium ferrite composite by coating Ag nanoparticles,” *J Alloys Compd*, vol. 615, pp. 749–753, Dec. 2014, doi: 10.1016/j.jallcom.2014.06.165.
- [192] G. Shen, Z. Xu, and Y. Li, “Absorbing properties and structural design of microwave absorbers based on W-type La-doped ferrite and carbon fiber composites,” *J Magn Mater*, vol. 301, no. 2, pp. 325–330, Jun. 2006, doi: 10.1016/j.jmmm.2005.07.007.
- [193] M. Thakur *et al.*, “Significantly improved magnetic parameters of Co–La co-doped strontium hexagonal ferrites for recording applications: structural, hysteresis, and mössbauer performance metrics,” *Journal of Materials Science: Materials in Electronics*, vol. 34, no. 29, p. 2002, Oct. 2023, doi: 10.1007/s10854-023-11328-3.
- [194] G. Feng *et al.*, “Lanthanum-substituted Ba<sub>0.4</sub>Ca<sub>0.6</sub>Fe<sub>11.4</sub>Co<sub>0.6</sub>O<sub>19</sub> ceramics with enhanced microwave absorption,” *Journal of Materials Science: Materials in Electronics*, vol. 31, no. 1, pp. 621–627, 2020, doi: 10.1007/s10854-019-02567-4.
- [195] M. Augustin and T. Balu, “Estimation of Lattice Stress and Strain in Zinc and Manganese Ferrite Nanoparticles by Williamson-Hall and Size-Strain Plot Methods,” *Int J Nanosci*, vol. 16, no. 3, pp. 1–7, 2017, doi: 10.1142/S0219581X16500356.

- [196] J. Mohammed *et al.*, “Structural, dielectric, and magneto-optical properties of Cu<sup>2+</sup>-Er<sup>3+</sup> substituted nanocrystalline strontium hexaferrite,” *Mater Res Express*, vol. 6, no. 5, 2019, doi: 10.1088/2053-1591/ab063b.
- [197] H. Mahajan, S. K. Godara, and A. K. Srivastava, “Synthesis and investigation of structural, morphological, and magnetic properties of the manganese doped cobalt-zinc spinel ferrite,” *J Alloys Compd*, vol. 896, p. 162966, 2021, doi: 10.1016/j.jallcom.2021.162966.
- [198] H. Moradmard, S. Farjami Shayesteh, P. Tohidi, Z. Abbas, and M. Khaleghi, “Structural, magnetic and dielectric properties of magnesium doped nickel ferrite nanoparticles,” *J Alloys Compd*, vol. 650, pp. 116–122, 2015, doi: 10.1016/j.jallcom.2015.07.269.
- [199] H. Kaur *et al.*, “Elucidation of microwave absorption mechanisms in Co–Ga substituted Ba–Sr hexaferrites in X-band,” *Journal of Materials Science: Materials in Electronics*, vol. 29, no. 17, pp. 14995–15005, 2018, doi: 10.1007/s10854-018-9638-3.
- [200] S. Bindra Narang and K. Pubby, “Nickel Spinel Ferrites: A Review,” *J Magn Magn Mater*, p. 167163, 2020, doi: 10.1016/j.jmmm.2020.167163.
- [201] T. T. Carol T., J. Mohammed, B. H. Bhat, S. Mishra, S. K. Godara, and A. K. Srivastava, “Effect of Cr–Bi substitution on the structural, optical, electrical and magnetic properties of strontium hexaferrites,” *Physica B Condens Matter*, vol. 575, no. August, p. 411681, 2019, doi: 10.1016/j.physb.2019.411681.
- [202] M. Thakur, C. Singh, H. Mahajan, S. K. Godara, P. K. Maji, and A. K. Srivastava, “Study the effect of Co<sup>2+</sup>-Dy<sup>3+</sup> on structural and magnetic properties of M-type calcium hexaferrite,” in *AIP Conference Proceedings*, American Institute of Physics Inc., Jun. 2023. doi: 10.1063/5.0159077.
- [203] M. Thakur, C. Singh, K. C. J. Raju, B. Arun, T. T. T. Carol, and A. K. Srivastava, “Fabrication of bicomponent Co–La substituted strontium hexaferrite for tunable microwave absorber application: Structural, morphological, reflection loss, input impedance metrics,” *Physica B Condens Matter*, vol. 679, Apr. 2024, doi: 10.1016/j.physb.2024.415735.
- [204] B. Zong and X. Niu, “Analysis of structure and magnetic behavior in M-type hexaferrite compounds Sr<sub>1-x</sub>Y<sub>x</sub>Fe<sub>10</sub>CoTiO<sub>19</sub>,” *Journal of Materials Science: Materials in Electronics*, vol. 31, no. 7, pp. 5290–5297, 2020, doi: 10.1007/s10854-020-03089-0.
- [205] T. Kaur, S. Kumar, B. H. Bhat, B. Want, and A. K. Srivastava, “Effect on dielectric, magnetic, optical and structural properties of Nd–Co substituted barium hexaferrite nanoparticles,” *Appl Phys A Mater Sci Process*, vol. 119, no. 4, pp. 1531–1540, 2015, doi: 10.1007/s00339-015-9134-z.
- [206] S. K. Chawla, S. S. Meena, P. Kaur, R. K. Mudsainiyan, and S. M. Yusuf, “Effect of site preferences on structural and magnetic switching properties of CO-Zr doped strontium hexaferrite SrCo<sub>x</sub>Zr<sub>x</sub>Fe<sub>(12-2x)</sub>O<sub>19</sub>,” *J Magn Magn Mater*, vol. 378, pp. 84–91, 2015, doi: 10.1016/j.jmmm.2014.10.168.

- [207] T. M. Meaz and C. B. Koch, "An investigation of trivalent substituted M-type hexagonal ferrite using X-ray and Mössbauer spectroscopy," *Hyperfine Interact*, vol. 166, no. 1–4, pp. 455–463, 2005, doi: 10.1007/s10751-006-9308-3.
- [208] G. A. Ashraf, L. Zhang, W. Abbas, and G. Murtaza, "Synthesis and characterizations of Al-Sm substituted Ba-Sr M-type hexagonal ferrite nanoparticles via sol-gel route," *Ceram Int*, vol. 44, no. 15, pp. 18678–18685, 2018, doi: 10.1016/j.ceramint.2018.07.096.
- [209] J. Xu, H. Zou, H. Li, G. Li, S. Gan, and G. Hong, "Influence of Nd<sup>3+</sup> substitution on the microstructure and electromagnetic properties of barium W-type hexaferrite," *J Alloys Compd*, vol. 490, no. 1–2, pp. 552–556, 2010, doi: 10.1016/j.jallcom.2009.10.079.
- [210] M. Thakur, C. Singh, R. B. Jotania, S. T. A. Naqvi, and A. K. Srivastava, "Frequency and Morphology Modulated Electrical, Dielectric, and Relaxation Metrics in Sol–Gel-Synthesized Sr Co<sub>1.5</sub>Zn<sub>0.5</sub>Fe<sub>12-2z</sub>O<sub>19</sub> Hexaferrite: Corroboration with Impedance Spectroscopy Software," *J Electron Mater*, 2024, doi: 10.1007/s11664-024-11195-6.
- [211] K. M. Battoo, S. Kumar, C. G. Lee, and Alimuddin, "Influence of Al doping on electrical properties of Ni-Cd nano ferrites," *Current Applied Physics*, vol. 9, no. 4, pp. 826–832, Jul. 2009, doi: 10.1016/j.cap.2008.08.001.
- [212] A. Aslam, M. U. Islam, I. Ali, M. S. Awan, M. Irfan, and A. Iftikhar, "High frequency electrical transport properties of CoFe<sub>2</sub>O<sub>4</sub> and Sr<sub>2</sub>NiMnFe<sub>12</sub>O<sub>22</sub> composite ferrites," *Ceram Int*, vol. 40, no. 1 PART A, pp. 155–162, 2014, doi: 10.1016/j.ceramint.2013.05.116.
- [213] E. J. W. Verwey and P. W. Haayman, "ELECTRONIC CONDUCTIVITY AND TRANSITION POINT OF MAGNETITE ('Fe<sub>3</sub>O<sub>4</sub>')," 1941.
- [214] E. J. W. Verwey and P. W. Haayman, "ELECTRONIC CONDUCTIVITY AND TRANSITION POINT OF MAGNETITE ('Fe<sub>3</sub>O<sub>4</sub>')," 1941.
- [215] M. M. Costa, G. F. M. Pires, A. J. Terezo, M. P. F. Graa, and A. S. B. Sombra, "Impedance and modulus studies of magnetic ceramic oxide Ba<sub>2</sub>Co<sub>2</sub>Fe<sub>12</sub>O<sub>22</sub> (Co<sub>2</sub>Y) doped with Bi<sub>2</sub>O<sub>3</sub>," *J Appl Phys*, vol. 110, no. 3, Aug. 2011, doi: 10.1063/1.3615935.
- [216] M. Nasri *et al.*, "Structural, dielectric, electrical and modulus spectroscopic characteristics of CoFeCuO<sub>4</sub> spinel ferrite nanoparticles," *Mater Sci Eng B Solid State Mater Adv Technol*, vol. 272, Oct. 2021, doi: 10.1016/j.mseb.2021.115331.
- [217] W. Chen, W. Zhu, O. K. Tan, and X. F. Chen, "Frequency and temperature dependent impedance spectroscopy of cobalt ferrite composite thick films," *J Appl Phys*, vol. 108, no. 3, Aug. 2010, doi: 10.1063/1.3457217.
- [218] R. B. Jotania, R. A. Nandotaria, C. C. Chauhan, M. Hashim, S. Singh Meena, and S. E. Shirsath, "Structural phases and Maxwell-Wagner relaxation in magnetically soft-ZnFe<sub>2</sub>O<sub>4</sub> and hard-Sr<sub>2</sub>Cu<sub>2</sub>Fe<sub>12</sub>O<sub>22</sub> nanocomposites," *Ceram Int*, vol. 42, no. 2, pp. 2289–2298, Feb. 2016, doi: 10.1016/j.ceramint.2015.10.023.



- [219] S. I. Ahmad, A. Rauf, T. Mohammed, A. Bahafi, D. Ravi Kumar, and M. B. Suresh, “Dielectric, impedance, AC conductivity and low-temperature magnetic studies of Ce and Sm co-substituted nanocrystalline cobalt ferrite,” *J Magn Magn Mater*, vol. 492, Dec. 2019, doi: 10.1016/j.jmmm.2019.165666.
- [220] M. Javid Iqbal, M. Nadeem, and M. M. Hassan, “Low temperature ac electrical study of  $\text{Pr}_{0.5-x}\text{La}_x\text{Ca}_{0.5}\text{MnO}_3$  ( $x=0.0-0.4$ ) ceramics by employing impedance spectroscopy,” *J Appl Phys*, vol. 114, no. 11, Sep. 2013, doi: 10.1063/1.4821957.
- [221] R. Nongjai, S. Khan, K. Asokan, H. Ahmed, and I. Khan, “Magnetic and electrical properties of in doped cobalt ferrite nanoparticles,” *J Appl Phys*, vol. 112, no. 8, Oct. 2012, doi: 10.1063/1.4759436.
- [222] C. Liu *et al.*, “Microstructure and magnetic properties of M-type strontium hexagonal ferrites with Y-Co substitution,” *J Magn Magn Mater*, vol. 436, pp. 126–129, 2017, doi: 10.1016/j.jmmm.2017.04.040.
- [223] H. S. Mund and B. L. Ahuja, “Structural and magnetic properties of Mg doped cobalt ferrite nano particles prepared by sol-gel method,” *Mater Res Bull*, vol. 85, pp. 228–233, 2017, doi: 10.1016/j.materresbull.2016.09.027.
- [224] C. C. Chauhan, T. Gupta, A. A. Gor, K. R. Jotania, and R. B. Jotania, “Effect of calcination temperature on structural and magnetic properties of lightly lanthanum substituted M-type strontium cobalt hexaferrites,” *Mater Today Proc*, vol. 47, no. xxxx, pp. 715–718, 2020, doi: 10.1016/j.matpr.2020.12.1184.
- [225] R. Nongjai, S. Khan, K. Asokan, H. Ahmed, and I. Khan, “Magnetic and electrical properties of in doped cobalt ferrite nanoparticles,” *J Appl Phys*, vol. 112, no. 8, 2012, doi: 10.1063/1.4759436.
- [226] M. V. Rane, D. Bahadur, A. K. Nigam, and C. M. Srivastava, “Mössbauer and FT-IR studies on non-stoichiometric barium hexaferrites,” *J Magn Magn Mater*, vol. 192, no. 2, pp. 288–296, 1999, doi: 10.1016/S0304-8853(98)00533-2.
- [227] C. Singh, S. B. Narang, I. S. Hudiar, Y. Bai, and K. Marina, “Hysteresis analysis of Co-Ti substituted M-type Ba-Sr hexagonal ferrite,” *Mater Lett*, vol. 63, no. 22, pp. 1921–1924, 2009, doi: 10.1016/j.matlet.2009.06.002.
- [228] J. Lee, E. J. Lee, T. Y. Hwang, J. Kim, and Y. H. Choa, “Anisotropic characteristics and improved magnetic performance of Ca–La–Co-substituted strontium hexaferrite nanomagnets,” *Sci Rep*, vol. 10, no. 1, pp. 1–9, 2020, doi: 10.1038/s41598-020-72608-0.
- [229] S. Kumar, M. Kumar Manglam, S. Supriya, H. Kumar Satyapal, R. Kumar Singh, and M. Kar, “Lattice strain mediated dielectric and magnetic properties in La doped barium hexaferrite,” *J Magn Magn Mater*, vol. 473, pp. 312–319, 2019, doi: 10.1016/j.jmmm.2018.10.085.
- [230] T. Ben Ghzaiel, W. Dhaoui, A. Pasko, and F. Mazaleyrat, “Effect of non-magnetic and magnetic trivalent ion substitutions on BaM-ferrite properties synthesized by hydrothermal method,” *J Alloys Compd*, vol. 671, pp. 245–253, 2016, doi: 10.1016/j.jallcom.2016.02.071.

- [231] A. Ghasemi and A. Morisako, "Static and high frequency magnetic properties of Mn-Co-Zr substituted Ba-ferrite," *J Alloys Compd*, vol. 456, no. 1–2, pp. 485–491, 2008, doi: 10.1016/j.jallcom.2007.02.101.
- [232] A. Kara, "EFFECT OF RARE-EARTH CO-DOPING ON THE MICROSTRUCTURAL AND MAGNETIC PROPERTIES OF BaFe<sub>12</sub>O<sub>19</sub>," vol. 20, no. 3, 2020, doi: 10.2478/adms-2020-0014.
- [233] N. Sivakumar, A. Narayanasamy, K. Shinoda, C. N. Chinnasamy, B. Jeyadevan, and J. M. Greneche, "Electrical and magnetic properties of chemically derived nanocrystalline cobalt ferrite," *J Appl Phys*, vol. 102, no. 1, pp. 0–8, 2007, doi: 10.1063/1.2752098.
- [234] D. Shekhawat and P. K. Roy, "Impact of yttrium on the physical, electro-magnetic and dielectric properties of auto-combustion synthesized nanocrystalline strontium hexaferrite," *Journal of Materials Science: Materials in Electronics*, vol. 30, no. 2, pp. 1187–1198, 2019, doi: 10.1007/s10854-018-0387-0.
- [235] J. Yang, W. Yang, F. Li, and Y. Yang, "Research and development of high-performance new microwave absorbers based on rare earth transition metal compounds: A review," *J Magn Magn Mater*, vol. 497, p. 165961, 2020, doi: 10.1016/j.jmmm.2019.165961.
- [236] C. Liu *et al.*, "Influence of the Eu substitution on the structure and magnetic properties of the Sr-hexaferrites," *Ceram Int*, vol. 46, no. 1, pp. 171–179, 2020, doi: 10.1016/j.ceramint.2019.08.245.
- [237] R. Srivastava and B. C. Yadav, "Ferrite materials: Introduction, synthesis techniques, and applications as sensors," *Int J Green Nanotechnol Biomed*, vol. 4, no. 2, pp. 141–154, 2012, doi: 10.1080/19430892.2012.676918.
- [238] R. Shams Alam, M. Moradi, H. Nikmanesh, J. Ventura, and M. Rostami, "Magnetic and microwave absorption properties of BaMg<sub>x</sub>/2Mn<sub>x</sub>/2Co<sub>x</sub>Ti<sub>2</sub>xFe<sub>12-4x</sub>O<sub>19</sub> hexaferrite nanoparticles," *J Magn Magn Mater*, vol. 402, pp. 20–27, 2016, doi: 10.1016/j.jmmm.2015.11.038.
- [239] J. Singh *et al.*, "Elucidation of phase evolution, microstructural, Mössbauer and magnetic properties of Co<sup>2+</sup>/Al<sup>3+</sup>-doped M-type Ba/Sr hexaferrites synthesized by a ceramic method," *J Alloys Compd*, vol. 695, pp. 1112–1121, 2017, doi: 10.1016/j.jallcom.2016.10.237.
- [240] A. Baykal, S. Yokuş, S. Güner, H. Güngüneş, H. Sözeri, and M. Amir, "Magneto-optical properties and Mössbauer Investigation of Ba<sub>x</sub>Sr<sub>y</sub>Pb<sub>z</sub>Fe<sub>12</sub>O<sub>19</sub> Hexaferrites," *Ceram Int*, vol. 43, no. 4, pp. 3475–3482, 2017, doi: 10.1016/j.ceramint.2016.10.013.
- [241] V. Dixit, D. Thapa, B. Lamichhane, C. N. Nandadasa, Y. K. Hong, and S. G. Kim, "Site preference and magnetic properties of Zn-Sn-substituted strontium hexaferrite," *J Appl Phys*, vol. 125, no. 17, pp. 6–13, 2019, doi: 10.1063/1.5084762.
- [242] A. Awadallah, S. H. Mahmood, Y. Maswadeh, I. Bsoul, and A. Aloqaily, "Structural and magnetic properties of vanadium doped M-type barium hexaferrite (BaFe<sub>12</sub>-

- xVxO19),” *IOP Conf Ser Mater Sci Eng*, vol. 92, no. 1, 2015, doi: 10.1088/1757-899X/92/1/012006.
- [243] J. H. De Araújo, J. M. Soares, M. F. Ginani, F. L. A. Machado, and J. B. M. Cunha, “Journal of Magnetism and Magnetic Materials Mössbauer and magnetic study of nanocrystalline strontium hexaferrite prepared by an ionic coordination reaction technique,” *J Magn Magn Mater*, vol. 343, no. 3, pp. 203–207, 2013, doi: 10.1016/j.jmmm.2013.04.077.
- [244] I. A. Auwal *et al.*, “Mössbauer Analysis and Cation Distribution of Zn Substituted BaFe<sub>12</sub>O<sub>19</sub> Hexaferrites,” *J Supercond Nov Magn*, vol. 31, no. 1, pp. 151–156, 2018, doi: 10.1007/s10948-017-4170-x.
- [245] M. Awawdeh, I. Bsoul, and S. H. Mahmood, “Magnetic properties and Mossbauer spectroscopy on Ga, Al, and Cr substituted hexaferrites,” *J Alloys Compd*, vol. 585, pp. 465–473, 2014, doi: 10.1016/j.jallcom.2013.09.174.
- [246] S. C. Bhandari, D. Guragain, J. Mohapatra, S. Yoon, J. P. Liu, and S. R. Mishra, “Magnetic and Mössbauer Effect Study of Ca-Sc Co-doped M-Type Strontium Hexaferrite,” 2021.
- [247] G. Qi *et al.*, “Lightweight Fe<sub>3</sub>C@Fe/C nanocomposites derived from wasted cornstalks with high-efficiency microwave absorption and ultrathin thickness,” *Adv Compos Hybrid Mater*, vol. 4, no. 4, pp. 1226–1238, Dec. 2021, doi: 10.1007/s42114-021-00368-0.
- [248] M. Thakur, C. Singh, S. K. Godara, B. A. Want, and A. K. Srivastava, “Fabrication of Bi-component Co–Cr doped M-type Sr-hexagonal ferrites: their structural, hysteresis, and susceptibility performance metrics,” *Journal of Materials Science: Materials in Electronics*, vol. 33, no. 28, pp. 22421–22434, Oct. 2022, doi: 10.1007/s10854-022-09019-6.
- [249] T. M. Meaz and C. B. Koch, “An investigation of trivalent substituted M-type hexagonal ferrite using X-ray and Mössbauer spectroscopy,” *Hyperfine Interact*, vol. 166, no. 1–4, pp. 455–463, Nov. 2005, doi: 10.1007/s10751-006-9308-3.
- [250] M. Thakur, C. Singh, V. Solanki, R. B. Jotania, H. Mahajan, and A. K. Srivastava, “Investigation of electrical, dielectric, and relaxation phenomenon of Co–Cr substituted SrM hexaferrite: Validation of measured and simulated parameters,” *Physica B Condens Matter*, p. 415515, Jan. 2023, doi: 10.1016/j.physb.2023.415515.
- [251] V. N. Dhage, M. L. Mane, S. B. Rathod, S. M. Rathod, and K. M. Jadhav, “Electric, dielectric and AC electrical conductivity study of Al<sup>3+</sup>-substituted barium hexaferrite nanoparticles synthesized by Sol-gel auto-combustion technique,” in *Materials Today: Proceedings*, Elsevier Ltd, 2021, pp. 1982–1987. doi: 10.1016/j.matpr.2021.04.119.
- [252] A. R. Kagdi *et al.*, “Influence of Mg substitution on structural, magnetic and dielectric properties of X-type barium–zinc hexaferrites Ba<sub>2</sub>Zn<sub>2-x</sub>Mg<sub>x</sub>Fe<sub>28</sub>O<sub>46</sub>,” *J Alloys Compd*, vol. 741, pp. 377–391, Apr. 2018, doi: 10.1016/j.jallcom.2018.01.092.
- [253] T. Gupta *et al.*, “Investigation on structural, hysteresis, Mössbauer properties and electrical parameters of lightly Erbium substituted X-type Ba<sub>2</sub>Co<sub>2</sub>Er<sub>x</sub>Fe<sub>28-x</sub>O<sub>46</sub>

- hexaferrites,” *Ceram Int*, vol. 46, no. 6, pp. 8209–8226, Apr. 2020, doi: 10.1016/j.ceramint.2019.12.049.
- [254] Y. Marouani *et al.*, “Electrical conductivity and dielectric properties of Sr doped M-type barium hexaferrite BaFe<sub>12</sub>O<sub>19</sub>,” *RSC Adv*, vol. 11, no. 3, pp. 1531–1542, Jan. 2021, doi: 10.1039/d0ra09465j.
- [255] M. Nasri *et al.*, “Structural, dielectric, electrical and modulus spectroscopic characteristics of CoFeCuO<sub>4</sub> spinel ferrite nanoparticles,” *Mater Sci Eng B Solid State Mater Adv Technol*, vol. 272, Oct. 2021, doi: 10.1016/j.mseb.2021.115331.
- [256] T. V. Sagar, T. S. Rao, and K. C. B. Naidu, “AC-electrical conductivity, magnetic susceptibility, dielectric modulus and impedance studies of sol-gel processed nano-NiMgZn ferrites,” *Mater Chem Phys*, vol. 258, Jan. 2021, doi: 10.1016/j.matchemphys.2020.123902.
- [257] H. Malik, M. A. Khan, A. Hussain, M. F. Warsi, A. Mahmood, and S. M. Ramay, “Structural, spectral, thermal and dielectric properties of Nd-Ni co-doped Sr-Ba-Cu hexagonal ferrites synthesized via sol-gel auto-combustion route,” *Ceram Int*, vol. 44, no. 1, pp. 605–612, Jan. 2018, doi: 10.1016/j.ceramint.2017.09.219.
- [258] S. K. Durrani, S. Naz, M. Mehmood, M. Nadeem, and M. Siddique, “Structural, impedance and Mössbauer studies of magnesium ferrite synthesized via sol-gel auto-combustion process,” *Journal of Saudi Chemical Society*, vol. 21, no. 8, pp. 899–910, Dec. 2017, doi: 10.1016/j.jscs.2015.12.006.
- [259] F. S. H. Abu-Samaha and M. I. M. Ismail, “AC conductivity of nanoparticles Co<sub>x</sub>Fe(1-x)Fe<sub>2</sub>O<sub>4</sub> (x=0, 0.25 and 1) ferrites,” *Mater Sci Semicond Process*, vol. 19, no. 1, pp. 50–56, Mar. 2014, doi: 10.1016/j.mssp.2013.11.027.
- [260] K. R. Hiremath, L. Zschiedrich, and F. Schmidt, “Numerical solution of nonlocal hydrodynamic Drude model for arbitrary shaped nano-plasmonic structures using Nédélec finite elements,” *J Comput Phys*, vol. 231, no. 17, pp. 5890–5896, Jul. 2012, doi: 10.1016/j.jcp.2012.05.013.
- [261] G. Hussain *et al.*, “Study of the role of dysprosium substitution in tuning structural, optical, electrical, dielectric, ferroelectric, and magnetic properties of bismuth ferrite multiferroic,” *J Alloys Compd*, vol. 919, Oct. 2022, doi: 10.1016/j.jallcom.2022.165743.
- [262] G. R. Gajula, L. R. Buddiga, C. K. Chidambara, A. K. Ch., and M. Dasari, “Dielectric, magnetic and magnetoelectric studies of lithium ferrite synthesized by solid state technique for wave propagation applications,” *Journal of Science: Advanced Materials and Devices*, vol. 3, no. 2, pp. 230–235, Jun. 2018, doi: 10.1016/j.jsamd.2018.04.007.
- [263] B. K. Jones, J. Santanat, and M. Mcpherson, “NEGATIVE CAPACITANCE EFFECTS IN SEMICONDUCTOR DIODES,” 1998.
- [264] A. Mallikarjuna *et al.*, “Structural transformation and high negative dielectric constant behavior in (1-x) (Al<sub>0.2</sub>La<sub>0.8</sub>TiO<sub>3</sub>) + (x) (BiFeO<sub>3</sub>) (x = 0.2–0.8) nanocomposites,” *Physica E Low Dimens Syst Nanostruct*, vol. 122, Aug. 2020, doi: 10.1016/j.physe.2020.114204.

- [265] E. Axelrod, A. Puzenko, Y. Haruvy, R. Reisfeld, and Y. Feldman, “Negative dielectric loss phenomenon in porous sol-gel glasses,” *J Non Cryst Solids*, vol. 352, no. 40-41 SPEC. ISS., pp. 4166–4173, Nov. 2006, doi: 10.1016/j.jnoncrysol.2006.07.008.
- [266] J. A. Bartkowska and D. Bochenek, “Microstructure and dielectric properties of BF–PFN ceramics with negative dielectric loss,” *Journal of Materials Science: Materials in Electronics*, vol. 29, no. 20, pp. 17262–17268, Oct. 2018, doi: 10.1007/s10854-018-9820-7.
- [267] M. Thakur *et al.*, “Exploration of structural, Mössbauer, and hysteresis performance metrics of SrCoxZnxFe12–2xO19 hexaferrite for recording applications,” *Appl Nanosci*, Nov. 2023, doi: 10.1007/s13204-023-02975-3.
- [268] S. E. Mousavi Ghahfarokhi, F. Ranjbar, and M. Zargar Shoushtari, “A study of the properties of SrFe12-xCoxO 19 nanoparticles,” *J Magn Magn Mater*, vol. 349, pp. 80–87, 2014, doi: 10.1016/j.jmmm.2013.08.036.
- [269] D. Lisjak *et al.*, “Magnetic phase formation in CoTi-substituted Ba hexaferrite coatings prepared with atmospheric plasma spraying,” *Journal of the American Ceramic Society*, vol. 93, no. 9, pp. 2579–2584, Sep. 2010, doi: 10.1111/j.1551-2916.2010.03770.x.
- [270] V. C. Chavan, S. E. Shirsath, M. L. Mane, R. H. Kadam, and S. S. More, “Transformation of hexagonal to mixed spinel crystal structure and magnetic properties of Co<sup>2+</sup> substituted BaFe12O19,” *J Magn Magn Mater*, vol. 398, no. May 2016, pp. 32–37, 2016, doi: 10.1016/j.jmmm.2015.09.002.
- [271] G. Sriramulu, N. Maramu, K. Praveena, and S. Katlakunta, “Effect of Cr<sup>3+</sup>–Al<sup>3+</sup> co-substitution on structural, magnetic and microwave absorption properties of Sr-hexaferrites,” *Journal of Materials Science: Materials in Electronics*, vol. 33, no. 35, pp. 26113–26123, Dec. 2022, doi: 10.1007/s10854-022-09298-z.
- [272] I. Mohammed, J. Mohammed, A. Sharma, H. Mahajan, A. Kaur, and A. K. Srivastava, “Influence of Mn<sup>2+</sup>-substitution on the structural, morphological and magnetic properties of Co<sub>2</sub>Y strontium hexaferrites,” *Mater Today Proc.*, vol. 61, pp. 1158–1162, Jan. 2022, doi: 10.1016/j.matpr.2021.12.514.
- [273] J. Xu, H. Zou, H. Li, G. Li, S. Gan, and G. Hong, “Influence of Nd<sup>3+</sup> substitution on the microstructure and electromagnetic properties of barium W-type hexaferrite,” *J Alloys Compd.*, vol. 490, no. 1–2, pp. 552–556, Feb. 2010, doi: 10.1016/j.jallcom.2009.10.079.
- [274] T. Zhang *et al.*, “Platelet-like hexagonal SrFe12O19 particles: Hydrothermal synthesis and their orientation in a magnetic field,” *J Magn Magn Mater*, vol. 412, pp. 102–106, Aug. 2016, doi: 10.1016/j.jmmm.2016.03.080.
- [275] S. M. Ramay, S. A. Siddiqi, S. Atiq, M. S. Awan, and S. Riaza, “Structural, magnetic, and electrical properties of Al<sup>3+</sup> substituted CuZn-ferrites,” *Chinese Journal of Chemical Physics*, vol. 23, no. 5, pp. 591–595, 2010, doi: 10.1088/1674-0068/23/05/591-595.



- [276] I. A. Auwal, H. Erdemi, H. Sözeri, H. Güngüneş, and A. Baykal, “Magnetic and dielectric properties of Bi<sup>3+</sup> substituted SrFe<sub>12</sub>O<sub>19</sub> hexaferrite,” *J Magn Magn Mater*, vol. 412, pp. 69–82, 2016, doi: 10.1016/j.jmmm.2016.03.066.
- [277] S. S. Jadhav, S. E. Shirsath, S. M. Patange, and K. M. Jadhav, “Effect of Zn substitution on magnetic properties of nanocrystalline cobalt ferrite,” *J Appl Phys*, vol. 108, no. 9, 2010, doi: 10.1063/1.3499346.
- [278] R. G. M. Oliveira *et al.*, “Dielectrical and structural studies of composite matrix BiVO<sub>4</sub>–CaTiO<sub>3</sub> and temperature effects by impedance spectroscopy,” *Journal of Materials Science: Materials in Electronics*, vol. 29, no. 19, pp. 16248–16258, 2018, doi: 10.1007/s10854-018-9714-8.
- [279] L. A. Ramajo, A. A. Cristóbal, P. M. Botta, J. M. Porto López, M. M. Reboredo, and M. S. Castro, “Dielectric and magnetic response of Fe<sub>3</sub>O<sub>4</sub>/epoxy composites,” *Compos Part A Appl Sci Manuf*, vol. 40, no. 4, pp. 388–393, Apr. 2009, doi: 10.1016/j.compositesa.2008.12.017.
- [280] H. Malik, M. A. Khan, A. Hussain, M. F. Warsi, A. Mahmood, and S. M. Ramay, “Structural, spectral, thermal and dielectric properties of Nd-Ni co-doped Sr-Ba-Cu hexagonal ferrites synthesized via sol-gel auto-combustion route,” *Ceram Int*, vol. 44, no. 1, pp. 605–612, Jan. 2018, doi: 10.1016/j.ceramint.2017.09.219.
- [281] S. K. Durrani, S. Naz, M. Mehmood, M. Nadeem, and M. Siddique, “Structural, impedance and Mössbauer studies of magnesium ferrite synthesized via sol–gel auto-combustion process,” *Journal of Saudi Chemical Society*, vol. 21, no. 8, pp. 899–910, Dec. 2017, doi: 10.1016/j.jscs.2015.12.006.
- [282] W. Chen, W. Zhu, O. K. Tan, and X. F. Chen, “Frequency and temperature dependent impedance spectroscopy of cobalt ferrite composite thick films,” *J Appl Phys*, vol. 108, no. 3, Aug. 2010, doi: 10.1063/1.3457217.
- [283] R. Nongjai, S. Khan, K. Asokan, H. Ahmed, and I. Khan, “Magnetic and electrical properties of in doped cobalt ferrite nanoparticles,” *J Appl Phys*, vol. 112, no. 8, Oct. 2012, doi: 10.1063/1.4759436.
- [284] A. Verma and R. Chatterjee, “Effect of zinc concentration on the structural, electrical and magnetic properties of mixed Mn-Zn and Ni-Zn ferrites synthesized by the citrate precursor technique,” *J Magn Magn Mater*, vol. 306, no. 2, pp. 313–320, 2006, doi: 10.1016/j.jmmm.2006.03.033.
- [285] J. H. You and S. I. Yoo, “Magnetic properties of Zn-substituted Y-type hexaferrites, Ba<sub>2</sub>Zn<sub>x</sub>Fe<sub>2–x</sub>Fe<sub>12</sub>O<sub>22</sub>,” *J Magn Magn Mater*, vol. 471, no. September 2018, pp. 255–261, 2019, doi: 10.1016/j.jmmm.2018.09.064.
- [286] V. Dixit, D. Thapa, B. Lamichhane, C. N. Nandadasa, Y. K. Hong, and S. G. Kim, “Site preference and magnetic properties of Zn-Sn-substituted strontium hexaferrite,” *J Appl Phys*, vol. 125, no. 17, May 2019, doi: 10.1063/1.5084762.
- [287] S. H. Mahmood *et al.*, “Magnetic Properties and Hyperfine Interactions in M-Type BaFe<sub>12–2x</sub>MoxZnxO<sub>19</sub> Hexaferrites Magnetic Properties and Hyperfine Interactions

- in M-Type BaFe<sub>12-2x</sub>Mo<sub>x</sub>Zn<sub>x</sub>O<sub>19</sub> Hexaferrites,” no. April, 2014, doi: 10.4236/jamp.2014.25011.
- [288] T. Ben Ghzaïel, W. Dhaoui, A. Pasko, and F. Mazaleyrat, “Effect of non-magnetic and magnetic trivalent ion substitutions on BaM-ferrite properties synthesized by hydrothermal method,” *J Alloys Compd*, vol. 671, pp. 245–253, 2016, doi: 10.1016/j.jallcom.2016.02.071.
- [289] G. D. Soria *et al.*, “Strontium hexaferrite platelets: a comprehensive soft X-ray absorption and Mössbauer spectroscopy study,” *Sci Rep*, vol. 9, no. 1, Dec. 2019, doi: 10.1038/s41598-019-48010-w.
- [290] J. H. De Araújo, J. M. Soares, M. F. Ginani, F. L. A. Machado, and J. B. M. Da Cunha, “Mössbauer and magnetic study of nanocrystalline strontium hexaferrite prepared by an ionic coordination reaction technique,” *J Magn Magn Mater*, vol. 343, pp. 203–207, 2013, doi: 10.1016/j.jmmm.2013.04.077.
- [291] J. Du, L. Lian, Y. Liu, and Y. Du, “Effect of Zn substitution on the structure and magnetic properties of Sr<sub>0.1</sub>La<sub>0.45</sub>Ca<sub>0.45</sub>Fe<sub>11.7-x</sub>Zn<sub>x</sub>Co<sub>0.3</sub>O<sub>19</sub> hexagonal ferrites,” *Journal of Materials Science: Materials in Electronics*, vol. 30, no. 21, pp. 19618–19624, Nov. 2019, doi: 10.1007/s10854-019-02335-4.
- [292] G. Sriramulu, N. Maramu, K. Praveena, and S. Katlakunta, “Effect of Cr<sup>3+</sup>–Al<sup>3+</sup> co-substitution on structural, magnetic and microwave absorption properties of Sr-hexaferrites,” *Journal of Materials Science: Materials in Electronics*, vol. 33, no. 35, pp. 26113–26123, Dec. 2022, doi: 10.1007/s10854-022-09298-z.
- [293] J. Mohammed *et al.*, “Effect of heat-treatment on the magnetic and optical properties of Sr<sub>0.7</sub>Al<sub>0.3</sub>Fe<sub>11.4</sub>Mn<sub>0.6</sub>O<sub>19</sub>,” *Mater Res Express*, vol. 5, no. 8, pp. 3–12, 2018, doi: 10.1088/2053-1591/aad1e5.
- [294] I. Mohammed, J. Mohammed, A. Sharma, H. Mahajan, A. Kaur, and A. K. Srivastava, “Influence of Mn<sup>2+</sup>-substitution on the structural, morphological and magnetic properties of Co<sub>2</sub>Y strontium hexaferrites,” *Mater Today Proc*, vol. 61, pp. 1158–1162, Jan. 2022, doi: 10.1016/j.matpr.2021.12.514.
- [295] P. Kuruva, P. Reddy Matli, B. Mohammad, S. Reddigari, and S. Katlakunta, “Effect of Ni-Zr codoping on dielectric and magnetic properties of SrFe<sub>12</sub>O<sub>19</sub> via sol-gel route,” *J Magn Magn Mater*, vol. 382, pp. 172–178, 2015, doi: 10.1016/j.jmmm.2015.01.050.
- [296] A. B. Kulkarni and S. N. Mathad, “Variation in structural and mechanical properties of Cd-doped Co-Zn ferrites,” *Mater Sci Energy Technol*, vol. 2, no. 3, pp. 455–462, Dec. 2019, doi: 10.1016/j.mset.2019.03.003.
- [297] M. N. Ashiq, M. J. Iqbal, and I. H. Gul, “Structural, magnetic and dielectric properties of Zr-Cd substituted strontium hexaferrite (SrFe<sub>12</sub>O<sub>19</sub>) nanoparticles,” *J Alloys Compd*, vol. 487, no. 1–2, pp. 341–345, Nov. 2009, doi: 10.1016/j.jallcom.2009.07.140.
- [298] R. Jasrotia, V. Pratap Singh, R. Kumar, K. Singha, M. Chandel, and M. Singh, “Analysis of Cd<sup>2+</sup> and In<sup>3+</sup> ions doping on microstructure, optical, magnetic and Mössbauer spectral properties of sol-gel synthesized BaM hexagonal ferrite based

- nanomaterials,” *Results Phys*, vol. 12, pp. 1933–1941, Mar. 2019, doi: 10.1016/j.rinp.2019.01.088.
- [299] G. L. Jadhav, P. P. Khirade, A. R. Chavan, C. M. Kale, and K. M. Jadhav, “Structural, Optical and Magnetic Properties of Diamagnetic Cd<sup>2+</sup> Incorporated Cobalt Ferrite Thin Films Deposited by Spray Pyrolysis,” *J Electron Mater*, vol. 50, no. 11, pp. 6525–6534, Nov. 2021, doi: 10.1007/s11664-021-09199-7.
- [300] R. Liu *et al.*, “Magnetocrystalline anisotropy study of Co-substituted M-type strontium hexaferrite single crystals,” *Ceram Int*, vol. 49, no. 2, pp. 1888–1895, Jan. 2023, doi: 10.1016/j.ceramint.2022.09.153.
- [301] J. Mohammed *et al.*, “Magnetic, Mössbauer and Raman spectroscopy of nanocrystalline Dy<sup>3+</sup>-Cr<sup>3+</sup> substituted barium hexagonal ferrites,” *Physica B Condens Matter*, vol. 585, May 2020, doi: 10.1016/j.physb.2020.412115.
- [302] L. M. Silva, R. B. da Silva, R. L. Silva, M. A. Morales, and J. H. de Araújo, “Improvement of (BH)<sub>max</sub> in Ba-hexaferrite doped with La and Co,” *Ceram Int*, vol. 48, no. 16, pp. 23224–23231, Aug. 2022, doi: 10.1016/j.ceramint.2022.04.306.
- [303] I. A. Auwal, H. Güngüneş, A. Baykal, S. Güner, S. E. Shirsath, and M. Sertkol, “Structural, morphological, optical, cation distribution and Mössbauer analysis of Bi<sup>3+</sup> substituted strontium hexaferrite,” *Ceram Int*, vol. 42, no. 7, pp. 8627–8635, 2016, doi: 10.1016/j.ceramint.2016.02.094.
- [304] M. Thakur, C. Singh, R. B. Jotania, A. K. Srivastava, and I. A. Abdel-Latif, “Investigation of electrical, dielectric, and relaxation metrics of SrFe<sub>12</sub>O<sub>19</sub>/Fe<sub>3</sub>O<sub>4</sub> hexaferrite composites,” *Appl Phys A Mater Sci Process*, vol. 130, no. 1, Jan. 2024, doi: 10.1007/s00339-023-07185-w.
- [305] P. Kaur, S. B. Narang, and S. Bahel, “Investigation of Electromagnetic Properties of La-Doped Strontium Ferrite in X and Ku Bands,” *J Supercond Nov Magn*, vol. 30, no. 8, pp. 2239–2245, Aug. 2017, doi: 10.1007/s10948-017-4024-6.
- [306] A. L. Guerrero-Serrano, M. Mirabal-García, and S. A. Palomares-Sánchez, “Synthesis and study of the lanthanum substitution in the lead M-type hexaferrite,” *J Supercond Nov Magn*, vol. 27, no. 7, pp. 1709–1713, 2014, doi: 10.1007/s10948-014-2489-0.
- [307] M. J. Iqbal and S. Farooq, “Enhancement of electrical resistivity of Sr<sub>0.5</sub>Ba<sub>0.5</sub>Fe<sub>12</sub>O<sub>19</sub> nanomaterials by doping with lanthanum and nickel,” *Mater Chem Phys*, vol. 118, no. 2–3, pp. 308–313, Dec. 2009, doi: 10.1016/j.matchemphys.2009.07.056.
- [308] J. Ji *et al.*, “Structural and magnetic properties of SrFe<sub>12</sub>O<sub>19</sub>/CoFe<sub>2</sub>O<sub>4</sub> composites with exchange coupling interaction,” *J Magn Magn Mater*, vol. 564, Dec. 2022, doi: 10.1016/j.jmmm.2022.170073.
- [309] L. Wang *et al.*, “The exchange coupling interaction in CoFe<sub>2</sub>O<sub>4</sub>/Fe<sub>3</sub>O<sub>4</sub> hard and soft magnetic nanocomposites,” *Vacuum*, vol. 181, Nov. 2020, doi: 10.1016/j.vacuum.2020.109751.

- [310] B. H. Bhat and B. Want, “Magnetic, dielectric and complex impedance properties of lanthanum and magnesium substituted strontium hexaferrite,” *Journal of Materials Science: Materials in Electronics*, vol. 27, no. 12, pp. 12582–12590, Dec. 2016, doi: 10.1007/s10854-016-5389-1.
- [311] I. A. Auwal *et al.*, “Electrical and Dielectric Properties of Y<sup>3+</sup>-Substituted Barium Hexaferrites,” *J Supercond Nov Magn*, vol. 30, no. 7, pp. 1813–1826, 2017, doi: 10.1007/s10948-017-3978-8.
- [312] G. R. Gajula, L. R. Buddiga, K. N. Chidambara Kumar, and M. Dasari, “Study on electric modulus, complex modulus and conductivity properties of Nb/Sm, Gd doped barium titanate-lithium ferrite ceramic composites,” *Results Phys*, vol. 17, Jun. 2020, doi: 10.1016/j.rinp.2020.103076.
- [313] M. Thakur, C. Singh, and A. K. Srivastava, “Tunable structural, morphological, and hysteresis characteristics of SrFe<sub>12</sub>O<sub>19</sub>/Fe<sub>3</sub>O<sub>4</sub> composites,” *Journal of Materials Science: Materials in Electronics*, vol. 35, no. 9, Mar. 2024, doi: 10.1007/s10854-024-12395-w.
- [314] F. Mohseni, R. C. Pullar, J. M. Vieira, and J. S. Amaral, “Enhancement of maximum energy product in exchange-coupled BaFe<sub>12</sub>O<sub>19</sub>/Fe<sub>3</sub>O<sub>4</sub> core-shell-like nanocomposites,” *J Alloys Compd*, vol. 806, pp. 120–126, Oct. 2019, doi: 10.1016/j.jallcom.2019.07.162.
- [315] M. A. Almessiere *et al.*, “Electronic, magnetic, and microwave properties of hard/soft nanocomposites based on hexaferrite SrNi<sub>0.02</sub>Zr<sub>0.02</sub>Fe<sub>11.96</sub>O<sub>19</sub> with variable spinel phase MFe<sub>2</sub>O<sub>4</sub> (M = Mn, Co, Cu, and Zn),” *Ceram Int*, vol. 47, no. 24, pp. 35209–35223, Dec. 2021, doi: 10.1016/j.ceramint.2021.09.064.
- [316] X. Wen, J. Dai, W. Feng, C. Cheng, and D. Huang, “SrFe<sub>12</sub>O<sub>19</sub>@ZnFe<sub>2</sub>O<sub>4</sub> core-shell composite fiber with enhanced exchange coupling interaction,” *J Magn Magn Mater*, vol. 568, Feb. 2023, doi: 10.1016/j.jmmm.2022.170278.
- [317] M. A. Almessiere *et al.*, “Review on functional bi-component nanocomposites based on hard/soft ferrites: Structural, magnetic, electrical and microwave absorption properties,” *Nano-Structures and Nano-Objects*, vol. 26. Elsevier B.V., Apr. 01, 2021. doi: 10.1016/j.nanoso.2021.100728.
- [318] M. Thakur, C. Singh, R. B. Jotania, T. T. Tekou Carol, and A. K. Srivastava, “Disk flower-like structure of PANI Modulated electronic transport dynamics of SrCo<sub>x</sub>Zn<sub>x</sub>Fe<sub>12-2x</sub>O<sub>19</sub> ferrite,” *Current Applied Physics*, vol. 63, pp. 72–89, Jul. 2024, doi: 10.1016/j.cap.2024.04.005.
- [319] H. K. Choudhary, R. Kumar, S. P. Pawar, S. Bose, and B. Sahoo, “Effect of Microstructure and Magnetic Properties of Ba-Pb-Hexaferrite Particles on EMI Shielding Behavior of Ba-Pb-Hexaferrite-Polyaniline-Wax Nanocomposites,” *J Electron Mater*, vol. 49, no. 3, pp. 1618–1629, Mar. 2020, doi: 10.1007/s11664-019-07478-y.

- [320] M. Javid Iqbal, M. Nadeem, and M. M. Hassan, “Low temperature ac electrical study of  $\text{Pr}_{0.5-x}\text{La}_x\text{Ca}_{0.5}\text{MnO}_3$  ( $x=0.0-0.4$ ) ceramics by employing impedance spectroscopy,” *J Appl Phys*, vol. 114, no. 11, Sep. 2013, doi: 10.1063/1.4821957.
- [321] S. A. Mathews, A. C. Ehrlich, and N. A. Charipar, “Hysteresis branch crossing and the Stoner–Wohlfarth model,” *Sci Rep*, vol. 10, no. 1, Dec. 2020, doi: 10.1038/s41598-020-72233-x.
- [322] S. K. Chawla, S. S. Meena, P. Kaur, R. K. Mudsainiyan, and S. M. Yusuf, “Effect of site preferences on structural and magnetic switching properties of CO-Zr doped strontium hexaferrite  $\text{SrCo}_x\text{Zr}_x\text{Fe}_{(12-2x)}\text{O}_{19}$ ,” *J Magn Magn Mater*, vol. 378, pp. 84–91, 2015, doi: 10.1016/j.jmmm.2014.10.168.



## **RESEARCH PUBLICATIONS (During Ph.D)**

**Manisha Thakur**, Charanjeet Singh, Sachin Kumar Godara, Basharat Ahmad Want and A. K. Srivastava. 2022. “Fabrication of Bi-component Co–Cr doped M-type Sr-hexagonal ferrites: their structural, hysteresis, and susceptibility performance metrics” *J Mater Sci: Mater Electron*: [10.1007/s10854-022-09019-6](https://doi.org/10.1007/s10854-022-09019-6) (Impact Factor- 2.8).

**Manisha Thakur**, Charanjeet Singh, Kirill D. Martinson, Ivan V. Buryanenko, Valentin G. Semenov, Sanjay R. Mishra, Md Farhan Azim, A.K. Srivastava, and Vadim I. Popkov. 2023. “Significantly improved magnetic parameters of Co–La co-doped strontium hexagonal ferrites for recording applications: structural, hysteresis, and mössbauer performance metrics” *J Mater Sci: Mater Electron*: [10.1007/s10854-023-11328-3](https://doi.org/10.1007/s10854-023-11328-3) (Impact Factor- 2.8).

**Manisha Thakur**, Charanjeet Singh, Kirill D. Martinson, Ivan V. Buryanenko, Valentin G. Semenov, Sanjay R. Mishra, Md Farhan Azim, A.K. Srivastava, and Vadim I. Popkov. 2023. “Exploration of Structural, Mössbauer, and Hysteresis Performance Metrics of SrCo<sub>x</sub>Zn<sub>x</sub>Fe<sub>12-2x</sub>O<sub>19</sub> Hexaferrite for Recording Applications” *Applied Nanosciences*. [10.1007/s13204-023-02975-3](https://doi.org/10.1007/s13204-023-02975-3) (Impact factor-3.869).

**Manisha Thakur**, Charanjeet Singh, R.B. Jotania, and Ajeet Kumar Srivastava “Investigating the Electrical, Dielectric, and Relaxation Phenomenon of Co-Cr Substituted SrM Hexaferrite: Validation of Measured and Simulated Parameters” *Physica b*: <https://doi.org/10.1016/j.physb.2023.415515> (Impact factor: 2.98).

**Manisha Thakur**, Charanjeet Singh, Hamnesh Mahajan, Sachin Kumar Godara, Pradip K Maji, and A.K. Srivastava. 2023. “Study the effect of Co<sup>2+</sup> - Dy<sup>3+</sup> on structural and magnetic properties of M-type calcium hexaferrite” *AIP Conference Proceedings*. <https://doi.org/10.1063/5.0159077> (Impact Factor- 0.189).

**Manisha Thakur**, Charanjeet Singh, A.K. Srivastava *et al.* Investigation of Electrical, Dielectric, and Relaxation Metrics of SrFe<sub>12</sub>O<sub>19</sub>/Fe<sub>3</sub>O<sub>4</sub> Hexaferrite Composites. *Applied Physics a*: [10.1007/s00339-023-07185-w](https://doi.org/10.1007/s00339-023-07185-w) (Impact factor: 2.983)

Mahajan, Hamnesh, Shammi Kumar, Anjori Sharma, Ibrahim Mohammed, **Manisha Thakur**, Simrandeep Kour, Amarjeet Kaur, and Ajeet Kumar Srivastava. 2022. “Structural, Morphological, and Electrochemical Investigation of Mn<sub>0.3</sub>Co<sub>0.2</sub>Zn<sub>0.5</sub>Fe<sub>2</sub>O<sub>4</sub>-Polyaniline Nanocomposite for Supercapacitor Application.” *Journal of Materials Science: Materials in Electronics*. doi: [10.1007/s10854-022-09335-x](https://doi.org/10.1007/s10854-022-09335-x). (Impact Factor: 2.478).

Mahajan H, Kumar S, Sharma A, Mohammed I, **Manisha Thakur**, Kaur A, et al. Effect of sintering temperature on structural, morphological, magnetic, and electrochemical properties of Mn<sub>0.3</sub>Co<sub>0.2</sub>Zn<sub>0.5</sub>Fe<sub>2</sub>O<sub>4</sub> Ferrite. *J Sol-Gel Sci Technol*. 2022; <https://doi.org/10.1007/s10971-022-06022-5> (Impact Factor: 2.326).

Mohammed, Ibrahim, J. Mohammed, Anjori Sharma, Hamnesh Mahajan, **Manisha Thakur**, and Ajeet Kumar Srivastava. 2022. “Structural, Morphological, Optical, Magnetic, and Microwave Properties of La<sup>3+</sup>-Mn<sup>2+</sup> Substituted Zn<sup>2+</sup>-Y-Type Barium-Strontium Hexaferrite.” *Chinese Journal of Physics* 78(April):377–90. doi: [10.1016/j.cjph.2022.06.025](https://doi.org/10.1016/j.cjph.2022.06.025). (Impact factor: 5.0).

**Manisha Thakur**, Charanjeet Singh, A.K. Srivastava *et al.* Experimental and Theoretical Realization of Morphology and Frequency Tuned Charge Transport Dynamics in Co-Zn Doped SrM Hexaferrite: Electrical, Impedance and Relaxation Realm, *ECS Journal of solid-state science and technology*: [10.1149/2162-8777/ad2196](https://doi.org/10.1149/2162-8777/ad2196) (Impact factor: 2.0)

**Manisha Thakur**, Charanjeet Singh, A.K. Srivastava *et al.* Tunable Structural, Morphological, and Hysteresis Characteristics of SrFe<sub>12</sub>O<sub>19</sub>/Fe<sub>3</sub>O<sub>4</sub> Composites: *J Mater Sci: Mater Electron* [10.1007/s10854-024-12395-w](https://doi.org/10.1007/s10854-024-12395-w) (Impact factor: 2.8)

**Manisha Thakur**, Charanjeet Singh, A.K. Srivastava *et al.* Disk Flower-like Structure of PANI Modulated Electronic Transport Dynamics of SrCo<sub>x</sub>Zn<sub>x</sub>Fe<sub>12-2x</sub>O<sub>19</sub> Ferrite, *Current Applied Physics* [10.1016/j.cap.2024.04.005](https://doi.org/10.1016/j.cap.2024.04.005) (Impact factor: 2.4)

**Manisha Thakur**, Charanjeet Singh, A.K. Srivastava *et al.* **Manisha Thakur**, Charanjeet Singh, A.K. Srivastava *et al.* Frequency and Morphology Modulated Electrical, Dielectric,

and Relaxation Metrics in Sol-gel Synthesized  $\text{SrCo}_{1.5z}\text{La}_{0.5z}\text{Fe}_{12-2z}\text{O}_{19}$  Hexaferrite: Corroboration with Impedance Spectroscopy Software, *J Electronic Mater.* (Impact factor: 2.0)

**Manisha Thakur**, Charanjeet Singh, A.K. Srivastava *et al.* Optimization of Performance Parameters of Co-La substituted Strontium Hexaferrite Based Microwave Absorbers: Structural, Morphological, Reflection Loss, Input Impedance Characteristics, *Physica b* 10.1016/j.physb.2024.415735 (Impact factor: 2.8).

### **COMMUNICATED PAPERS**

Structural, Mössbauer, and Hysteresis Performance Metrics of Co-Cd Co-doped SrM Hexaferrite for Recording Applications, *Physica Scripta* (Impact factor: 3.081)

### **TO BE COMMUNICATED PAPERS**

Microwave absorption properties of  $\text{SrFe}_{12}\text{O}_{19}/\text{Fe}_3\text{O}_4$  Composites.

Microwave absorption properties of  $\text{SrFe}_{12}\text{O}_{19}/\text{CoFe}_2\text{O}_4$  Composites.

### **ORAL PRESENTATION**

- ✓ “Study the effect of  $\text{Co}^{2+}$ - $\text{Dy}^{3+}$  on structural and magnetic properties of M-type Calcium Hexaferrite”. National Conference on “Recent Advancement in Physical Sciences” organized by NIT Uttarakhand held on 19-20 December 2021.
- ✓ “Effect of Heat treatment on structural and optical properties of  $\text{CaCo}_{0.2}\text{Dy}_{0.4}\text{Fe}_{11.4}\text{O}_{19}$  hexaferrite”. International Conference on Materials for Emerging Technologies (ICMET-21) held on 18-19 February 2022.

## CURRICULUM VITAE

**Name:** Manisha Thakur  
**Date of Birth:** 20<sup>th</sup> October 1995  
**Sex:** Female  
**Nationality:** Indian  
**Marital Status:** Married  
**Telephone No:** 7018556321  
**Email:** [thakurmanisha2022@gmail.com](mailto:thakurmanisha2022@gmail.com)  
**Home Address:** House No. 458/34 Aman Nagar, Jalandhar-144001



### EDUCATIONAL QUALIFICATION

- M.Sc. Physics from G.N.D.U Amritsar in 2018 secured First class with 70%.
- B.Sc. Non-Medical from G.N.D.U Amritsar in 2016 secured First class with 73%.
- Higher Secondary education (Non-Medical), P.S.E.B in 2013 secured first class with 91%.

### CERTIFICATIONS

- Qualified Himachal Pradesh State Eligibility Test of Assistant Professor 2018
- Certified by IIT Kanpur for NPTEL coursework “PHYSICS OF SEMICONDUCTOR”
- The second position in the “DISTRICT LEVEL SCIENCE SEMINAR”

### AREA OF EXPERTISE

- Proficient in ORIGIN software, EIS software, Xpert High Score, ImageJ, VNA analysis, VSM, FESEM, EDX, etc.

### SKILL HIGHLIGHT

- Punctual
- Leadership quality
- Accepting challenges
- Team spirit
- Innovative

### LANGUAGES

- English
- Hindi
- Punjabi